Plastic Waste Upcycling via Carbon Dioxide Valorisation

Juliette DELCORPS

A dissertation submitted in partial fulfilment of the requirements for the degree of Doctor of Philosophy in Chemical Sciences

2022 – 2026

University of Mons

Under the Supervision of Pr. Olivier Coulembier

Jury :

Pr. Pascal Gerbaux (UMons), Chair
Pr. Carmela APRILE (UNamur), Secretary
Dr. Christophe DETREMBLEUR (ULiège)
Pr. Philippe DUBOIS (UMons)
Pr. Daniel TATON (Université de Bordeaux)

SUMMARY

The continuous rise in anthropogenic carbon dioxide (CO_2) emissions and the persistent accumulation of plastic waste rank among the most pressing environmental challenges of the 21st century. Although traditionally addressed as independent issues, both problematics share a common origin in our heavy reliance on fossil resources and call for the development of more integrated valorisation strategies. Against this background, the present thesis explores a combined approach in which CO_2 is activated through organic carriers and covalently incorporated into post-modified polyolefin backbones.

The work is structured around three interconnected axes. The first concerns the preparation of CO_2-binding organic liquids (CO_2BOLs) and the study of their reactivity toward model electrophiles. Combining experimental observations with density functional theory (DFT) calculations, a unique metal-free, cation-assisted ion-pair mechanism is uncovered, enabling the selective synthesis of linear dialkyl carbonates from alkyl iodides. The second axis transposes this chemistry to two macromolecular substrates, namely pristine and iodinated poly(vinyl chloride) (PVC), through the use of alcohol (CO_2BALs) and amine (CO_2BAMs) analogues of these CO_2BOLs, thereby demonstrating the feasibility of covalently incorporating CO_2 along a polymer backbone under mild conditions while limiting competing elimination pathways.

The third axis addresses the selective functionalisation of the chemically inert C-H bonds of polyolefins. A solvent-free iodination protocol implemented by twin-screw extrusion at 106 °C, using iodoform and sodium hydroxide, enables the incorporation of substantial iodine contents into polyethylene (PE) and isotactic polypropylene (*i*PP) without detectable chain cleavage. By finely tuning the balance between iodination and elimination, the same mechanochemical process affords the stereoselective formation of conjugated polyene sequences in the *cis* configuration - typically accessed only through cryogenic routes - and opens the way to further post-functionalisation reactions such as reactive-extrusion epoxidation.

Taken together, these investigations establish a coherent framework combining CO_2 activation through organic carriers and the functionalisation of commodity polyolefins and pave the way for integrated upcycling strategies at the interface between CO_2 valorisation and plastic recycling.

REMERCIEMENTS

Ces quatre années de thèse ont été d'une richesse incroyable, tant par les rencontres faites que par les expériences vécues. Ces quelques lignes sont l'occasion d'exprimer ma gratitude à toutes les personnes qui ont jalonné ce parcours et contribué, de près ou de loin, à le rendre aussi précieux.

Tout d'abord, mes remerciements les plus sincères vont à mon promoteur, Olivier, pour son implication constante, sa pédagogie, sa disponibilité et les nombreuses opportunités qu'il m'a offertes tout au long de ces années. Merci surtout d'avoir cru en moi du début à la fin, particulièrement dans les moments où je n'y croyais pas moi-même. Sans ta confiance, ce travail n'aurait jamais vu le jour.

Un immense merci à Emna, dont la contribution à cette thèse est incommensurable. Merci pour le travail gargantuesque que tu as fourni, sans lequel ce manuscrit ne serait pas ce qu'il est. Merci aussi et surtout pour ta bonne humeur, ta positivité et ta capacité à me comprendre et à me rassurer dans les moments difficiles.

Je souhaite également remercier l'AXA Research Fund, dont le soutien financier a rendu cette thèse possible.

Je tiens à remercier les membres du jury d'avoir accepté d'évaluer ce travail de thèse. Merci au Professeur Pascal Gerbaux d'en avoir assuré la présidence, ainsi qu'à la Professeure Carmela Aprile, au Docteur Christophe Detrembleur, au Professeur Philippe Dubois et au Professeur Daniel Taton pour le temps et l'attention qu'ils ont bien voulu consacrer à la lecture et à la discussion de ce manuscrit.

Ce travail doit beaucoup à de nombreuses collaborations. Pour leurs contributions au deuxième chapitre, je remercie Kuber Singh Rawat et la Professeure Véronique Van Speybroeck de l'Université de Gand, Mathilde Wells et le Professeur Bertrand Blankert du Service d'Analyse Pharmaceutique de l'UMons, Bruno Grignard et Christophe Detrembleur de l'Université de Liège, ainsi que le Professeur Pascal Gerbaux du Service de Synthèse et Spectrométrie de Masse Organiques de l'UMons. Merci également à Yinghui Zhang et au Professeur Jean-François Gohy pour notre collaboration sur le chapitre figurant en annexe.

Je tiens à exprimer ma reconnaissance à l'équipe de la Professeure Christine Jérôme de l'Université de Liège pour leur accueil chaleureux et leur bienveillance lors de mon séjour parmi eux.

A very special thank you goes to Professor Tanja Junkers and her entire team at Monash University in Melbourne - Gayathri, Vianna, Lakshani, Bo, WeiNian, Igor, Amna, Krittin, Mengyuan, Lachie and Sanket - for their warm welcome, their guidance, their kindness, and the

wonderful moments we shared during my three-month stay with them. This experience will remain one of the most enriching of my journey. Ce séjour australien n'aurait pas été le même sans les belles rencontres faites en dehors du laboratoire. Un merci tout particulier à Anne-Cécile et Pascal, qui m'ont ouvert les portes de leur maison pendant ces trois mois et m'ont fait me sentir chez moi à l'autre bout du monde. J'espère pouvoir revenir vous rendre visite un jour.

À mes collègues du Service des Matériaux Polymères et Composites - Léa, Simon, Anthony, Sylvie, Elora, Noémie, Seb, et tous les autres - merci pour la bonne ambiance au quotidien, les discussions de couloir et l'entraide qui rendent le labo bien plus qu'un simple lieu de travail.

À mes amis, une mention toute particulière. Pierre, Baptiste, Pauline et Valentine, merci d'être toujours là, fidèlement, depuis notre première année à l'université. Clem, Titi et Clara, vous êtes devenus bien plus que des collègues. À chacun d'entre vous, merci. Votre présence a rendu ces années infiniment plus précieuses.

À ma famille enfin. Papa, Maman, Victor : merci pour votre soutien et vos encouragements indéfectibles, dans les bons moments mais surtout dans les moins bons. À Sébastien, mon compagnon, futur mari et meilleur ami depuis onze ans : il n'y a pas de mots à la hauteur. Merci pour tout. Vraiment tout.

Enfin, un clin d'œil à Emile et Syrah, mes fidèles compagnons à quatre pattes, ainsi qu'à tous les animaux croisés en Australie, en Tanzanie ou à Pairi Daiza. Vous m'avez offert, et continuerez de m'offrir, ce réconfort et ces sourires que les humains ne parviennent pas toujours à susciter.

TABLE OF CONTENTS

ABBREVIATION TABLE **1**

GENERAL INTRODUCTION **9**

General Background - Plastic Waste and Carbon Dioxide Management **13**

I. Introduction *16*

II. Plastic Waste Management *18*
A. Recycling Methods 19
B. Recycling and Upcycling of Thermoplastics 33
C. Alternative Valorisation Pathways 41
D. Intermediate Conclusion 45

III. Carbon Dioxide Management *46*
A. Atmospheric CO_2 Removal 47
B. Carbon Capture 52
C. CO_2-Binding Organic Liquids 69
D. Intermediate Conclusion 72

IV. Conclusion and Objectives of the Work *73*

V. References *76*

Turning Carbon Dioxide into Dialkyl Carbonates through Guanidinium-Assisted S_N2 Ion-Pair Process **93**

I. INTRODUCTION *96*

II. RESULTS AND DISCUSSION *99*
A. Preparation of TBD-based CO_2BOLs 99
B. Preparation of Linear Dialkyl Carbonates from TBD-based CO_2BOLs 107

III. CONCLUSION *116*

IV. EXPERIMENTAL *117*
A. Materials 117
B. Procedures 117
C. Methods 118

V. SUPPORTING INFORMATION *121*

VI. REFERENCES *127*

CO_2-Binding Alcohols as Potential Candidates for Poly(Vinyl Chloride) Upcycling **133**

I. INTRODUCTION *136*

II. RESULTS AND DISCUSSION *138*
A. Thermal properties of CO_2BALs: Melting points and degradation 140
B. Reaction between PVC and CO_2BALs in solution 143

III. CONCLUSION *148*

IV. EXPERIMENTAL *149*
A. Materials 149
B. Procedures 149

C. Methods 150

V. SUPPORTING INFORMATION *152*

VI. REFERENCES *160*

Boosting PVC Reactivity through Iodination for CO_2-Derived Functionalisation 163

I. INTRODUCTION *166*

II. RESULTS AND DISCUSSION *168*

A. PVC iodination 168

B. CO_2BAM selection and reaction with iodinated PVC 172

III. CONCLUSION *176*

IV. EXPERIMENTAL *177*

A. Materials 177

B. Procedures 177

C. Methods 178

V. SUPPORTING INFORMATION *180*

VI. REFERENCES *188*

Solvent-Free Iodination of Polyethylene via Twin-Screw Extrusion: A Scalable Approach 191

I. INTRODUCTION *194*

II. RESULTS AND DISCUSSION *197*

A. Direct Iodination using n-Hexadecane as a Small-Molecule Model 197

B. Direct Iodination of Polyethylene by Twin-Screw Reactive Extrusion 201

C. Extrapolation to TSE-based Polypropylene Iodination 207

III. CONCLUSION *209*

IV. EXPERIMENTAL *210*

A. Materials 210

B. Procedures 210

C. Methods 211

V. SUPPORTING INFORMATION *213*

VI. REFERENCES *219*

From Polyethylene to Conjugated Polyenes: A Mechanochemical One-Pot Upcycling Strategy for Selective Functionalisation 223

I. INTRODUCTION *226*

II. RESULTS AND DISCUSSION *228*

III. CONCLUSION *237*

IV. EXPERIMENTAL *238*

A. Materials 238

B. Procedures 238

C. Methods 239

V. SUPPORTING INFORMATION *242*

VI. REFERENCES *244*

Conclusion And Perspectives 247

Evaluation of CO_2-Binding Organic Liquids as Electrolytes 255

I. INTRODUCTION 258

II. RESULTS AND DISCUSSION 260

A. CO_2BOL screening 260
B. Temperature dependence and activation energy 265
C. Conductivity recovery and impedance evolution 267
D. ACN–based solutions: concentration dependence and LiTFSI compatibility 273

III. CONCLUSION 276

IV. EXPERIMENTAL 277

A. Materials 277
B. Procedures 277
C. Methods 279

V. SUPPORTING INFORMATION 281

VI. REFERENCES 289

ABBREVIATION TABLE

^{1}H / ^{13}C NMR	Proton / Carbon 13 nuclear magnetic resonance
3Rs	Reduce, Reuse, Recycle
ACN	Acetonitrile
AFOLU	Agriculture, Forestry and Other Land Uses
AIBN	Azobisisobutyronitrile
AMP	2-amino-2-methyl-1-propanol
AP	As prepared
ASTM	American Society for Testing and Materials
ATR	Attenuated total reflectance
B3LYP	Becke, 3-parameter, Lee-Yang-Parr
BECCS	Bioenergy with carbon capture and sequestration
$ButNH_2$	Butylamine
ButOH	Butanol
CAE	Constant analyser energy
c-AFM	Conductive atomic force microscopy
CAN	Covalent adaptable network
CCS	Carbon capture and sequestration/storage
CCU	Carbon capture and utilisation
$CDCl_3$	Deuterated chloroform
CDR	Carbon dioxide removal
C-F	Conant-Finkelstein
CHO	Cyclohexene oxide
CHP	Combined heat and power
CI	Chemical ionisation
CLC	Chemical looping combustion
CLOU	Chemical looping with oxygen uncoupling

CO	Carbon monoxide
CO_2	Carbon dioxide
CO_2BAL	CO_2-binding alcohol
CO_2BAM	CO_2-binding amine
CO_2BOL	CO_2-binding organic liquid
CO_2e	CO_2 equivalent
CO_2-EOR	CO_2-enhanced oil recovery
CO_2RR	CO_2 reduction reaction
COF	Covalent organic framework
C-PCM	Conductor-like polarisable continuum model
CPE	Chlorinated polyethylene
CP-MAS	Cross polarisation magic angle spinning
CRI	Carbon recycling international
DAC	Direct air capture
DACCS	Direct air capture and storage
DACCU	Direct air capture and utilisation
DBN	1,5-diazabicyclo[4.3.0]non-5-ene
DBU	1,8-diazabicyclo[5.4.0]undec-7-ene
DEC	Diethyl carbonate
DE-XRT	Dual-energy X-ray transmission
DFT	Density functional theory
DMC	Double metal cyanide
DMC	Dimethyl carbonate
DME	1,2-dimethoxyethane
DMF	*N,N*-Dimethylformamide
DMSO	Dimethyl sulfoxide
DSC	Differential scanning calorimetry
E2	Bimolecular elimination

EC	Ethylene carbonate
EGEE	Ethylene glycol ethyl ether
EGME	Ethylene glycol methyl ether
EIS	Electrochemical impedance spectroscopy
EOR	Enhance oil recovery
e-PE	Epoxidised PE
ESI-MS	Electrospray ionisation coupled to mass spectrometry
FCC	Fluid catalytic cracking
FT	Fischer-Tropsch
FT-IR	Fourrier Transform Infrared
GC-MS	Gass chromatography coupled to mass spectrometry
GHG	Greenhouse gas
GWP	Global Warming Potential
H_2	Hydrogen
HAT	Hydrogen atom transfer
HCl	Hydrochloric acid
HDPE	High density polyethylene
$HexNH_2$	Hexylamine
HexOH	Hexanol
HTL	Hydrothermal liquefaction
IEA	International Energy Agency
IGCC	Integrated gasification combined cycle
IL-CCS	Illinois Inudtrial Carbon Capture and Storage
IPCC	Intergovernmental Panel on Climate Change
I-PE	Iodinated PE
iPP	Isotactic polypropylene
I-PP	Iodinated PP
ISO	International Organization for Standardization

LDPE	Low density polyethylene
LED	Light emitting diode
LIBS	Laser-induced breakdown spectroscopy
LiTFSI	Lithium bis(trifluoromethanesulfonyl)imide
LLDPE	Linear low density polyethylene
LSV	Linear sweep voltametry
LULUCF	Land Use, Land Use Change, and Forestry
MA	Maleic anhydride
***m*CPBA**	Meta-chloroperoxybenzoic acid
MD	Molecular dynamics
MDEA	Methyldiethanolamine
MDT	Maximal degradation temperature
MEA	Monoehtanolamine
MEK	Methyl ethyl ketone
MFI	Melt flow index
M_n	Number-average molecular weight
M_n th	Theoretical M_n
M_n/M_w SEC	M_n or M_w determined by SEC
MOF	Metal-organic framework
MTT	tetrazolium dye 3-(4,5-dimethylthiazol-2-yl)-2,5-diphenyltetrazolium bromide
MVA	Monitoring, verification and accounting
M_w	Weight-average molecular weight
***n*-C16**	*n*-hexadecane
NCI	Non-covalent interaction
NECCS	Negative emissions carbon capture and storage
NHPI	*N*-hydroxyphthalimide
NIPU	Non-isocyanate polyurethane
OCV	Open-circuit voltage

PC	polycarbonate
PC	Propylene carbonate
PCHC	Poly(cyclohexene carbonate)
PE	Polyethylene
PE-g-MA	Polyethylene-grafted maleic anhydride
PET	Poly(ethylene terephthalate)
PHU	Poly(hydroxyurethane)
PINO	Phthalimido-*N*-oxyl
PMMA	Poly(methyl methacrylate)
PO	Propylene oxide
POSS	Polyhedral oligomeric silsesquioxane
PP	Polypropylene
PPC	Poly(propylene carbonate)
PP-g-MA	Polypropylene-grafted maleic anhydride
PS	Polystyrene
PSA	Pressure swing adsorption
PSAR	Polarity-swing-assisted recovery
PTC	Phase-transfer catalysis
PU	Polyurethane
PVC	Poly(vinyl chloride)
PVC-I	Iodinated PVC
PVDC	Polyvinylidene chloride
ROCOP	Ring-opening copolymerisation
RWGS	Reverse water gas shift
SAFT	Statistical Associating Fluid Theory
SDD(I)	Small delay defect (for the iodine atom)
SDG	Sustainable Development Goals
SEC	Size exclusion chromatography

SET	Single electron transfer
S_N	Nucleophilic substitution
S_N2	Bimolecular nucleophilic substitution
SPI	Society of the Plastics Industry
SS	Screw speed
SS	Stainless steel
Syngas	Synthesis gas
TBAB	Tetrabutylammonium bromide
TBD	1,5,7-triazabicyclo[4.4.0]dec-5-ene
TGA	Thermogravimetric analysis
THF	Tetrahydrofuran
TMG	1,1,3,3-tetramethylguanidine
TMS	Tetramethyl silane
$TMSN_3$	Azidotrimethylsilane
ToF	Time of flight
TRL	Technology readiness level
TS	Transition state
TSA	Temperature swing adsorption
TSE	Twin screw extrusion
TVSA	Temperature-vacuum swing adsorption
UNEP	United Nations Environment Programme
UPO	Unsaturated polyolefin
VMD	Visual molecular dynamics
VTF	Vogel-Tamman-Fulcher
WGS	Water gas shift
Wt%	Weight percent
WTE	Waste-to-energy
XPS	X-ray photoelectron spectroscopy

XRF	X-ray fluorescence
ZSM-5	Zeolite Socony Mobil-5

GENERAL INTRODUCTION

The rapid increase in anthropogenic carbon dioxide (CO_2) emissions and the accumulation of plastic waste represent two of the most pressing environmental challenges of the 21st century. The extensive use of fossil resources for energy and chemical production has led to a continuous rise in atmospheric CO_2 levels, contributing significantly to climate change and its associated impacts. At the same time, the widespread production and use of plastics - particularly polyolefins such as polyethylene and polypropylene - have generated vast quantities of persistent waste, the majority of which is not effectively recycled and instead accumulates in landfills or the natural environment. These materials are highly resistant to degradation, leading to long-term ecological consequences. Conventional approaches to addressing these issues typically consider them separately, focusing either on carbon capture and storage or on mechanical and chemical recycling of plastics. However, such strategies often suffer from economic or technical limitations. In this context, the development of innovative solutions that simultaneously address both CO_2 emissions and plastic waste is of growing interest. In particular, the transformation of CO_2 into value-added chemical building blocks, coupled with the functionalisation and upgrading of polymeric materials, offers a promising route toward more sustainable and circular processes. By integrating these approaches, it becomes possible to envision new pathways for waste valorisation that contribute to both resource efficiency and environmental protection.

This PhD work aims to address these two major waste streams through the development of an integrated recycling strategy. This approach relies on the functionalisation of polymers, in particular the halogenation of polyolefins, followed by their reaction with CO_2-derived compounds.

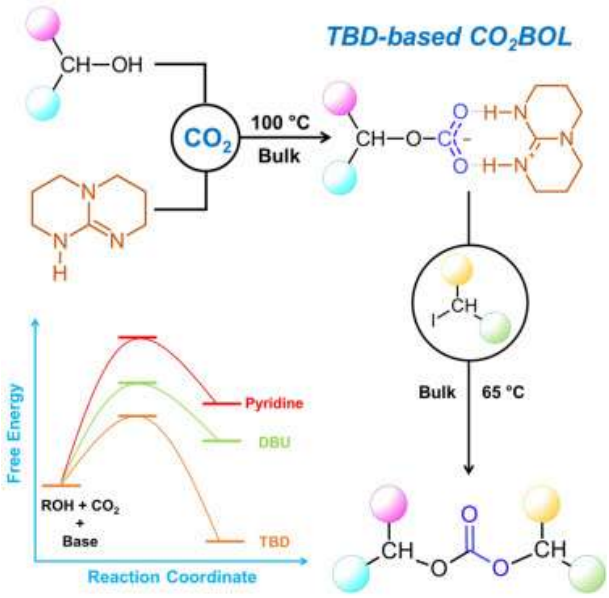
In this context, the objectives of this research are threefold. First, the synthesis of CO_2-derived compounds and their reactivity toward small model molecules will be investigated and optimised. In parallel, the halogenation of polyolefins will be developed and refined. Finally, these two research directions will be combined through the reaction between the resulting products, with the overall aim of enabling the upcycling of plastic waste via CO_2 valorisation. Each of these objectives is pursued with the aim of developing a strategy that is both as environmentally and economically viable as possible.

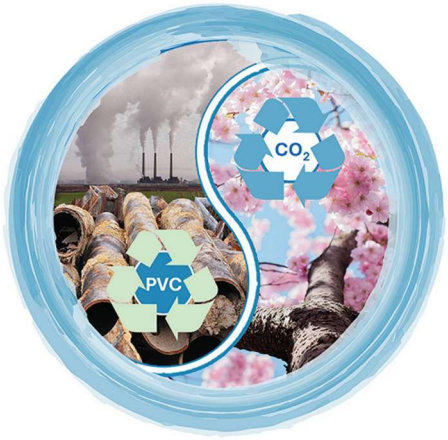
This manuscript is divided into six chapters, which are presented according to the aforementioned objectives and summarised below.

Chapter 1 is dedicated to the contextualisation and state-of-the-art regarding the problematics of plastic waste and carbon dioxide management. Strategies currently in use or under research are presented. A detailed description of mechanical and chemical recycling technologies is first provided in the plastic waste management section of this chapter. Particular

attention is then given to the recycling of the most common thermoplastic polymers, highlighting both established and emerging approaches specific to these widely used materials. Finally, alternative plastic waste recycling strategies including, post-synthetic functionalisation and plastic waste upcycling, are discussed. The second section of this chapter focuses on CO_2 management strategies. These include atmospheric CO_2 removal, carbon capture and storage (CCS), and carbon capture and utilisation (CCU), each covering a large array of technologies. Finally, this section and chapter are concluded by a state-of-the-art on CO_2-binding organic liquids (CO_2BOLs), a specific class of organic compounds notably used for the capture of CO_2 at the industrial scale. Building on this background, the first part of this PhD work focused on the valorisation of CO_2 through organic pathways, before moving toward the treatment of commodity plastics.

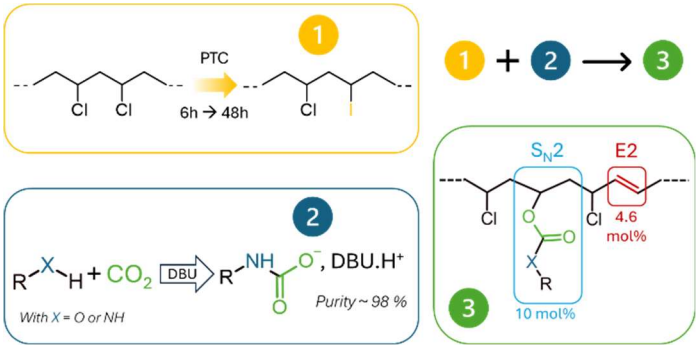
In **Chapter 2**, we describe the selective bimolecular nucleophilic substitution (S_N2) reaction between primary and secondary alkyl iodides with 1,5,7-triazabicyclo[4.4.0]dec-5-ene (TBD)-based CO_2BOLs. We show that TBD is a great candidate for bulk carbon dioxide and alcohol binding at 100 °C. TBD-based carbonate salts are selective for S_N2 processes, allowing them to work with highly reactive alkyl iodide while eliminating unwanted base quaternisation either in acetonitrile or in bulk at both 21 °C and 65 °C. The high reactivity of these TBD-based CO_2BOLs toward backside S_N2 processes at low temperature is explained by the presence of the TBD.H$^+$ guanidinium, revealing a unique metal-free cation-assisted S_N2 ion-pair process. The unique nature of this mechanism led us to investigate the reactivity of our TBD-based CO_2BOLs toward one of the most problematic polymers in terms of recycling to date, namely poly(vinyl chloride) (PVC).





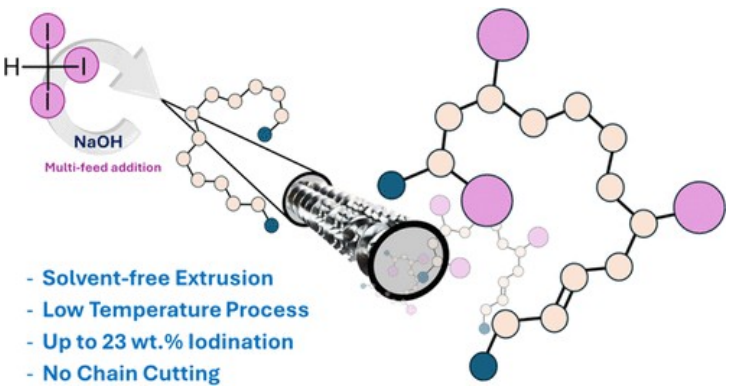
Chapter 3 explores the use of TBD-based CO_2-binding alcohols - hereafter referred to as CO_2BALs to distinguish them from their amine-based counterparts (CO_2BAMs, introduced in Chapter 4) - as nucleophiles for PVC functionalisation, aiming to enhance its upcycling potential. The impact of solvent polarity, CO_2BAL conversion, and reaction time on the substitution-to-elimination ratio was systematically investigated. Although the degree of substitution remained below 10 wt%, a

promising S_N2/E2 selectivity of 94/6 was achieved. The functionalised materials were characterised using ^{1}H NMR, FT-IR, SEC, and TGA, confirming the successful grafting of carbonate moieties and highlighting thermal stability trends. While CO_2BAL stabilisation in polar solvents may limit reactivity, alternative approaches were considered to improve substitution efficiency and are presented in the next chapter. This work provides new insights into CO_2-based strategies for PVC modification, bridging the gap between polymer upcycling and sustainable chemistry.



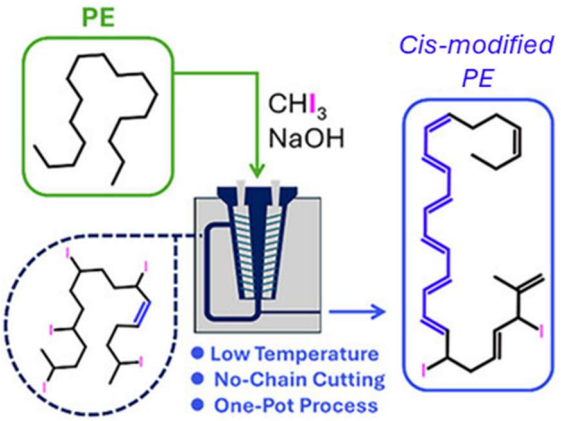
To recover the high reactivity of iodinated electrophiles evidenced in Chapter 2, we then decided to modify the nature of PVC itself through a partial iodination reaction, thereby enhancing its reactivity toward CO_2BOLs - in this case, CO_2BAMs. To this end, **Chapter 4** describes an aqueous phase-transfer catalysis strategy enabling the selective iodination of PVC under mild and sustainable conditions. The subsequent reaction with a 1,8-diazabicyclo[5.4.0]undec-7-une (DBU)-based CO_2BAM achieves efficient S_N2 substitution at CH-X centres, improving CO_2 incorporation fourfold relative to previous CO_2BAL strategies. The polymer remains fully soluble, demonstrating a greener, safer, and effective approach to PVC structural modification.

Building on the findings of these last two chapters, the iodination of polyolefins became the cornerstone of this work. In this context, **Chapter 5** presents a novel, solvent-free approach for the iodination of polyethylene (PE) using twin-screw extrusion under mild conditions. The iodination process, typically challenging due to the inertness of PE, was successfully carried out using iodoform (CHI_3) as the iodine source and NaOH as the initiator, all at a low reaction temperature of 106 °C. Initial optimisation using *n*-hexadecane as a model compound yielded efficient mono-iodination, which was then extended to PE, achieving iodine incorporation levels of up to 23 wt%. The process was further applied to isotactic polypropylene (*i*PP), reaching iodine contents of approximately 22 wt%. The resulting iodinated polymers were characterised using ^{1}H NMR, SEC, FT-IR, TGA, and XPS, confirming successful iodine incorporation and the absence of polyolefin chain cleavage. Thermal analysis revealed significant changes in crystallinity and melting temperatures, directly correlated with the iodine content, especially for PE. This scalable,



environmentally friendly method opens new avenues for polyolefin functionalisation, enhancing their potential in advanced materials, including biomedical imaging and diagnostics, where iodine's high atomic number improves radiopacity, as well as flame-retardant polymers and polymers with improved coating and adhesion properties.

Chapter 6 naturally emerged from exploiting the limitations of the iodination process developed in Chapter 5, namely the formation of unsaturations. This chapter thus presents a solvent-free, mechanochemical approach to introduce conjugated polyene sequences into polyethylene (PE) via a twin-screw extrusion process. The controlled iodination/elimination strategy enables the stereoselective formation of *cis* polyenes, a configuration typically achieved under cryogenic conditions but here accessible at higher temperatures (106 °C) in a melt-processing environment. This novel approach is confirmed through spectroscopic characterisation, including ATR-FTIR, Raman, and CP-MAS ^{13}C NMR, and a Diels–Alder reaction that verified the stereochemistry of the resulting polyene. The polymer shows remarkable oxidative stability, with no degradation observed even after six months under ambient conditions. The unsaturated fragments within the polymer exhibit distinct reactivity, allowing selective post-functionalisation via epoxidation under reactive extrusion conditions. Mechanochemical epoxidation with *m*-chloroperoxybenzoic acid (*m*CPBA) improves solubility and processability without chain fragmentation, as evidenced by SEC analysis. This work presents a scalable route for the selective functionalisation of polyolefins, opening new avenues for their valorisation into advanced materials and demonstrating the feasibility of high-temperature processing for the formation of conjugated polyenes.



Finally, the main findings of this work are summarised in the general conclusion, along with the perspectives that naturally emerge from it, ranging from the convergence between the TSE-iodinated polyolefins of Chapter 5 and the CO_2BOL chemistry developed in Chapters 2-4, to the direct use of CO_2 as a reactive partner for the epoxidised polyethylene of Chapter 6, as well as alternative chemistries for tethering CO_2-derived functionalities onto polyolefin backbones.

CHAPTER 1

General Background

Plastic Waste and Carbon Dioxide Management



TABLE OF CONTENTS

I. Introduction 16

II. Plastic Waste Management 18

A. Recycling Methods 19
1. Mechanical Recycling 20
2. Chemical Recycling 26

B. Recycling and Upcycling of Thermoplastics 33
1. Polyethylene 34
2. Polypropylene 36
3. Poly(Vinyl Chloride) 38

C. Alternative Valorisation Pathways 41

D. Intermediate Conclusion 45

III. Carbon Dioxide Management 46

A. Atmospheric CO_2 Removal 47
1. Bioenergy with Carbon Capture and Storage 47
2. Direct Air Capture 50

B. Carbon Capture 52
1. Carbon Capture and Storage 59
2. Carbon Capture and Utilisation 61

C. CO_2-Binding Organic Liquids 69

D. Intermediate Conclusion 72

IV. Conclusion and Objectives of the Work 73

V. References 76

I. Introduction

The emergence of plastic materials can be traced back to the mid-1800s with the invention of cellulose-based materials such as Parkesine and Celluloid.[1] However, the first fully synthetic plastic wasn't invented until 1907, when Leo Baekeland introduced Bakelite.[1,2] In the decades that followed, plastic production diversified and industrialised rapidly, with World War II acting as a catalyst for mass manufacturing.[3] By the 1960s, concerns over plastic pollution and its environmental impact began to surface. Indeed, it quickly became clear that the properties that made plastics such attractive materials, were also their biggest drawback when reaching the end of their use life.[4]

Today, the annual global production of plastics has exceeded 400 Mt.[3,5] In other words, a 200-fold increase in production has been observed in the span of 70 years (**Figure 1.1**). Since two thirds of those plastics only have a short lifetime, the production of such large amounts can only generate nearly as much waste. Furthermore, most of this waste is not managed properly, leading to its accumulation in the natural environment and the devastating consequences that come with it.[3,6]

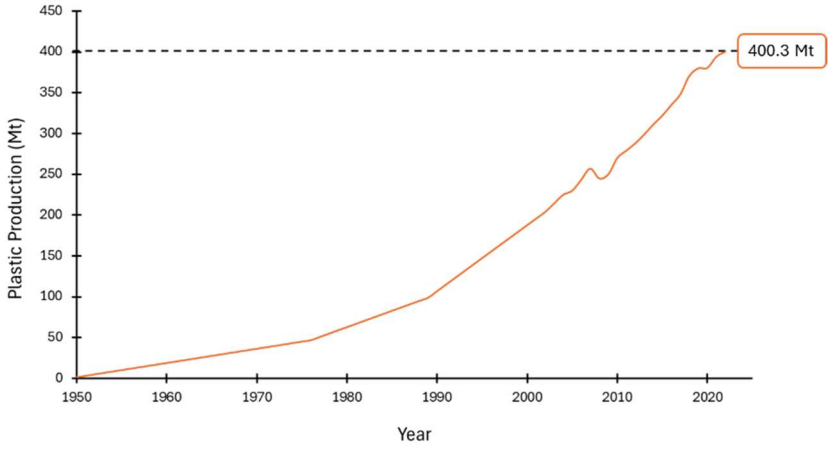


Figure 1.1. Historical growth of global plastic production (1950 – 2022). Adapted from *Enviraj*.[7]

Currently, there are three main ways to handle plastic waste: recycling, incineration, or landfilling.[8] Although Europe recycled about 27 % of its plastic waste in 2022, around 24 % was still sent to landfill while the remaining 49 % was incinerated.[5] As encouraging as these figures may seem, global statistics reflect a far less optimistic reality. Indeed, according to the United Nations Environment Programme, less than 10 % of plastic waste is recycled globally (**Figure 1.2**).[9] Thus, tremendous effort is still required if a circular plastics economy is to be reached.

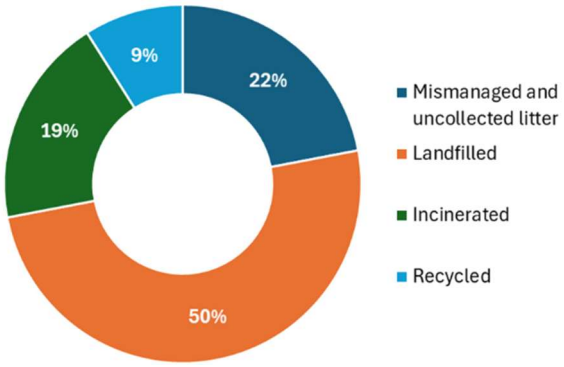


Figure 1.2. Global plastic waste management distribution. Adapted from *OECD*.[10]

Moreover, the production, use, and disposal of conventional fossil fuel-based plastics was responsible for the emission of an estimated 1.7 gigatons of carbon dioxide equivalent* ($GtCO_2e$) in 2015.[9] A truly circular plastics economy would therefore allow to not only reduce plastic pollution, but also mitigate greenhouse gas (GHG) emissions, thereby tackling two of the most pressing environmental challenges of our time.

Unfortunately, plastics are not the only ones at fault when it comes to GHG emissions. Indeed, in 2023, an all-time new record for global GHG emissions was set with 57.1 $GtCO_2e$, most of which is linked to energy consumption (**Figure 1.3**). The largest contributor, accounting for approximately 75 %, is the notorious carbon dioxide.[12] Hence, although the recycling of plastic waste would indeed help mitigate GHG emissions, more impactful actions need to be taken.

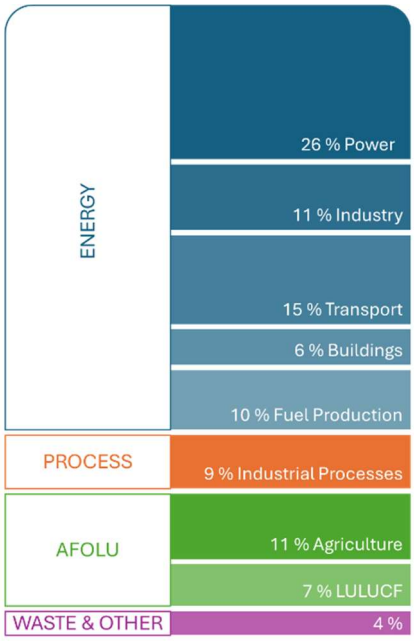


Figure 1.3. Global GHG emissions by sector (2023). AFOLU = "Agriculture, Forestry, and other Land Use" and LULUCF "Land Use, Land-Use Change, and Forestry". Adapted from *UNEP Emissions Gap Report 2024*.[12]

* Carbon dioxide equivalent (CO_2e) is a standardized metric used to compare emissions from different greenhouse gases based on their global warming potential (GWP), by converting the quantity of each gas into the amount of CO_2 that would produce an equivalent warming effect over a given time horizon.[11]

Two main strategies exist for tackling CO_2 emissions. The first one consists in upstream mitigation. It involves reducing emissions at the source, mainly by decreasing our reliance on fossil fuels. Despite this, CO_2 production might be unavoidable in a society as industrialised as ours. Therefore, downstream solutions such as removal from the atmosphere, carbon capture and storage (CCS), and carbon capture and utilisation (CCU) are also a possibility.

This first chapter provides an overview of the current state of the art in two key environmental challenges: plastic waste recycling and CO_2 management. To address these topics effectively, the chapter is divided into two main sections. The first section explores the technologies currently employed in plastic waste recycling, with a particular focus on polyethylene (PE), polypropylene (PP), and poly(vinyl chloride) (PVC). It also reviews alternative plastic waste valorisation pathways. The second section shifts focus to CO_2 management, covering various strategies such as atmospheric CO_2 removal, CCS, and CCU. Special attention is also given to CO_2-binding organic liquids (CO_2BOLs), highlighting their potential applications.

II. Plastic Waste Management

As previously outlined, plastic waste is generally managed in three different ways: landfilling, incineration, or recycling. Although landfilling appears as the path of least resistance, one cannot consider it as a sustainable approach to plastic waste management. Indeed, despite presenting advantages - such as low energy requirement, cost effectiveness, or high waste throughput - the drawbacks of this method significantly outweigh its benefits.[3] When placed in landfill, plastic waste can be leaked into the environment and lead to the contamination of waterbodies and soils.[3,4] Once in the environment, whether marine or terrestrial, a butterfly effect is triggered leading to devastating consequences for biodiversity, but also impacting public health and socio-economic systems.[3] This is why several European countries, including Belgium, have implemented landfill bans.[5]

Incineration of plastic waste, also known as waste-to-energy (WTE) or energy recovery, represents an equally environmentally damaging waste management strategy. It consists in burning plastics to recover the energy generated from the heat. However, while it allows for reduction of waste volumes, WTE mostly exhibits disadvantages. First of all, it produces more GHG emissions than other forms of energy production such as coal, oil, and natural gas.[13] Additionally, it also releases toxic compounds into the environment both via direct emission into the atmosphere and the disposal of the byproducts (ash and wastewater), leading to serious health issues.[14–19] Despite being more economically attractive, incineration offers little justification as a long term strategy, especially when more sustainable, low-impact waste management strategies like recycling are available.[20–22]

Per the hierarchy established by the 3Rs (Reduce, Reuse, Recycle) principle of plastics waste management, recycling is the most sustainable strategy after reducing the amounts of

generated waste and reusing products already available on the market.[3] Although energy recovery is often still considered a form of recycling, this view is no longer supported by current standards: the ASTM (American Society for Testing and Materials) D7209 guide, which encompassed energy recovery within its scope of plastics waste management practices, was withdrawn in 2015 and has not been replaced.[21–24] In contrast, the International Organization for Standardization (ISO) explicitly defines recycling as "processing of plastics waste materials for the original purpose or for other purposes, excluding energy recovery"[25] (ISO 15270:2008).[†] The methodologies that are encompassed by this definition are discussed below.

A. Recycling Methods

Depending on the nature of the polymer that is to be recycled, various methods can be considered, and some may be preferred over others. According to the same ISO standard (ISO 15270:2008), there are three different approaches to recycling defined as follows: [25]

- **Mechanical recycling:** Processing of plastics waste into secondary raw material or products without significantly changing the chemical structure of the material.
- **Feedstock recycling (or chemical recycling):** Conversion to monomer or production of new raw materials by changing the chemical structure of plastics waste through cracking, gasification, or depolymerisation, excluding energy recovery and incineration.
- **Biological recycling (or organic recycling):** Aerobic (composting) or anaerobic (digestion) treatment of biodegradable plastics waste under controlled conditions using micro-organisms to produce, in the presence of oxygen, stabilised organic residues, carbon dioxide and water or, in the absence of oxygen, stabilised organic residues, methane, carbon dioxide and water.

While biological recycling is outside the scope of this thesis, readers seeking a more in-depth discussion on the subject are invited to refer to recent reviews by Liu et al.[26] as well as Getino et al.[27]

[†] ISO 15270:2008 is currently under revision and is expected to be replaced by a five-part series (ISO 15270-1 to ISO 15270-5). As all parts have not yet been published at the time of writing, the definitions used here are those of the latest confirmed version of ISO 15270:2008 (last reviewed in 2018), which remains the current standard.

1. Mechanical Recycling

Generally, mechanical recycling of plastic waste is seen as merely a two-step process involving melting and reshaping of the materials. In reality, these operations represent only the final stages of a much more complex system (**Figure 1.4**). The process begins with waste collection, followed by sorting, washing, and grinding steps, which may occur in different sequences and be repeated multiple times. Each stage is critical, as high-purity polymer streams are required to obtain higher-quality recycled materials. Only after these conditions are met are the resulting plastic flakes melted and reprocessed using various methods.[3,6,8,21,28–30]

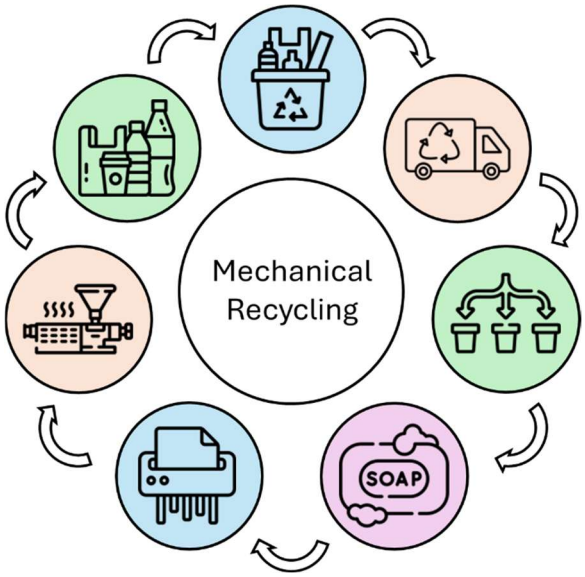


Figure 1.4. Mechanical recycling steps for post-consumer plastic waste. Clockwise from the top : plastic waste, collection, sorting, washing, grinding, reprocessing, and new product.

As the first step, collection is just as essential to the efficiency of mechanical recycling as the rest of the process. More specifically, separate waste collection, which relies on an initial separation at the consumer level, is crucial in order to facilitate processing of the waste.[31,32] According to the 2024 report published by Plastics Europe, when comparing recycling rates for plastics collected separately to those of mixed waste streams, the former exceed the latter thirteen-fold.[5] Moreover, literature shows that adopting door-to-door collection schemes both decreases waste generation and increases purity of the waste stream, thereby increasing recycling rates.[31,33]

Despite separate waste collection, plastic waste streams still consist of a wide variety of polymers characterised by an even larger array of properties. This means that there is no one-size-fits-all method for plastics recycling. The waste thus needs to be further sorted following collection. This generally happens at a sorting facility before the sorted waste fractions can go on to recycling plants. Indeed, due to the lack of a universal recycling method, facilities generally specialise in the recycling of one polymer type. Hence, different companies deal with different steps of the recycling process.

Plastic waste sorting relies on the materials' physicochemical properties like size, density, colour, or even surface wettability.[34,35] However, it typically starts with operators manually removing large and/or non-recyclable items from the waste stream.[34,36] Then depending on the plant, many different sorting techniques can be associated. Mechanical methods use sieves / screens to separate the waste based on size. Regardless of the type of screen (disc, rotating drum, or oscillating / vibrating), they all contain specific size openings through which waste of the appropriate size falls. Usually, three fractions are collected. In the first one, items are smaller than 30 mm, while the other two contain items bigger than 150 mm (oversize) and those of intermediate size (30 < x < 150 mm), respectively.[37,38] **Figure 1.5** schematises a simplified side view of a vibrating screen separator and the resulting size segregation of the waste.

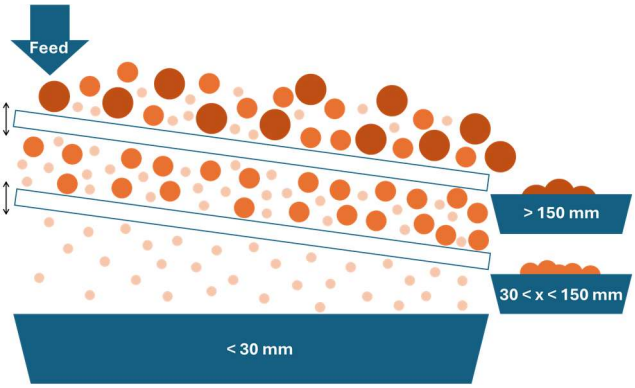


Figure 1.5. Simplified side view of a vibrating screen separator.[38,39]

There are also several ways through which metallic items can be separated from the plastic waste stream. On the one hand, ferrous metals are extracted using magnetic devices such as overbelt magnets, magnetic head pulleys or magnetic drums as depicted in **Figures 1.6a-c**. In each case, the magnet is used to attract the metallic items and retain them longer than non-magnetic materials, thereby leading to separation.[34] On the other hand, non-ferrous metals (i.e. aluminium, copper, zinc), which are not magnetic, are separated from the rest of the stream using a method known as Eddy current separation (**Figure 1.6d**). In this technique, a high-speed magnetic rotor creates an alternating magnetic field, which induces an electric current (Eddy current) in conducting metals passing through the field. This induced current in turn generates a secondary magnetic field opposed to that of the rotor. This triggers repulsive forces between the rotor and the metallic item and thus separation from the waste stream.[34,40,41] As with mechanical or magnetic separation techniques, various types of Eddy current separators exist depending on the type of rotor it uses.[40] Moreover, both magnetic and Eddy current separation are often associated with mechanical methods at the beginning of the sorting process.[8,38]

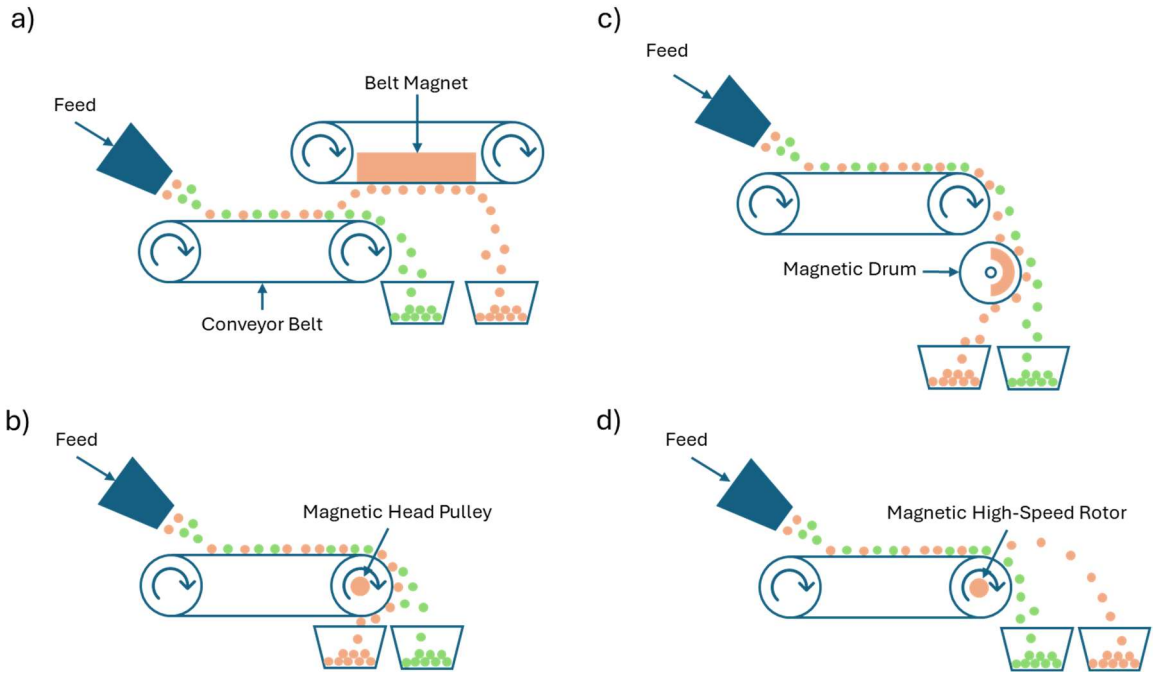


Figure 1.6. Schematic representation of techniques used to sort ferrous **(a-c)** and non-ferrous **(d)** metals out of the waste stream. **(a)** Overbelt magnetic separator, **(b)** magnetic head pulley separator, **(c)** magnetic drum separator, and **(d)** Eddy current separator. Metallic items are represented in orange while non-metallic ones are represented in green. (Reproduced from reference 34)

Other widely used sorting technologies rely on material density. These methods can be classified into two categories: dry and wet techniques. Dry techniques such as wind sifters, ballistic separators, or film grippers, use airflow to separate lighter items from heavier ones. Conversely, wet techniques are based on the differences in density between the material and a liquid medium. For example, in sink–float separation using water (density = 1 $g.cm^{-3}$), polymers with densities below 1 $g.cm^{-3}$, such as polyethylene (PE, 0.925 – 0.96 $g.cm^{-3}$) and polypropylene (PP, 0.905 $g.cm^{-3}$), float, while polymers with higher densities, such as polyethylene terephthalate (PET, 1.35 $g.cm^{-3}$) and polyvinyl chloride (PVC, 1.30 – 1.58 $g.cm^{-3}$), sink.[8,34,42] However, further separation is often not possible due to overlapping density ranges among different materials.[8,43] Consequently, additional techniques must be applied. These include magnetic density separation,[41] froth flotation,[45] triboelectric (or electrostatic) separation[46] and / or sensor-based technologies. The latter rely on various detection methods operating across a wide range of the electromagnetic spectrum, from X-ray to terahertz wavelengths.[8,34,35,47] The most widely used sensor technologies for plastic waste sorting at the industrial level include dual-energy X-ray transmission (DE-XRT) and X-ray fluorescence (XRF) spectroscopies, colour line-scan cameras, infrared and hyperspectral cameras, as well as laser-induced breakdown spectroscopy (LIBS).[47] Regardless of the detection method, the sensor is generally placed above the conveyor belt on which the waste stream is fed. Following detection and upon reaching the end of the belt, items of specific composition are separated from the rest of the waste stream via short blasts of dry air (**Figure 1.7**).[34,47]

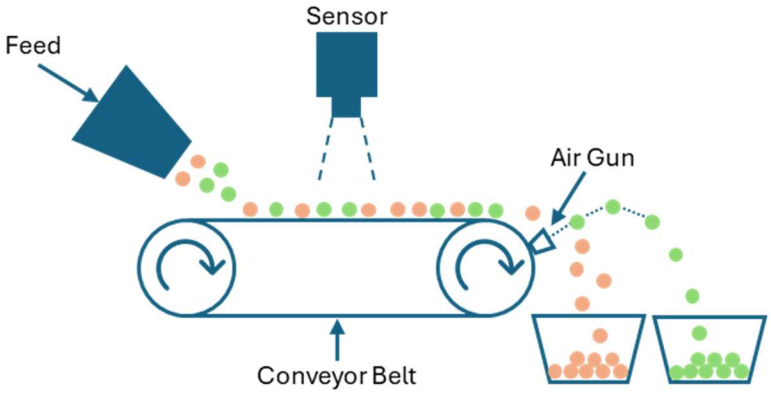


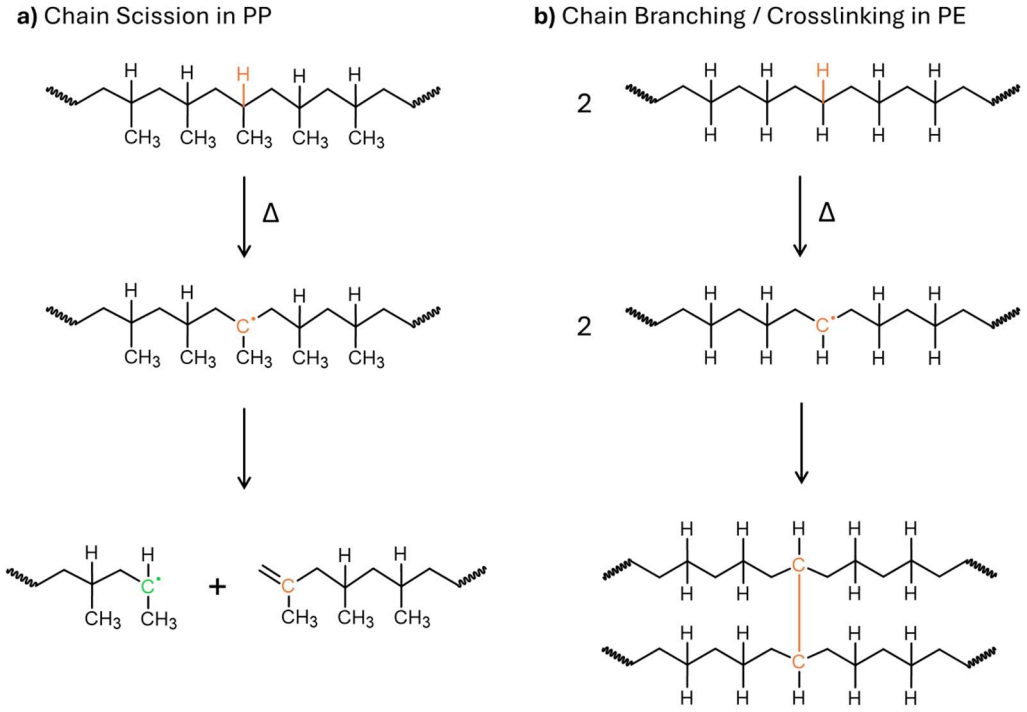
Figure 1.7. General representation of sensor-based sorting techniques. (Reproduced from reference 34)

In addition to the sorting of the plastic waste, its washing is also essential in order to remove as many contaminants (i.e. labels, adhesives, organic matter, etc.) as possible from the different polymer streams.[35,48,49] Similar to sorting technologies, washing techniques can be classified into dry and wet methods. The former use friction to remove impurities, while the latter use water with or without caustic and surfactant solutions. Some wet methods also combine the use of friction and water washing (with or without caustic and surfactant solutions).[48,50] Moreover, wet washing can be performed either at room temperature (25 °C) or at higher temperatures (hot washing) depending on how heavy or persistent the contamination is.[35,48] Techniques are selected based on the nature of the initial material and the recyclate quality requirements. Following washing, the plastic waste is dried mechanically (centrifugal dryer) or thermally.[35]

Between the sorting and washing stages, waste materials typically undergo at least one size-reduction step.[8] Shredding or grinding produces flakes that improve sorting and cleaning efficiency and facilitate handling during subsequent reprocessing.[51] These flakes are then generally extruded and pelletised before being sent to manufacturers, where they will be further processed using different methods (i.e. injection moulding, blow moulding, etc.) depending on the final product.[52]

While mechanical recycling presents numerous advantages (low energy demand, reduced CO_2 emissions, cost efficiency, high material retention) and is the most widespread recycling method, it presents several drawbacks as well.[53] First of all, mechanical recycling, as it is generally understood and described above, is limited to thermoplastic materials.[29,30] Indeed, owing to the irreversibility of their three-dimensional crosslinked structure, thermoset polymers (e.g. epoxy resins, polyurethanes, silicones, etc.) cannot be melted. This means that, unlike thermoplastics, they cannot be reprocessed through extrusion and are therefore considered difficult to recycle. Generally, mechanical recycling of thermoset materials actually stops at the sorting, cleaning and size reduction steps and they are then used as fillers or reinforcements in other materials. In other words, the mechanical recycling of thermosets leads to the downcycling of the material, i.e. the material loses value upon recycling.[54,55]

The second drawback stems from the thermal reprocessing itself. In addition to the potential degradation polymers sustain over the course of their use life, the heat and mechanical shear they are subjected to during the extrusion process can cause further damage to the material's structure. The most commonly observed forms of degradation can be classified into two categories based on the effect they have on the polymer's molecular weight (M_w). On one hand, chain scission leads to a decrease in M_w, while on the other hand branching and crosslinking yield higher molecular weights. The prevalence of one type of degradation over the other is dictated by factors such as the nature of the polymer, its initial M_w, and extrusion conditions. For example, PE is more prone to chain branching and crosslinking, whereas PP is more likely to undergo chain scission (**Scheme 1.1**). Either way, both are radical processes which, in the absence of oxygen, are generally initiated by the thermally induced abstraction of hydrogen atoms.[8,24,53,56]



Scheme 1.1. Thermo-mechanical degradation pathways. (a) Chain scission pictured in the case of PP **(b)** Chain branching / crosslinking pictured in the case of PE. Adapted from reference 56.

Regardless of the degradation pathway, material properties are negatively affected. Notably, mechanical properties, especially tensile strength and impact resistance, as well as thermal (melting and glass transition temperature) and rheological (viscosity and elasticity) properties are directly impacted and diminished by thermo-mechanical degradation. Eventually, after being subjected to several reprocessing cycles, such properties modifications become detrimental to the material's quality, inevitably leading to its downcycling.[53,57] Generally, recycled products are therefore not entirely constituted of recycled materials. Rather, manufacturers incorporate a fraction of recycled polymer with the virgin one.[24,58]

Finally, the third and probably most significant drawback of mechanical recycling lies in its inability to handle waste stream contamination, which further reduces recyclate quality.[30] Although continuous research efforts seek to improve cleaning and sorting techniques,[59,60] in practice some residues remain difficult to remove completely and pure, single-polymer waste streams are rarely achieved. Contaminants therefore include compounds such as adhesives, pigments, inks, labels, or lubricants, as well as other polymers.[29] The presence of these additional polymers may result from inefficient sorting, but multilayer materials also contribute significantly to the generation of mixed plastic waste streams.[29] Two main challenges generally arise with the reprocessing of such mixed polymer streams. The first one is caused by the differences in melting temperatures between the different polymers (**Figure 1.8**). Typically, reprocessing temperature is determined by the polymer exhibiting the highest melting temperature within the mixture. This can thus lead to degradation of the lower-melting polymers of the mixture. A recurring example is that of PVC traces in PET streams. Generally speaking, the presence of PVC needs to be reduced as much as possible during the reprocessing of other polymer streams as it undergoes dehydrochlorination at higher temperatures. This not only causes equipment corrosion and air pollution but, in the case of PET, it also lead to the catalysis of the degradation process and the resulting loss of properties.[8,24,61,62]

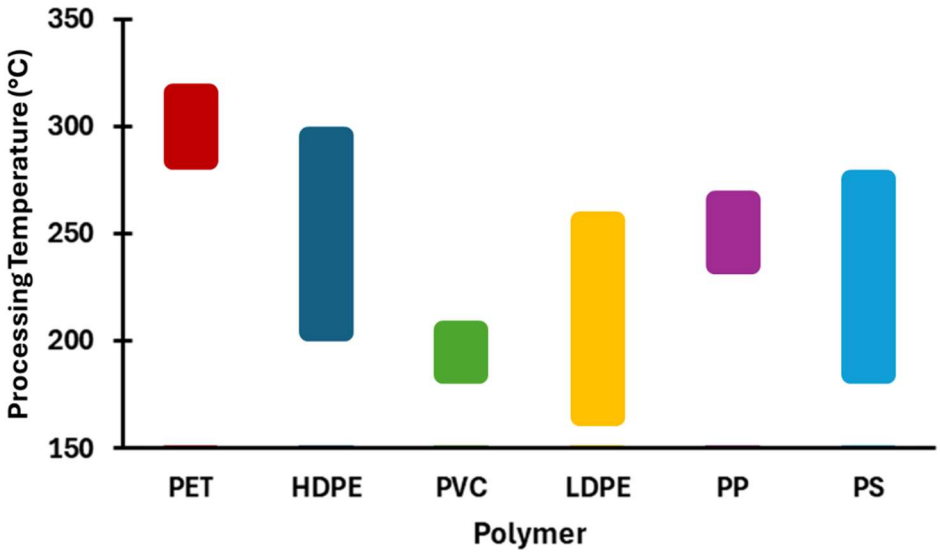


Figure 1.8. Processing temperature ranges for the most common thermoplastic polymers. Adapted from references 8 and 24. (PET = Poly(Ethylene Terephthalate), HDPE = High Density Poly(Ethylene), PVC = Poly(Vinyl Chloride), LDPE = Low Density Poly(Ethylene), PP = Poly(Propylene), and PS = Poly(Styrene)).

Additionally, the reprocessing of mixed polymer waste streams produces polymer blends, which pose challenges of their own. Among these challenges, the immiscibility and incompatibility of most polymer pairs prevail.[63] In such polymer blends, two phases can be observed, where one of the polymers forms the matrix phase while the other makes up the dispersed phase. These phases can present under various morphologies, from spheres and cylinders to sheets, as well as continuous segments (**Figure 1.9**).[64,65] Such phase separation yields poor mechanical properties due to high interfacial tension. More specifically, tensile

strength and impact resistance are highly influenced by the distribution of the dispersed phase because of inadequate stress and strain transfer between the phases.[24]

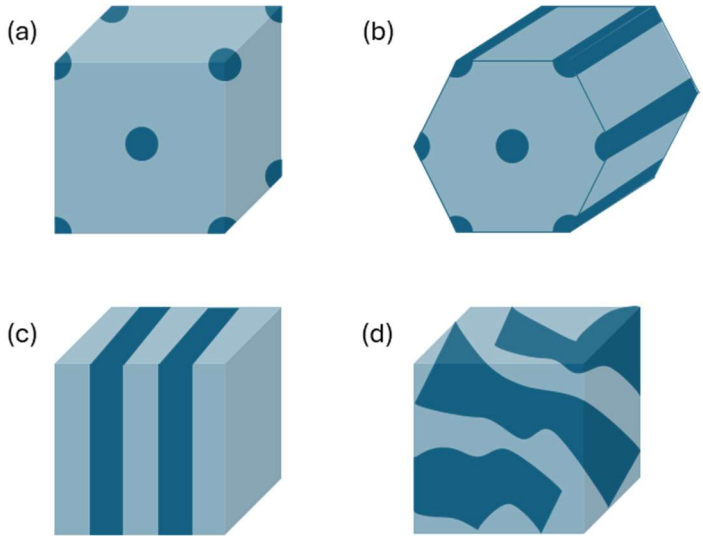


Figure 1.9. Immiscible polymer blends morphologies. (a) spheres, **(b)** cylinders, **(c)** sheets, and **(d)** continuous. Adapted from reference 8.

The loss of properties resulting from thermo-mechanical degradation or the formation of polymer blends is generally remedied through the use of various additives such as heat stabilisers, impact modifiers, compatibilisers,[66–68] pigments and fillers.[8,24] However, this prevents additional recycling cycles as it can hinder sorting and further reduce polymer stream purity.[55] Mechanical recycling may therefore not always be suitable for closed-loop recycling, i.e. the recycling of materials to products of equivalent quality and intended for the same application as their virgin predecessor, especially for applications such as food packaging, which are subjected to strict guidelines.[55,61,69] Considering that packaging accounts for about 40 % of European plastic production, 60 % of which is actually food packaging, other recycling methods, such as chemical recycling, are therefore necessary.[5,70]

2. Chemical Recycling

Chemical recycling encompasses a range of technologies that transform plastic waste into smaller molecular compounds through chemical reactions. These technologies are generally classified into two categories : the monomer loop and the molecular loop (**Figure 1.10**).[57] The former involves the conversion of the polymer back into its monomeric constituents, while the latter transforms it into other value-added compounds, such as fuels or syngas. In contrast to mechanical recycling, which retains the polymer backbone (polymer loop)[57] and is therefore sensitive to contamination and degradation, chemical recycling involves the breakdown of polymer chains into their fundamental building blocks, enabling the production of high-purity secondary materials. This fundamental difference allows chemical recycling to address limitations inherent to mechanical processes, particularly in handling heterogeneous, contaminated, or multi-layer plastic waste streams.[71] As a result, chemical recycling is

increasingly positioned as a complementary pathway rather than a competing one. While mechanical recycling remains preferable for clean and homogeneous waste due to its lower energy demand and cost, chemical recycling can process fractions that would otherwise be incinerated or landfilled.[72]

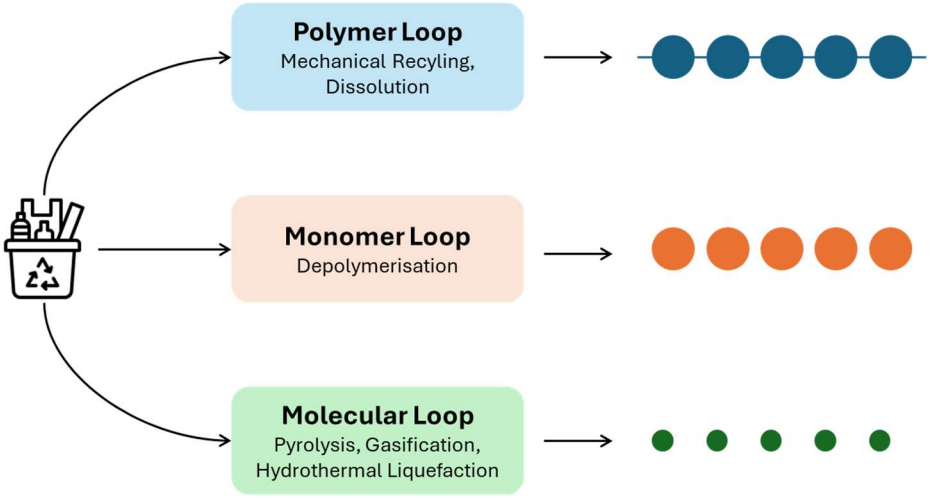


Figure 1.10. Output-based classification of recycling technologies - polymer, monomer, and molecular loop.

Although specific configurations vary depending on the technology, chemical recycling processes generally follow a similar sequence of steps. As with mechanical recycling, plastic waste intended for chemical recycling is collected from municipal, commercial, or industrial sources and subjected to pre-treatment steps such as sorting, cleaning, and size reduction to ensure suitable feedstock quality.[73] The prepared feedstock is then introduced into a reactor, where it undergoes chemical transformation under controlled conditions. While the choice of reactor type depends on the specific process, key operational parameters remain the same and include temperature, pressure, residence time, and catalyst presence (if applicable).[74] The resulting products are then separated into different fractions (gas, liquid, solid) and further purified using techniques such as distillation, condensation, or filtration. Finally, recovered products are upgraded to meet industry specifications and can be reintegrated into existing petrochemical systems (**Figure 1.11**). For example, pyrolysis oil can be used as a feedstock in steam crackers to produce new olefins.[73]

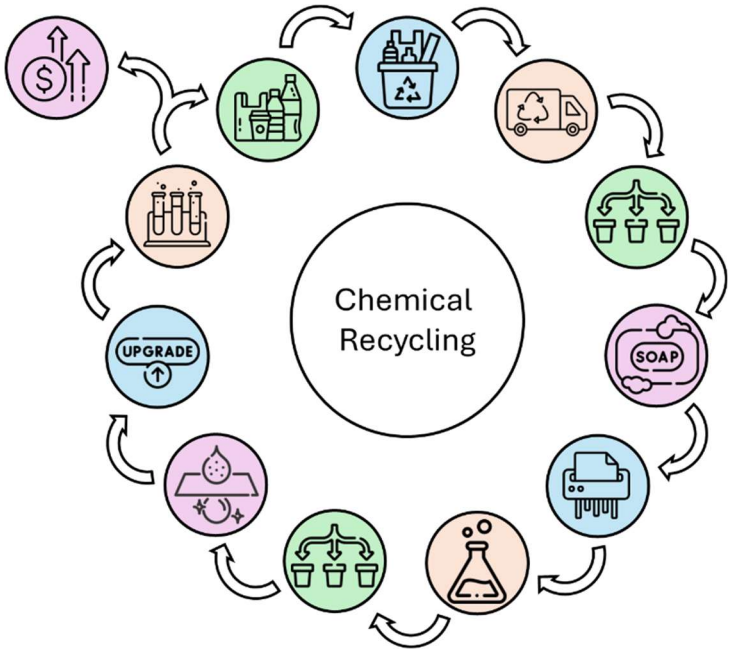


Figure 1.11. Chemical recycling steps for post-consumer plastic waste. Clockwise from the top : plastic waste, collection, sorting, washing, grinding, chemical transformation, separation, purification, upgrade, and new product, which can be reintegrated into the cycle or not.

Chemical recycling comprises several distinct technological pathways, each characterised by specific reaction mechanisms, feedstock requirements, and output products. While some new and existing methods are continuously being developed and improved, the most common ones include dissolution, depolymerisation, pyrolysis, gasification, and hydrothermal liquefaction.[75]

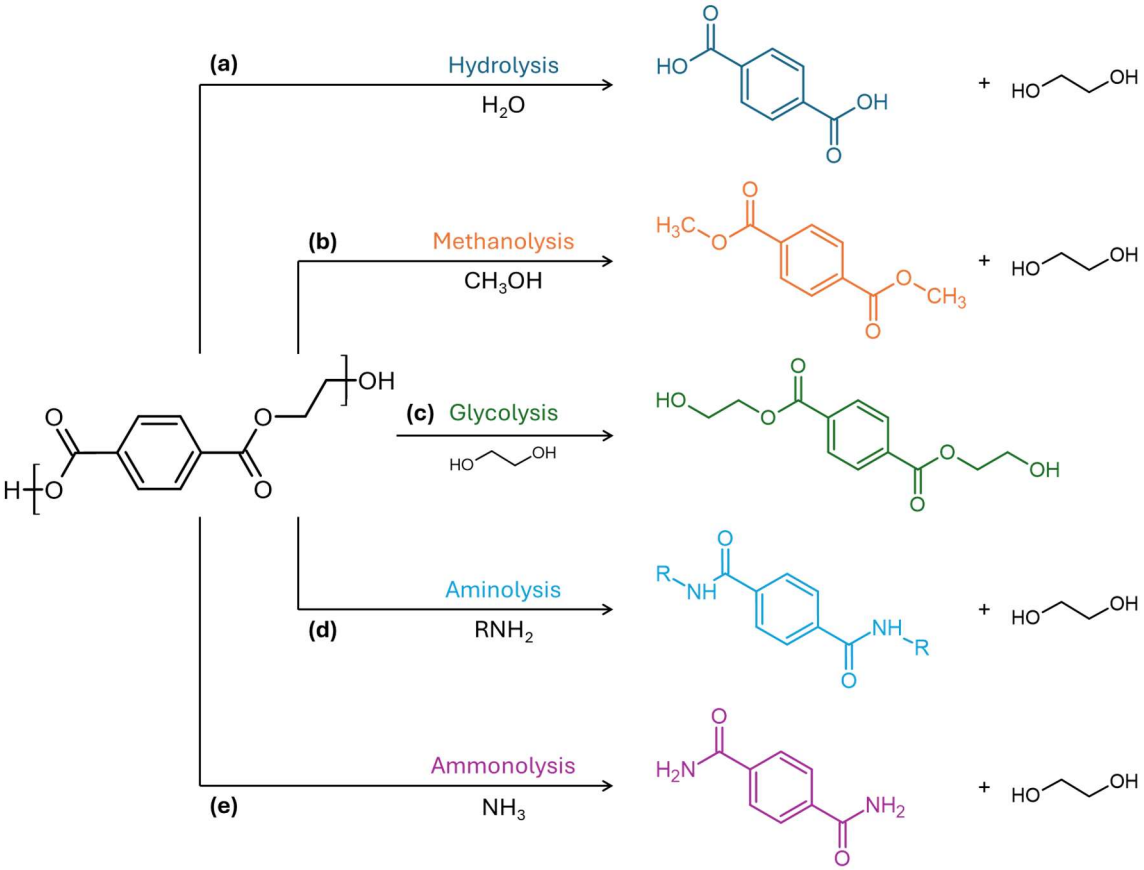
Dissolution

The dissolution approach does not involve any chemical transformation or break down of polymer chains. Instead, it involves isolation of specific polymers from mixed waste streams while preserving their molecular structure via their selective dissolution in suitable solvents, followed by purification and precipitation. While dissolution is technically a physical recycling method, it is often included in chemical recycling. This method is particularly advantageous for treating complex and multi-layer materials, where different polymers are combined in a single product. By carefully selecting solvents, individual polymers can be separated and recovered with high purity.[76] As a result, dissolution-based processes can handle feedstocks that are challenging for both mechanical recycling and certain chemical recycling methods.[73] The recovered polymers can then be reused in applications similar to virgin materials, provided that the purification process effectively removes additives and contaminants.[77] However, the process relies heavily on efficient solvent recovery systems to minimise environmental impact and operational costs.[73]

Depolymerisation

Depolymerisation processes aim to break down polymers into their constituent monomers or other valuable intermediates by reversing the polymerisation reaction. This approach is particularly suitable for condensation polymers such as polyethylene terephthalate (PET), polyamides, and polyurethanes, which can be chemically cleaved into well-defined molecules.[55]

Depolymerisation is generally performed using solvolysis. Different solvolysis methods exist, including hydrolysis, glycolysis, methanolysis, aminolysis, and ammonolysis, based on the solvent that induces chain scission. These processes can yield high-purity monomers such as terephthalic acid or ethylene glycol in the case of PET, which can be directly reused in polymer production (**Scheme 1.2**).[78] The ability to recover monomers with near-virgin quality represents a major advantage, as it enables true closed-loop recycling. Moreover, solvolysis is tolerant of most additives and polymer mixtures and blends due to its specificity to certain chemical functionalities and can therefore be used to selectively separate constituents.[55,79] However, depolymerisation still requires relatively clean and homogeneous feedstocks to ensure high product quality as the presence of too many contaminants would complexify the purification process, in turn jeopardising economic viability.[55]



Scheme 1.2. Solvolysis of PET. From top to bottom : Hydrolysis, Methanolysis, Glycolysis, Aminolysis, and Ammonolysis. Adapted from reference 78.

Pyrolysis

Pyrolysis is a thermochemical process in which plastic waste is heated in the absence of oxygen, typically at temperatures between 300 °C and 700 °C. Under these conditions, long polymer chains undergo thermal cracking, resulting in a mixture of liquid hydrocarbons (pyrolysis oil), non-condensable gases, and solid residues (char).[80] The primary product of pyrolysis, pyrolysis oil, is a complex mixture of hydrocarbons that can be further refined and used as a substitute for fossil-derived feedstocks such as naphtha in steam crackers, enabling the production of new plastics.[55] Non-condensable gases are typically reused within the process to provide heat, improving overall energy efficiency,[55] while char is generally considered a low-value by-product, although potential applications are being explored (**Figure 1.12**).[81–83]

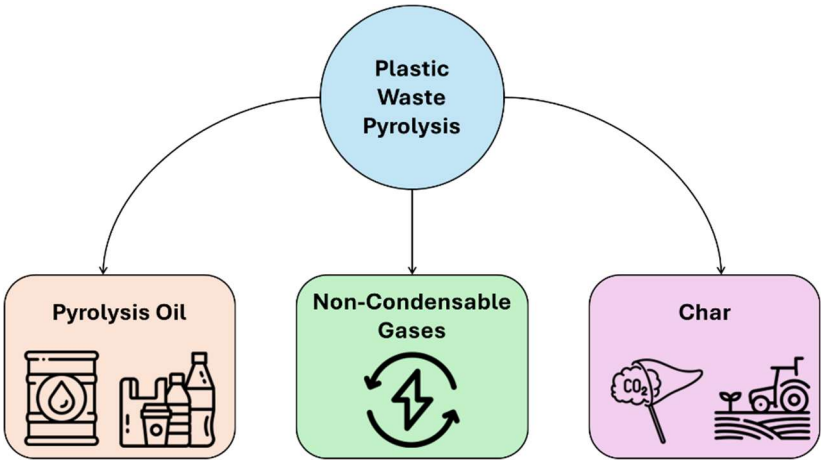


Figure 1.12. Plastic waste pyrolysis products and their applications. From left to right : pyrolysis oil – fuels, new plastic products, non-condensable gases – energy, and char – CO_2 capture, agriculture.

The process can be conducted with or without catalysts, with catalytic pyrolysis offering improved control over product distribution and quality.[8,84] In catalytic pyrolysis, solid acid catalysts - most commonly zeolites such as ZSM-5 - are introduced into the reactor to promote specific cracking reactions.[74,85] As a result, product composition can be significantly impacted. Typically, the use of catalysts in pyrolysis leads to increased yields of lighter iso-hydrocarbons and aromatics (C_5-C_{15} range) and reduces char formation / increases liquid and gaseous products proportions.[8,86] Moreover, it allows the process to be operated under milder conditions, thereby reducing energy consumption.[8] However, catalytic pyrolysis also introduces additional challenges. Catalyst deactivation is a major issue, primarily due to coke formation on the catalyst surface, which blocks active sites and reduces efficiency over time. In addition, catalysts can be sensitive to impurities in the feedstock, such as metals, chlorine, or sulphur, which may poison active sites or accelerate degradation. Consequently, catalyst regeneration and feedstock pre-treatment become important considerations in process design.[80]

An important variation of this process is hydropyrolysis, in which hydrogen is introduced during thermal degradation, often in the presence of a catalyst.[79] The addition of hydrogen promotes hydrogenation reactions that stabilise intermediate species, reducing the formation of

char and unsaturated compounds.[6] As a result, hydropyrolysis can improve the yield and quality of liquid products, producing oils with lower aromatic content and fewer impurities. This can simplify downstream upgrading and make the resulting products more suitable for direct integration into petrochemical processes. However, the requirement for hydrogen supply and additional process control increases both complexity and cost, which may limit its current industrial deployment.[8]

From a feedstock perspective, pyrolysis is particularly well suited to polyolefin-rich waste streams, including PE and PP, due to their simple hydrocarbon structure devoid of heteroatoms such as chlorine, nitrogen, or oxygen. This allow for these polyolefins to be efficiently cracked into smaller hydrocarbon molecules during pyrolysis, resulting in high yields of liquid oil and gaseous products. In contrast, polymers containing heteroatoms, such as PVC, PET, or polyurethanes (PU), can introduce significant challenges.[87] For example, PVC releases hydrogen chloride (HCl) during thermal degradation, which can lead to equipment corrosion and the formation of hazardous compounds.[55,79] Similarly, oxygen-containing polymers may produce more complex product distributions, including oxygenated compounds that require additional upgrading. Consequently, although pyrolysis can tolerate a certain degree of mixed plastic waste, pre-treatment steps such as sorting, shredding, and drying are often necessary to limit the presence of problematic materials and ensure process stability.[87]

Gasification

Gasification involves the partial oxidation of plastic waste at high temperatures, typically above 700 °C, in the presence of a controlled amount of oxygen or steam. Unlike pyrolysis, which produces liquid hydrocarbons, gasification converts plastics into synthesis gas (syngas), primarily composed of carbon monoxide (CO) and hydrogen (H_2).[88]

A key advantage of gasification is its high tolerance to heterogeneous and contaminated feedstocks. Mixed plastic waste, including materials that are difficult to separate or recycle mechanically, can be processed with relatively limited pre-sorting.[89] However, pre-treatment steps such as size reduction and removal of non-combustible materials are still required to ensure efficient reactor operation.[90]

The main product, syngas, is a highly versatile intermediate that can be used in a wide range of downstream applications. It can be converted into fuels through processes such as Fischer–Tropsch synthesis or used to produce chemicals like methanol and ammonia. This flexibility allows gasification to integrate into existing chemical and energy systems. However, the need for extensive gas cleaning to remove contaminants such as tar, particulates, and acid gases increases both process complexity and cost.[74]

Hydrothermal Liquefaction

Hydrothermal liquefaction (HTL) is a thermochemical conversion process that uses water at elevated temperatures and pressures - typically between 250 °C and 400 °C and 10-25 MPa - to convert plastic waste into liquid hydrocarbons. Under these conditions, water exists in a subcritical or near-critical state, where its physicochemical properties (e.g., dielectric constant, ionic product) are significantly altered. This enables it to act both as a solvent and as a reactive medium, facilitating the breakdown of polymer chains without the need for prior drying.[74,91,92]

One of the key advantages of HTL is its ability to process wet or contaminated feedstocks, which distinguishes it from pyrolysis and gasification. This makes HTL particularly attractive for waste streams that include moisture-rich materials or are difficult to dry economically. HTL can handle mixed waste streams and is especially relevant when plastics are co-processed with biomass, sewage sludge, or other organic waste fractions.[91,93]

From a feedstock perspective, HTL is suitable for a wide range of polymers, although the efficiency and product distribution depend strongly on polymer type. Polyolefins (PE, PP) can be converted into oil-like products similar to those obtained via pyrolysis, while oxygen-containing polymers such as PET may undergo hydrolysis reactions, producing oxygenated compounds such as terephthalic acid and other intermediates. The presence of water can therefore be advantageous for certain polymers by promoting specific reaction pathways that are not accessible in dry processes.[74,92]

The primary product of HTL is a liquid oil phase, often referred to as biocrude or hydrothermal oil, which consists of a complex mixture of hydrocarbons and oxygenated compounds. This oil can be further upgraded through hydrotreatment or refining to produce fuels or chemical feedstocks. In addition to the liquid phase, HTL generates an aqueous phase containing dissolved organics, a gaseous fraction (mainly CO_2 and light hydrocarbons), and a small amount of solid residue.[91,93]

Despite its advantages, HTL faces several challenges. The requirement for high pressures increases reactor complexity and capital costs compared to atmospheric processes such as pyrolysis. In addition, the composition of the aqueous phase can pose environmental concerns and requires appropriate treatment.[94] Product upgrading is often necessary to improve stability and remove oxygenated compounds, particularly when processing mixed or oxygen-rich feedstocks.[93]

B. Recycling and Upcycling of Thermoplastics

While mechanical and chemical recycling technologies provide a general framework for plastic waste valorisation, their implementation and efficiency are highly dependent on the nature of the targeted polymers. To help their sorting and recycling, polymers are commonly classified into seven categories described by the Society of the Plastics Industry (SPI), each one assigned an identification code from 1 to 7 (**Figure 1.13**). The first six correspond to the most common commodity plastics, i.e. PET (1), HDPE (2), PVC (3), LDPE (4), PP (5), and PS (6), while all other plastics fall into category number 7 (e.g. polycarbonates (PC), polyurethanes (PU), poly(methyl methacrylate) (PMMA), nylons, etc.).[23,95]

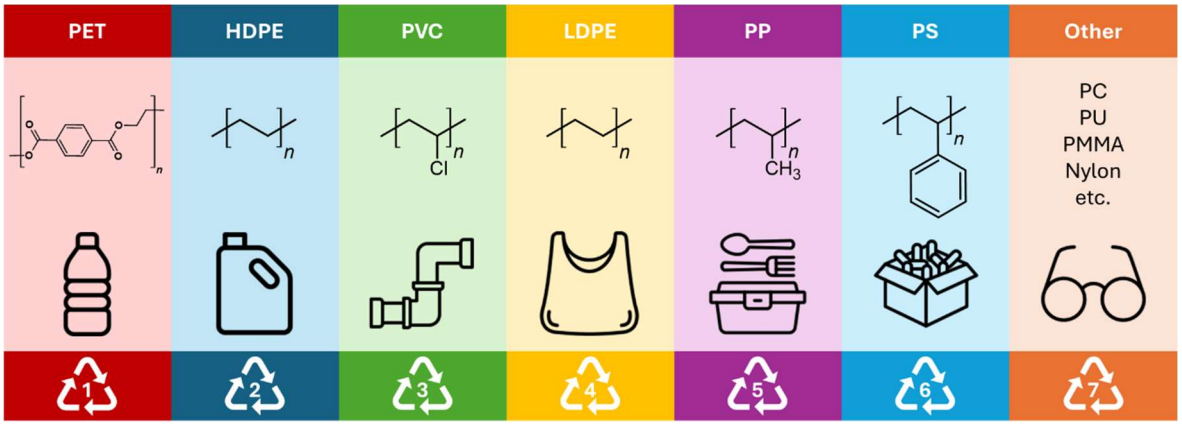


Figure 1.13. SPI classification of polymers.

Thermoplastics, which represent the largest share of global plastics production (~ 86 % in 2024),[96] exhibit significant differences in terms of processability, degradation pathways, and recyclability. Despite their shared thermoplastic nature, these polymers therefore exhibit markedly different behaviours during processing and recycling. For instance, polyolefins such as HDPE, LDPE, and PP are relatively easy to reprocess due to their simple hydrocarbon backbone, but they are prone to thermo-oxidative degradation and chain scission during repeated extrusion cycles, leading to a deterioration of their porperties.[97,98] In contrast, condensation polymers such as PET are more sensitive to hydrolysis due to the presence of ester linkages, which can significantly reduce molecular weight during mechanical recycling but also enables efficient chemical depolymerisation.[72,99] Other polymers, such as PVC and PS, present additional challenges related to the release of hazardous compounds or the formation of undesired by-products during thermal treatment.[100,101] These differences strongly influence the choice and efficiency of recycling strategies.

This section examines these materials individually, with an emphasis on established and emerging recycling strategies. More specifically, the focus is set on PE (HDPE and LDPE), PP, and PVC as they represent the top three most produced polymers globally. In contrast, PET and PS fall out of the scope of this thesis as they represent a smaller fraction of plastic waste. For more information on the recycling of these two polymers, readers are directed to reviews such as those by Muringayil Joseph *et al.*[102] and Xu *et al.*[103]

1. Polyethylene

Polyethylene (PE), encompassing high-density polyethylene (HDPE) and low-density polyethylene (LDPE), is the most widely produced class of thermoplastics and represents a major fraction of global plastic waste streams.[95,96] Its saturated hydrocarbon backbone, composed exclusively of C-C and C-H bonds, confers high chemical stability but also renders it intrinsically resistant to depolymerisation.[104] This chemical inertness has historically limited recycling strategies to mechanical reprocessing and high-temperature thermochemical conversion.[105]

The primary distinction between HDPE and LDPE lies in their molecular architecture, which directly impacts their physicochemical properties and, consequently, their recycling behaviour. HDPE is characterised by a largely linear polymer structure, allowing for close chain packing and resulting in high crystallinity, density, and mechanical strength. In contrast, LDPE exhibits a highly branched structure, which hinders chain packing and leads to lower crystallinity, reduced density, and increased flexibility (**Figure 1.14**).[106] These structural differences not only determine their respective applications, with HDPE predominantly used in rigid containers and LDPE in flexible films, but also influence their behaviour during processing and recycling. In particular, the higher crystallinity of HDPE generally confers better mechanical stability during reprocessing, whereas the branched architecture of LDPE results in lower viscosity and different rheological behaviour, which can affect melt processing and product performance.

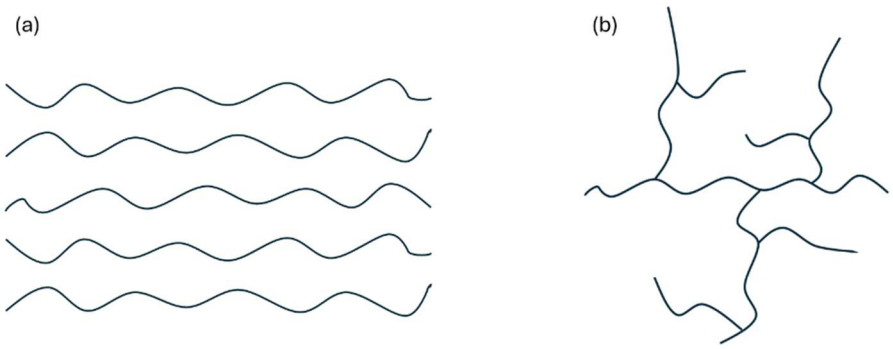


Figure 1.14. PE structures : (a) HDPE and **(b)** LDPE.

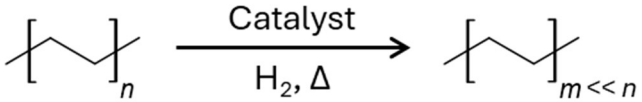
As a result, mechanical recycling is more readily implemented for HDPE, which benefits from relatively homogeneous waste streams such as bottle-grade materials. However, repeated extrusion cycles subject the polymer to thermal and mechanical stresses that promote radical-mediated degradation.[105] In a recent study published in Nature Communications, Patel *et al.* used rheology-simulated and extrusion-based recycling experiments to systematically investigate the degradation pathways of HDPE.[107] They demonstrated that chain scission dominates during the initial stages of reprocessing, while increasing exposure to oxygen progressively shifts the dominant mechanism toward long-chain branching. These findings are consistent with earlier observations by Akhras *et al.*, who showed through multiple reprocessing

cycles of several polyolefin grades that HDPE undergoes concurrent chain scission and branching, with the relative prevalence of each mechanism depending on the specific material grade and processing conditions.[98] Importantly, such structural changes translate directly into altered rheological and mechanical properties, ultimately limiting the number of viable recycling loops and the range of applications for the recyclate.[53,97]

In contrast, LDPE, which is predominantly used in films, suffers less from intrinsic thermo-mechanical degradation than from upstream challenges. Its collection and sorting are significantly hindered by contamination and the prevalence of multilayer structures, in which LDPE is combined with other polymers or aluminium foil. These composite materials are particularly difficult to separate into pure polymer streams, ultimately limiting effective LDPE recycling rates.[8,29] Furthermore, the thin and lightweight nature of LDPE films makes them prone to clogging sorting equipment, which adds operational complexity.[108]

To overcome these limitations, significant research efforts have been devoted to chemical recycling and upcycling of polyethylene. Conventional thermal pyrolysis, typically performed at temperatures above 400 °C, produces a broad distribution of hydrocarbons through radical mechanisms. While robust, this approach lacks selectivity and requires extensive downstream upgrading.[80,87] This has motivated the development of catalytic alternatives aimed at achieving greater control over product distribution.

A major advance in this field was reported in 2019 by Celik *et al.*, who demonstrated that platinum nanoparticles supported on strontium titanate ($Pt/SrTiO_3$) can catalyse the hydrogenolysis of HDPE into liquid lubricants and waxes at 300 °C under hydrogen pressure, with near-complete conversion.[109] Importantly, this work established catalytic hydrogenolysis as a viable strategy for polyolefin upcycling. Around the same time, Rorrer, Beckham, and Román-Leshkov showed that ruthenium-based catalysts supported on carbon (Ru/C) enable the conversion of polyethylene into liquid alkanes under mild conditions (200 °C, 20 bar H_2), providing improved selectivity toward shorter-chain products.[110] Building on this concept, Jia *et al.* further demonstrated that Ru catalysts can deconstruct HDPE into liquid hydrocarbon fuels and lubricants, with the product distribution being tuneable through the adjustment of reaction conditions such as temperature and hydrogen pressure.[111] (**Scheme 1.3**)



Scheme 1.3. Polyethylene hydrogenolysis.

More recently, attention has shifted toward enhancing selectivity and reducing energy input through rational catalyst design. For instance, Chauhan *et al.* developed single-site ruthenium dihydride catalysts confined within metal–organic frameworks (MOFs), which converted LDPE into a narrow distribution of liquid hydrocarbons (C_8–C_{24}) at only 200 °C, achieving up to 80 %

selectivity and 98 % conversion.[112] The confinement effect of the MOF pores was shown to play a critical role in controlling product chain length. In another approach, Nogueroles-Langa *et al.* reported that bimetallic Ru–Ni alloy nanoparticles supported on titania yield up to 55 % liquid C_6–C_{45} products from HDPE bottle caps under optimised conditions, while monometallic Ru produced virtually no liquids under the same conditions.[113] By integrating life cycle and techno-economic analyses, the authors further demonstrated that the process could be profitable with substantially lower CO_2 emissions when using green hydrogen, highlighting the importance of sustainability-driven catalyst design.

In parallel to catalytic hydrogenolysis, tandem catalytic systems combining multiple functionalities have been explored to further improve selectivity. For example, the Scott group pioneered a tandem hydrogenolysis–aromatisation route using Pt/γ-Al_2O_3 that selectively converts PE into long-chain alkylaromatics at 280 °C, coupling the exothermic hydrogenolysis with endothermic aromatisation to make the overall process thermodynamically favourable.[114] Additionally, selective oxidation strategies have emerged as a promising complementary pathway. Huang *et al.* recently demonstrated a method for transforming PE and PP at approximately 80 % conversion into fatty acids via temperature-gradient thermolysis followed by oxidation over manganese stearate, with the resulting fatty acids further converted into high-value surfactants.[115] Industrial-scale techno-economic analysis suggested economic viability without the need for subsidies, representing a significant step toward practical implementation.

Despite these advances, significant challenges remain in translating these technologies to industrial scale. Feedstock heterogeneity, catalyst deactivation - particularly through coking and poisoning by contaminants such as heteroatoms or metals -, and process economics continue to limit large-scale deployment.[29,80,87] As a result, polyethylene recycling remains dominated by mechanical processes, while chemical recycling strategies are still in the process of maturation.[104]

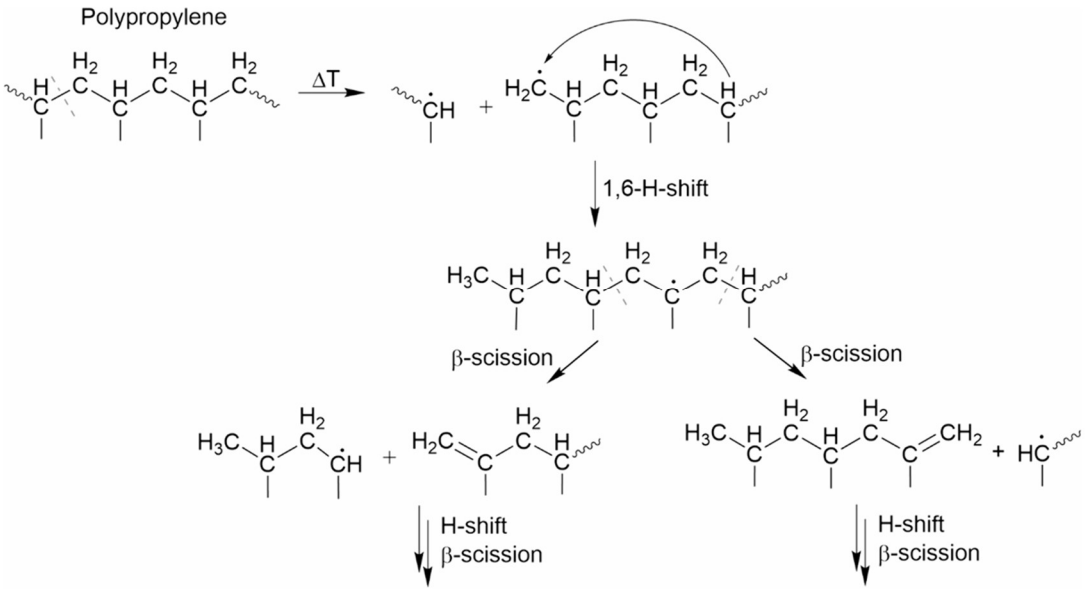
2. Polypropylene

Polypropylene (PP) is one of the most widely used thermoplastics, with applications spanning packaging, automotive components, textiles, and consumer goods, owing to its low density, chemical resistance, and favourable mechanical properties.[5,72,95] Like polyethylene, PP consists of a saturated hydrocarbon backbone. However, the presence of pendant methyl groups on every other carbon introduces tertiary carbon atoms that significantly influence its degradation behaviour (**Scheme 1.1a**, **p16**). In particular, these tertiary sites are highly susceptible to hydrogen abstraction and radical formation, making PP considerably more prone to thermo-oxidative chain scission during melt processing than PE.[6]

As a consequence, mechanical recycling of PP is systematically accompanied by pronounced chain scission, leading to a progressive decrease in molecular weight and embrittlement of the material. This phenomenon has been investigated in several systematic

studies. Douiri *et al*. examined the reprocessing of impact copolymer polypropylene over multiple extrusion–injection moulding cycles and observed that chain scission was evident as early as the first reprocessing loop, as indicated by a continuous increase in melt flow index (MFI).[116] Despite this, injection moulding processability was maintained for at least three consecutive cycles, as the decrease in viscosity at high shear rates partially compensated for the loss in molecular weight. Similarly, Akhras *et al*. confirmed that PP and PE exhibit fundamentally different degradation behaviours during reprocessing: while PP undergoes a gradual decrease in molecular weight due to chain scission, PE grades instead show an opposite trend toward higher molecular weights, consistent with branching and crosslinking reactions.[98] The practical implication is that the number of viable recycling loops for PP is generally more limited than for PE, and that stabilisers (antioxidants) play a critical role in extending reprocessability.[86]

Beyond mechanical recycling, the chemical recycling of polypropylene has been extensively explored, although it remains fundamentally constrained by the absence of hydrolysable functional groups along the polymer backbone. Conventional thermal pyrolysis of PP proceeds via radical chain mechanisms, primarily initiated by homolytic C-C bond cleavage followed by stabilisation of the resulting radicals through intramolecular hydrogen transfer (1,6-H-shift) and subsequent β-scission (**Scheme 1.4**).[117] While robust, such processes yield a broad distribution of hydrocarbons including alkanes, alkenes, and aromatics, which complicates downstream valorisation and typically requires extensive upgrading.[118,119]



Scheme 1.4. Degradation of PP. Thermally-induced homolytic cleavage and radical stabilisation via 1,6-H-shift.[117]

In this context, catalytic pyrolysis using zeolite-based catalysts, particularly ZSM-5, has been extensively studied as a means to steer product distributions toward lighter hydrocarbons and aromatics.[85,86] ZSM-5 promotes cracking through carbocation intermediates on its Brønsted acid

sites, drawing strong parallels with fluid catalytic cracking (FCC) technologies used in the petroleum industry.[74] However, similar to PE, challenges related to catalyst deactivation through coking, as well as sensitivity to feedstock impurities (metals, halogens), remain significant obstacles.[8,80,87]

More recently, catalytic hydrogenolysis has emerged as a promising alternative for PP upcycling under milder conditions. Kots *et al*. demonstrated that Ru/TiO_2 catalysts can convert polypropylene into liquid lubricant-range hydrocarbons at 250 °C under hydrogen pressure, with high selectivity toward branched alkanes.[120] This work illustrated that the methyl branches inherent to PP's structure can be exploited to produce valuable branched hydrocarbons that are difficult to obtain from PE. Sun *et al*. further investigated the structure sensitivity of carbon-supported ruthenium nanoparticles in the hydrogenolysis of waste PP, demonstrating that small, disordered Ru nanoclusters are effective in C–C bond scission, whereas larger nanoparticles promote stereoisomerisation of the polymer backbone, highlighting the importance of catalyst nanostructure in controlling activity, selectivity, and product microstructure.[121]

Furthermore, significant research efforts have targeted selective upcycling approaches that aim to produce high-value chemicals rather than fuels. In a notable example, Xu *et al*. demonstrated that polypropylene can be converted into fatty acids via controlled temperature-gradient thermolysis followed by oxidation.[115] The PP wax yield remained high even when processed in air (eliminating the need for inert gas), and the resulting fatty acids were further converted to surfactants.

Another innovative strategy was recently reported by Le *et al.*, who investigated low-temperature pyrolysis (300 - 320 °C) of PP to tailor the molecular weight distribution of the resulting solid residue while imparting terminal vinylidene functionality - approximately two per chain - that can serve as reactive handles for further chemical transformations.[122] By maintaining solid residue yields above 90 wt% under these mild conditions, this approach retains much of the polymer's value in solid form while enabling its subsequent upcycling into new materials.

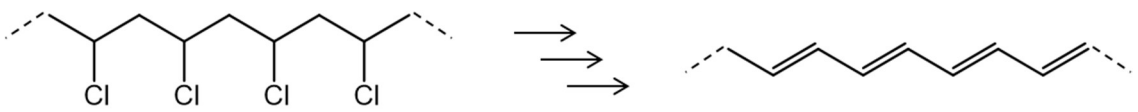
Despite these advances, several challenges remain. Catalyst deactivation, sensitivity to feedstock impurities, and the inherent complexity of radical degradation pathways continue to limit the efficiency and selectivity of PP chemical recycling processes. Consequently, while polypropylene is technically amenable to both mechanical and chemical recycling, achieving efficient and selective closed-loop processes remains a significant scientific and technological challenge.

3. Poly(Vinyl Chloride)

Poly(vinyl chloride) (PVC) is a widely used thermoplastic, particularly in construction and infrastructure applications (pipes, window frames, cables, flooring), where its durability, chemical resistance, and flame-retardant properties are highly valued.[100] In contrast to

polyolefins, PVC contains approximately 57 wt% chlorine along its backbone, which profoundly influences its physicochemical properties and, more critically, its degradation behaviour.[123] In addition, commercial PVC formulations typically include substantial amounts of additives - such as plasticisers (e.g. phthalates), heat stabilisers (metal soaps, organotin compounds), and fillers - resulting in highly heterogeneous materials that further complicate recycling processes.[124]

A defining feature of PVC is its thermal instability, which is dominated by dehydrochlorination reactions occurring at relatively low temperatures, typically between 250 and 320 °C.[125] This process involves the sequential elimination of hydrogen chloride (HCl) molecules and the formation of conjugated polyene sequences along the backbone (**Scheme 1.5**), which are responsible for the characteristic discolouration of degraded PVC. Importantly, this reaction is autocatalytic: the HCl released catalyses further dehydrochlorination, leading to a self-accelerating degradation cascade.[125,126] The mechanistic aspects of this pathway have been extensively studied and although the precise molecular mechanism of polyene propagation remains debated, the initiation step is well established. Dehydrochlorination in PVC is known to initiate at structurally defective sites, particularly allylic and tertiary chlorines formed during polymerisation, which act as labile sites with reduced activation energies for C-Cl cleavage.[127] This intrinsic instability poses major challenges for both processing and recycling, as the release of HCl not only accelerates polymer degradation but also leads to severe corrosion of processing equipment and the potential formation of hazardous by-products.[8,24]



Scheme 1.5. Formation of polyene sequences upon thermal degradation of PVC.

From a mechanical recycling perspective, PVC recycling is feasible for relatively pure and well-sorted waste streams, particularly in rigid PVC applications such as pipes and window profiles, which benefit from long service lives and relatively clean return streams. The European PVC industry has notably established the VinylPlus® programme, which has recycled over 700,000 tonnes of PVC waste in 2024.[128] However, mechanical recycling of PVC faces inherent limitations. The compositional variability of PVC products, particularly between rigid (unplasticised) and flexible (plasticised) formulations, complicates sorting and blending. Furthermore, the presence of legacy additives - including heavy metal stabilisers (lead, cadmium) that are now restricted under European regulations - in older PVC products poses health and environmental concerns during reprocessing.[124]

Thermal treatment routes such as pyrolysis are particularly complicated by PVC's chlorine content, as dehydrochlorination occurs at temperatures well below those required for backbone degradation (250-320 °C vs. > 350 °C).[125] As highlighted in the systematic review by Tian *et al.*, managing chlorine throughout the recycling chain requires a multi-stage approach encompassing pretreatment dechlorination, simultaneous chlorine removal during pyrolysis,

and downstream purification of the hydrocarbon products to avoid contamination and reactor corrosion (**Figure 1.15**).[129] Considerable research has therefore focused on developing effective dechlorination strategies. Hydrothermal treatment has been proposed as a means to remove chlorine under relatively mild conditions. In a recent study, Li *et al.* demonstrated a co-hydrothermal carbonisation approach combining PVC with corncob biomass, where hydroxyl and other active species generated during biomass hydrolysis significantly reduced the activation energy for PVC dehydrochlorination from 190 to 110 kJ/mol, achieving efficient dechlorination at 280 °C with residual chlorine content below 0.05 %.[130]

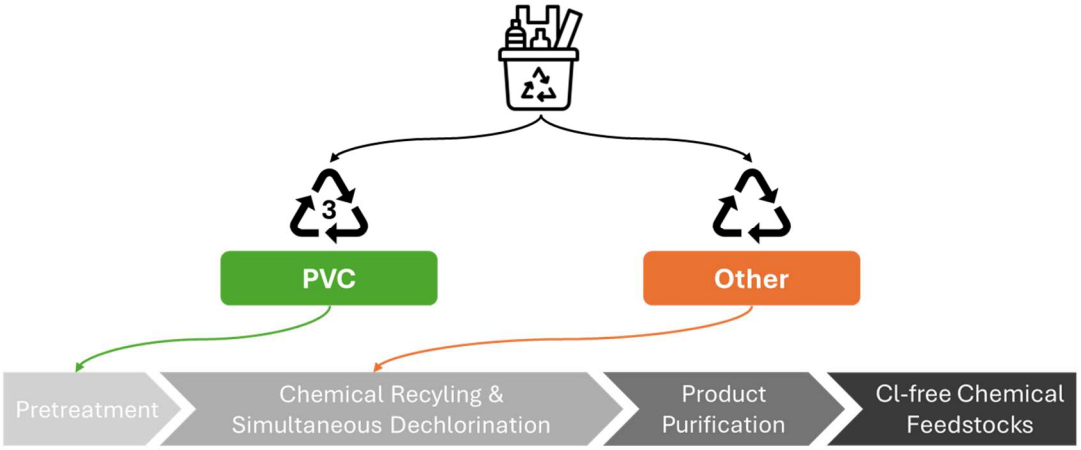


Figure 1.15. Integrated dechlorination strategy for PVC chemical recycling. Adapted from reference 128.

Catalytic approaches have also shown considerable promise. In a notable example, Vos *et al.* at KU Leuven recently reported a novel upcycling route for chlorinated plastics - including PVC, polyvinylidene chloride (PVDC), and chlorinated polyethylene (CPE) - based on consecutive dehydrochlorination-hydrogenation with HCl trapping and olefin metathesis.[131] In this tandem process, $ZnCl_2$-catalysed dehydrochlorination is combined with Ru-catalysed hydrogenation and metal oxide sorbents for HCl capture, converting each chlorinated plastic type into an unsaturated polyolefin (UPO) containing up to 11 double bonds per 100 carbons. The resulting UPOs can then be chemically cleaved via metathesis into α,ω-dienes, which are valuable chemical building blocks. This work represents a significant step toward the integrated chemical recycling of chlorinated waste streams.

In parallel, solvent-based recycling strategies have been explored to selectively dissolve PVC and separate it from other polymers and additives.[73,124] Alshaikh *et al.* demonstrated an innovative approach in which PVC is first fractionated using "green" solvents (acetone, ethyl acetate), and then subjected to sequential dehydrochlorination–hydrogenation cycles.[132] The polyene segments formed during dehydrochlorination are hydrogenated to produce aliphatic $-(CH_2)_n-$ segments, progressively modifying the polymer backbone. This process can be repeated over multiple cycles, progressively transforming PVC into a polyethylene-like material with tuneable properties.

Despite these advances, PVC remains one of the most challenging thermoplastics to recycle due to the combined effects of its chlorine content, additive complexity, and degradation chemistry.[124,125] Future progress will depend on the development of efficient and scalable dechlorination technologies, improved sorting strategies that can distinguish between rigid and flexible PVC formulations (and identify legacy additive content), and potentially the redesign of PVC formulations to enhance their compatibility with circular recycling processes. For a comprehensive perspective on PVC degradation and emerging valorisation pathways, the reader is referred to the recent review by Havaei *et al.*[124]

C. Alternative Valorisation Pathways

While mechanical and chemical recycling technologies aim to recover materials or chemical feedstocks from plastic waste, the limitations discussed in the preceding sections highlight the need for complementary strategies that go beyond conventional recycling paradigms. Mechanical recycling is constrained by material degradation and strict feedstock requirements, whereas chemical recycling often involves high energy consumption, complex processing conditions, and significant economic challenges.[71]

In this context, increasing attention has been directed toward alternative valorisation pathways that seek not only to recover value from plastic waste, but also to transform it into new materials with enhanced or entirely different properties. Rather than focusing solely on closing the loop within existing polymer applications, these approaches explore opportunities to upcycle plastic waste into higher-value products through innovative processing techniques.[133,134] Two strategies emerging as particularly promising are the post-synthesis functionalisation of polymer chains, and the use of mechanochemical processes - including reactive extrusion - to induce chemical transformations under solvent-free conditions.

The post-synthesis functionalisation of polymers involves modifying existing polymer chains to introduce new chemical functionalities or improve material properties (**Figure 1.16**). Unlike depolymerisation-based recycling, this strategy retains much of the original polymer structure while enhancing its performance or applicability.[55] When applied to post-consumer plastic waste, such modifications can effectively transform low-value recyclates into higher-performance materials.[135]

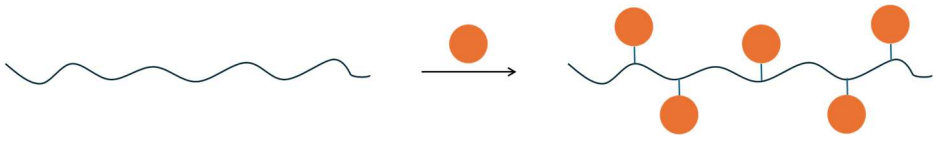


Figure 1.16. Polymer post-synthesis functionalisation. (● = Functional Group).

This approach is particularly relevant for commodity polyolefins such as PE and PP, whose saturated hydrocarbon backbones lack reactive functional groups and exhibit inherently low surface energy, poor adhesion, and limited compatibility with polar materials.[136] These

shortcomings restrict the use of recycled polyolefins in applications requiring interfacial adhesion, paintability, printability, or blending with polar polymers and fillers. As reviewed by Zhao, Li, and Jiang, significant progress has been made in recent years in the development of homogeneous C-H functionalisation methods applicable to polyolefin substrates, enabling the direct installation of C-C, C-O, C-N, C-S, and C-halogen bonds onto the polymer backbone.[135] These strategies encompass thermal and photoinduced radical additions, metal-catalysed C-H oxidation and amination, as well as photoredox and selenium-catalysed approaches, all of which can introduce polar moieties without requiring the development of new polymerisation processes. Importantly, the density of functionalisation can be tuned predictably by adjusting reagent stoichiometry and reaction conditions, allowing optimisation of material properties such as surface adhesion, toughness, and solvent resistance.

A well-established industrial example is the production of maleic anhydride-grafted polyolefins (PE-g-MA, PP-g-MA) via reactive extrusion, a process based on radical C-H addition that has been widely used as a coupling agent between polyolefins and inorganic fillers or natural fibres, as well as a compatibilisers in immiscible polymer blends.[135] In the context of recycling, compatibilisers play a critical role in upgrading mixed polyolefin waste streams. Self *et al.* demonstrated that block copolymer additives can dramatically improve the interfacial adhesion and mechanical properties of PE/PP recycled blends,[66] and Zervoudakis *et al.* showed that such compatibilisers can be effective at very low loadings (< 1 wt%), making the approach economically viable for industrial implementation.[67]

A more demanding challenge arises when waste streams contain chemically dissimilar polymers rather than blends of polyolefins alone. Clarke *et al.* proposed a strategy for reusing mixed-plastics waste by introducing dynamic cross-linkers into polymer mixtures. The specifically designed cross-linkers render immiscible polymer chains compatible and generate *in situ* graft multiblock copolymers, yielding reprocessable thermosets with enhanced tensile strength and creep resistance compared to virgin plastics while maintaining recyclability over multiple cycles.[6,137] More recently, Zhang *et al.* developed a versatile C-H insertion strategy to synthesise polyolefins bearing polar pendant groups, which act as effective compatibilisers for PET/HDPE, PET/LDPE, and PET/iPP blends at loadings as low as 0.5-1.0 wt%.[138] Notably, this approach was demonstrated using post-consumer HDPE bottle caps as the starting material, highlighting its practical applicability.

Beyond compatibilisation, more ambitious functionalisation strategies have been explored to create entirely new material classes from waste polyolefins. In a landmark study, Neidhart *et al.* modified branched polyolefins and post-consumer polyethylene through radical C-H functionalisation using thiosulfonates, followed by crosslinking with polytopic amines to form dynamic covalent polyolefin networks.[139] The resulting materials exhibited a ~4.5-fold increase in toughness and significantly reduced creep deformation compared to the parent LLDPE, while retaining full reprocessability through associative bond exchange of the diketoenamine

crosslinks. This work illustrates how post-synthesis functionalisation can transform commodity plastic waste into performance-advantaged thermoset-like materials that remain compatible with circular processing. More broadly, Hassanian-Moghaddam *et al.* have discussed how such covalent adaptable networks (CANs) applied to polyolefins represent a paradigm shift, combining the recyclability of thermoplastics with the dimensional stability and solvent resistance of crosslinked networks.[6]

Overall, post-synthesis functionalisation offers a powerful complement to conventional recycling strategies. By retaining the polymer backbone while introducing tailored functionalities, this approach enables the creation of materials with properties that can surpass those of the original polymer - from improved interfacial adhesion and blend compatibility to entirely new network architectures. As such, it represents a shift from simple material recovery toward the design of advanced functional materials derived from plastic waste.

In parallel, mechanochemical approaches have emerged as a promising alternative strategy for inducing chemical transformations in polymers. Mechanochemistry relies on the application of mechanical forces (e.g. grinding or shearing), typically delivered through techniques like ball milling or reactive extrusion, to activate chemical reactions, generating localised high-energy conditions that can lead to bond scission, radical formation, and subsequent chemical transformations without the need for bulk solvents. The historical development of polymer mechanochemistry can be traced back to the pioneering work of Staudinger and Heuer in 1934, who first observed that polystyrene undergoes chain scission upon mechanical treatment, as reflected by a decreasing viscosity. However, it is only in the past decade that the field has expanded beyond simple degradation toward controlled and selective chemical transformations.[140]

During mechanical processing, highly reactive intermediates known as mechanoradicals are generated. While these species have traditionally been viewed as undesirable by-products leading to degradation, recent work has demonstrated that they can be deliberately harnessed as reactive handles for polymer functionalisation. As reviewed by Krusenbaum *et al.*, mechanoradicals formed *in situ* during ball milling can undergo radical coupling with functional small molecules.[141] For instance, Kubota *et al.* demonstrated that macroradicals generated from PS, PE, PMMA, and polysulfone react with prefluorescent nitroxide reagents to yield luminescent polymeric materials in a single mechanochemical step.[142] More recently, Skala, Zeitler, and Golder demonstrated that liquid-assisted grinding can graft CF_3 groups onto commercial and waste polystyrene with tuneable functionalisation densities of 0.6-1.0 mol%.[143] These examples illustrate how mechanochemistry is evolving from a mere degradation tool toward a platform for the selective chemical modification of otherwise inert polymer backbones under solvent-free or near-solvent-free conditions.

A key advantage of mechanochemistry lies in its alignment with green chemistry principles: reactions can be conducted without solvents, at ambient or near-ambient temperatures, and with reduced energy input compared to thermal processes.[140] However, challenges remain regarding the scalability of batch mechanochemical techniques, the controlled and site-selective activation of polymer backbones, and the need to direct force-induced reactivity toward desired functionalisation pathways while suppressing competing chain scission and radical-mediated side reactions.[141,144]

Within this framework, reactive extrusion can be considered a continuous and industrially relevant form of mechanochemical processing. In reactive extrusion, chemical reactions are carried out during melt processing in an extruder, where mechanical shear, heat, and intensive mixing collectively promote transformations such as grafting, chain extension, crosslinking, or vitrimerisation.[145] As highlighted in a recent Perspective, reactive melt extrusion leverages polymer processing infrastructure - single- and twin-screw extruders - to achieve solvent-free polymer functionalisation and upcycling, aligning with the principles of green chemistry (**Figure 1.17**).[145,146]

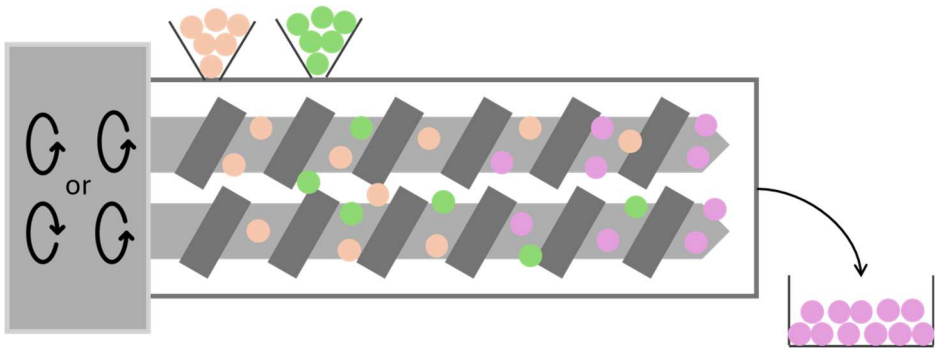


Figure 1.17. Reactive extrusion – Twin-screw extrusion. *Adapted from reference 144*.

Current research focuses on adapting reactive extrusion specifically for plastic waste valorisation. A striking recent example was reported by Vialon *et al.*, who demonstrated that an azidotriazine-based grafting agent enables the direct upcycling of PE/PP waste blends into high-performance materials via reactive extrusion at industrially relevant processing temperatures.[147] The azidotriazine thermally decomposes during extrusion to form a reactive nitrene species, which induces a combination of grafting, oligomerisation, and crosslinking reactions *in situ*. Untreated PE/PP blends, which typically exhibit poor mechanical properties suitable only for low-value applications, were transformed into materials with significantly enhanced tensile strength and modulus, demonstrating that reactive extrusion can overcome the immiscibility-related property losses that plague conventional mechanical recycling of mixed polyolefin waste. In another example, Kar *et al.* demonstrated the scalable vitrimerisation of thermoplastic polyolefins through reactive extrusion, using maleic anhydride grafting followed by transesterification-based dynamic crosslinking to produce reprocessable thermoset-like materials with improved creep resistance.[148]

Overall, alternative valorisation pathways based on post-synthesis functionalisation - including mechanochemical processing and its industrial implementation through reactive extrusion - offer new opportunities for transforming plastic waste into higher-value materials. By focusing on property enhancement and value creation rather than simple material recovery, these approaches extend the scope of plastic waste management and contribute to the development of a more diversified and resilient circular economy.

D. Intermediate Conclusion

This first section has provided an overview of the current landscape of plastic waste management, with a particular emphasis on the recycling technologies available for the three most produced thermoplastics: polyethylene, polypropylene, and poly(vinyl chloride).

Mechanical recycling remains the most established and widely practised approach, offering the advantages of relatively low energy demand, reduced CO_2 emissions, and cost efficiency. However, it is inherently limited by the progressive degradation of material properties upon repeated reprocessing cycles - chain scission in the case of PP, and a combination of chain scission and long-chain branching for PE - as well as by its sensitivity to waste stream contamination and the challenges posed by mixed polymer waste. These limitations often lead to downcycling, restricting the use of mechanically recycled materials for high-quality or food-contact applications.

Chemical recycling technologies offer a complementary pathway by deconstructing polymer chains into molecular building blocks, thereby circumventing the quality limitations of mechanical processes. Among these technologies, catalytic hydrogenolysis has emerged as a particularly promising approach for polyolefin upcycling, enabling the conversion of PE and PP into valuable liquid hydrocarbons, lubricants, or chemical feedstocks under relatively mild conditions. However, challenges related to catalyst stability, feedstock heterogeneity, and process economics remain significant barriers to industrial deployment. For PVC, the high chlorine content and the associated dehydrochlorination reactions introduce additional complexity, requiring dedicated dechlorination strategies before or during chemical processing. Recent advances, such as tandem catalytic systems combining dehydrochlorination, hydrogenation, and metathesis, offer promising but still early-stage solutions.

Beyond conventional recycling, alternative valorisation pathways - including post-synthesis functionalisation, mechanochemical processing, and reactive extrusion - open new perspectives for transforming plastic waste into higher-value materials. These approaches, which focus on property enhancement and chemical modification rather than simple material recovery, have the potential to expand the range of applications for recycled plastics and contribute to a more circular economy (**Table 1.1**).

Table 1.1. Plastic waste upcycling strategies

Strategy	Polymer(s)	Products Obtained	Ref.
Catalytic hydrogenolysis of polyolefins	PE, PP	Liquid hydrocarbons: lubricants, waxes, fuels, and branched/aromatic alkanes	109-114, 120, 121
Thermolysis / pyrolysis-based upcycling	PE, PP	Fatty acids (-> surfactants); solid residues with reactive vinylidene end-groups	115, 122
Dechlorination-based upcycling	PVC (PVDC, CPE)	Unsaturated polyolefins / alpha,omega-dienes; polyethylene-like materials	131, 132
Compatibilization of polymer blends	PE/PP, PET/polyolefin blends	Compatibilized blends and reprocessable thermosets with improved adhesion/strength	135, 66, 67, 6, 137, 138
Radical C-H functionalisation & mechanochemistry	PE, PS, PMMA, polysulfone	Dynamic covalent networks, luminescent polymers, CF3-functionalised polymers	139, 142, 143
Reactive extrusion upcycling	PE/PP blends, polyolefins	High-performance, reprocessable thermoset-like materials with enhanced properties	147, 148

In the context of this thesis, these insights highlight the importance of developing versatile chemical approaches capable of simultaneously addressing the challenges of polyolefin inertness, PVC's chlorine-related constraints, and the heterogeneity of real-world plastic waste streams. The following chapters will build upon this foundation by exploring specific strategies for the chemical valorisation of these materials.

III. Carbon Dioxide Management

As outlined in the introduction, CO_2 constitutes approximately 75 % of global greenhouse gas emissions, with a record 57.1 $GtCO_2e$ emitted in 2023.[12] While transitioning away from fossil fuels represents the most direct route to emission reduction, certain industrial sectors - including aviation, shipping, cement, and steel - involve process emissions that cannot be eliminated through fuel switching alone.[149] Furthermore, the limited remaining global carbon budget means that even aggressive emission reductions may prove insufficient to stabilise

global temperatures within the targets set by the Paris Agreement without complementary removal and capture strategies.[150]

Two broad categories of downstream approaches have therefore emerged: carbon dioxide removal (CDR), which aims to extract CO_2 already present in the atmosphere, and carbon capture, which targets CO_2 at point sources before it reaches the atmosphere. Within the latter category, a further distinction is made between carbon capture and storage (CCS), where the captured CO_2 is permanently sequestered in geological formations, and carbon capture and utilisation (CCU), where CO_2 is converted into value-added products (**Figure 1.18**).[151] These strategies are not mutually exclusive; rather, they form a complementary portfolio whose deployment depends on technological maturity, economic viability, and the specific emission context. This section provides an overview of the current state of the art across these approaches, with particular attention to bioenergy with CCS (BECCS) and direct air capture (DAC) as CDR technologies, point-source carbon capture technologies and their coupling with storage or utilisation, and CO_2-binding organic liquids (CO_2BOLs) as a promising class of capture solvents with potential applications in both CCS and CCU.

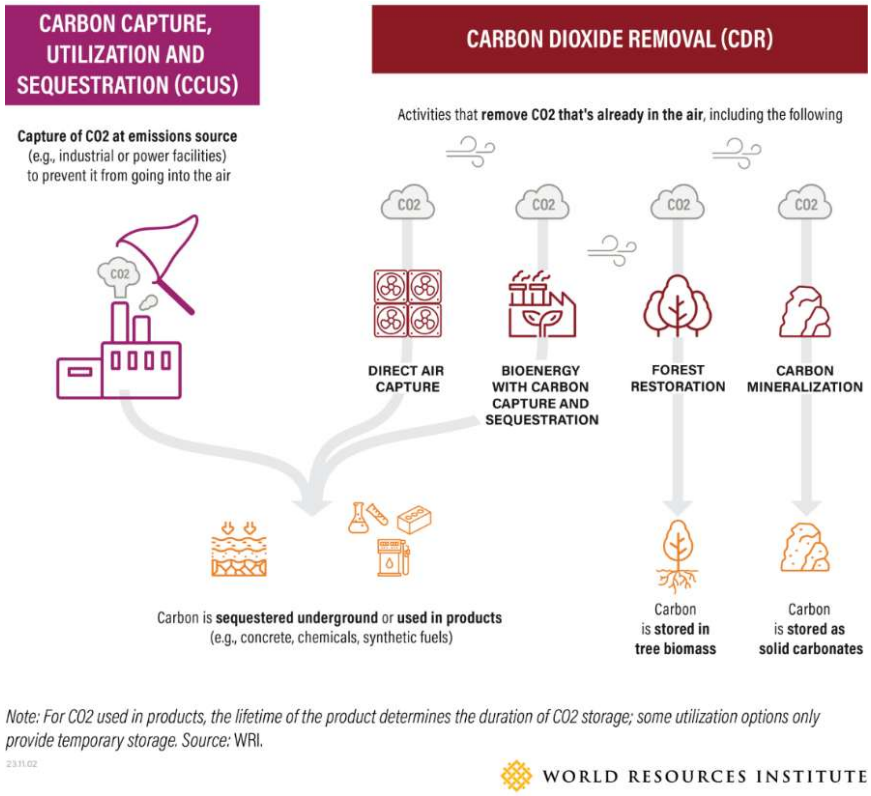


Figure 1.18. Distinction between carbon capture and carbon dioxide removal.[151]

A. Atmospheric CO_2 Removal

Atmospheric CO_2 removal encompasses a range of approaches aimed at reducing the concentration of CO_2 already present in the atmosphere. These can be broadly classified into nature-based ("conventional") and technology-based ("novel") methods.[152] Nature-based CDR includes afforestation and reforestation, soil carbon sequestration, enhanced rock weathering,

ocean alkalinity enhancement, and biochar production. While these approaches currently account for the vast majority of CDR activity - approximately 2 $GtCO_2$ per year, almost entirely from conventional land management - their scalability is ultimately constrained by land availability, permanence uncertainties, and saturation effects.[152,153] Technology-based CDR methods, in contrast, remain nascent but are increasingly viewed as indispensable for achieving net-zero and net-negative emission targets. Among these, BECCS and DAC have received the most attention and are the two technology-based CDR approaches most prominently featured in the mitigation pathways of the Intergovernmental Panel on Climate Change (IPCC).[11] Both approaches are discussed below.

1. Bioenergy with Carbon Capture and Storage

Among technology-based CDR approaches, BECCS has historically occupied the most prominent position in climate mitigation scenarios. It couples bioenergy production with the capture and permanent geological storage of the resulting CO_2. Because biomass absorbs atmospheric CO_2 during growth via photosynthesis, capturing the CO_2 released at the energy conversion step transfers atmospheric carbon into permanent geological storage, yielding net-negative emissions when the full life cycle is managed sustainably (**Figure 1.19**).[153]

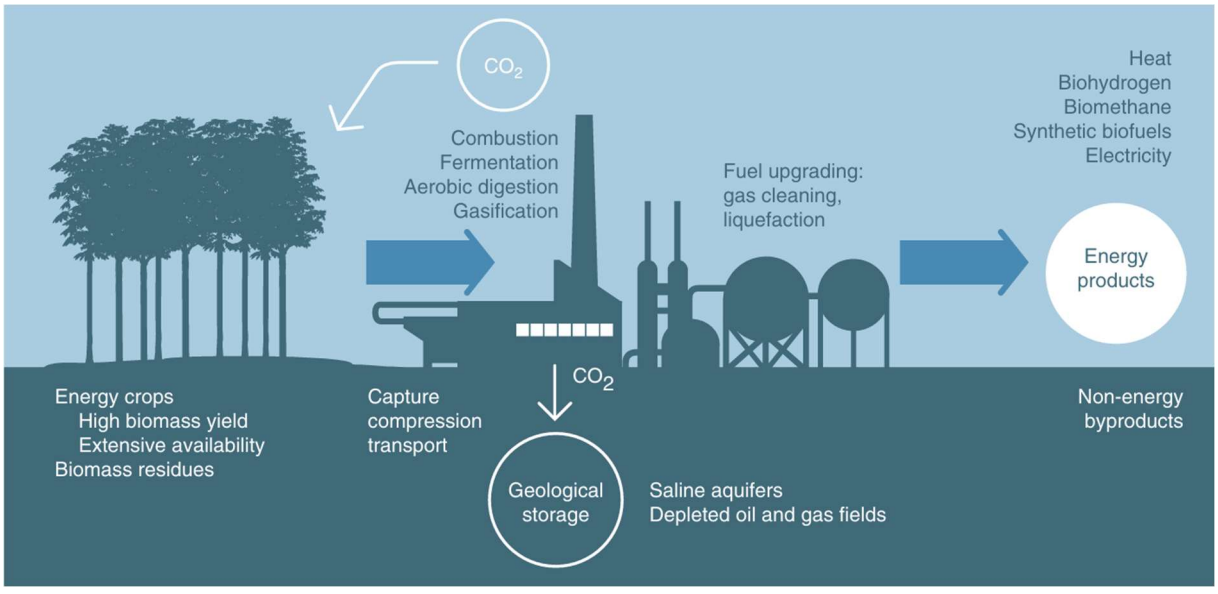


Figure 1.19. Schematic representation of the bioenergy with carbon capture and storage concept.[154]

BECCS can be integrated into several bioenergy pathways, including biomass combustion for power and heat generation, biomass gasification, and bioethanol or biomethane production via fermentation. Each pathway presents distinct CO_2 concentrations in the output stream, which in turn affects the choice and cost of the capture technology applied.[155] For example, CO_2 from bioethanol fermentation is produced at high purity (> 95 %), requiring only dehydration and compression before transport and storage, which makes it the lowest-cost BECCS pathway currently available.[155] In contrast, biomass combustion for power generation produces dilute CO_2 streams (10-15 %), necessitating the same energy-intensive post-combustion capture

technologies (e.g. amine scrubbing) as fossil fuel power plants, with similar energy penalties.[155,156]

BECCS occupies a central place in the Intergovernmental Panel on Climate Change (IPCC) mitigation pathways, contributing a median cumulative removal of approximately 334 $GtCO_2$ by 2100 across scenarios consistent with limiting warming to 1.5 °C.[11] Operational deployment, however, lags far behind this ambition: while the IEA Net Zero Emissions Scenario calls for around 185 $MtCO_2$/year of biogenic capture by 2030, the current project pipeline points to no more than 60 $MtCO_2$/year.[157] As of 2024, only four large-scale BECCS facilities were operating worldwide, all associated with bioethanol production in the United States.[158] The most notable is the Illinois Industrial Carbon Capture and Storage (IL-CCS) project at the ADM corn ethanol plant in Decatur, which captured approximately 1 $MtCO_2$ from fermentation between 2011 and 2014 and injected it into the Mount Simon Sandstone saline aquifer. A 3-year post-closure monitoring programme has since confirmed successful containment with no detected leakage.[159,160] Activity is now expanding beyond bioethanol, particularly in northern Europe: the Danish Energy Agency awarded CCUS contracts to two combined heat and power (CHP) plants in 2023 and to three further BECCS projects in 2024, while Stockholm Exergi is constructing one of the world's largest BECCS facilities at its biomass-fired CHP plant, targeting approximately 0.8 MtCO2/year of permanent removal once operational.[157,161]

Despite its prominence in integrated assessment models, BECCS faces several critical challenges that explain this deployment gap. The most fundamental concerns biomass sustainability: large-scale deployment would require substantial supply, raising concerns about competition with food production, biodiversity impacts, and land-use change emissions. Fajardy and Mac Dowell have shown that the net carbon balance of BECCS is highly sensitive to biomass type and origin, the fate of the original land cover, and the energy penalty of the capture process.[156] Translating these dependencies into a global estimate, Hanssen *et al*. used a spatially explicit model - assessing biomass yields region by region under strict land-use constraints that exclude any expansion onto forests or existing croplands - to derive a biophysical potential of approximately 2.5 $GtCO_2$/year for lignocellulosic-crop BECCS electricity on a 30-year horizon, rising to 40 $GtCO_2$/year over 80 years as plantations mature.[162] These figures represent an upper bound compatible with sustainability constraints. However, in practice, the full life-cycle balance is even less favourable. Cultivation, harvesting, processing, transport, indirect land-use change, and the capture energy penalty can each erode or even negate the negative emission potential.[155,163] Hayat *et al*. found that some configurations, particularly those involving long-distance biomass transport or energy-intensive feedstock processing, are unlikely to deliver net-negative emissions under realistic conditions.[163] This underscores the importance of pathway-specific life cycle assessment rather than blanket assumptions about BECCS carbon negativity.

A further difficulty is structural: BECCS inherits all the infrastructure needs of conventional CCS - transport networks, storage capacity, long-term monitoring - while adding an upstream biological supply chain that is rarely co-located with capture facilities. Regions with the highest biomass potential, such as South America and sub-Saharan Africa, do not generally coincide with those of well-characterised geological storage capacity, such as northern Europe or the United States.[155] This spatial disconnect creates additional CO_2 transport requirements and complicates the allocation of removal credits across the multiple stakeholders involved in the value chain. BECCS deployment is, in this sense, intrinsically dependent on the prior existence of a CCS economy, which itself remains constrained by low investor confidence and by the financial risks associated with full value chain integration.[155]

Fourth, the cost of BECCS varies considerably depending on the pathway. A comprehensive synthesis of the literature reports costs ranging from 15 to 400 $/tCO$_2$, with Minx *et al.* assessing a central range of 100-200 $/tCO$_2$.[150] The lower end of this range corresponds to bioethanol fermentation, where the high purity of the CO_2 stream (> 95 %) minimises capture costs, while the upper end reflects biomass combustion for power generation, where dilute flue gas streams require energy-intensive post-combustion capture with costs comparable to fossil CCS.[150,155] Current policy instruments, including the U.S. 45Q tax credit (85 $/tCO$_2$ for dedicated storage) and the Danish NECCS Fund, are beginning to close the economic gap for lower-cost pathways, but higher-cost applications in power and industry remain uneconomic without additional support.[157,164]

Despite these challenges, BECCS remains a cornerstone of most climate mitigation scenarios due to its unique ability to generate both energy and negative emissions simultaneously.[11] Its deployment is therefore likely to focus first on low-cost, high-purity pathways such as bioethanol and biogas upgrading, before extending to more capital-intensive biomass power and gasification applications as costs decrease and policy frameworks mature.[157]

2. Direct Air Capture

DAC refers to the engineered extraction of CO_2 directly from ambient air, where its concentration of approximately 0.04% (420 ppm) is two to three orders of magnitude lower than in industrial flue gases (5-15%) - corresponding to a CO_2 partial pressure nearly 300 times lower than in a typical coal flue gas.[165,166] This extreme dilution constitutes the fundamental thermodynamic challenge of DAC: the minimum theoretical energy required to separate CO_2 from ambient air is approximately 20 kJ/mol CO_2, compared to about 8.4 kJ/mol CO_2 from flue gas.[167] In practice, actual energy requirements are substantially higher due to process inefficiencies.

Two main technological approaches to DAC have reached commercial or near-commercial deployment: liquid solvent-based systems and solid sorbent-based systems.[165,168]

In liquid solvent DAC, ambient air is passed through large air contactors where it comes into contact with an aqueous alkaline solution, most commonly potassium hydroxide (KOH). The CO_2 reacts with the hydroxide to form potassium carbonate (K_2CO_3), which is subsequently processed through a causticisation loop involving calcium hydroxide ($Ca(OH)_2$) to regenerate KOH and produce calcium carbonate ($CaCO_3$). The $CaCO_3$ is then calcined at temperatures exceeding 900 °C to release a concentrated stream of CO_2 and regenerate the calcium oxide (CaO) sorbent (**Figure 1.20**). This approach, pioneered by Carbon Engineering (now part of Occidental Petroleum), benefits from continuous operation, high single-pass CO_2 capture efficiency, and the use of well-established industrial chemistry. However, the high-temperature calcination step imposes substantial energy requirements and necessitates either natural gas combustion with integrated carbon capture or access to high-temperature heat from alternative sources.[165,169]

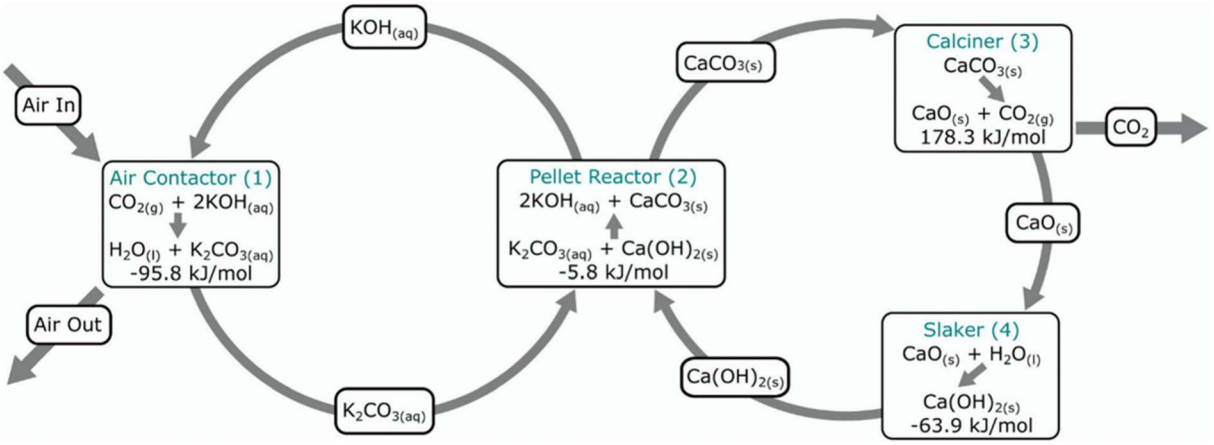


Figure 1.20. Carbon Engineering DAC process.[165,169]

Solid sorbent DAC systems employ a range of porous materials - including amine-functionalised supports, alkali carbonates on silica or activated carbon, and anionic resins - that chemically bind CO_2 from ambient air at near-ambient conditions. Regeneration is achieved through temperature-vacuum swing adsorption (TVSA), typically at temperatures between 80 and 100 °C, releasing a concentrated CO_2 stream while regenerating the sorbent for reuse.[168,170] The Swiss company Climeworks has been the most prominent developer of this approach, operating the Orca plant in Iceland (4,000 tCO_2/year, commissioned in 2021)[171] and the larger Mammoth facility (36,000 tCO_2/year, commissioned in 2024).[172] The modular nature of solid sorbent systems allows for incremental scaling, and the low regeneration temperatures enable the use of waste heat or low-grade geothermal energy. However, these systems are sensitive to ambient humidity and temperature variations, sorbent degradation remains a concern over extended cycling, and the requirement for vacuum adds to energy consumption and equipment complexity.[166,170]

More recently, electrochemical DAC approaches have emerged as a promising third pathway. These systems use electrochemical processes to drive CO_2 capture and release, potentially

offering improved energy efficiency by avoiding thermal regeneration entirely. Companies such as Verdox (USA) and Mission Zero Technologies (UK) have demonstrated pilot-scale electrochemical DAC units, reaching technology readiness level (TRL) 4 as of 2024.[173] While still in the early stages of development, electrochemical DAC could offer fundamental advantages in terms of energy efficiency and process flexibility, although durability and cost challenges remain to be addressed.

As of 2024, global DAC capacity stood at approximately 0.01 $MtCO_2$/year.[168] This figure is orders of magnitude below the 7 to 9 $GtCO_2$/year of removal estimated to be necessary by 2050 to maintain a realistic path toward the 1.5 °C target.[168,174] Current costs for DAC remain high, ranging from approximately 600 to 1,000 \$/tCO_2. Optimistic projections suggest costs could decrease to \$250-\$300/tCO_2 by the end of the decade with the development of multi-megaton-capacity facilities, and potentially reach around \$200/tCO_2 further in the future through technological learning, economies of scale, and industrial maturation - though achieving the more ambitious target of \$100/tCO_2 is considered unlikely without substantial policy support.[175] The U.S. Department of Energy's Carbon Negative Shot initiative has set 100 \$/tCO_2 as the target cost for DAC with durable storage.[168] Achieving such cost reductions will require advances in all three pillars of DAC technology: the air contactor (improving gas–sorbent/solvent contact efficiency and minimising pressure drop), the sorbent or solvent (enhancing CO_2 capacity, selectivity, kinetics, and long-term stability), and the regeneration process (reducing energy consumption and enabling the use of renewable or waste heat sources).[165,166]

Despite these challenges, DAC presents unique advantages that justify continued investment and development. Unlike nature-based CDR, DAC has a small land footprint and can be sited flexibly - ideally near CO_2 storage sites or renewable energy sources - without competing for arable land. It can address both distributed and legacy emissions, and the captured CO_2 can be stored permanently underground (DACCS) or used as a feedstock for synthetic fuels, chemicals, or building materials (DACCU).[165,167] As a result, DAC is increasingly integrated into long-term climate mitigation scenarios as an essential component of the CDR portfolio.

B. Carbon Capture

While DAC addresses CO_2 already dispersed in the atmosphere, carbon capture from point sources targets emissions at their origin - typically large industrial facilities and power plants where CO_2 concentrations are significantly higher (2-30 %) than in ambient air.[176] This concentration advantage translates into lower thermodynamic and practical energy requirements for separation, making point-source capture a more immediately cost-effective strategy for large-scale emission reduction. According to the International Energy Agency (IEA), as of the first quarter of 2025, just over 50 $MtCO_2$/year of capture capacity was in operation globally, with the project pipeline suggesting that this could grow to approximately 430 $MtCO_2$/year by 2030.[177] Three main technological approaches have been developed for point-

source carbon capture: post-combustion capture, pre-combustion capture, and oxy-fuel combustion capture.[137,178,179]

Post-combustion capture involves the separation of CO_2 from the flue gas produced after combustion in conventional power plants or industrial processes. Because the CO_2 is dilute (typically 10-15 % in coal-fired plants, 3-4 % in gas-fired plants) and at low pressure, chemical absorption using aqueous amine solutions - most commonly monoethanolamine (MEA) at 30 wt% - is the dominant technology.[179,180] In this process, flue gas is contacted with the amine solution in an absorber column, where CO_2 reacts exothermically with the amine to form carbamate and bicarbonate species. The CO_2-rich solvent is then heated in a stripper column to approximately 120-140 °C to reverse the reaction and release a concentrated CO_2 stream for compression, while the regenerated solvent is recycled (**Figure 1.21**). Post-combustion capture is the most technologically mature approach and offers the critical advantage of being retrofittable to existing infrastructure without requiring fundamental modifications to the combustion process.[179,181] However, the major drawback of MEA-based capture is its high energy penalty: solvent regeneration consumes approximately 3.6-4.0 GJ/tCO_2, translating into a 9-13 % reduction in net plant efficiency.[179,180] This substantial energy consumption, combined with issues of solvent degradation, corrosion, and amine emissions, has driven extensive research into advanced solvents, sorbents, and membranes aimed at reducing the parasitic energy load.[179,181]

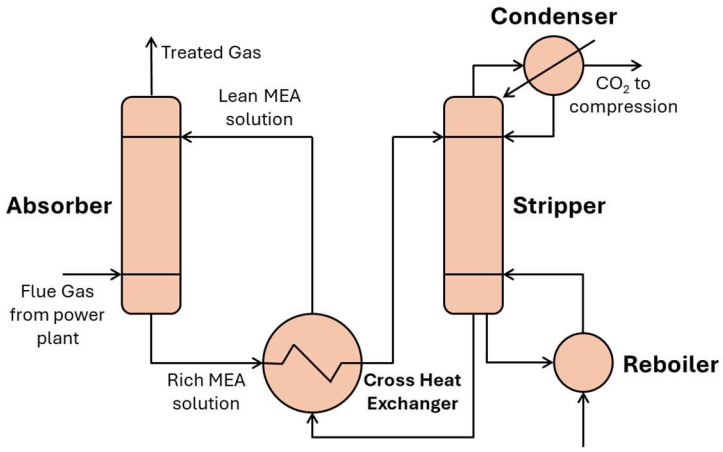


Figure 1.21. Post-combustion capture process based on chemical absorption. Adapted from reference 181.

Pre-combustion capture is primarily applicable to integrated gasification combined cycle (IGCC)[‡] power plants and hydrogen production facilities. In this approach, the fuel (coal or natural gas) is first converted to syngas (CO + H_2) through gasification or reforming. The CO component is then shifted to CO_2 via the water-gas shift (WGS) reaction, producing a gas stream with high CO_2 (35-40 %) and H_2 concentrations. The CO_2 is separated - typically using physical

[‡] IGCC is a process that combines gasification of organic feedstock to produce synthesis gas with a combined cycle system that recovers exhaust heat to generate additional electricity, resulting in higher efficiency and reduced carbon dioxide emissions.[182]

solvents such as Selexol (dimethyl ether of polyethylene glycol) or Rectisol (chilled methanol), which exploit the high CO_2 partial pressure - and the remaining hydrogen-rich gas is used for power generation (**Figure 1.22**).[176,179] The higher CO_2 concentration and pressure in pre-combustion systems yield a greater thermodynamic driving force for separation, potentially reducing the energy penalty compared to post-combustion capture.[176] However, the capital cost of the upstream gasification or reforming infrastructure is significantly higher, and the technology is not readily retrofittable to existing combustion-based plants.[179]

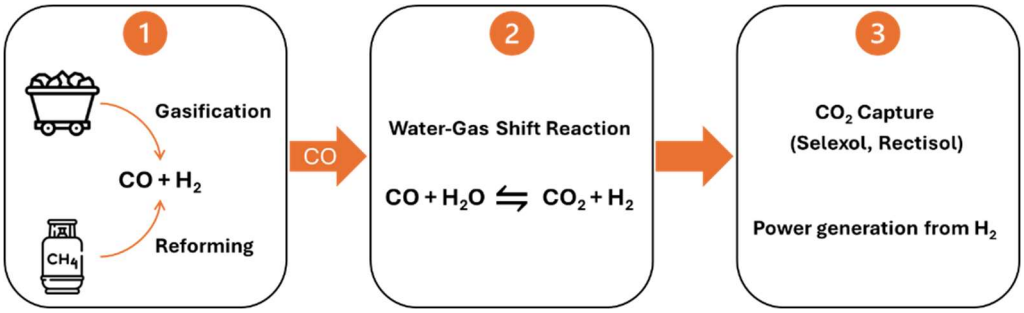


Figure 1.22. Pre-combustion capture approach.

Oxy-fuel combustion replaces air with a mixture of pure oxygen and recycled flue gas as the combustion oxidant, resulting in a flue gas composed primarily of CO_2 (up to 90 % on a dry basis) and water vapour. A simple condensation step then yields a high-purity CO_2 stream ready for compression and storage.[179,180] The elimination of nitrogen from the combustion environment not only simplifies CO_2 separation but also significantly reduces NO_X emissions.[180] The principal drawback is the energy-intensive cryogenic air separation unit (ASU) required to produce the oxygen feed, which imposes a substantial parasitic load on the power plant.[176,179,180] Research efforts are therefore focused on developing more efficient oxygen production technologies, such as ion transport membranes.[183]

Each capture approach offers distinct advantages and faces specific challenges. Post-combustion capture remains the most widely deployed due to its retrofitability and technological maturity, with capture costs typically ranging from 36 to 111 \$/tCO_2 depending on the CO_2 source concentration and the specific process configuration.[184] Pre-combustion capture can achieve lower marginal capture costs in greenfield IGCC installations, though higher capital investments are required.[184] Oxy-fuel combustion offers potentially high capture rates (> 95 %) with simplified downstream CO_2 purification but remains less commercially mature than the other two approaches.[180]

Regardless of the capture configuration (post-combustion, pre-combustion, or oxy-fuel), the actual separation of CO_2 from the gas mixture relies on one or more separation technologies. Five principal methods have been developed to varying degrees of technological maturity: chemical or physical absorption and adsorption, membrane separation, cryogenic separation, and chemical looping (**Figure 1.23**).[179,185]

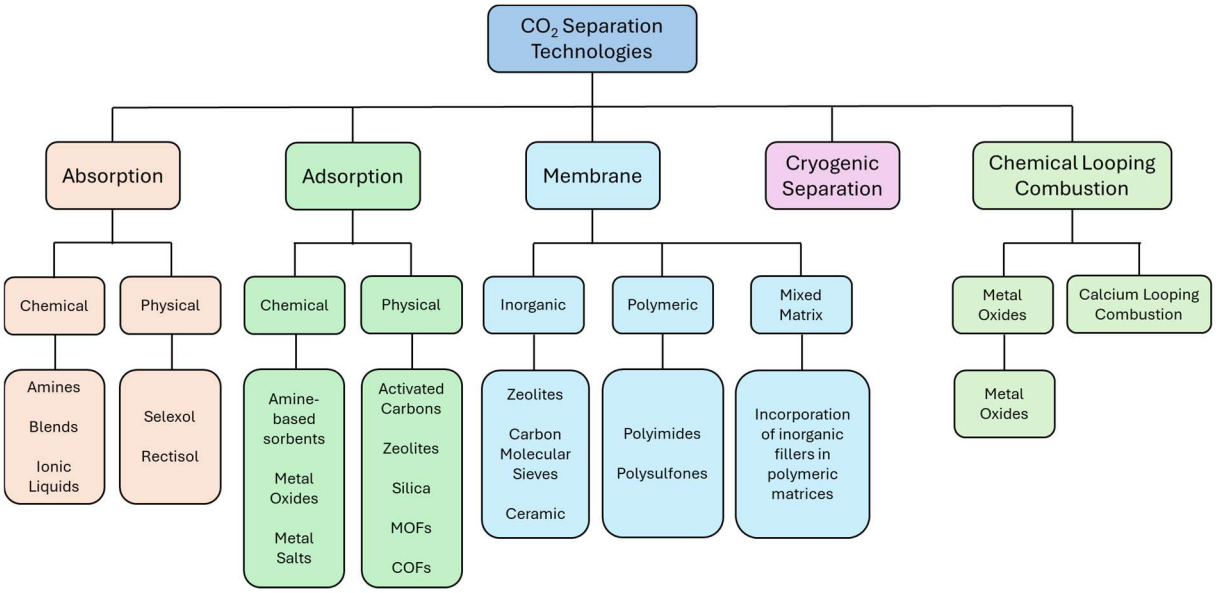


Figure 1.23. CO_2 separation technologies. Adapted from reference 186.

Chemical absorption is the most technologically mature and widely deployed CO_2 separation method at industrial scale. As introduced above, it relies on the reversible chemical reaction between CO_2 and a liquid solvent - most commonly an aqueous solution of a primary or secondary alkanolamine such as monoethanolamine (MEA, 30 wt%) - in an absorber-stripper configuration.[179,180] The CO_2-rich solvent is subsequently heated in a regeneration column (typically at 120-140 °C) to release a concentrated CO_2 stream and regenerate the solvent for reuse. While MEA-based absorption achieves high capture rates (> 90 %) and is compatible with a wide range of CO_2 partial pressures, its high regeneration energy (3.6-4.0 GJ/tCO_2), solvent degradation in the presence of oxygen and sulphur compounds, equipment corrosion, and fugitive amine emissions constitute significant drawbacks.[179–181,186] To address these limitations, considerable research effort has been directed toward the development of advanced solvents, including sterically hindered amines (e.g., 2-amino-2-methyl-1-propanol, AMP), blended amine systems (e.g. MEA/MDEA (methyldiethanolamine), piperazine/MDEA), and phase-change solvents that undergo liquid-liquid phase separation upon CO_2 loading, allowing only the CO_2-rich phase to be sent to the stripper.[186,187] Phase-change absorbents have demonstrated the potential to reduce regeneration energy to approximately 1.7-2.0 GJ/tCO_2.[187] Additionally, non-aqueous solvents - including ionic liquids and CO_2-binding organic liquids (CO_2BOLs), which are discussed in detail in a later section - have attracted increasing attention due to the elimination of the water-related energy penalty.[188]

Physical absorption is preferred when the CO_2 partial pressure is high, as in pre-combustion capture or natural gas processing. In contrast to chemical absorption, physical solvents such as Selexol (dimethyl ether of polyethylene glycol) or Rectisol (chilled methanol) dissolve CO_2 without chemical reaction. The absorbed CO_2 can then be released by reducing the pressure (pressure swing) rather than by heating, resulting in lower regeneration energy requirements.[179]

However, physical solvents are less effective at the low CO_2 partial pressures encountered in post-combustion flue gases.

Adsorption employs porous solid sorbent materials (**Figure 1.24**)[189] to capture CO_2 from gas streams through either physisorption (van der Waals interactions) or chemisorption (chemical bonding with surface functional groups).[185,190] In practice, CO_2 capture by adsorption is operated as a cyclic process alternating between an adsorption step and a desorption (or regeneration) step, during which the captured CO_2 is released and the sorbent restored for reuse. These cycles are classified according to the thermodynamic variable that is modulated to drive adsorption and desorption. In temperature swing adsorption (TSA), desorption is driven by raising the sorbent temperature while pressure swing adsorption (PSA) reduces the total pressure, and vacuum swing adsorption (VSA) applies sub-atmospheric pressure.[191] Conventional adsorbents include activated carbons, zeolites (e.g., 13X, ZSM-5), and silica supports, which offer moderate CO_2 capacities (typically ~ 1-7.5 mmol/g) and fast kinetics but limited selectivity, particularly in the presence of moisture.[185,191] More recently, a new generation of advanced porous materials has attracted significant attention. Metal-organic frameworks (MOFs) - crystalline materials composed of metal nodes connected by organic linkers - exhibit exceptionally high surface areas (up to > 6,000 m^2/g),[192] tuneable pore sizes, and chemically modifiable internal surfaces, enabling CO_2 adsorption capacities exceeding 20 mmol/g under high-pressure conditions.[193,194] Amine-functionalised MOFs and solid amine sorbents (amines grafted onto or impregnated into mesoporous silica supports) combine the selectivity of chemical absorption with the practical advantages of solid handling, and are the basis of several solid sorbent DAC systems discussed earlier.[191,195] Covalent organic frameworks (COFs), which are structurally analogous to MOFs but composed entirely of light elements (C, H, N, O, B) linked by covalent bonds, represent another emerging class of adsorbents with high thermal and chemical stability.[196] Despite these advances, challenges related to sorbent stability over extended cycling, scalability of synthesis, and competition from water vapour remain significant barriers to large-scale deployment of adsorption-based CO_2 capture.[167,185]

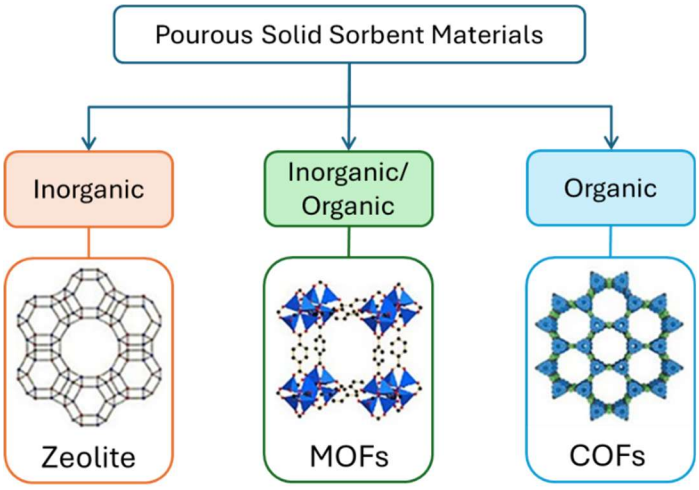


Figure 1.24. Classification of porous solid materials for CO_2 adsorption. Adapted from reference 189.

Membrane separation exploits differences in the permeability of gas components through a semi-permeable barrier to achieve CO_2 separation.[197] Membranes offer several attractive features: continuous operation without the need for chemical reagents or thermal regeneration, compact footprint, modularity, and the potential for low energy consumption.[197,198] CO_2 separation through membranes is driven by the partial pressure difference across the membrane (the transmembrane driving force) and depends on two key material properties: permeability (the rate at which CO_2 passes through the membrane) and selectivity (the preferential permeation of CO_2 over other gases, particularly N_2 or CH_4).[198] Membrane materials are broadly classified into three categories: polymeric membranes (e.g. polyimides, polysulfones, polymers of intrinsic microporosity), inorganic membranes (e.g. zeolite, carbon molecular sieve, ceramic), and mixed-matrix membranes (MMMs), which incorporate inorganic fillers (zeolites, MOFs, or other nanoparticles) within a polymer matrix to combine the processability of polymers with the superior separation properties of inorganic materials.[197,198] A fundamental trade-off exists in membrane design between permeability and selectivity, described by the Robeson upper bound: materials with high gas permeability tend to exhibit lower separation selectivity, and vice versa (**Figure 1.25**).[197,199,200] Recent research has focused on surpassing this upper bound through the development of thermally rearranged polymers, ultra-thin composite membranes, and facilitated transport membranes incorporating CO_2-reactive carriers (e.g. amines, carbonate salts, ionic liquids).[197,198] At the industrial level, membrane-based CO_2 capture has been commercially deployed for natural gas sweetening and biogas upgrading, where CO_2 concentrations are relatively high (> 20 %). For post-combustion capture, where the low CO_2 partial pressure in flue gas reduces the transmembrane driving force, multi-stage membrane configurations or hybrid membrane-absorption systems are being investigated to achieve the required capture rates and purity.[198] Recent techno-economic analyses have shown that optimised membrane systems could reduce capture costs to approximately 57 \$/tCO_2 for natural gas combined cycle applications - a 55 % reduction compared to conventional amine-based capture.[201]

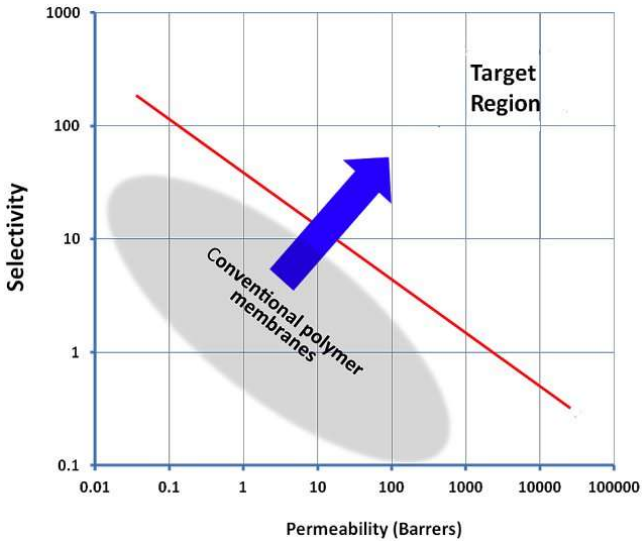


Figure 1.25. Robeson's upper bound for gas separation.[202]

Cryogenic separation involves cooling and compressing the gas mixture to temperatures at which CO_2 condenses or solidifies (desublimation), allowing it to be physically separated from the remaining gases.[179,203] This approach can yield very high-purity CO_2 (> 99.9 %) in liquid form, ready for transport without further compression.[203] However, the substantial refrigeration energy required makes it economically viable only for gas streams with high CO_2 concentrations (> 50 %), such as those produced by oxy-fuel combustion or certain industrial processes.[203,204] In addition, the presence of impurities such as water and gas traces can cause operational problems (e.g. frost formation, plugging) that require upstream conditioning.[205,206] Cryogenic processes are therefore most commonly used in combination with other separation technologies rather than as standalone capture solutions.[207]

Chemical looping combustion (CLC) represents a fundamentally different approach to carbon capture in which CO_2 separation is inherent to the combustion process itself, rather than being performed as a downstream operation.[208,209] In CLC, the fuel does not come into direct contact with air. Instead, a solid oxygen carrier - typically a metal oxide such as Fe_2O_3, NiO, CuO, or Mn_3O_4 - is circulated between two interconnected reactors.[208,210] In the fuel reactor, the oxygen carrier is reduced by the fuel, producing a flue gas consisting almost exclusively of CO_2 and H_2O. A simple condensation step then yields a concentrated CO_2 stream. In the air reactor, the reduced oxygen carrier is re-oxidised by air, regenerating it for the next cycle (**Figure 1.26**). Because nitrogen from the air never mixes with the combustion products, no energy-intensive gas separation step is required.[208–210] This inherent separation gives CLC the potential for uniquely low energy penalties and costs for CO_2 capture compared to conventional post-combustion methods.[208–210] Research and development in CLC has progressed significantly over the past two decades, with pilot- and demonstration-scale studies validated across diverse fuels and reactor configurations, including interconnected fluidised beds, packed beds, moving beds, and rotating reactors.[208,210] The main challenges concern the development of oxygen carriers that combine high oxygen transport capacity, fast redox kinetics, mechanical stability (resistance to attrition, sintering, and agglomeration), and low cost over extended operation.[208,209,211] Iron-based carriers (ilmenite, natural iron ores) and manganese-based oxygen carriers have attracted particular interest due to their low cost, availability, and environmental compatibility, while copper-based carriers offer the unique ability to release gaseous oxygen in the fuel reactor (chemical looping with oxygen uncoupling, CLOU).[208–210] Despite significant progress, critical challenges remain - including oxygen carrier durability, reactor scale-up, and system integration under industrial conditions - and further development toward large-scale commercial deployment is required.[208–211]

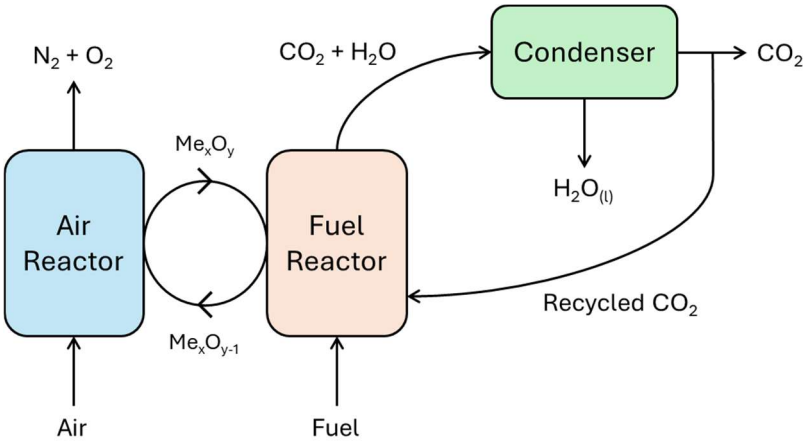


Figure 1.26. Idealised schematic description of the CLC process. Adapted from reference 204.

Once captured, CO_2 must either be permanently stored or converted into useful products. The following sub-sections examine these two complementary strategies.

1. Carbon Capture and Storage

Carbon capture and storage (CCS) refers to the permanent sequestration of captured CO_2 in geological formations, thereby preventing its release into the atmosphere. The complete CCS chain comprises three steps: capture (discussed above), transport, and geological storage.[158,212]

Following capture, CO_2 is compressed to a supercritical or dense phase (typically above 7.4 MPa)[213] and transported to the storage site. The choice of transport mode depends on the distance, volume, and geographical constraints. The two main options for large-scale CO_2 transport are pipeline and ship, although for short distances and small volumes, truck or rail transport are also possible.[214] The vast majority of CO_2 transportation is expected to occur via pipeline. In fact, several CO_2 pipeline networks are already in operation, particularly in North America, where more than 8,000 km of onshore CO_2 pipelines support enhanced oil recovery (EOR) operations.[214] However, ship transport may be preferable over long distances (> 1,500 km) and is emerging as a viable option for offshore storage and cross-border CO_2 trade.[212]

Geological storage of CO_2 relies on injecting the compressed CO_2 into deep subsurface formations - typically at depths exceeding 800 m, where temperature and pressure conditions maintain CO_2 in a supercritical state with density approaching that of a liquid. Three main types of geological formations are considered suitable for CO_2 storage: deep saline aquifers, depleted oil and gas reservoirs, and unmineable coal seams.[213,215]

Deep saline aquifers represent the largest potential storage resource globally. These porous and permeable sedimentary formations, saturated with brine and sealed by impermeable caprocks, offer vast storage capacities estimated in the thousands of gigatonnes of CO_2.[213] The Sleipner project in Norway, operational since 1996, was the first commercial-scale CO_2 storage project in a saline aquifer and has successfully injected more than 16 Mt CO_2 over its first twenty years, with extensive monitoring confirming containment integrity.[216,217]

Depleted oil and gas reservoirs benefit from well-characterised geology and existing infrastructure, including wells and surface facilities. Their proven ability to trap hydrocarbons over geological timescales provides confidence in seal integrity. Moreover, CO_2 injection into depleted or partially depleted reservoirs can serve a dual purpose through enhanced oil recovery (CO_2-EOR), where the injected CO_2 miscibly displaces residual oil, increasing production while simultaneously achieving permanent storage. However, the presence of legacy wellbores constitutes a potential leakage pathway that requires careful assessment and remediation.[213,218]

Four primary trapping mechanisms contribute to the long-term security of geological CO_2 storage (**Figure 1.27a** and **b**): structural trapping (physical containment beneath an impermeable caprock), residual trapping (immobilisation of CO_2 as disconnected droplets in pore spaces), solubility trapping (dissolution of CO_2 in formation brine to form carbonic acid), and mineral trapping (reaction of dissolved CO_2 with formation minerals to precipitate stable carbonate phases).[213,219] These mechanisms operate over different timescales, with structural trapping dominating in the short term and mineral trapping providing the most permanent form of storage over thousands to millions of years (**Figure 1.27c**).

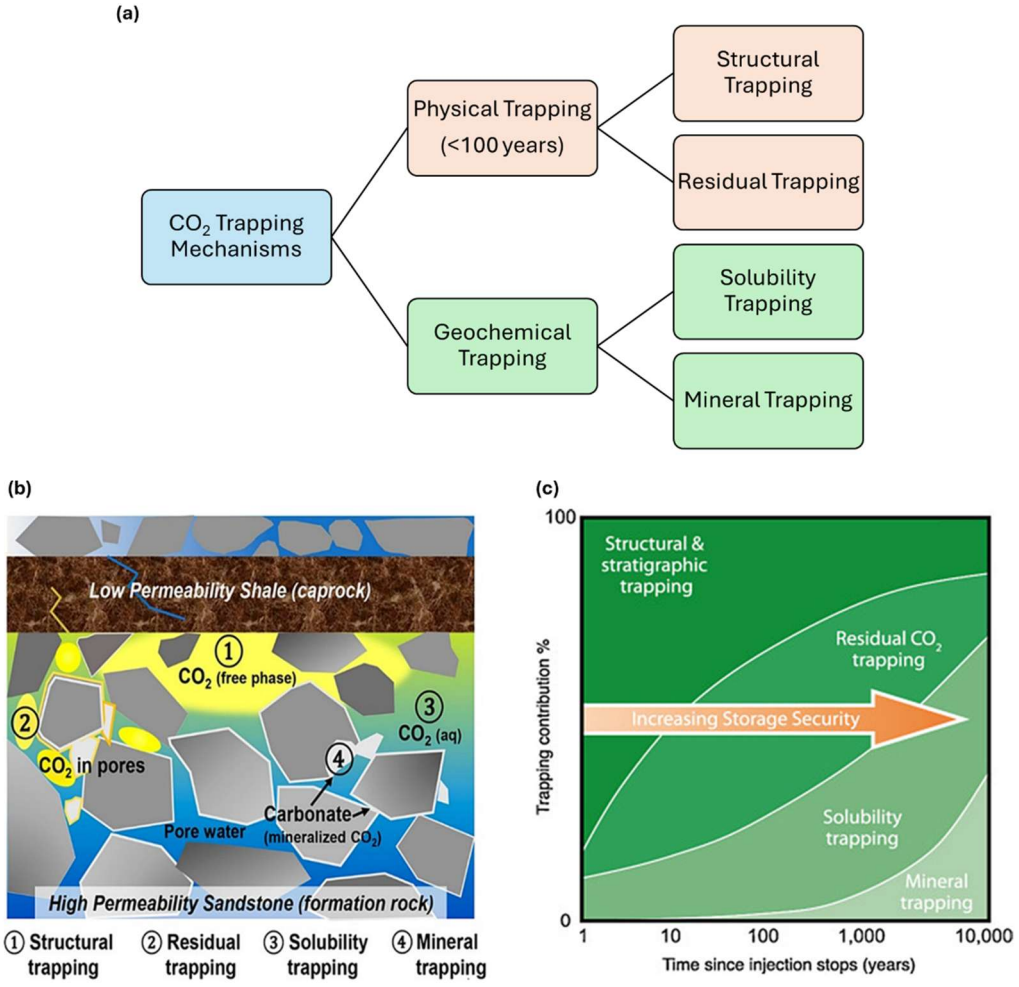


Figure 1.27. Geological CO_2 storage trapping mechanisms. (a) Classification (Adapted from reference 209), **(b)** Schematic representation,[219] and **(c)** Performance over time.[219]

A recent analysis published in *Nature* by Gidden *et al.* established a risk-based estimate for the prudent planetary limit of geological CO_2 storage at approximately 1,460 (1,290-2,710) $GtCO_2$, demonstrating that while substantial capacity exists, it is finite and must be treated as a limited intergenerational resource.[220] This study further showed that only stringent near-term emission reductions can lower the risk of exceeding this limit before 2200, underscoring the need for CO_2 storage to complement - not replace - emission reduction efforts.

Despite the theoretical promise and several successful large-scale demonstrations, CCS deployment has been slower than initially anticipated. As of early 2025, operational CCS capacity stood at approximately 50 $MtCO_2$/year - a fraction of the gigatonne-scale deployment envisioned in most climate stabilisation scenarios.[177] Key barriers include high capital costs, long project development timescales, the absence of robust carbon pricing in many jurisdictions, public acceptance concerns (particularly for onshore storage), and residual uncertainties regarding long-term containment integrity and liability frameworks.[212,221] Monitoring, verification, and accounting (MVA) frameworks remain an active area of development, with techniques including seismic surveys, well-based measurements, surface monitoring, and atmospheric detection being deployed and refined.[213]

2. Carbon Capture and Utilisation

Carbon capture and utilisation (CCU) represents an alternative paradigm in which captured CO_2 is not stored underground but is instead used in a broad range of applications. These applications can be broadly classified into two categories : direct utilisation and conversion-based utilisation, where CO_2 is converted to feedstock for the production of fuels, chemicals, polymers, or building materials (**Figure 1.28**).[212,222,223]

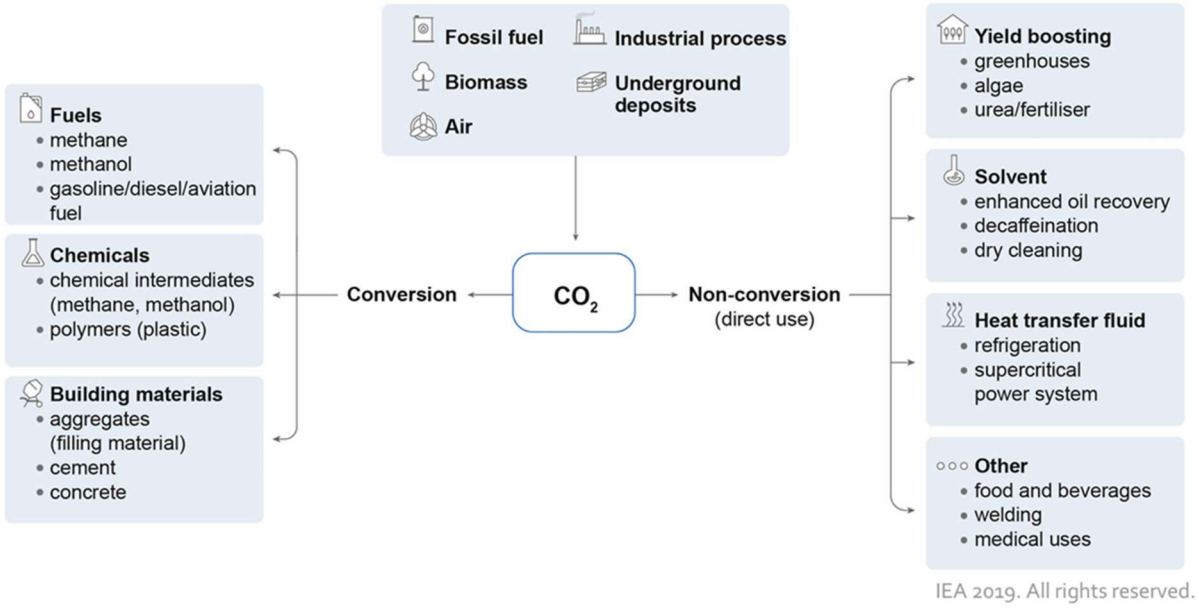
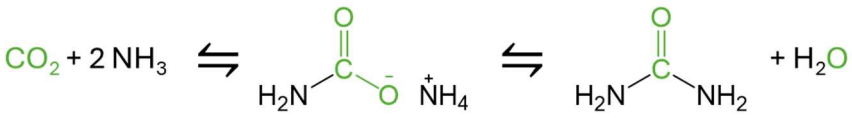


Figure 1.28. Classification of CO_2 utilisation pathways.[223]

According to the IEA's 2019 report *Putting CO_2 to Use*, which presents data for the year 2015, approximately 230 Mt of CO_2 were consumed annually across both direct and conversion-based applications.[223] The single largest consumer was the fertiliser industry, where approximately 130 Mt CO_2 per year is chemically transformed into urea via reaction with ammonia (**Scheme 1.6**).[223,224] Although this figure has not been officially revised since, global urea production has increased substantially from approximately 175 Mt in 2015 to 195.5 Mt in 2023,[225] suggesting that the corresponding CO_2 consumption has likely grown to approximately 140-145 Mt per year, and that total global CO_2 utilisation now exceeds 250 Mt per year.[§] Regardless of the exact current figures, urea synthesis constitutes the most mature and voluminous example of conversion-based CO_2 utilisation, yet it does not result in net emission reduction, as the CO_2 is released when the urea is applied as fertiliser and hydrolysed in soils.[226] Among direct (non-conversion) applications, enhanced oil recovery (discussed above)[218] accounted for 70-80 Mt CO_2 per year, while food and beverage production, metal fabrication, and other industrial uses consumed approximately 20 Mt CO_2 per year.[223] Beyond urea, the current demand for CO_2 in the production of fuels, other chemicals, and building materials through emerging conversion pathways remains negligible by comparison, though this is expected to change as technologies mature and policy frameworks evolve.[223]



Scheme 1.6. Urea synthesis from ammonia and CO_2.

The case of urea illustrates a broader and critically important point: using CO_2 as a feedstock does not automatically equate to reducing emissions. More generally, the climate benefit of a CO_2-derived product depends on five interrelated factors: (i) the source of the CO_2 (fossil, biogenic, or atmospheric), (ii) the product or service being displaced, (iii) the carbon intensity of the energy used for the conversion process, (iv) the duration of carbon retention in the product, and (v) the scale of the opportunity.[223] Unlike CCS, where CO_2 is permanently sequestered, most conversion-based CCU pathways ultimately release the CO_2 back to the atmosphere - either rapidly, as in the case of fuels that are combusted, or over intermediate timescales, as in the case of chemicals such as urea.[223,227] Only applications involving permanent carbon retention - most notably the mineralisation of CO_2 into building materials - can approach the permanence of geological storage.[223] Moreover, for CCU pathways involving fuels and chemical intermediates, the use of low-carbon energy throughout the conversion process is essential; otherwise, the life-cycle emissions of the CO_2-derived product may exceed those of its conventionally produced counterpart, thereby negating any climate benefit.[223,228]

Within conversion-based CCU, the IEA has identified five key categories of CO_2-derived products and services: (i) fuels, (ii) chemicals, (iii) building materials from minerals, (iv) building

[§] Calculations performed based on the stoichiometry of the reaction presented in Scheme 1.6.

materials from waste, and (v) CO_2 use to enhance the yield of biological processes.[223] These categories span a wide range of technological maturity, energy requirements, and carbon retention timescales, as discussed below.

CO_2-Derived Building Materials

The mineralisation of CO_2 into building materials is arguably the most promising CCU pathway from a climate perspective, owing to the combination of permanent carbon storage in thermodynamically stable carbonate phases, low energy requirements for the exothermic carbonation reactions, and the enormous scale of the global construction materials market (~30 billion tonnes of concrete per year).[223,229] Three main approaches have been developed: CO_2-cured concrete, in which CO_2 replaces or supplements steam during the curing process; CO_2-based cement, in which calcium or magnesium silicate clinkers are designed to harden through carbonation rather than hydration; and the conversion of industrial waste streams (e.g. steel slag, coal fly ash) into carbonate aggregates.[229] CO_2 curing exploits the reaction between CO_2 and the calcium silicate phases present in Portland cement or their hydration products to form $CaCO_3$ and amorphous silica gel, a process that not only sequesters CO_2 but can also improve the compressive strength and durability of the cured product.[229,230] Companies such as CarbonCure Technologies (Canada) and Solidia Technologies (USA) have commercialised CO_2-based concrete processes, with CarbonCure's technology deployed in over 800 concrete plants worldwide.[229,231] The theoretical potential is substantial - replacing all conventional concrete with CO_2-cured alternatives could create a demand for up to 1,000-1,200 Mt CO_2 per year globally.[223] However, a recent assessment by Myers *et al.* cautioned that the claimed decarbonisation potentials of several commercial mineralisation technologies are overstated when full life-cycle emissions are rigorously accounted for, and that few are currently more economical than CSS for reducing CO_2 emissions.[232]

CO_2-Derived Fuels

CO_2 can be converted into a broad range of synthetic fuels - including methane, methanol, gasoline, and aviation fuels - via catalytic hydrogenation, the reverse water-gas shift (RWGS) reaction followed by Fischer–Tropsch (FT) synthesis, or co-electrolysis (**Figure 1.29**).[223,233] The most technologically mature pathways are the direct hydrogenation of CO_2 to methanol ($CO_2 + 3H_2 \rightarrow CH_3OH + H_2O$) and the Sabatier reaction for methanation ($CO_2 + 4H_2 \rightarrow CH_4 + 2H_2O$), both of which employ heterogeneous catalysts at elevated temperatures and pressures.[234–237] The CO_2 utilisation rates are substantial, with methanol synthesis requiring approximately 1.37 t CO_2 per tonne of product and methanation requiring approximately 2.74 t CO_2 per tonne of product, assuming complete conversion.[223]

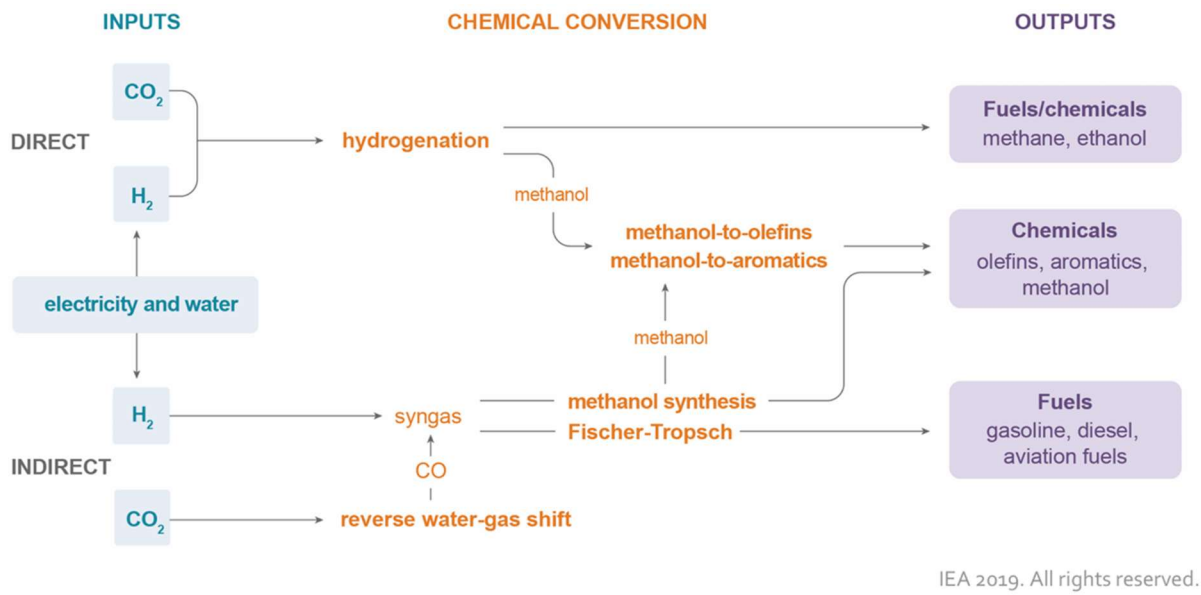


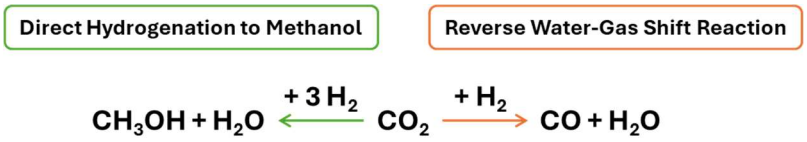
Figure 1.29. Mature conversion routes for CO_2-derived fuels and chemical intermediates.[223]

The primary challenge in producing fuels from CO_2 lies in the molecule's thermodynamic stability ($\Delta G°_f$ = -396 kJ/mol), which necessitates large energy inputs - predominantly in the form of hydrogen - and the use of catalysts to drive the conversion.[224] The overall energy efficiency of the conversion chain ranges from approximately 40 to 55 %, meaning that a significant fraction of the input energy is lost during the process (45 to 60 %). Consequently, the production costs of CO_2-derived methanol and methane are currently two to seven times higher than those of their fossil-derived counterparts, depending on local electricity and hydrogen prices.[223]

Despite these economic barriers, CO_2-derived fuels are attracting increasing attention for applications in which direct electrification is impractical, most notably long-haul aviation. In this context, the European Union's ReFuelEU Aviation regulation has mandated minimum blending shares of synthetic aviation fuels, increasing from 0.7 % in 2030 to 28 % in 2050, providing a demand-side driver for scale-up.[228] Several commercial and demonstration-scale facilities are already in operation. The George Olah Renewable Methanol plant in Svartsengi, Iceland, operated by Carbon Recycling International (CRI) since 2012, produces approximately 4,000 tonnes per year of methanol from geothermal CO_2 (5,500 Mt per year) and electrolytic hydrogen.[238,239] In Germany, the Audi e-gas plant in Werlte has produced synthetic methane from CO_2 and renewable hydrogen since 2013.[223] As of early 2024, around 15 additional large-scale capture facilities targeting CO_2 utilisation for synthetic hydrocarbon fuels were in various stages of planning and construction, with a combined potential to capture and utilise approximately 8 Mt CO_2 by 2030.[228]

From a catalyst development perspective, the industrial standard for CO_2 hydrogenation to methanol remains the $Cu/ZnO/Al_2O_3$ system, originally optimised for syngas-based methanol synthesis.[234,235] However, this catalyst suffers from limited CO_2 conversion and methanol selectivity due to competition from the reverse water-gas shift reaction (**Scheme 1.7**), which leads to catalyst deactivation as well.[235,240] Significant recent research has therefore focused on

alternative catalytic systems, including noble metal-based catalysts,[241] oxides (e.g. In_2O_3-based),[240] hybrid oxides (e.g. ZnO-ZrO_2 solid solutions),[242,243] and bimetallic formulations,[244,245] which have demonstrated improved selectivity and stability under CO_2-rich conditions.[235]

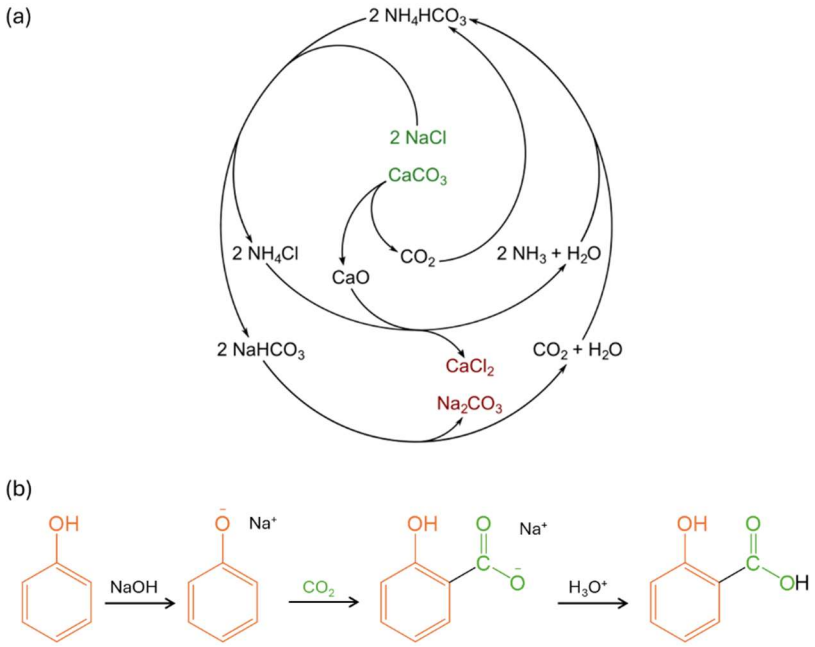


Scheme 1.7. Competition between the direct hydrogenation of CO_2 to methanol and the reverse water-gas shift reaction.

CO_2-Derived Chemicals and Polymers

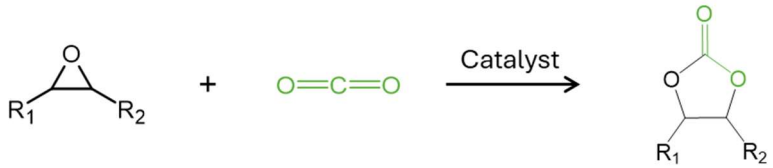
Beyond fuels and building materials, CO_2 can serve as a C_1 building block for the synthesis of a wide range of chemicals, including organic carbonates (cyclic and linear), polycarbonates, polyurethane precursors, carbamates, and carboxylates.[224,233] Several of these transformation pathways require significantly less energy input than the production of fuels, because the carbon atom retains its +4 oxidation state in the product (as in carbonates, carbamates, and polycarbonates) or is only slightly reduced to +3 (as in carboxylates), with the necessary energy being contributed by the electron-rich co-reagent rather than by an external source.[224]

As discussed above, the most established chemical utilisation of CO_2 is urea synthesis, which consumed approximately 130 Mt CO_2 per year as of 2015 and has likely grown since but does not contribute to net emission reduction.[223,226,246] Other mature CO_2-based chemical processes include the production of inorganic carbonates - principally precipitated calcium carbonate (~114 Mt/y) and sodium carbonate (~50 Mt/y) via the Solvay process (**Scheme 1.8a**) - which collectively consume approximately 90 Mt CO_2 per year, and the synthesis of salicylic acid via the Kolbe-Schmitt reaction (**Scheme 1.8b**), which consumes only about 29 kt CO_2 per year.[224,246]



Scheme 1.8. (a) The Solvay process[247] ; **(b)** The Kolbe-Schmitt reaction.[248]

The cycloaddition of CO_2 to epoxides to form five-membered cyclic carbonates (**Scheme 1.9**) is also a well-established process, which benefits from 100 % atom economy, relatively mild reaction conditions, and a wide applicability of the resulting products.[246,249–251] Cyclic carbonates find use as electrolyte solvents for lithium-ion batteries - a rapidly growing market driven by the electrification of transport - as green polar aprotic solvents replacing toxic alternatives such as dimethylformamide (DMF), and as versatile intermediates for the synthesis of polycarbonates, polyurethanes, and fine chemicals.[249–251]

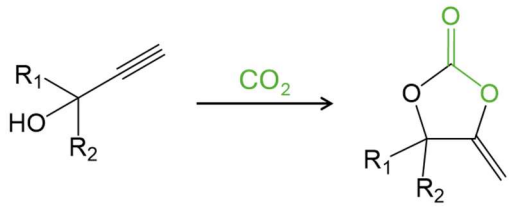


Scheme 1.9. Five-membered cyclic carbonate synthesis from epoxides and CO_2.

This reaction has been the subject of intense catalytic research over the past two decades, with the development of increasingly efficient and selective catalytic systems.[249–251] Early approaches relied on metal-salen complexes - particularly those based on aluminium, chromium, and cobalt - often in combination with co-catalytic nucleophiles.[250,251] More recently, significant progress has been made with metal-organic frameworks (MOFs) and porous organic polymers, which offer high surface areas, tuneable pore environments, and the possibility of incorporating catalytically active sites directly into the framework structure.[249–251] A particularly successful design strategy in this context is the development of fully heterogeneous bifunctional catalysts in which a Lewis-acidic metal centre and a nucleophilic halide are co-immobilised in close proximity on the same support, exploiting their spatial vicinity to synergistically activate both the epoxide and the CO_2 molecule during the catalytic cycle. Aprile and co-workers have systematically implemented this concept on a variety of platforms - including silsesquioxane

(POSS)-supported metalloporphyrin–imidazolium cross-linked networks,[252,253] multi-walled carbon nanotube-supported metal-phthalocyanine/imidazolium copolymers,[254] and metal-doped imidazolium-functionalised low-dimensional silica nanostructures[255] - consistently demonstrating that the proximity between the two catalytic sites is a key parameter governing activity, selectivity, and recyclability under solvent-free conditions. In parallel, metal-free organocatalytic approaches have gained prominence, including systems based on ionic liquids, hydrogen-bond donors, and strong organic bases such as amidines and guanidines, which can activate both the epoxide substrate and the CO_2 molecule through cooperative mechanisms.[250,251,256]

Beyond catalyst design, the structural diversification of CO_2-derived cyclic carbonates themselves has emerged as a complementary lever to expand their utility in polymer synthesis. A representative example is the development by Gennen *et al.* of α-alkylidene cyclic carbonates obtained directly from CO_2 and propargylic alcohols (**Scheme 1.10**), which display markedly higher reactivity toward nucleophiles than their saturated counterparts and enable the synthesis of regioregular polyurethanes and polycarbonates under milder conditions.[257]



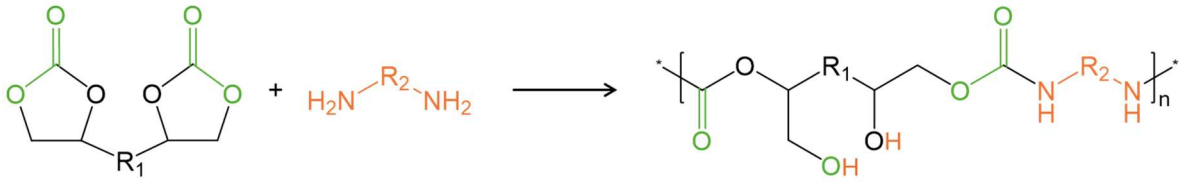
Scheme 1.10. α-Alkylidene cyclic carbonates synthesis from CO_2 and propargylic alcohols.

The copolymerisation of CO_2 with epoxides to produce aliphatic polycarbonates represents another major pathway, yielding materials that can incorporate 30-50 wt% CO_2 and that exhibit properties suitable for a range of applications.[258] The ring-opening copolymerisation (ROCOP) of CO_2 with propylene oxide (PO) to form poly(propylene carbonate) (PPC) and with cyclohexene oxide (CHO) to form poly(cyclohexene carbonate) (PCHC) are the most extensively studied systems, employing catalysts based on zinc, cobalt, or chromium-salen and β-diiminate complexes.[259,260] Successful large-scale PO/CO_2 copolymerisation processes have been developed by companies including Novomer (now part of Saudi Aramco) and Empower Materials.[260]

In a related but distinct approach, the copolymerisation of CO_2 and PO catalysed by double metal cyanide (DMC) catalysts yields poly(ether-co-carbonate) polyols which serve as precursors for polyurethane (PU) production.[260,261] Covestro (Germany) has incorporated such polyols into isocyanate-based PU formulations as soft segments to design flexible foams, commercialised under the cardyon™ brand.[260] A life-cycle analysis by von der Assen and Bardow demonstrated that poly(ether-co-carbonate) polyols with 20 wt% CO_2 content can achieve life-cycle GHG emission reductions of 11-19 % relative to conventional polyether polyols, with the

climate benefits exceeding the amount of CO_2 directly incorporated because the use of CO_2 as a comonomer displaces the production of energy-intensive epoxide monomers.[262]

In addition to these isocyanate-based PU routes, CO_2-derived cyclic carbonates can serve as precursors for the synthesis of non-isocyanate polyurethanes (NIPUs) via polyaddition with diamines, offering a phosgene-free and isocyanate-free route to poly(hydroxyurethane) (PHU) materials (**Scheme 1.11**).[260,263] PHUs differ from conventional polyurethanes by the presence of primary and secondary hydroxyl pendant groups, which impart higher chemical resistance and lower gas permeability but whose influence on water absorption and thermal stability remains debated.[260] Although alternatives to isocyanates are known to provide lower molecular weight polymers - partly because side reactions render the selective synthesis of high M_n PHUs challenging - this pathway has emerged as one of the most promising approaches for producing polyurethanes without using toxic isocyanate reagents while simultaneously incorporating CO_2 as a C_1 building block.[260,263] The synthetic strategies developed within this framework, together with their translation into emerging applications such as self-blowing NIPU foams that exploit the in situ release of CO_2 from cyclic carbonate precursors as a non-toxic, endogenous blowing agent, have been recently reviewed in detail by Grignard *et al.*[264]



Scheme 1.11. PHU synthesis via cyclic carbonate and diamine polyaddition.

More recently, the electrochemical reduction of CO_2 (CO_2RR) has emerged as a particularly promising conversion route, offering the possibility of coupling CO_2 conversion directly with renewable electricity without requiring an intermediate hydrogen production step.[265] Electrochemical CO_2 reduction can yield a wide range of products depending on the catalyst employed and the reaction conditions. On tin (Sn), bismuth (Bi), and lead (Pb) electrodes, the primary product is formate/formic acid (HCOOH), while gold (Au) and silver (Ag) catalysts favour carbon monoxide (CO) production.[265] Copper remains the only elemental catalyst capable of producing significant quantities of multicarbon (C_{2+}) products - most notably ethylene (C_2H_4) and ethanol (C_2H_5OH) - from CO_2, although achieving high selectivity and current density simultaneously remains challenging due to the complex reaction network involving the critical C-C coupling step.[265,266] Recent advances have demonstrated Faradaic efficiencies exceeding 70 % for ethylene production in flow cell configurations, using oxide-derived copper and nanostructured copper–zinc alloy catalysts.[267,268] Solid oxide electrolyser-based CO_2-to-CO conversion is the most technologically mature CO_2 electrolysis pathway, having been commercially deployed by Topsoe under the name eCOs™, with demonstration units commissioned since 2016 and full-size commercial plants under operation.[269] Nevertheless, challenges related to catalyst stability, product selectivity under sustained operation, and the

overall energy efficiency of the process continue to limit large-scale industrial deployment of more complex CO_2RR products.[270]

Outlook for Conversion-Based CCU

Among the five categories of CO_2-derived products, fuels exhibit the greatest volumetric potential (> 5 Gt CO_2/year) owing to the vast global energy market, while building materials offer the greatest net climate benefit per tonne of CO_2 used, primarily because of their low energy requirements and permanent carbon retention.[223] Chemicals and polymers occupy an intermediate position, with significant value creation potential but more limited volumes (1-5 and < 1 Gt CO_2/year, respectively).[223] Biological yield boosting - the use of CO_2 to enhance crop growth in greenhouses or to support algae cultivation - is commercially mature in certain regions (notably the Netherlands, which consumes approximately 5-6 Mt CO_2 per year for horticultural applications) but offers relatively modest scaling potential compared to the other categories.[223]

It is important to emphasise that CCU cannot replace CCS in delivering the gigatonne-scale emission reductions required to meet Paris Agreement targets.[223,227] The expected smaller scale of many CCU opportunities, the temporary nature of carbon storage in fuels and most chemicals, and the early stage of technological and market development all limit the near-term mitigation impact of CCU relative to geological storage.[223] Nevertheless, CCU fulfils a complementary role by providing economic value to captured CO_2, thereby improving the business case for carbon capture infrastructure, and by offering pathways to decarbonise products that will continue to require carbon - such as aviation fuels, platform chemicals, and construction materials - in a net-zero economy.[223,271]

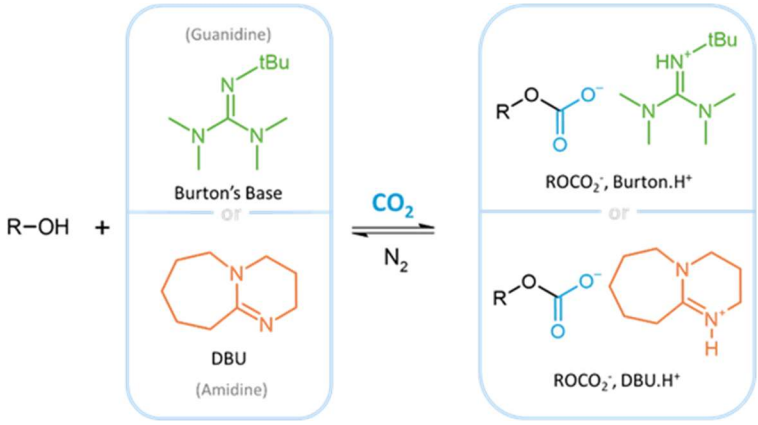
As highlighted above, the chemistry of CO_2 fixation into carbonates and other value-added products is intimately connected to the chemistry of CO_2 capture, particularly through the shared use of strong organic bases - amidines and guanidines - as both capture agents and catalysts. This molecular convergence between capture and utilisation is exemplified by CO_2-binding organic liquids (CO_2BOLs), discussed in the following section, which exploit the reversible reactivity of these nitrogen bases with CO_2 and hold potential for integrated capture-utilisation strategies.

C. CO_2-Binding Organic Liquids

Among the various classes of advanced solvents being developed for CO_2 capture, CO_2-binding organic liquids (CO_2BOLs) represent a particularly intriguing category of switchable solvents with distinctive properties.[188,272] First introduced by Jessop, Heldebrant *et al.* in 2005 as a broader class of CO_2-triggered switchable polarity solvents, CO_2BOLs have since been extensively investigated as potential alternatives to conventional aqueous amine systems for post-combustion CO_2 capture.[273]

CO_2BOLs are anhydrous organic liquids composed of a strong organic base - typically an amidine (e.g. 1,8-diazabicyclo[5.4.0]undec-7-ene (DBU)) or a guanidine (e.g. 1,1,3,3-

tetramethylguanidine (TMG) or Barton's base) - combined with an alcohol.[272,274] Upon exposure to CO_2, the base deprotonates the alcohol, which then reacts with CO_2 to form an alkylcarbonate anion, producing an amidinium or guanidinium alkylcarbonate ionic liquid (**Scheme 1.12**).[188,274] This transformation is fully reversible: the ionic liquid reverts to the original neutral organic mixture upon mild heating (typically 50-90 °C) or by purging with an inert gas, releasing the captured CO_2.[274,275] This dramatic and reversible polarity switch - from a non-polar molecular liquid to a polar ionic liquid - is the defining characteristic of CO_2BOLs and underpins their potential advantages for CO_2 capture.



Scheme 1.12. CO_2BOL formation from Burton's base (top) and DBU (bottom).

The development of CO_2BOLs has progressed through several generations. The first generation consisted of dual-component systems - a mixture of a free base and a free high-boiling alcohol - which exhibited high CO_2 capture capacity (up to 19 wt%)[274] but suffered from high volatility.[272] To address this limitation, single-component CO_2BOLs were developed by covalently linking the base and alcohol functionalities within a single molecule, forming alkanolamidines or alkanolguanidines.[276] These single-component systems exhibited reduced volatility and produced zwitterionic species upon CO_2 binding rather than an ion pair.[276] However, they introduced a new challenge: extremely high viscosity upon CO_2 loading, exceeding 2,000 cP in some cases, which would severely impede mass transfer and pumping in industrial absorber/stripper configurations.[277] A subsequent advancement involved the design of low-viscosity single-component CO_2BOLs based on alkanolguanidines with an imidazolidine core structure, which significantly mitigated the viscosity issue while maintaining favourable capture performance.[188,277]

A distinctive advantage of CO_2BOLs over aqueous amine systems is their anhydrous nature. In conventional MEA processes, a significant fraction of the regeneration duty is not consumed by the CO_2-amine reaction itself but by the surrounding water. Two water-related contributions dominate this penalty: the sensible heat required to raise the temperature of the bulk aqueous solvent from absorber to stripper conditions, and the latent heat associated with its partial vaporisation during steam stripping.[278] By replacing water with a non-volatile organic medium of lower specific heat, CO_2BOLs eliminate both contributions and shift the energy balance of the

capture process in favour of the reaction itself.[278] This intrinsic thermodynamic advantage has motivated further process-level strategies aimed at lowering the regeneration duty beyond what the absence of water alone can achieve. One such strategy is polarity-swing-assisted regeneration (PSAR), introduced by Mathias *et al.*, in which a chemically inert non-polar antisolvent (e.g. hexadecane) is added to the CO_2-loaded CO_2BOL to shift the equilibrium toward CO_2 release by lowering the overall polarity of the mixture.[279] This polarity-driven approach reduced the required regeneration temperature by as much as 73 °C compared to conventional thermal swing, with the antisolvent being easily recovered by cooling the mixture to induce phase separation.[279]

More recent research has focused on further optimising CO_2BOL performance through three-component formulations and the exploration of novel hydroxyl compounds. Yue *et al.* investigated ternary CO_2BOLs comprising DBN (1,5-diazabicyclo[4.3.0]non-5-ene), ethylene glycol, and MEA, achieving an optimal absorption capacity of 0.267 g CO_2/g solvent at 40 °C and 1 bar while elucidating the effect of component molar ratios on the reaction mechanism.[280] Hedayati and Feyzi developed water-insensitive three-component CO_2BOLs based on TMG, an alkanol, and an amine promoter, finding that the preferred TMG/methanol/MEA system (molar ratio 0.3/0.6/0.1) achieved an equilibrium CO_2 loading of 0.396 mol CO_2/mol solvent while demonstrating tolerance to water - a critical requirement for practical flue gas applications where moisture is inevitably present.[281] Spectroscopic characterisation revealed that MEA inhibits the formation of bicarbonate precipitates, thereby maintaining the homogeneous liquid state of the solvent and reducing the energy required for regeneration.[281]

In parallel, computational approaches have played an increasingly important role in CO_2BOL development, both for exploring novel binary formulations and for understanding the molecular origins of solvent behaviour. Anwer *et al.* combined experimental measurements with soft-SAFT thermodynamic modelling to evaluate DBU-based CO_2BOLs in which conventional alkanols were replaced by ether-alcohols (ethylene glycol methyl ether, EGME, and ethylene glycol ethyl ether, EGEE). The ether formulations yielded 10-20 % higher CO_2 uptake and 8 % lower heat of absorption than their alkanol counterparts, and the model identified DBU:EGME (1:2) as the best-performing candidate, with a projected regeneration energy of only 1.87 GJ/tCO_2 - less than half that of aqueous MEA.[282] Whereas Anwer *et al.* used modelling to project performance for a given solvent structure, Cantu *et al.* turned to molecular dynamics (MD) simulations to identify the structural features that determine solvent behaviour in the first place. They showed that the overall hydrogen-bonding topology of the CO_2-loaded zwitterion is a key determinant of viscosity: intermolecular H-bonds between neighbouring zwitterions extend the interaction network and raise viscosity, whereas intramolecular H-bonds localise the charge within a single molecule and reduce it. Building on this insight, they proposed tuning the acid-zwitterion equilibrium to increase the fraction of neutral species, thereby lowering viscosity without compromising CO_2 loading.[283]

Beyond their application in CO_2 capture, CO_2BOLs and related switchable solvents have demonstrated potential in broader chemical contexts, bridging the gap between CO_2 capture and utilisation. Their switchable polarity has been exploited for the extraction and separation of bioactive compounds from complex natural matrices,[284] for the dissolution and processing of biomass - most notably cellulose, which can be regenerated in controlled morphologies or homogeneously modified without recourse to conventional toxic solvents,[285] and as reaction media whose properties can be reversibly tuned by CO_2 addition and removal to facilitate product-catalyst separations.[286]

Despite these promising developments, several challenges must be addressed before CO_2BOLs can achieve industrial deployment. The development of formulations that simultaneously satisfy requirements for low viscosity, high CO_2 capacity, rapid kinetics, and low regeneration energy, together with long-term solvent durability and integration into existing capture infrastructure, all require further investigation.[278,287] Recent techno-economic analyses have begun to quantify these performance targets: comprehensive evaluations of CO_2BOL-based capture processes project costs in the range of $38-47 per tonne CO_2, representing a 12-23% reduction compared to aqueous amine benchmarks, yet further solvent development, process optimisation and testing at larger scales remain necessary to validate these projections and reduce the risks of commercialisation.[288,289]

D. Intermediate Conclusion

This section has provided an overview of the current landscape of CO_2 management, encompassing atmospheric removal, point-source capture, geological storage, chemical utilisation, and advanced capture solvents.

Atmospheric CO_2 removal encompasses both nature-based approaches, which currently account for the vast majority of CDR activity, and technology-based methods such as bioenergy with carbon capture and storage (BECCS) and direct air capture (DAC). BECCS has historically occupied the most prominent position in IPCC (International Panel on Climate Change) mitigation scenarios, yet its operational deployment remains modest: only a handful of large-scale facilities are in operation globally, all associated with bioethanol production in the United States, and the current project pipeline falls well short of the capacity envisaged in IEA (International Energy Agency) Net Zero scenarios. This deployment gap reflects critical challenges related to biomass sustainability, life-cycle emissions, and the inherent dependence on a mature CCS infrastructure. Direct air capture lags even further behind, with only pilot- and demonstration-scale facilities in operation and costs that remain well above those of point-source capture. Nevertheless, DAC is increasingly viewed as indispensable for addressing legacy and distributed emissions. Both liquid solvent and solid sorbent approaches have reached commercial deployment, and emerging electrochemical methods hold promise for further efficiency gains. Neither BECCS nor DAC alone can close the gap between current

emissions and climate targets. Rather, they must be deployed as part of a diversified portfolio of mitigation and removal strategies.

Point-source carbon capture is comparatively more mature in terms of operational capacity, with an established global deployment and a substantial announced project pipeline expected to expand over the coming years. Post-combustion capture using amine-based solvents remains the dominant technology due to its retrofitability, though its high energy penalty continues to drive the search for improved solvents and alternative capture approaches. Carbon capture and storage in geological formations has been demonstrated at scale through long-running projects, and recent risk-based analyses have established a finite but substantial prudent planetary limit for geological storage. Carbon capture and utilisation offers complementary value through the conversion of CO_2 into fuels, chemicals, and materials, although the net climate benefit of CCU pathways depends critically on the carbon intensity of the energy inputs and the durability of the products.

Among advanced capture solvents, CO_2BOLs have emerged as a compelling class of switchable materials whose anhydrous nature eliminates the sensible and latent heat penalties associated with water in aqueous amine systems, thereby shifting the regeneration energy balance in favour of the CO_2-base reaction itself. Recent developments - including ether-based formulations with markedly reduced regeneration energies, water-tolerant three-component formulations and polarity-swing-assisted regeneration strategies - have brought CO_2BOLs closer to practical relevance, with techno-economic analyses projecting capture costs below those of aqueous amine benchmarks.

In the context of this thesis, the CO_2 management landscape highlights the need for materials and processes that can bridge the gap between capture and utilisation. CO_2BOLs, with their switchable properties and tuneable chemistry, are particularly well positioned in this regard. The following chapters will explore specific strategies that leverage these molecular platforms for the development of integrated capture-utilisation approaches.

IV. Conclusion and Objectives of the Work

This first chapter has provided a comprehensive overview of the current state of the art regarding two of the most pressing environmental challenges of the 21st century: the accumulation of plastic waste and the continuously rising atmospheric emissions of carbon dioxide. Although typically addressed as independent problems, both originate from our heavy reliance on fossil resources, and both call for more ambitious and integrated valorisation strategies than those currently available at scale.

On the plastic waste front, mechanical recycling - although widely implemented and economically attractive - suffers from progressive property degradation upon repeated reprocessing and from a limited tolerance toward contaminated or mixed polymer streams,

frequently resulting in downcycling rather than closed-loop recycling. Chemical recycling offers an attractive complement by converting polymer waste back into molecular building blocks but remains hindered by catalyst deactivation, feedstock heterogeneity, and unfavourable process economics. These limitations are particularly pronounced for the three most produced commodity thermoplastics: polyethylene (PE) and polypropylene (PP), whose sensitivity to thermo-oxidative degradation and chain scission upon repeated reprocessing typically restricts their recycled output to lower-value applications, and poly(vinyl chloride) (PVC), whose chlorine content and propensity for dehydrochlorination raise additional safety and compatibility issues. Within this landscape, alternative valorisation strategies - including the post-synthetic functionalisation of polymer chains and their integration into mechanochemical processes such as reactive extrusion - have emerged as particularly appealing pathways, opening the door to upcycling approaches that not only recover material but also create additional value.

With regard to CO_2 management, the persistent growth in global greenhouse gas emissions demonstrates that upstream mitigation alone will not suffice to meet the targets of the Paris Agreement. Downstream strategies encompassing atmospheric CO_2 removal, carbon capture and storage (CCS), and carbon capture and utilisation (CCU) will therefore have to be deployed at increasingly large scales. Among the solvents developed for carbon capture, CO_2-binding organic liquids (CO_2BOLs) have emerged as a particularly promising class of switchable materials. Their anhydrous nature circumvents the energy penalties associated with aqueous amines, while the reactive carbonate and carbamate species formed upon CO_2 binding endow them with a chemistry that extends well beyond mere storage: these species are nucleophilic enough to engage in subsequent transformations, effectively positioning CO_2BOLs at the interface between capture and utilisation.

Bringing these two threads together reveals a compelling opportunity. The very chemistry that drives efficient CO_2 capture by CO_2BOLs can, in principle, be redirected toward the functionalisation of halogenated polymers through nucleophilic substitution, thereby addressing plastic waste valorisation and CO_2 utilisation within a single integrated process. Realising such an approach, however, requires overcoming a series of complementary challenges. On the CO_2BOL side, the nucleophilicity of the CO_2-derived species must be demonstrated and the selectivity of the substitution reaction established on well-defined model substrates, while competing pathways such as base quaternisation and elimination must be kept under control. On the polymer side, the chemical inertness of polyolefins and the fragility of PVC backbones impose the development of mild, selective, and ideally solvent-free halogenation protocols that introduce reactive handles without compromising molecular integrity. Coupling these two research lines defines the overarching objective of the present thesis.

Against this background, the present thesis is structured around three interconnected goals. A first axis is directed toward the preparation of CO_2BOLs and the characterisation of their

reactivity toward simple, well-defined electrophiles used as models. A second axis focuses on the halogenation of polyolefins, with the aim of turning these chemically inert materials into reactive substrates amenable to further modification. The third and final axis brings the two previous lines together: the halogenated polymers are reacted with the CO_2BOLs so as to achieve the upcycling of plastic waste through the covalent incorporation of CO_2. Throughout, particular attention is paid to the environmental and economic viability of the proposed strategies.

V. References

1 S. C. Rasmussen, *Angew. Chem. Int. Ed.*, 2021, **60**, 8012–8016.

2 *Report of the Basic Energy Sciences Roundtable on Chemical Upcycling of Polymers*, U.S. Department of Energy, Office of Science, Nairobi, 2019.

3 P. G. C. Nayanathara Thathsarani Pilapitiya and A. S. Ratnayake, *Cleaner Materials*, 2024, **11**, 100220.

4 A. Chamas, H. Moon, J. Zheng, Y. Qiu, T. Tabassum, J. H. Jang, M. Abu-Omar, S. L. Scott and S. Suh, *ACS Sustainable Chem. Eng.*, 2020, **8**, 3494–3511.

5 *The Circular economy for Plastics - A European Analysis*, Plastics Europe, 2024.

6 D. Hassanian-Moghaddam, N. Asghari and M. Ahmadi, *Macromolecules*, 2023, **56**, 5679–5697.

7 Global Plastic Production (1950 - 2022), https://oer.enviraj.com/charts/global-plastic-production/, (accessed 13 May 2025).

8 K. Ragaert, L. Delva and K. Van Geem, *Waste Management*, 2017, **69**, 24–58.

9 *From Pollution to Solution - A Global Assessment of Marine Litter and Plastic Pollution*, United Nations Environment Programme, 2021.

10 OECD, *Global Plastics Outlook: Economic Drivers, Environmental Impacts and Policy Options*, OECD, 2022.

11 Intergovernmental Panel On Climate Change (IPCC), Ed., *Climate Change 2022 - Mitigation of Climate Change: Working Group III Contribution to the Sixth Assessment Report of the Intergovernmental Panel on Climate Change*, Cambridge University Press, 1st edn., 2023.

12 *Emissions Gap Report 2024: No more hot air … please!*, United Nations Environment Programme, 2024.

13 N. Tangri, *PLOS Clim*, 2023, **2**, e0000100.

14 P. W. Tait, J. Brew, A. Che, A. Costanzo, A. Danyluk, M. Davis, A. Khalaf, K. McMahon, A. Watson, K. Rowcliff and D. Bowles, *Australian and New Zealand Journal of Public Health*, 2020, **44**, 40–48.

15 M. Allsopp, P. Costner and P. Johnston, *Environ. Sci. & Pollut. Res.*, 2001, **8**, 141–145.

16 J. García-Pérez, P. Fernández-Navarro, A. Castelló, M. F. López-Cima, R. Ramis, E. Boldo and G. López-Abente, *Environment International*, 2013, **51**, 31–44.

17 National Research Council (U.S.), Ed., *Waste incineration & public health*, National Academy Press, Washington, D.C, 2000.

18 K. Rogers and I. Jaspers, *Toxicological Sciences*, 2025, **206**, 230–232.

19 M. A. Fayshal, *Heliyon*, 2024, **10**, e40838.

20 D. Crîstiu, F. d'Amore and F. Bezzo, *Computers & Chemical Engineering*, 2024, **180**, 108503.

21 C. W. S. Yeung, J. Y. Q. Teo, X. J. Loh and J. Y. C. Lim, *ACS Materials Lett.*, 2021, **3**, 1660–1676.

22 *Basic Energy Sciences Roundtable - Chemical Upcycling of Polymers*, U.S. Department of Energy, Office of Science, 2019.

23 M. Chanda, *Advanced Industrial and Engineering Polymer Research*, 2021, **4**, 133–150.

24 Z. O. G. Schyns and M. P. Shaver, *Macromol. Rapid Commun.*, 2021, **42**, 2000415.

25 International Organization for Standardization, Plastics — Guidelines for the recovery and recycling of plastics waste (ISO Standard No. 15270:2008), https://www.iso.org/standard/45089.html, (accessed 1 December 2025).

26 W. Liu, J. Wang and M. Habibi, *Process Biochemistry*, 2025, **159**, 82–101.

27 L. Getino, J. A. Revilla-Gómez, L. M. Ariza-Carmona, S. Thijs, C. Didierjean and A. Chamizo-Ampudia, *Bacteria*, 2025, **4**, 44.

28 E. Bezeraj, S. Debrie, F. J. Arraez, P. Reyes, P. H. M. Van Steenberge, D. R. D'hooge and M. Edeleva, *RSC Sustainability*, 2025, **3**, 1996–2047.

29 *Chemical Recycling and the Role of Mass Balance Explained*, Plastics Europe, 2022.

30 R. A. Clark and M. P. Shaver, *Chem. Rev.*, 2024, **124**, 2617–2650.

31 P. F. Albizzati, I. Antonopoulos, D. Caro, J. Cristobal Garcia, L. Egle, P. Gaudillat, G. Foster, S. Manfredi, R. Marschinski, D. Martinez Turegano, E. Pierri, H. Saveyn and D. Tonini, *Development of an EU harmonised model for separate municipal waste collection and related policy support*, European Commission, 2022.

32 M. Dri, P. Canfora, I. Antonopoulos and P. Gaudillat, *Best Environmental Management Practice for the Waste Management Sector*, European Commission, 2018.

33 G. Degli Antoni and G. Vittucci Marzetti, *Ecological Economics*, 2019, **161**, 321–329.

34 S. Serranti and G. Bonifazi, in *Use of Recycled Plastics in Eco-efficient Concrete*, Elsevier, 2019, 9–37.

35 L. E. P. Real, *Recycled Materials for Construction Applications: Plastic Products and Composites*, Springer International Publishing, Cham, 2023.

36 The Plastic Recycling Process, https://plasticsrecycling.org/how-recycling-works/the-plastic-recycling-process/, (accessed 14 January 2026).

37 M. Jansen, A. Feil and T. Pretz, in *Waste Management*, TK Verlag, 2012, pp. 169–175.

38 D. Wiedner and A. Sarkady, Optimal processing of REFUSE DERIVED FUEL | Shredding, screening, sorting | RDF recycling technology, https://www.youtube.com/watch?v=f4X2j9_-yHw, (accessed 14 January 2026).

39 Screening Machines, https://www.spaleck.eu/screening-machines/, (accessed 13 January 2026).

40 How does an Eddy Current Separator Work ?, https://gtekmagnet.com/how-does-an-eddy-current-separator-work/, (accessed 15 January 2026).

41 Y. R. Smith, J. R. Nagel and R. K. Rajamani, *Minerals Engineering*, 2019, **133**, 149–159.

42 W. D. Jr. Callister and D. G. Rethwisch, *Materials Science and Engineering - An Introduction*, Wiley, 10th edn., 2018.

43 S. Van Den Eynde, S. Waumans, T. Dimas, D. J. Díaz-Romero, I. Zaplana and J. Peeters, *Resources, Conservation and Recycling*, 2024, **209**, 107753.

44 E. J. Bakker, P. C. Rem and N. Fraunholcz, *Waste Management*, 2009, **29**, 1712–1717.

45 C. Wang, H. Wang, J. Fu and Y. Liu, *Waste Management*, 2015, **41**, 28–38.

46 M. Saeki, *Particulate Science and Technology*, 2008, **26**, 494–506.

47 T. Längle and G. Maier, in *Springer Handbook of Circular Plastics Economy*, eds. A. Buettner and E. Weidner, Springer Nature Switzerland, Cham, 2025, pp. 375–390.

48 K. Tumu, M. Munshi, K. Vorst and G. Curtzwiler, *Advances in Materials Science and Engineering*, 2025, **2025**, 8041388.

49 *Polyolefin Standard Laboratory Processing Practices*, Association of Plastic Recyclers, 2025.

50 J. M. Soto, M. A. Martín-Lara, G. Blázquez, V. Godoy, L. Quesada and M. Calero, *Process Safety and Environmental Protection*, 2020, **139**, 315–324.

51 Panchal Plastic Machinery Pvt Ltd., The Significance of Size Reduction in Recycling Operations, https://recyclinginside.com/recycling-technology/size-reduction/the-significance-of-size-reduction-in-recycling-operations/#:~:text=Improved%20efficiency:%20Size%20reduction%20can,from%20large%20pieces%20of%20material., (accessed 28 January 2026).

52 S. M. Al-Salem, P. Lettieri and J. Baeyens, *Waste Management*, 2009, **29**, 2625–2643.

53 M. Namjoufar, Y. Wei, K. J.-R. Maloney, M. Laghaei, J. Patadiya, S. A. Hadigheh, M. Naebe and O. Zabihi, *Journal of Environmental Chemical Engineering*, 2026, **14**, 121559.

54 E. Morici and N. Tz. Dintcheva, *Polymers*, 2022, **14**, 4153.

55 J.-P. Lange, *ACS Sustainable Chem. Eng.*, 2021, **9**, 15722–15738.

56 S. Saikrishnan, D. Jubinville, C. Tzoganakis and T. H. Mekonnen, *Polymer Degradation and Stability*, 2020, **182**, 109390.

57 S. Billiet and S. R. Trenor, *ACS Macro Lett.*, 2020, **9**, 1376–1390.

58 M. K. Eriksen, J. D. Christiansen, A. E. Daugaard and T. F. Astrup, *Waste Management*, 2019, **96**, 75–85.

59 R. R. Larder and F. L. Hatton, *ACS Polym. Au*, 2023, **3**, 182–201.

60 L. Roming, F. Kronenwett, P. Bäcker, J. Josekutty, G. Maier and T. Längle, *Waste Management*, 2026, **209**, 115175.

61 J. N. Hahladakis and E. Iacovidou, *Journal of Hazardous Materials*, 2019, **380**, 120887.

62 R. Möller and U. Jeske, *Recycling von PVC. Grundlagen, Stand der Technik, Handlungsmöglichkeiten*, Karlsruhe, 1995.

63 I. Fortelný, D. Michálková and Z. Kruliš, *Polymer Degradation and Stability*, 2004, **85**, 975–979.

64 P. J. Flory, *Principles of polymer chemistry*, Cornell university press, Ithaca (N.Y.) London, 1992.

65 T. Liu and G. Liu, *J. Mater. Chem. A*, 2019, **7**, 23476–23488.

66 J. L. Self, A. J. Zervoudakis, X. Peng, W. R. Lenart, C. W. Macosko and C. J. Ellison, *JACS Au*, 2022, **2**, 310–321.

67 A. J. Zervoudakis, C. S. Sample, X. Peng, D. Lake, M. A. Hillmyer and C. J. Ellison, *ACS Macro Lett.*, 2022, **11**, 1396–1402.

68 S. Xie, K. M. Karnaukh, K.-C. Yang, D. Sun, K. T. Delaney, J. Read De Alaniz, G. H. Fredrickson and R. A. Segalman, *Macromolecules*, 2023, **56**, 3617–3630.

69 EFSA Panel on Food Contact Materials, Enzymes and Processing Aids (CEP), C. Lambré, J. M. Barat Baviera, C. Bolognesi, A. Chesson, P. S. Cocconcelli, R. Crebelli, D. M. Gott, K. Grob, M. Mengelers, A. Mortensen, G. Rivière, I. Steffensen, C. Tlustos, H. Van Loveren, L. Vernis, H. Zorn, V. Dudler, M. R. Milana, C. Papaspyrides, M. de F. Tavares Poças, G. Colombo, D. Comandella, A. Lioupis, R. Marano, I. P. Munoz Guajardo, E. Savini, V. Sfika, E. Tsochatzis, K. Volk and E. Lampi, *EFSA Journal*, 2024, **22**, e8879.

70 S. Ceballos-Santos, D. B. De Sousa, P. G. García, J. Laso, M. Margallo and R. Aldaco, *Science of The Total Environment*, 2024, **951**, 175452.

71 S. Kumagai, K. M. Knauer, G. W. Huber and C. R. Bening, *Cell Reports Sustainability*, 2025, **2**, 100465.

72 D. Peti, J. Dobránsky and P. Michalík, *Polymers*, 2025, **17**, 603.

73 I. Vollmer, M. J. F. Jenks, M. C. P. Roelands, R. J. White, T. Van Harmelen, P. De Wild, G. P. Van Der Laan, F. Meirer, J. T. F. Keurentjes and B. M. Weckhuysen, *Angew. Chem. Int. Ed.*, 2020, **59**, 15402–15423.

74 T. Lee, D. Kwon, S. Lee, Y. Kim, J. Y. Kim, H. Song, S. Jung, J. Lee, Y. F. Tsang, K.-H. Kim and E. E. Kwon, *Progress in Energy and Combustion Science*, 2025, **108**, 101219.

75 International Organization for Standardization, Plastics — Guidelines for the recovery and recycling of plastics waste — Part 1: General Principles (ISO/DIS 15270-1 Draft), https://www.iso.org/obp/ui/en/#iso:std:iso:15270:-1:dis:ed-1:v1:en, (accessed 24 March 2026).

76 T. W. Walker, N. Frelka, Z. Shen, A. K. Chew, J. Banick, S. Grey, M. S. Kim, J. A. Dumesic, R. C. Van Lehn and G. W. Huber, *Sci. Adv.*, 2020, **6**, eaba7599.

77 G. Pappa, C. Boukouvalas, C. Giannaris, N. Ntaras, V. Zografos, K. Magoulas, A. Lygeros and D. Tassios, *Resources, Conservation and Recycling*, 2001, **34**, 33–44.

78 L. Umdagas, R. Orozco, K. Heeley, W. Thom and B. Al-Duri, *Polymer Degradation and Stability*, 2025, **234**, 111246.

79 J. J. M. Pang, Y. H. Lee, H. Zhao, A. Ong and J. Y. C. Lim, *Green Chem.*, 2025, **27**, 14978–15001.

80 S. M. Al-Salem, A. Antelava, A. Constantinou, G. Manos and A. Dutta, *Journal of Environmental Management*, 2017, **197**, 177–198.

81 D. A. Wijesekara, P. Sargent, C. J. Ennis and D. Hughes, *Journal of Cleaner Production*, 2021, **317**, 128212.

82 A. Ligero, M. Calero, A. Pérez, R. R. Solís, M. J. Muñoz-Batista and M. Á. Martín-Lara, *Process Safety and Environmental Protection*, 2023, **173**, 558–566.

83 W. R. Athembo, J. Redshaw and S. Jeffery, *Cleaner and Circular Bioeconomy*, 2025, **12**, 100189.

84 J. Schirmer, J. S. Kim and E. Klemm, *Journal of Analytical and Applied Pyrolysis*, 2001, **60**, 205–217.

85 R. Miandad, M. A. Barakat, A. S. Aburiazaiza, M. Rehan and A. S. Nizami, *Process Safety and Environmental Protection*, 2016, **102**, 822–838.

86 J. E. Lee, D. Lee, J. Lee and Y.-K. Park, *Chemosphere*, 2025, **370**, 143978.

87 M. Kusenberg, A. Zayoud, M. Roosen, H. D. Thi, M. S. Abbas-Abadi, A. Eschenbacher, U. Kresovic, S. De Meester and K. M. Van Geem, *Fuel Processing Technology*, 2022, **227**, 107090.

88 U. Arena, *Waste Management*, 2012, **32**, 625–639.

89 O. Dogu, M. Pelucchi, R. Van De Vijver, P. H. M. Van Steenberge, D. R. D'hooge, A. Cuoci, M. Mehl, A. Frassoldati, T. Faravelli and K. M. Van Geem, *Progress in Energy and Combustion Science*, 2021, **84**, 100901.

90 H. Xu and B. Shi, *Processes*, 2022, **10**, 499.

91 M. J. Boel, H. Wang, A. Al Farra, L. Megido, J. M. González-LaFuente and N. R. Shiju, *React. Chem. Eng.*, 2024, **9**, 1014–1031.

92 G. C. Laredo, J. Reza and E. Meneses Ruiz, *Cleaner Chemical Engineering*, 2023, **5**, 100094.

93 A. Moustafa, K. Abdelrahman, A. Abdelhaleem and I. S. Fahim, *Journal of Analytical and Applied Pyrolysis*, 2025, **189**, 107112.

94 I. Harasymchuk, V. Kočí and M. Vitvarová, *International Journal of Sustainable Engineering*, 2024, **17**, 124–148.

95 M. T. Chin and T. Diao, *ACS Catal.*, 2024, **14**, 12437–12453.

96 *Plastics the Fast Facts 2025 - Global and European plastics production and economic indicators*, Plastics Europe, 2025.

97 A. Lamtai, S. Elkoun, M. Robert, F. Mighri and C. Diez, *Waste*, 2023, **1**, 860–883.

98 M. H. Akhras, J. Langwieser, S. Czaker, A. Felgel-Farnholz and J. Fischer, *Clean Techn Environ Policy*, 2024, **26**, 3507–3526.

99 D. S. Achilias, *Euro-Mediterr. J. Environ. Integr.*, 2025, **10**, 2605–2618.

100 R. Huang, J. Meng and X. Jiang, *Green Energy & Environment*, 2026, **11**, 283–316.

101 D. Royuela, A. Veses, T. García, R. Murillo and J. D. Martínez, *Journal of Environmental Chemical Engineering*, 2026, **14**, 121633.

102 T. Muringayil Joseph, S. Azat, Z. Ahmadi, O. Moini Jazani, A. Esmaeili, E. Kianfar, J. Haponiuk and S. Thomas, *Case Studies in Chemical and Environmental Engineering*, 2024, **9**, 100673.

103 Z. Xu, D. Sun, J. Xu, R. Yang, J. D. Russell and G. Liu, *ChemSusChem*, 2024, **17**, e202400474.

104 H. Luo, H. Tyrrell, J. Bai, R. Ibrahim Muazu and X. Long, *Green Chem.*, 2024, **26**, 11444–11467.

105 A. Rahimi and J. M. García, *Nat. Rev. Chem.*, 2017, **1**, 0046.

106 A. Ravve, *Principles of Polymer Chemistry*, Springer New York, New York, NY, 2012.

107 A. D. Patel, Z. O. G. Schyns, T. W. Franklin and M. P. Shaver, *Nat. Commun.*, 2024, **15**, 8733.

108 J. Dill, Challenges and potential solutions for polyethylene film recycling, https://spnews.com/potential-solutions/, (accessed 2 April 2026).

109 G. Celik, R. M. Kennedy, R. A. Hackler, M. Ferrandon, A. Tennakoon, S. Patnaik, A. M. LaPointe, S. C. Ammal, A. Heyden, F. A. Perras, M. Pruski, S. L. Scott, K. R. Poeppelmeier, A. D. Sadow and M. Delferro, *ACS Cent. Sci.*, 2019, **5**, 1795–1803.

110 J. E. Rorrer, G. T. Beckham and Y. Román-Leshkov, *JACS Au*, 2021, **1**, 8–12.

111 C. Jia, S. Xie, W. Zhang, N. N. Intan, J. Sampath, J. Pfaendtner and H. Lin, *Chem Catalysis*, 2021, **1**, 437–455.

112 M. Chauhan, C. Thadhani, B. Rana, P. Gupta, B. Ghosh and K. Manna, *Chem. Mater.*, 2024, **36**, 10670–10679.

113 I. Nogueroles-Langa, Y. Ge, C. Salah, S. D. Jaydev, J. Morales-Vidal, P. S. Berman, H. Eliasson, R. Erni, G. Guillén-Gosálbez, N. López, A. J. Martín and J. Pérez-Ramírez, *Nat. Commun.*, 2025, **16**, 9791.

114 F. Zhang, M. Zeng, R. D. Yappert, J. Sun, Y.-H. Lee, A. M. LaPointe, B. Peters, M. M. Abu-Omar and S. L. Scott, *Science*, 2020, **370**, 437–441.

115 Z. Xu, N. E. Munyaneza, Q. Zhang, M. Sun, C. Posada, P. Venturo, N. A. Rorrer, J. Miscall, B. G. Sumpter and G. Liu, *Science*, 2023, **381**, 666–671.

116 L. Douiri, H. Jdidi, S. Kordoghli, G. El Hajj Sleiman and Y. Béreaux, *Polymer Degradation and Stability*, 2024, **219**, 110617.

117 A. Schade, M. Melzer, S. Zimmermann, T. Schwarz, K. Stoewe and H. Kuhn, *ACS Sustainable Chem. Eng.*, 2024, **12**, 12270–12288.

118 K. Yun, X. Lian, S. Wang, R. Shan, H. Yuan and Y. Chen, *Journal of the Energy Institute*, 2025, **123**, 102279.

119 W. Li, M. Zheng, J. Li, C. Ren and X. Li, *Polymer Degradation and Stability*, 2025, **239**, 111419.

120 P. A. Kots, S. Liu, B. C. Vance, C. Wang, J. D. Sheehan and D. G. Vlachos, *ACS Catal.*, 2021, **11**, 8104–8115.

121 J. A. Sun, P. A. Kots, Z. R. Hinton, N. S. Marinkovic, L. Ma, S. N. Ehrlich, W. Zheng, T. H. Epps, L. T. J. Korley and D. G. Vlachos, *ACS Catal.*, 2024, **14**, 3228–3240.

122 A. N. Le, R. Herrera Monegro, I. Mountziaris, Y. Avila-Martinez, B. P. Carrow, M. L. Robertson and R. Krishnamoorti, *Macromolecules*, 2025, **58**, 8360–8368.

123 A. Mohammed, G. A. El-Hiti, E. Yousif, A. A. Ahmed, D. S. Ahmed and M. H. Alotaibi, *Polymers*, 2020, **12**, 969.

124 M. Havaei, O. Akin, A. Locaspi, R. John Varghese, F. Minette, E. Romers, S. De Meester and K. M. Van Geem, *Waste Management*, 2025, **193**, 105–134.

125 J. Yu, L. Sun, C. Ma, Y. Qiao and H. Yao, *Waste Management*, 2016, **48**, 300–314.

126 J. Wu, K. G. Papanikolaou, F. Cheng, B. Addison, A. A. Cuthbertson, M. Mavrikakis and G. W. Huber, *ACS Sustainable Chem. Eng.*, 2024, **12**, 7402–7413.

127 T. Tetičkovič, D. Klinar, K. Rižnar and D. Pečar, *Molecules*, 2026, **31**, 202.

128 *Progress Report 2025*, Vinyl Plus, 2025.

129 Y. Tian, M. Han, D. Gu, Z. Bi, N. Gu, T. Hu, G. Li, N. Zhang and J. Lu, *Sustainability*, 2024, **16**, 8331.

130 Z. Li, S. Niu, J. Liu and Y. Wang, *Science of The Total Environment*, 2022, **843**, 157082.

131 C. Vos, G. O'Rourke and D. De Vos, *ACS Sustainable Chem. Eng.*, 2026, **14**, 2595–2605.

132 A. Alshaikh, S. Ezendu, D. Ryoo, P. S. Shinde, J. L. Anderson, T. Szilvási, P. A. Rupar and J. E. Bara, *ACS Appl. Polym. Mater.*, 2024, **6**, 9656–9662.

133 R. Balu, N. K. Dutta and N. Roy Choudhury, *Polymers*, 2022, **14**, 4788.

134 Z. Zhang, B. Y. Zhang, Q. Tang, M. Mrugala, D. Zhang, G. Li, W. Li and J. Z. Ou, *Adv. Materials Technologies*, 2026, **11**, e01385.

135 Y. Zhao, D. Li and X. Jiang, *Eur. J. Org. Chem.*, 2023, **26**, e202300664.

136 N. K. Boaen and M. A. Hillmyer, *Chem. Soc. Rev.*, 2005, **34**, 267–275.

137 R. W. Clarke, T. Sandmeier, K. A. Franklin, D. Reich, X. Zhang, N. Vengallur, T. K. Patra, R. J. Tannenbaum, S. Adhikari, S. K. Kumar, T. Rovis and E. Y.-X. Chen, *Nature*, 2023, **616**, 731–739.

138 M. Zhang, M. Kränzlein, S. Cui, A. M. LaPointe and G. W. Coates, *J. Am. Chem. Soc.*, 2026, **148**, 4599–4604.

139 E. K. Neidhart, M. Hua, Z. Peng, L. T. Kearney, V. Bhat, F. Vashahi, E. J. Alexanian, S. S. Sheiko, C. Wang, B. A. Helms and F. A. Leibfarth, *J. Am. Chem. Soc.*, 2023, **145**, 27450–27458.

140 S. Aydonat, A. H. Hergesell, C. L. Seitzinger, R. Lennarz, G. Chang, C. Sievers, J. Meisner, I. Vollmer and R. Göstl, *Polym. J.*, 2024, **56**, 249–268.

141 A. Krusenbaum, S. Grätz, G. T. Tigineh, L. Borchardt and J. G. Kim, *Chem. Soc. Rev.*, 2022, **51**, 2873–2905.

142 K. Kubota, N. Toyoshima, D. Miura, J. Jiang, S. Maeda, M. Jin and H. Ito, *Angew. Chem. Int. Ed.*, 2021, **60**, 16003–16008.

143 M. E. Skala, S. M. Zeitler and M. R. Golder, *Chem. Sci.*, 2024, **15**, 10900–10907.

144 A. Rizzo and G. I. Peterson, *Progress in Polymer Science*, 2024, **159**, 101900.

145 J. A. Nettles, T. E. Long and K. Jin, *JACS Au*, 2026, **6**, 720–730.

146 R. R. A. Bolt, J. A. Leitch, A. C. Jones, W. I. Nicholson and D. L. Browne, *Chem. Soc. Rev.*, 2022, **51**, 4243–4260.

147 T. Vialon, H. Sun, G. J. M. Formon, P. Galanopoulo, C. Guibert, F. Averseng, M.-N. Rager, A. Percot, Y. Guillaneuf, N. J. Van Zee and R. Nicolaÿ, *J. Am. Chem. Soc.*, 2024, **146**, 2673–2684.

148 G. P. Kar, M. O. Saed and E. M. Terentjev, *J. Mater. Chem. A*, 2020, **8**, 24137–24147.

149 S. J. Davis, N. S. Lewis, M. Shaner, S. Aggarwal, D. Arent, I. L. Azevedo, S. M. Benson, T. Bradley, J. Brouwer, Y.-M. Chiang, C. T. M. Clack, A. Cohen, S. Doig, J. Edmonds, P. Fennell, C. B. Field, B. Hannegan, B.-M. Hodge, M. I. Hoffert, E. Ingersoll, P. Jaramillo, K. S. Lackner, K. J. Mach, M. Mastrandrea, J. Ogden, P. F. Peterson, D. L. Sanchez, D. Sperling, J. Stagner, J. E. Trancik, C.-J. Yang and K. Caldeira, *Science*, 2018, **360**, eaas9793.

150 J. C. Minx, W. F. Lamb, M. W. Callaghan, S. Fuss, J. Hilaire, F. Creutzig, T. Amann, T. Beringer, W. De Oliveira Garcia, J. Hartmann, T. Khanna, D. Lenzi, G. Luderer, G. F. Nemet, J. Rogelj, P. Smith, J. L. Vicente Vicente, J. Wilcox and M. Del Mar Zamora Dominguez, *Environ. Res. Lett.*, 2018, **13**, 063001.

151 K. Lebling, A. Gangorta, K. Hausker and Z. Byrum, 7 Things to Know About Carbon Capture, Utilization and Sequestration, https://www.wri.org/insights/carbon-capture-

technology?utm_campaign=socialmedia&utm_source=linkedin&utm_medium=world+resources+institute, (accessed 8 April 2026).

152 W. F. Lamb, J. Minx, M. Callaghan, F. Schenuit, T. Gasser, T. Repke, A. Cowie, F. Müller-Hansen, G. F. Nemet, J. Steinhauser, R. Bellamy, S. Lueck, Keywan Riahi, G. Grassi, Aniruddh Mohan, C. Powis, O. Geden, J. M. Valenzuela, J. Strefler, G. Peters, S. Fuss, E. Cox, S. Smith, J. Greene, Yoga Pratama and M. Gidden, *State of Carbon Dioxide Removal - 1st Edition*, OSF, 2023.

153 S. Fuss, W. F. Lamb, M. W. Callaghan, J. Hilaire, F. Creutzig, T. Amann, T. Beringer, W. De Oliveira Garcia, J. Hartmann, T. Khanna, G. Luderer, G. F. Nemet, J. Rogelj, P. Smith, J. L. V. Vicente, J. Wilcox, M. Del Mar Zamora Dominguez and J. C. Minx, *Environ. Res. Lett.*, 2018, **13**, 063002.

154 J. G. Canadell and E. D. Schulze, *Nat. Commun.*, 2014, **5**, 5282.

155 M. Fajardy, A. Köberle, N. Mac Dowell and A. Fantuzzi, *BECCS deployment: a reality check*, Imperial College London, 2019.

156 M. Fajardy and N. Mac Dowell, *Energy Environ. Sci.*, 2017, **10**, 1389–1426.

157 M. Fajardy and C. Greenfield, Bioenergy with Carbon Capture and Storage, https://www.iea.org/energy-system/carbon-capture-utilisation-and-storage/bioenergy-with-carbon-capture-and-storage, (accessed 9 April 2026).

158 *Global Status of CCS 2024*, Global CCS Institute, Australia, 2024.

159 J. Kemper, *International Journal of Greenhouse Gas Control*, 2015, **40**, 401–430.

160 R. J. Finley, *Greenhouse Gases*, 2014, **4**, 571–579.

161 BECCS Stockholm, https://www.stockholmexergi.se/en/beccs/, (accessed 9 April 2026).

162 S. V. Hanssen, V. Daioglou, Z. J. N. Steinmann, J. C. Doelman, D. P. Van Vuuren and M. A. J. Huijbregts, *Nat. Clim. Chang.*, 2020, **10**, 1023–1029.

163 M. A. Hayat, K. Alhadhrami and A. M. Elshurafa, *International Journal of Greenhouse Gas Control*, 2024, **135**, 104164.

164 45Q Tax Credit for Carbon Capture Projects, https://carboncapturecoalition.org/resource/45q-tax-credit-for-carbon-capture-projects/?utm_source=chatgpt.com, (accessed 9 April 2026).

165 M. Erans, E. S. Sanz-Pérez, D. P. Hanak, Z. Clulow, D. M. Reiner and G. A. Mutch, *Energy Environ. Sci.*, 2022, **15**, 1360–1405.

166 M. Ozkan, S. P. Nayak, A. D. Ruiz and W. Jiang, *iScience*, 2022, **25**, 103990.

167 E. S. Sanz-Pérez, C. R. Murdock, S. A. Didas and C. W. Jones, *Chem. Rev.*, 2016, **116**, 11840–11876.

168 *Direct Air Capture - A key technology for net zero*, International Energy Agency, 2024.

169 D. W. Keith, G. Holmes, D. St. Angelo and K. Heidel, *Joule*, 2018, **2**, 1573–1594.

170 S. Deutz and A. Bardow, *Nat. Energy*, 2021, **6**, 203–213.

171 Orca: the first large-scale plant, https://climeworks.com/plant-orca, (accessed 9 April 2026).

172 Mammoth: our newest facility, https://climeworks.com/plant-mammoth, (accessed 9 April 2026).

173 F. Bisotti, K. A. Hoff, A. Mathisen and J. Hovland, *Chemical Engineering Science*, 2024, **283**, 119416.

174 J. Minx, J. Burke, I. Schulte, B. Probst, F. Müller-Hansen, S. Roe, H. Buck, S. Smith, Injy Johnstone, G. F. Nemet, M. Edwards, M. Gidden, F. Schenuit, S. Fuss, W. F. Lamb, O. Geden, J. Pongratz, N. Vaughan and E. Cox, *The State of Carbon Dioxide Removal - 2nd Edition*, OSF, 2024.

175 M. Ozkan, *MRS Energy & Sustainability*, 2024, **12**, 46–61.

176 D. Obi, S. Onyekuru and A. Orga, *Energy Science & Engineering*, 2025, **13**, 1749–1770.

177 M. Fajardy, C. Greenfield and J. Tweneboah Koduah, CCUS projects around the world are reaching new milestones, https://www.iea.org/commentaries/ccus-projects-around-the-world-are-reaching-new-milestones, (accessed 11 April 2026).

178 R. M. Cuéllar-Franca and A. Azapagic, *Journal of CO_2 Utilization*, 2015, **9**, 82–102.

179 J. A. Garcia, M. Villen-Guzman, J. M. Rodriguez-Maroto and J. M. Paz-Garcia, *Journal of Environmental Chemical Engineering*, 2022, **10**, 108470.

180 S. Talei, D. Fozer, P. S. Varbanov, A. Szanyi and P. Mizsey, *ACS Omega*, 2024, acsomega.3c05034.

181 E. Oko, M. Wang and A. S. Joel, *Int. J. Coal Sci. Technol.*, 2017, **4**, 5–14.

182 B. B. Krishna, B. Biswas and T. Bhaskar, in *Biofuels: Alternative Feedstocks and Conversion Processes for the Production of Liquid and Gaseous Biofuels*, Elsevier, 2019, pp. 285–300.

183 S. Yadav and S. S. Mondal, *Fuel*, 2022, **308**, 122057.

184 E. S. Rubin, J. E. Davison and H. J. Herzog, *International Journal of Greenhouse Gas Control*, 2015, **40**, 378–400.

185 M. Karimi, M. Shirzad, J. A. C. Silva and A. E. Rodrigues, *Environ. Chem. Lett.*, 2023, **21**, 2041–2084.

186 X. Y. D. Soo, J. J. C. Lee, W.-Y. Wu, L. Tao, C. Wang, Q. Zhu and J. Bu, *Journal of CO_2 Utilization*, 2024, **81**, 102727.

187 S. Shen, X. Shi, C. Li, H. Guo, Q. Long, S. Wang and X. Yin, *Separation and Purification Technology*, 2022, **300**, 121908.

188 Y. Park, K.-Y. A. Lin, A.-H. A. Park and C. Petit, *Front. Energy Res.*, 2015, **3**, 42.

189 R. Xue, H. Guo, W. Yang, S.-L. Huang and G.-Y. Yang, *Adv Compos Hybrid Mater*, 2022, **5**, 1595–1611.

190 A. H. Berger and A. S. Bhown, *Energy Procedia*, 2011, **4**, 562–567.

191 A. Samanta, A. Zhao, G. K. H. Shimizu, P. Sarkar and R. Gupta, *Ind. Eng. Chem. Res.*, 2012, **51**, 1438–1463.

192 O. K. Farha, I. Eryazici, N. C. Jeong, B. G. Hauser, C. E. Wilmer, A. A. Sarjeant, R. Q. Snurr, S. T. Nguyen, A. Ö. Yazaydın and J. T. Hupp, *J. Am. Chem. Soc.*, 2012, **134**, 15016–15021.

193 F. Kong and W. Chen, *Nanomaterials*, 2024, **14**, 1340.

194 A. R. Millward and O. M. Yaghi, *J. Am. Chem. Soc.*, 2005, **127**, 17998–17999.

195 J. Hack, N. Maeda and D. M. Meier, *ACS Omega*, 2022, **7**, 39520–39530.

196 H. Li, A. Dilipkumar, S. Abubakar and D. Zhao, *Chem. Soc. Rev.*, 2023, **52**, 6294–6329.

197 E. Kamio, T. Yoshioka and H. Matsuyama, *Journal of Chemical Engineering of Japan*, 2023, **56**, 2222000.

198 S. Nakao, K. Yogo, K. Goto, T. Kai and H. Yamada, *Advanced CO_2 Capture Technologies: Absorption, Adsorption, and Membrane Separation Methods*, Springer International Publishing, Cham, 2019.

199 L. M. Robeson, *Journal of Membrane Science*, 1991, **62**, 165–185.

200 L. M. Robeson, *Journal of Membrane Science*, 2008, **320**, 390–400.

201 J. W. Park, S. Heo, J.-G. Yeo, S. Lee, J.-K. Kim and J. H. Lee, *Membranes*, 2025, **15**, 200.

202 N. Panapitiya, S. Wijenayake, D. Nguyen, C. Karunaweera, Y. Huang, K. Balkus, I. Musselman and J. Ferraris, *Materials*, 2016, **9**, 643.

203 C. Song, Q. Liu, S. Deng, H. Li and Y. Kitamura, *Renewable and Sustainable Energy Reviews*, 2019, **101**, 265–278.

204 D. Berstad, R. Anantharaman and P. Nekså, *International Journal of Refrigeration*, 2013, **36**, 1403–1416.

205 M. Shen, L. Tong, S. Yin, C. Liu, L. Wang, W. Feng and Y. Ding, *Separation and Purification Technology*, 2022, **299**, 121734.

206 A. M. Aneesh and A. A. Sam, *Front. Energy Res.*, 2023, **11**, 1167099.

207 C. Song, Q. Liu, N. Ji, S. Deng, J. Zhao, Y. Li, Y. Song and H. Li, *Renewable and Sustainable Energy Reviews*, 2018, **82**, 215–231.

208 N. Mahinpey, S. Daneshmand-Jahromi, K. Pirzadeh, A. Abdalla, M. H. Sedghkerdar and D. Karami, *Ind. Eng. Chem. Res.*, 2026, **65**, 4200–4233.

209 Y. Zhang, H. Han, N. Zhu, Y. Che, X. Zhang, Y. Xue, J. Deng, C. Wu, H. Wang, Y. Chen and S. Yi, *Ind. Eng. Chem. Res.*, 2025, **64**, 1933–1967.

210 A. Lyngfelt, *Energy Fuels*, 2020, **34**, 9077–9093.

211 B. Narindri Rara Winayu, T.-K. Tseng and H. Chu, *Processes*, 2023, **11**, 3164.

212 M. Bui, C. S. Adjiman, A. Bardow, E. J. Anthony, A. Boston, S. Brown, P. S. Fennell, S. Fuss, A. Galindo, L. A. Hackett, J. P. Hallett, H. J. Herzog, G. Jackson, J. Kemper, S. Krevor, G. C. Maitland, M. Matuszewski, I. S. Metcalfe, C. Petit, G. Puxty, J. Reimer, D. M. Reiner, E. S. Rubin, S. A. Scott, N. Shah, B. Smit, J. P. M. Trusler, P. Webley, J. Wilcox and N. Mac Dowell, *Energy Environ. Sci.*, 2018, **11**, 1062–1176.

213 T. Ajayi, J. S. Gomes and A. Bera, *Pet. Sci.*, 2019, **16**, 1028–1063.

214 About CCUS, https://www.iea.org/reports/about-ccus, (accessed 13 April 2026).

215 P. S. Ringrose, A.-K. Furre, S. M. V. Gilfillan, S. Krevor, M. Landrø, R. Leslie, T. Meckel, B. Nazarian and A. Zahid, *Annu. Rev. Chem. Biomol. Eng.*, 2021, **12**, 471–494.

216 A.-K. Furre, O. Eiken, H. Alnes, J. N. Vevatne and A. F. Kiær, *Energy Procedia*, 2017, **114**, 3916–3926.

217 O. Eiken, in *Geophysics and Geosequestration*, eds. T. L. Davis, M. Landrø and M. Wilson, Cambridge University Press, 1st edn., 2019, 209–234.

218 V. Núñez-López and E. Moskal, *Front. Clim.*, 2019, **1**, 5.

219 A. Bashir, M. Ali, S. Patil, M. S. Aljawad, M. Mahmoud, D. Al-Shehri, H. Hoteit and M. S. Kamal, *Earth-Science Reviews*, 2024, **249**, 104672.

220 M. J. Gidden, S. Joshi, J. J. Armitage, A.-B. Christ, M. Boettcher, E. Brutschin, A. C. Köberle, K. Riahi, H. J. Schellnhuber, C.-F. Schleussner and J. Rogelj, *Nature*, 2025, **645**, 124–132.

221 S. Krevor, H. De Coninck, S. E. Gasda, N. S. Ghaleigh, V. De Gooyert, H. Hajibeygi, R. Juanes, J. Neufeld, J. J. Roberts and F. Swennenhuis, *Nat. Rev. Earth Environ.*, 2023, **4**, 102–118.

222 A. Rafiee, K. Rajab Khalilpour, D. Milani and M. Panahi, *Journal of Environmental Chemical Engineering*, 2018, **6**, 5771–5794.

223 *Putting CO_2 to Use : Creating value from emissions*, International Energy Agency, 2019.

224 M. Aresta, A. Dibenedetto and A. Angelini, *Chem. Rev.*, 2014, **114**, 1709–1742.

225 L. Cross, Global fertilizer demand begins its recovery after a rocky two years, https://gpcachem.org/2024/09/27/global-fertilizer-demand-begins-its-recovery-after-a-rocky-two-years/, (accessed 15 April 2026).

226 *2006 IPCC Guidelines for National Greenhouse Gas Inventories - Volume 4 : Agriculture, Forestry and Other Land Use*, Intergovernmental Panel on Climate Change (IPCC), 2023.

227 N. Mac Dowell, P. S. Fennell, N. Shah and G. C. Maitland, *Nature Clim. Change*, 2017, **7**, 243–249.

228 M. Fajardy and G. Carl, CO_2 Capture and Utilisation, https://www.iea.org/energy-system/carbon-capture-utilisation-and-storage/co2-capture-and-utilisation, (accessed 15 April 2026).

229 M. Hanifa, R. Agarwal, U. Sharma, P. C. Thapliyal and L. P. Singh, *Journal of CO_2 Utilization*, 2023, **67**, 102292.

230 D. Stefaniuk, M. Hajduczek, J. C. Weaver, F. J. Ulm and A. Masic, *PNAS Nexus*, 2023, **2**, pgad052.

231 CarbonCure Celebrates Milestone of 50 Million Cubic Yards of Lower Carbon Concrete, https://www.carboncure.com/news/carboncure-marks-50-million-cubic-yards-milestone/#:~:text=Today%2C%20more%20than%20800%20CarbonCure,in%20the%20past%20365%20days, (accessed 15 April 2026).

232 J. G. Driver, E. Bernard, P. Patrizio, P. S. Fennell, K. Scrivener and R. J. Myers, *Proc. Natl. Acad. Sci. U.S.A.*, 2024, **121**, e2313475121.

233 J. Artz, T. E. Müller, K. Thenert, J. Kleinekorte, R. Meys, A. Sternberg, A. Bardow and W. Leitner, *Chem. Rev.*, 2018, **118**, 434–504.

234 X. Jiang, X. Nie, X. Guo, C. Song and J. G. Chen, *Chem. Rev.*, 2020, **120**, 7984–8034.

235 J. Zhong, X. Yang, Z. Wu, B. Liang, Y. Huang and T. Zhang, *Chem. Soc. Rev.*, 2020, **49**, 1385–1413.

236 M. Younas, L. Loong Kong, M. J. K. Bashir, H. Nadeem, A. Shehzad and S. Sethupathi, *Energy Fuels*, 2016, **30**, 8815–8831.

237 S. Rönsch, J. Schneider, S. Matthischke, M. Schlüter, M. Götz, J. Lefebvre, P. Prabhakaran and S. Bajohr, *Fuel*, 2016, **166**, 276–296.

238 S. Sollai, A. Porcu, V. Tola, F. Ferrara and A. Pettinau, *Journal of CO_2 Utilization*, 2023, **68**, 102345.

239 George Olah, https://carbonrecycling.com/projects/george-olah, (accessed 16 April 2026).

240 J. Wang, G. Zhang, J. Zhu, X. Zhang, F. Ding, A. Zhang, X. Guo and C. Song, *ACS Catal.*, 2021, **11**, 1406–1423.

241 L. H. Vieira, L. F. Rasteiro, C. S. Santana, G. L. Catuzo, A. H. M. Da Silva, J. M. Assaf and E. M. Assaf, *ChemCatChem*, 2023, **15**, e202300493.

242 J. Wang, G. Li, Z. Li, C. Tang, Z. Feng, H. An, H. Liu, T. Liu and C. Li, *Sci. Adv.*, 2017, **3**, e1701290.

243 Z. Han, C. Tang, F. Sha, S. Tang, J. Wang and C. Li, *Journal of Catalysis*, 2021, **396**, 242–250.

244 Q. Wu, S. Liang, T. Zhang, B. Louis and Q. Wang, *Fuel*, 2022, **313**, 122963.

245 T. Pinheiro Araújo, J. Morales-Vidal, T. Zou, M. Agrachev, S. Verstraeten, P. O. Willi, R. N. Grass, G. Jeschke, S. Mitchell, N. López and J. Pérez-Ramírez, *Advanced Energy Materials*, 2023, **13**, 2204122.

246 A. W. Kleij, M. North and A. Urakawa, *ChemSusChem*, 2017, **10**, 1036–1038.

247 T. Di Marco, Soda & Reforms. The 150th Anniversary of Solvay., https://www.scienceonthenet.eu/content/article/marco-taddia/soda-reforms-150th-anniversary-solvay/maggio-2013, (accessed 28 April 2026).

248 J. Clayden, N. Greeves and S. Warren, *Organic Chemistry*, Oxford Univ. Press, Second Edition., 2012.

249 T. Yan, H. Liu, Z. X. Zeng and W. G. Pan, *Journal of CO_2 Utilization*, 2023, **68**, 102355.

250 A. J. Kamphuis, F. Picchioni and P. P. Pescarmona, *Green Chem.*, 2019, **21**, 406–448.

251 V. Mishra and S. C. Peter, *Chem Catalysis*, 2024, **4**, 100796.

252 A. Morena, V. Campisciano, A. Santiago-Portillo, M. Gruttadauria, F. Giacalone and C. Aprile, *Fuel*, 2023, **336**, 126819.

253 A. Morena, L. Valentino, L. Fusaro, M. Gruttadauria, F. Giacalone and C. Aprile, *Journal of CO_2 Utilization*, 2026, **106**, 103382.

254 B. Taormina, R. Jouclas, A. Dsouza, A. Morena, M. Gruttadauria, C. Aprile and F. Giacalone, *Carbon*, 2025, **243**, 120508.

255 C. Célis, A. Morena, V. Marsala, L. Fusaro and C. Aprile, *Journal of Environmental Chemical Engineering*, 2026, 122884.

256 M. Alves, B. Grignard, R. Mereau, C. Jerome, T. Tassaing and C. Detrembleur, *Catal. Sci. Technol.*, 2017, **7**, 2651–2684.

257 S. Gennen, B. Grignard, T. Tassaing, C. Jérôme and C. Detrembleur, *Angew. Chem. Int. Ed.*, 2017, **56**, 10394–10398.

258 Y. Zhu, C. Romain and C. K. Williams, *Nature*, 2016, **540**, 354–362.

259 G. W. Coates and D. R. Moore, *Angew. Chem. Int. Ed.*, 2004, **43**, 6618–6639.

260 B. Grignard, S. Gennen, C. Jérôme, A. W. Kleij and C. Detrembleur, *Chem. Soc. Rev.*, 2019, **48**, 4466–4514.

261 J. Langanke, A. Wolf, J. Hofmann, K. Böhm, M. A. Subhani, T. E. Müller, W. Leitner and C. Gürtler, *Green Chem.*, 2014, **16**, 1865–1870.

262 N. Von Der Assen and A. Bardow, *Green Chem.*, 2014, **16**, 3272–3280.

263 R. Turnaturi, C. Zagni, V. Patamia, V. Barbera, G. Floresta and A. Rescifina, *Green Chem.*, 2023, **25**, 9574–9602.

264 B. Grignard, M. Bourguignon, F. Monie, T. Vidil, H. Cramail, G. Perli, H. Sardon, J.-M. Raquez, S. Caillol and C. Detrembleur, *Chem. Soc. Rev.*, 2026, Advance Article.

265 S. Nitopi, E. Bertheussen, S. B. Scott, X. Liu, A. K. Engstfeld, S. Horch, B. Seger, I. E. L. Stephens, K. Chan, C. Hahn, J. K. Nørskov, T. F. Jaramillo and I. Chorkendorff, *Chem. Rev.*, 2019, **119**, 7610–7672.

266 D. Gao, R. M. Arán-Ais, H. S. Jeon and B. Roldan Cuenya, *Nat. Catal.*, 2019, **2**, 198–210.

267 W. Liu, P. Zhai, A. Li, B. Wei, K. Si, Y. Wei, X. Wang, G. Zhu, Q. Chen, X. Gu, R. Zhang, W. Zhou and Y. Gong, *Nat. Commun.*, 2022, **13**, 1877.

268 J. Zhang, C. Guo, S. Fang, X. Zhao, L. Li, H. Jiang, Z. Liu, Z. Fan, W. Xu, J. Xiao and M. Zhong, *Nat. Commun.*, 2023, **14**, 1298.

269 R. Küngas, *J. Electrochem. Soc.*, 2020, **167**, 044508.

270 X. She, Y. Wang, H. Xu, S. Chi Edman Tsang and S. Ping Lau, *Angewandte Chemie*, 2022, **134**, e202211396.

271 Committee on Carbon Utilization Infrastructure, Markets, Research and Development, Board on Energy and Environmental Systems, Board on Chemical Sciences and Technology, Division on Engineering and Physical Sciences, Division on Earth and Life Studies, and National Academies of Sciences, Engineering, and Medicine, *Carbon Utilization Infrastructure, Markets, and Research and Development: A Final Report*, National Academies Press, Washington, D.C., 2024.

272 S. Kumar, J. H. Cho and I. Moon, *International Journal of Greenhouse Gas Control*, 2014, **20**, 87–116.

273 P. G. Jessop, D. J. Heldebrant, X. Li, C. A. Eckert and C. L. Liotta, *Nature*, 2005, **436**, 1102–1102.

274 D. J. Heldebrant, C. R. Yonker, P. G. Jessop and L. Phan, *Energy Environ. Sci.*, 2008, **1**, 487–493.

275 L. Phan, D. Chiu, D. J. Heldebrant, H. Huttenhower, E. John, X. Li, P. Pollet, R. Wang, C. A. Eckert, C. L. Liotta and P. G. Jessop, *Ind. Eng. Chem. Res.*, 2008, **47**, 539–545.

276 D. J. Heldebrant, P. K. Koech, M. T. C. Ang, C. Liang, J. E. Rainbolt, C. R. Yonker and P. G. Jessop, *Green Chem.*, 2010, **12**, 713–721.

277 P. K. Koech, J. Zhang, I. V. Kutnyakov, L. Cosimbescu, S.-J. Lee, M. E. Bowden, T. D. Smurthwaite and D. J. Heldebrant, *RSC Adv.*, 2013, **3**, 566–572.

278 D. J. Heldebrant, P. K. Koech, V.-A. Glezakou, R. Rousseau, D. Malhotra and D. C. Cantu, *Chem. Rev.*, 2017, **117**, 9594–9624.

279 Paul. M. Mathias, K. Afshar, F. Zheng, M. D. Bearden, C. J. Freeman, T. Andrea, P. K. Koech, I. Kutnyakov, A. Zwoster, A. R. Smith, P. G. Jessop, O. G. Nik and D. J. Heldebrant, *Energy Environ. Sci.*, 2013, **6**, 2233–2242.

280 W. Yue, W. Han, M. Yuan, X. Zhou and H. Fu, *Journal of Molecular Liquids*, 2024, **399**, 124400.

281 A. Hedayati and F. Feyzi, *ACS Sustainable Chem. Eng.*, 2020, **8**, 7909–7920.

282 S. Anwer, I. I. I. Alkhatib, H. A. Salih, I. AlNashef and L. F. Vega, *Chemical Engineering Journal*, 2025, **503**, 158297.

283 D. C. Cantu, J. Lee, M.-S. Lee, D. J. Heldebrant, P. K. Koech, C. J. Freeman, R. Rousseau and V.-A. Glezakou, *J. Phys. Chem. Lett.*, 2016, **7**, 1646–1652.

284 S. Wei, Y. Wu and J. Xi, *Food Chemistry*, 2025, **463**, 141170.

285 P. McNeice and B. L. Feringa, *Green Chem.*, 2024, **26**, 11747–11772.

286 P. G. Jessop, S. M. Mercer and D. J. Heldebrant, *Energy Environ. Sci.*, 2012, **5**, 7240–7253.

287 R. R. Wanderley, D. D. D. Pinto and H. K. Knuutila, *Separation and Purification Technology*, 2021, **260**, 118193.

288 Y. Jiang, P. M. Mathias, C. J. Freeman, J. A. Swisher, R. F. Zheng, G. A. Whyatt and D. J. Heldebrant, *International Journal of Greenhouse Gas Control*, 2021, **106**, 103279.

289 Y. Jiang, P. M. Mathias, R. F. Zheng, C. J. Freeman, D. Barpaga, D. Malhotra, P. K. Koech, A. Zwoster and D. J. Heldebrant, *Journal of Cleaner Production*, 2023, **388**, 135696.

CHAPTER 2

Turning Carbon Dioxide into Dialkyl Carbonates through Guanidinium-Assisted S_N2 Ion-Pair Process



Delcorps J., Singh Rawat K., Wells M., Ben Ayed E., Grignard B., Detrembleur C., Blankert B., Gerbaux P., Van Speybroeck V., Coulembier O., *Cell Reports Physical Science*, 2024, 5, 7, 102057. https://doi.org/10.1016/j.xcrp.2024.102057

TABLE OF CONTENTS

I. INTRODUCTION....96

II. RESULTS AND DISCUSSION....99

A. Preparation of TBD-based CO_2BOLs....99

B. Preparation of Linear Dialkyl Carbonates from TBD-based CO_2BOLs....107

III. CONCLUSION....116

IV. EXPERIMENTAL....117

A. Materials....117

B. Procedures....117

C. Methods....118

V. SUPPORTING INFORMATION....121

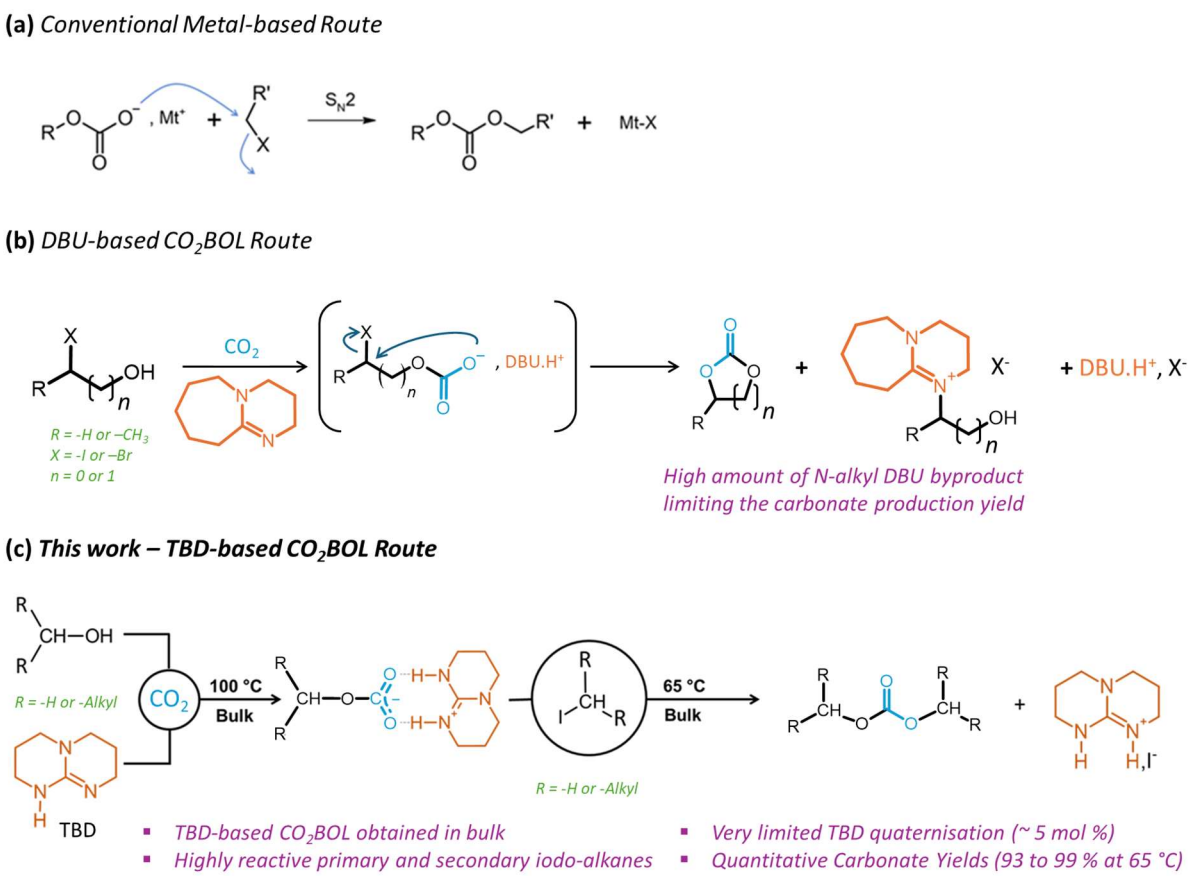
VI. REFERENCES....127

I. INTRODUCTION

As outlined in Chapter 1, the management of anthropogenic CO_2 emissions encompasses several complementary strategies. Among these, the conversion of CO_2 into value-added products has attracted particular attention from the chemistry community, motivated by the prospect of reframing an abundant waste stream as a renewable C1 feedstock.[1–3] From hydrogenation-based to chemical fixation-based products, CO_2 allows for a vast array of valuable chemical compounds to be prepared and designed for specific applications.[4–6] If groundbreaking work on catalyst design now allows for CO_2 to be transformed efficiently, only a few of the technologies available today are economically viable and scalable, such as the production of urea and carbonate-based polymers.[2] Aliphatic polycarbonates are attractive biomaterials owing to the potential CO_2 utilisation involved in their production, which is estimated to reach 10-50 Mt/year by 2050.[2] In the current market structure, carbonate-based polymers are mainly prepared by copolymerisation of CO_2 and epoxides.[7] However, they could also be obtained from carbonate-based synthons, either cyclic or linear, themselves potentially derived from CO_2. Since the best strategy for producing polycarbonates - in which carbonate linkages are connected by more than three carbon atoms - is the condensation polymerisation of diols and dialkyl carbonates,[8] a high-scale production of the latter is of utmost importance for the plastics industry. In addition to being used as simple intermediates in polymer production, dialkyl carbonates are also important chemical compounds due to their potential use as polar aprotic solvents, monomers for organic glasses-based polymers, synthetic lubricants, plasticisers, intermediates of pharmaceuticals, energy storage enhancers and CO_2 scavengers.[9–14]

Dialkyl carbonates, especially the dimethyl and diethyl forms (DMC & DEC),[15–19] have been commercially synthesised through the phosgene, Bayer non-phosgene,[20] ENIChem alcohol oxycarboxylation,[21] UBE alkyl nitrate carbonylation,[22] and the Asahi-Kasei transesterification processes.[15,17,23–25] Although the values of Gibbs free energy indicate that these conventional routes are advantageous,[20] they quickly become unattractive in terms of safety, toxicity and environment, driving both scientific and industrial interests to CO_2-based processes. In general, there are three main synthetic routes to dialkyl carbonates from CO_2, i.e. the direct carboxylation of alcohols, the alcoholysis of urea, and the transesterification of cyclic carbonates with alcohols.[17,26–28] Surprisingly, bimolecular nucleophilic substitution (S_N2) processes between carbonate salts and alkyl halides are not typically used to prepare dialkyl carbonates (**Scheme 2.1a**). Although this method offers a simple technological process, the low yield for dialkyl carbonates and rigorous operation conditions generally prevent its popularisation. When dialkyl carbonates are prepared from metal-based carbonate salts, the high temperatures adopted to circumvent the poor nucleophilicity of the carbonate active site are generally incompatible with either the carbonate salt's thermal stability or the substrate

functionalities. To that end, exotic organic solvents such as *N*-methyl-2-pyrrolidone or *N*,*N*-dimethylacetamide are necessary to maintain the solubility of the metal salts.[28]

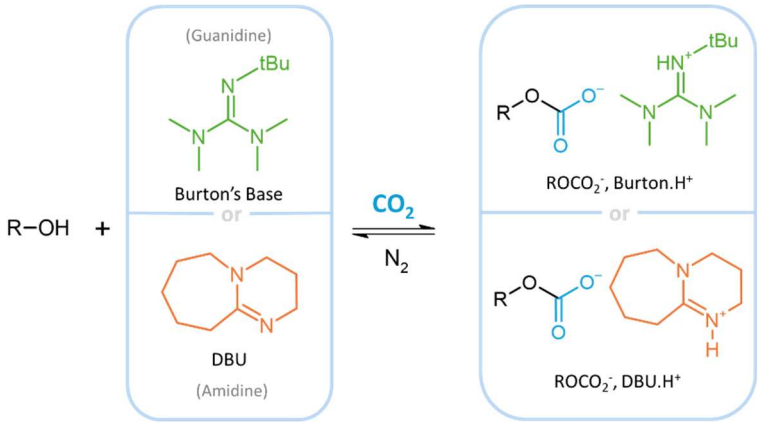


Scheme 2.1. Preparation of Carbonates: S_N2 Methods and DBU- and TBD-Based CO_2BOL Routes. (a) General reaction scheme for the dialkyl carbonate ($ROCO_2CH_2R'$) preparation from a S_N2 reaction between a metal-based carbonate salt ($ROCO_2^-$,Mt^+) and a primary alkyl halide ($R'CH_2X$), **(b)** DBU-based CO_2BOL route employed for the preparation of ethylene and propylene carbonates, **(c)** This work: a TBD-based CO_2BOL route.

Organic compounds, such as ionic liquids, could moderately improve the S_N2 reaction by enhancing the nucleophilicity of metal-based carbonate salts.[29] As organic molecules offer many advantages over metals (e.g. lower toxicity, milder reaction conditions, etc.), it would be unfortunate to see them as mere additives to metals.[30] To date, only a handful of studies have focused on the preparation of linear dialkyl carbonates using organo-based carbonate salts.[31,32] While Rossi *et al*. have reported the synthesis of organic carbonates from tetrabutylammonium alkyl carbonates, Bratt and Taylor developed an innovative process based on the use of intermediate methanesulfonyl carbonates. If the latter process suffers from harsh conditions such as high temperatures (> 150 °C), the former necessitates the synthesis of highly hygroscopic and non-commercially available tetrabutylammonium alkyl carbonates.

Highly interesting for the CO_2 capture and sequestration, organic solvent systems known as carbon dioxide-binding organic liquids (CO_2BOLs) have been developed. CO_2BOLs are based on

a liquid mixture of an alcohol and amidine or guanidine base, especially DBU and Burton's base, that chemically binds CO_2 to form amidinium or guanidinium carbonate salts (**Scheme 2.2**).[33,34]



Scheme 2.2. CO_2BOL synthesis from Burton's guanidine base and the 1,8-diazabicyclo[5.4.0]undec-7-ene (DBU) amidine base.

In 2019, Khokarale and Mikkola described a one-pot process for the synthesis of 5- and 6-membered cyclic carbonates such as ethylene carbonate (EC) and propylene carbonate (PC) based on the CO_2BOL concept (**Scheme 2.1b**).[35] They demonstrated that in presence of the DBU superbase, halohydrins can be effectively converted to cyclic carbonates except 2-bromo and 2-iodoethanol which react equivalently with the amidine and form *N*-alkyl DBU salts. Surprisingly, the authors made no mention of the extremely mild conditions under which the syntheses were carried out, nor of the glaring difference in the reactivity of the carbonate salts when they are produced from DBU rather than metals. Although the ease of reaction can obviously be partly explained by the thermodynamic stability of the as-prepared 5- and 6-membered cycles, it is not excluded to envisage that the R-OCO_2^-, DBU.H^+/R'X system also presents similarities to anion-π interactions-based systems[36,37] or to rare ion-pair S_N2 processes[38–41] in which reaction intermediate and transition state are stabilised.

While guanidines such as 1,1,3,3-tetramethylguanidine (TMG) and Barton's base have already been studied to prepare CO_2BOLs, no one has ever considered the attractive alternative of 1,5,7-triazabicyclo[4.4.0]dec-5-ene (TBD) guanidine. Comparatively to both TMG and Barton's base, TBD is a unique organic structure due to its high basicity but, more importantly, to its bifunctionality characterised by two reactive sites at close distance.[42] While its catalytic abilities have already been exploited in various organic reactions, including transesterification,[43,44] transcarbonylation,[45] amidation,[46–54] Michael-addition and aldol reactions,[55,56] it also appears as a "magic catalyst" for the polymer community.[57] Ready-to-apply liquid formulations of TBD are also available, allowing to overcome the complicated handling of its crystalline delivery form and its rather limited market availability.[42]

This chapter describes the selective S_N2 reaction of primary and secondary alkyl iodides with TBD-based CO_2BOLs (**Scheme 2.1c**). By crossing experimental observations and molecular

modelling to reveal the most preferred reaction mechanism, we demonstrate that TBD is the most favourable candidate for binding CO_2 and alcohols, especially primary ones. As compared to DBU-based CO_2BOLs, the TBD-based ones are selective to S_N2 processes allowing to work with highly reactive alkyl iodides while getting rid of undesirable base quaternisation. The high reactivity of those TBD-based CO_2BOLs towards backside S_N2 processes is unambiguously explained by the presence of the TBD.H^+ guanidinium revealing a unique metal-free cation-assisted S_N2 ion-pair process.

II. RESULTS AND DISCUSSION

A. Preparation of TBD-based CO_2BOLs

A fast, selective and potentially industrially scalable preparation of dialkyl carbonates from a CO_2BOL salt requires adapting to the use of different types of commercially available alkyl halides, especially those bearing excellent leaving groups such as bromide and iodide. Despite iodo-based compounds having been excluded by Khokarale and Mikkola due to their ease to quaternise DBU during the preparation of EC and PC,[35] we decided to face the challenge by only working with such extremely reactive alkyl halides, thus necessitating the design of a metal-free carbonate salt which is easy to prepare, cheap and highly selective to a S_N2 process.

Physical and chemical properties of CO_2BOLs can be manipulated by changing alcohol/base pairs. Appropriate organic bases include amidines, guanidines, some amines and phosphazenes. In comparison to nucleophilic DBU,[58] non-nucleophilic tertiary amines such as triethylamine and Hünig's base (N,N-diisopropylethylamine) seem attractive to get rid of the unwanted *N*-alkylation of the base. However, they have been demonstrated ineffective for CO_2BOLs preparation under regular conditions of temperature and pressure.[59] On the other hand, phosphazene superbases present some concerns about toxicological issues[60,61] and are not produced on an industrial scale, excluding applications in the chemical industry and to the present study.

To evaluate the relevance of using TBD to prepare CO_2BOLs from alcohols, we priorly decided to compare its efficiency to the one of the well-known DBU base. In the presence of DBU, the rate of CO_2 uptake from an alcohol is mainly dependent on the stirring rate of the medium since the reaction is a function of the mass-transfer of CO_2 from the gas phase into solution.[33] Under optimal stirring rate conditions, a few seconds are sufficient to almost quantitatively transform a primary alcohol/DBU mixture into a CO_2BOL. In order to make an efficient comparison between DBU and TBD, we then deliberately decided to primarily work on a static open medium (no stirring rate applied) by simply bubbling CO_2 into the alcohol/base mixture (pCO_2 = 0.2 bar). Conversions were monitored gravimetrically and confirmed from time to time by ^{1}H NMR spectroscopy. As presented by **Figure 2.1a**, such simple experimental modification has a

tremendous impact on the overall CO_2 uptake when CO_2BOLs are prepared from different alcohols and the DBU base ($[alcohol]_0/[DBU]_0$ = 1) in bulk (no solvent). While there is a little preference for methanol, ethanol, 1-propanol over a longer 1-hexanol, those primary alcohols are preferred over secondary alcohols (isopropanol, cyclohexanol and butan-2-ol) and very strongly preferred over phenol. If such observations appear in perfect line with the ones of Heldebrant,[33] the maximal CO_2 uptake of this exothermic system, here obtained from primary alcohols, is limited to 52-56 % reaching a plateau after 5 to 10 minutes. Considering those values as reasonable in terms of conversion and kinetics to easily compare the DBU and the TBD bases, we selected those experimental conditions and ethanol as the representative alcohol for our CO_2BOL preparation study with TBD.

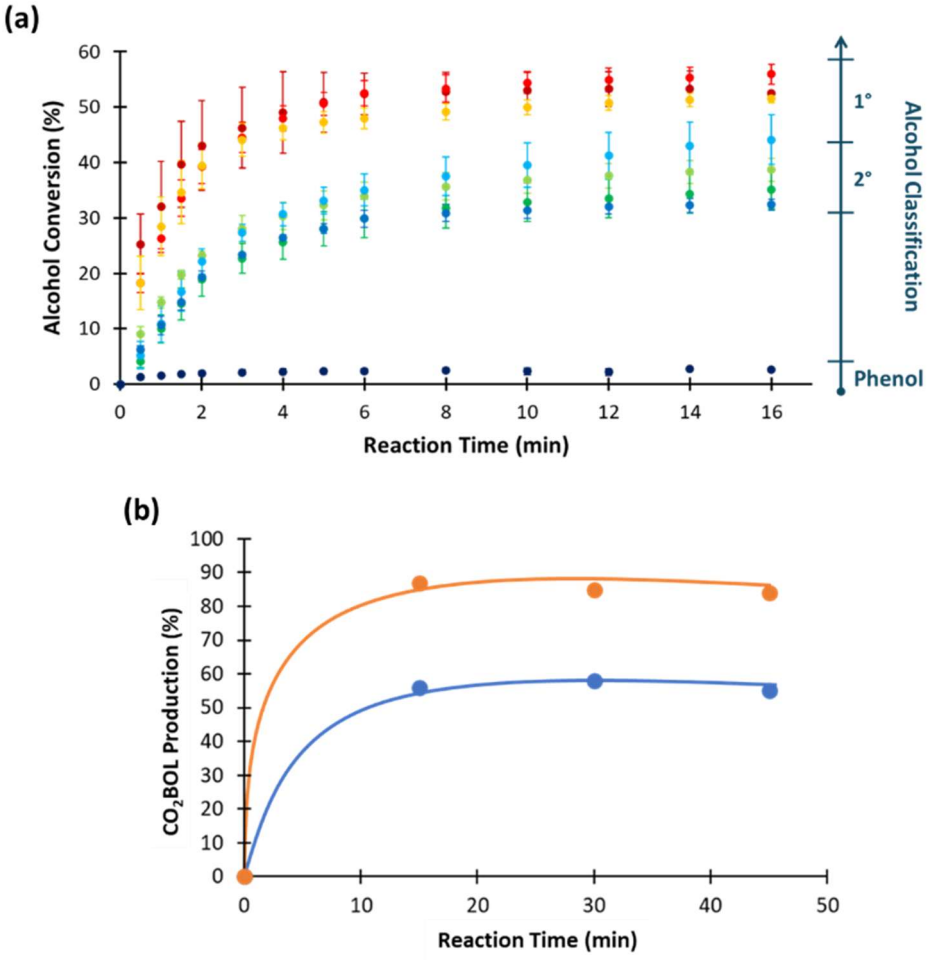


Figure 2.1. (a) CO_2BOLs Production from Various Alcohols Activated by DBU at 21 °C under CO_2 Bubbling. CO_2BOLs production from primary alcohols (● methanol, ● ethanol, ● 1-propanol, ● 1-hexanol), secondary alcohols (● iso-propanol, ● butan-2-ol, ● cyclo-hexanol) and phenol (●) as activated by DBU ($[alcohol]_0/[DBU]_0$ = 1) at 21 °C and under CO_2 bubbling (pCO_2 = 0.2 bar). Error bars represent the standard deviation of 3 trials. **(b) TBD and DBU Efficiencies Comparison in CO_2BOL Production.** CO_2BOLs production obtained from ethanol as activated by TBD (●) and DBU (●) in MEK ($[ethanol]_0$ = $[DBU]_0$ = $[TBD]_0$ = 3 M) at 21 °C (pCO_2 = 0.2 bar).

Because the semi-crystalline version of TBD has been used, efficiencies of both DBU and TBD bases were experimentally compared by reactions performed in solution for an initial concentration in bases and ethanol of ~ 3 M. The degree of CO_2 loading in CO_2BOLs is known to control the polarity of the solvent but conversely the polarity has also been exploited as means to control CO_2 loading.[62] Since non-polar solvents aid in the de-complexing of CO_2 from CO_2BOLs, we first decided to compare both DBU and TBD's respective activities by selecting the polar methyl ethyl ketone (MEK) solvent also known for its great ability to dissolve CO_2 as compared to other solvents such as alcohols.[63]

As expected, the use of TBD considerably increases the overall kinetics of the CO_2BOL production and improves the maximal CO_2BOL production value to ~87 % (**Figure 2.1b**), at least in MEK. By comparing the relative integration of the $CH_3C\underline{H_2}OCO_2^-$ to the $TBD.H^+$ methylene signal, the ^1H NMR spectroscopy analysis reveals that the quasi-quantitative CO_2 conversion is attributed to a partial evaporation of the ethanol during the exothermic CO_2BOL formation. Moreover, the oxygen-bound methylene of the ethyl group of the sample shifted from the normal position of ethanol (3.52 ppm in $CDCl_3$) to 3.81 ppm, which is close to the chemical shifts of the DBU-based hexyl carbonate salts (3.90 ppm)[64] or the dihexylcarbonate (4.13 ppm in CCl_4).[65]

To gain further insights into the reaction mechanism and reactivity of both DBU and TBD in the CO_2 conversion towards CO_2BOL, we collaborated with Dr. Kuber Singh Rawat from the team of Pr. Veronique Van Speybroeck (UGhent). They conducted a detailed investigation using density functional theory (DFT) calculations ($CPCM_{(toluene)}$/B3LYP-D3(BJ)/ 6-311++G**,SDD(I) level of theory). Further computational details are given the Experimental Procedures section. To better evaluate the relevance of the as-obtained DBU- and TBD-based results, an extra comparison with a non-efficient pyridine base has also been performed (**Figure 2.2**).

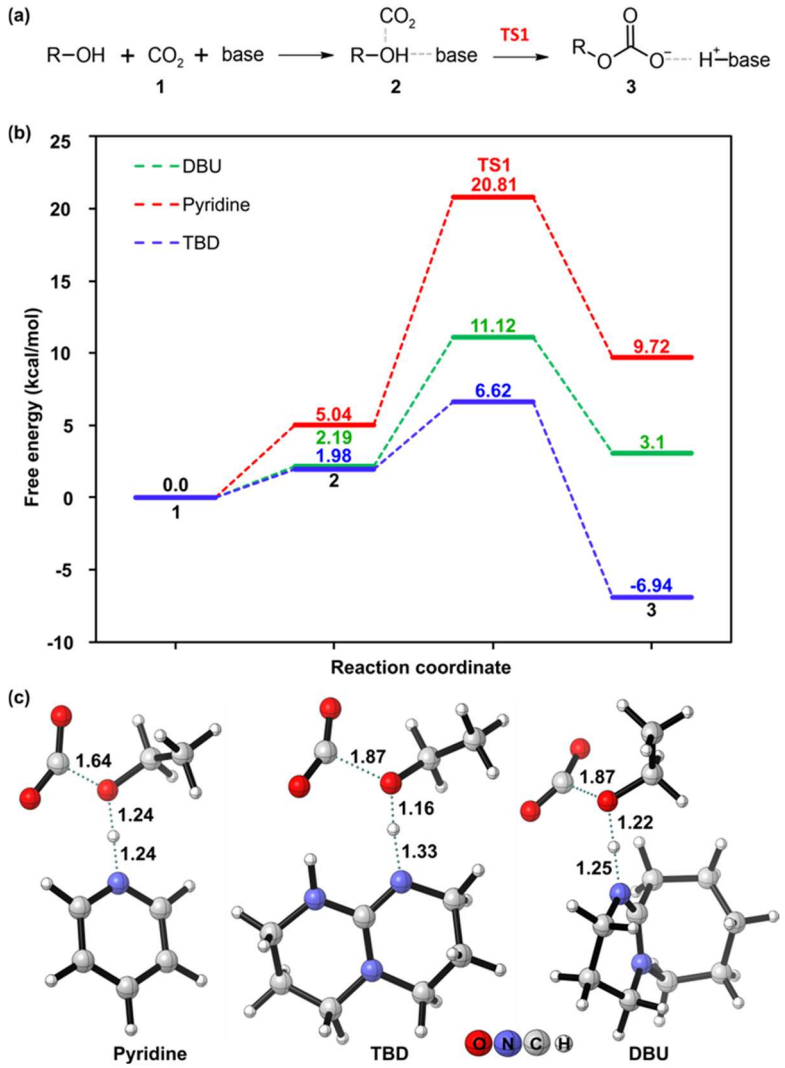


Figure 2.2. CO_2 Activation via Ethanol and Organic Bases: Pathway, Energy Profiles, and Transition State Geometries. (a) possible reaction pathway, **(b)** calculated free energy profiles at $CPCM_{(toluene)}$/B3LYP-D3(BJ)/ 6-311++G** level of theory, and **(c)** optimised geometries for transition states with bond lengths (in Å). The atom colours are elaborated in the figure.

The reaction initiates with the interaction between a CO_2 molecule and the base along with ethanol (**1→2**). The calculated free energies (ΔG) for this reaction were 5.04, 2.19, and 1.98 kcal/mol (**Figure 2.2b**) for the pyridine, DBU, and TBD bases, respectively. Next, the transition from intermediate **2** to the final product **3** (**2→3**) occurs via a concerted transition state (**TS1**) instead of a stepwise process. Upon closer inspection, it can be observed that in these transition states, the carbon atom of the CO_2 molecule participates in a reaction with the oxygen atom of ethanol while the base simultaneously abstracts the proton from the alcohol (representative structures are depicted in **Figure 2.2c**). The calculated energy barriers ($\Delta G^{\ddagger}$) for pyridine, DBU and TBD were determined to be 15.77, 8.93, and 4.64 kcal/mol, respectively. These results are in agreement with our experiments and indicate that TBD is the most favourable candidate for this reaction compared to the other two bases, and most importantly DBU. Moreover, the overall reaction free energy profile also reveals a strong interaction between the carbonate anion and TBD.H^+ leading to an overall exothermic reaction-free energy of -6.94

kcal/mol compared to the endothermicity observed for DBU.H$^+$ (3.1 kcal/mol) and pyridine.H$^+$ (9.72 kcal/mol).

The CO_2 activation using the base only was also explored as in previous reports[66,67] and we found that in this scenario as well, activation by TBD (2.89 kcal/mol) requires a lower energy barrier compared to DBU (6.56 kcal/mol) (**Figure 2.3**). These barriers are lower compared to the CO_2 activation by ethanol in the presence of bases. Nevertheless, the final products are found to be 5.09 kcal/mol and 5.81 kcal/mol more favourable for TBD and DBU, respectively, when CO_2 reacts with ethanol rather than with base alone.

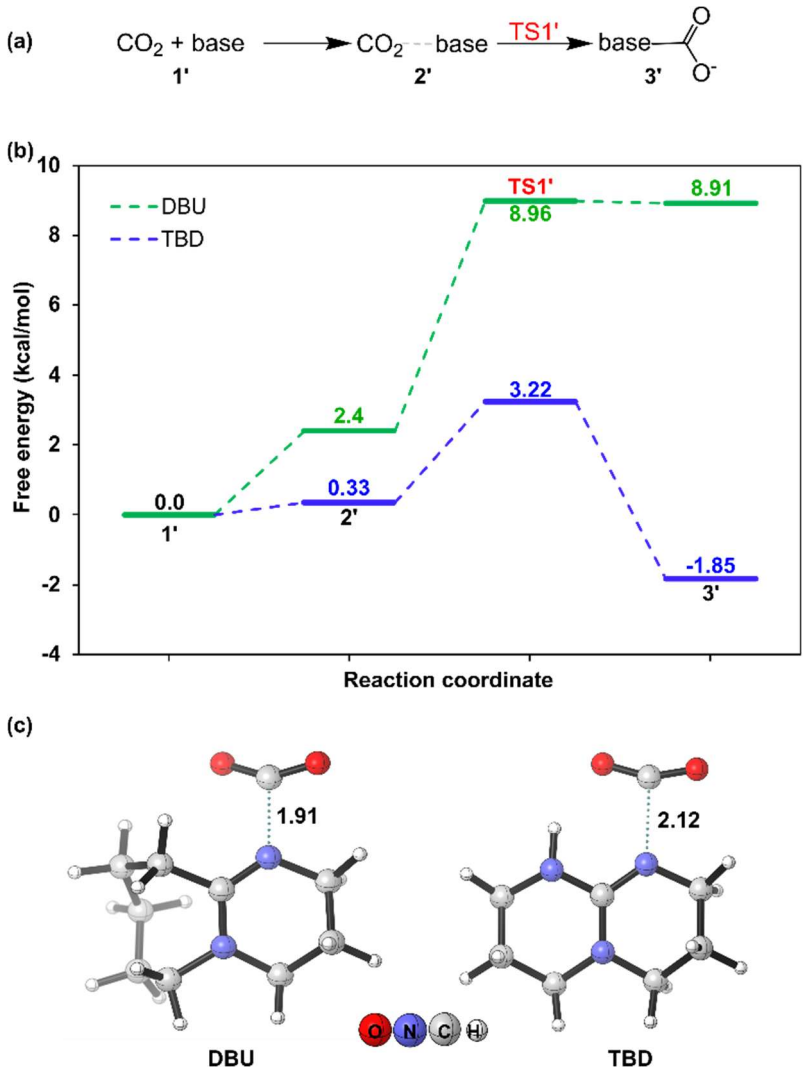


Figure 2.3. CO_2 activation using bases only. (a) Possible reaction pathway, **(b)** calculated free energy profile at $CPCM_{(toluene)}$/B3LYP-D3(BJ)/ 6-311++G** level of theory, and **(c)** Optimised geometries for transition states with bond lengths (in Å). The atom colours are indicated in the figure.

To demonstrate that the preparation of CO_2BOLs from TBD is a promising and efficient process, the ability of the guanidine base to quantitatively convert longer primary alcohols into carbonate salts has been investigated by adjusting the experimental conditions to improve the CO_2BOL conversion. Long primary alcohols do not solubilise the semi-crystalline version of TBD

at room temperature, thus requiring to either use an efficient solvent to solubilise reactants while stabilising the as-produced carbonate salt, or to generate CO_2BOLs in the melt state. To the best of our knowledge, the second strategy has never been studied and could represent a real breakthrough for the industrial production of CO_2BOLs. 1-Heptanol has been used as a representative candidate for the rest of our study.

In 2008, Jessop *et al*. briefly stated that the production of CO_2BOLs from DBU and alcohols proceeds to great conversion in $CDCl_3$.[64] To get rid of the relatively slow kinetics observed under static conditions, 1-heptanol and TBD were therefore solubilised in this solvent ($[1\text{-heptanol}]_0$ = 4 M, $[OH]_0/[TBD]_0$ = 1) and subjected to a CO_2 bubbling treatment (pCO_2 = 0.2 bar, 2-to-3 bubbles per second) under high stirring rate (~ 500 rpm).[33] Under those experimental conditions, our ^{1}H NMR data show that the reaction proceeds to very high conversions. Specifically, the proton assignable to the OH function of the 1-heptanol initially shifts downfield and then completely disappears after 10 minutes of reaction. Concomitantly, the N-H signal of the TBD shifts downfield by + 0.53 ppm to the benefit of the guanidium protons signal (**Figure 2.4**). By comparing integration values before and after reaction, a conversion of 95 ± 5 % is calculated. Considering the moderate accuracy of the ^{1}H NMR integration, such result indicates either a complete or an almost-complete conversion to the alkyl carbonate salt.

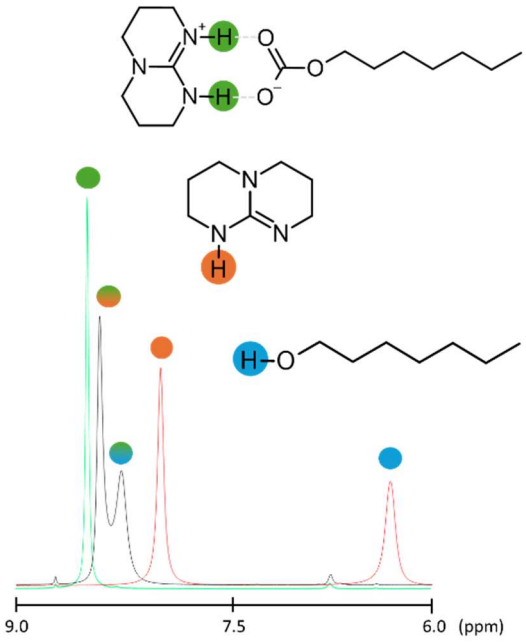


Figure 2.4. Enhanced CO_2BOL Production via TBD-assisted Alcohol Activation under CO_2 Bubbling and High Stirring. ^{1}H NMR spectra (zoomed between δ = 6 ppm and 9 ppm) of an equimolar mixture of 1-heptanol and TBD before (red) and after 5 (black) and 10 minutes (green) of CO_2 treatment.

To complement our observation and clearly visualise the important role of the chloroform solvent, the CO_2 activation was also evaluated when the carbonate salt is produced under $CHCl_3$ solvation. Appropriate DFT calculations were then investigated and compared to a representative toluene-based medium. The calculated energy barriers (**TS1**) for DBU and TBD in

$CHCl_3$ were found to be 7.15 and 3.99 kcal/mol, respectively (**Figure 2.5a**). These energy barriers were 1.78 and 0.65 kcal/mol lower compared to the toluene solvent for DBU and TBD, respectively (**Figure 2.2b** and **Figure 2.5a**). Furthermore, the comprehensive analysis of the reaction's free energy profile indicated that the final product (**3**) is more favoured when $CHCl_3$ is the solvent, with an additional free energy stabilisation of 2.93 and 2.08 kcal/mol for DBU and TBD, respectively. Moreover, TBD exhibited a more favourable reaction free energy (-9.02 kcal/mol) when compared to DBU (0.17 kcal/mol). This observation aligns well with the experimental results, suggesting that TBD is a better base for CO_2 activation compared to DBU, especially in $CHCl_3$. Additionally, we performed a comparative analysis of various solvents in the activation of CO_2 using TBD. Our computational findings, as illustrated in **Figure 2.5b**, indicate that acetonitrile (ACN) leads to a greater thermodynamic stability compared to toluene and $CHCl_3$.

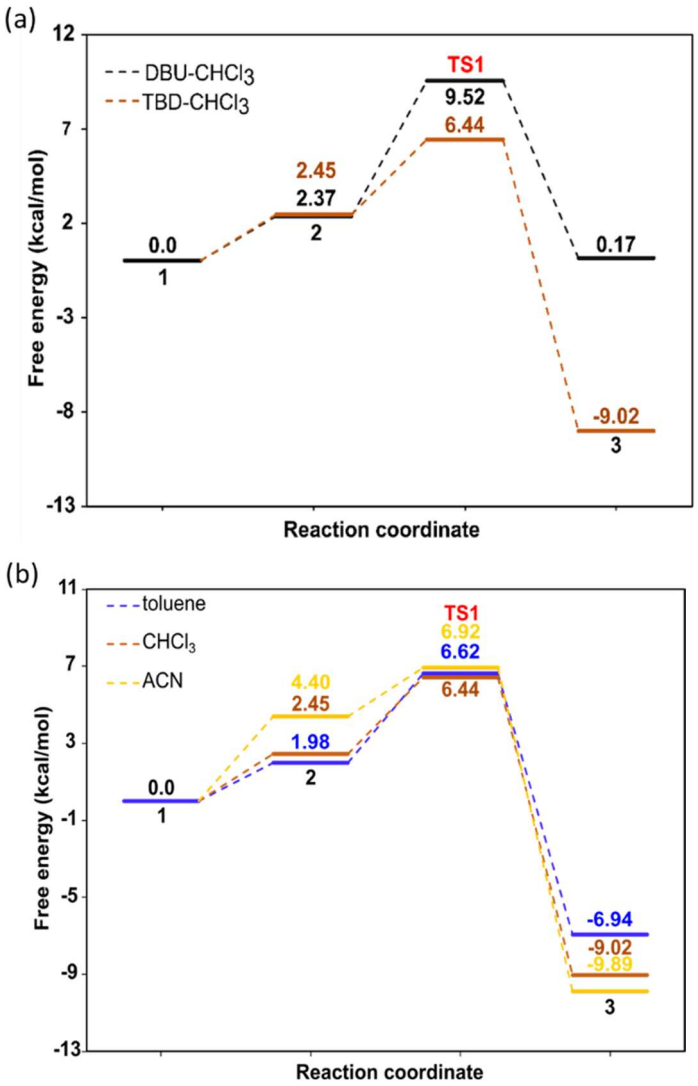


Figure 2.5. Theoretical Energy Profiles of CO_2 Activation with (a) DBU and TBD in Ethanol: $CHCl_3$ Solvent Analysis. The calculated free energy profile for CO_2 activation via ethanol in the presence of DBU and TBD bases using $CHCl_3$ solvent. Values were calculated at $CPCM_{(CHCl3)}$/B3LYP-D3(BJ)/ 6-311++G** level of theory. **(b) Using TBD base in different solvents** at $CPCM_{(toluene)}$/B3LYP-D3(BJ)/ 6-311++G** level of theory.

Although academically very interesting, producing CO_2BOLs in organic solvents presents certain disadvantages. Generally speaking, in the limited context of a single production of CO_2BOLs, the use of solvent considerably reduces any interest in industrial production. In the more specific context of our study, and in view of the DFT results presented above, chloroform contributes considerably to the general stabilisation of CO_2BOLs, limiting *de facto* their reactivity towards the alkyl halides used to prepare dialkyl carbonates through a one-pot S_N2 reaction. To get rid of such a problem, we investigated the possibility to produce CO_2BOLs at a temperature sufficiently high to solubilise TBD into the alcohol without using any solvent.

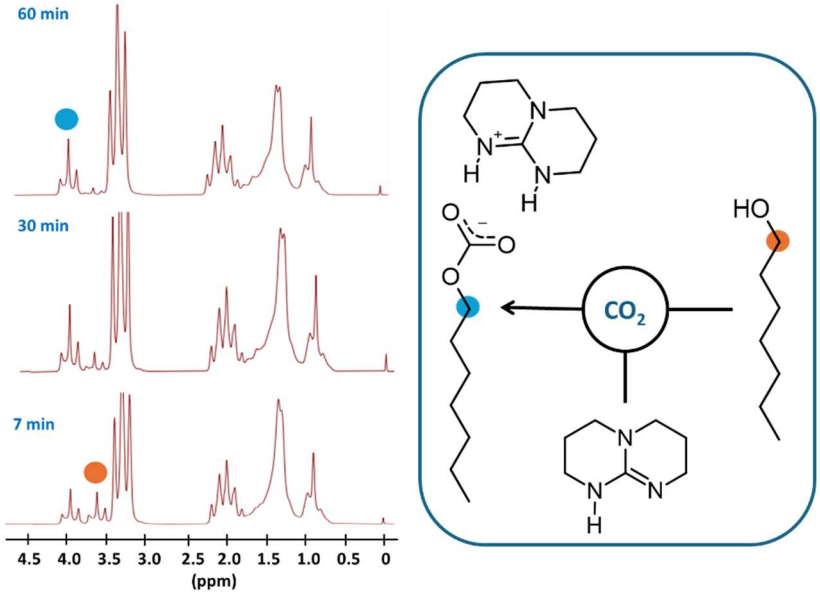


Figure 2.6. Bulk Production of CO_2BOLs via Heat-Activated TBD and 1-Heptanol Mixture under CO_2 Exposure. ^{1}H NMR spectra (zoomed between δ = 0 ppm and 4.5 ppm) of an equimolar mixture of 1-heptanol and TBD during a CO_2 treatment (pCO_2 = 0.2 bar) at 100 °C. (See also Figure S2.1, in the Supporting Information section, page 109)

As already stated, liquid long primary alcohols such as 1-heptanol do not solubilise the semi-crystalline version of TBD completely at 21 °C. When heated at 100 °C for few seconds, the two-phases mixture turns into a clear fluid solution. By cooling down the medium to room temperature, the TBD starts to recrystallise producing the heterogenous 1-heptanol/guanidine mixture back. To produce the corresponding CO_2BOL in bulk, the equimolar mixture of 1-heptanol and TBD was therefore heated up and subjected to a CO_2 exposure (pCO_2 = 0.2 bar) under high stirring rate (~ 500 rpm), at a constant temperature of 100 °C. Although slower than in $CHCl_3$ solution, treating the homogeneous mixture at 100 °C under a CO_2 atmosphere enables the corresponding carbonate salt to be produced selectively in a near-quantitative yield (~ 96%), after one hour of reaction and without the use of solvent (**Figure 2.6** and **Figure S2.1**, **p. 121**). Evidently, the working temperature must be sufficiently high to allow the complete solubilisation of TBD, but also below the decomposition temperature of the CO_2BOL to prevent potential thermal release of CO_2 from the TBD-based salt, a topic slated for further investigation. However, this liberation of CO_2 from the CO_2BOL suggests a potential avenue for recyclability.

Indeed, examination of the TBD-based salt's thermal stability revealed that, under a nitrogen flow (pN_2 = 0.2 bar), it takes 1.5 h to achieve approximately 90% degradation at 90 °C, whereas complete degradation occurs within 0.5 h at 110 °C (**Figure 2.7**). Subsequent to thermal degradation, the alcohol and TBD are recovered (**Figure S2.2**, **p. 121**). Consequently, the CO_2BOL could be readily regenerated by reintroducing CO_2 into the mixture.

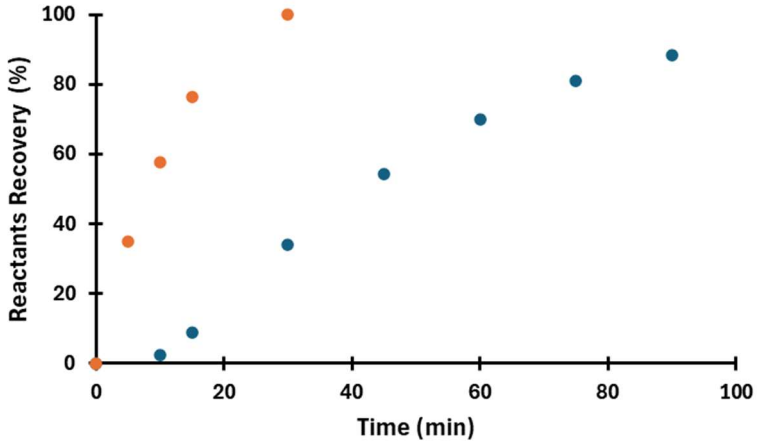


Figure 2.7. Alcohol and TBD recovery rate when bubbling N_2 (pN_2 = 0.2 bar) over the CO_2BOL at 90 °C (●) and 110 °C (●).

B. Preparation of Linear Dialkyl Carbonates from TBD-based CO_2BOLs

Taking into account the experimental data in the literature on reactions involving the use of DBU-based carbonate salts and alkyl halides, it would appear that, leaving aside the poisoning alkylation reactions of DBU, the production of carbonates is somehow based on a nucleophilic substitution (S_N) mechanism. The primary nature of the alkyl halides generally used seems to support the fact that the mechanism involved implies a bimolecular nucleophilic substitution (S_N2) process. Despite this, the generally mild experimental conditions, compared to those adopted for the use of metal-based carbonate salts, make the exact nature of this process unclear. This is all the more true as the nucleophilic nature of carbonate salts is supposed to be very weak, making the process theoretically fastidious. In order to remove the doubt and define this reaction as accurately as possible, a series of experimental carbonatations were carried out and supplemented by DFT theoretical calculations.

Various linear dialkyl carbonate syntheses were performed by adding primary and secondary alkyl iodides to an heptyl-OCO_2^-,TBD.H^+ salt, pre-generated by treatment of an equimolar mixture of 1-heptanol and TBD under CO_2 bubbling for 1.5 hours at 100 °C (Conv. ~ 95%). Iodoethane and 1-iodooctane were selected as primary alkyl iodides, while 2-iodopropane was used as a representative secondary alkyl halide. Reactions were performed for 24 hours under air by using one equivalent of alkyl iodide as compared to the initial 1-heptanol. Since all reactants are liquid, nucleophilic substitution reactions were performed in ACN (2M) but also in

bulk at 21 and 65 °C (**Table 2.1**). Carrying out these S_N reactions without solvent should favour the formation of the expected solid TBD.H$^+$, I$^-$ salt by-product, simplifying the separation process and easily enhancing reaction purity.

Table 2.1. Reaction yields

Alkyl iodide	Entry	Bulk		Entry	ACN	
		Yield (%) at 21 °C	Yield (%) at 65 °C		Yield (%) at 21 °C	Yield (%) at 65 °C
Iodoethane	1	~ 99	~ 99	4	93	~ 99
1-Iodooctane	2	23	~ 99	5	67	93
2-Iodopropane	3	67	96	6	97	95

Yields of heptyl-OCO_2^-, TBD.H$^+$ salt with different alkyl iodides as reacted in bulk and ACN (2M) at 21 °C and 65 °C. Yields are determined by ^{1}H NMR analysis from the crude mixture taking into account the engaged TBD-based salt content.

Carrying out the carbonatation reactions in ACN gives high yields whatever the temperature and the nature of the alkyl iodide (**Table 2.1**, entries 4 – 6). This observation highlights a reaction mechanism based on a S_N2 process. Since the frontside pathway is highly disfavoured because of the increased steric repulsion as a result of the proximity of the carbonate nucleophile and I$^-$ leaving group in the transition state, the hypothesis of a S_N2 backside process appears more convincing. Very interestingly, the overall polarity of the solvent is not crucial since high yield of reactions are also obtained in bulk, especially at 65 °C (**Table 2.1**, entries 1 – 3). Moreover, it is worth noting that the yields observed when iodoethane is used as the alkyl iodide are somehow identical with or without ACN (**Table 2.1**, entries 1 & 4). Although results obtained when using 1-iodooctane have to be discarded due to a partial crystallisation of the carbonate produced in bulk at 21 °C (**Table 2.1**, entry 2), the use of 2-iodopropane also provides highly acceptable results in the absence of solvent at room temperature, considering the secondary nature of this alkyl iodide (**Table 2.1**, entry 3). Based on the concept of ion-pairs introduced and developed by Winstein,[68] all these observations suggest that the hypothetical backside S_N2 process does not proceed from free ions or solvent-separated ions but by contact ion-pairs where the countercation (*i.e.*, the TBD.H$^+$ guanidinium) and the anion (*i.e.*, the heptyl-OCO_2^- carbonate anion) are in close proximity to each other.

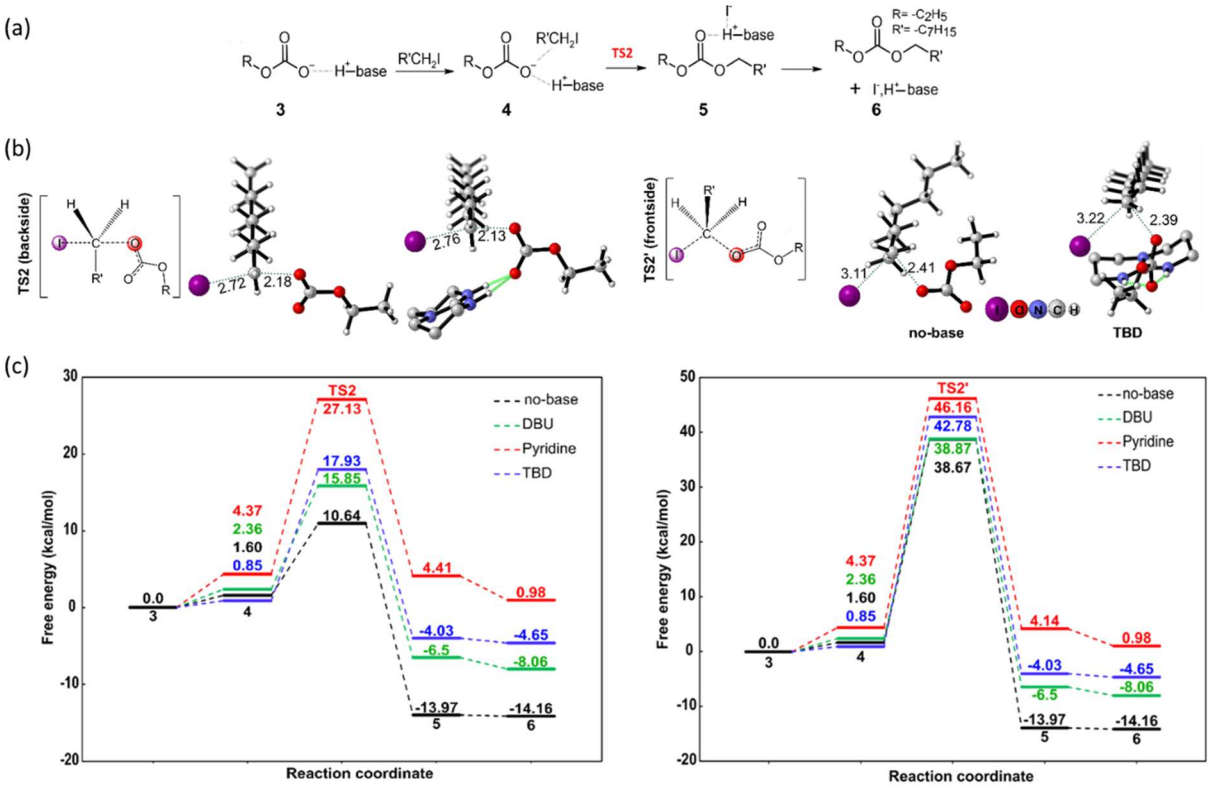


Figure 2.8. DFT Mechanistic Investigation of TBD-Based CO_2BOL Reactivity towards Alkyl Iodides: Comparison with and without DBU and Pyridine. (a) possible reaction pathway, **(b)** optimised geometries for transition states (Bond lengths in Å), and **(c)** calculated free energy profile for the backside (left) and frontside (right) attacks at $CPCM_{(toluene)}$/B3LYP-D3(BJ)/ 6-311++G**, SDD(I) level of theory. H atoms are omitted from TBD for clarity. The atom colours are elaborated in the figure.

To understand the high reactivity of the TBD-based CO_2BOLs with regards to the alkyl iodides and to shed some light on the mechanism involved, mechanistic investigations at the DFT level were performed. To make an accurate comparison, the reactivity of TBD-based CO_2BOLs was compared to the ones hypothetically obtained from both DBU and pyridine bases. Simulations were performed by considering intermediate **3** (**Figure 2.2a**, **p. 102**) and 1-iodooctane. The proposed reaction pathway is illustrated in **Figure 2.8a**. Two scenarios have been hypothesised : one in which the mechanism implies a carbonate anion in absence of its TBD.H^+ countercation (labelled "no-base") and another in the presence of the protonated base cation (labelled "pyridine", "DBU" and "TBD"). In each scenario, the S_N2 reaction was examined via two distinct transition states (**Figure 2.8b**) : (i) the carbonate anion attacks via the backside (**TS2**) of the leaving group (I^-) or (ii) the carbonate anion attacks from the frontside of the leaving group (**TS2'**). Based on the calculated free energy barriers (**Figure 2.8c**), it is evident that the backside attack is more favourable in all the cases. Interestingly, a backside attack without TBD.H^+ shows the most favourable path with a free energy barrier of 9.04 kcal/mol, which is 28.03 kcal/mol lower compared to when the carbonate anion approaches from the frontside. On the other hand, the calculated barriers via **TS2** are 13.48, 17.08, and 22.76 kcal/mol for DBU, TBD, and pyridine, respectively. This indicates that, compared to an amidinium cation, the involvement of a

guanidinium cation demands a higher barrier to accomplish the process. The reason stems from the disruption of the strong interaction between the cation and the carbonate anion during the substitution process. As a result, the separation of the carbonate anion and base.H^+ in intermediate **3** requires large free energies of 44.23 kcal/mol and 38.22 kcal/mol (**Figure S2.11**, **p. 126**) for TBD and DBU, respectively. Such high energy barriers confirm that free ions are not involved and that contact ion-pairs are acting as nucleophiles in the S_N2 process. Nevertheless, noncovalent interaction (NCI) analysis[69] reveals that the energy required to break the interaction can be counterbalanced by stabilising both the leaving and attacking groups through the formation of noncovalent interactions with TBD.H^+ in transition state (**TS2**). To investigate the role of these interactions, various configurations of **TS2** (**Figure 2.9**) were computed by altering the manner in which TBD.H^+ interacts with the leaving I^- ion and attacking carbonate anion groups. When both I^- and the unreactive O atom of the carbonate anion engage in interactions with TBD.H^+ (I···TBD and N−H···O), a barrier of 17.08 kcal/mol is required (**Figure 2.9a**). As clearly represented by the **Figure 2.9e**, such an optimised transition state induces an attractive noncovalent interaction between the TBD.H^+ and the leaving I^-, strongly supporting a guanidinium-assisted S_N2 ion-pair process. Any alteration in these interactions (**Figure 2.9f-h**) leads to a higher barrier.

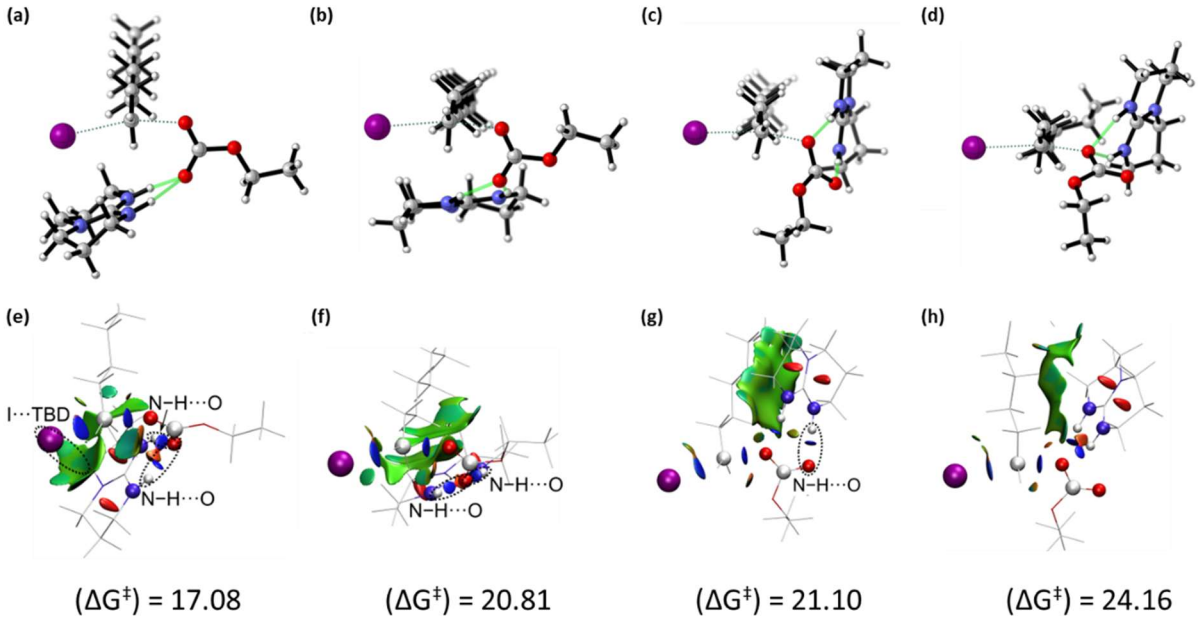


Figure 2.9. Transition State Geometries and NCI Analysis of TBD-Based S_N2 Reaction: Impact of Noncovalent Interactions on Energy Barriers. (a-d) Optimised geometries for transition states (**TS2**) involving TBD in a backside attack S_N2 reaction, considering various noncovalent interactions between TBD.H^+ and both the leaving I^- and the attacking carbonate anion groups. The calculated energy barriers (in kcal/mol) are presented alongside their **(e-h)** corresponding NCI plots, providing a detailed visualisation of the impact of these interactions on the energy barriers. Isosurface colours reflect the nature and strength of the interactions, with blue indicating regions of strong attractive interactions, green representing areas of attractive interactions, and red highlighting regions of repulsion.

Overall, as compared to DBU and pyridine, the presence of TBD is quite crucial to assist the CO_2 activation and subsequent S_N2 reaction with alkyl iodides through a unique guanidinium-assisted S_N2 ion-pair process. A combined free energy profile for the reaction gives an additional support for the role of different bases (**Figure 2.10**).

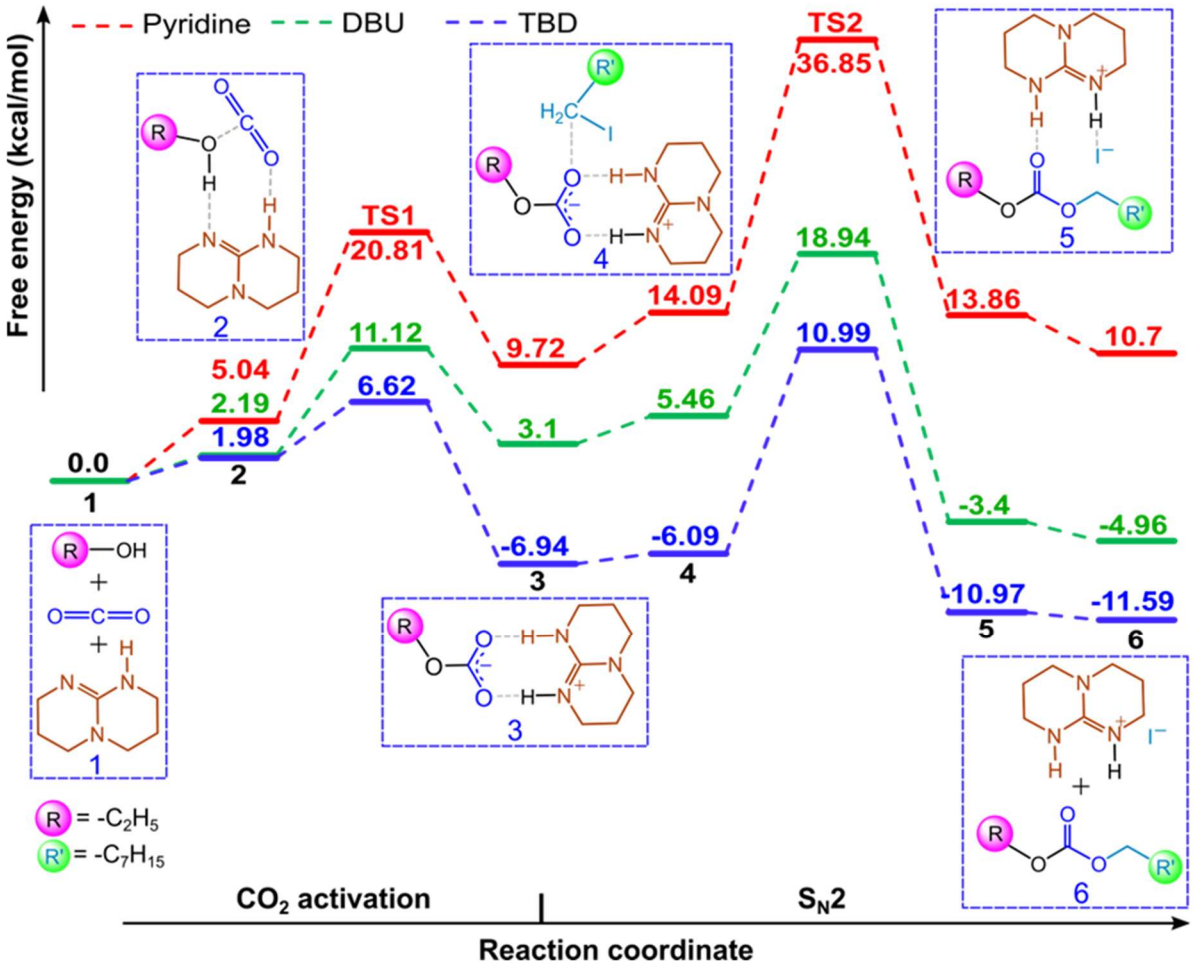


Figure 2.10. Role of TBD in CO_2 Activation and S_N2 Reaction: Comparative Free Energy Profile with DBU and Pyridine. A combined free energy profile for CO_2 activation and S_N2 ion-pair reaction using different bases calculated at $CPCM_{(toluene)}$/B3LYP-D3(BJ)/ 6-311++G**, SDD(I) level of theory. The reactants, products, and intermediates of TBD are enclosed in a blue dashed box.

We also explored the free energy profile employing ACN, toluene and $CHCl_3$ solvents for the TBD base (**Figure S2.12**, **p. 126**). A comprehensive analysis of the overall reaction free energy profile shows a preference for ACN, showcasing energy advantages of 6.99 kcal/mol and 2.85 kcal/mol over toluene and $CHCl_3$, respectively. This observation aligns well with our experimental results, demonstrating that ACN exhibits improved catalytic performance compared to the bulk.

Considering the reactants involved, performing reactions in bulk presents an interesting asset, *i.e.* the precipitation of the $TBD.H^+,I^-$ salt and its simple isolation from the crude medium. Whatever the alkyl iodide used, and after only a few minutes, a significant amount of a white

compound indeed starts to precipitate, making its isolation by filtration easy. While the ^{1}H NMR analysis of that compound confirms the presence of a protonated guanidinium (TBD.H^{+}) (**Figure S2.9**, **p. 125**), the presence of an iodide counteranion has been unambiguously certified by electrospray ionisation mass spectrometry analysis (ESI-MS), performed by Pr. Pascal Gerbaux and his team (**Figure S2.10**, **p. 125**). Indeed, besides ions corresponding to the cationic part of organic salts, such as ionic liquids, aggregate ions associating the parent ion with one or more ionic liquid molecules are often detected upon ESI in the positive ion mode,[70] making the identification of both the cationic and anionic parts of an organic salt possible in a single MS analysis. In **Figure S2.10** (see p. 125), besides the dominant signals at *m/z* 140.1 and 279.2 that are readily ascribed to [TBD+H]$^{+}$ and [2TBD+H]$^{+}$ ions, the singly charged ions detected at *m/z* 407.1 correspond to such an aggregate associating two protonated TBD molecules to a single iodide anion, typically [2TBD+2H+I]$^{+}$, whose detection supports our first hypothesis. Satellite signals at *m/z* 168.1, 196.2 and 435.2 are also detected and attest for the presence of TBD molecules that have been quaternised by iodoethane. To our opinion, the detection of those signals is attributed to the presence of at least 5 mol% of TBD^{+}C$_2$H$_5$. Such *N*-quaternised TBD comes from the fact that iodoethane has been used in slight excess as compared to the heptyl-OCO$_2^{-}$, TBD.H^{+} salt initially produced at ~ 95 mol% from the 1-heptanol ([iodoethane]$_0$ = [TBD]$_0$ = [1-heptanol]$_0$ ~ (100/95).[heptyl-OCO$_2^{-}$, TBD.H^{+}]).

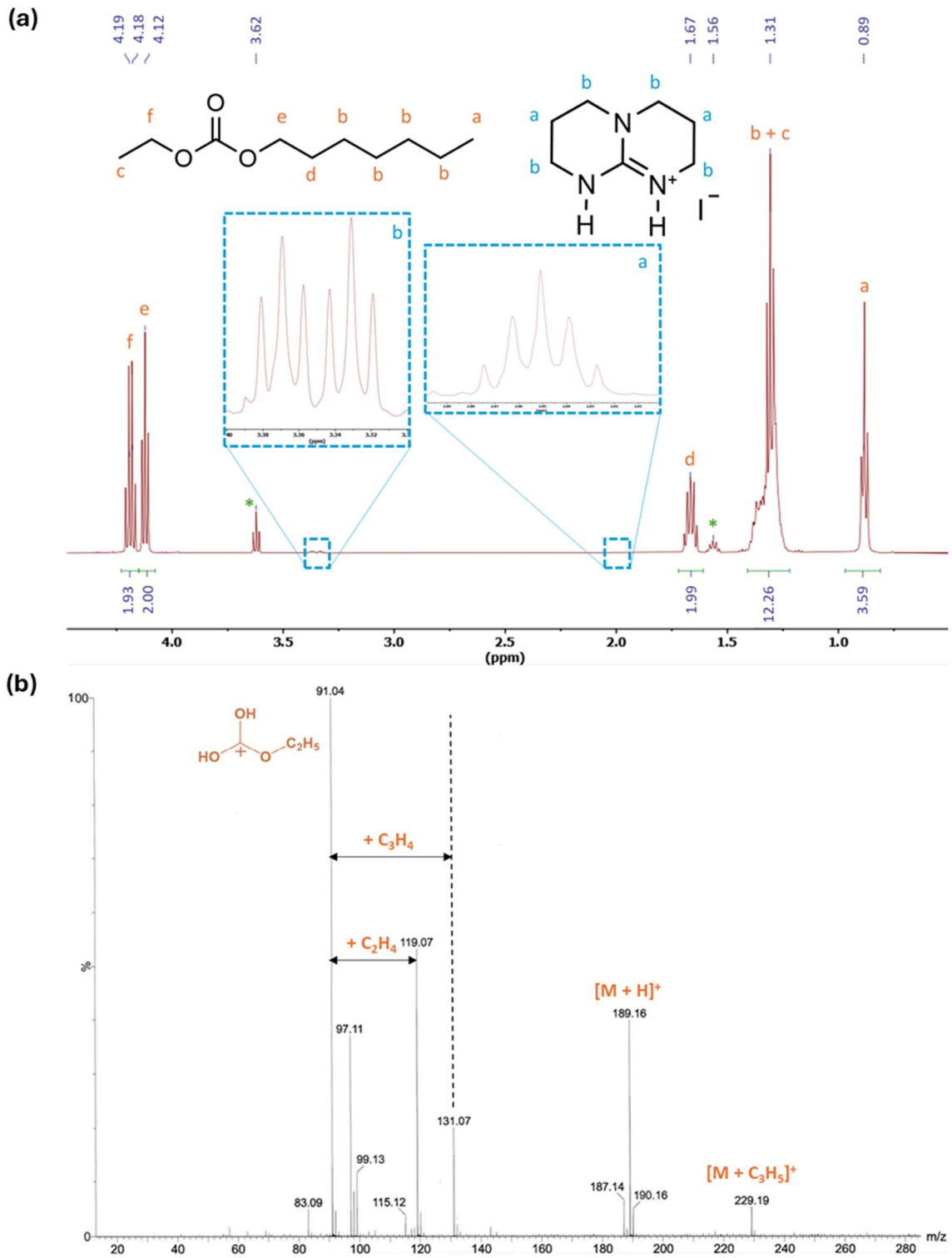


Figure 2.11. Characterisation of Heptyl-Ethyl Carbonate by ^{1}H NMR and GC-MS Analysis. (a) ^{1}H NMR ($CDCl_3$, 500 MHz) of the heptyl-ethyl carbonate (Table 1, entry 1) zoomed between δ = 0.5 and 4.5 ppm (with * signals belonging to the residual 1-heptanol) and **(b)** its corresponding GC-MS analysis (CI (CH_4) HRMS $C_{10}H_{21}O_3$ $[M + H]^+$ m/z_{exp} = 189.1517, m/z_{th} = 189.1491 ; Δ = 2.6 mDa).

All linear dialkyl carbonates were characterised by ^{1}H NMR spectroscopy and gas chromatography mass spectrometry (GC-MS) (**Figures S2.3 – S2.8, p. 122 – 124**). **Figure 2.11** shows a representative example of carbonate obtained in bulk at 21 °C after filtration of the

TBD.H$^+$,I$^-$ by-product (**Table 2.1**, entry 1). GC-MS analyses have been performed under chemical ionisation (CI) conditions using methane as the CI gas, as no molecular ions were detected under electron ionisation conditions. Under CI(CH_4), the C_7H_{15}-O-C(=O)-O-C_2H_5 carbonate is detected as protonated molecules, $[M+H]^+$, at *m/z* 189.2. Note that the adduct ions at *m/z* 217.2 and 229.2 are generated in the ionisation source running at high pressure in methane. Besides the quasi-molecular ions, the fragment ions detected at *m/z* 91.0, 119.1 and 131.1 arise from a 98 u loss (C_7H_{14}) from the *m/z* 189.2, 217.2 and 229.2 parent ions, respectively. We further confirm the elemental composition of the *m/z* 189.2 ions as $[C_{10}H_{20}O_3+H]^+$ using accurate mass measurement (High Resolution MS) experiment, confirming the presence of the C_7H_{15}-O-C(=O)-O-C_2H_5 composition. This last sample was finally analysed by FT-IR spectroscopy along with both 1-heptanol and the heptylOCO_2^-,TBD.H$^+$ CO_2BOL salt (**Figure 2.12**). When comparing the spectra, distinctive changes are clearly visible, constituting reliable evidence for the formation of the dialkyl carbonate function, supporting *de facto* the S_N2 ion-pair process. Before reacting with 1-iodoethane, the CO_2BOL exhibits a C=N ring stretching vibration at 1570 cm^{-1} and N-H stretching at 3152 and 3232 cm^{-1}, confirming the presence of the protonated TBD. This is consistent with the ^{1}H NMR data. Additionally, the strong absorption at 1655 cm^{-1} and the weak peak at 1388 cm^{-1} correspond to the stretching vibrations of C=O and C-O- groups of the carbonate anion, respectively. In comparison, the IR spectrum of the C_7H_{15}-O-C(=O)-O-C_2H_5 dialkyl carbonate shows a distinctive absorption at 1744 cm^{-1}, attributed to the asymmetric stretching vibration of the C=O group, and a band at approximately 1251 cm^{-1}, corresponding to the symmetric stretching vibration of the C-O-C linkage within the carbonate group.

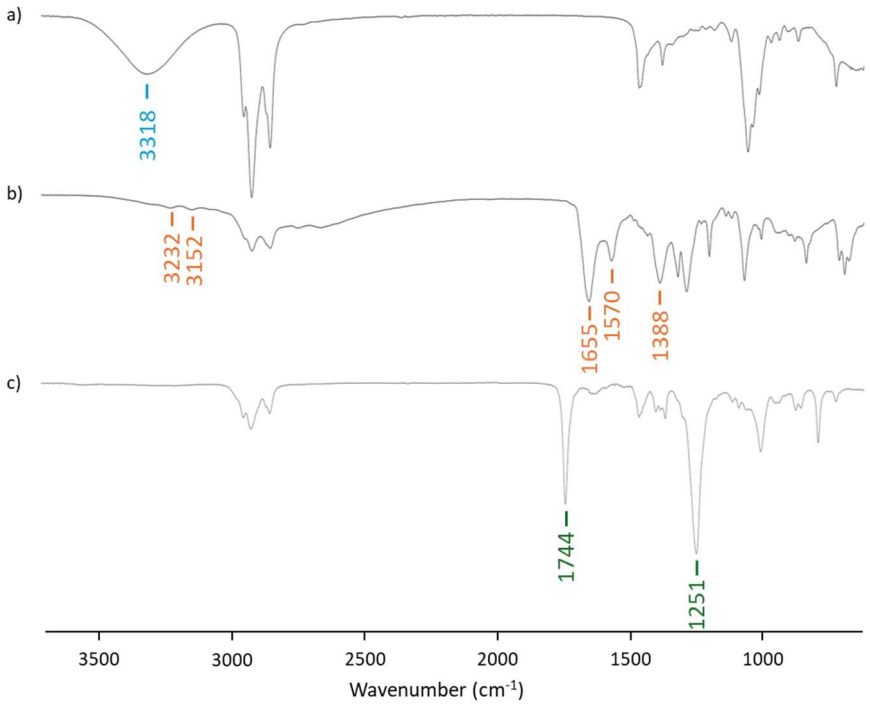


Figure 2.12. FT-IR spectra of **(a)** 1-heptanol, **(b)** heptyl-OCO_2^-, TBD.H$^+$ salt, and **(c)** the reaction product between heptyl-OCO_2^-, TBD.H$^+$ salt and 1-iodoethane (after elimination of TBD.H$^+$,I$^-$ salt).

While the nature of the isolated TBD.H$^+$,I$^-$ salt might suggest a possible reconversion as solar cells component or as catalyst for the fixation of CO_2 to epoxides,[71–73] whatever the linear dialkyl carbonate produced in bulk, the residual presence of the guanidinium salt (< 1 mol % based on ^{1}H NMR analysis) was always pointed out (**Figure 2.11a,** insets between δ = 3.3 ppm and 3.4 ppm and between δ = 2.0 ppm and 2.1 ppm). To avoid a tedious extraction process involving the use of a large quantity of organic solvent, we reasoned that the salt could be considered an 'acceptable contaminant' regarding the final application of the as-produced carbonate. Because linear dialkyl carbonates represent an important class of intermediates for pharmaceuticals, a salt toxicity test was undertaken in collaboration with Dr. Mathilde Wells from Pr. Bertrand Blankert's team. The study was performed on foetal human epithelial cells FHs74Int (ATCC®, CCL-241). Cells were incubated at 37 °C for 24h before being treated with a series of two-fold dilutions of the TBD.H$^+$,I$^-$ salt. The effective tested concentrations ranged from 0.78 to 200 µM. After 24h, cell viability was assessed through an MTT assay.[74] Cell viability (%) was calculated and compared to a negative control. Within the tested concentration range, the TBD.H$^+$,I$^-$ salt displayed no significant toxicity on FHs74Int cells (**Figure 2.13**). The slope of the curve was shown to be non-significantly different from zero following a Fisher-Snedecor test (P value = 0.7151). This wide interval of concentrations was chosen as it is presumed to be far above the likely residual levels of the catalyst. FHs74Int cells were selected as they are derived from non-pathological human intestinal tissue and constitute a good model to study the toxicity of any compound/food that could potentially come into contact with the intestinal epithelial barrier.[75] Although these preliminary results are promising, other cell lines could also be investigated in the future, notably liver-derived cells to evaluate the effect of a potential metabolisation on the cytotoxicity of TBD.H$^+$,I$^-$.

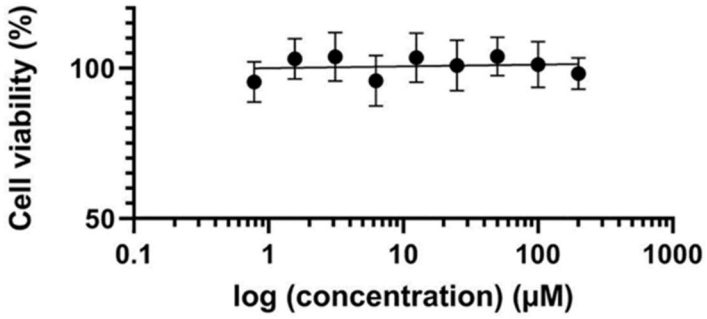


Figure 2.13. Toxicity Assessment of TBD.H$^+$,I$^-$ Salt on FHs74Int Cells. Dose-response curve following cell exposure to increasing TBD.H$^+$,I$^-$ salt concentrations. Data was generated using GraphPad Prism 8 (San Diego, CA, USA). Error bars represent the standard deviation of 6 trials.

III. CONCLUSION

We compared the formation of DBU- and TBD-based CO_2BOLs both experimentally and theoretically and came to the conclusion that TBD is a better candidate for the formation of CO_2BOLs. We also demonstrated the ability of TBD to form CO_2BOLs in bulk with quasi quantitative yields. This allowed us to attempt a bimolecular nucleophilic substitution on the as-prepared CO_2BOLs using various alkyl iodides without performing any prior purification. Experiments and DFT calculations showed that despite a significant energy barrier, the reaction still proceeded without much difficulty. TBD-based carbonate salts exhibited remarkable selectivity for S_N2 processes, consistently achieving yields above 90% across a range of conditions in both acetonitrile and bulk settings at temperatures from 21 to 65 °C. This underscores the robustness and versatility of TBD-based carbonate salts in promoting S_N2 reactions with highly reactive alkyl iodides. The high reactivity of these TBD-based CO_2BOLs towards backside S_N2 processes at low temperature is explained by the presence of the TBD.H^+ guanidinium, revealing a unique metal-free cation-assisted S_N2 ion-pair process. By performing reactions in bulk, the TBD.H^+,I^- by-product crashes out and is easily filtered out. In the pharmaceutical use of dialkyl carbonates, the presence of residual guanidinium salt is unlikely to pose a problem as it showed no cytotoxicity toward FHs74Int cells. Nevertheless, further evaluation in other cell types would be required to fully assess its safety.

The unique S_N2 selectivity of TBD-based carbonate salts, combined with their suppression of elimination and quaternisation pathways, naturally raised the question of whether this chemistry could be translated to macromolecular substrates bearing C-X bonds. Poly(vinyl chloride) (PVC) - one of the most problematic commodity plastics in terms of recyclability - offers precisely this type of sp^3 C-X electrophilic sites along its backbone. The next chapter therefore extends this chemistry to PVC, using TBD-based CO_2-binding alcohols - hereafter referred to as CO_2BALs, to distinguish them from the amine-based CO_2BAMs introduced later - as nucleophiles to graft CO_2-derived carbonate moieties onto the polymer, taking a first step toward the upcycling of plastic waste through CO_2 valorisation.

Beyond their use for dialkyl carbonate synthesis, CO_2BOLs were also considered as potential electrolytes for Li-ion batteries. This work was performed in collaboration with Yinghui Zang and Pr. Dr. Jean-François Gohy from UCLouvain. The results that stemmed from this study are found in the Appendix at the end of this manuscript (see page 241).

IV. EXPERIMENTAL

A. Materials

Carbon dioxide N50 (≥ 99.999 %) was supplied by Air Liquide. 1-Propanol (99+ %), 2-butanol (99 %), 1-hexanol (anhydrous, ≥ 99 %), deuterated chloroform (0.03 vol% TMS, deuteration degree min. 99.8% for NMR spectroscopy, stabilised with silver), as well as 1-heptanol were purchased from Sigma-Aldrich. Methanol (GPR Rectapur) and propan-2-ol were purchased from VWR. Iodoethane (98+ %, stabilised with copper) and 1-iodooctane were acquired from Alfa Aesar. Cyclohexanol (99 %) and 1,8-diazabicyclo[5.4.0]undec-7-ene (DBU, 98+ %) were supplied by Thermoscientific. Phenol (99+ %, for biochemistry, loose crystals) and 2-butanone (or methyl ethyl ketone (MEK), ACS Reagent) were acquired from Acros Organics. Ethanol (denaturated with 3% diethylether, Desinfectol) was purchased from Chemlab. 1,5,7-Triazabicyclo[4.4.0]dec-5-ene (TBD) was supplied by Apollo Scientific. 2-Iodopropane (stabilised with copper chip) was purchased from TCI.

B. Procedures

General procedure for the synthesis of DBU-based CO_2BOLs

A vial equipped with a septum is charged with DBU (3 ml, 0.0201 mol) and an alcohol (0.0201 mol). Two needles (20G), one of which is connected to the CO_2 tank, are then used to pierce the septum and bubble carbon dioxide (pCO_2 = 0.2 bar) onto the reaction mixture. The reaction is performed at room temperature and kinetically studied by gravimetry or ^{1}H NMR (60 MHz).

General procedure for the synthesis of TBD-based CO_2BOLs in MEK

A vial equipped with a septum is charged with TBD (2.7979 g, 0.0201 mol), ethanol (1.170 ml, 0.0201 mol) and MEK (6.7 ml, C_{TBD} = 3M). Two needles (20G), one of which is connected to the CO_2 tank, are then used to pierce the septum and bubble carbon dioxide (pCO_2 = 0.2 bar) onto the reaction mixture. The reaction is performed at room temperature and kinetically studied by gravimetry or ^{1}H NMR (60 MHz).

General procedure for the synthesis of TBD-based CO_2BOLs from 1-heptanol

A vial equipped with a septum and a stir bar is charged with a mixture of TBD (2.7979 g, 0.0201 mol) and 1-heptanol (2.8414 ml, 0.0201 mol) in $CHCl_3$ (5 ml, C_{TBD} = 4M) or in bulk. Two needles (20G), one of which is connected to the CO_2 tank, are then used to pierce the septum and bubble carbon dioxide (pCO_2 = 0.2 bar) onto the reaction mixture. The reaction is performed at room temperature (in $CHCl_3$) or at 100 °C (in bulk) and under 500 rpm stirring. Reaction kinetics were studied by ^{1}H NMR spectroscopy. ^{1}H NMR (500 MHz, $CDCl_3$) : δ = 3.90 (t, 2H), 3.30 (dt, 8H), 2.00 (quint, 4H), 1.60 (quint, 2H), 1.30 (m, 8H), 0.87 (t, 3H).

General procedure for the alkylation of CO_2BOLs

Alkylation reactions were performed on CO_2BOLs obtained according to the procedure described in the previous section. No treatments or purifications were performed on the reaction mixtures. Selected alkyl iodides (0.0201 mol) were added to the vial after the completion of the CO_2BOLs' synthesis. Reactions were performed at room temperature (21 °C) or 65 °C and under 500 rpm stirring for 24 hours in bulk or in acetonitrile. Reaction kinetics were studied by ^{1}H NMR spectroscopy. The TBD.H$^+$,I$^-$ salt was eliminated via filtration in the case of the bulk reactions and via liquid-liquid extraction (diethyl ether/water, 1:1 v/v) for the reactions performed in acetonitrile. Reaction products and by-products were analysed by ^{1}H NMR spectroscopy and mass spectrometry.

- Ethyl-heptyl carbonate : ^{1}H NMR (500 MHz, $CDCl_3$) : δ = 4.18 (q, 2H), 4.12 (t, 2H), 1.67 (quint, 2H), 1.31 (t, 8H), 0.89 (t, 3H). GC-MS : CI (CH_4) HRMS $C_{10}H_{21}O_3$ $[M + H]^+$ m/z_{exp} = 189.1517, m/z_{th} = 189.1491 ; Δ = 2.6 mDa.

- Octyl-heptyl carbonate : ^{1}H NMR (500 MHz, $CDCl_3$) : δ = 4.12 (t, 4H), 1.66 (quint, 4H), 1.30 (br. s, 18H), 0.89 (t, 6H). GC-MS : CI (CH_4) HRMS $C_{16}H_{33}O_3$ $[M + H]^+$ m/z_{exp} = 273.2432, m/z_{th} = 273.2430 ; Δ = 0.2 mDa.

- isoPropyl-heptyl carbonate : ^{1}H NMR (500 MHz, $CDCl_3$) : δ = 4.87 (m, 1H), 4.12 (t, 2H), 1.66 (quint, 4H), 1.29 (d, 14H), 0.88 (t, 3H). GC-MS : CI (CH_4) HRMS $C_{11}H_{23}O_3$ $[M + H]^+$ m/z_{exp} = 203.1644, m/z_{th} = 203.1647 ; Δ = -0.3 mDa.

- TBD.H$^+$, I$^-$: ^{1}H NMR (500 MHz, $CDCl_3$) : δ = 3.35 (dt, 8H), 2.03 (quint, 4H). MS : ESI HRMS $C_{14}H_{28}N_6I$ [2 TBDH$^+$ + I$^-$] m/z_{exp} = 407.1413, m/z_{th} = 407.1420 ; Δ = -0.7 mDa.

C. Methods

NMR Spectroscopy

CO_2 conversion kinetics were followed time-to-time through ^{1}H nuclear magnetic resonance (NMR) using a Spinsolve 60 Ultrabenchtop NMR spectrometer (Magritek, Aachen, Germany). All spectra were acquired according to the following parameters: aq = 6.4 sec, repetition time = 10 sec, pulse angle = 90, ns = 32.

Final dialkyl carbonate products were all characterised by ^{1}H NMR using a Bruker AVANCEII 500 MHz apparatus at room temperature in chloroform-d_1 ($CDCl_3$). All spectra were acquired according to the following parameters: aq = 2.75 sec, d1 = 1 sec, sw = 20, ns = 32.

FT-IR Spectroscopy

Fourier Transform InfraRed spectroscopy was performed to further demonstrate the formation of both the heptyl-OCO_2^-,TBD.H^+ salt and the ethyl-heptyl carbonate using a Bruker Tensor 27 spectrometer.

Mass Spectrometry

Gas chromatography coupled to mass spectrometry (GC-MS) analyses were performed using a GCT-Premier (Waters), equipped with a chemical ionisation (CI) source, with methane as the CI gas, and a Time of Flight (ToF) analyser. The GC system is equipped with a Phenomenex ZEBRON-ZB-5MS (30 m x 0.25 mm x 0.25 µm). The thin film of 0.25 µm is composed of a 5 % phenyl-arylene / 95 % dimethylpolysiloxane phase. Helium was used as the carrier gas at a flow rate of 1 $ml.min^{-1}$. Sample solutions were prepared in HPLC-grade hexane at a concentration of 1 $mg.mL^{-1}$ and subsequently diluted 1000-fold. After dilution, 1 µl of the solutions was injected into the GC injector, maintained at 200 °C to ensure the volatilisation of the sample. The oven temperature program was set as follows: initial temperature of 60 °C, ramped to 260 °C over 25 minutes, held at 260 °C for 10 minutes and finally returned to 60 °C within 15 minutes. High-resolution mass spectrometry (HRMS) analyses were performed to determine the elemental composition of the detected ions. Perfluorotributylamine (PFTBA) was used as an external calibrant (lock mass) to ensure accurate mass measurement.

The ESI-MS analyses were performed in positive ionisation mode on commercially available instruments, Waters QToF US. Instrumental parameters were set as follows : capillary voltage of +3.1 kV, cone voltage of 30 V, source and desolvation temperatures of 80 °C and 120 °C respectively, N_2 flow rate of 50 $L.h^{-1}$ for the gas cone and 500 $L.h^{-1}$ for the desolvation, and finally a resolution of ~8000 (m/z 472). Sample solutions were prepared in HPLC-grade MeOH at a concentration of 1 $mg.mL^{-1}$. After dilution (1000 x), the solutions were injected into the ESI source using a syringe pump at a flow rate of 5 $\mu L.min^{-1}$. Finally, HRMS analyses were performed to determine the elemental composition of the detected ions. NaI was used as an external calibrant (lock mass) to ensure accurate mass measurement.

DFT Calculations

All the calculations were performed using the density functional theory (DFT) as implemented in Gaussian 16 package[76] with Becke's three-parameter hybrid exchange and Lee–Yang–Parr's correlation functional (B3LYP).[77,78] A mixed basis set of SDD for I atom and 6-311++G** basis set for all other atoms were considered.[79–81] To account for the solvent effect of toluene, a conductor-like polarisable continuum model (C-PCM) was applied.[82] Chloroform and acetonitrile solvents were also considered for comparison. All the structures were optimised using Grimme's dispersion correction D3(BJ) to consider non-covalent interactions.[83,84] Confirmation of intermediates and transition states was achieved through harmonic vibrational

frequencies, ensuring absence of imaginary frequencies for intermediates and the presence of one imaginary frequency for transition states corresponding to the desired transformation. Free energies and free energy barriers were calculated at 298.15 K and 1 atm pressure. NCI plot was employed and depicted using VMD to gain more insight into the crucial non-covalent interactions between base and reactants in the transition state.[69,85] All the optimised structures were illustrated using the visualisation package CYLview.[86]

Cytotoxicity tests

Foetal human epithelial cells FHs74Int (ATCCÒ, CCL-241) were cultivated and seeded in 96-well plates (2 x 104 cells per well). Cells were incubated at 37 °C for 24h before being treated with a series of two-fold dilutions of the TBD.H^+,I^- salt. Culture medium (Hybri-Care medium (ATCCÒ) supplemented with 10% FBS) was used for the dilutions and the effective tested concentrations ranged from 0.78 to 200 µM. After 24 h, cell viability was assessed through an MTT assay, a colorimetric test which allows the measurement of cellular metabolic activity. Briefly, the cell medium was discarded and replaced by 200 µL of MTT [3(-(4,5-dimethylthiazol-2-yl)-2,5-diphenyltetrazolium bromide)] solution at 0.5 mg/mL in PBS. Following a 4-hour incubation period, the MTT solution was removed from the plates and DMSO was added to dissolve the formed formazan crystals. The absorbance was measured at 570 nm using a SpectraMaxÒ M2 (Molecular Devices, San Jose, CA, USA). Cell viability (%) was calculated compared to a negative control (untreated cells in presence of culture medium).

V. SUPPORTING INFORMATION

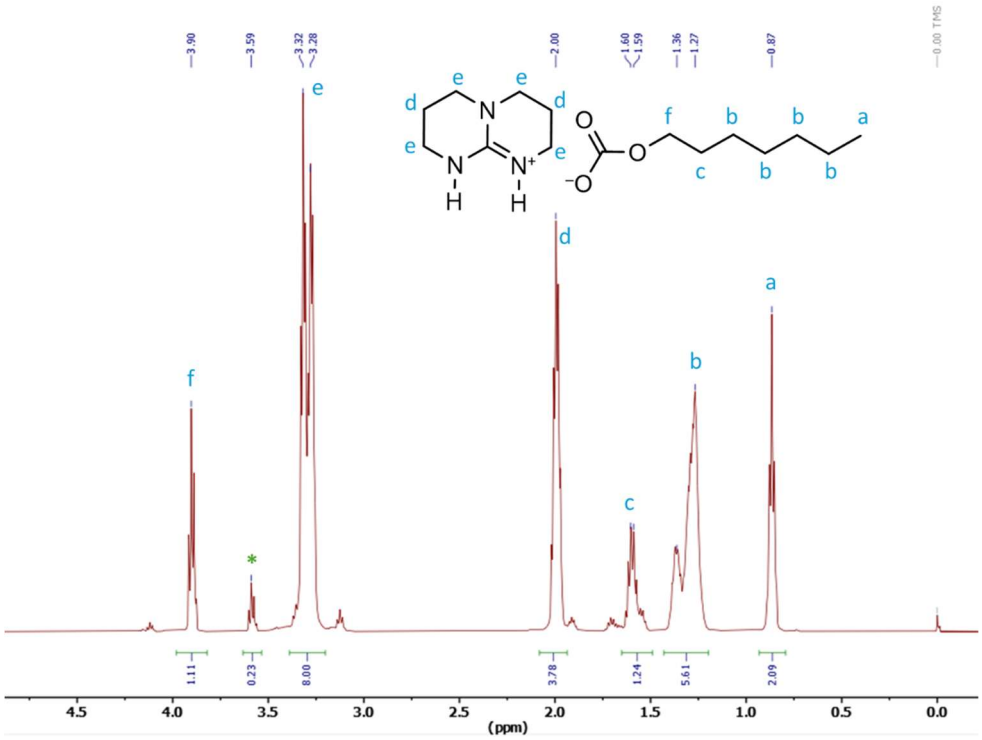


Figure S2.1. ^{1}H NMR spectrum (zoomed between δ = 0 ppm and δ = 4.5 ppm) of the product of the reaction between 1-heptanol and TBD under CO_2 bubbling (pCO_2 = 0.2 bar), with * signals belonging to the residual 1-heptanol.

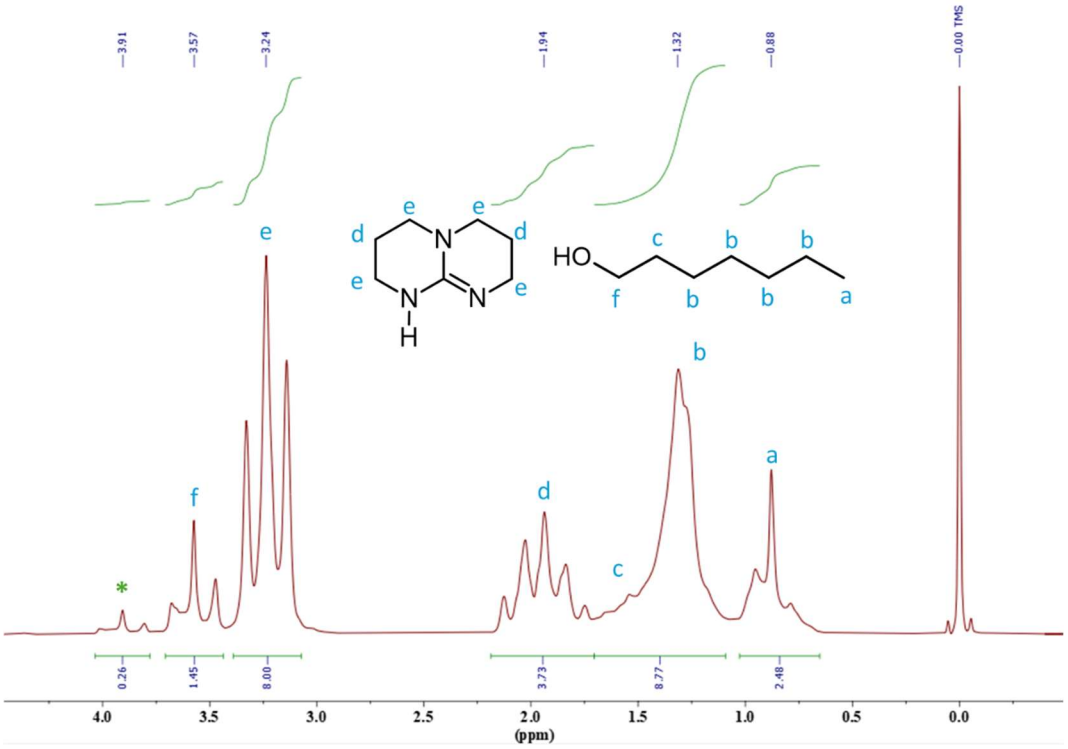


Figure S2.2. ^{1}H NMR spectrum (zoomed between δ = 0 ppm and δ = 4.5 ppm) of the product of degradation of 1-heptylcarbonate, TBD.H$^+$ under N_2 bubbling (pN_2 = 0.2 bar) after 1h30 at 90 °C, with * signals belonging to the residual CO_2BOL.

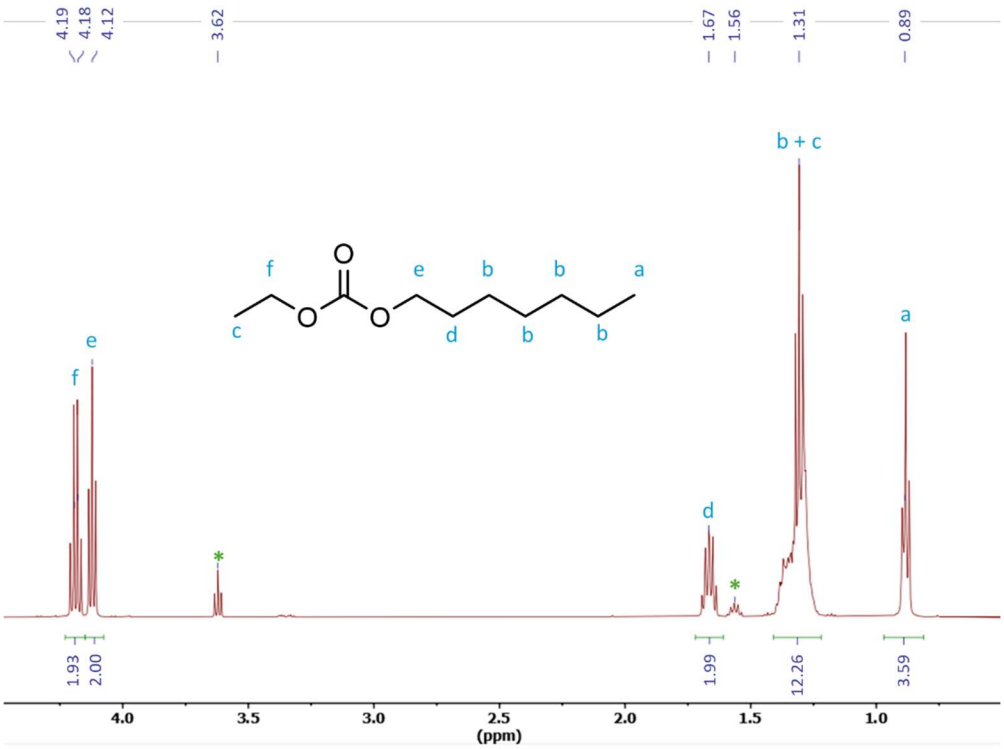


Figure S2.3. ^{1}H NMR spectrum (zoomed between δ = 0 ppm and δ = 4.5 ppm) of the reaction product between heptyl-OCO_2^-, TBD.H^+ salt and iodoethane after elimination of TBD.H^+,I^-, with * signals belonging to the residual 1-heptanol.

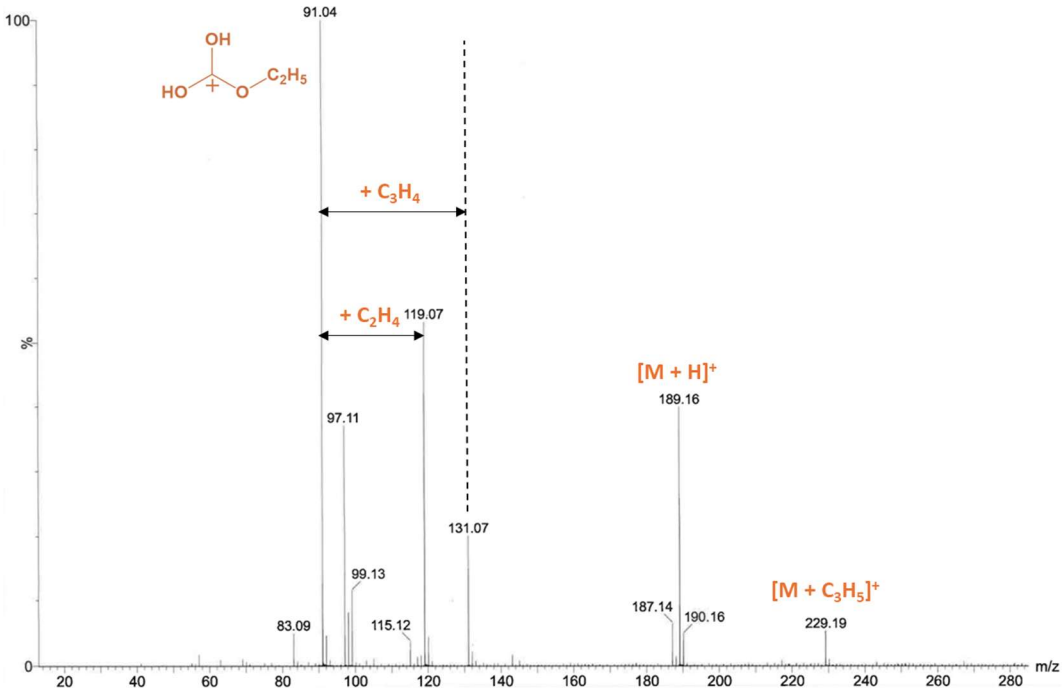


Figure S2.4. GC-MS spectrum of the reaction product between heptyl-OCO_2^-, TBD.H^+ salt and iodoethane after elimination of TBD.H^+,I^- (time of elution : 9.33 min).

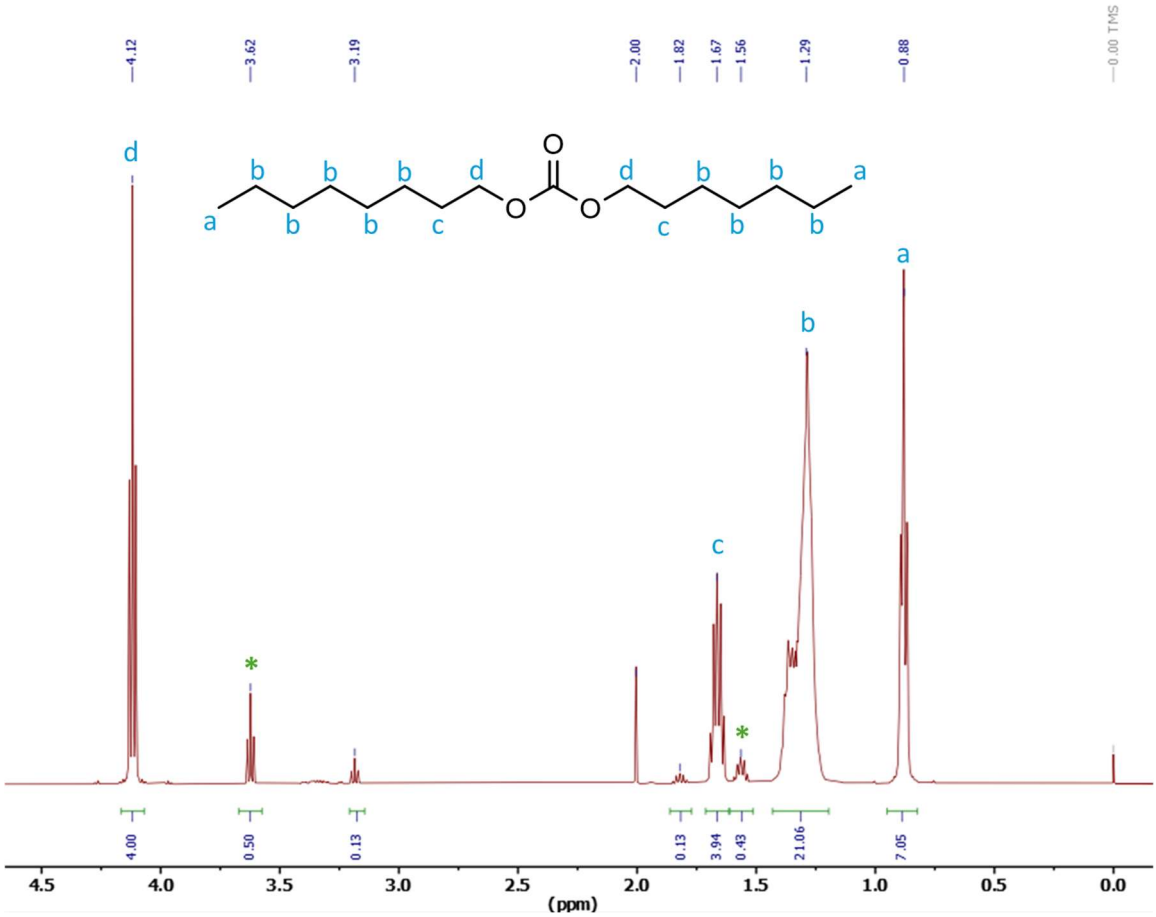


Figure S2.5. ^{1}H NMR spectrum (zoomed between δ = 0 ppm and δ = 4.5 ppm) of the reaction product between heptyl-OCO_2^-, TBD.H$^+$ salt and 1-iodooctane after elimination of TBD.H$^+$,I$^-$, with * signals belonging to the residual 1-heptanol.

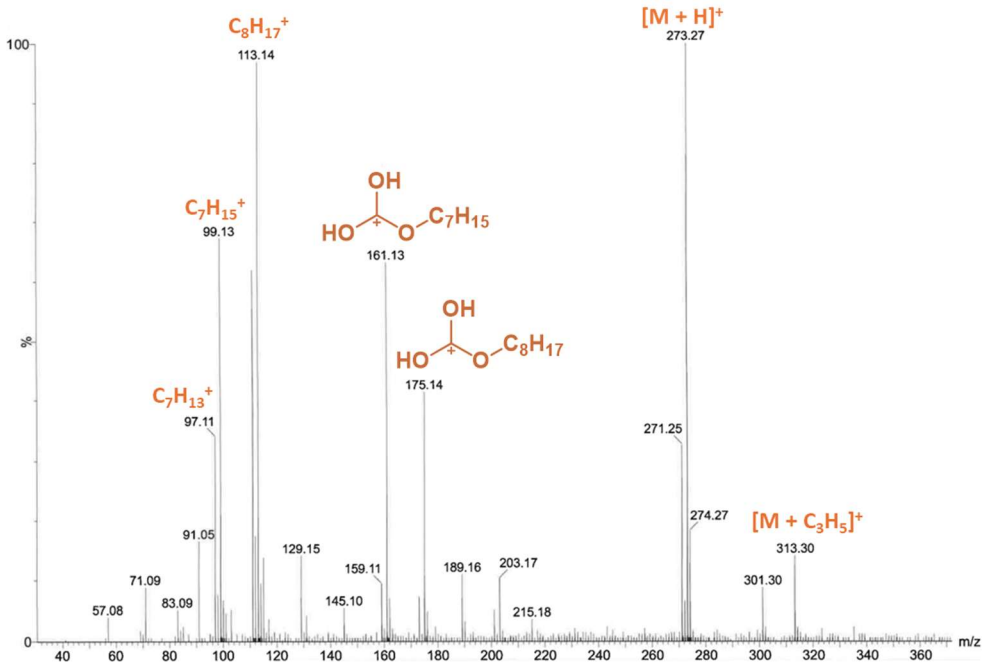


Figure S2.6. GC-MS spectrum of the reaction product between heptyl-OCO_2^-, TBD.H$^+$ salt and 1-iodooctane after elimination of TBD.H$^+$,I$^-$ (time of elution : 16.41 min).

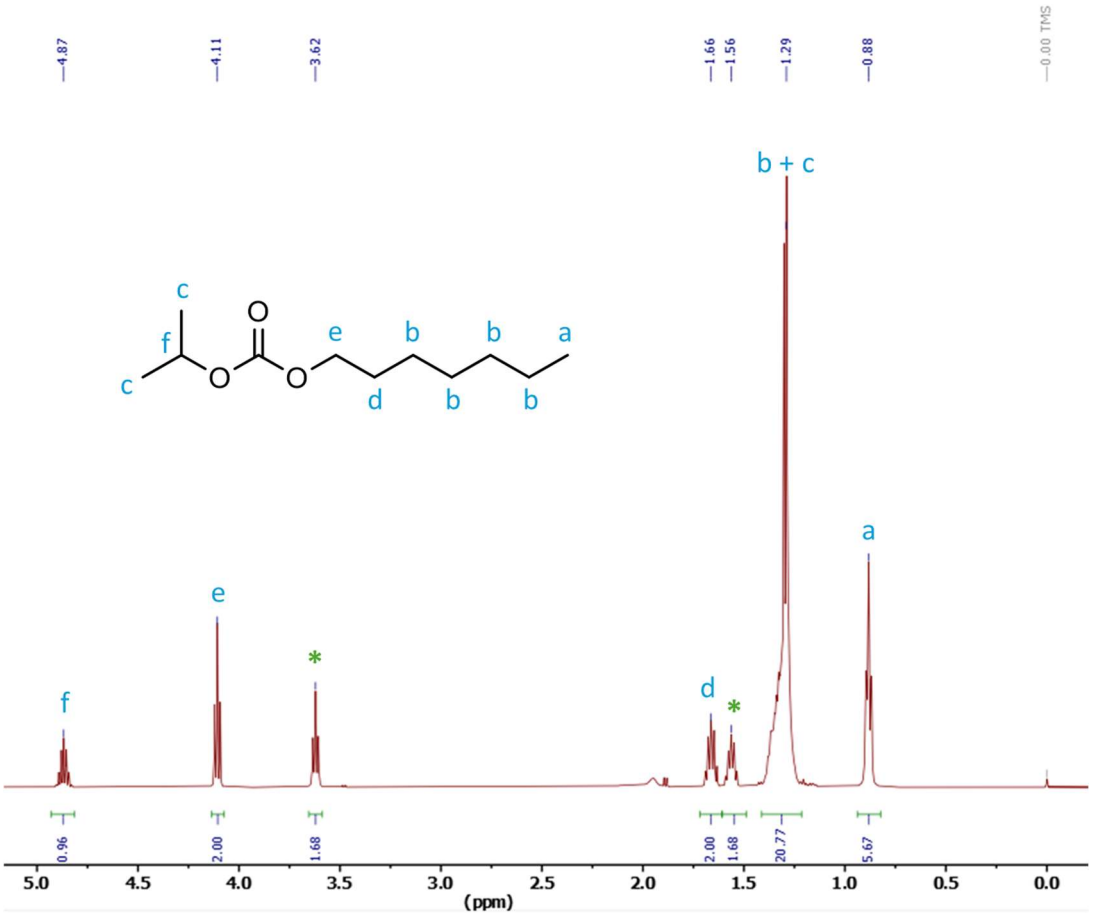


Figure S2.7. ^{1}H NMR spectrum (zoomed between δ = 0 ppm and δ = 5 ppm) of the reaction product between heptyl-OCO_2^-, TBD.H^+ salt and 2-iodopropane after elimination of TBD.H^+,I^-, with * signals belonging to the residual 1-heptanol.

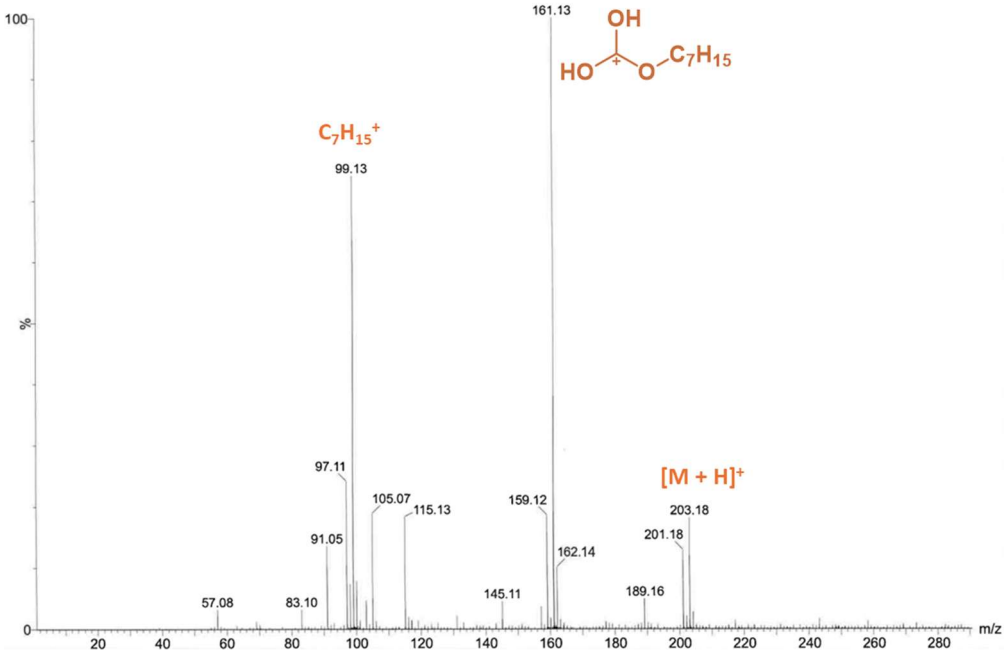


Figure S2.8. GC-MS spectrum of the reaction product between heptyl-OCO_2^-, TBD.H^+ salt and 2-iodopropane after elimination of TBD.H^+,I^- (time of elution : 9.86 min).

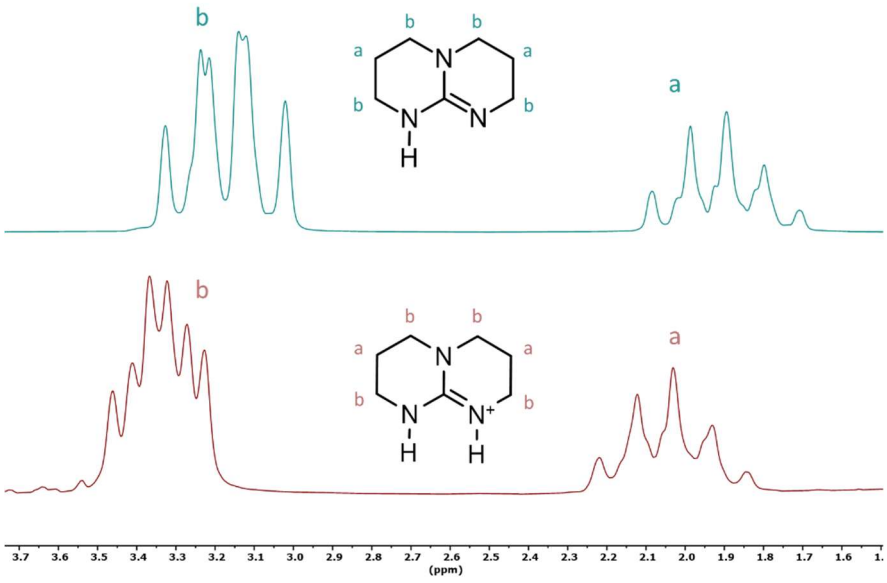


Figure S2.9. ^{1}H NMR spectra (zoomed between δ = 1.5 ppm and δ = 3.7 ppm) of pristine TBD (top) and the white precipitate obtained after reaction between heptyl-OCO_2^-, TBD.H^+ salt and iodoethane (bottom).

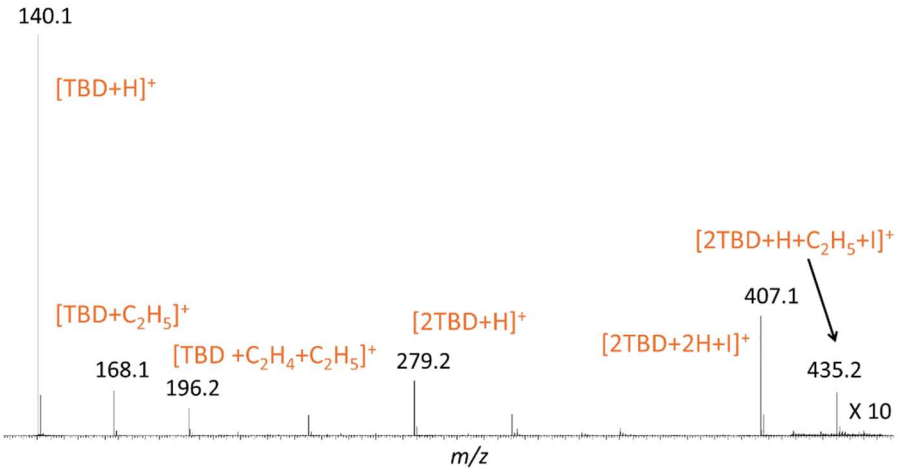


Figure S2.10. Electrospray ionisation mass spectrometry analysis of an aqueous solution of the white precipitate, confirming the formation of TBD.H^+,I^- salt.

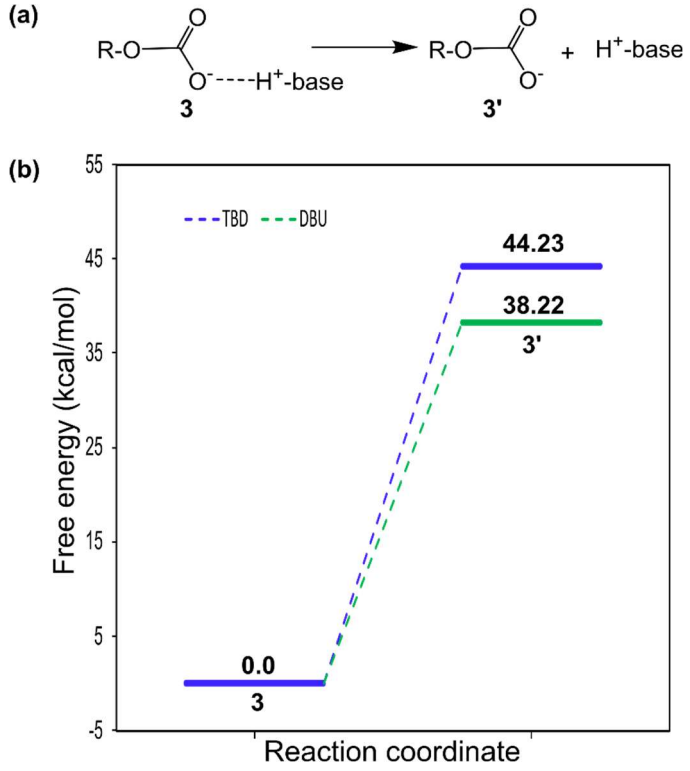


Figure S2.11. Free energy profile for separation of carbonate anion and base.H^+ from intermediate **3**.

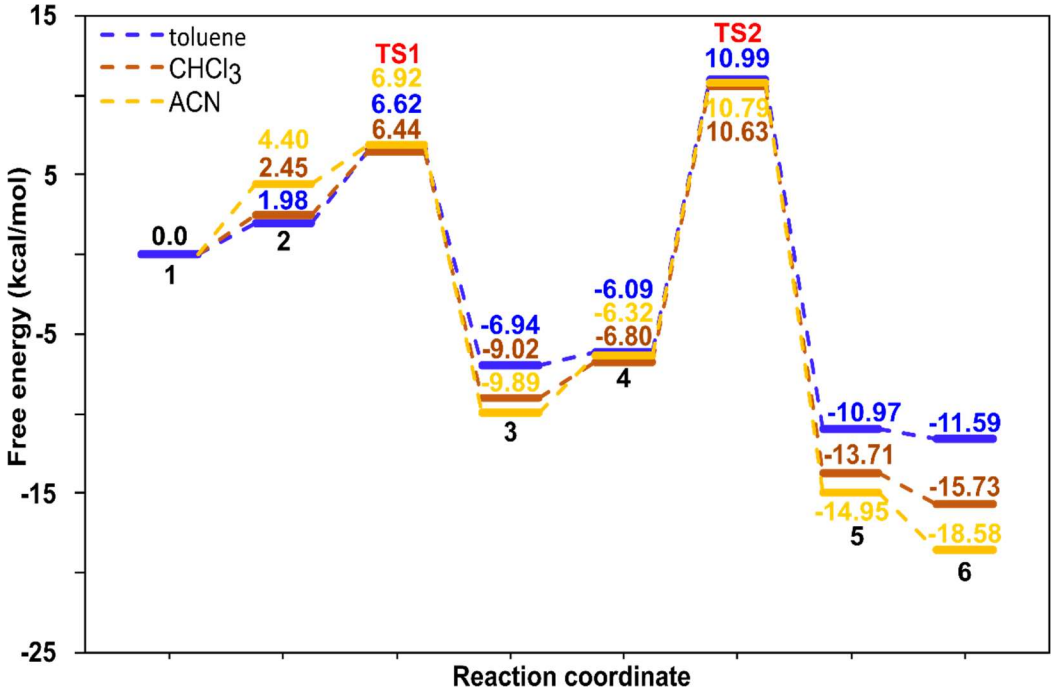


Figure S2.12. A combined free energy profile for CO_2 activation and S_N2 ion-pair reaction using TBD base in different solvents at $CPCM_{(solvent)}$/B3LYP-D3(BJ)/ 6-311++G**, SDD(I) level of theory.

VI. REFERENCES

1 M. Aresta, A. Dibenedetto and A. Angelini, *Chemical Reviews*, 2014, **114**, 1709–1742.

2 C. Hepburn, E. Adlen, J. Beddington, E. A. Carter, S. Fuss, N. Mac Dowell, J. C. Minx, P. Smith and C. K. Williams, *Nature*, 2019, **575**, 87–97.

3 Y. Liu and X.-B. Lu, *Macromolecules*, 2023, **56**, 1759–1777.

4 Y.-N. Li, L.-N. He, Z.-F. Diao and Z.-Z. Yang, in *Advances in Inorganic Chemistry*, Elsevier, 2014, vol. 66, 289–345.

5 G. Centi and F. Signori, *Green Carbon Dioxide: Advances in CO_2 Utilization*, Wiley, 2014.

6 B. Hu and S. L. Suib, in *Green Carbon Dioxide*, eds. G. Centi and S. Perathoner, Wiley, 1st edn., 2014, 51–97.

7 P. Wei, G. A. Bhat and D. J. Darensbourg, *Angew. Chem. Int. Ed.*, 2023, **62**, e202307507.

8 J. H. Park, J. Y. Jeon, J. J. Lee, Y. Jang, J. K. Varghese and B. Y. Lee, *Macromolecules*, 2013, **46**, 3301–3308.

9 B. Schäffner, F. Schäffner, S. P. Verevkin and A. Börner, *Chem. Rev.*, 2010, **110**, 4554–4581.

10 S. Gryglewicz, F. A. Oko and G. Gryglewicz, *Ind. Eng. Chem. Res.*, 2003, **42**, 5007–5010.

11 Y. Ono, *Applied Catalysis A: General*, 1997, **155**, 133–166.

12 V. V. Chaban and N. A. Andreeva, *Journal of Molecular Liquids*, 2022, **367**, 120454.

13 V. V. Chaban, N. A. Andreeva, F. L. Bernard, L. M. Dos Santos and S. Einloft, *Phys. Chem. Chem. Phys.*, 2023, **25**, 9320–9335.

14 P. Tundo and F. Aricò, *ChemSusChem*, 2023, **16**, e202300748.

15 K. Shukla and V. C. Srivastava, *RSC Adv.*, 2016, **6**, 32624–32645.

16 Y. Zhou, Z. Fu, S. Wang, M. Xiao, D. Han and Y. Meng, *RSC Adv.*, 2016, **6**, 40010–40016.

17 S. Huang, B. Yan, S. Wang and X. Ma, *Chemical Society Reviews*, 2015, **44**, 3079–3116.

18 H. Jin Lee, T. Tung Nguyen, A. Vy Tran, H. Sik Kim, Y.-W. Suh, J. Baek and Y. Jin Kim, *Journal of Industrial and Engineering Chemistry*, 2023, **123**, 140–149.

19 Y. Cao, H. Cheng, L. Ma, F. Liu and Z. Liu, *Catal. Surv. Asia*, 2012, **16**, 138–147.

20 P. Kongpanna, V. Pavarajarn, R. Gani and S. Assabumrungrat, *Chemical Engineering Research and Design*, 2015, **93**, 496–510.

21 K. Tomishige, T. Sakaihori, S. Sakai and K. Fujimoto, *Applied Catalysis A: General*, 1999, **181**, 95–102.

22 T. Matsuzaki and A. Nakamura, *Catalysis Surveys from Japan*, 1997, **1**, 77–88.

23 S. Dabral and T. Schaub, *Advanced Synthesis & Catalysis*, 2019, **361**, 223–246.

24 I. Omae, *Coordination Chemistry Reviews*, 2012, **256**, 1384–1405.

25 A. Dibenedetto and A. Angelini, in *Advances in Inorganic Chemistry*, Elsevier, 2014, vol. 66, 25–81.

26 V. V. Chaban, N. A. Andreeva, L. Moreira Dos Santos and S. Einloft, *Journal of Molecular Liquids*, 2024, **394**, 123743.

27 V. V. Chaban, L. M. D. Santos and S. Einloft, *Journal of Molecular Liquids*, 2024, **399**, 124417.

28 V. V. Chaban, *Journal of Molecular Liquids*, 2023, **391**, 123244.

29 Y. R. Jorapur and D. Y. Chi, *The Journal of Organic Chemistry*, 2005, **70**, 10774–10777.

30 A. Zafar, M. A. Iqbal, G. Iram, U. S. Shoukat, F. Jamil, M. Saleem, M. Yousif, Z. U. Abidin and M. Asad, *RSC Adv.*, 2024, **14**, 20365–20389.

31 M. Verdecchia, M. Feroci, L. Palombi and L. Rossi, *The Journal of Organic Chemistry*, 2002, **67**, 8287–8289.

32 M. O. Bratt and P. C. Taylor, *The Journal of Organic Chemistry*, 2003, **68**, 5439–5444.

33 D. J. Heldebrant, C. R. Yonker, P. G. Jessop and L. Phan, *Energy Environ. Sci.*, 2008, **1**, 487–493.

34 D. J. Heldebrant, P. G. Jessop, C. A. Thomas, C. A. Eckert and C. L. Liotta, *The Journal of Organic Chemistry*, 2005, **70**, 5335–5338.

35 S. G. Khokarale and J.-P. Mikkola, *RSC Adv.*, 2019, **9**, 34023–34031.

36 B. L. Schottel, H. T. Chifotides and K. R. Dunbar, *Chem. Soc. Rev.*, 2008, **37**, 68–83.

37 N. Luo, Y. Ao, D. Wang and Q. Wang, *Chemistry – A European Journal*, 2021, **28**, e202103303.

38 S. Harder, A. Streitwieser, J. T. Petty and P. von Schleyer, *Journal of the American Chemical Society*, 1995, **117**, 3253–3259.

39 A. Streitwieser, G. S.-C. Choy and F. Abu-Hasanayn, *Journal of the American Chemical Society*, 1997, **119**, 5013–5019.

40 A. Ebrahimi, M. Habibi and A. Amirmijani, *Journal of Molecular Structure: THEOCHEM*, 2007, **809**, 115–124.

41 T. A. Hamlin, M. Swart and F. M. Bickelhaupt, *ChemPhysChem*, 2018, **19**, 1315–1330.

42 E. Fritz-Langhals, *Org. Process Res. Dev.*, 2022, **26**, 3015–3023.

43 X. Fu and C.-H. Tan, *Chemical Communications*, 2011, **47**, 8210–8222.

44 L. A. Anderson and A. K. Franz, *Energy & Fuels*, 2012, **26**, 6404–6410.

45 G. Trapasso, C. Salaris, M. Reich, E. Logunova, C. Salata, K. Kümmerer, A. Figoli and F. Aricò, *Sustainable Chemistry and Pharmacy*, 2022, **26**, 100639.

46 F. J. Weiberth, Y. Yu, W. Subotkowski and C. Pemberton, *Organic Process Research & Development*, 2012, **16**, 1967–1969.

47 C. Sabot, K. A. Kumar, S. Meunier and C. Mioskowski, *Tetrahedron Letters*, 2007, **48**, 3863–3866.

48 B. Vigante, M. Rucins, A. Plotniece, K. Pajuste, I. Luntena, B. Cekavicus, E. Bisenieks, R. Smits, G. Duburs and A. Sobolev, *Molecules*, 2015, **20**, 20341–20354.

49 J. L. Hickey and S. Lin, *Peptide Science*, 2020, **112**, e24161.

50 J. F. R. Van Guyse, J. Verjans, S. Vandewalle, K. De Bruycker, F. E. Du Prez and R. Hoogenboom, *Macromolecules*, 2019, **52**, 5102–5109.

51 R. Hoogenboom and J. Van Guyse, US Pat., 11332554B2, 2022.

52 H. Mutlu and M. A. R. Meier, *Macromolecular Chemistry and Physics*, 2009, **210**, 1019–1025.

53 W. Guo, J. E. Gómez, L. Martínez-Rodríguez, N. A. G. Bandeira, C. Bo and A. W. Kleij, *ChemSusChem*, 2017, **10**, 1969–1975.

54 D. A. Rankic, C. M. Stiff, C. W. am Ende and J. M. Humphrey, *The Journal of Organic Chemistry*, 2017, **82**, 12791–12797.

55 A. Horváth, *Tetrahedron Letters*, 1996, **37**, 4423–4426.

56 C. Ghobril, C. Sabot, C. Mioskowski and R. Baati, *Eur. J. Org. Chem.*, 2008, **2008**, 4104–4108.

57 M. K. Kiesewetter, M. D. Scholten, N. Kirn, R. L. Weber, J. L. Hedrick and R. M. Waymouth, *J. Org. Chem.*, 2009, **74**, 9490–9496.

58 M. Baidya and H. Mayr, *Chemical Communications*, 2008, 1792.

59 P. Munshi, A. D. Main, J. C. Linehan, C.-C. Tai and P. G. Jessop, *Journal of the American Chemical Society*, 2002, **124**, 7963–7971.

60 Y. Xia, J. Shen, H. Alamri, N. Hadjichristidis, J. Zhao, Y. Wang and G. Zhang, *Biomacromolecules*, 2017, **18**, 3233–3237.

61 A. Khalil, S. Saba, C. Ribault, M. Vlach, P. Loyer, O. Coulembier and S. Cammas-Marion, *Polymers*, 2020, **12**, 1705.

62 P. M. Mathias, K. Afshar, F. Zheng, M. D. Bearden, C. J. Freeman, T. Andrea, P. K. Koech, I. Kutnyakov, A. Zwoster, A. R. Smith, P. G. Jessop, O. G. Nik and D. J. Heldebrant, *Energy Environ. Sci.*, 2013, **6**, 2233–2242.

63 X. Gui, Z. Tang and W. Fei, *J. Chem. Eng. Data*, 2011, **56**, 2420–2429.

64 L. Phan, D. Chiu, D. J. Heldebrant, H. Huttenhower, E. John, X. Li, P. Pollet, R. Wang, C. A. Eckert, C. L. Liotta and P. G. Jessop, *Ind. Eng. Chem. Res.*, 2008, **47**, 539–545.

65 S. Sakai, Y. Kobayashi and Y. Ishii, *J. Org. Chem.*, 1971, **36**, 1176–1180.

66 E. R. Pérez, R. H. A. Santos, M. T. P. Gambardella, L. G. M. De Macedo, U. P. Rodrigues-Filho, J.-C. Launay and D. W. Franco, *J. Org. Chem.*, 2004, **69**, 8005–8011.

67 C. Villiers, J.-P. Dognon, R. Pollet, P. Thuéry and M. Ephritikhine, *Angewandte Chemie International Edition*, 2010, **49**, 3465–3468.

68 S. Winstein, E. Clippinger, A. H. Fainberg, R. Heck and G. C. Robinson, *Journal of the American Chemical Society*, 1956, **78**, 328–335.

69 J. Contreras-García, E. R. Johnson, S. Keinan, R. Chaudret, J.-P. Piquemal, D. N. Beratan and W. Yang, *J. Chem. Theory Comput.*, 2011, **7**, 625–632.

70 Z. B. Alfassi, R. E. Huie, B. L. Milman and P. Neta, *Analytical and Bioanalytical Chemistry*, 2003, **377**, 159–164.

71 P. Wang, S. M. Zakeeruddin, M. Grätzel, W. Kantlehner, J. Mezger, E. V. Stoyanov and O. Scherr, *Appl. Phys. A*, 2004, **79**, 73–77.

72 C. Yi, J. Luo, S. Meloni, A. Boziki, N. Ashari-Astani, C. Grätzel, S. M. Zakeeruddin, U. Röthlisberger and M. Grätzel, *Energy Environ. Sci.*, 2016, **9**, 656–662.

73 Á. Mesías-Salazar, R. S. Rojas, F. Carrillo-Hermosilla, J. Martinez, A. Antiñolo, O. S. Trofymchuk, F. M. Nachtigall, L. S. Santos and C. G. Daniliuc, *New J. Chem.*, 2024, **48**, 105–111.

74 T. Mosmann, *Journal of Immunological Methods*, 1983, **65**, 55–63.

75 J. R. Kanwar and R. K. Kanwar, *BMC Immunol*, 2009, **10**, 7.

76 M. J. Frisch, G. W. Trucks, H. B. Schlegel, G. E. Scuseria, M. A. Robb, J. R. Cheeseman, G. Scalmani, V. Barone, G. A. Petersson, H. Nakatsuji, X. Li, M. Caricato, A. V. Marenich, J. Bloino, B. G. Janesko, R. Gomperts, B. Mennucci, H. P. Hratchian, J. V. Ortiz, A. F. Izmaylov, J. L. Sonnenberg, D. Williams-Young, F. Ding, F. Lipparini, F. Egidi, J. Goings, B. Peng, A. Petrone, T. Henderson, D. Ranasinghe, V. G. Zakrzewski, J. Gao, N. Rega, G. Zheng, W. Liang, M. Hada, M. Ehara, K. Toyota, R. Fukuda, J. Hasegawa, M. Ishida, T. Nakajima, Y. Honda, O. Kitao, H. Nakai, T. Vreven, K. Throssell, J. A. Montgomery Jr., J. E. Peralta, F. Ogliaro, M. J. Bearpark, J. J. Heyd, E. N. Brothers, K. N. Kudin, V. N. Staroverov, T. A. Keith, R. Kobayashi, J. Normand, K. Raghavachari, A. P. Rendell, J. C. Burant, S. S. Iyengar, J. Tomasi, M. Cossi, J. M. Millam, M. Klene, C. Adamo, R. Cammi, J. W. Ochterski, R. L. Martin, K. Morokuma, O. Farkas, J. B. Foresman and D. J. Fox, 2016.

77 A. D. Becke, *The Journal of Chemical Physics*, 1993, **98**, 5648–5652.

78 C. Lee, W. Yang and R. G. Parr, *Phys. Rev. B*, 1988, **37**, 785–789.

79 D. Andrae, U. Häussermann, M. Dolg, H. Stoll and H. Preuss, *Theoret. Chim. Acta*, 1990, **77**, 123–141.

80 T. Clark, J. Chandrasekhar, G. W. Spitznagel and P. V. R. Schleyer, *J. Comput. Chem.*, 1983, **4**, 294–301.

81 R. Krishnan, J. S. Binkley, R. Seeger and J. A. Pople, *The Journal of Chemical Physics*, 1980, **72**, 650–654.

82 M. Cossi, N. Rega, G. Scalmani and V. Barone, *J. Comput. Chem.*, 2003, **24**, 669–681.

83 S. Grimme, J. Antony, S. Ehrlich and H. Krieg, *The Journal of Chemical Physics*, 2010, **132**, 154104.

84 S. Grimme, S. Ehrlich and L. Goerigk, *J. Comput. Chem.*, 2011, **32**, 1456–1465.

85 W. Humphrey, A. Dalke and K. Schulten, *Journal of Molecular Graphics*, 1996, **14**, 33–38.

86 C. Y. Legault, CYLview (version 1.0b) Université de Sherbrooke 2009.

CHAPTER 3

CO_2-Binding Alcohols as Potential Candidates for Poly(Vinyl Chloride) Upcycling



Delcorps J., Ben Ayed A., Coulembier O., *Polymer Chemistry*, 2025, 16, 25, 2923-2932.
https://doi.org/10.1039/D5PY00350D

TABLE OF CONTENTS

I. INTRODUCTION....136

II. RESULTS AND DISCUSSION....138

A. Thermal properties of CO_2BALs: Melting points and degradation....140

B. Reaction between PVC and CO_2BALs in solution....143

III. CONCLUSION....148

IV. EXPERIMENTAL....149

A. Materials....149

B. Procedures....149

C. Methods....150

V. SUPPORTING INFORMATION....152

VI. REFERENCES....160

I. INTRODUCTION

With a global annual production of 45 million metric tons in 2022 and a projected increase to 65 million metric tons by 2030,[1] poly(vinyl chloride) (PVC) ranks as the third most produced polymer worldwide, following polyethylene (PE) and polypropylene (PP).[2] Its widespread use makes it a key target for the scientific community recycling efforts. Despite its reputation as a challenging material to recycle, Europe has seen significant progress in this area through initiatives such as Vinyl2010 and VinylPlus.[3] These programs have driven an impressive increase in PVC recycling, from just 18,000 tons in 2004 to 264,000 tons in 2010, and further to 731,000 tons in 2020. Projections suggest this figure could reach 1 million tons per year by 2030.[4–6] However, with an annual production of 6.5 million tons across the EU-27, Norway, Switzerland, and the United Kingdom,[2] the current recycling rates leave room for considerable improvement.

Two main approaches are currently employed for large-scale PVC recycling, *i.e.* mechanical recycling and feedstock (or chemical) recycling.[4–7] Unfortunately, both methods face significant limitations. Mechanical recycling requires thoroughly sorted and homogeneous PVC waste to produce a material with properties comparable to the original polymer.[5–7] This stringent requirement complicates waste management, and the process itself often degrades polymer chains, leading to a loss of physical and mechanical properties that restrict the applications of the recycled material.[5] Feedstock recycling, on the other hand, is hindered by PVC's high chlorine content. This method typically involves thermal treatments, during which the easily broken C-Cl bond releases chlorinated derivatives (**Figure 3.1a**). If not effectively captured, these emissions can cause equipment corrosion and air pollution. Moreover, dehydrochlorination generates conjugated polyene sequences that may undergo cyclisation to form regular and chlorinated aromatic compounds, further increasing the environmental burden of feedstock recycling.[7] The recovery of chlorine from PVC and other chlorinated polymers, such as polyvinylidene chloride (PVDC), is thus crucial to their recycling process.[8–10]

To overcome the limitations of traditional recycling methods, innovative approaches such as biological and electrochemical recycling,[8] as well as chemical upcycling,[11] have been explored and warrant further research.[5,12] Among these, chemical upcycling through nucleophilic substitution has garnered significant attention.[13] However, the efficiency of these substitution reactions is influenced by a variety of factors, including the leaving group properties, the polymer structure, and the reaction environment.[14–16] For instance, while chlorine is a modest leaving group that can undergo substitution and elimination reactions under various conditions,[17] product selectivity remains a challenge due to the competition between these pathways. Factors such as solvent polarity, nucleophile identity, temperature, and nucleophile concentration play a critical role in directing the reaction.[17] Polar aprotic solvents like dimethylformamide (DMF) have been shown to favour substitution over elimination, while higher temperatures tend to promote elimination.[18,19] Similarly, less basic nucleophiles increase substitution selectivity,[17] offering avenues for tailoring reaction conditions to improve outcomes.

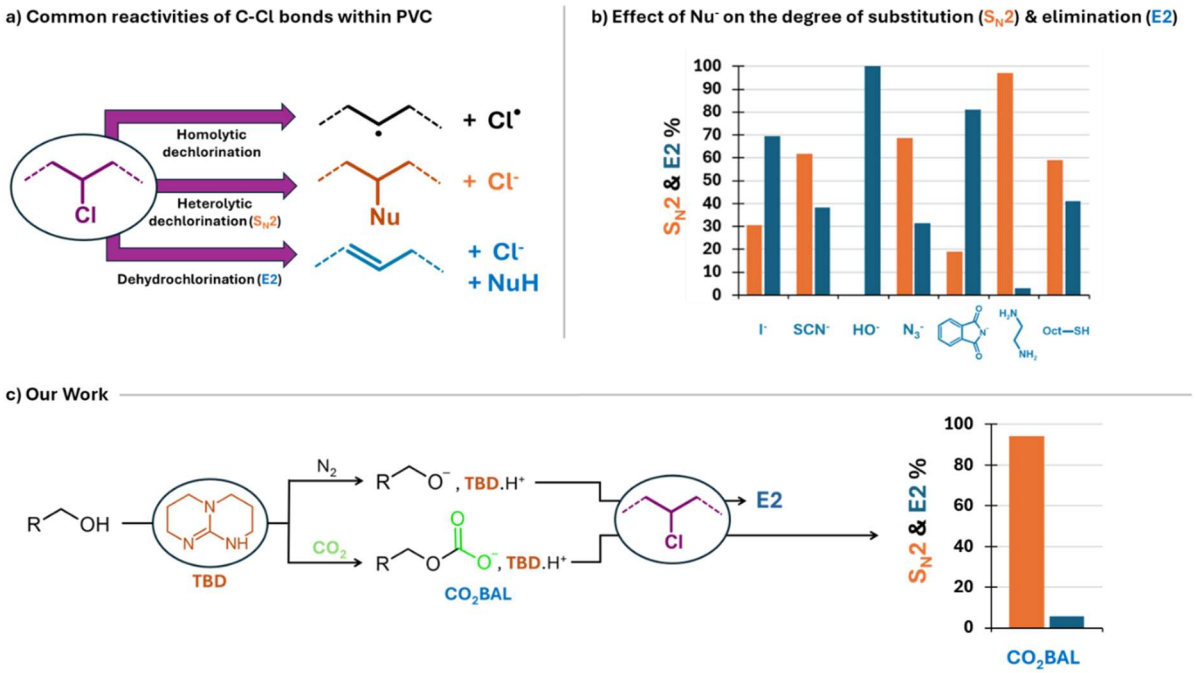


Figure 3.1. Chlorine Reactivity and Selectivity in PVC Modifications: a) Common Reactivities of C-Cl Bonds in PVC, **b)** Nucleophile-Dependent Substitution (S_N2) and Elimination (E2) Ratios (I^- in DMF at 60 °C, SCN^- in DMF at 100 °C, HO^- in DMF at 21 °C, N_3^- in DMF at 100 °C, Phthalimide anion in DMF at 60 °C, Ethylenediamine at 75 °C in bulk, 1-octanethiol/K_2CO_3 in DMF at 40 °C), and **c)** Enhanced Selectivity Using CO_2BALs in Our Work (R = Decyl).

Substitution reactions with nucleophiles offer the potential to convert PVC into new polymeric materials for specialised applications, including catalysis,[20,21] separations,[22,23] and antimicrobial polymers.[24] Nevertheless, such transformations often face practical limitations due to incomplete dechlorination and competition with elimination, leading to residual chlorine atoms and alkenes that can alter polymer properties.[25] These challenges underscore the need for innovative strategies to enhance both the efficiency and selectivity of substitution reactions, as demonstrated by recent studies.[26]

Optimising these reaction parameters could enable the development of versatile and sustainable recycling methods for PVC. For instance, a variety of nucleophiles, including iodide anion, hydroxide, azide, and thiocyanate, have been explored for PVC substitution reactions (**Figure 3.1b**).[19] Thiols have also been employed, with Lu *et al*. achieving partial substitution of PVC chlorine atoms using potassium carbonate and *N,N*-diisopropylethylamine.[27] Additionally, amination of PVC has enabled its upcycling into carbon dioxide absorbents, as demonstrated by Sneddon *et al*.[28] However, while the use of nucleophiles for PVC modification has been extensively studied, research on employing carbonates as nucleophiles remains notably sparse. This gap is particularly surprising given the potential for carbonates to provide functionalised PVC materials with unique properties. Furthermore, although substitution reactions are often accompanied by elimination processes, the latter is either underreported or dominates in most studies,[16] underscoring the need for approaches that favour selective substitution over elimination.

In this work, we aimed to functionalise PVC using 1,5,7-triazabicyclo[4.4.0]dec-5-ene (TBD)-based CO_2-binding alcohol-derived materials (CO_2BALs), previously developed for the synthesis of "simple" dialkyl carbonates in Chapter 2 (**Figure 3.1c**).[29] The effects of temperature, solvent polarity, CO_2BAL conversion, and reaction time were systematically studied to evaluate their impact on both the degree of substitution and the substitution-to-elimination ratio. Although substitution levels higher than 10 wt.% were not achieved in optimal conditions, this result makes the CO_2BAL approach particularly appealing, as the nature of the by-product is a TBD.HCl salt, which has potential applications in biochemistry.[30,31] However, for future investigations, it will be necessary to consider other functionalisation strategies.

II. RESULTS AND DISCUSSION

As detailed in Chapter 2, carbon dioxide-binding organic liquids (CO_2BOLs) are an innovative class of materials formed by combining alcohols with liquid organic bases, such as amidines or guanidines.[32–35] These systems are capable of binding CO_2 through reversible interactions, making them highly versatile for applications in CO_2 capture and utilisation.

CO_2BOLs form intermediates that can act as nucleophiles in substitution reactions,[29,36–38] opening new avenues for polymer transformations and upcycling strategies. Among the organic bases used in CO_2BOLs, 1,5,7-triazabicyclo[4.4.0]dec-5-ene (TBD) has recently garnered particular attention.[39] TBD-based CO_2BOLs exhibit a unique ability to promote selective S_N2 (bimolecular nucleophilic substitution) reactions with primary and secondary iodo-alkanes.[29] This selectivity primarily arises from the formation of a TBD.H^+ guanidinium cation during the reaction, which interacts with and stabilises the iodide ion released as the leaving group in the S_N2 process. By minimising competing reactions such as elimination or base quaternisation, this mechanism enables highly efficient and controlled transformations.

Table 3.1. Main differences, environmental impact and major innovation between TBD-based CO_2BOLs used for small-molecule synthesis (Chapter 2 / Ref. 29) and this work.

Criteria	Chapter 2 / Ref. 29	This Work
Main Objective	Dialkyl carbonates synthesis via S_N2 with TBD-based CO_2BOLs	PVC upcycling with CO_2BOLs for sustainable valorisation
Main Substrates	Primary and secondary alkyl iodides	PVC secondary methine chlorides
Final Product	Dialkyl carbonates	Carbonate-modified PVC through an almost exclusively S_N2 process and a limited HCl-liberating E2 reaction
Reaction Temperature	21 – 65 °C	21 °C (optimal conditions)
Solvents Used	Acetonitrile or solvent-free condition	DMF (optimal conditions)
Environmental Impact	Green alternative to toxic metal-based methods	Plastic waste valorisation, reduction of HCl waste by-product by an exclusive TBD.HCl benign salt production
Major Innovation	Guanidinium-assisted S_N2 ion-pair process	Extension to polymers, contribution to PVC recycling by CO_2 valorisation

Building on these properties, this study extends the application of TBD-based CO_2BOLs beyond small-molecule transformations to the upcycling of poly(vinyl chloride) (PVC), a widely used polymer with significant recycling challenges. To better highlight the improvements introduced in this chapter, several key aspects are compared in **Table 3.1**, showcasing the differences between TBD-based CO_2BOLs used for small-molecule synthesis (*cfr*. Chapter 2 / Ref. 29) and their application in PVC recycling. As far as the environmental impact is concerned, it was hypothesised that these systems could limit the release of chloride ions during both dechlorination and dehydrochlorination (**Figure 3.2**). By leveraging the chloride-trapping ability of TBD.H^+, this approach seeks to reduce the formation of toxic by-products while enhancing substitution efficiency on the PVC backbone. Moreover, this work underscores the dual sustainability of the proposed method: integrating CO_2 into the reaction process transforms this abundant greenhouse gas into a valuable resource for polymer modification. This innovative use of CO_2 not only aligns with broader goals in carbon capture and utilisation but also addresses critical challenges in PVC recycling.

To better reflect the versatility of the systems explored in this study, the term CO_2BALs ("CO_2-binding alcohols") is proposed to describe alcohol-based systems that extend beyond the liquid-phase CO_2BOLs typically described in the literature. This broader definition emphasises the adaptability of CO_2BALs in enabling sustainable and efficient polymer transformations.

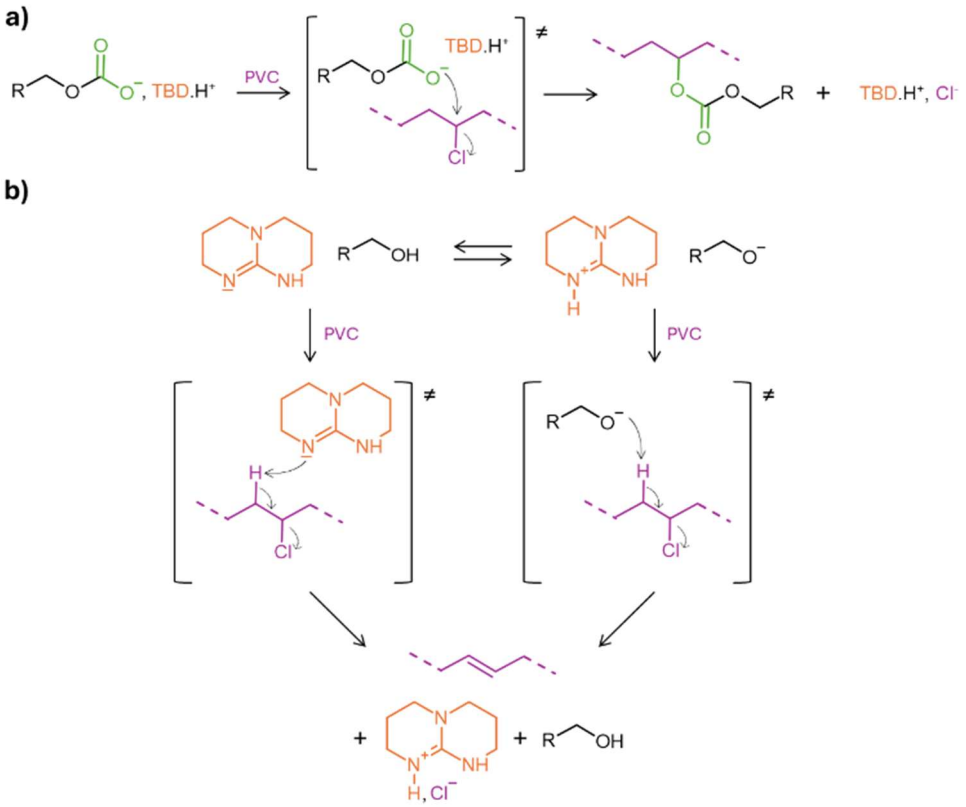


Figure 3.2. Trapping of chloride by guanidinium TBD.H$^+$ during **a)** dechlorination (S_N2) and **b)** dehydrochlorination (E2) reactions.

A. Thermal properties of CO_2BALs: Melting points and degradation

In developing a method to functionalise PVC using CO_2BALs, a solvent-free approach was prioritised to enhance the environmental sustainability of the process and minimise waste generation. Such an approach requires both reactants to be in a compatible physical state to ensure effective interaction. For PVC, this means operating above its Vicat softening temperature (~92 °C)[40] but below its thermal degradation threshold (~250 °C).[41] The CO_2BALs, on the other hand, must remain liquid under these conditions, as this enhances their ability to mix with the polymer and facilitates reactivity.

To evaluate the feasibility of these conditions, the melting points and thermal stability of CO_2BALs were studied. A series of TBD alkylcarbonate salts were prepared by mixing equimolar amounts of alcohol and TBD in bulk, as previously detailed in Chapter 2.[29] Mixtures were then heated to a constant temperature and exposed to CO_2 (pCO_2 = 0.2 bar) under vigorous stirring (500 rpm). The temperature was maintained at 50 °C for methanol, ethanol, and 1-propanol, while 90 °C was used for 1-butanol, 1-hexanol, 1-octanol, and 1-decanol (**Figures S3.1 – S3.6, p. 152 – 154**). The thermal properties of the obtained CO_2BALs were evaluated by determining their melting points, which are influenced by the length of the alkyl chain. As shown in **Figure 3.3**, with the exception of the TBD butylcarbonate salt (which remains a viscous liquid with a melting temperature of 13.5 °C), all other CO_2BALs are solid at room temperature. The melting points

follow a clear trend: they decrease with the length of the alkyl chain down to a minimum for the 1-butanol-based salt, after which they slightly increase for longer chains. These results were compared to those of 1,8-diazabicyclo[5.4.0]undec-7-ene (DBU)- and 1,1,3,3-tetramethylguanidine (TMG)-based CO_2BALs,[35] with the latter exhibiting negative melting points across all investigated alkyl chain lengths. Notably, the melting points of the TBD-based CO_2BALs are generally higher than those of DBU-based salts, particularly for shorter alkyl chains such as methanol, ethanol, and 1-propanol. This suggests that the TBD salts form more stable crystalline structures compared to DBU and TMG salts. This thermal behaviour is significant when considering the conditions required for the upcycling of PVC, as the melting point influences both the stability and reactivity of the CO_2BALs during polymer functionalisation.

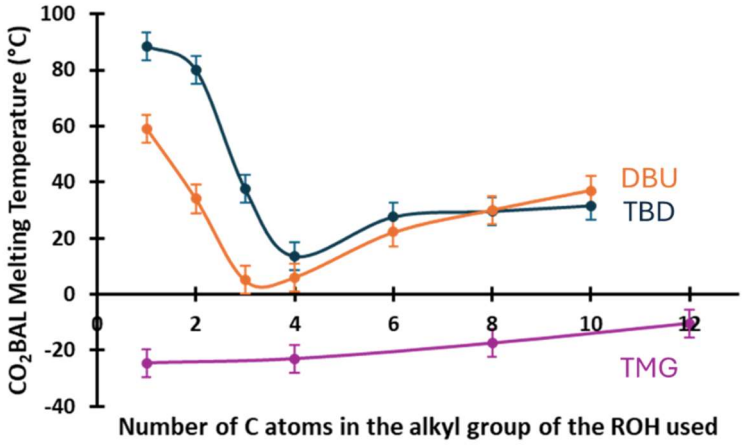


Figure 3.3. Melting points of TBD-based CO_2BALs as a function of the alkyl chain length, compared with the melting points of DBU- and TMG-based CO_2BALs. Thermal data for DBU and TMG are adapted from Ref.35.

Initially encouraged by the relatively high melting points of CO_2BALs derived from methanol, ethanol, and 1-propanol, we faced a critical limitation when examining their thermal stability. Thermogravimetric analyses (TGA) revealed that the degradation onset temperatures (T5%) of these salts are consistently close to their melting points (ca. 80 - 85 °C, **Figures S3.8 – S3.10, p. 155 – 156**), excluding their use in liquid form at temperatures compatible with PVC's Vicat softening point. Furthermore, the TGA data showed that the degradation temperatures of CO_2BALs are independent of alkyl chain length, falling within a narrow range of 80 - 90 °C (**Figures S3.8 – S3.14, p. 155 – 157**).

To gain deeper insight into the thermal behaviour of CO_2BALs, we sought to determine the activation energy (E_a) and pre-exponential factor (A) by applying the Arrhenius equation across a broad temperature range (40 - 110 °C). This required selecting a CO_2BAL with a melting point sufficiently distinct from its T5% to ensure reliable thermal measurements. The 1-decanol-based CO_2BAL emerged as a good candidate, with a melting point of 31.5 °C and a degradation onset temperature of 86.4 °C. These properties provided a stable and practical platform for assessing thermal stability and reactivity. It should also be noted that, as previously reported,[29] the longer alkyl chain of 1-decanol poses a barrier to achieving quantitative carbonate

conversion. The synthesis of the corresponding CO_2BAL used here was indeed limited to ~80% conversion, as determined by ^{1}H NMR analysis (**Figure S3.7c**, **p.155**). Despite this slight limitation, the thermal properties of this compound made it a good choice for the subsequent experiments.

In the simplest approach, the decarboxylation reaction rate constant for the 1-decanol-based CO_2BAL, *k*, can be calculated according to equation 3.1:

$$ln\left(\frac{[CO_2BAL]_0}{[CO_2BAL]_t}\right) = k.t \qquad (3.1)$$

where $[CO_2BAL]_0$ and $[CO_2BAL]_t$ represent the concentration in CO_2BAL at time 0 and *t* minutes, respectively. The decarboxylation rate constant, *k*, can, therefore be calculated from the gradient for each semi-log plots at the different selected temperatures (**Figure 3.4a**).

Examination of the liberation of CO_2 from the TBD-based salt under a constant nitrogen flow (pN_2 = 0.2 bar), reveals that it takes 10 h to achieve ~ 50% degradation at 40 °C, whereas an almost complete degradation occurs within 0.3 h at 110 °C. The Arrhenius plot is then applied to calculate the activation energy (**Figure 3.4b**), E_a, and the pre-exponential factor, *A*, according to equation 3.2:

$$\ln k = \ln A - \frac{E_a}{R.T} \qquad (3.2)$$

where *R* is the universal gas constant (8.3144 J.mol^{-1}.K^{-1}).

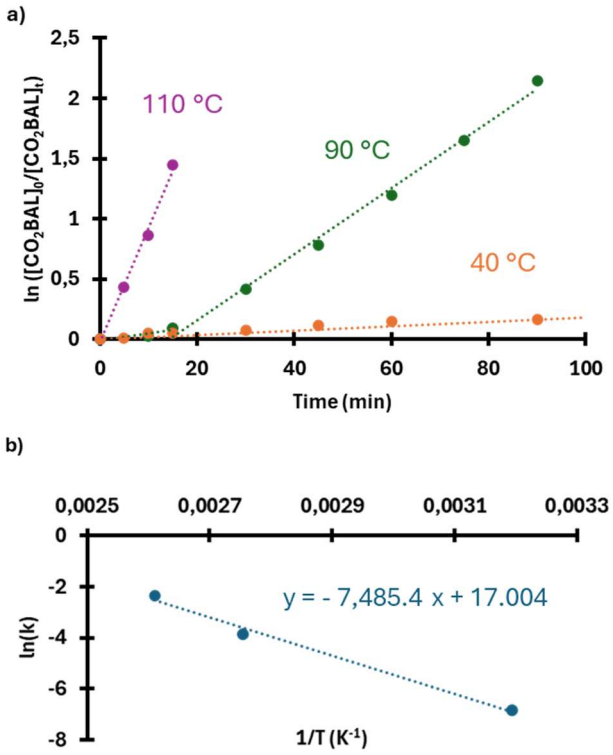


Figure 3.4. a) Decarboxylation kinetics of 1-decanol-based CO_2BAL at different temperatures and **b)** corresponding Arrhenius plot.

The activation energy (E_a) and pre-exponential factor (A) obtained for the 1-decanol-based CO_2BAL (62 kJ.mol^{-1} and 2.4 x 10^7 min^{-1}) fall within the typical range observed for first-order reactions involving complex organic transformations. For instance, Moreno *et al.* reported a E_a values of 58.7 - 70.5 kJ.mol^{-1} for cannabinoid decarboxylation,[42] illustrating that the thermal behaviour of the 1-decanol-based CO_2BAL is comparable to other thermally activated systems. While this moderate E_a reflects a certain degree of thermal stability, it also indicates that degradation becomes non-negligible at elevated temperatures. Combined with the relatively low degradation onset temperature (T5% = 86.4 °C), this limits the practical use of the CO_2BAL in bulk conditions, particularly for PVC functionalisation near its Vicat softening temperature (~92 °C). These findings further justify transitioning to solution-phase reactions, where thermal constraints are minimised, allowing for more controlled and efficient reactivity.

B. Reaction between PVC and CO_2BALs in solution

Unlike high-temperature bulk processes, solution-phase methods offer greater flexibility in selecting both the reaction temperature and the polarity of the medium. For PVC, only tetrahydrofuran (THF, dipole moment = 1.75 D), *N,N*-dimethylformamide (DMF, dipole moment = 3.82 D), and methyl ethyl ketone (MEK, dipole moment = 2.81 D) have been considered to investigate the ability of CO_2BAL to react with PVC at room temperature.[43–46] While THF is known to dissolve PVC completely, it was directly discarded due to its inability to solubilise 1-decanol-based CO_2BAL (conv. ~ 80 %) whatever its concentration. DMF and MEK, which exhibit satisfactory PVC dissolution performances and known to perfectly solubilise CO_2BALs, have then been compared.

Before initiating any reaction, the absolute number-average molar mass of PVC was determined. The theoretical number-average molar mass (M_nth) provided by Sigma is estimated at 48,000 g.mol^{-1}. Experimentally, Size Exclusion Chromatography (SEC) was performed using a polystyrene (PS) standard calibration in THF at 25 °C, with the Mark-Houwink relationship applied for both PS and PVC ($[\eta] = KM^a$, where K_{PS} = 1.1 x 10^{-4} dL.g^{-1} and a_{PS} = 0.725 for PS; K_{PVC} = 1.658 x 10^{-4} dL.g^{-1} and a_{PVC} = 0.76 for PVC).[47] This analysis yielded an experimental number-average molar mass (M_nSEC) of 41,400 g.mol^{-1} and a dispersity value ($Đ_M = M_w/M_n$) of 2.2. Prior to correction, the relative M_nSEC was 63,500 g.mol^{-1}.

To limit the significance of elimination reactions, which typically play a major role in the S_N2-E2 competition with PVC,[19,27,28] reactions were performed at 21 °C by reacting a CO_2BAL of 1-decanol (conv. ~ 80%) in a PVC solution ($[PVC]_0$ = 0.7 mmol.L^{-1}) for an initial $[Cl]_0$-to-$[CO_2BAL]_0$ molar ratio of 1. Even though MEK is capable of perfectly dissolving both PVC and the CO_2BAL of 1-decanol individually, their combination in this solvent and under the applied concentration conditions renders the CO_2BAL of 1-decanol insoluble. Under vigorous stirring, and after several hours, the insolubilisation of CO_2BAL gradually diminishes, eventually disappearing and leaving behind an insoluble black precipitate that does not dissolve in any of the organic solvents used.

In our opinion, such a black insoluble precipitate is likely due to the formation of a polyacetylene-like structure, possibly resulting from the degradation of CO_2BAL, which releases 1-decanol and TBD into the solution. The free TBD, or the alkoxide formed by deprotonation of 1-decanol by the guanidine, could then act as a base, promoting E2 elimination reactions on the PVC. Interestingly, the rate of insolubilisation has been observed variable with the degree of CO_2BAL conversion, *i.e.*, CO_2BALs of varying degrees of carbonate conversion.

Two TBD decanol-based carbonate salts with different degrees of carbonate conversion were then prepared under CO_2 by mixing equimolar amounts of 1-decanol and TBD at 90 °C for different reaction times. This approach allowed us to prepare new CO_2BALs with carbonate conversions of 50 and 75 mol% (**Figure S3.7a** and **b**, **p. 155**). Note that a conversion of 75% corresponds to a salt composed of 75 mol% carbonate and 25 mol% TBD alkoxide. A TBD alkoxide (referred to as the "0% conversion") also served as a reference for a CO_2BAL system entirely devoid of CO_2. These CO_2BALs were then reacted with PVC previously dissolved in MEK ($[PVC]_0$ = 0.7 mmol.L^{-1}) for a reaction time limited to 1 hour and a $[Cl]_0$-to-$[1\text{-decanol}]_0$ = 1. ^{1}H NMR analyses of the three reactions reveal no apparent reaction with the CO_2BAL but a substantial increase in vinyl protons showing up at δ = 5.5 - 6 ppm (**Figures S3.15** and **S3.16**, **p.158**). By integrating these protons relative to the CH-Cl signals of PVC (δ = 4.35 - 4.65 ppm), the proportion of E2 elimination per chain (= 100 x $(I_{5.5\text{-}6}/2)/[(I_{5.5\text{-}6}/2)+I_{4.35\text{-}4.65}]$) rises with decreasing CO_2BAL conversion. Moreover, the relative M_nSEC values also decrease accordingly, in agreement with the literature.[48] These trends are summarised in **Figure 3.5**, which compares the proportion of E2 elimination with the corresponding M_nSEC values. It should be noted that for the sample obtained with CO_2BAL 0% (*i.e.*, an equimolar mixture of 1-decanol and TBD), only the soluble fraction was analysed by SEC, while the majority remained insoluble in the SEC eluent, likely due to a high unsaturation content.

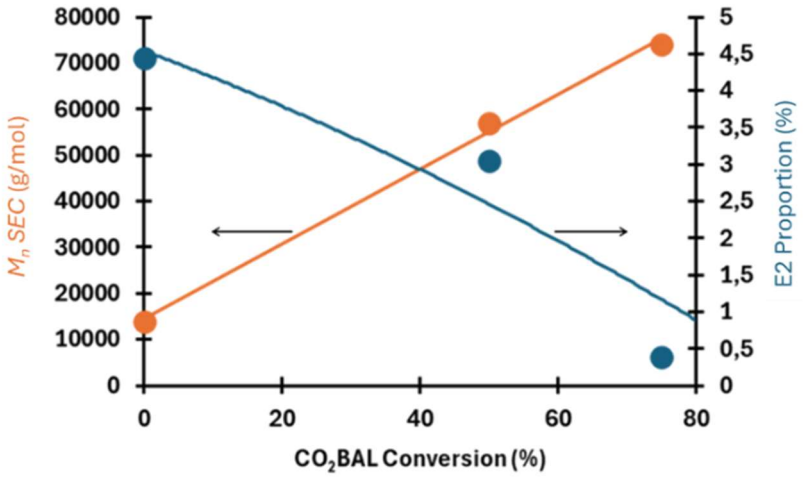


Figure 3.5. Influence of CO_2BAL carbonate conversion on the reaction outcome with PVC in MEK at 21 °C ($[PVC]_0$ = 0.7 mmol.L^{-1}, $[Cl]_0$-to-$[1\text{-decanol}]_0$ = 1, reaction time = 1 h). The relative M_nSEC values (in orange) and the proportion of E2 elimination (in blue) are plotted as a function of the CO_2BAL carbonate conversion.

To overcome the limitations observed in MEK, reactions were finally carried out at 21 °C in DMF, a solvent ensuring complete solubilisation of both PVC and the 1-decanol CO_2BAL. Five functionalisation reactions were performed in parallel for reaction times of 30 minutes, 1, 2, 18, and 72 hours, respectively. Each reaction medium was subsequently precipitated, washed, and dried to ensure complete removal of decanol derivatives. ^{1}H NMR analyses revealed signals associated with the α-methine proton of a decyl carbonate, which typically appears at δ = 4.87 ppm for alkyl carbonates and δ = 4.97 ppm for acyl carbonates.[29,49] In the present case, a signal was detected at approximately δ = 4.76 ppm, overlapping with the PVC methine protons, suggesting the formation of a decyl-based carbonate. Additionally, a triplet at δ = 0.89 ppm, corresponding to terminal methyl protons of decyl chains, confirmed the successful reaction of CO_2BAL with PVC (**Figure 3.6a**). Notably, vinyl proton signals (δ = 5.5 - 6 ppm) first appeared at the 2-hour mark, corresponding to a S_N2/E2 ratio of 94/6. Beyond this point, the selectivity shifted in favour of elimination, with S_N2/E2 ratios decreasing to 54/46 after 18 hours and 38/62 after 72 hours. This shift was accompanied by a decrease in relative M_nSEC values, which initially increased from 63,500 g/mol for PVC to over 89,000 g/mol after 2 hours, before declining for longer reaction times (**Figure S3.17 – S3.18**, **p. 159**). The degree of substitution followed the same trend, increasing over the first two hours of reaction before decreasing at longer reaction times. These observations suggest that prolonged reaction times lead to kinetic instability and the gradual release of free TBD into the reaction medium, promoting elimination over substitution. Moreover, the decreasing degree of substitution also suggests that longer reaction times allow for the elimination of previously grafted moieties.

The success of the reaction was further confirmed by Fourier Transform Infrared (FTIR) spectroscopy. The spectrum of the sample obtained after 2 hours of reaction exhibited a new absorption band at 1744 cm^{-1}, attributed to the asymmetric stretching of the C=O bond. This frequency matches that observed for a model small molecule in Chapter 2 (**Figure 3.6b**).[29] Notably, no significant absorption bands corresponding to C=C stretching vibrations were detected, indicating that vinyl unsaturations formed via elimination remain below the FT-IR detection limit.

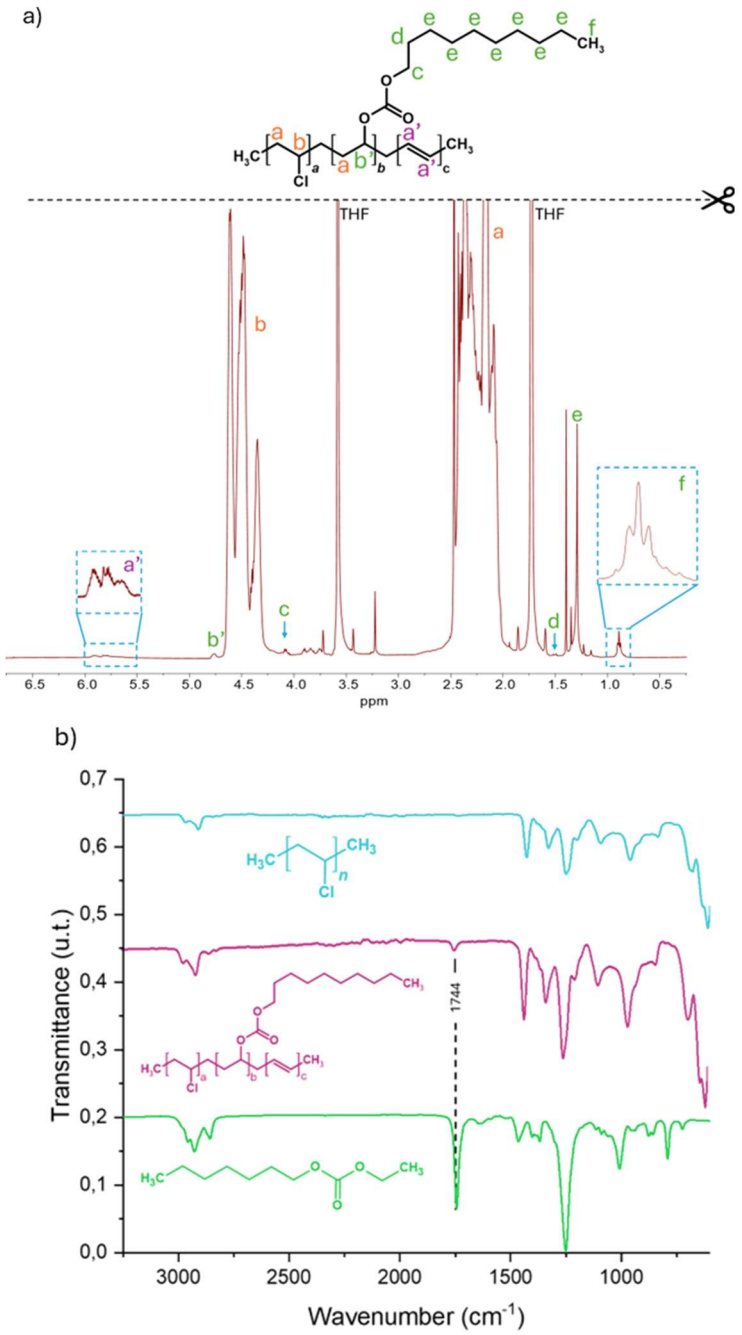


Figure 3.6. a) ^{1}H NMR (THF-d_8, 500 MHz) of modified PVC **b)** FT-IR of PVC (blue), modified PVC (purple), and a heptyl-ethyl carbonate (green) used in comparison and prepared as reported in Chapter 2.

The sample obtained after 2 hours of reaction was further analysed by thermogravimetric analysis (TGA) to accurately determine the mass fraction of grafted carbonate moieties and compared to the pristine PVC (**Figure 3.7**). As expected, the thermogram of pristine PVC exhibits thermal stability up to 230 °C, beyond which rapid dehydrochlorination occurs, spanning the temperature range of 230 to 370 °C.[50] Between 375 and 525 °C, the degraded polyene structures undergo transformation into condensed aromatic hydrocarbons, eventually yielding infusible coke with a residual carbon content of approximately 6.8% at 650 °C. Three key differences were observed in the thermogram of modified PVC. First, an additional mass loss step appears at *ca.*

125 °C, attributed to the degradation of the grafted carbonate groups. Second, the chlorinated backbone of PVC is destabilised upon functionalisation, as evidenced by a shift in the dehydrochlorination onset temperature from 230 °C (pristine PVC) to approximately 180 °C. This phenomenon is well-documented in the literature.[27,28,51,52] Finally, the coke residue at 650 °C is slightly higher for modified PVC compared to pristine PVC, likely reflecting the small proportion of elimination reactions detected by ^{1}H NMR spectroscopy.

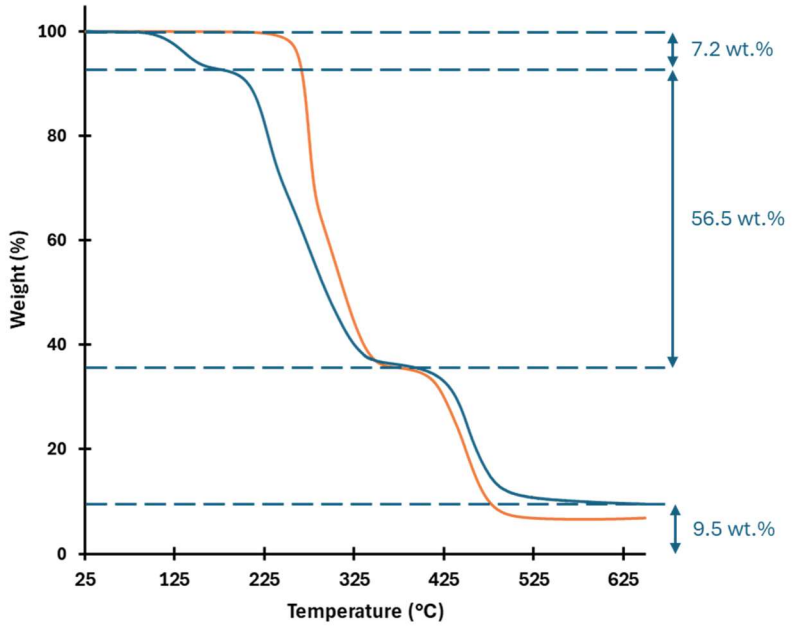
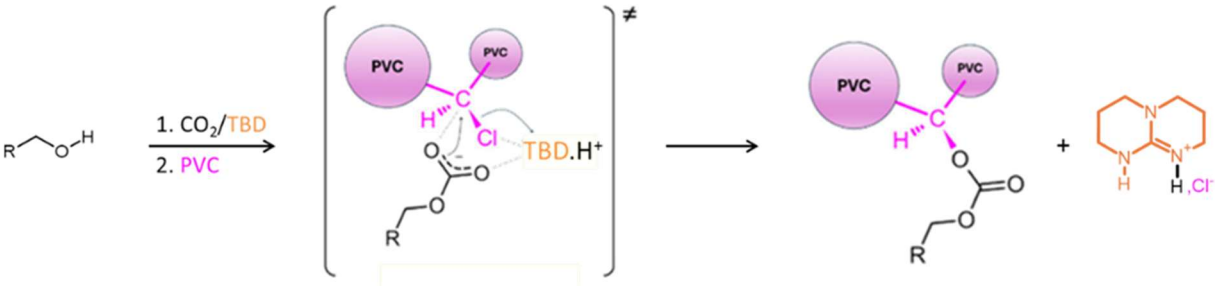


Figure 3.7. Thermal stability of pristine PVC (orange) and PVC modified with 1-decanol-based CO_2BAL (conv. 80%) in DMF for 2 hours (blue).

The limited grafting efficiency observed in DMF can be attributed to a combination of steric and electronic factors. CO_2BALs are known to be significantly stabilised in highly polar solvents like DMF due to dipolar interactions (see Chapter 2),[29] which reduces their overall reactivity and may hinder efficient nucleophilic attack. In S_N2 reactions, the substitution of the halogenated carbon is governed by both the dynamics and reactivity of the system.[53] Typically, S_N2 reactions proceed *via* a backside attack, resulting in Walden inversion. However, the introduction of bulky substituents can sterically hinder this pathway, potentially favouring a S_N2 frontside mechanism despite its slightly higher energetic cost. In the case of PVC, a statistical coil polymer with randomly distributed CH-Cl electrophilic sites, steric hindrance plays a crucial role in dictating the reaction pathway. The steric environment likely promotes frontside S_N2 substitution, especially when assisted by a guanidinium ion-pair mechanism (**Scheme 3.1**).[29] The combination of CO_2BAL stabilisation in DMF and steric constraints on the PVC backbone could thus explain the observed limitation in grafting efficiency.



Scheme 3.1. Mechanism proposed for PVC substitution from CO_2BAL by a frontside approach.

III. CONCLUSION

Thermal properties assessment revealed that CO_2BALs undergo degradation under bulk-phase reaction conditions, necessitating the use of solution-phase functionalisation for efficient PVC modification at 21 °C. Despite a moderate degree of substitution (<10 wt.%) compared to some already existing strategies mentioned in the introduction, this approach achieved a remarkable S_N2 selectivity (94/6) while generating a single, benign by-product (TBD.HCl). Spectroscopic and thermal analyses confirmed the successful grafting of carbonate functionalities, though solvent effects influenced reaction efficiency. Specifically, the strong stabilisation of CO_2BALs in polar solvents like DMF reduced their nucleophilicity at room temperature, highlighting the need for alternative strategies to enhance substitution yields. Beyond PVC functionalisation, this strategy holds broader environmental benefits. The use of CO_2BALs introduces a novel approach for integrating CO_2 into polymer modifications, aligning with circular economy principles. A potential concern for large-scale implementation may be the cost of TBD. However, this limitation can be mitigated, as demonstrated by Fritz-Langhals, who developed a straightforward and cost-effective one-pot synthesis of a liquid TBD formulation.[39] Moreover, the generation of a single, benign by-product (TBD.HCl) enhances the process sustainability. As a guanidinium chloride, TBD.HCl has well-established applications in biochemistry, notably as a protein denaturant and nucleic acid stabiliser,[30,31] which supports its potential for recovery and reuse. By bridging CO_2 utilisation with PVC upcycling, this work contributes to the development of greener methodologies for the valorisation of chlorine-rich polymers.

To overcome the limited substitution efficiency observed here, the next chapter combines two complementary strategy modifications. On the electrophile side, a fraction of the C-Cl bonds of PVC is converted into C-I bonds through an aqueous phase-transfer catalysis strategy, restoring the high reactivity of iodinated electrophiles evidenced in Chapter 2, as iodide is a far better leaving group than chloride. On the nucleophile side, the TBD-based CO_2BAL is replaced by a DBU-based CO_2-binding amine (CO_2BAM), taking advantage of the considerably lower cost of DBU compared to TBD and the higher CO_2 conversion rates.

IV. EXPERIMENTAL

A. Materials

Carbon dioxide N50 (≥ 99.999 %) was supplied by Air Liquide. 1-Propanol (99+ %), 1-butanol (≥99.4 %, ACS reagent), 1-hexanol (anhydrous, ≥ 99 %), deuterated chloroform (0.03 vol% TMS, deuteration degree min. 99.8 % for NMR spectroscopy, stabilised with silver), 1-decanol (for synthesis), poly(vinyl chloride) (low molecular weight), as well as N,N-dimethylformamide (anhydrous, 99.8 %) were purchased from Sigma-Aldrich. Methanol (GPR Rectapur) and octan-1-ol (purified) were purchased from VWR. 2-Butanone (or methyl ethyl ketone (MEK), ACS Reagent) was acquired from Acros Organics. Ethanol (denaturated with 3 % diethylether, Desinfectol) was purchased from Chemlab. 1,5,7-Triazabicyclo[4.4.0]dec-5-ene (TBD) was supplied by Apollo Scientific. Deuterated tetrahydrofuran (99.5 % D) was supplied by CortecNet.

B. Procedures

General procedure for the synthesis of CO_2BALs

The general protocol was adapted from the one described in Chapter 2. A Schlenk tube, equipped with a septum and a stir bar, is charged with a mixture of TBD (1.3990 g, 0.01005 mol) and an alcohol (0.01005 mol or 0.03015 mol for methanol, and 0.05025 mol for ethanol and 1-propanol) in bulk. A butyl pipe is used to link the CO_2 tank and the Schlenk tube and a needle (20G) is used to pierce the septum, allowing carbon dioxide (pCO_2 = 0.2 bar) to be bubbled onto the reaction mixture in a continuous flow. For most CO_2BOLs the reaction is performed at 90 °C in an oil bath and under 500 rpm stirring for 1h30. In the case of methanol, ethanol and 1-propanol, the reaction is performed at 50 °C in an oil bath.

- $MeOCO_2^-$,$TBD.H^+$: ^{1}H NMR (60 MHz, $CDCl_3$) : δ = 3.59 (s, 3H), 3.29 (dt, 8H), 1.98 (quint, 4H).
- $EtOCO_2^-$,$TBD.H^+$: ^{1}H NMR (60 MHz, $CDCl_3$) : δ = 4.03 (q, 2H), 3.29 (dt, 8H), 1.98 (quint, 4H), 1.23 (t, 3H).
- $PrOCO_2^-$,$TBD.H^+$: ^{1}H NMR (60 MHz, $CDCl_3$) : δ = 3.87 (q, 2H), 3.29 (dt, 8H), 1.98 (quint, 4H), 1.57 (quint, 2H), 0.94 (t, 3H).
- $ButOCO_2^-$,$TBD.H^+$: ^{1}H NMR (500 MHz, $CDCl_3$) : δ = 3.91 (q, 2H), 3.29 (dt, 8H), 1.98 (quint, 4H), 1.59 (quint,2H), 1.40 (m, 2H), 0.91 (t, 3H).
- $HexOCO_2^-$,$TBD.H^+$: ^{1}H NMR (500 MHz, $CDCl_3$) : δ = 3.91 (q, 2H), 3.29 (dt, 8H), 1.98 (quint, 4H), 1.61 (quint, 2H), 1.38 (m, 2H), 1.28 (m, 4H), 0.87 (t, 3H).
- $OctOCO_2^-$,$TBD.H^+$: ^{1}H NMR (500 MHz, $CDCl_3$) : δ = 3.91 (q, 2H), 3.30 (dt, 8H), 1.99 (quint, 4H), 1.61 (quint, 2H), 1.37 (m, 2H), 1.27 (m, 8H), 0.87 (t, 3H).

- $DecOCO_2^-$,TBD.H^+ : ^{1}H NMR (500 MHz, $CDCl_3$) : δ = 3.90 (q, 2H), 3.30 (dt, 8H), 1.99 (quint, 4H), 1.60 (quint, 2H), 1.38 (m, 2H), 1.25 (m, 12H), 0.87 (t, 3H).

$\tilde{\nu}_{max}$ (cm^{-1}) : 3232 (NH), 3152 (NH), 1655 (C=O), 1570 (C=N), 1388 (CO).

General procedure for the reaction between CO_2BALs and PVC

PVC (0.01005 mol Cl, 0.6245g PVC) was dissolved in MEK or DMF (20 ml). The CO_2BAL (0.01005 mol) was then added to the solution. The reaction was performed at room temperature, under 500 rpm stirring, and CO_2 atmosphere for 0.5, 1, 2, 18 or 72 hours. After each reaction, the product is purified through a three-step process. First, water is used to precipitate and wash the product. Then, the precipitate is solubilised in THF. Finally, the solution from the previous step is precipitated in water, and the product is filtrated, thoroughly washed with methanol and dried before analysis.

Modified PVC : ^{1}H NMR (500 MHz, THF-d_8) : δ = 5.79 (br. t, 2H), 4.75 (br. t, 1H), 4.49 (br. t, 1H), 4.09 (br. t, 1H), 2.24 (br. m, 2H), 1.46 (t, 2H), 1.29 (br. m, 14H), 0.89 (t, 3H).

$\tilde{\nu}_{max}$ (cm^{-1}) : 1744 (C=O), 1429 (PVC), 1330 (PVC), 1250 (PVC), 1117 (C-O), 964 (PVC).

C. Methods

Melting point determination

The melting point of each CO_2BAL was determined visually by heating a pre-cooled sealed NMR tube containing CO_2BAL compounds, at a rate of 1 °C per minute in an oil bath.

Thermal stability – TGA and Degradation Kinetics

CO_2BALs were subjected to thermogravimetric analysis (TGA) to determine their degradation temperature. Measurements were performed under nitrogen flow at a rate of 5 °C per minute using a TA Q500 TGA.

Products of the reaction between CO_2BAL and PVC were subjected to TGA as well. This allowed for thermal stability evaluation as well as the determination of the substitution rate. Measurements were performed under nitrogen flow at a rate of 2.5 °C per minute using a TA Q500 TGA.

In order to evaluate the CO_2BALs' thermal stability, degradation kinetics analysis was performed. Samples were therefore subjected to a nitrogen flow ($p(N_2)$ = 0.2 bar) at different temperatures, using the same experimental setup as for their synthesis. Degradation was monitored regularly through ^{1}H NMR spectroscopy. The neperian logarithm of the degradation percentage was plotted against time. After linear regression, the slope obtained gave the kinetic constant of the degradation reaction (k) at each temperature. Consequently, the plot of ln(k) against 1/T (K^{-1}) allowed to work out the frequency factor (A) and the activation energy (E_a) parameters of the Arrhenius equation for the degradation reaction.

FT-IR spectroscopy

Fourier Transform InfraRed spectroscopy was performed using a Bruker Tensor 27 spectrometer to give an indication regarding the success of the substitution reaction between PVC and CO_2BALs.

NMR spectroscopy

CO_2 conversion was followed time-to-time through ^{1}H nuclear magnetic resonance (NMR) using a Spinsolve 60 Ultrabenchtop NMR spectrometer (Magritek, Aachen, Germany). All spectra were acquired according to the following parameters: aq = 6.4 sec, repetition time = 10 sec, pulse angle = 90, ns = 32.

Final CO_2BAL and substitution products were all characterised by ^{1}H NMR using a Bruker AVANCEII 500 MHz apparatus at room temperature in chloroform-d_1 ($CDCl_3$) and THF-d_8, respectively. All spectra were acquired according to the following parameters: aq = 2.75 sec, d1 = 1 sec, sw = 20, ns = 32 for small molecules and 512 for PVC-based compounds.

SEC

Substitution products were subjected to size exclusion chromatography (SEC) in THF at 25 °C using a Triple Detection Polymer Laboratories liquid chromatograph equipped with a refractive index (ERMA 7517), a UV detector (254 nm), a capillary viscometry, a light scattering RALS (Viscotek T-60) (Polymer Laboratories GPC-RI/CV / RALS) and an automatic injector (Polymer Laboratories GPC-RI/UV) and four columns: a PL gel 10 µm guard column and three PL gel Mixed-B 10 µm columns (linear columns for separation of M_w PS ranging from 500 to 10^6 daltons). All samples for SEC analyses were prepared according to the following concentration: 1 mg of polymer sample in 1 mL of THF.

V. SUPPORTING INFORMATION

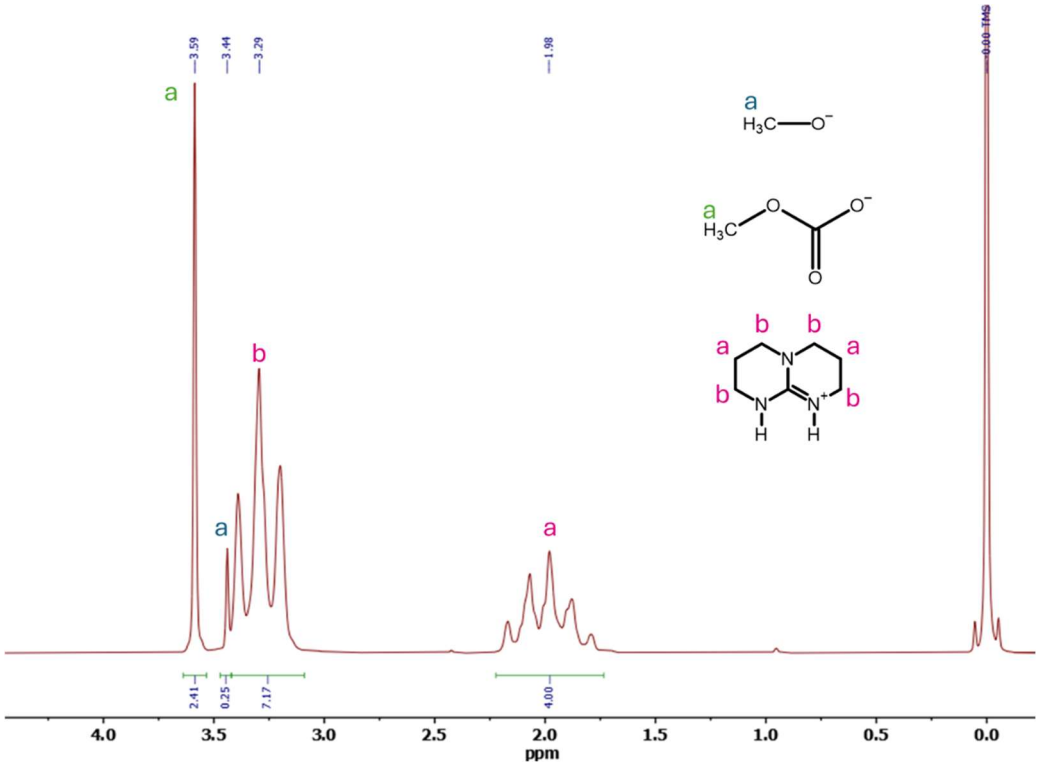


Figure S3.1. ^{1}H NMR spectrum (60 MHz, $CDCl_3$, zoomed between δ = 0 ppm and δ = 4.5 ppm) of the product of the reaction between methanol and TBD under CO_2 bubbling.

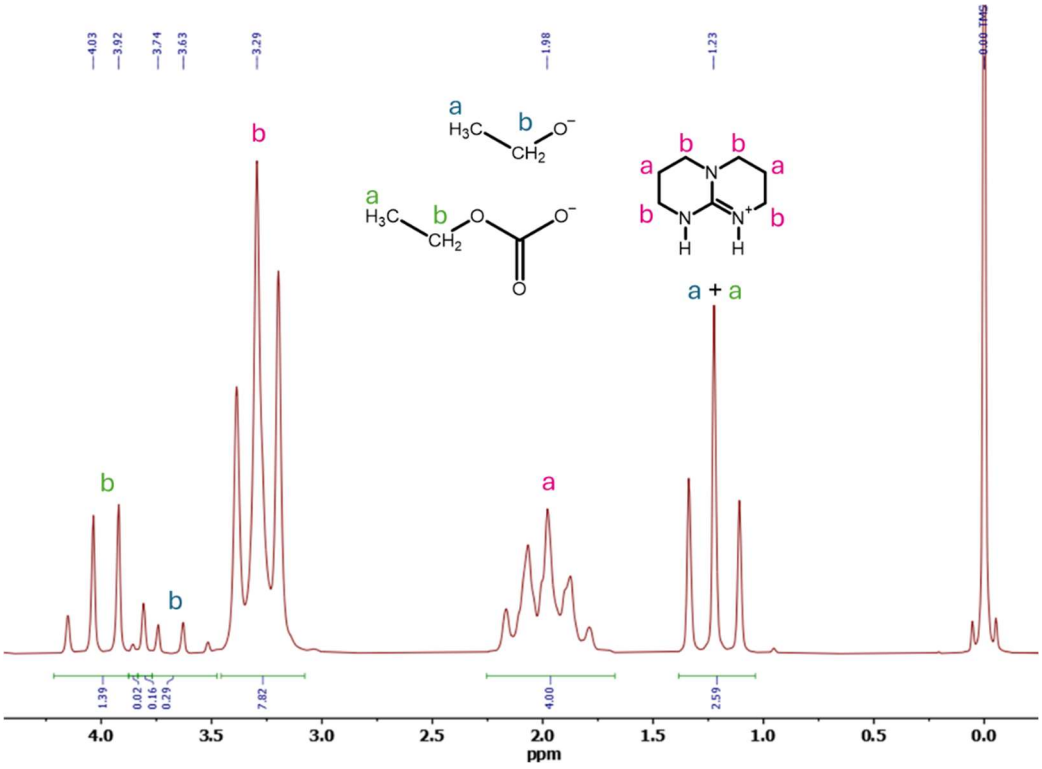


Figure S3.2. ^{1}H NMR spectrum (60 MHz, $CDCl_3$, zoomed between δ = 0 ppm and δ = 4.5 ppm) of the product of the reaction between ethanol and TBD under CO_2 bubbling.

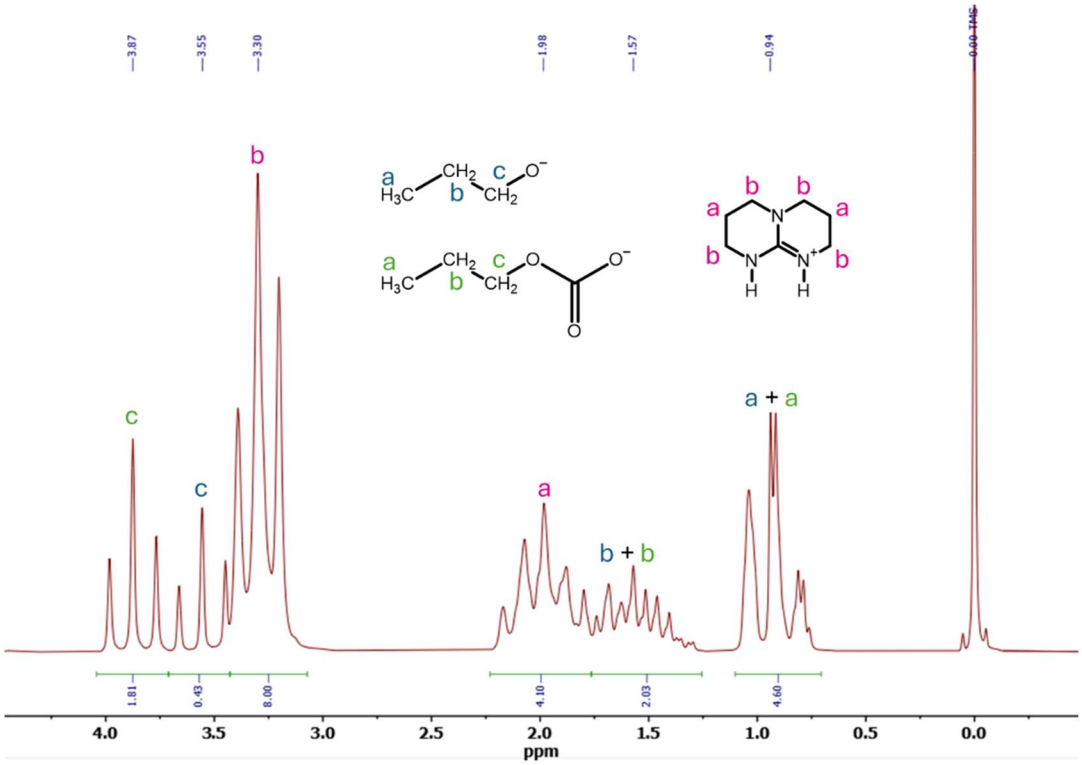


Figure S3.3. ^{1}H NMR spectrum (60 MHz, $CDCl_3$, zoomed between δ = 0 ppm and δ = 4.5 ppm) of the product of the reaction between 1-propanol and TBD under CO_2 bubbling.

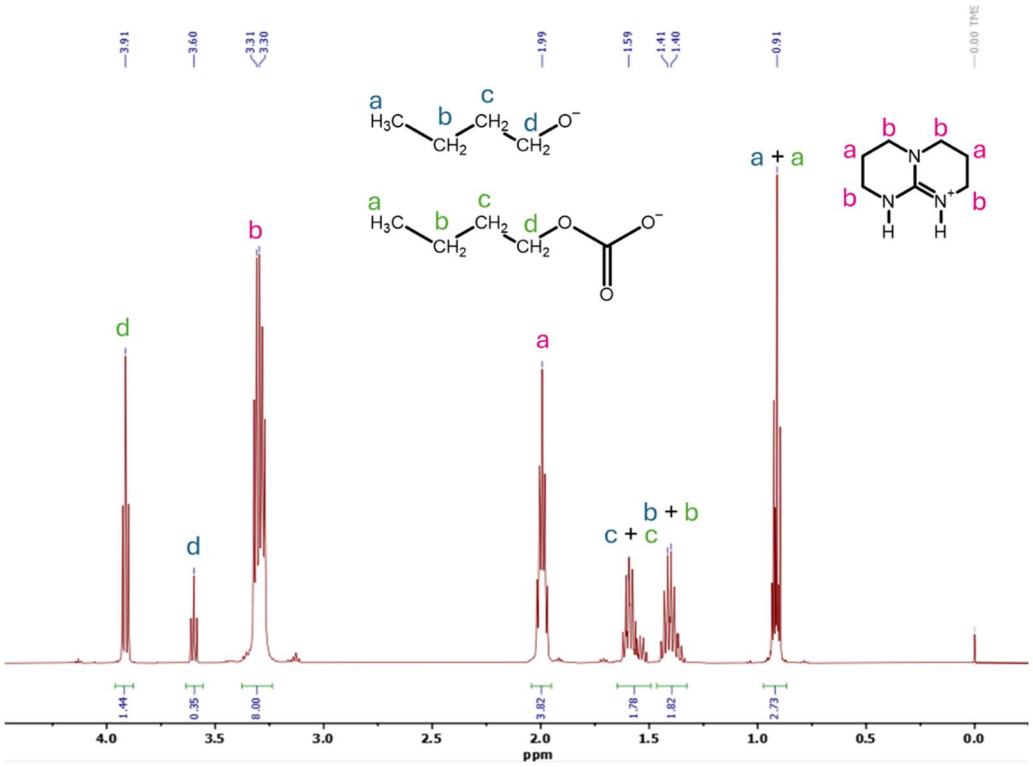


Figure S3.4. ^{1}H NMR spectrum (500 MHz, $CDCl_3$, zoomed between δ = 0 ppm and δ = 4.5 ppm) of the product of the reaction between 1-butanol and TBD under CO_2 bubbling.

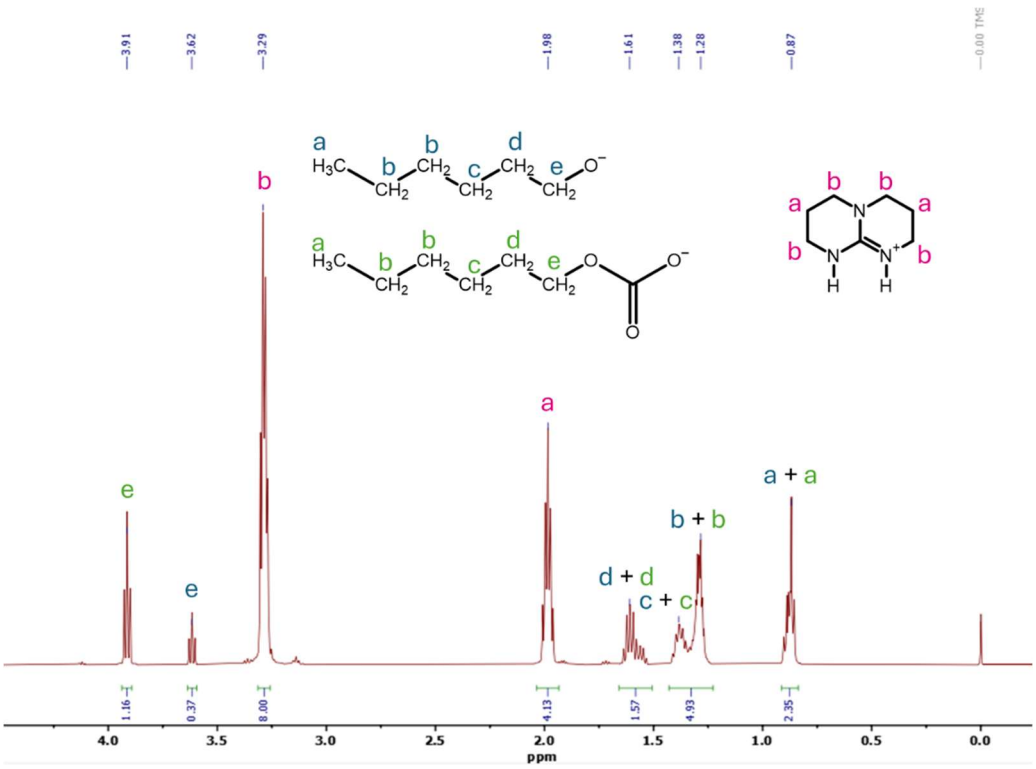


Figure S3.5. ^{1}H NMR spectrum (500 MHz, $CDCl_3$, zoomed between δ = 0 ppm and δ = 4.5 ppm) of the product of the reaction between 1-hexanol and TBD under CO_2 bubbling.

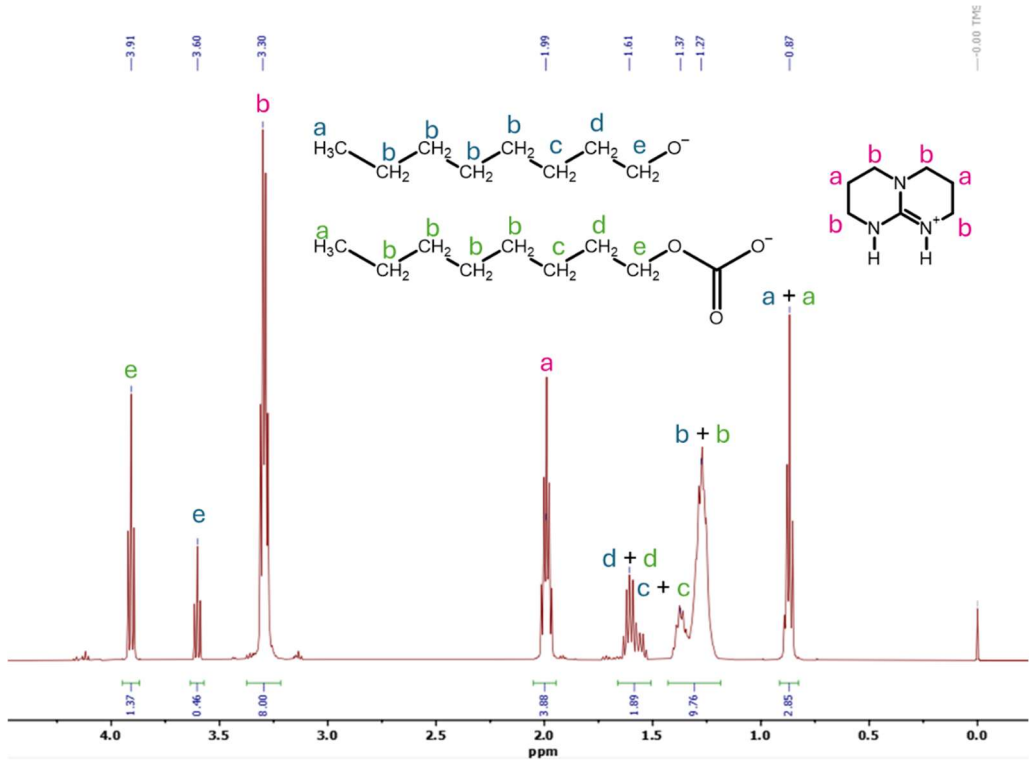


Figure S3.6. ^{1}H NMR spectrum (500 MHz, $CDCl_3$, zoomed between δ = 0 ppm and δ = 4.5 ppm) of the product of the reaction between 1-octanol and TBD under CO_2 bubbling.

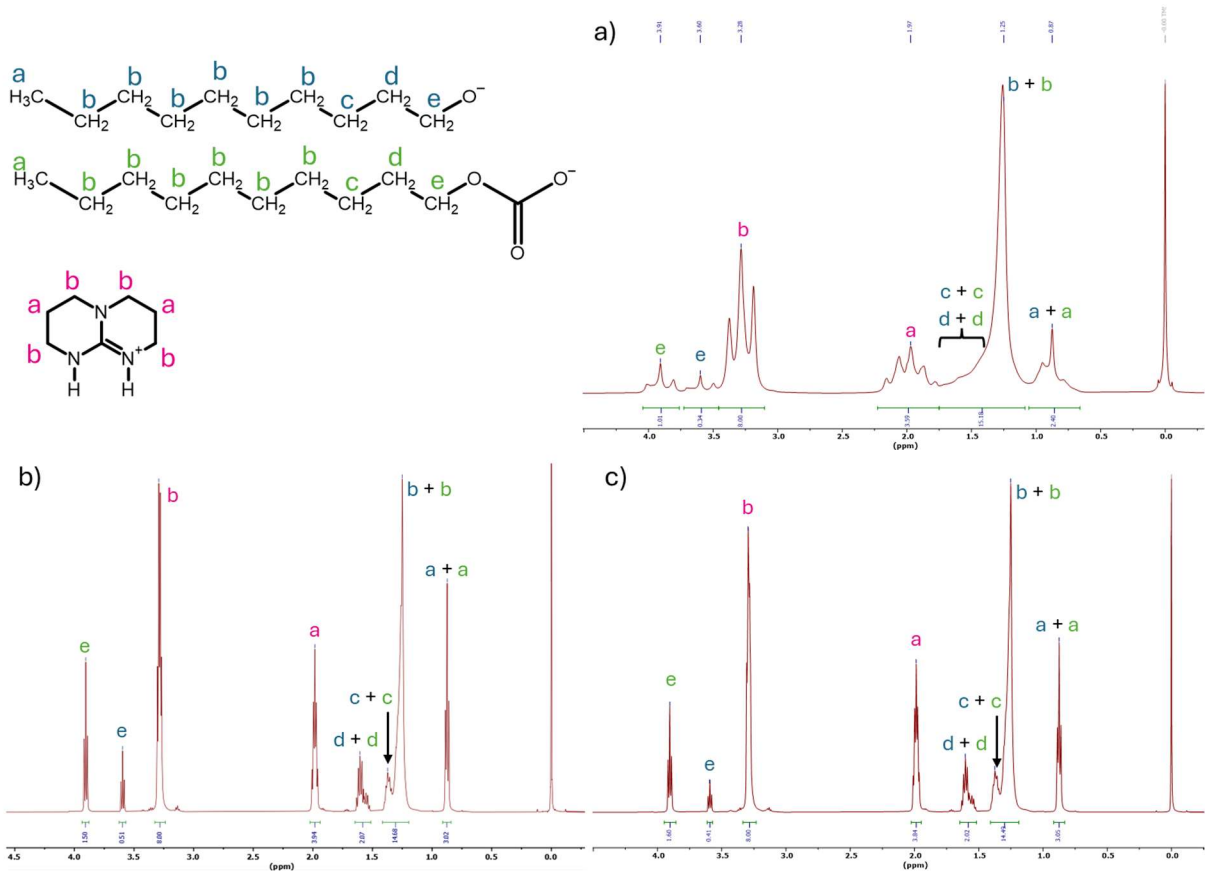


Figure S3.7. ^{1}H NMR spectrum (500 MHz, $CDCl_3$, zoomed between δ = 0 ppm and δ = 4.5 ppm) of the product of the reaction between 1-decanol and TBD under CO_2 bubbling : **a)** 50 %, **b)** 75 %, and **c)** 80 % conversion, respectively.

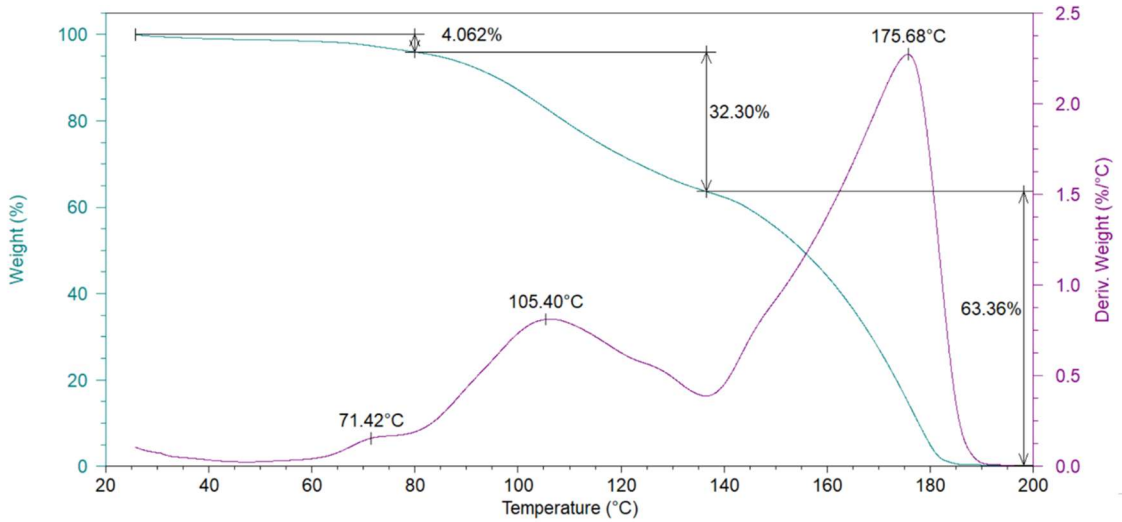


Figure S3.8. Thermogravimetric analysis (TGA) of the product of the reaction between methanol and TBD under CO_2 bubbling.

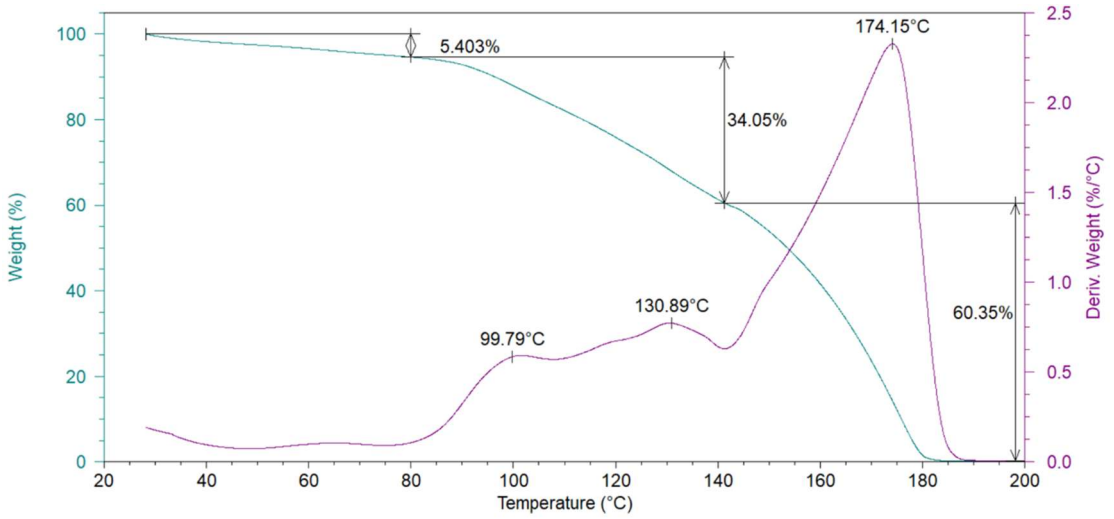


Figure S3.9. TGA of the product of the reaction between ethanol and TBD under CO_2 bubbling.

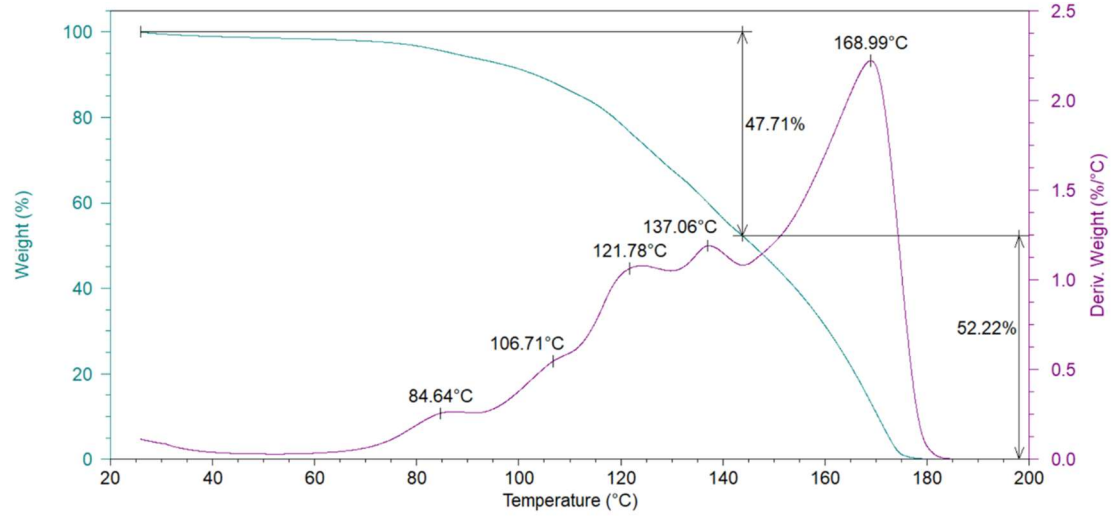


Figure S3.10. TGA of the product of the reaction between 1-propanol and TBD under CO_2 bubbling.

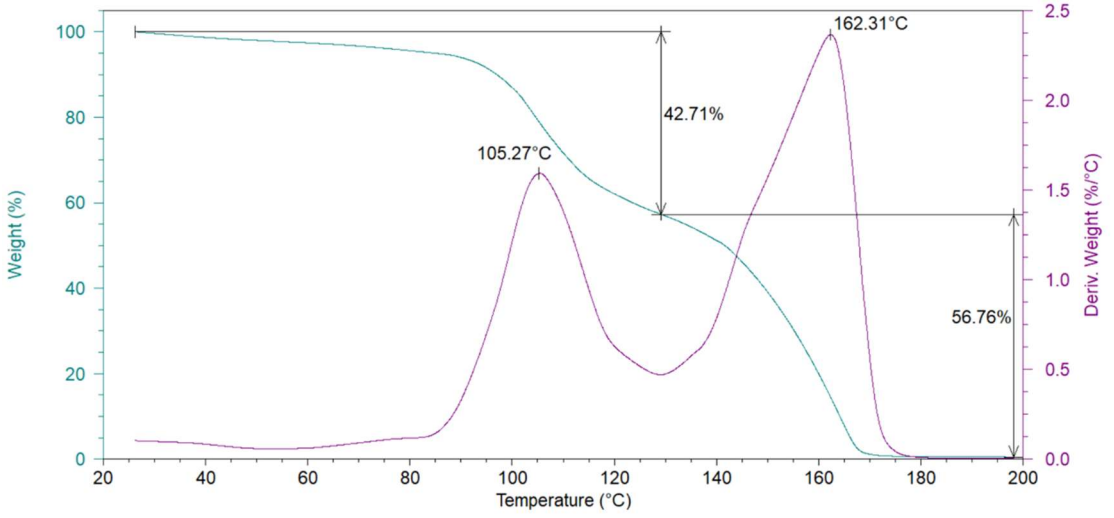


Figure S3.11. TGA of the product of the reaction between 1-butanol and TBD under CO_2 bubbling.

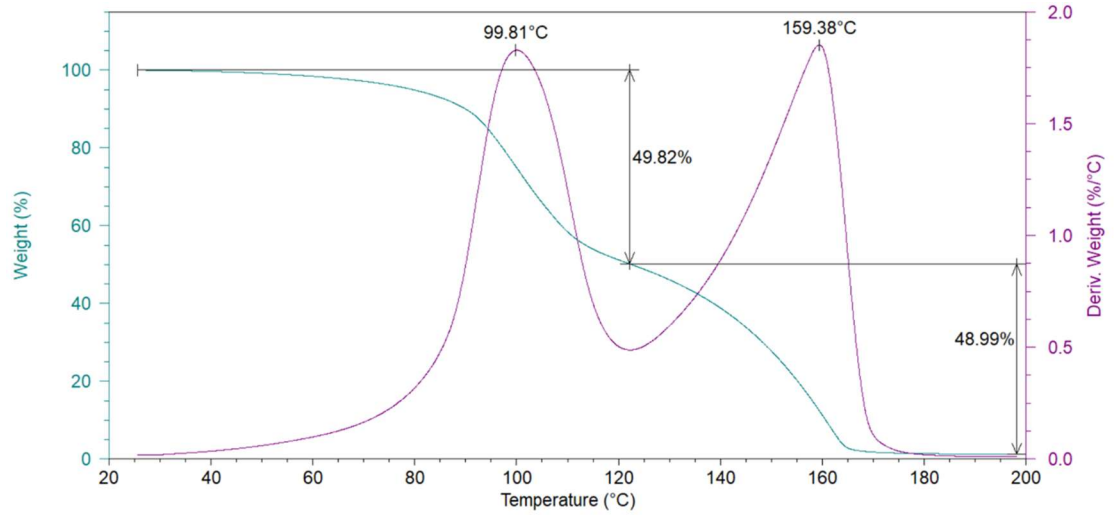


Figure S3.12. TGA of the product of the reaction between 1-hexanol and TBD under CO_2 bubbling.

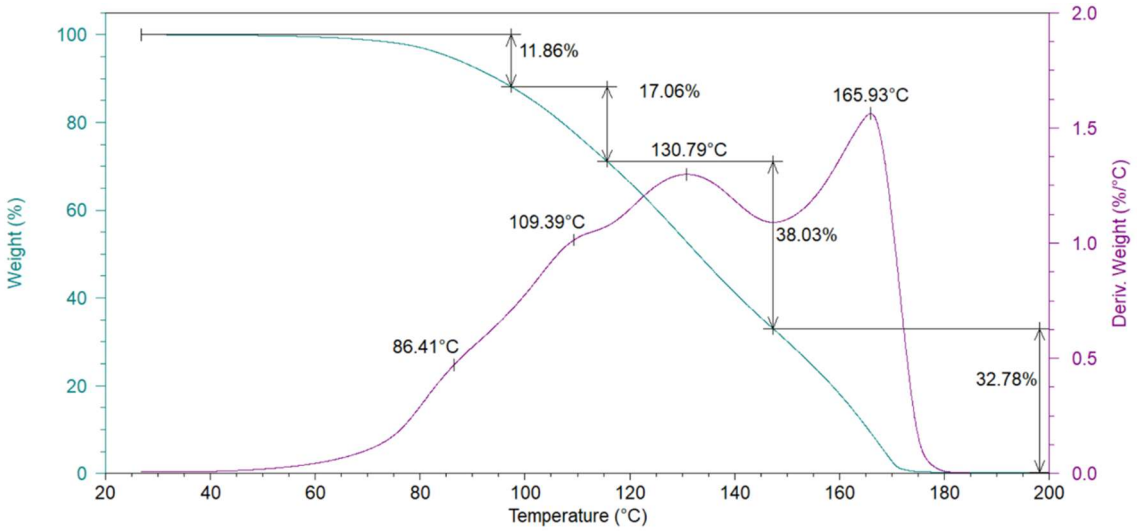


Figure S3.13. TGA of the product of the reaction between 1-octanol and TBD under CO_2 bubbling.

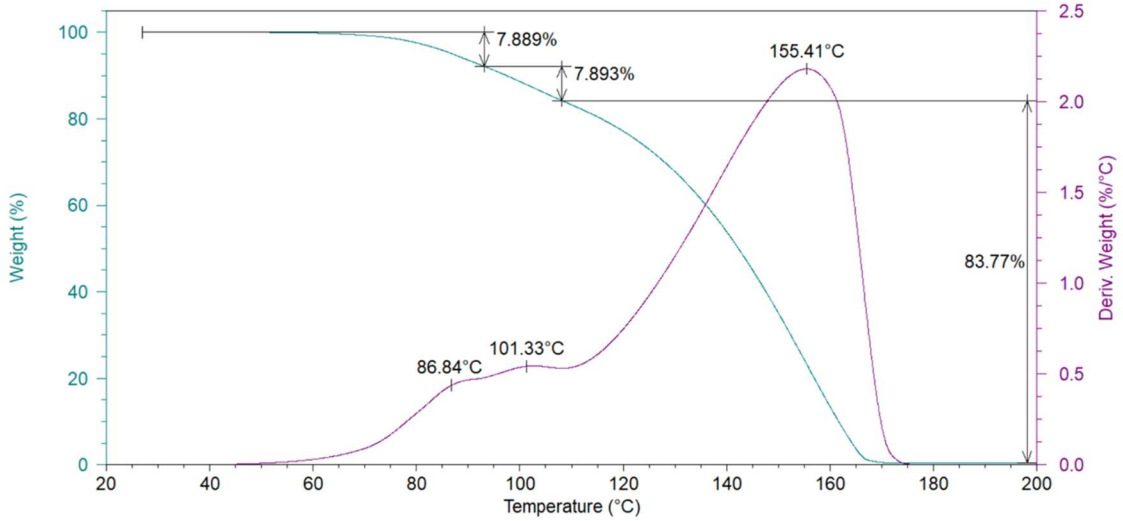


Figure S3.14. TGA of the product of the reaction between 1-decanol and TBD under CO_2 bubbling.

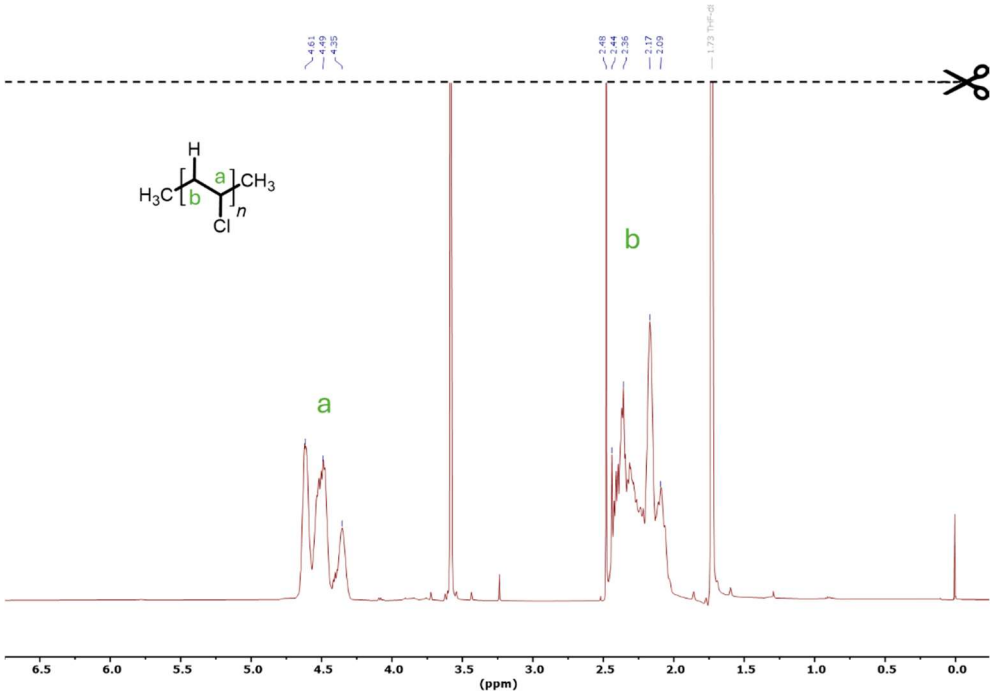


Figure S3.15. ^{1}H NMR spectrum (500 MHz, THF-d_8, zoomed between δ = 0 ppm and δ = 6.75 ppm) of pristine PVC.

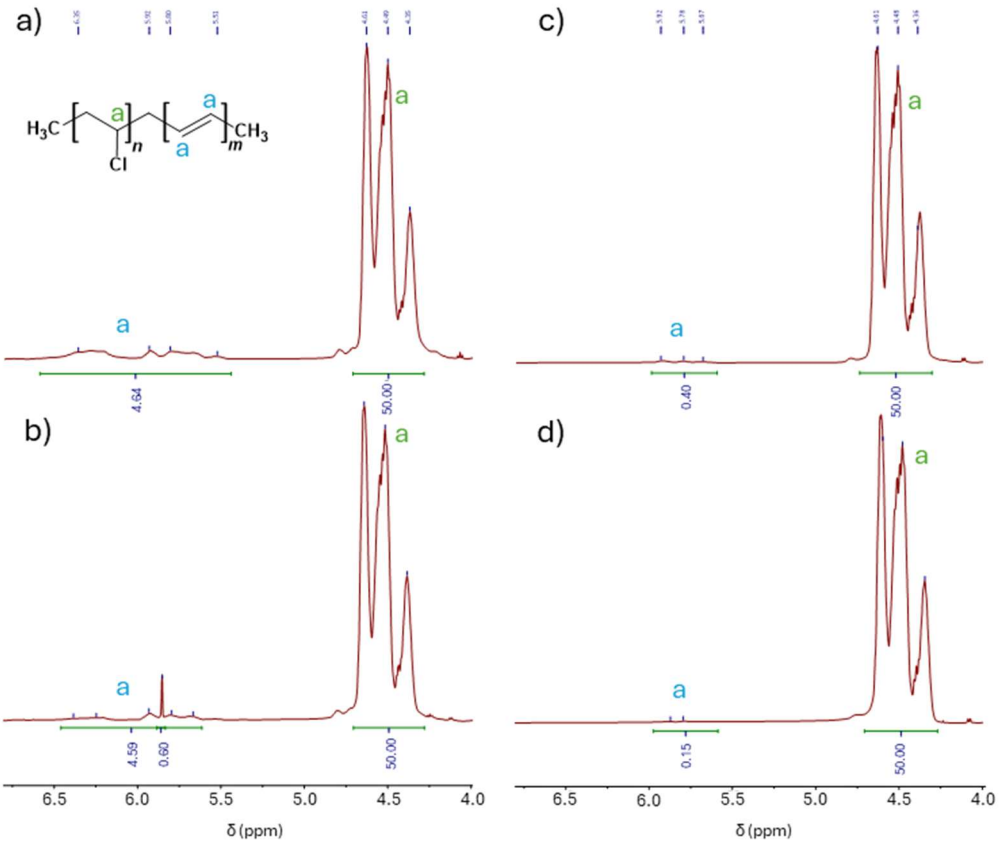


Figure S3.16. ^{1}H NMR spectrum (500 MHz, THF-d_8, zoomed between δ = 4.0 ppm and δ = 6.75 ppm) of the product of the reaction between 1-decylcarbonate, TBD.H^{+} (CO_2BAL conv. = **a)** 0%, **b)** 50%, **c)** 75%, and **d)** 80%) and PVC in MEK for 1 hour.

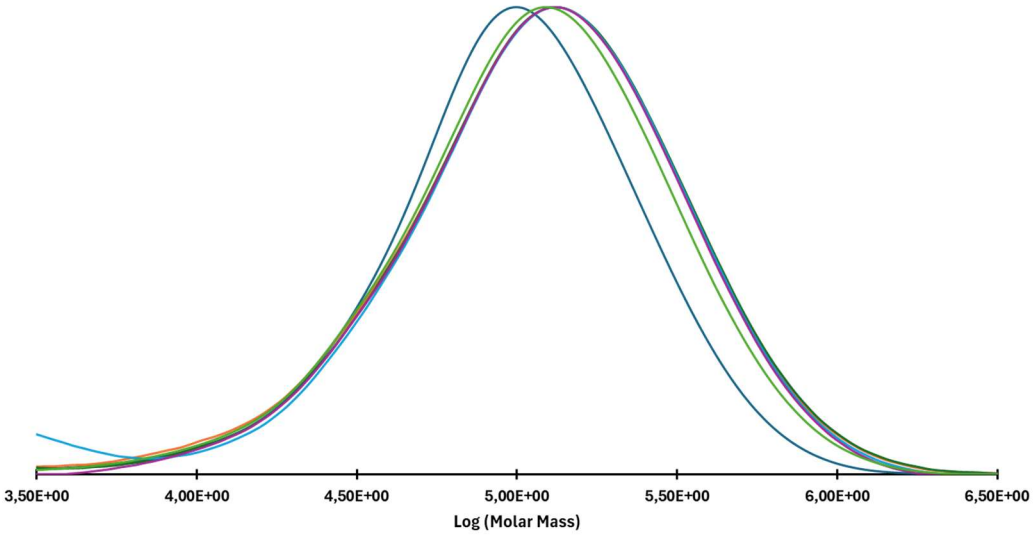


Figure S3.17. SEC traces of pristine PVC (dark blue) and the product of the reaction between 1-decylcarbonate, TBD.H^+ and PVC in DMF for 30 minutes (orange), 1 hour (dark green), 2 hours (light blue), 18 hours (purple), and 72 hours (light green).

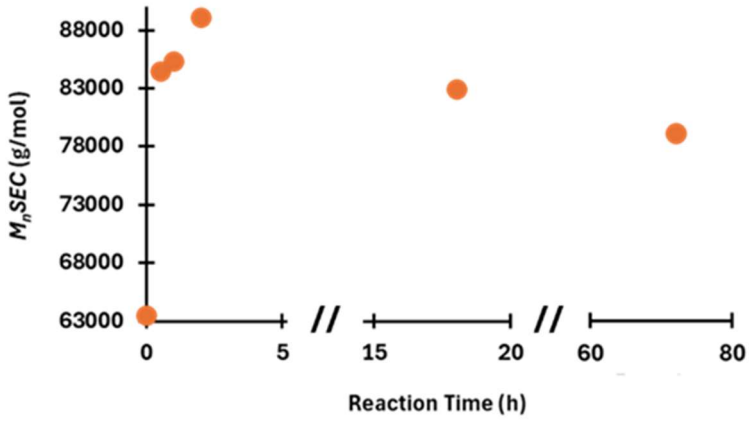


Figure S3.18. Effect of reaction time on the polymer's relative M_n determined by SEC.

VI. REFERENCES

1 Poly Vinyl Chloride (PVC) Market Analysis, https://www.chemanalyst.com/industry-report/polyvinyl-chloride-pvc-market-60, (accessed 15 April 2024).

2 *The Circular economy for Plastics - A European Analysis*, Plastics Europe, 2024.

3 A. Buekens and A. Sevenster, *J. Mater. Cycles Waste Manag.*, 2010, **12**, 184–192.

4 K. Lewandowski and K. Skórczewska, *Polymers*, 2022, **14**, 3035.

5 Z. Ait-Touchente, M. Khellaf, G. Raffin, N. Lebaz and A. Elaissari, *Polymers for Advanced Techs*, 2024, **35**, e6228.

6 M. Sadat-Shojai and G.-R. Bakhshandeh, *Polymer Degradation and Stability*, 2011, **96**, 404–415.

7 X. Jiang, B. Zhu and M. Zhu, *Green Chem.*, 2023, **25**, 6971–7025.

8 D. E. Fagnani, D. Kim, S. I. Camarero, J. F. Alfaro and A. J. McNeil, *Nat. Chem.*, 2023, **15**, 222–229.

9 M. Liu, X. Wu and P. J. Dyson, *Nat. Chem.*, 2024, **16**, 700–708.

10 S. Mishra, S. Kar, R. Rangappa, P. Patil, V. Kadam, S. H. Chikkali and R. C. Samanta, *Chemistry A European J.*, 2025, **31**, e202403980.

11 J. L. S. Zackasee, V. Srivardhan, B. L. Truesdell, E. J. Vrana and C. S. Sevov, *Chem*, 2025, **11**, 102298.

12 S. Zhang, H. Han, M. Cao, Y. Xie and J. Chen, *Interdisciplinary Materials*, 2025, **4**, 5–23.

13 T. Yoshioka and G. Grause, in *Topical Themes in Energy and Resources*, eds. Y. Tanaka, M. Norton and Y.-Y. Li, Springer Japan, Tokyo, 2015, pp. 195–214.

14 S. Moulay, *J. Res. Updates Polym. Sci.*, 2015, **4**, 79–122.

15 S. Moulay, *Progress in Polymer Science*, 2010, **35**, 303–331.

16 R. K. Jha, B. J. Neyhouse, M. S. Young, D. E. Fagnani and A. J. McNeil, *Chem. Sci.*, 2024, **15**, 5802–5813.

17 Z. O. G. Schyns and M. P. Shaver, *Macromol. Rapid Commun.*, 2021, **42**, 2000415.

18 G. Martinez, N. Guarrotxena, J. M. Gomez-Elvira and J. Millan, *Polymer Bulletin*, 1992, **28**, 427–433.

19 T. Kameda, M. Ono, G. Grause, T. Mizoguchi and T. Yoshioka, *Polymer Degradation and Stability*, 2009, **94**, 107–112.

20 L. Shao, C. Qi and X.-M. Zhang, *RSC Adv.*, 2014, **4**, 53105–53108.

21 M. Bakherad, A. Keivanloo and S. Samangooei, *Chinese Journal of Catalysis*, 2014, **35**, 324–328.

22 J. Zhu, Y. Su, X. Zhao, Y. Li, J. Zhao, X. Fan and Z. Jiang, *Ind. Eng. Chem. Res.*, 2014, **53**, 14046–14055.

23 A. Siekierka, J. Wolska, W. Kujawski and M. Bryjak, *Separation Science and Technology*, 2018, **53**, 1191–1197.

24 S. Rabie, D. Ali, N. Khaireldin, M. El-Hashash, M. Elsaidi, A. El-Sayed and N. Wahed, *Egypt. J. Chem.*, 2020, **63**, 4833–4849.

25 E. J. Park, B. C. Park, Y. J. Kim, A. Canlier and T. S. Hwang, *Macromol. Res.*, 2018, **26**, 913–923.

26 N. G. Bush, M. K. Assefa, S. Bac, S. Mallikarjun Sharada and M. E. Fieser, *Mater. Horiz.*, 2023, **10**, 2047–2052.

27 L. Lu, S. Kumagai, T. Kameda, L. Luo and T. Yoshioka, *RSC Adv.*, 2019, **9**, 28870–28875.

28 G. Sneddon, J. C. McGlynn, M. S. Neumann, H. M. Aydin, H. H. P. Yiu and A. Y. Ganin, *J. Mater. Chem. A*, 2017, **5**, 11864–11872.

29 J. Delcorps, K. S. Rawat, M. Wells, E. Ben Ayed, B. Grignard, C. Detrembleur, B. Blankert, P. Gerbaux, V. Van Speybroeck and O. Coulembier, *Cell Reports Physical Science*, 2024, **5**, 102057.

30 K. C. Aune and C. Tanford, *Biochemistry*, 1969, **8**, 4579–4585.

31 L. M. Mayr and F. X. Schmid, *Biochemistry*, 1993, **32**, 7994–7998.

32 D. J. Heldebrant, C. R. Yonker, P. G. Jessop and L. Phan, *Energy Procedia*, 2009, **1**, 1187–1195.

33 D. J. Heldebrant, C. R. Yonker, P. G. Jessop and L. Phan, *Energy Environ. Sci.*, 2008, **1**, 487–493.

34 D. J. Heldebrant, P. K. Koech, M. T. C. Ang, C. Liang, J. E. Rainbolt, C. R. Yonker and P. G. Jessop, *Green Chem.*, 2010, **12**, 713–721.

35 L. Phan, D. Chiu, D. J. Heldebrant, H. Huttenhower, E. John, X. Li, P. Pollet, R. Wang, C. A. Eckert, C. L. Liotta and P. G. Jessop, *Ind. Eng. Chem. Res.*, 2008, **47**, 539–545.

36 M. Verdecchia, M. Feroci, L. Palombi and L. Rossi, *J. Org. Chem.*, 2002, **67**, 8287–8289.

37 Á. Mesías-Salazar, R. S. Rojas, F. Carrillo-Hermosilla, J. Martínez, A. Antiñolo, O. S. Trofymchuk, F. M. Nachtigall, L. S. Santos and C. G. Daniliuc, *New J. Chem.*, 2024, **48**, 105–111.

38 S. G. Khokarale and J.-P. Mikkola, *RSC Adv.*, 2019, **9**, 34023–34031.

39 E. Fritz-Langhals, *Org. Process Res. Dev.*, 2022, **26**, 3015–3023.

40 Heat distortion temperature, https://pvc.org/about-pvc/pvcs-physical-properties/heat-distortion-temperature/, (accessed 9 August 2024).

41 J. Yu, L. Sun, C. Ma, Y. Qiao and H. Yao, *Waste Management*, 2016, **48**, 300–314.

42 T. Moreno, P. Dyer and S. Tallon, *Ind. Eng. Chem. Res.*, 2020, **59**, 20307–20315.

43 G. Grause, A. Buekens, Y. Sakata, A. Okuwaki and T. Yoshioka, *J. Mater. Cycles Waste Manag.*, 2011, **13**, 265–282.

44 Z. Hou and R. M. Broughton, *Journal of Coated Fabrics*, 1998, **28**, 37–55.

45 S. Adanur, Z. Hou and R. M. Broughton, *Journal of Coated Fabrics*, 1998, **28**, 145–168.

46 G. Grause, S. Hirahashi, H. Toyoda, T. Kameda and T. Yoshioka, *J. Mater. Cycles Waste Manag.*, 2017, **19**, 612–622.

47 A. J. De Vries, C. Bonnebat and M. Carrega, *Pure and Applied Chemistry*, 1971, **26**, 209–240.

48 A. Wirsén and P. Flodin, *J. of Applied Polymer Sci.*, 1978, **22**, 3039–3056.

49 S. Y. Lee, J. M. Murphy, A. Ukai and G. C. Fu, *J. Am. Chem. Soc.*, 2012, **134**, 15149–15153.

50 N. Choudhury, A. Kim, M. Kim and B.-S. Kim, *Advanced Materials*, 2023, **35**, 2304113.

51 A. Salazar Avalos, M. Hakkarainen and K. Odelius, *Polymers*, 2017, **9**, 84.

52 P. Jia, M. Zhang, L. Hu, R. Wang, C. Sun and Y. Zhou, *Polymers*, 2017, **9**, 621.

53 E. Carrascosa, J. Meyer, J. Zhang, M. Stei, T. Michaelsen, W. L. Hase, L. Yang and R. Wester, *Nat Commun*, 2017, **8**, 25.

CHAPTER 4

Boosting PVC Reactivity through Iodination for CO_2-Derived Functionalisation



Delcorps J., Ben Ayed E., Coulembier O., RSC Advances, 2026, 16, 14, 12798-12805.
https://doi.org/10.1039/D6RA00749J

TABLE OF CONTENTS

I. INTRODUCTION 166

II. RESULTS AND DISCUSSION 168

A. PVC iodination 168

B. CO_2BAM selection and reaction with iodinated PVC 172

III. CONCLUSION 176

IV. EXPERIMENTAL 177

A. Materials 177

B. Procedures 177

C. Methods 178

V. SUPPORTING INFORMATION 180

VI. REFERENCES 188

I. INTRODUCTION

Among the many challenges facing sustainable materials science, the simultaneous management of carbon dioxide (CO_2) and halogenated plastics stands out as both urgent and conceptually rich. Poly(vinyl chloride) (PVC), the third most produced polymer worldwide, combines large-scale utility with a notorious resistance to circularity.[1–5] Its chlorine content hinders conventional recycling, while its incineration generates corrosive and toxic emissions.[6] In parallel, the chemical community continues to seek viable strategies for CO_2 utilisation, not merely for capture, but for its integration into value-added materials.[7–13] Bringing these two issues together, the chemical modification of PVC through CO_2-based chemistry represents a promising step toward genuine carbon circularity.

In Chapter 3, we explored this concept using CO_2-binding alcohols (CO_2BALs), a subclass of CO_2-binding organic liquids (CO_2BOLs).[14] These dual-function reagents acted both as CO_2 carriers and as nucleophiles capable of reacting with PVC through substitution, enabling the partial incorporation of carbonate functionalities into the polymer backbone.[15] The CO_2BAL was generated from 1-decanol and 1,5,7-triazabicyclo[4.4.0]dec-5-ene (TBD) by bubbling CO_2 at 0.2 bar and 90 °C, reaching a conversion of approximately 80%. While this approach demonstrated the feasibility of CO_2-mediated PVC functionalisation, the overall degree of incorporation remained limited to a 7 wt% mass substitution corresponding to only *ca*. 2.5 mol % of the methine sites along the chain, after 2 hours of reaction. In terms of CO_2 loading, this corresponds to a maximum of 17.6 g per kg of PVC (**Figure 4.1a**).

Reasoning that a greener and more efficient CO_2-mediated functionalisation of PVC would benefit from the use of safer and renewable reagents while improving reaction selectivity, we turned our attention to amine-based CO_2-binding agents (CO_2BAMs). In contrast to the carbonate linkages formed with CO_2BALs, the carbamate bonds formed by CO_2BAMs are thermodynamically more stable due to resonance delocalisation between the nitrogen lone pair and the carbonyl group. This higher stability is expected to improve the durability of the grafted structure,[16,17] its compatibility with further transformations, and ultimately the sustainability of an expected upcycling process.

In this framework, primary amines were identified as the most suitable nucleophilic partners for CO_2 activation.[18] Among them, 1-hexylamine was selected for its favourable green chemistry profile and potential renewability. Linear aliphatic amines such as 1-hexylamine can be synthesised from biomass-derived alcohols via catalytic “hydrogen-borrowing” amination.[19] This transformation is fully atom-economic, producing only water as a by-product and aligning with principles of green chemistry. In parallel, we sought to replace the costly and moisture-sensitive TBD guanidine used in CO_2BAL synthesis with a more affordable and robust organic base. 1,8-Diazabicyclo[5.4.0]undec-7-ene (DBU) was selected for its economic advantage (100 mL costs approximately €109, whereas 5 g of TBD amounts to €55.4) as well as for its distinct mechanistic benefits.[20,21] As reported by McGhee *et al.*,[22] DBU efficiently promotes carbamate anion

formation and enhances S_N2 selectivity in urethane-type bond formation under mild CO_2 pressure, a feature recently exploited in continuous flow conditions by Stagel *et al*.[23]

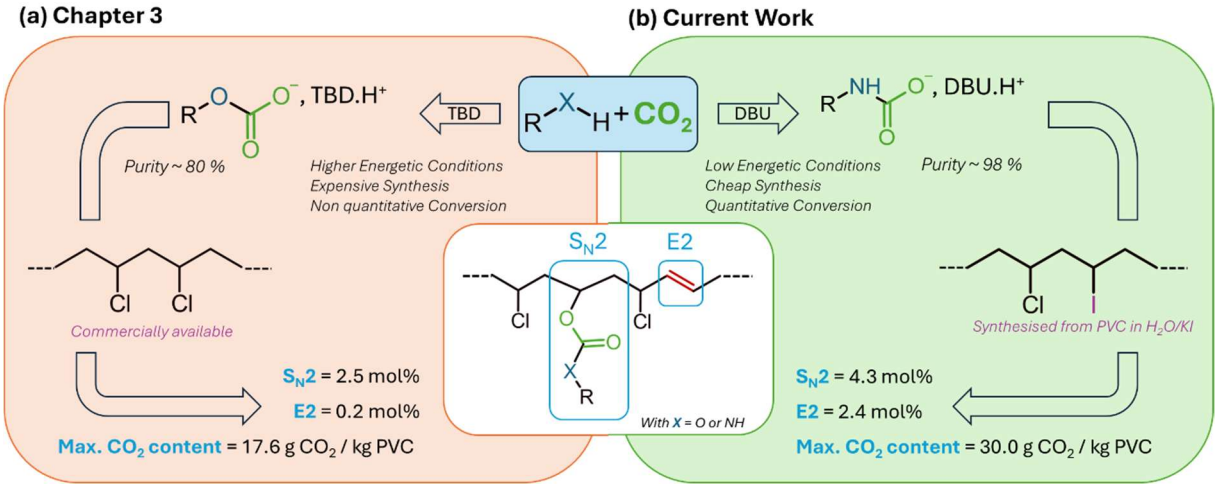


Figure 4.1. (a) Previously reported reactivity of CO_2BALs in S_N2 with pristine PVC. See Chapter 3 / reference 14; **(b)** This work: enhancement of substitution rate via PVC iodination and the use of CO_2BAMs. With TBD = 1,5,7-triazabicyclo[4.4.0]dec-5-ene, DBU = 1,8-diazabicyclo[5.4.0]undec-7-ene, S_N2 = second-order nucleophilic substitution and E2 = second-order elimination.

To further enhance substitution kinetics while addressing one of the major safety and sustainability issues of PVC recycling, *i.e.* the release of corrosive hydrogen chloride, we reasoned that a partial iodination of PVC prior to CO_2BAM treatment could mitigate acid-gas formation. Although hydrogen iodide is a stronger acid than hydrogen chloride, its vapours are less corrosive toward metallic equipment and form less volatile metal halides.[24–26] In addition, iodinated PVC displays higher S_N2 reactivity, facilitating more efficient CO_2 incorporation under mild conditions.

Overall, as presented herein, this dual approach, combining CO_2BAMs with a greener preparation of iodinated PVC (**Figure 4.1b**), provides a safer and more sustainable pathway for covalent CO_2 upcycling into polymeric materials. Under conditions directly comparable to those previously employed for CO_2BAL-mediated functionalisation, this strategy increases the efficiency of S_N2 substitution by roughly twofold (4.3 mol % substitution rate and max. CO_2 content ~ 30.0 g per kg of polymer), yielding a polymer that remains fully soluble in organic media despite the formation of some vinyl groups via E2 elimination. Together, these features highlight a clear improvement in both the efficiency and versatility of CO_2 incorporation into PVC (**Table 4.1**).

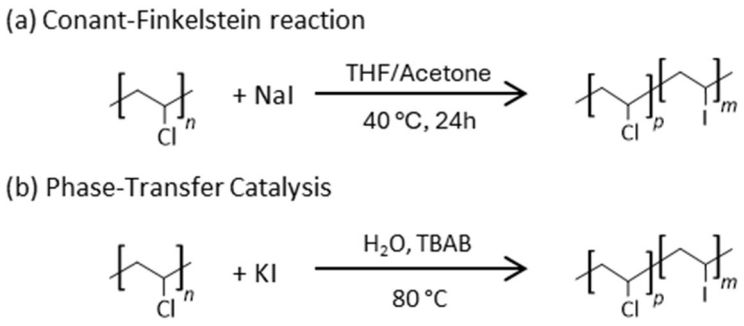
Table 4.1. Comparative overview of the CO_2BAL and CO_2BAM strategies under identical reaction conditions ($[PVC]_0 = [PVC\text{-}I]_0 = 0.7$ mmol.L^{-1}, $[Cl]_0/[CO_2BAM \text{ or } CO_2BAL]_0 = 1$, 21 °C, 2 h, DMF).

Parameter	**CO_2BAL Strategy** Chapter 3	**CO_2BAM Strategy** This work
Polymer support	PVC	Partially iodinated PVC
CO_2 carrier activation	1-decanol + TBD	1-hexylamine + DBU
Purity of activated species	~ 80% (20 mol% free base)	~ 98%
Nucleophile	Carbonate	Carbamate
Bond formed	Carbonate linkage	Carbamate linkage
S_N2/E2 behaviour	Limited substitution	Enhanced S_N2 selectivity
Degree of substitution	~ 2.5 mol%	~ 4.3 mol%
Max CO_2 content	~ 17.6 g/kg	~ 30.0 g/kg
Solubility	Soluble	Fully soluble
Base	TBD (moisture sensitive, costly)	DBU (robust, affordable)

II. RESULTS AND DISCUSSION

A. PVC iodination

In the literature, the iodination of PVC is most frequently carried out through the Conant-Finkelstein reaction using NaI in THF/acetone (**Scheme 4.1a**).[27–29] However, this protocol relies on a problematic solvent system[30] and does not consistently deliver high iodination efficiency. Although bio-based THF has been reported,[31–33] replacing this mixture with safer and more sustainable media remains an important objective. An alternative route proposed by Lakshmi and Jayakrishnan uses water as the solvent under phase-transfer catalysis (PTC, **Scheme 4.1b**),[34] offering a greener and underexplored approach.



Scheme 4.1. PVC iodination via **(a)** the Conant-Finkelstein reaction and **(b)** phase-transfer catalysis. TBAB = tetrabutylammonium bromide.

To establish a clear baseline for comparison, the conventional Conant-Finkelstein reaction was first reproduced on a smaller scale following the protocol of Rusen *et al.*[29] This benchmark experiment not only provided direct insight into the substitution pattern and material response under classical conditions but also served as a reference for assessing the efficiency, selectivity,

and environmental performance of the PTC-based alternative developed herein. After 24 hours at 40 °C, the polymer exhibited a faint yellow colouration, consistent with partial chlorine-to-iodine substitution (**Figure 4.3**). Size exclusion chromatography (SEC) revealed a moderate increase in number-average molar mass (M_n), while thermogravimetric analysis (TGA) showed a 32 °C decrease of the maximal degradation temperature (MDT), both supporting a PVC backbone substitution (**Figures 4.2**). However, conventional spectroscopic techniques such as ^{1}H and ^{13}C NMR or FT-IR failed to provide unambiguous structural evidence, as the spectral features of PVC remain largely unaffected (**Figure S4.2**, **p. 180**).

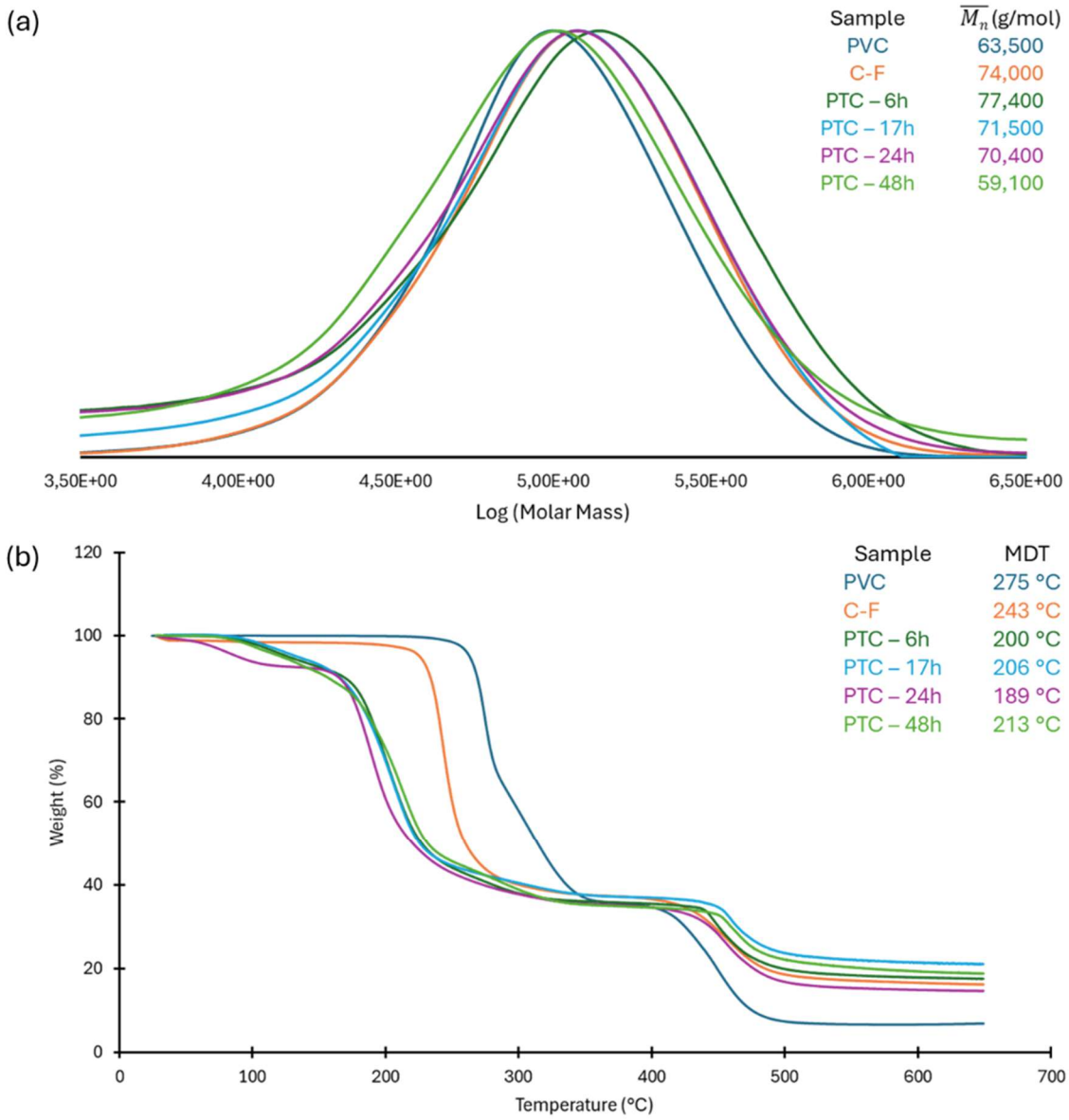


Figure 4.2. (a) SEC chromatograms and **(b)** TGA thermograms of PVC and modified PVC samples iodinated via the Conant-Finkelstein reaction (C-F) or phase transfer catalysis (PTC) for 6, 17, 24, or 48 hours.

To obtain quantitative insight, X-ray photoelectron spectroscopy (XPS) was employed to determine the surface iodine content, within the 1-10 nm sampling depth (**Figures S4.3** and

S4.4, **p. 181**). Although this technique does not probe the bulk of the film (*ca.* 70 mm thick), it offers a reliable benchmark for comparing different iodination methods. The XPS spectrum indicated an iodine content of 0.10 at%, confirming a moderated successful chlorine substitution ≤ 3% (**Figure S4.4**, **p. 181** and **Table S4.1 - entry 2**, **p. 183**). A minor sodium signal was also detected, suggesting the presence of residual NaI despite purification. Consequently, this value likely represents a slight overestimation of the true iodine incorporation. Overall, this experiment establishes the Conant-Finkelstein reaction as an effective yet limited benchmark, providing a quantitative baseline for evaluating greener iodination strategies under comparable conditions.

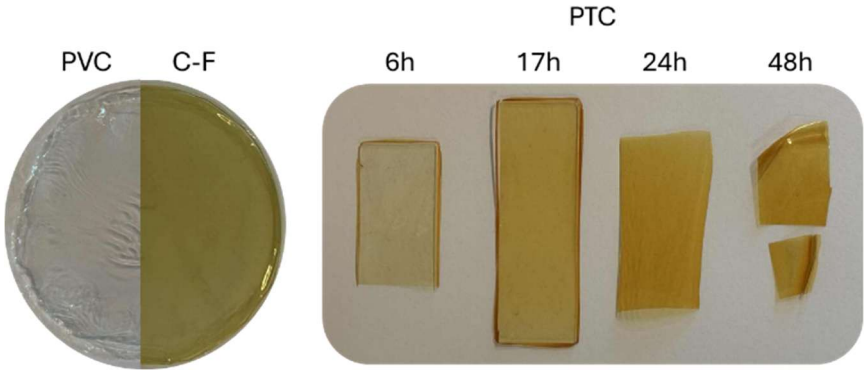


Figure 4.3. Colour evolution of PVC after 24 h via the Conant-Finkelstein (C-F) reaction, and after 0, 6, 17, 24, and 48 h of iodination via PTC.

Building on the promising report by Lakshmi and Jayakrishnan,[34] the phase-transfer-catalysed (PTC) iodination of PVC was then reinvestigated. The optimised conditions reported in their original study were maintained, while reaction times were increased to enhance substitution efficiency. Reactions were thus conducted with tetrabutylammonium bromide (TBAB) used as transfer agent at 80 °C for durations of 6, 17, 24, and 48 h ($[KI]_0$ = 6M, $[KI]_0/[TBAB]_0$ = 40). After completion, the samples were thoroughly washed, dried, and solvent-casted into thin films suitable for subsequent analysis. A simple visual inspection immediately reflected the progress of iodination; while pristine PVC films remained transparent, the treated samples displayed a distinct yellow colouration that deepened with increasing reaction time (**Figure 4.3**). Importantly, all materials remained soluble in conventional PVC solvents (THF and DMF), and none exhibited the darkening typical of extensive dehydrohalogenation. ^{1}H NMR and FT-IR analyses further confirmed that elimination reactions were minimal, with the fraction of unsaturated sites remaining below 1 mol% even after 48 h (**Figures S4.1** and **S4.2**, **p. 180**). This negligible degradation attests to the mildness and selectivity of the PTC approach, which proceeds efficiently under aqueous conditions without compromising polymer integrity. With the exception of the 6 h sample, all PTC-treated films exhibited a deeper yellow hue than the Conant-Finkelstein analogue, suggesting higher iodination levels. This trend was confirmed by TGA, which revealed a more pronounced MDT decrease upon increasing reaction time (**Figure 4.2b**). The relatively modest MDTs variation in TGA thermograms among the PTC samples aligns

with earlier observations by Lakshmi *et al.*, who reported that substitution efficiency plateaued after prolonged exposure.[34]

SEC data showed an initial increase in M_n during the first 6 hours of reaction, followed by a gradual decrease at longer times (**Figure 4.2a**). Since SEC determines apparent molar masses based on hydrodynamic volume rather than absolute molecular weight, these variations reflect conformational changes in solution rather than backbone scission. Attractive intramolecular interactions are known to reduce the hydrodynamic radius of polymer chains in solution, leading to lower apparent molar masses when calibrated against polystyrene standards.[35] Given the negligible extent of elimination, the progressive decrease in M_n at longer reaction times is therefore attributed to a reduction in hydrodynamic volume as the polymer backbone becomes increasingly iodinated. As the most polarisable and least electronegative halogen, iodine exhibits the strongest σ-hole donor character and forms particularly robust halogen bonds.[36] Increasing iodine content thus enhances the likelihood of intra- and intermolecular halogen-bonding interactions, which promote chain compaction in solution and consequently lower the apparent M_n.

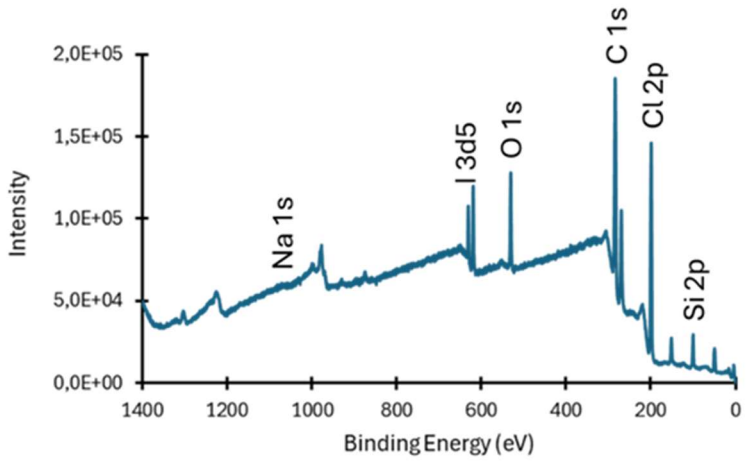


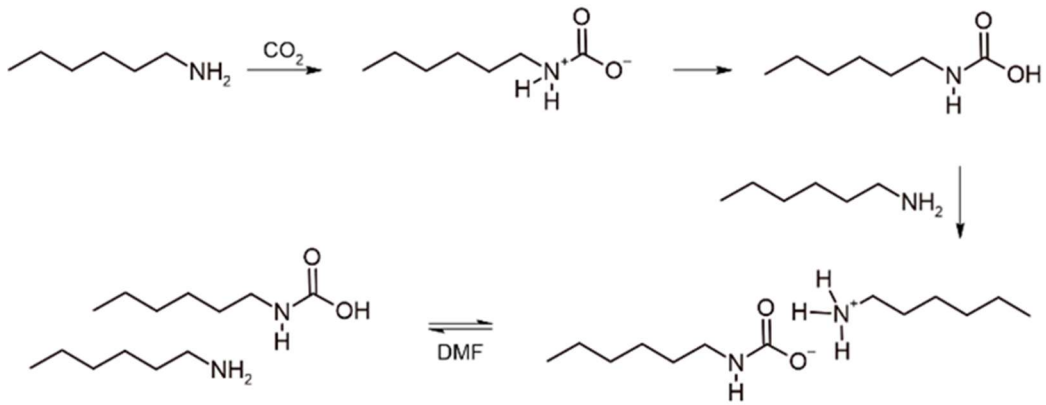
Figure 4.4. XPS spectrum of PVC iodinated via phase transfer catalysis (PTC) for 48 hours.

XPS measurements substantiated these findings, revealing a steady increase in iodine surface content up to 0.84 at% after 48 h, suggesting a chlorine substitution ≤ 24.5% (**Figure 4.4, Figures S4.3-S4.7**, **p. 181 – 182**, and **Table S4.1 - entries 3-6**, **p. 183**). In parallel, water static contact-angle measurements showed no statistically significant change between pristine PVC (85.6 ± 1.7°) and PTC-iodinated films (83.4 ± 4.3°, after 48 h), indicating that the surface wettability remains essentially unchanged despite iodine incorporation. Conversely and in accord with the XPS measurements, DSC analysis showed a pronounced decrease in the glass-transition temperature, T_g (from 86 °C for pristine PVC to 50 °C after 48 h of iodination), reflecting local structural relaxation induced by the introduction of bulky iodinated groups (**Figure S4.8**, **p. 169** and **Table S4.1**, **p. 183**). Residual TBAB still detected by ^{1}H NMR after purification was found to be negligible and therefore cannot account for the observed decrease in T_g. Instead, this reduction is attributed to a self-plasticisation effect arising from the incorporation of iodinated substituents, consistent with previous reports on bulky-substituted PVC derivatives.[37,38]

Taken together, the absence of a resolvable CH-I resonance in the ^{1}H spectra, despite the substantial iodine content indicated by XPS, likely reflects the convergence of several compounding factors rather than a single cause. First, for methine (CHX) environments structurally analogous to the PVC backbone, a heavy-atom spin-orbit coupling contribution to proton shielding is known to enhance deshielding of CH-I relative to CH-Cl,[39] but only modestly (~0.3-0.4 ppm),[40] placing the expected signal within the broad and already complex methine envelope of PVC. Second, XPS probes only the outermost 1-10 nm of the film, whereas NMR reports on the bulk. The iodine content averaged over the full sample volume could therefore be substantially lower than the surface-derived value reported. Finally, the halogen-bonding-driven chain compaction already inferred from the SEC data[36] would be expected to locally restrict the mobility of iodinated methine sites engaged in such intra- or intermolecular interactions, broadening the corresponding CH-I resonance and further reducing its already low signal-to-noise ratio. Together, these effects make the CH-I signal difficult to resolve - overlapping in position with the existing CH-Cl envelope, and further attenuated in intensity by the low bulk iodine content and by broadening from restricted local mobility - rather than genuinely absent.

B. CO_2BAM selection and reaction with iodinated PVC

Primary and secondary alkylamines react readily with CO_2 at ambient pressure and temperature, forming carbamate or carbamic acid adducts,[18] depending on the nature of the medium. Early reports also highlighted that the addition of organic superbases, such as amidines or guanidines, is critical for stabilising certain amine carboxylations, enhancing both yield and nucleophilicity.[18,41,42] Guided by this principle, three CO_2-binding amines (CO_2BAMs) were prepared from the representative primary amine, 1-hexylamine, for comparative evaluation. When CO_2 was bubbled into the pristine liquid alkylamine, ^{1}H NMR analysis of the medium indicated that approximately 43 % of the amine reacted (**Figure S4.9**, **p. 183**). In this polar protic medium, and mirroring reactions performed in water,[43] the reaction proceeds via formation of the carbamic acid, which is immediately deprotonated by another molecule of free amine (**Scheme 4.2**). By adding one equivalent of strong base such as 1,8-diazabicyclo[5.4.0]undec-7-ene (DBU) or 1,5,7-triazabicyclo[4.4.0]dec-5-ene (TBD), only the 1-hexylamine acts as a Lewis base while the superbase acts as Brønsted base pushing conversions in carbamate salts to 95 and 90%, respectively (**Figures S4.10 & S4.11**, **p. 184**).



Scheme 4.2. Preparation of a CO_2BAM of 1-hexylamine through CO_2 activation. In DMF, the carbamate form should be in equilibrium with its carbamic acid homologue.

Performing nucleophilic substitution directly in the bulk iodinated PVC represents the greenest approach to avoid the use of solvents entirely. Pristine PVC softens around 92 °C,[44] whereas iodination lowers its T_g to 50-55 °C, suggesting a softening temperature near 60 °C. The three CO_2BAMs were thus subjected to a TGA analysis to estimate their degradation onset temperatures (T5%, **Figure S4.13**, **p.186**). Even the most thermally robust DBU-based CO_2BAM (T5% = 65 °C) leaves only a narrow margin, precluding safe bulk processing, making the solvent-free strategy impractical, and the choice of a solvent necessary.

DMF was selected to ensure solubility of both iodinated PVC and carbamate salts. Although DMF is not ideal from a toxicity standpoint, the reaction conditions (see Experimental Section) produce only aqueous DMF effluents, which can be efficiently recovered via membrane-based techniques (pervaporation, nanofiltration), avoiding high-energy distillation or incineration.[45] The use of DMF also informs the choice of CO_2BAM for S_N2 functionalisation of iodinated PVC. Under a saturated CO_2 atmosphere, the carbamate form of CO_2BAM obtained without an organic strong base exists in equilibrium with its carbamic acid form (**Scheme 4.2**),[18] precluding its use as a nucleophile and making it ineffective for S_N2 substitution of the iodinated PVC. For CO_2BAMs prepared with DBU or TBD, we previously showed that residual free base in CO_2-binding alcohols (CO_2BALs) promotes dehydrochlorination, forming carbon-carbon double bonds and provoking precipitation of the modified PVC. Among the CO_2BAMs tested here, DBU provides the highest conversion in carbamate form (95 %), whereas TBD reaches only 90 % conversion. Considering its lower basicity ($pKa_{DBU.H+}$= 24.3 *vs* $pKa_{TBD.H+}$= 26.0 in ACN), as well as the greater accessibility and lower cost of DBU, the DBU-based CO_2BAM was selected as the optimal reagent for nucleophilic substitution on iodinated PVC. This choice is further supported by the excellent stability of the DBU-based CO_2BAM in DMF over time (**Figure S4.12**, **p. 185**). Under identical experimental conditions as those used for the subsequent reaction with iodinated PVC ($[CO_2BAM]_0$ = 0.5 M, 21 °C, CO_2-saturated atmosphere), the carbamate salt indeed remained fully stable for at least 24 h, with very little to no sign of CO_2 release.

Considering the limitations of our analytical methods, it was not possible to reliably determine the iodine content of PVC-I. TGA of the iodinated material after 48 h shows an initial mass-loss event of 11-12 wt% between 90 and 140 °C, followed by a broader 53-54 wt% degradation from 140 to 400 °C (**Figure 4.2b**). For comparison, unmodified PVC typically exhibits a two-step thermal decomposition, with a major initial mass loss of ~63 wt% and a plateau associated with char formation.[46] This first step is often attributed to HCl elimination, but the overall mechanism is highly complex, defect-dependent, and involves overlapping processes such as dehydrohalogenation and backbone scission.[47] In PVC-I, the splitting of the initial mass loss into two distinct events likely reflects the same intrinsic complexity, and the early 12 wt% loss cannot be unambiguously assigned to iodine elimination alone. Notably, this initial mass loss is substantially higher than the iodine surface content inferred from XPS (0.84 at%), further emphasising the fundamentally different information depth of both techniques and precluding any direct quantitative comparison. Consequently, neither TGA, XPS nor NMR spectroscopy provides a reliable estimate of the degree of iodination. As a result, the absolute molar mass of PVC-I remains inaccessible, preventing accurate determination of a defined $[halogen]_0/[CO_2BAM]_0$ ratio.

To allow a meaningful comparison with the reactivity of pristine PVC toward CO_2BALs reported in our previous study,[15] we therefore elected to use the absolute number-average molar mass of unmodified PVC (M_nSEC = 41 400 g.mol^{-1}, $Đ_M = M_w/M_n$ = 2.2), determined in THF at 25 °C using PS calibration and Mark-Houwink corrections, as the reference value to compute the amount of CO_2BAM. The reaction in DMF at 21 °C with the DBU-based CO_2BAM derived from 1-hexylamine was thus conducted using this M_nSEC to impose an initial $[halogen]_0/[CO_2BAM]_0$ molar ratio of 1, enabling direct comparison with the corresponding S_N2 reactivity observed in the CO_2BAL series. In our previous study, we demonstrated that the degree of carbonatation reached 2.5 mol% after 2 hours at 21 °C.[15] As a proof-of-concept of our new strategy, the reaction between PVC-I and the DBU-based CO_2BAM was then reiterated in DMF for 2 hours only ($[PVC\text{-}I]_0$ = 0.7 mmol.L^{-1}). The reaction medium was subsequently precipitated in cold water, washed, and dried to ensure complete removal of CO_2BAM derivatives. The structural changes induced by the reaction between PVC-I and the DBU-based CO_2BAM were first evaluated by FTIR spectroscopy (**Figure S4.14**, **p. 186**). The appearance of a weak band at 1724 cm^{-1} is consistent with the presence of carbonyl groups, in line with the partial formation of carbamate-type motifs upon nucleophilic substitution. Concomitantly, a distinct absorption at 1643 cm^{-1} clearly evidences the formation of C=C double bonds, confirming that elimination processes also occur under these conditions. Additional features, namely the irregular envelope between 2000 - 2400 cm^{-1} and the broad, intense band between 3100 - 3600 cm^{-1}, are characteristic of overlapping O-H, N-H and weak overtone/combination contributions.

More detailed insight was obtained from the ^{13}C NMR spectrum of the modified polymer (**Figure 4.5**). While the characteristic triplet-type CH–X pattern of PVC (δ = 56.87, 57.76 and 58.75 ppm, with X = Cl or I) is preserved, three new resonances emerge at δ = 57.08, 58.03 and 59.05 ppm.

Their chemical-shift proximity and analogous triplet-like distribution strongly suggest that the modification remains localised at the CH–X carbons of the polymer backbone. The slight downfield displacement of these new signals (~ 0.2-0.3 ppm) is consistent with partial nucleophilic substitution by CO_2BAM-derived species or by hexylamine liberated *in situ*, although the relative contributions of carbamate retention and CO_2 loss cannot be unambiguously established at this stage. Nevertheless, the appearance of these carbon resonances provides direct spectroscopic evidence for covalent grafting at the CH–X positions, supporting the occurrence of S_N2-type substitution in competition with elimination.

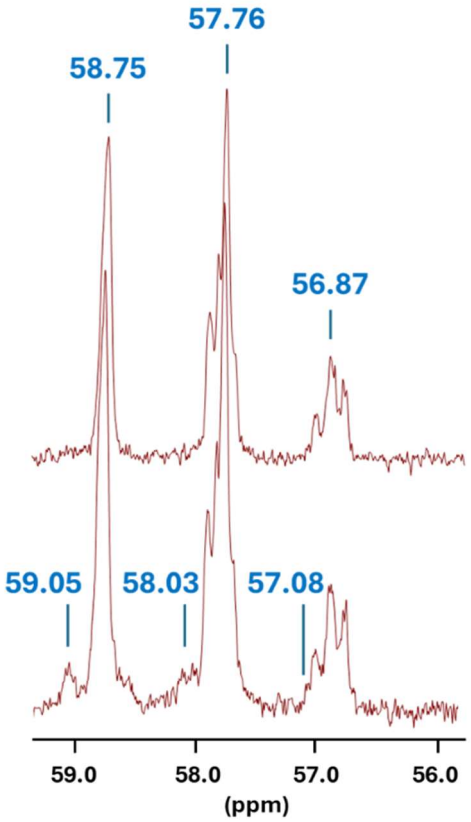


Figure 4.5. Enlarged ^{13}C NMR region (δ = 56.0-59.2 ppm). **Top:** PVC-I after 48 h iodination via PTC, showing the characteristic CH–X triplet. **Bottom:** same region after reaction with the DBU-based CO_2BAM of 1-hexylamine (2 h, 21 °C). Spectra recorded in THF-d_8 at 21 °C (126 MHz).

The ^1H NMR spectrum corroborates this mixed reactivity (**Figure S4.15**, **p. 187**). Integration of the vinylic protons (δ = 5.5-6.0 ppm) indicates 2.4 mol % of unsaturation, while signals attributable to the grafted hexyl group (δ = 0.7-1.5 ppm) correspond to 4.3 mol% of covalent incorporation. Taken together, these spectroscopic data depict a reaction manifold in which CO_2BAM-derived nucleophiles engage in efficient substitution at the CH–X centres of PVC-I while a concomitant fraction of sites undergo base-promoted elimination, ultimately yielding a functionalised material with dual substitution–elimination character. Importantly, despite the formation of unsaturations, the polymer remained fully soluble throughout the reaction, in contrast to our previous observations with TBD-derived CO_2BALs.[15] This preserved solubility strongly suggests that the substantially higher degree of substitution achieved under

CO_2BAM/DBU conditions effectively outcompetes the elimination-inducing pathways observed in our earlier study.

Although the ^{13}C signals of the carbamate carbonyl (theoretically close to δ = 155 ppm) and the olefinic carbons arising from dehydrohalogenation (theoretically close to δ = 125-135 ppm)[48] were not detected in the spectrum, this is consistent with the low abundance of both functional groups (4.3 and 2.4 mol% of the repeat units, respectively), which, combined with the intrinsically low sensitivity of ^{13}C NMR (1.1% natural abundance) for a polymer sample, places both signals close to the practical detection limit under the acquisition conditions used (ns = 4096, d1 = 2 s). This limitation is expected to be most severe for the carbamate function. Being quaternary and non-protonated, it lacks NOE enhancement under standard proton-decoupled acquisition and is expected to relax considerably more slowly than protonated backbone carbons, by analogy with quaternary carbons reported to exhibit substantially longer T1 relaxation times than their protonated counterparts in related carbamate-forming systems (T1 = 4-16 s, depending on structure).[49] Reliable detection of such slowly relaxing, low-abundance quaternary carbons typically requires recycle delays on the order of several tens of seconds (≥5×T1),[49] well beyond the d1 = 2 s used in the present acquisition (see Experimental section, **p. 178**), such that the carbonyl signal would be strongly attenuated relative to its real abundance. The olefinic carbons, while protonated and thus less impacted by this relaxation limitation, remain a comparably minor species (2.4 mol%) and may be further broadened by the heterogeneous local environments of isolated, non-conjugated double bonds, lowering their peak height below the baseline noise level of the acquired spectrum.

III. CONCLUSION

This chapter presented a sustainable, dual-strategy approach for covalent CO_2 incorporation into PVC. Aqueous PTC-mediated iodination enhances S_N2 reactivity, while DBU-based CO_2BAMs provide stable, efficient nucleophiles for functionalisation. This method increases substitution efficiency compared to CO_2BALs, preserves polymer solubility and highlights an efficient and greener pathway for PVC chemical modification.

Systematic investigations of CO_2BAMs bearing different alkyl substituents, as well as studies on reaction time and the resulting polymer properties, are still required to move this work beyond the proof-of-concept stage.

In parallel, our group sought to broaden the scope and extend this approach to other polymers. Namely, polyethylene (PE) and polypropylene (PP), the two most produced polymers globally, ahead of PVC. The following chapter addresses the first part of the strategy, i.e. the iodination of PE and PP.

IV. EXPERIMENTAL

A. Materials

Poly(vinyl chloride) (low molecular weight, $M_n th$ ~ 48 kg/mol, $M_n SEC$ ~ 41.4 kg/mol)[15], tetrabutylammonium bromide (TBAB), and N,N-dimethylformamide (anhydrous, 99.8%) were purchased from Sigma-Aldrich. Potassium iodide (KI), acetone p., and methanol p. were supplied by Chemlab. Sodium iodide (NaI) as well as deuterated tetrahydrofuran (99.5% D) were acquired from VWR. 1-Hexylamine (99%) and 1,8-diazabicyclo[5.4.0]undec-7-ene (98+%) were supplied by Thermo Scientific. Finally, carbon dioxide N50 (≥99.999%), 1,5,7-triazabicycl[4.4.0]dec-5-ene, and deuterated chloroform (99.8 %D + 0.03% TMS V/V, for NMR spectroscopy) were purchased from Air Liquide, Apollo Scientific, and Eurisotop, respectively.

B. Procedures

PVC iodination via phase transfer catalysis (PTC)

In a 100 ml single-neck round-bottom flask equipped with a stir bar were introduced 600 mg (1.25 x 10^{-5} mol) of PVC, 30g (0.18 mol) of KI, 1.441g (0.0045 mol) of TBAB, and 30 ml of demineralised water. The reaction medium was stirred at 80 °C for 6, 17, 24 or 48 hours. After the allotted reaction time, the reaction mixture was filtered onto a Büchner funnel and thoroughly washed with water. In order to eliminate as much unreacted TBAB and KI as possible, the sample was then solubilised in THF or MEK and reprecipitated in water.

PVC iodination via the Conant-Finkelstein reaction

In a 50 ml round-bottom flask equipped with a stir bar were introduced 1 g (2.1 x 10^{-5} mol) of PVC, 2.4 g (0.016 mol) of NaI, and 12 ml of a THF/acetone (1:2) mixture. The reaction mixture was then stirred under nitrogen at 40 °C for 24 hours. Once the 24 hours were up, the reaction medium was precipitated in a methanol/water (2:1) mixture. The precipitate was then dried overnight under vacuum at 40 °C.

CO_2BAM synthesis

A Schlenk tube, equipped with a septum and a stir bar, is charged with a mixture of hexylamine (0.010 mol) and a base (0.010 mol DBU, TBD, or hexylamine itself) in bulk. A butyl pipe is used to link the Schlenk tube to a Schlenk line. This Schlenk line is used to first put the reaction mixture under vacuum, then under a carbon dioxide atmosphere (pCO_2 = 0.2 bar). In the case of the DBU-based and amine only CO_2BAMs, the reaction starts at room temperature until the exothermicity subsides (about 15 to 20 minutes). The conversion is then maximised at 90 °C in an oil bath and under maximum stirring for 30 minutes. In the case of the TBD-based CO_2BAM, the reaction is performed directly at 90°C for 1 hour in order to solubilise the TBD in hexylamine.

Substitution reaction between iodinated PVC and CO_2BAM

Iodinated PVC sample (0.010 mol Cl, 0.6245 g PVC) was dissolved in DMF (20 ml). The CO_2BAM (0.010 mol) was then added to the solution. The reaction was performed at room temperature, under maximum stirring, and CO_2 atmosphere for 2 hours. After the reaction, the product is purified through a three-step process. First, water is used to precipitate and wash the product. Then, the precipitate is solubilised in THF. Finally, the solution from the previous step is precipitated and washed with methanol.

C. Methods

Thermogravimetric analysis (TGA)

The CO_2BAMs were subjected to thermogravimetric analysis to determine their degradation onset temperature. Measurements were performed under nitrogen flow at a rate of 5 °C per minute using a TA Q500 TGA. All PVC-based samples were subjected to TGA as well. Measurements were performed under nitrogen flow at a rate of 2.5 °C per minute using a TA Q500 TGA.

Fourier Transform InfraRed (FT-IR) spectroscopy

FT-IR spectroscopy was performed using a Bruker Tensor 27 spectrometer to give an indication regarding the success of the substitution reaction between PVC and CO_2BAM.

Nuclear Magnetic Resonance (NMR) spectroscopy

CO_2 conversion was followed time-to time through ^{1}H NMR using a Spinsolve 60 Ultrabenchtop NMR spectrometer (Magritek, Aachen, Germany). All spectra were acquired according to the following parameters: aq = 6.4 s, repetition time = 10 s, pulse angle = 90, ns = 32. Final CO_2BAM and substitution products were all characterised by ^{1}H NMR using a Bruker AVANCEII 500 MHz apparatus at room temperature in chloroform-*d1* ($CDCl_3$) and THF-*d8*, respectively. All spectra were acquired according to the following parameters: aq = 2.75 s, d1 = 1 s, sw = 20, ns = 32 for small molecules and 512 for PVC-based compounds. ^{13}C NMR spectra were also acquired using a Bruker AVANCEII 500 MHz apparatus at room temperature in THF-*d8* according to the following parameters: aq = 1.1 s, d1 = 2 s, sw = 240, ns = 4096.

Size Exclusion Chromatography (SEC)

All PVC-based samples were subjected to SEC in THF at 25 °C using a Triple Detection Polymer Laboratories liquid chromatograph equipped with a refractive index (ERMA 7517), a UV detector (254 nm), a capillary viscometer, a light scattering RALS (Viscotek T-60) (Polymer Laboratories GPC-RI/CV/RALS), an automatic injector (Polymer Laboratories GPC-RI/UV), and four columns: a PL gel 10 µm guard column and three PL gel Mixed-B 10 µm columns (linear columns for separation of M_w PS ranging from 500 to 10^6 daltons). All samples for SEC analyses were prepared according to the following concentration: 1 mg of polymer sample in 1 mL of THF.

Differential Scanning Calorimetry (DSC)

DSC analysis was conducted using a DSC Q2000 from TA instruments under inert atmosphere (N_2/ 50 ml/min). Samples of 3-4 mg were sealed in aluminium DSC pans, placed in the DSC cell and heated from -20 to 80 or 100 °C with a heating rate of 10 °C.min^{-1}. The glass transition temperature (T_g) was measured on the second heating scan.

X-ray Photoelectron Spectroscopy (XPS)

The sample composition was evaluated using XPS with a VERSAPROBE PHI 5000 instrument from Physical Electronics. The instrument was equipped with a monochromatic Al Kα X-ray source. X-ray photoelectron spectra were collected at a take-off angle of 45°, and the electron energy analyser was operated in the CAE (constant analyser energy) mode. To compensate for the built-up charge on the sample surface during measurements, a dual beam charge neutralisation system consisting of an electron gun (approximately 1 eV) and an Ar ion gun (less than or equal to 10 eV) was employed. The binding energies were referenced to the C1s peak at 284.6 eV. Atomic concentration percentages were determined using CasaXPS software based on the XPS data.

Contact Angle

To perform contact angle measurements, films were made out of each sample by solvent casting. These films were casted directly onto microscope slides for easier handling. These measurements were performed using a Krüss Drop Shape Analysis System DSA 10 Mk2. 20 µl droplets of demineralised water were deposited in various places on the polymer film and contact angles were measured using the Drop Shape Analysis software.

V. SUPPORTING INFORMATION

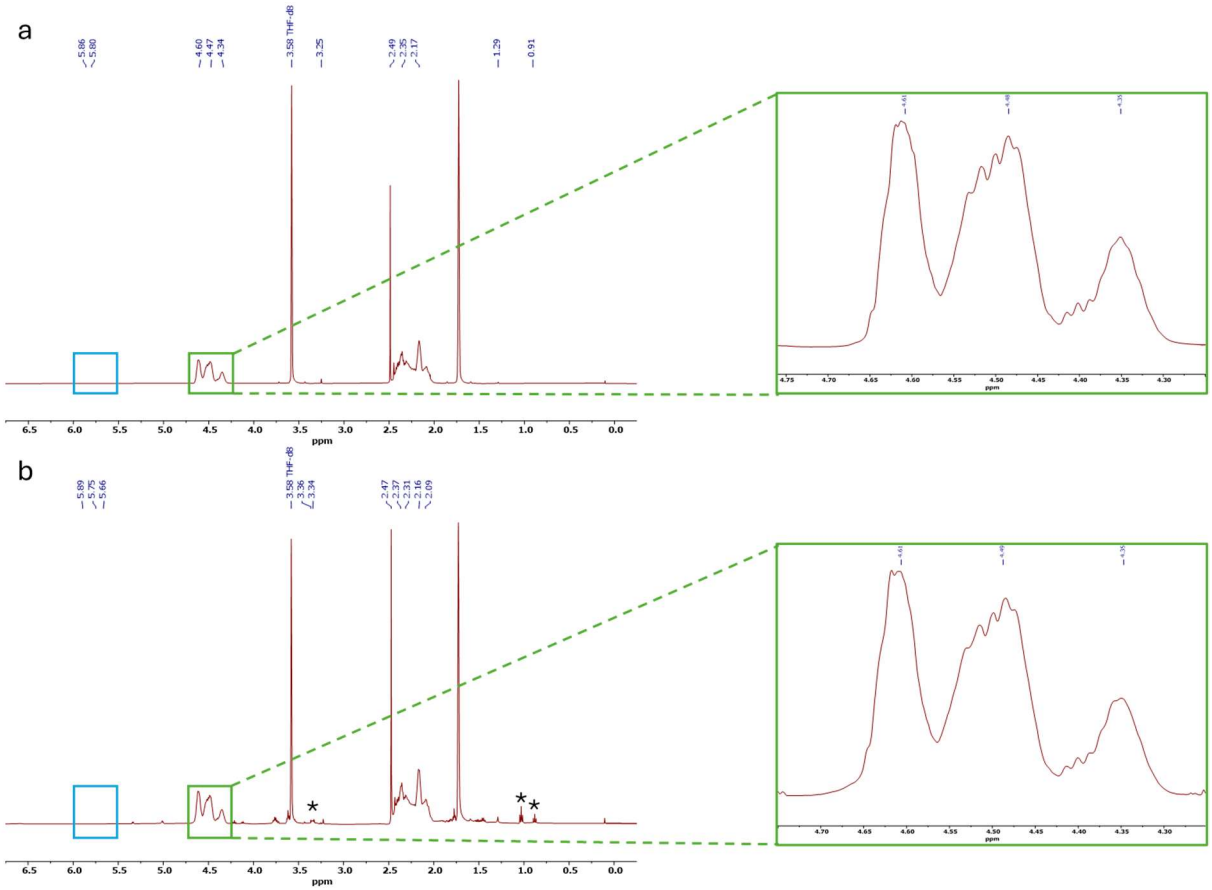


Figure S4.1. ^{1}H NMR spectra of **a)** PVC and **b)** PVC iodinated via phase-transfer catalysis for 24h. The remaining TBAB in b) is designated by asterisks (*).

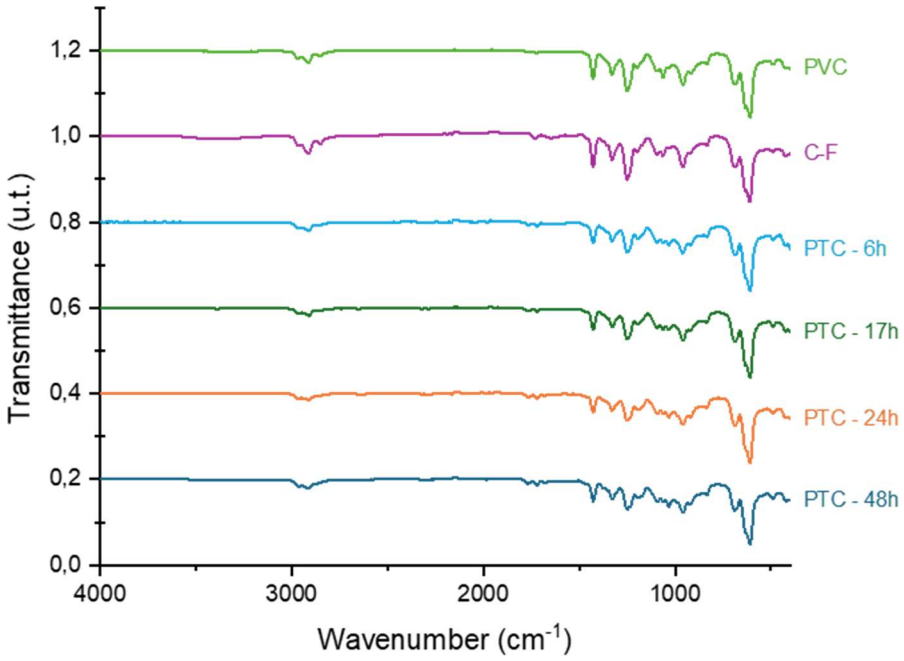


Figure S4.2. FT-IR of PVC and modified PVC samples iodinated via the Conant-Finkelstein reaction (C-F) or phase transfer catalysis (PTC) for 6, 17, 24, or 48 hours.

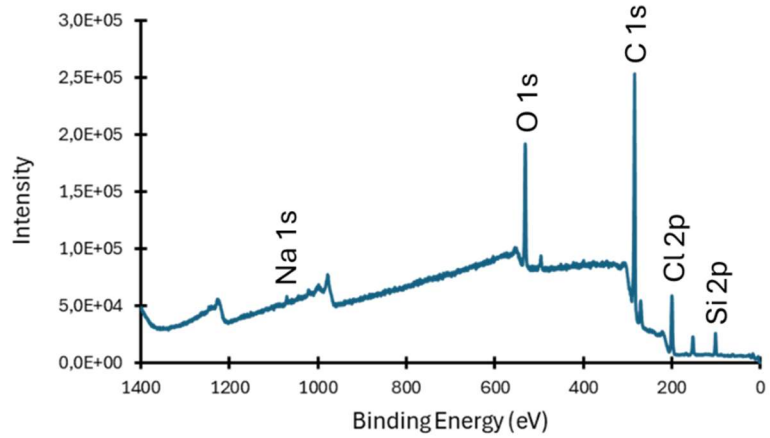


Figure S4.3. XPS spectrum of PVC.

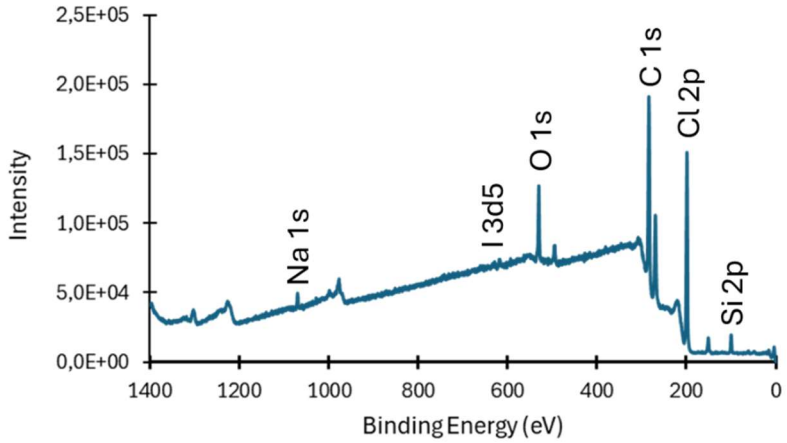


Figure S4.4. XPS spectrum of PVC iodinated via the Conant-Finkelstein reaction.

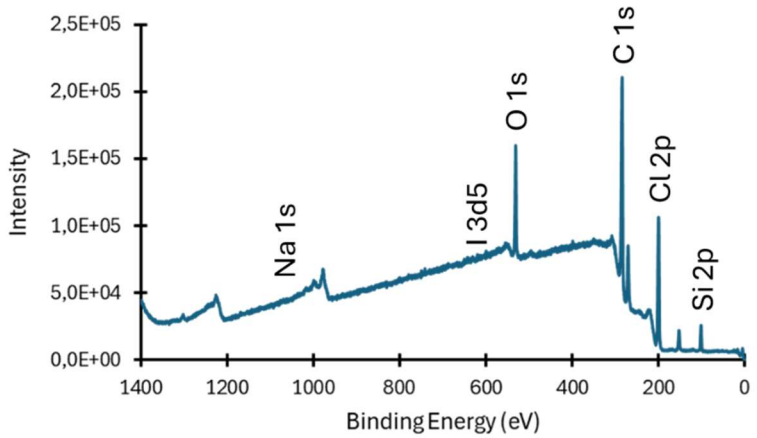


Figure S4.5. XPS spectrum of PVC iodinated via phase transfer catalysis for 6 hours.

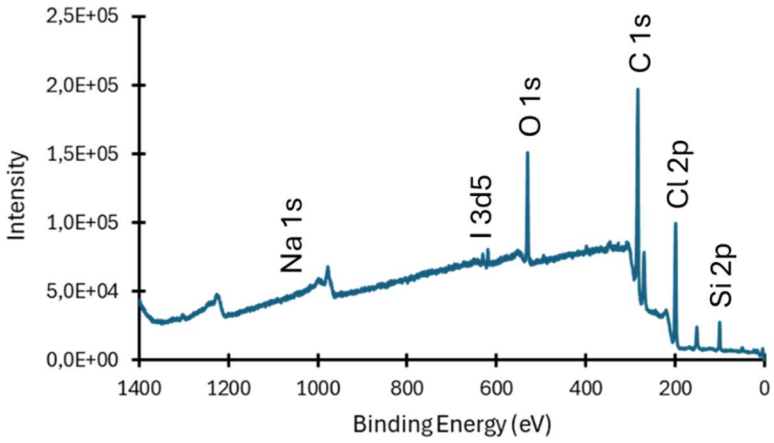


Figure S4.6. XPS spectrum of PVC iodinated via phase transfer catalysis for 17 hours.

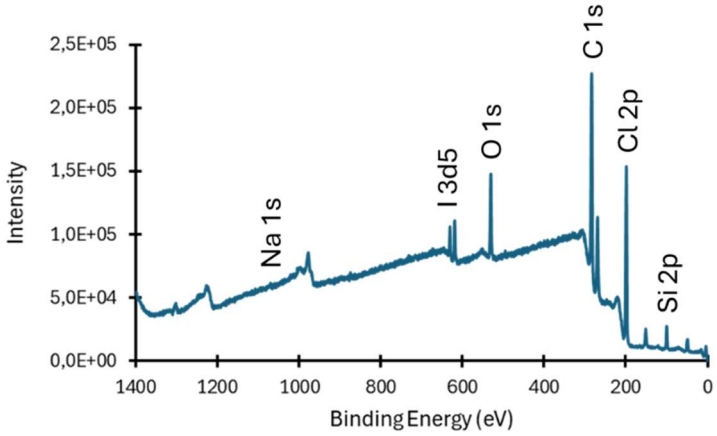


Figure S4.7. XPS spectrum of PVC iodinated via phase transfer catalysis for 24 hours.

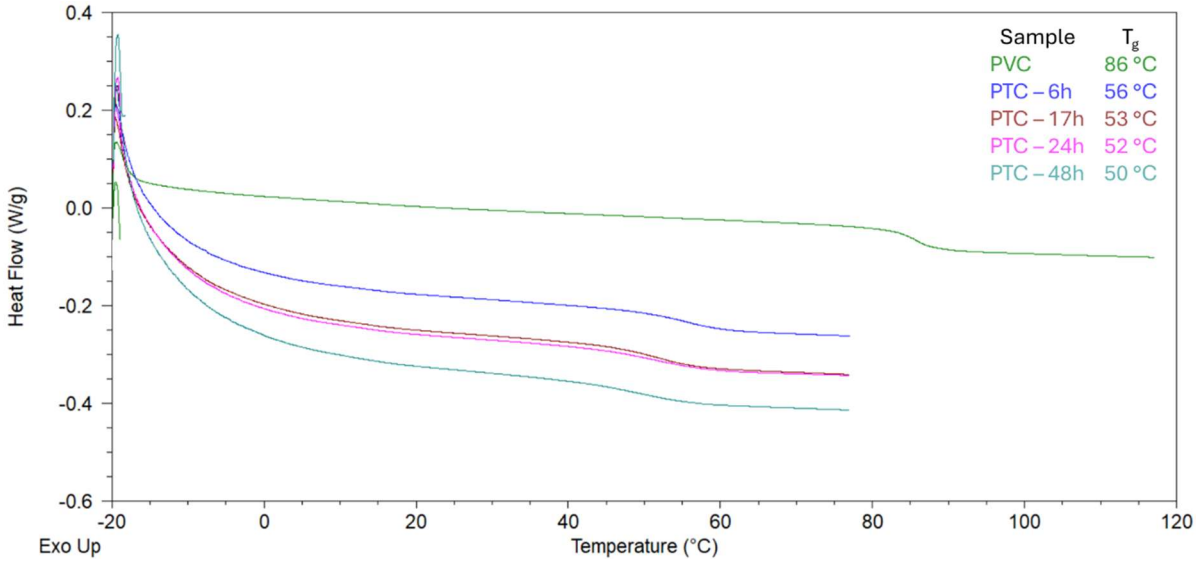


Figure S4.8. DSC of PVC and modified PVC samples iodinated via phase transfer catalysis (PTC) for 6, 17, 24, or 48 hours.

Table S4.1. Summary of physicochemical and thermal properties of pristine and iodinated PVC samples.

	Method	t (h)	MDT (°C)	$\overline{M_n}$ (g/mol)	C 1s (at%)	Cl 2p (at%)	I 3d5 (at%)	Na 1s (at%)	T_g (°C)	Contact angle (°)
1	PVC	0	275	63,500	73.52	6.53	0	0.49	86	85.6 ± 1.7
2	C-F	24	243	74,000	67.30	19.23	0.10	1.52	/	/
3	PTC	6	200	77,400	69.78	12.48	0.05	0.25	56	86.8 ± 1.1
4	PTC	17	206	71,500	70.29	12.14	0.18	0	53	85.5 ± 2.3
5	PTC	24	189	70,400	69.87	15.79	0.48	0.16	52	85.9 ± 1.6
6	PTC	48	213	59,100	67.47	17.37	0.84	0.23	50	83.4 ± 4.3

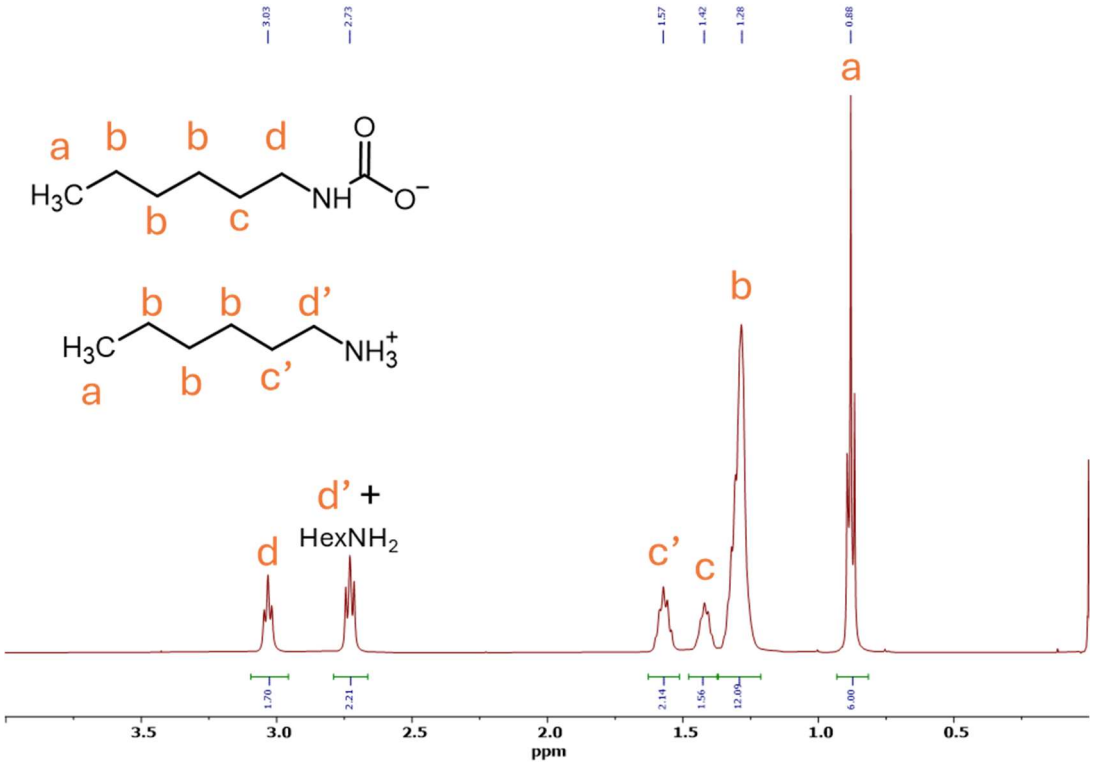


Figure S4.9. ^{1}H NMR spectrum of the amine only-based CO_2BAM.

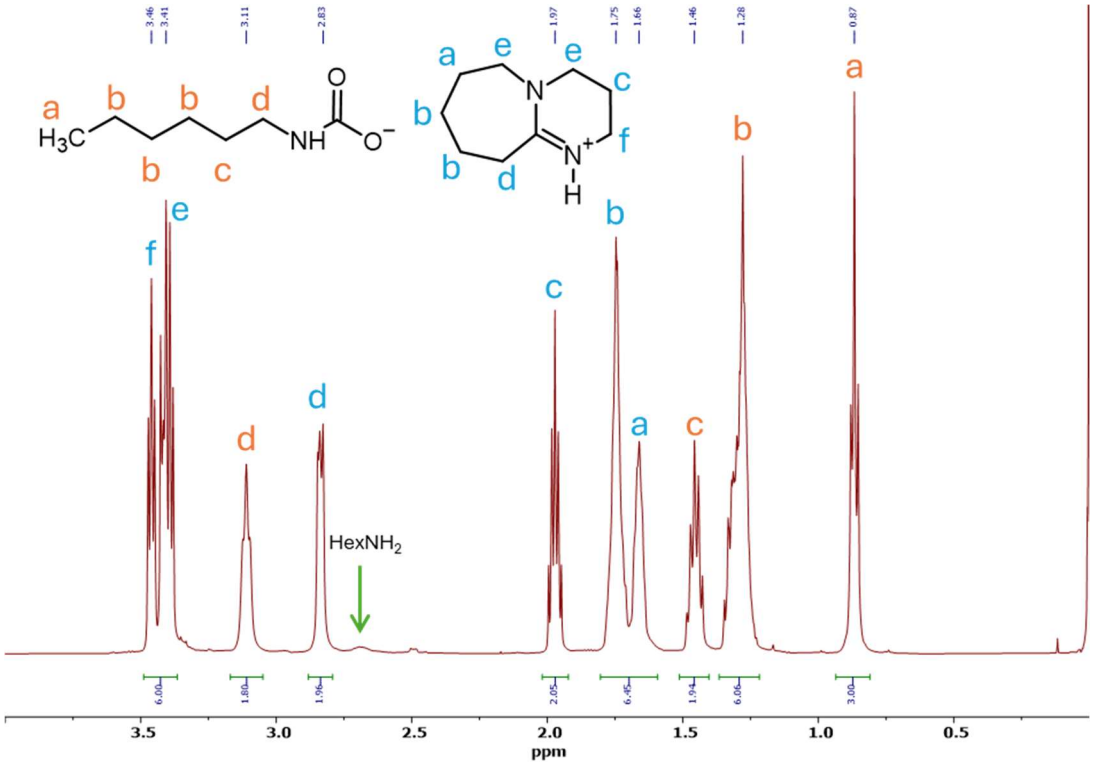


Figure S4.10. ^{1}H NMR spectrum of the hexylamine and DBU-based CO_2BAM.

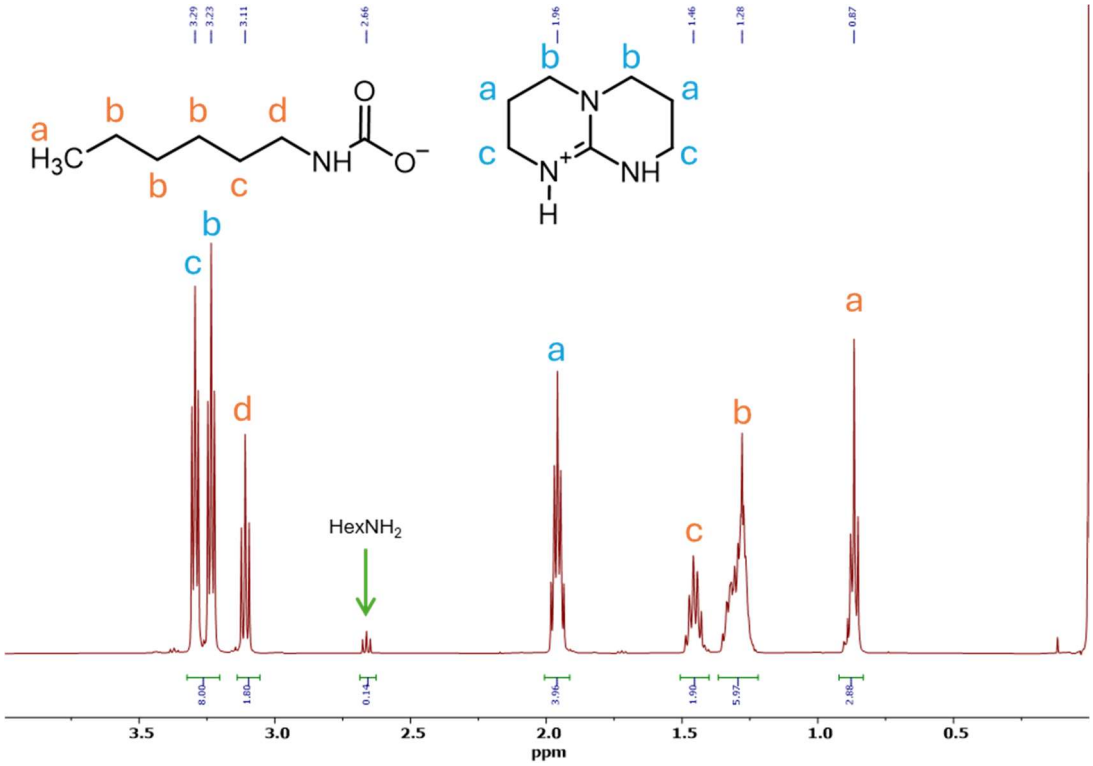


Figure S4.11. ^{1}H NMR spectrum of the hexylamine and TBD-based CO_2BAM.

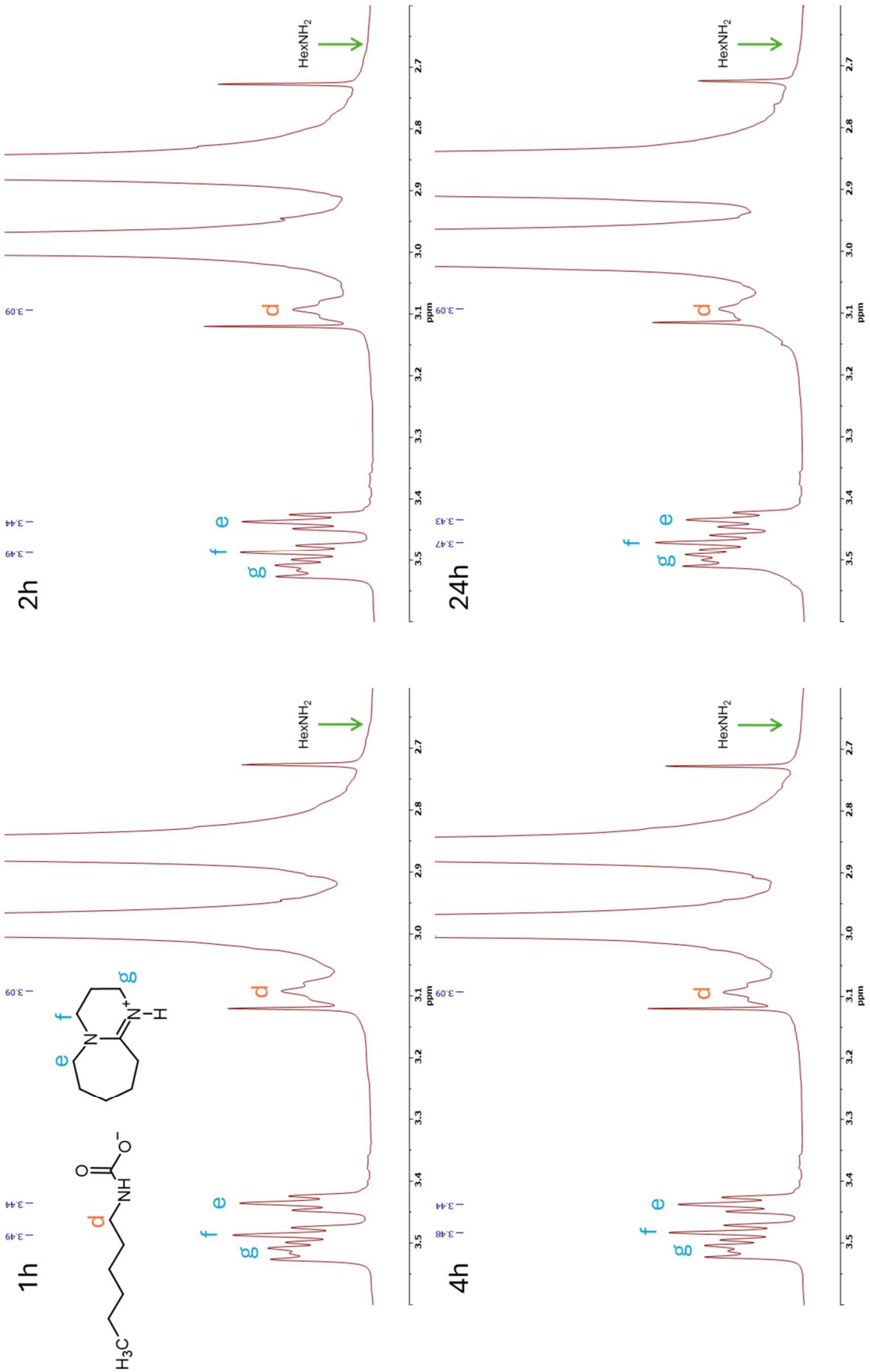


Figure S4.12. Stability of DBU-based CO_2BAM of 1-hexylamine in solution in DMF studied by ^{1}H NMR spectroscopy. The green arrow indicates where free hexylamine should appear in case of CO_2BAM degradation.

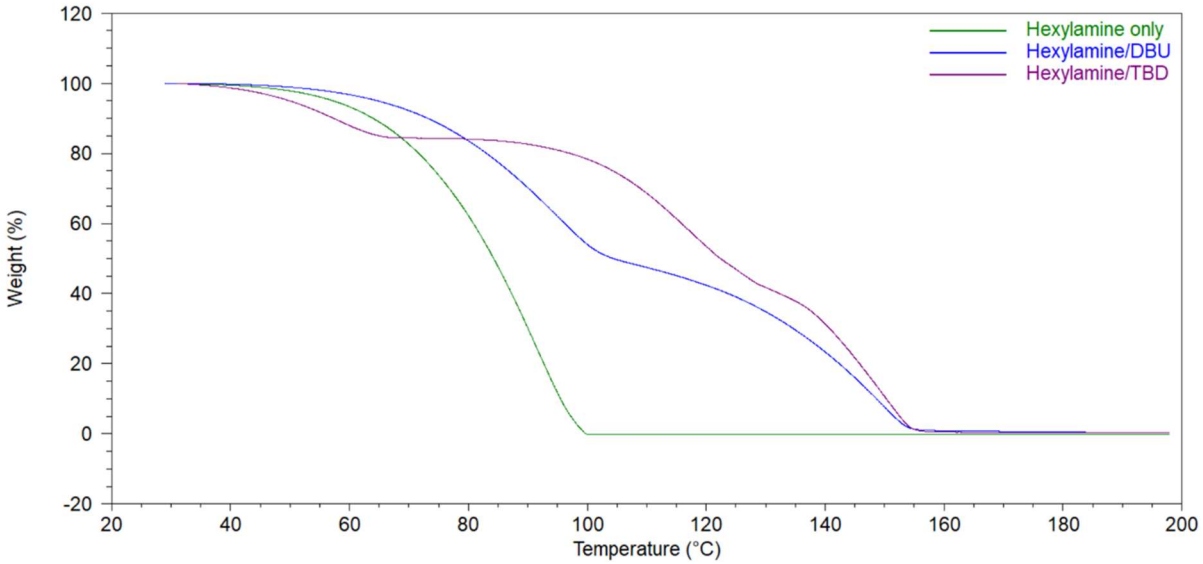


Figure S4.13. TGA thermograms of pristine 1-hexylamine, hexylamine/DBU, and hexylamine/TBD-based CO_2BAMs.

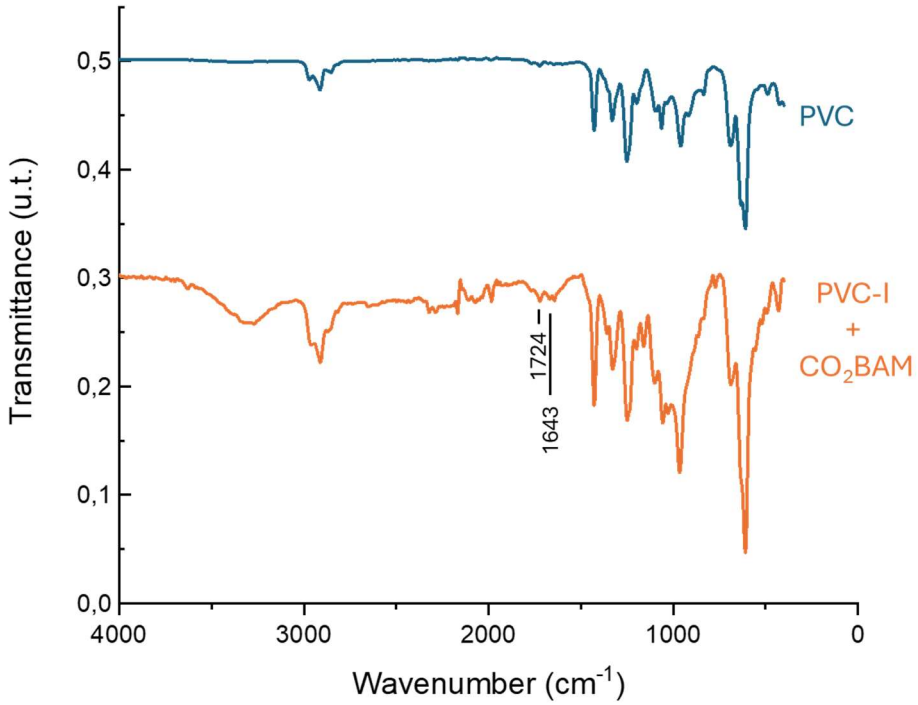


Figure S4.14. FT-IR spectra of pristine PVC and the product of reaction between PVC-I and the DBU-based CO_2BAM of 1-hexylamine.

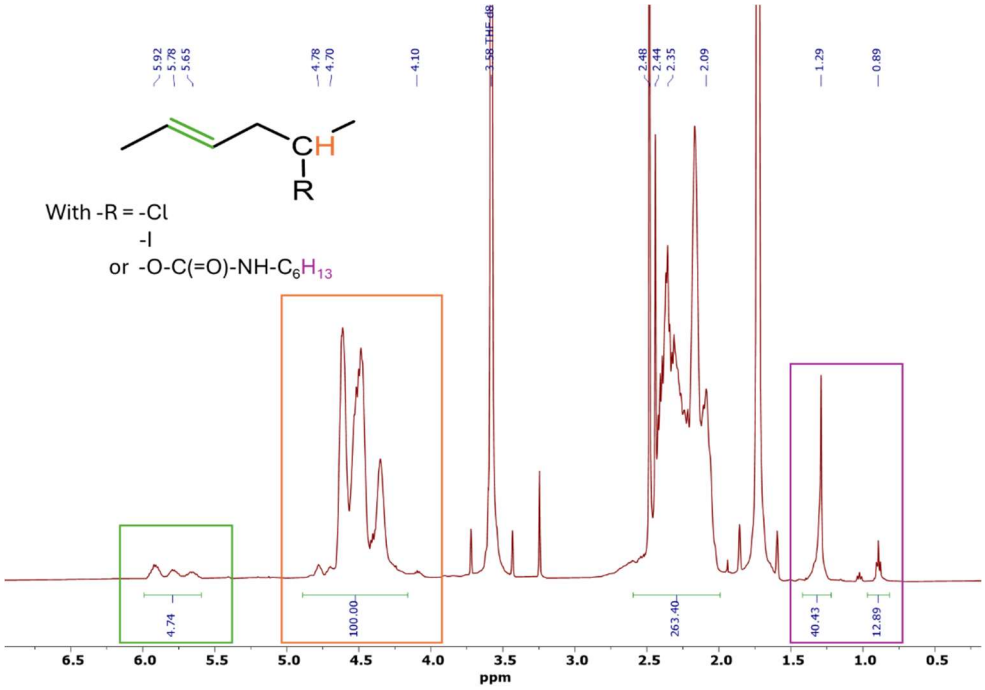


Figure S4.15. ^{1}H NMR spectrum of the reaction product between PVC-I and the DBU-based CO_2BAM of 1-hexylamine.

VI. REFERENCES

1 *The Circular economy for Plastics - A European Analysis*, Plastics Europe, 2024.

2 A. Buekens and A. Sevenster, *J. Mater. Cycles Waste Manag.*, 2010, **12**, 184–192.

3 K. Lewandowski and K. Skórczewska, *Polymers*, 2022, **14**, 3035.

4 Z. Ait-Touchente, M. Khellaf, G. Raffin, N. Lebaz and A. Elaissari, *Polymers for Advanced Techs*, 2024, **35**, e6228.

5 M. Sadat-Shojai and G.-R. Bakhshandeh, *Polymer Degradation and Stability*, 2011, **96**, 404–415.

6 X. Jiang, B. Zhu and M. Zhu, *Green Chem.*, 2023, **25**, 6971–7025.

7 S. H. Kim, K. H. Kim and S. H. Hong, *Angew. Chem. Int. Ed.*, 2014, **53**, 771–774.

8 Q. Liu, L. Wu, R. Jackstell and M. Beller, *Nat. Commun.*, 2015, **6**, 5933.

9 B. Grignard, S. Gennen, C. Jérôme, A. W. Kleij and C. Detrembleur, *Chem. Soc. Rev.*, 2019, **48**, 4466–4514.

10 C. Hepburn, E. Adlen, J. Beddington, E. A. Carter, S. Fuss, N. Mac Dowell, J. C. Minx, P. Smith and C. K. Williams, *Nature*, 2019, **575**, 87–97.

11 Y. Liu and X.-B. Lu, *Macromolecules*, 2023, **56**, 1759–1777.

12 X. Xiaoding and J. A. Moulijn, *Energy Fuels*, 1996, **10**, 305–325.

13 Z. Li, R. Shi, Y. Ma, J. Zhao and T. Zhang, *J. Phys. Chem. Lett.*, 2022, **13**, 5291–5303.

14 J. Delcorps, K. S. Rawat, M. Wells, E. Ben Ayed, B. Grignard, C. Detrembleur, B. Blankert, P. Gerbaux, V. Van Speybroeck and O. Coulembier, *Cell Reports Physical Science*, 2024, **5**, 102057.

15 J. Delcorps, E. Ben Ayed and O. Coulembier, *Polym. Chem.*, 2025, **16**, 2923–2932.

16 L. W. Dittert and T. Higuchi, *Journal of Pharmaceutical Sciences*, 1963, **52**, 852–857.

17 M. Takahashi, S. Sakamoto, N. Sakamoto, S. Nishimura, S. Hwang, J. Kim and M. Hosokawa, *Journal of Pharmaceutical Sciences*, 2026, **115**, 104146.

18 J. K. Mannisto, L. Pavlovic, T. Tiainen, M. Nieger, A. Sahari, K. H. Hopmann and T. Repo, *Catal. Sci. Technol.*, 2021, **11**, 6877–6886.

19 A. M. Afanasenko, N. Deak, J. October, R. Sole and K. Barta, *Green Chem.*, 2025, **27**, 5947–5981.

20 D. J. Heldebrant, C. R. Yonker, P. G. Jessop and L. Phan, *Energy Environ. Sci.*, 2008, **1**, 487–493.

21 D. J. Heldebrant, P. G. Jessop, C. A. Thomas, C. A. Eckert and C. L. Liotta, *J. Org. Chem.*, 2005, **70**, 5335–5338.

22 W. McGhee, D. Riley, K. Christ, Y. Pan and B. Parnas, *J. Org. Chem.*, 1995, **60**, 2820–2830.

23 K. Stagel, L. Ielo and K. Bica-Schröder, *ACS Omega*, 2023, **8**, 48444–48450.

24 Y. Imai, Y. Kanda, H. Sasaki and H. Togano, *Corrosion Engineering*, 1982, **31**, 714–721.

25 J. Y. Choi, Y. S. Kim, I. Sah, H. C. No and C. Jang, *International Journal of Hydrogen Energy*, 2014, **39**, 14557–14564.

26 R. Kaczmarczyk and S. Gurgul, *Energies*, 2024, **17**, 3223.

27 S. Moulay and Z. Zeffouni, *J. Polym. Res.*, 2006, **13**, 267–275.

28 N. A. El-Ghamaz and H. A. Ghaly, *Chemical Physics Letters*, 2016, **648**, 66–74.

29 E. Rusen, Raluca Şomoghi, C. Busuioc and A. Diacon, *RSC Adv.*, 2020, **10**, 35692–35700.

30 O. Clavilier, D. Foy and F. Byrne, *Green Chem.*, 2025, **27**, 12151–12159.

31 Y. Zhu, J. Yang, F. Mei, X. Li and C. Zhao, *Green Chem.*, 2022, **24**, 6450–6466.

32 J. Lange and S. H. Wadman, *ChemSusChem*, 2020, **13**, 5329–5337.

33 V. M. Shinde, G. N. Patil, A. Katariya and Y. S. Mahajan, *Chemical Engineering and Processing: Process Intensification*, 2015, **95**, 241–248.

34 S. Lakshmi and A. Jayakrishnan, *J. of Applied Polymer Sci.*, 2002, **84**, 493–499.

35 A. M. Striegel, *Anal. Bioanal. Chem.*, 2012, **402**, 77–81.

36 G. Cavallo, P. Metrangolo, R. Milani, T. Pilati, A. Priimagi, G. Resnati and G. Terraneo, *Chem. Rev.*, 2016, **116**, 2478–2601.

37 P. Jia, M. Zhang, L. Hu, R. Wang, C. Sun and Y. Zhou, *Polymers*, 2017, **9**, 621.

38 L. Lu, S. Kumagai, T. Kameda, L. Luo and T. Yoshioka, *RSC Adv.*, 2019, **9**, 28870–28875.

39 J. Vícha, J. Novotný, S. Komorovsky, M. Straka, M. Kaupp and R. Marek, *Chemical Reviews*, 2020, **120**, 7065-7103.

40 R. J. Abraham, M. A. Warne and L. Griffiths, *Journal of the Chemical Society, Perkin Transactions 2*, 1997, **26**, 2151-2160.

41 W. D. McGhee, D. P. Riley, M. E. Christ and K. M. Christ, *Organometallics*, 1993, **12**, 1429–1433.

42 M. Costa, G. P. Chiusoli and M. Rizzardi, *Chem. Commun.*, 1996, 1699–1700.

43 P. V. Kortunov, M. Siskin, L. S. Baugh and D. C. Calabro, *Energy Fuels*, 2015, **29**, 5919–5939.

44 Heat distortion temperature, https://pvc.org/about-pvc/pvcs-physical-properties/heat-distortion-temperature/, (accessed 9 August 2024).

45 Z. Zhang, F. Ruan, S. Xu, W. Wu, S. Shi and G. Xiao, *Process Safety and Environmental Protection*, 2022, **159**, 779–794.

46 N. Choudhury, A. Kim, M. Kim and B.-S. Kim, *Advanced Materials*, 2023, **35**, 2304113.

47 K. G. Papanikolaou, J. Wu, G. W. Huber and M. Mavrikakis, *J. Polym. Res.*, 2023, **30**, 83.

48 G. O'Rourke, T. Hennebel, M. Stalpaert, A. Skorynina, A. Bugaev, K. Janssens, L. Van Emelen, V. Lemmens, R. De Oliveira Silva, C. Colemonts, P. Gabriels, D. Sakellariou and D. De Vos, *Chem. Sci.*, 2023, **14**, 4401-4412.

49 A. F. Ciftja, A. Hartono, H. F. Svendsen, *Int. J. Greenh. Gas Control*, 2013, **16**, 224-232.

CHAPTER 5

Solvent-Free Iodination of Polyethylene via Twin-Screw Extrusion: A Scalable Approach



Ben Ayed E., Delcorps J., Coulembier O., *Industrial & Engineering Chemistry Research*, 2024, 63, 49, 21455-21465.
https://doi.org/10.1021/acs.iecr.4c03434 - (Patent : ARC-IP Ref P1711-WO HaloPE)

TABLE OF CONTENTS

I. INTRODUCTION 194

II. RESULTS AND DISCUSSION 197

A. Direct Iodination using n-Hexadecane as a Small-Molecule Model 197

B. Direct Iodination of Polyethylene by Twin-Screw Reactive Extrusion 201

C. Extrapolation to TSE-based Polypropylene Iodination 207

III. CONCLUSION 209

IV. EXPERIMENTAL 210

A. Materials 210

B. Procedures 210

C. Methods 211

V. SUPPORTING INFORMATION 213

VI. REFERENCES 219

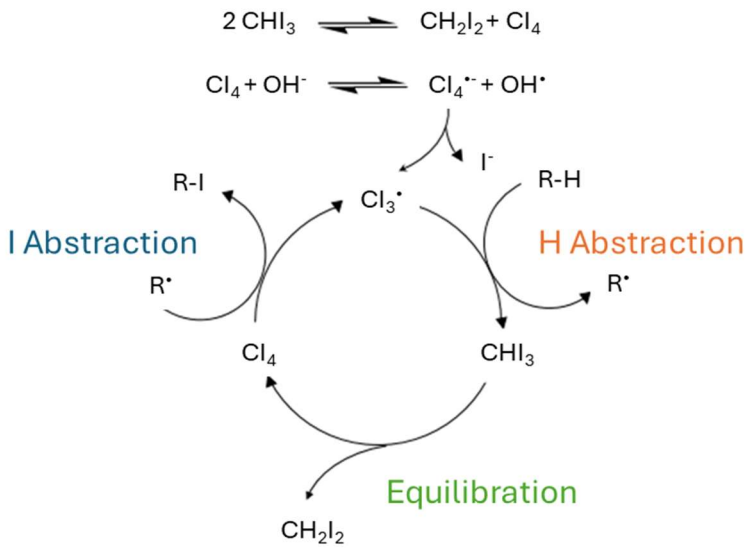
I. INTRODUCTION

The direct functionalisation of unactivated C-H bonds in aliphatic hydrocarbons is a well-known concept that has remained a subject of continued relevance among the scientific community.[1–6] This growing curiosity and interest have led to substantial work on the transformations of the C-H bond, given its significant importance as the building block of the majority of non-metallic materials, ranging from small molecules to long-chain macromolecules. Most synthetic activation strategies reported in the literature have utilised transition metal complexes,[7] metal carbenoids,[8,9] or catalysts[10] for amination,[11] hydroxylation,[12] azidation,[13] alkylation,[14] dehydrogenation,[15] and halogenation[16,17] reactions on low molecular weight compounds. In the early 2000s, Hartwig and Hillmayer[18] introduced the concept of C-H borylation[19] followed by the oxidation of a polyolefin using metallic complexes to achieve controlled, regioselective functionalisation of polypropylenes. This breakthrough drew significant attention to the synthetic value of C-H activation chemistry in the field of materials.[20] These methods are undeniably appealing and diverse, with a strong capability to provide desired synthetic pathways for hydrocarbons. However, limitations such as scalability issues, harsh reaction conditions, sensitivity, and high costs of these metallic complexes or catalysts, along with their non-negligible impact on human health and the environment, cannot be disregarded.

Given these considerations, extensive research has been conducted to explore new, straightforward approaches that offer improved economic and environmental viability while maintaining or even enhancing the efficiency of existing methods.[21–23] Arguably, the most conventional metal-free method for the direct conversion of aliphatic C-H bonds in organic chemistry textbooks is the free radical process.[24] This approach has sparked significant research interest, leading to intensified efforts to expand its applicability to a variety of hydrocarbon molecules. Several studies have unveiled fascinating catalytic C-H transformations involving specialised precursors or catalysts to achieve desired products while avoiding hydrocracking, isomerisation, or oligomerisation of the target molecules.[20] For instance, Minisci *et al*. reported the catalytic monohalogenation of alkanes using *N*-hydroxyphthalimide (NHPI) as a precursor, which generates the phthalimido-N-oxyl (PINO) radical responsible for hydrogen abstraction from the alkane's C-H bond.[25] Similarly, another group used the same NHPI precursor and PINO radical for selective amination of aliphatic C-H bonds.[26] In 2014, Alexanian's group developed intermolecular C-H bromination[27] and chlorination[28] reactions by employing amidyl radicals derived from *N*-haloamide reagents under visible light irradiation. This strategy has proven to be highly efficient due to the ability of nitrogen-centred radicals to achieve facile hydrogen atom transfer (HAT) across a broad spectrum of substrates, from small alkanes to complex molecules in late-stage synthesis.[29] Additionally, these halogenation reactions were conducted with the substrate as the limiting reagent, whereas traditional C-H functionalisation approaches typically require a large excess of

the starting material.[27,30] Building upon these remarkable characteristics, the same research group extended this protocol to C-H xanthylation in 2016.[31]

While the field of C-H diversification is rapidly expanding, certain C-H transformations, such as the iodination of aliphatic alkanes, remain highly restricted.[30] Iodine is considered an excellent leaving group because of its large atomic size and low electronegativity. These properties allow it to stabilise negative charge efficiently and form a relatively weak C–I bond,[32] making it particularly favourable in nucleophilic substitution (S_N) reactions. However, due to the unfavourable thermodynamics associated with iodine itself (characterised by a large positive enthalpy of hydrogen abstraction),[33] only a limited number of articles have addressed the direct iodination of low-molecular-weight alkanes. Currently, most direct iodination methods rely on highly electrophilic entities such as perfluoroalkyl radicals,[34] *tert*-butyl hypoiodite (generated *in situ*),[35,36] or a combination of hypervalent iodine, I_2, and azidotrimethylsilane ($TMSN_3$).[37] While these strategies offer operational convenience for alkane iodination, they can be challenging and impractical due to the high instability of certain generated reagents[36] or the toxic and explosive nature of others.[38] To overcome these limitations, Schreiner *et al*. developed a promising phase transfer single electron (SET) approach utilising crushed NaOH and iodoform (CHI_3) under mild conditions (**Scheme 5.1**).[33] This method has been successfully applied to a wide range of strained aliphatic and polycyclic hydrocarbons. In 2017, in collaboration with Schreiner, Artaryan *et al*. achieved the first iodination of hydrocarbons using an *N*-iodoamide at 100 °C under white LED irradiation.[32] However, while the iodination methods mentioned earlier exhibit a certain degree of diversity, they have primarily been restricted to small molecules. In contrast, other halogens or polar groups have been successfully incorporated into complex molecules and even polyolefins.[39]



Scheme 5.1. Mechanism for the iodination of alkanes (R-H) using iodoform (CHI_3) and NaOH, as postulated by Schreiner *et al*.[33]

Polyethylene (PE) is a low-cost commodity polymer extensively used in various applications, such as food storage, packaging, and biomedical devices.[40] However, its inert nature severely limits its interaction with polar additives, fillers, plastic blends, and materials like glass and metal.[34,35,41,42] To overcome these limitations and enhance the PE properties without compromising its performance, polar functional groups have been introduced along the polymer backbone.[43–45] This strategy has gained significant popularity due to its ability to greatly modify the physical properties of the final product, expanding its applicability in high-performance engineering applications. Numerous methods have been extensively developed and documented in several reviews, encompassing both metal and metal-free approaches.[39,46,47] For instance, Zhou *et al*. achieved the first direct amination of PE using NHPI as an organic catalyst to cleave C-H bonds.[41] In another study, the same group[42] introduced chlorine and bromine atoms into PE chains in a controlled manner using *N*-chloroamide[28] and *N*-bromoamide[27] reagents developed by Alexanian *et al*. Regioselective functionalisation of PE using a *N*-xanthylamide reagent under blue light exposure was reported by Williamson *et al*.[48] More recently, Cluzeau *et al*. reported a metal-free, dual-mode nitrosation of PE based on tert-butyl nitrite (t-BuONO), enabling the selective installation of oxime or carbonyl groups along the polymer backbone. Notably, this transformation could be performed either under visible-light irradiation in solution or directly by twin-screw reactive extrusion, highlighting the relevance of solvent-free melt-processing for the radical C-H functionalisation of polyolefins.[49] Regarding iodinated PE, only a few reports have been published, relying on plasma technology where polymer films were exposed to iodine vapours for controlled durations.[46,47,50–52] XPS analysis indicated that after 141 days of exposure, an incorporation of 0.34 wt% iodine was achieved.[53] This finding suggests that iodination methods for PE as reported can be effective, but they necessitate significantly longer reaction times.

In this chapter, we report for the first time the iodination of C-H bonds in PE under mechanochemical conditions (twin-screw extrusion) without organic solvents and under mild experimental conditions. Our initial studies on a linear alkane (*n*-hexadecane) revealed high conversion yields after optimisation of the protocol suggested by Schreiner *et al*.,[33] which employs iodoform as a cheap and stable iodine source and powdered NaOH as the initiator for the iodination reaction. The ratios of the reactants (alkane/CHI_3/NaOH), reaction duration, temperature, and shearing forces were carefully controlled to minimise any typical side reactions that could negatively affect the transformation of the alkane. This process was then extended to PE using a twin-screw extruder. Additionally, to a lesser extent, our conditions for iodination were successfully applied to polypropylene (PP). The work-up of this reaction is a one-step process followed by purification and characterisation of the functionalised polymer.

II. RESULTS AND DISCUSSION

A. Direct Iodination using n-Hexadecane as a Small-Molecule Model

The combination of solid NaOH and iodoform powder has demonstrated efficient mono-halogenation of cyclohexane, lightweight linear alkanes, and cyclic alkanes.[20,21,33,54,55] These transformations typically require the substrate to be used in large excess for optimal yield. High yields (calculated relative to iodoform) were achieved in these transformations. However, these conditions are not suitable for iodinating polyolefins and the reaction conditions, such as reactant ratios, time, temperature, and shearing forces first need to be optimised. Additionally, understanding the reaction mechanism and identifying potential side reactions that could cause crosslinking or degradation of polyolefins, such as polyethylene (PE), is crucial.

To determine the appropriate conditions for iodinating PE, several reactions were performed using *n*-hexadecane (*n*-C16) as a model compound. This choice was based on the characteristics of *n*-C16 as a long-chain hydrocarbon with only aliphatic C-H bonds, closely resembling the properties of PE. At first, the iodination reactions were conducted at 40 °C for 24 hours using a combination of solid NaOH and iodoform (CHI_3). Experimental conditions mimicked those reported by Schreiner *et al.*[33] by using both *n*-C16 and the base in excess with regards to CHI_3 ($[n\text{-C16}]_0/[CHI_3]_0/[NaOH]_0$ = 50/1/12.5). ^{1}H NMR analysis of the crude product in $CDCl_3$ revealed that the reaction predominantly produced mono-iodinated *n*-C16, with iodination occurring selectively at secondary carbons (δ = 4 – 4.2 ppm). The conversion yield, calculated relative to CHI_3, was approximately 1% (**Table 5.1**, **entry 1**). The analysis also showed the presence of unreacted starting material CHI_3 at δ = 4.89 ppm, and the formation of a side product, CH_2I_2, at δ = 3.86 ppm (**Figure S5.1**, **p. 213**).

Table 5.1. Experimental conditions and conversion yields for the iodination of *n*-hexadecane at 40 °C for 24 hours using various bases and iodinating agents.[a]

Entry	Iodine source/Base	Conversion Yield [b] (%)
1	CHI_3/NaOH	≈ 1
2	CI_4/NaOH	≈ 1.6
3	CHI_3/Cs_2CO_3	≈ 0.5
4	CHI_3/ K_2CO_3	≈ 0.3
5	CHI_3/KOH	≈ 1.6

[a] Experimental conditions: **0.92** mole of *n*-hexadecane, **0.0178** mole of iodinating agent and **0.25** mole of base, 24 hours at 40 °C; [b] Conversion yields (relative to CHI_3 or CI_4 initial content) were determined based on ^{1}H NMR analysis of the crude iodination reaction product.

This selection of reagents and conditions allowed us to evaluate the efficiency of NaOH and CHI_3 as a pair. At this stage, our primary aim was not to optimise conversion yields, but to justify the selection of these specific reagents (NaOH and CHI_3) for subsequent iodination reactions,

acknowledging that adjustments could potentially affect overall conversions. While elemental iodine (I_2) and diiodomethane (CH_2I_2) did not yield iodoalkane, which was expected due to the endergonic nature of I_2 and the limited reactivity of CH_2I_2 as an iodine donor,[55] tetraiodomethane (CI_4) successfully facilitated the desired reaction, yielding approximately 1.6% conversion, as confirmed by ^{1}H NMR analysis of the crude product (**Table 5.1**, **entry 2** and **Figure S5.2**, **p. 213**). During the reaction both CHI_3 and CI_4 coexist in equilibrium, as previously reported by Schreiner *et al*. (**Scheme 5.1**, **p.195**).[33] Given its superior stability, safety benefits, and cost-effectiveness,[33] iodoform was selected as the preferred reagent for the rest of our study.

In exploring alternative bases, various inorganic compounds were first evaluated. Carbonate salts such as caesium carbonate (Cs_2CO_3) and potassium carbonate (K_2CO_3) were employed in the reaction (**Table 5.1**, **entries 3** and **4**). Although iodoalkane formation occurred, the conversion yields did not exceed 0.5%. This low yield can be attributed to the reactivity of the ions released during the initiation stage of the iodination reaction, where hydroxide ions are more reactive than carbonate ones. By using potassium hydroxide (KOH), the reaction proceeded with a slight improvement in the conversion yield (**Table 5.1**, **entry 5**). This increase can be attributed to the greater reactivity of the base due to the larger ionic radius of K^+ compared to Na^+. KOH, however, is not practical for large-scale processes due to its higher cost and increased corrosiveness compared to NaOH. Organic bases such as 1,8-diazabicyclo[5.4.0]undec-7-ene (DBU) and 1,5,7-triazabicyclo[4.4.0]dec-5-ene (TBD) were also tested, but no formation of the iodoalkane was observed. Additionally, azobisisobutyronitrile (AIBN), a well-known radical initiator, was evaluated as a substitute for NaOH, but it did not result in the desired product. These findings indicate that the interactive coupling between CHI_3 and NaOH in this reaction system is not solely governed by basicity alone, implying that other factors play a crucial role. This observation underscores the complexity of the reaction mechanism, where considerations such as the specific reactivity of hydroxide ions and potential interactions between the reactants are pivotal.

As previously stated, while the combination of iodoform and NaOH has demonstrated effectiveness in the iodination of *n*-C16, the conversion yield of the desired product remains notably low. Our efforts were then directed towards optimising the reactant ratios to enhance results. Additionally, the influence of temperature on the reaction was investigated to understand its impact on both the conversion rate and the potential formation of shorter chain products resulting from C-C bond cleavage or any side products other than the concomitant production of CH_2I_2. It is worth noting that to extrapolate our model study to the iodination of PE, the highest temperature investigated needs to be below the degradation temperature of the main CHI_3 reactant (T_d = 150 °C; **Figure S5.3**, **p. 214**), should not exceed the melting point of the PE, and should ideally be close to the softening temperature of the PE chains ($T \leq 106$ °C).[56] This balance ensures that the PE remains in a suitable state for reactive extrusion without becoming fully liquid.

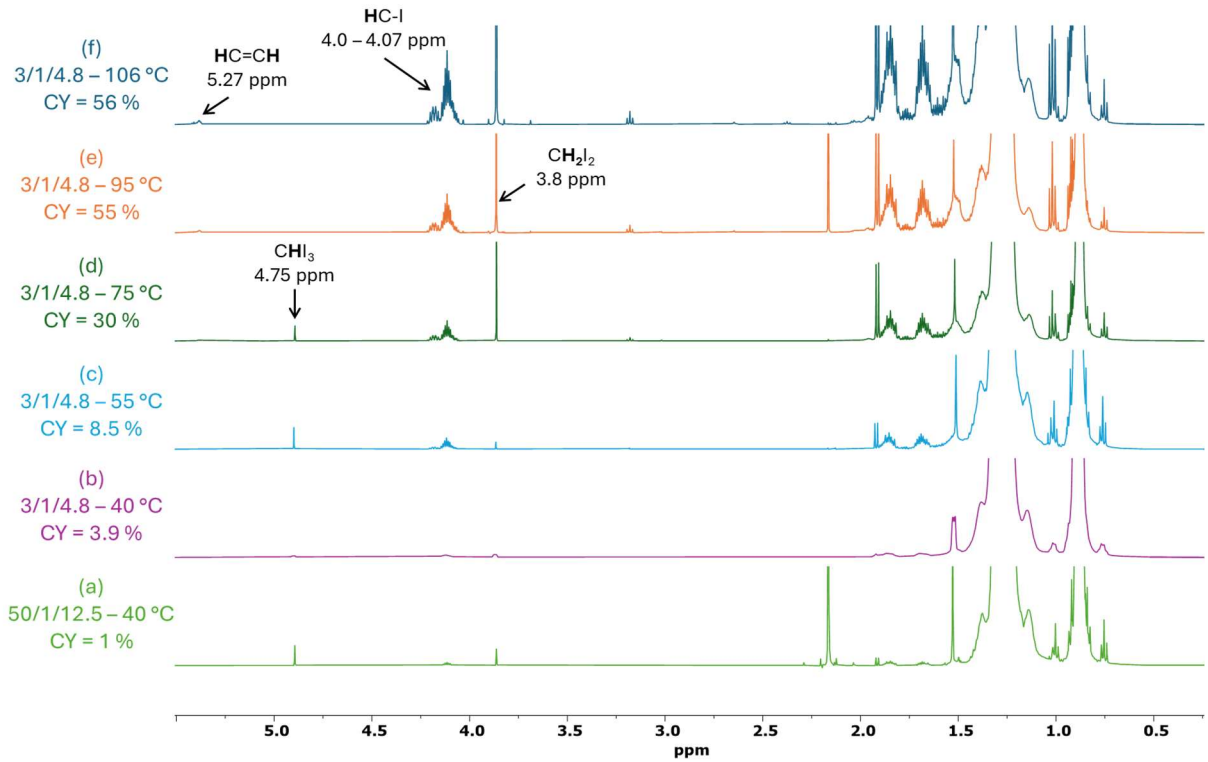


Figure 5.1. Conversion yields (CY %) of *n*-hexadecane after iodination under varying [*n*-C16]$_0$/[CHI_3]$_0$/[NaOH]$_0$ ratios and reaction temperatures, supported by stacked ^{1}H NMR spectra (recorded in $CDCl_3$ at 21 °C).

Figure 5.1 presents stacked ^{1}H NMR spectra of the iodinated *n*-hexadecane crude product obtained under various temperature conditions and initial [*n*-C16]$_0$/[CHI_3]$_0$/[NaOH]$_0$ ratios. At 40 °C, increasing the concentration of the CHI_3/NaOH duo relative to the initial *n*-hexadecane content ([*n*-C16]$_0$/[CHI_3]$_0$/[NaOH]$_0$ = 50/1/12.5 < 3/1/4.8) enhances the overall conversion from 1 to 4% (**Figure 5.1a-b**). Furthermore, maintaining the same ratio of components at 3/1/4.8 while increasing the temperature from 40 to 106 °C drastically enhances the conversion yield to 56% (**Figure 5.1c-f**). All spectra show no abnormalities or unrecognisable signals that could indicate the formation of smaller iodinated molecules resulting from C-C cleavage. However, under the specific experimental conditions employed, low molecular weight compounds (such as CI_4, C_2I_4, C_2HI_5) or iodide salts could potentially be present in the resulting product while remaining undetected by ^{1}H NMR spectroscopy.[57] Prominent signals appearing at δ = 4.07 ppm (attributed to a proton adjacent to the iodine atom) and δ = 5.27 ppm (indicative of olefinic protons) suggest that iodination at this specific ratio and under elevated temperature conditions enhances efficiency. This also increases the potential for alkane polyhalogenation, which is a desirable outcome in our study.

Monitoring reaction time is crucial to prevent degradation, especially when applying this model to PE iodination. At 95 °C for example, and for an initial ratio of [*n*-C16]$_0$/[CHI_3]$_0$/[NaOH]$_0$ of 3/1/4.8, the iodination degree increases with time, reaching a maximum of 55% after 24 hours

before declining due to the elimination of iodine atoms (**Figure 5.2a**), as indicated by the appearance of olefinic protons in the ^{1}H NMR spectrum (**Figure S5.4**, **p. 214**).

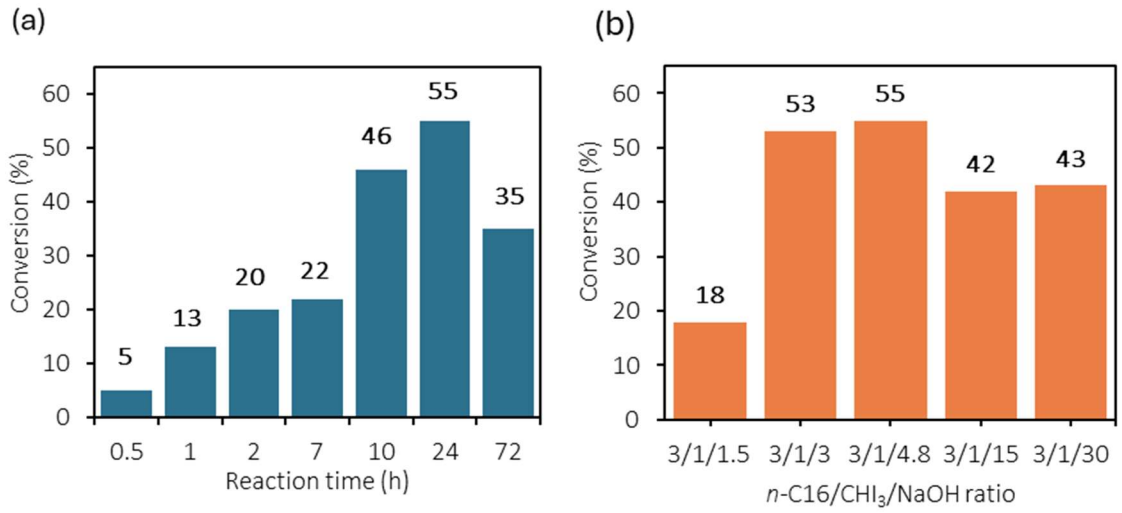


Figure 5.2. Iodination of *n*-hexadecane at 95 °C. (a) Influence of reaction time for an initial ratio of $[n\text{-C16}]_0/[CHI_3]_0/[NaOH]_0$ of 3/1/4.8; **(b)** Influence of initial ratio of $[n\text{-C16}]_0/[CHI_3]_0/[NaOH]_0$ after 24 hours.

Figure 5.2b explores the effect of NaOH concentration on conversion. At low NaOH content (3/1/1.5) the apparent conversion remains limited, while increasing the ratio to 3/1/3 or 3/1/4.8 maximises yield (53-55%), beyond which further increases in NaOH concentration lead to a decline in yield. The ^{1}H NMR spectra showed no notable differences, but the changing CHI_3/NaOH ratio impacts the distribution of active species (**Figure S5.5**, **p. 215**). According to Schreiner *et al.*, NaOH acts as a reducing agent, not a base, initiating the reaction by reducing *in situ* generated CI_4, forming triiodomethyl radicals ($^{\bullet}CI_3$).[33] These radicals abstract hydrogen from alkanes, forming CHI_3 and alkyl radicals. Alkyl radicals then react with CI_4, producing iodinated alkanes and regenerating $^{\bullet}CI_3$, continuing the cycle (**Scheme 5.1**, **p.195**).[57–59]

Categorised as a phase transfer catalysis reaction, the mass transfer aspect significantly influences the overall conversion.[21,53] Therefore, the effect of system agitation speeds ranging from 0 to 400 rpm was investigated. Conversions were measured after 2 hours of reaction at 95 °C with an initial ratio of $[n\text{-C16}]_0/[CHI_3]_0/[NaOH]_0$ of 3/1/4.8 (**Figure 5.3**). Without agitation, the conversion was low but increased with higher speeds, reaching up to 19%. However, excessively high agitation speeds and temperatures can cause the reaction mixture to adhere to the flask walls, impeding mass transfer and reducing conversion efficiency. Adding iodoform powder in fractions every 30 minutes under constant stirring at 400 rpm significantly improved yields from 19% to 30% (**Figure S5.6**, **p. 216**), demonstrating the effectiveness of this approach.

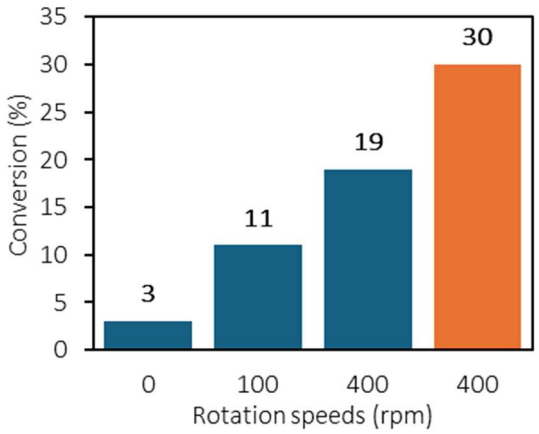


Figure 5.3. Overall impact of magnetic stirring speeds on the conversion of *n*-hexadecane at 95 °C ([*n*-C16]$_0$/[CHI_3]$_0$/[NaOH]$_0$ of 3/1/4.8) in a one-pot process (blue, one addition, reaction time = 2h) *vs*. a multi-feed process (orange, 4 additions every 30 minutes).

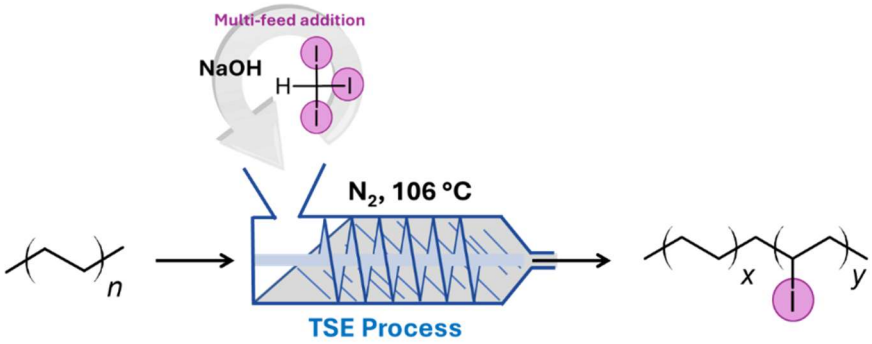
B. Direct Iodination of Polyethylene by Twin-Screw Reactive Extrusion

After optimising the reaction conditions using a model light alkane molecule, a series of iodinated polyethylene (**I-PE**) samples were prepared using a twin-screw reactive extrusion (TSE) process. To the best of our knowledge, no previous studies have reported the iodination of PE in solvent-free conditions using a TSE process. In order to facilitate comprehensive molecular characterisation, including ^{1}H NMR spectroscopy and Size Exclusion Chromatography (SEC), we selected PE with a low molecular weight (Theoretical molar mass, M_nth ~ 1500 g/mol; M_wSEC = 7500 g/mol). This choice was crucial since higher molecular weight PE tends to be insoluble, limiting the range of analytical techniques that can be effectively applied. By using low molecular weight PE, we ensured that the iodinated samples remained soluble, thus allowing for a more detailed analysis of the reaction products and their structural attributes.

Although the initial conditions were optimised for a model alkane, these were adapted for the iodination of PE to better suit the polymer's characteristics. Based on findings with *n*-hexadecane, where an excess of NaOH relative to CHI_3 led to the generation of unsaturations due to the elimination of iodine atoms, a molar ratio of 1:1 for CHI_3/NaOH was selected for the PE iodination process. This choice was made to favour iodination over elimination, while acknowledging that the latter is an inescapable feature of this reactive system. An excessive amount of NaOH would shift the iodination/elimination balance too far towards the elimination pathway and, more critically, would also promote radical-induced intermolecular crosslinking. Such crosslinking would be detrimental under extrusion conditions, as it could lower the polymer's decomposition temperature and alter its crystallinity. Additionally, an excess of NaOH could present experimental challenges, such as difficulties in achieving uniform mixing and complications in process control during extrusion.

To avoid these risks, the quantity of NaOH was carefully limited, and for PE, only the effects of shearing force, *i.e.*, screw speed (SS), and reaction time were systematically studied. The reaction conditions were meticulously controlled to maintain a 1:1 molar ratio between CHI_3 and NaOH. Results are presented based on the ratio $[Ethylene]_0/[CHI_3]_0/[NaOH]_0$, with all reactions conducted under nitrogen at 106 °C using a multi-feed addition method. In this approach, reagents were incrementally added every 30 minutes over a specific period of time. The detailed experimental conditions and results are provided in **Table 5.2**. It should be noted, however, that in contrast to the iodination process of *n*-hexadecane, which involved simple physical filtration of the remaining starting materials, iodinated PEs were thoroughly washed and purified to remove excess iodoform powder (See Experimental Procedure), ensuring the accuracy of the experimental results.

Table 5.2. Impact of Extrusion and Reaction Conditions on Polyethylene Iodination.



Entry	Sample Code	$[Ethylene]_0/[CHI_3]_0/[NaOH]_0$	Reaction time (h)	SS [a] (rpm)	M_wSEC [b] (g/mol)	T_m [c] (°C)	X_c [c] (%)	Iodine (wt%)		
								XPS	^{1}H NMR	TGA
1	I-PE_1	3/1/1	2	100	9600	89.3	11.4	-	7	9
2	I-PE_2	2/1/1	2	100	12100	87.5	10.8	-	9	11
3	I-PE_3	1/1/1	2	100	15000	78.6	6	-	-	16
4	I-PE_4	1/1/1	2	200	13900	83.3	7	10	16	15
5	I-PE_5	1/1/1	2	300	12000	75	5	-	-	23
6	I-PE_6	1/1/1	1	100	-	87.4	6	-	13	9
7	I-PE_7	1/1/1	5	100	-	68	5	-	-	15

[a] SS = screw speed. [b] Weight-average molecular mass as determined by SEC (THF as the eluent; 50 °C) with polystyrene standards for calibration. [c] Melting temperature and crystallinity percentage as determined by DSC.

Our study began by adjusting the feed ratio of the ethylene unit to the CHI_3/NaOH duo (**Table 5.2**, **entries 1-3**) for 2 hours at a screw speed of 100 rpm. By combining results from ^{1}H NMR and thermogravimetric analysis (TGA), it was found that iodine weight percentages decreased when the amounts of CHI_3 and NaOH were reduced in comparison to the repeating ethylene units, indicating a decrease in PE iodination levels. This finding is consistent with the observations

made for *n*-hexadecane. Therefore, to achieve a higher iodine content with minimal side reactions, we chose to maintain an equimolar ratio between the ethylene repeating unit, the haloform, and the base ($[Ethylene]_0/[CHI_3]_0/[NaOH]_0$ = 1) while varying the experimental conditions from one experiment to the next (**Table 5.2**, **entries 3-7**).

TGA is invaluable not only for evaluating how functional groups influenced the polymer's thermal properties but also for estimating the degree of halogenation in the samples. Typically, for halogenated polyolefins, the weight loss observed in the first stage closely corresponds with values obtained using more precise techniques such as ^{1}H NMR.[42,60,61] Most TGA traces of iodinated polyethylene (**I-PE**) (**Figure 5.4a** and **Figure S5.7**, **p. 217**) exhibit a three-stage degradation pattern, in contrast to pristine PE, which degrades in a single, smooth step starting at 350 °C and reaching complete degradation at 530 °C. For **I-PE**s, the first degradation step begins around 250 °C, depending on the degree of functionalisation, followed by significant decomposition between 400 °C and 550 °C, attributed to molecular scission and breakdown of the polymer's hydrocarbon skeleton. The final degradation stage starts at 650 °C, corresponding to the formation of crosslinked structures at higher temperatures. It is important to note that these crosslinking reactions are driven by the presence of carbon-carbon double bonds, whose quantity cannot be directly inferred from TGA.

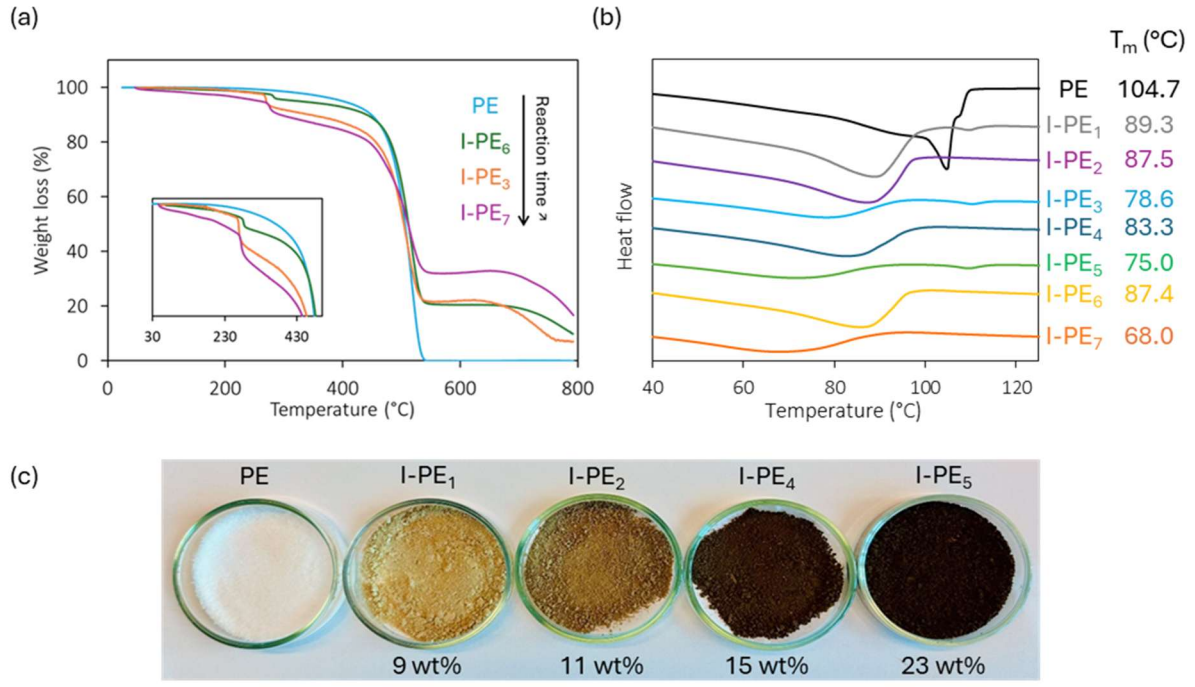


Figure 5.4. (a) TGA curves of the PE starting material and modified samples at different reaction durations; **(b)** DSC curves displaying the T_m of all the iodinated PE with all DSC data obtained from the 2nd heating cycle at a rate of 10 °C/min (Exo up); **(c)** Photograph of selected samples with increasing iodination rates.

The iodine content in the functionalisation process is strongly influenced by various parameters. For instance, higher shearing rates (**I-PE$_5$**, 300 rpm) significantly increases iodine content compared to **I-PE$_3$** (100 rpm) and **I-PE$_4$** (200 rpm). This enhanced shearing promotes

greater homogeneity and increases the polymer's active surface area relative to the halogenating reactant and the base. However, as the iodine content increases, the concurrent formation of double bonds intensifies, leading to crosslinking and the production of a more resistant material that becomes difficult to dissolve and characterise using techniques other than TGA.

Reaction time also proved to be a key factor in influencing the rate of functionalisation. For example, after one hour, the iodine content reaches 9 wt% (**I-PE$_6$**), while extending the reaction to two hours nearly doubles the iodine content (**I-PE$_3$**, 16 wt%). Yet, longer reaction times did not improve the final outcome (**I-PE$_7$**, 15 wt%). Interestingly, the residual mass of **I-PE$_7$** was higher than that of the other samples, suggesting that iodination eventually reaches a saturation point, and prolonged exposure to shearing forces may induce dehydrohalogenation, favouring the formation of additional carbon-carbon double bonds in the polymer structure, as evidenced by a pronounced and broad peak appearing at 1645-1569 cm^{-1} in the FT-IR data (**Figure S5.8b**, **p. 217**). This increase in iodination levels, combined with the confirmed presence of carbon-carbon double bonds as shown by ^{1}H NMR and TGA, also leads to a noticeable darkening of the sample colour. In contrast, **I-PE** samples with lower mass iodination degrees exhibit colours ranging from yellow to light brown (**Figure 5.4c**). This colour variation provides a visual indication of the degree of functionalisation, with higher iodine content correlating with a darker final product. Although these elimination reactions constitute a limitation of the iodination process itself, they can conversely be exploited to generate conjugated polyene sequences directly along the PE backbone under similar twin-screw extrusion conditions - a complementary strategy developed in Chapter 6.

The melting temperature (T_m) of all modified samples was affected compared to the unfunctionalised PE, which has a T_m of 104.7 °C (**Figure 5.4b**). The reduction in T_m values is expected due to the incorporation of functional groups that act as defects within the crystalline regions, disrupting the crystallinity of the parent polymer, even at low iodine contents. Iodine, with a van der Waals radius of 1.98 Å, is a large, bulky functional group that can easily alter the crystallinity of PE. A previous study by Plummer *et al*. demonstrated that the incorporation of halogens like chlorine and bromine into PE chains affects crystallinity, with bromine causing more pronounced changes due to its larger atomic radius compared to chlorine.[42]

In addition to the thermal analyses, ^{1}H NMR spectroscopy provided further insights into the structural modifications induced by iodination. **I-PE**s with an iodine content ≤ 15 wt% (**Table 5.2**, **entries 1, 2, 4, & 6**) exhibited good solubility in deuterated chloroform at 50 °C. The samples were analysed promptly to prevent polymer recrystallisation, showing an acceptable, though not perfect, correlation with the iodination weight content determined by TGA. **Figure 5.5** illustrates the ^{1}H NMR spectrum of a selected iodinated PE sample (**I-PE$_4$**), used as an illustrative example to confirm functionalisation. Compared to the unmodified PE (**Figure S5.9**, **p.218**), the spectrum reveals new chemical shifts: around δ = 4.11 ppm for α-hydrogens adjacent to the iodine atom

and around δ = 1.7-1.9 ppm for β-hydrogens from neighbouring -CH_2- units. These shifts are consistent with those observed in iodinated *n*-hexadecane, highlighting the changes induced by iodination on the polyolefin chain.

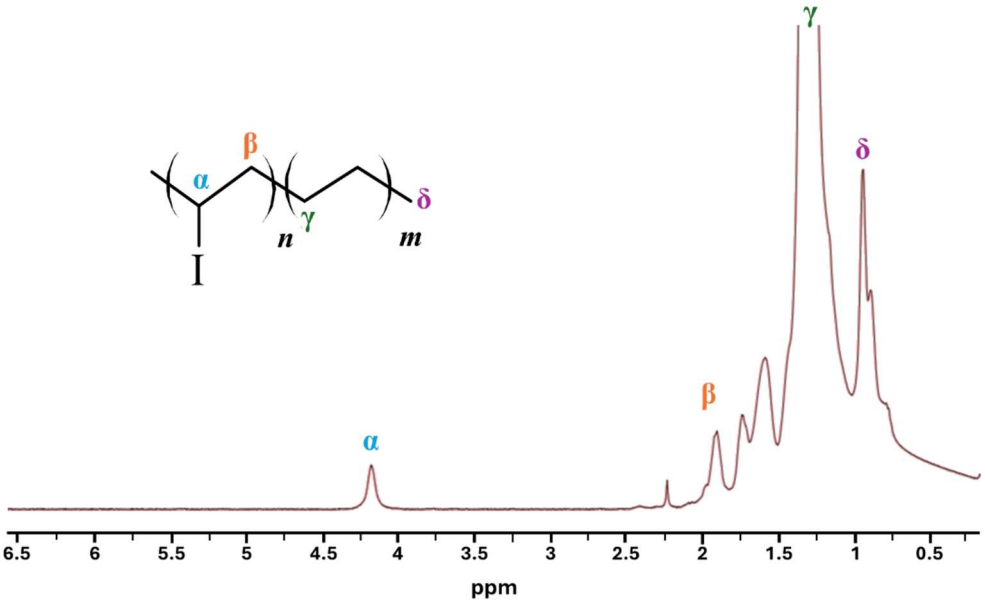


Figure 5.5. ^{1}H NMR spectrum of **I-PE$_4$** in $CDCl_3$ solvent at room temperature (zoomed between δ = 0 ppm and δ = 6.5 ppm).

To complement these findings and to gain a deeper understanding of the structural changes, ATR-FTIR spectroscopy was employed. **Figure 5.6a** presents the results of the iodination reaction conducted at different shearing rates, ranging from 100 rpm to 300 rpm (**Table 5.2**, **entries 3-5**). Visually, the intensity of PE's characteristic absorption peaks remained unchanged. However, an interesting observation was made regarding the doublets typically observed at 1470 and 720 cm^{-1}, which are associated with CH_2 bending and rocking deformation, respectively.[61] In **I-PE** sample, these doublets were merged into a single peak, indicating a modification in the crystalline packing of the polymer due to the incorporation of iodine atoms into the polymer backbone.[59] Furthermore, the intensity of the terminal groups, characterised by the CH_3 deformation peak at 1369 cm^{-1}, did not increase, suggesting that chain scission did not occur.[62] While the C-I stretching modes, usually found in the range of 600-200 cm^{-1}, were not visible with a germanium crystal,[63] new peaks appeared in the spectra of the modified samples. For example, the C-H deformation modes observed at 1326 cm^{-1} suggested alterations in the C-H environment around the polymer after modification. This is most likely explained by the higher electronegativity of both the iodine atoms as well as the sp^2 hybridised carbon of the new C=C double bonds, which can lower the frequency of neighbouring groups.[64] Indeed, a broad peak ranging from 1645-1569 cm^{-1}, assigned to C=C stretching modes, and a sharp peak at 779 cm^{-1}, corresponding to the =C-H out-of-plane bending mode of the *cis* conformation of an alkene, were also detected.[64] Interestingly, such transformations usually yield the *trans* isomer, for which the =C-H out-of-plane bending mode appears around 970-960 cm^{-1}.[64] The intensity and broadness of these peaks were notably heightened under conditions of increased shearing (**I-**

PE$_5$) and extended durations of the iodination reaction (**I-PE$_7$**) (**Figure S5.8b**, **p. 217**). Although the vinylene moiety was not detectable using ^{1}H NMR in the modified PEs, it was present in the spectra of iodinated *n*-hexadecane, which presented higher iodine content, albeit with variations in the ratio of double bond (0.4 mol%) to iodine content (23 mol%). Moreover, the final products exhibited very low to no solubility in organic solvents. This observation suggests that physical cross-linking likely occurred due to π-π stacking interactions between the polyene sequences introduced along the polymer backbone (see Chapter 6). Notably, no evidence of oxidation of the double bonds was observed, as indicated by the absence of carbonyl groups characterised by an absorption band at 1710 cm^{-1} in all samples.[65]

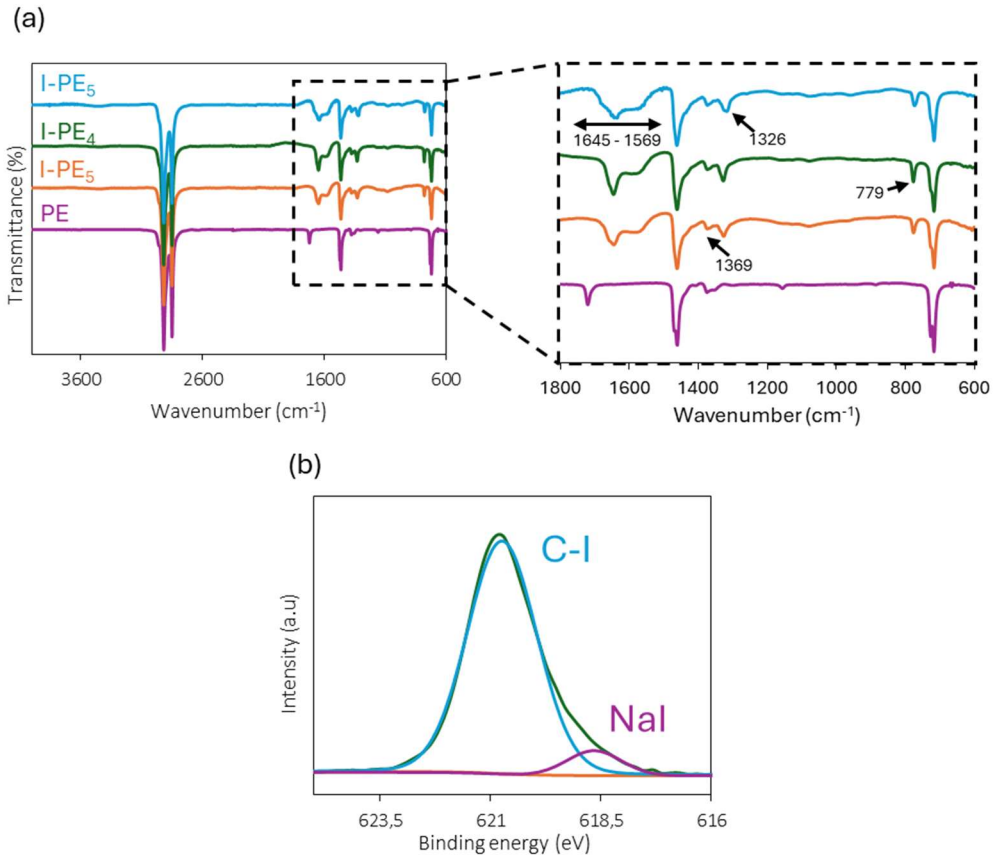


Figure 5.6. **(a)** FT-IR spectra of the PE starting material and iodinated PEs subjected to varying shearing rates; **(b)** XPS spectrum showing the I 3d region of **I-PE$_4$**.

X-ray photoelectron spectroscopy (XPS), while primarily a surface-sensitive technique, provided valuable elemental analysis, confirming iodine grafting onto the polymer chains. As shown in **Figure 5.6b**, the examination of the selected sample **I-PE$_4$** revealed a new peak at 620.7 eV, attributed to chemically bonded iodine on carbon atoms.[47] Additionally, impurities from additives in PE and salts such as NaI, resulting from side products during the iodination reaction and/or purification, were identified. The C1s spectra of the sample exhibited a strong, singular C-C absorption peak at 285 eV (**Figure S5.10**, **p. 218**), with no splitting or emergence of new, lower intensity peaks within the same range, indicating a lack of complex structures.[66] The level of C sp^2 hybridisation was not detected in the spectrum, suggesting that the vinylene

moieties are internal or of very low amount, at least for **I-PE$_4$**. The iodine atomic percentage post-modification for 2 hours using TSE was estimated at 1.72%, which corresponds to a mass percentage of 10 to 11% iodine in the polymer. Notably higher than the 0.34 wt% achieved after 141 days of exposure through I_2 plasma surface modification of polyethylene,[52] this iodine content is in agreement with the results obtained from ^{1}H NMR and TGA analyses, confirming the accuracy of the iodine content measurement.

C. Extrapolation to TSE-based Polypropylene Iodination

The successful iodination of PE using TSE prompted us to consider applying a similar procedure to isotactic polypropylene (*i*PP), a widely used polyolefin feedstock appreciated for its high chemical resistance and exceptional mechanical properties.[67] Similar to PE, *i*PP consists of a saturated C-C backbone, but with pendant methyl groups attached to every other backbone carbon, rendering it more susceptible to degradation during functionalisation, particularly under thermomechanical conditions. In the frame of our investigation an *i*PP with a $M_n th$ ~ 5000 g/mol was selected. Literature extensively covers grafting reactions on PP in the melt state, particularly focusing on the grafting of polar synthons such as maleic anhydride, glycidyl methacrylate, and styrene. These reactions are typically initiated by free radicals generated from the thermal decomposition of organic peroxides, which preferentially attack the tertiary C-H bonds, leading to β-scission, coupling and isomerisation side reactions.[68–70] To preserve the integrity of the parent polymer during the iodination of PP, the same procedure as for the functionalisation of PE was adopted ($[Propylene]_0/[CHI_3]_0/[NaOH]_0$ = 1, SS = 200 rpm), with the gradual addition of the CHI_3/NaOH duo over a 2-hour cycle under nitrogen at 106 °C, a temperature close to the Vicat softening point of the polymer.[71,72] No solvents or additives were added during the process.

Although the final product was successfully collected and purified, its resistance to dissolution in organic solvents posed significant challenges for characterisation. As a result, obtaining a complete ^{1}H NMR spectrum, or employing other techniques requiring solubility, was difficult. Nevertheless, we managed to conduct several tests on the collected iodinated PP (**I-PP**) using TGA, DSC, and FT-IR analyses.

The FT-IR analysis of **I-PP** reveals the same stretching, deformation, and rocking vibrations of CH_3 at 2953 cm^{-1}, 2873 cm^{-1}, 1377 cm^{-1}, 1156 cm^{-1}, and 971 cm^{-1}, as well as stretching and flexural vibrations of CH_2 at 2917 cm^{-1}, 2845 cm^{-1}, and 1459 cm^{-1}, found in the original *i*PP spectrum.[73] A closer examination of the fingerprint region highlights the presence of internal *cis* C=C bonds, evidenced by the broad signal within the range of 1645-1569 cm^{-1} and the one at 781 cm^{-1} (**Figure 5.7a**). However, while these signals are present, they are less pronounced compared to those in the **I-PE** samples, even when comparing samples with identical iodine content. This suggests a lower degree of C=C bond formation in **I-PP**, indicating differences in the modification mechanism between PP and PE, despite similar levels of functionalisation. This is confirmed by TGA analysis, which, in addition to a first 22 wt% dehalogenation step, observed

between 230 and 450 °C, shows a charring percentage of 9 wt%, significantly lower than that observed in the analysis of **I-PE** samples (**Figure 5.7b** and **Figure 5.4a**). Although the charring rate cannot be directly correlated to the percentage of carbon-carbon double bonds in a sample, a lower charring value suggests fewer C=C bonds, and thus fewer elimination reactions during the modification of PP.

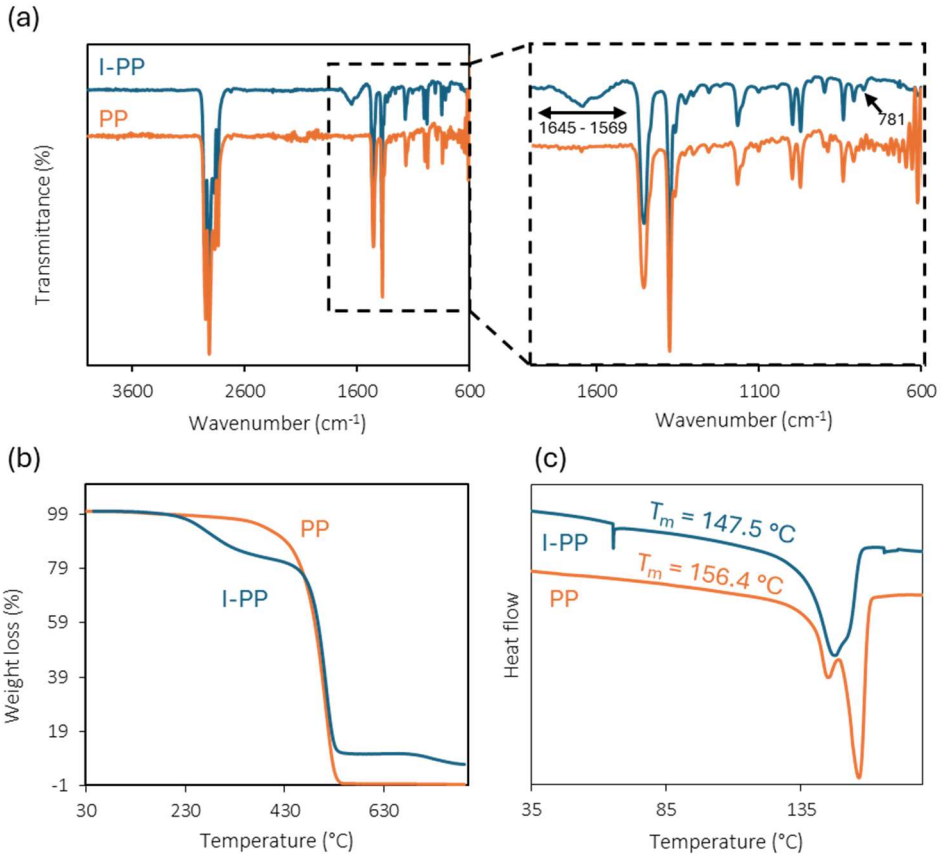


Figure 5.7. (a) FT-IR spectra of original PP and corresponding **I-PP**; **(b)** TGA curves of both *i*PP and **I-PP**; **(c)** Second heating DSC curves of original *i*PP and **I-PP** (Exo up).

Interestingly, the as-obtained **I-PP** exhibits a melting transition at 147.5 °C, which is slightly lower than that of the original *i*PP (T_m = 156.4 °C), while maintaining a relatively high degree of crystallinity (X_c = 23% for **I-PP** compared to 40% for *i*PP, **Figure 5.7c**). These results clearly indicate that modifying PP under these conditions is an effective approach to functionalise the polyolefin while partially preserving its crystalline structure and physical characteristics, which are valuable for various applications. However, despite the successful modifications achieved, further investigation is needed to fully understand the regioselectivity of the iodination reaction on PP.

III. CONCLUSION

In this chapter, we successfully demonstrate a novel and scalable solvent-free method for the iodination of polyethylene (PE) via twin-screw extrusion (TSE). Using iodoform (CHI_3) as an iodine source and NaOH as an initiator under mild conditions, iodine was efficiently incorporated into the PE chains, achieving up to 23 wt% iodine content, while minimising side reactions and polymer chain degradation. The iodinated polymers exhibited substantial changes in crystallinity and melting temperatures, directly correlated with iodine content, as confirmed by FT-IR, TGA, and NMR analyses. The application of this method to isotactic polypropylene (*i*PP) also yielded promising results, with iodine incorporation reaching 22 wt%. Furthermore, the results show that TSE-based iodination is not only environmentally friendly but also compatible with industrial-scale processes.

This work paves the way for new opportunities in the functionalisation of polyolefins, enhancing their potential use in advanced material applications such as medical devices, packaging, and high-performance technologies.

Beyond the iodination reaction itself, the secondary formation of carbon-carbon double bonds observed under extended extrusion conditions emerged as a phenomenon worth investigating in its own right. Building on these observations, Chapter 6 deliberately amplifies this elimination pathway to access conjugated polyene sequences directly embedded within the PE backbone, opening new avenues for the post-functionalisation of commodity polyolefins.

Many thanks to Emna, to whom this chapter is owed. Beyond carrying out the experimental work she authored the original article on which this chapter is based and played a central role in the filing of the associated patent.

IV. EXPERIMENTAL

A. Materials

n-hexadecane (*n*-C16, 99%), sodium hydroxide beads (NaOH, >98.5%), iodoform (CHI_3, 99+%), tetraiodomethane (CI_4, ≥97.0%), iodine (I_2, 99.8%), potassium tert-butoxide (C_4H_9KO, ≥98%), deuterated chloroform (0.03 vol% TMS, deuteration degree min. 99.8% for NMR spectroscopy, stabilised with silver), polyethylene (PE, lot SKU 427772, M_n ~ 1.5 kg/mol, Đ =2.2) and isotactic polypropylene (iPP, lot 428116, M_n ~ 5 kg/mol) were purchased from Sigma Aldrich. 1,5,7-Triazabicyclo[4.4.0]dec-5-ene (TBD) was supplied by Apollo Scientific. 1,8-Diazabicyclo[5.4.0]undec-7-ene (DBU, 98+ %) was supplied by Thermoscientific. Chloroform ($CHCl_3$, 99+% stabilised with amylene), methanol (GPR rectapur) and xylene 99+% (mixture of isomers) were obtained from Chemlab.

B. Procedures

Iodination of *n*-Hexadecane

In a brown glass round-bottom flask equipped with a reflux condenser and a magnetic stirrer bar, *n*-hexadecane (33.96 g, 0.15 mol, 3 eq.), an initial fraction of CHI_3 (4.9 g, 0.0125 mol, 0.25 eq.), and finely powdered NaOH (2.5 g, 0.0675 mol, 1.2 eq.) were combined. The flask was immersed in a silicone oil bath maintained at 106 °C. Every 30 minutes, additional portions of CHI_3 (4.9 g, 0.0125 mol) and NaOH (2.5 g, 0.0675 mol) were added. After two hours, the total amount of CHI_3 was 19.6 g (0.05 mol, 1 eq.) and NaOH was 10 g (0.25 mol, 4.8 eq.) relative to *n*-hexadecane. The reaction mixture was kept at 106 °C under vigorous magnetic stirring for a total of 24 hours. The mixture was then allowed to cool to room temperature and was filtered under vacuum to remove solid by-products. The crude liquid product was collected and subjected to ^{1}H NMR spectroscopy for structural analysis. Conversion yields (CY) are calculated is calculated from the NMR spectrum of said product.

$$CY\ (\%) = \frac{I_{4.12}}{I_{4.12} + \frac{I_{1.26}}{28}}$$

Where $I_{4.12}$ is the integral corresponding to the proton geminal to the iodine atom, which appears at 4.12 ppm, and $I_{1.26}$ is the integral of the fourteen CH_2 of *n*-hexadecane.

Iodination of Polyolefins via Twin-Screw Reactive Extrusion

The samples were prepared using an Xplore DSM vertical microcompounder with a 5 cm^3 capacity. This microcompounder was equipped with intermeshing conical twin-screws that operated at a speed of 200 rpm and included a continuous nitrogen purge. A manual floodgate allowed for either extrusion or recirculation during the reactive extrusion process. To initiate the reaction, 35.7 mmol of polyethylene/polypropylene was loaded into the preheated extruder

chamber at 106 °C. Every 30 minutes, portions of iodoform (CHI_3) and sodium hydroxide (NaOH) were added, with a total of 14 g of iodoform and 1.42 g of sodium hydroxide used. The reaction was maintained at a constant speed for 2 hours. Upon completion, the polymer was recovered and stored in a sample holder for 24 hours to equilibrate to ambient relative humidity. The polymer was then purified by dissolving it in a 50:50 volume mixture of xylene/water (for PE) or toluene/water (for PP), followed by precipitation in methanol. The resulting mixture was vacuum filtered, and the solid was rinsed with methanol and dried overnight under vacuum before characterisation.

C. Methods

NMR Spectroscopy

^{1}H NMR spectra were acquired using a Bruker AVANCEII 500 MHz apparatus at room temperature in chloroform-*d1* ($CDCl_3$). All spectra were recorded at 21 °C according to the following parameters: aq = 2.75 s, d1 = 1 s, sw = 20, with a ns = 32 for *n*-hexadecane and of 512 for PE. The relative error of ^{1}H NMR is in the range of 2 to 5 %.

Fourier Transform Infrared Spectroscopy

The Fourier transform infrared spectra of the samples were acquired by using the attenuated total reflectance (ATR) technique (Bruker, Tensor 27) with OPUS 6.5 software. The spectra were acquired over the wavelength range of 4000– 600 cm^{-1} with 32 spectral scans.

X-ray photoelectron spectroscopy

The sample composition was evaluated using X-ray photoelectron spectroscopy (XPS) with a VERSAPROBE PHI 5000 instrument from Physical Electronics. The instrument was equipped with a monochromatic Al Kα X-ray source. X-ray photoelectron spectra were collected at a take-off angle of 45°, and the electron energy analyser was operated in the CAE (constant analyser energy) mode. To compensate for the built-up charge on the sample surface during measurements, a dual beam charge neutralisation system consisting of an electron gun (approximately 1 eV) and an Ar ion gun (less than or equal to 10 eV) was employed. The binding energies were referenced to the C1s peak at 284.6 eV. Atomic concentration percentages were determined using CasaXPS software based on the XPS data.

Size exclusion chromatography

Size exclusion chromatography (SEC) was performed in THF at 50 °C using a Triple Detection Polymer Laboratories liquid chromatograph equipped with a refractive index (ERMA 7517), a UV detector (254 nm), a capillary viscometry, a light scattering RALS (Viscotek T-60) (Polymer Laboratories GPC-RI/CV / RALS), an automatic injector (Polymer Laboratories GPC-RI/UV) and four columns: a PL gel 10 µm guard column and three PL gel Mixed-B 10 µm columns (linear columns for separation of M_w PS ranging from 500 to 10^6 Daltons). All samples for SEC analyses

were prepared according to the following concentration: 1-5 mg of polymer sample in 1 mL of THF.

Thermogravimetric analysis

Thermal decomposition of samples was studied by thermogravimetric analysis (TGA). The analysis was performed with a TGA Q500 (TA Instruments®, New Castle, USA). Samples of 5-10 mg were loaded into a platinum pan and were heated from 30 to 800 °C with a heating rate of 10 °C.min^{-1} under nitrogen gas.

Differential scanning calorimetry

DSC analysis was conducted using a DSC Q2000 from TA instruments under inert atmosphere (N_2, 50 ml/min). Samples of 5-7 mg were sealed in aluminium DSC pans, placed in the DSC cell and heated from -60 to 150 °C with a heating rate of 10 °C.min^{-1}. The melting temperature (T_m) was based on the second heating scan. The crystallinity degree (X_c) was calculated according to the following equation (1).

$$\chi_c\ (\%) = \frac{\Delta H_f}{\Delta H_f^0}\ x\ 100 \qquad (1)$$

Where ΔH_f is the melting enthalpy of the PE and PP samples while ΔH_f^0 is the standard melting enthalpy of PE (293 J/g) and iPP (207 J/g).

V. SUPPORTING INFORMATION

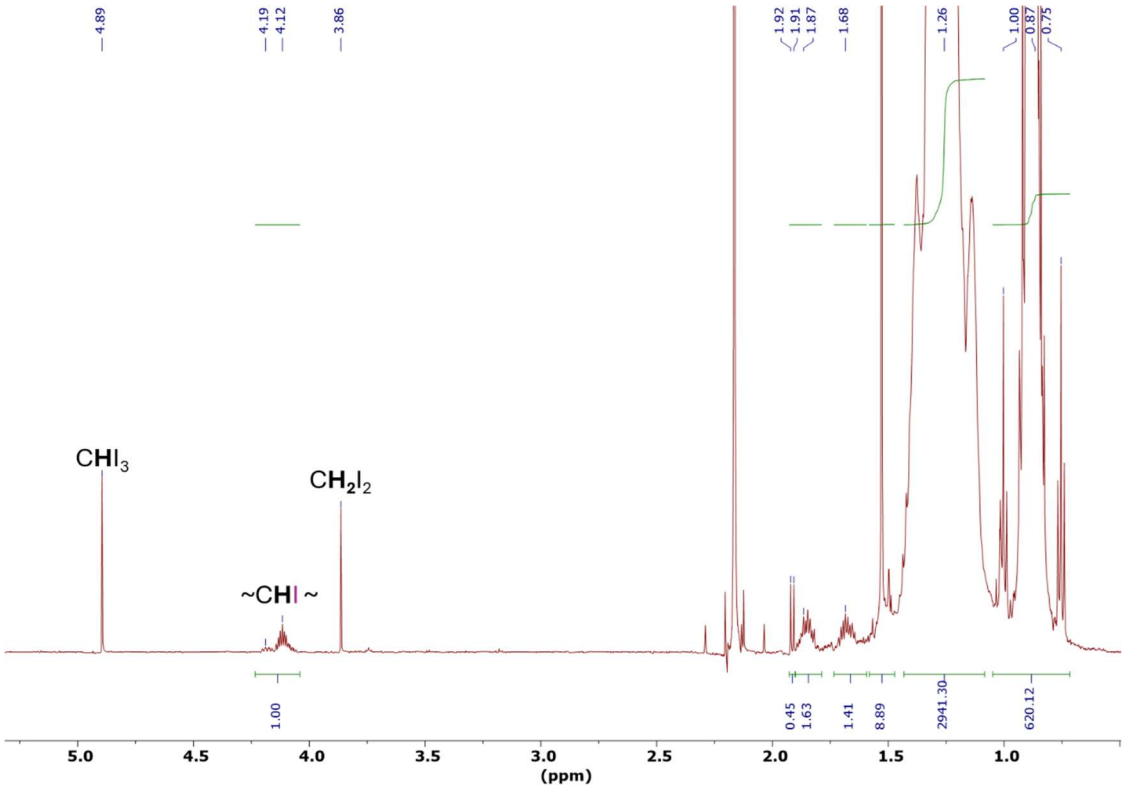


Figure S5.1. ^{1}H NMR spectrum of iodinated *n*-hexadecane (**Table S5.1**, **entry 1**) in $CDCl_3$ (zoomed between δ = 0.5 – 5.25 ppm).

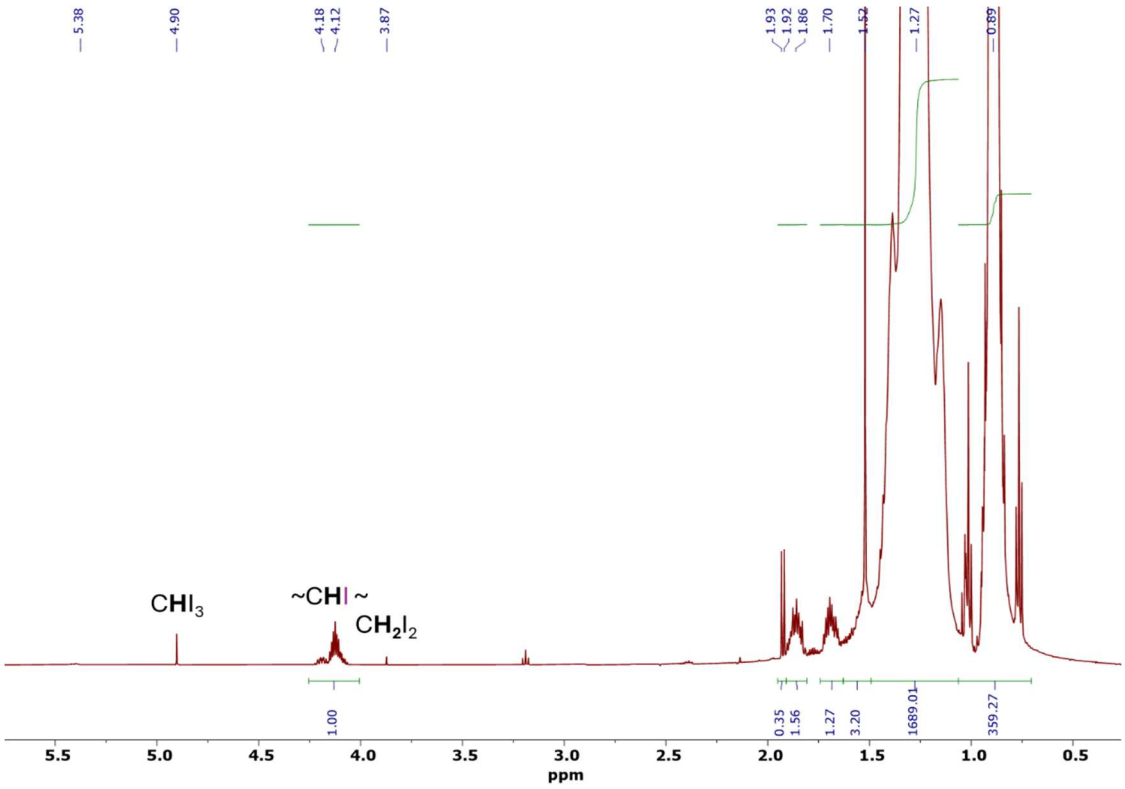


Figure S5.2. ^{1}H NMR spectrum of iodinated *n*-hexadecane (**Table S5.1**, **entry 2**) in $CDCl_3$ (zoomed between δ = 0.3 – 5.8 ppm).

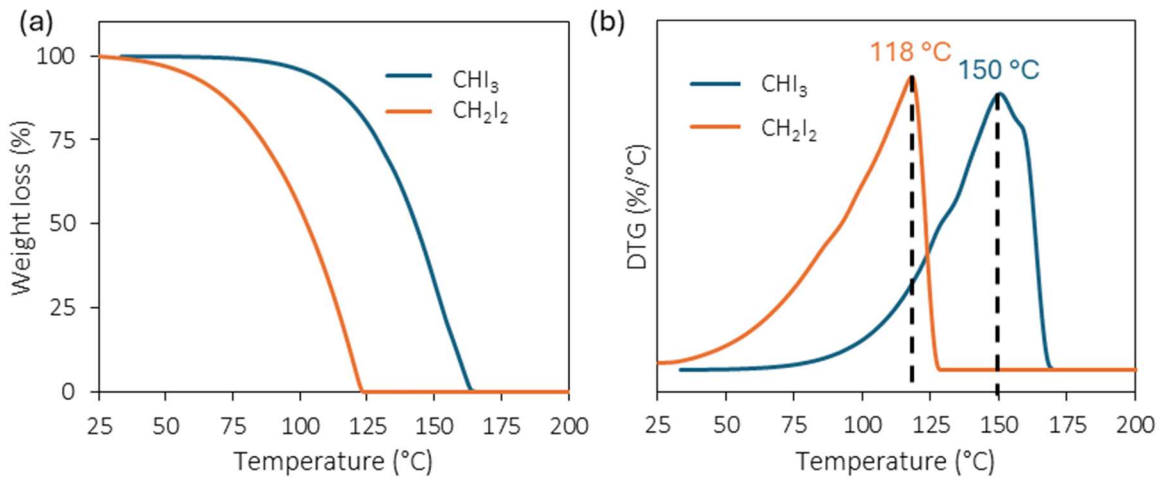


Figure S5.3. (a) TGA and **(b)** corresponding DTG curves of both iodoform (CHI_3, blue) and diiodomethane (CH_2I_2, orange), recorded under nitrogen atmosphere at a rate of 10 °C.min^{-1}.

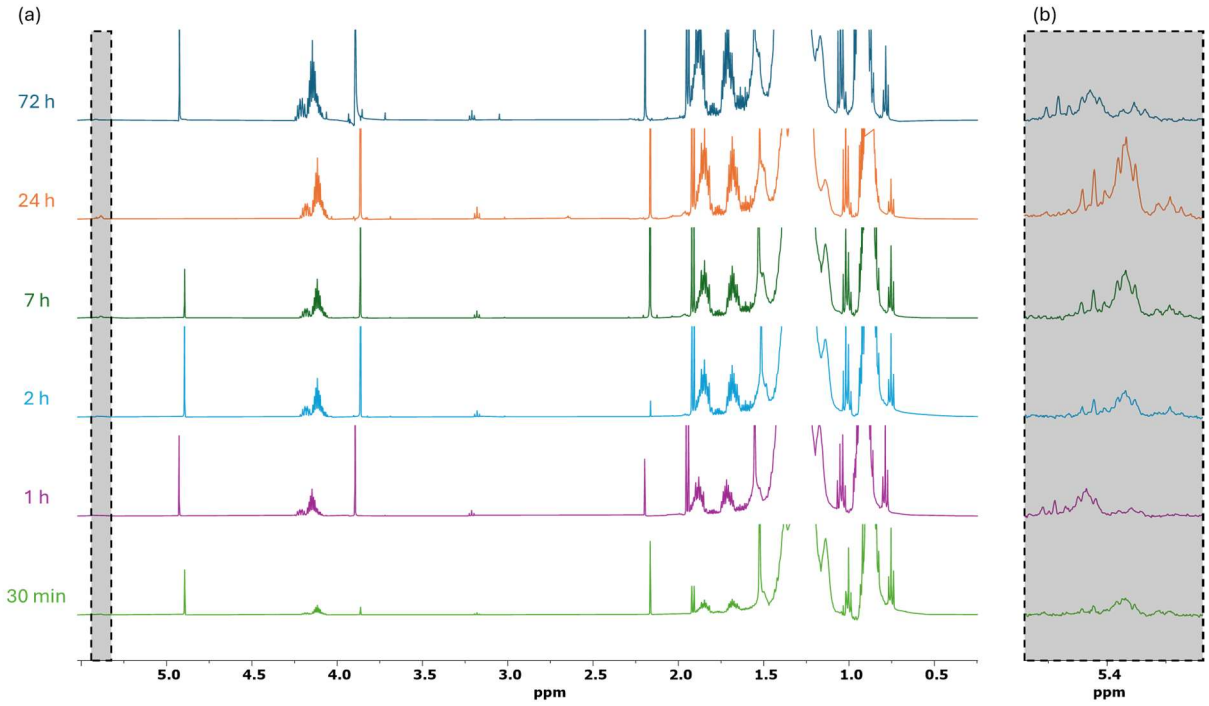


Figure S5.4. Time-dependent iodination of *n*-hexadecane at 95 °C with a ratio of $[n\text{-C16}]_0/[CHI_3]_0/[NaOH]_0$ of 3/1/4.8 monitored by ^{1}H NMR spectroscopy in $CDCl_3$. **(a)** Stack of spectra between δ = 0 and 5.5 ppm and **(b)** corresponding expended spectra at δ = 5.3 – 5.5 ppm focusing on olefinic protons.

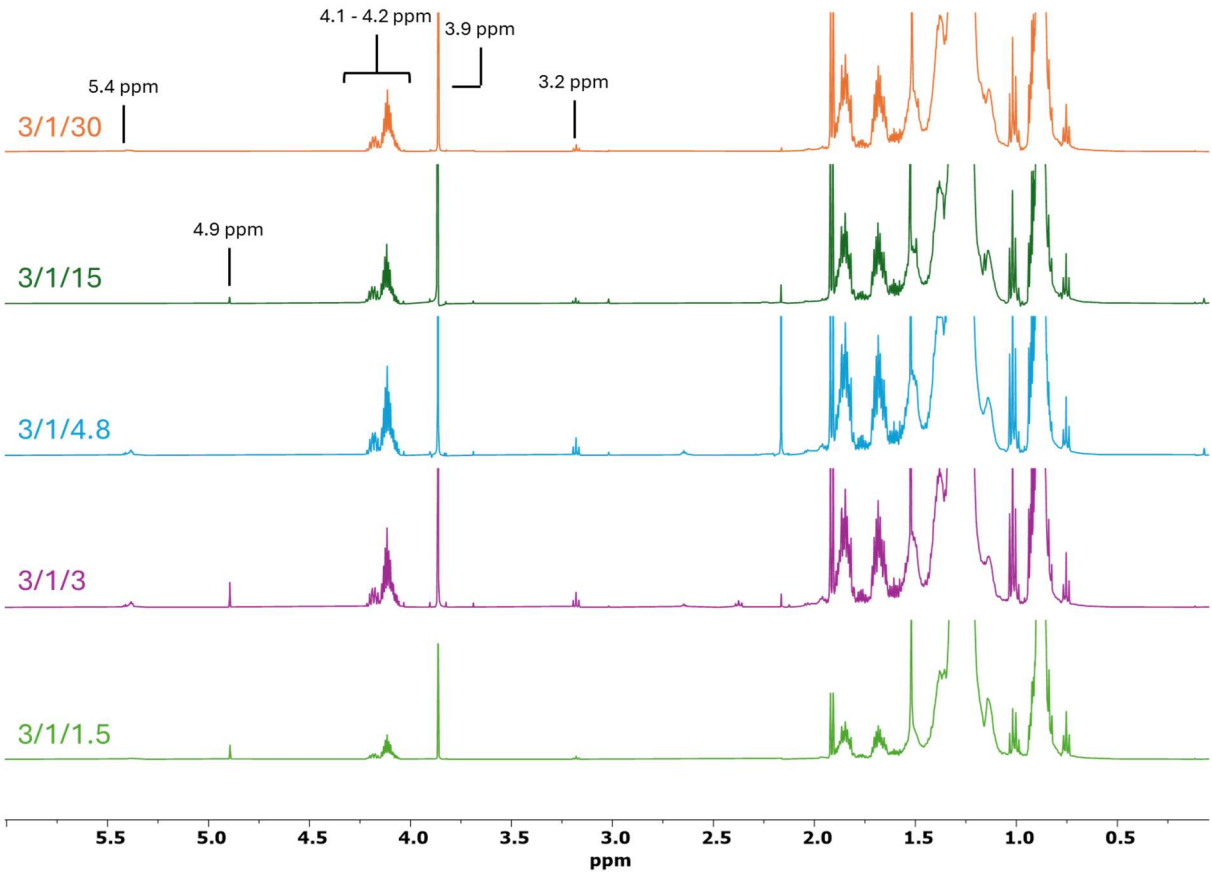


Figure S5.5. NaOH content-dependent iodination of *n*-hexadecane at 95 °C for 24 hours monitored by ^{1}H NMR spectroscopy in $CDCl_3$. Zoomed spectra between δ = 0 ppm and δ = 6 ppm.

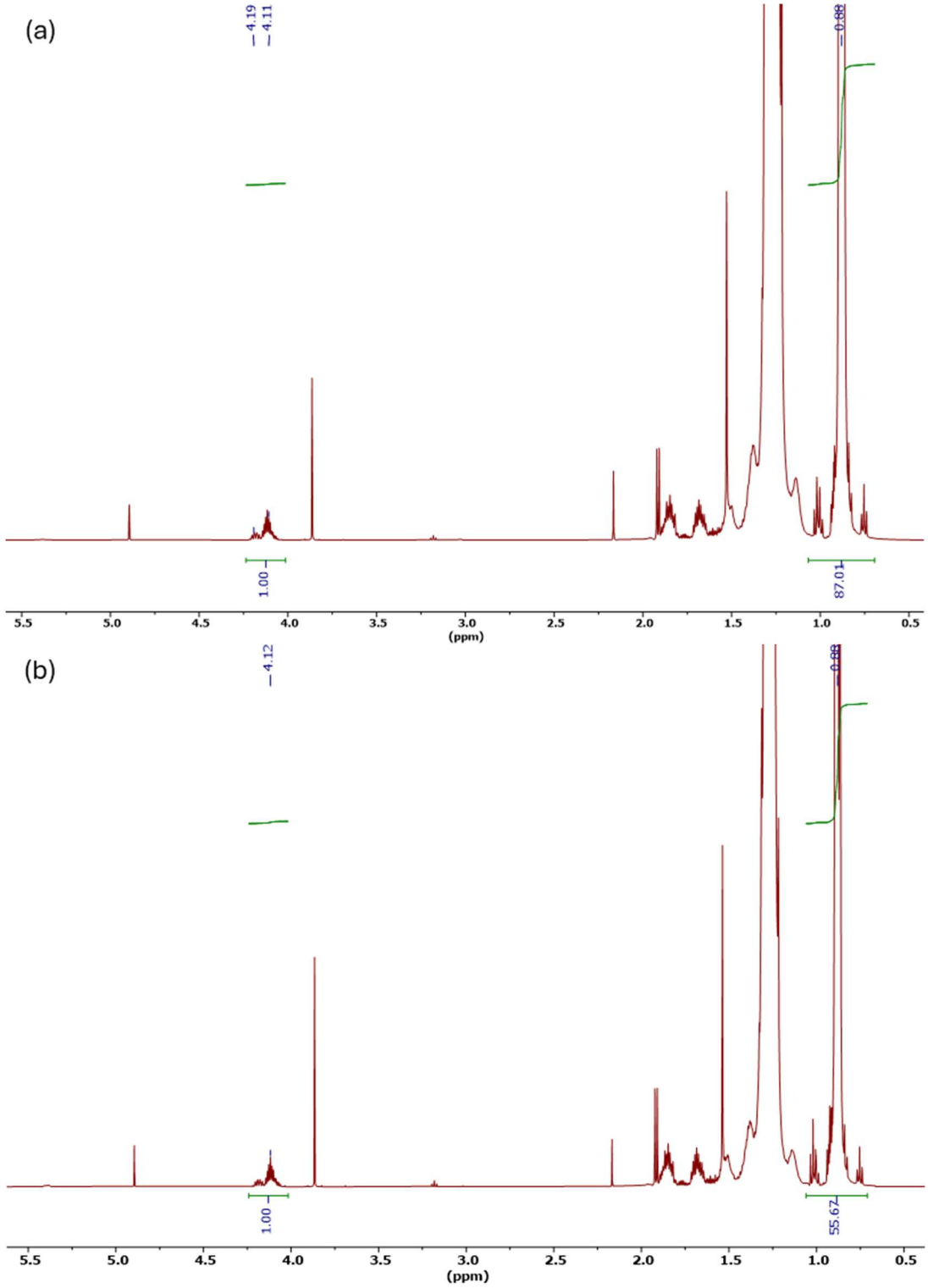


Figure S5.6. ^{1}H NMR spectra of iodinated n-hexadecane subjected to magnetic stirring at 400 rpm for a duration of 2 hours at 95 °C ($CDCl_3$, zoomed between δ = 0.5 and 5.5 ppm). **(a)** Product of the iodination reaction under standard conditions, and **(b)** product obtained after gradual addition of CHI_3 and NaOH every 30 minutes for the same duration.

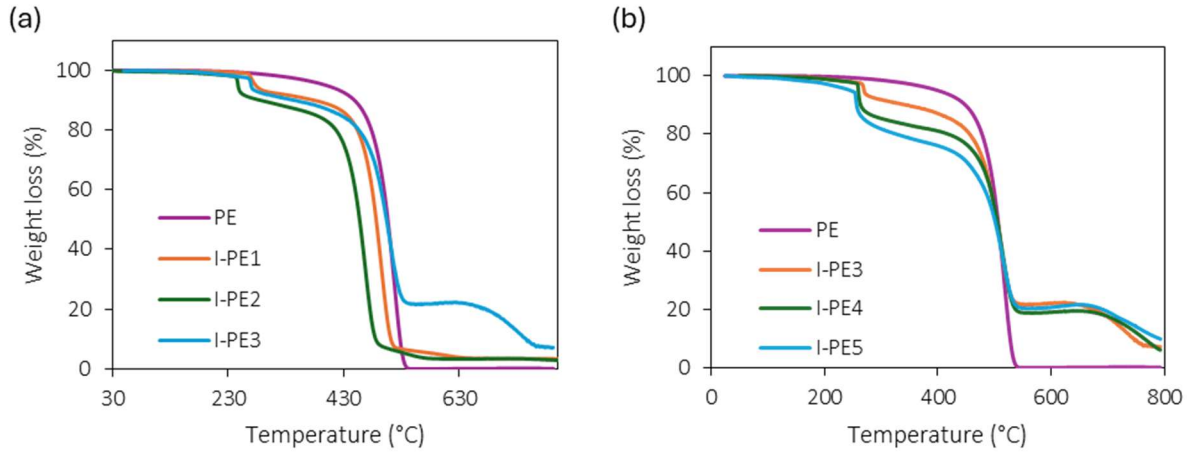


Figure S5.7. TGA curves of **(a)** iodinated PE obtained from different $[Ethylene]_0/[CHI_3]_0/[NaOH]_0$ ratios and **(b)** iodinated PE subjected to different shearing forces under an inert atmosphere (N_2) at a rate of 10 °C.min^{-1}.

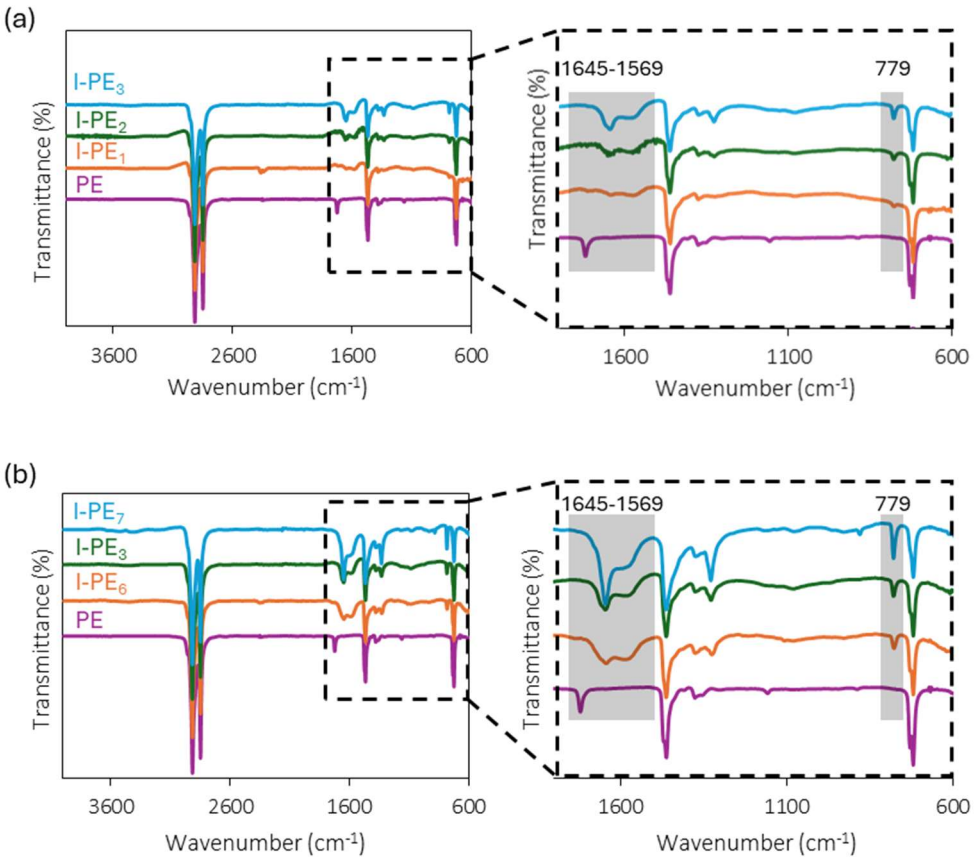


Figure S5.8. ATR-FTIR spectra of the PE starting material and some iodinated PE with **(a)** different feeding ratios and at **(b)** different residence times.

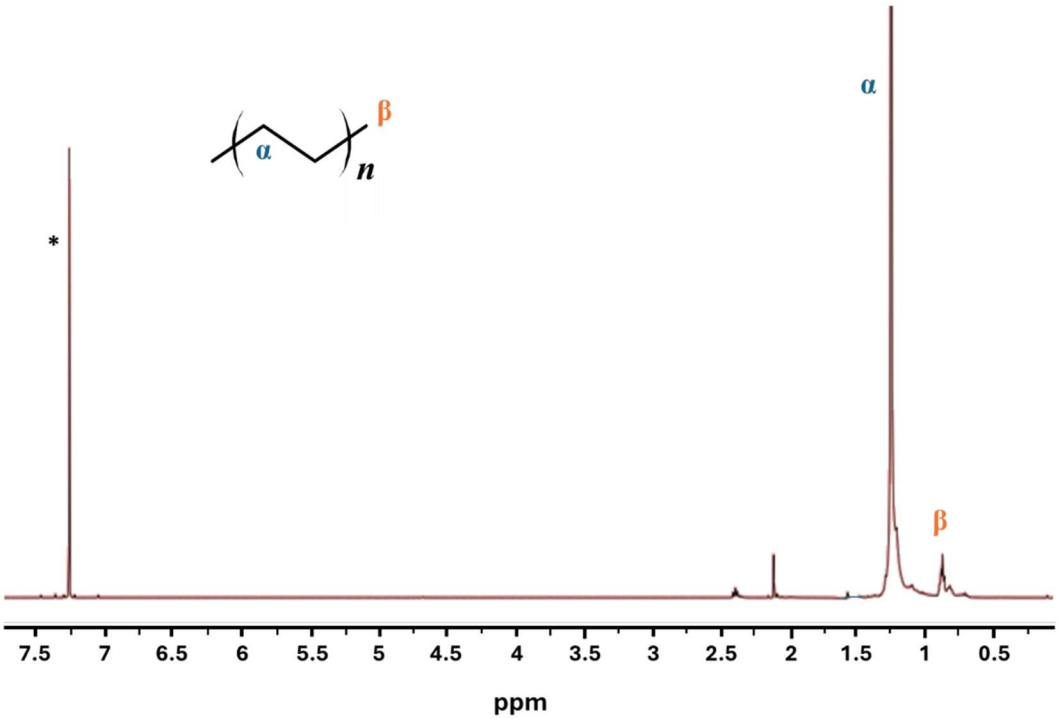


Figure S5.9. ^{1}H NMR spectrum of unmodified PE in chloroform ($CDCl_3$) at room temperature. *$CHCl_3$

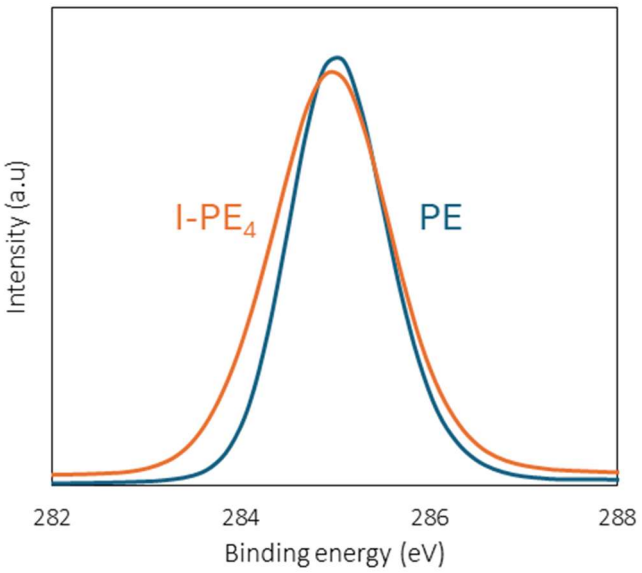


Figure S5.10. C1s XPS spectra of untreated polyethylene and iodinated PE (**I-PE$_4$** = $[Ethylene]_0/[CHI_3]_0/[NaOH]_0$= 1/1/1; 2 hours; SS= 200 rpm).

VI. REFERENCES

1 B. A. Arndtsen, R. G. Bergman, T. A. Mobley and T. H. Peterson, *Accounts of Chemical Research*, 1995, **28**, 154–162.

2 K. M. Engle, T.-S. Mei, M. Wasa and J.-Q. Yu, *Accounts of Chemical Research*, 2012, **45**, 788–802.

3 J. Yamaguchi, A. D. Yamaguchi and K. Itami, *Angewandte Chemie International Edition*, 2012, **51**, 8960–9009.

4 W. R. Gutekunst and P. S. Baran, *Chemical Society Reviews*, 2011, **40**, 1976–1991.

5 H. M. L. Davies and D. Morton, *The Journal of Organic Chemistry*, 2016, **81**, 343–350.

6 J. F. Hartwig and M. A. Larsen, *ACS Central Science*, 2016, **2**, 281–292.

7 A. E. Shilov, *Activation of Saturated Hydrocarbons by Transition Metal Complexes*, Springer Netherlands, 1984.

8 H. M. L. Davies and J. R. Manning, *Nature*, 2008, **451**, 417–424.

9 M. P. Doyle, R. Duffy, M. Ratnikov and L. Zhou, *Chemical Reviews*, 2010, **110**, 704–724.

10 R. H. Crabtree, *Journal of the Chemical Society, Dalton Transactions*, 2001, **17**, 2437–2450.

11 R. Breslow and S. H. Gellman, *Journal of the Chemical Society, Chemical Communications*, 1982, **24**, 1400–1401.

12 J. T. Groves, T. E. Nemo and R. S. Myers, *Journal of the American Chemical Society*, 1979, **101**, 1032–1033.

13 M. Goswami and B. de Bruin, *European Journal of Organic Chemistry*, 2017, **2017**, 1152–1176.

14 A. Demonceau, A. F. Noels, A. J. Hubert and P. Teyssié, *Bulletin des Sociétés Chimiques Belges*, 1984, **93**, 945–948.

15 R. H. Crabtree, J. M. Mihelcic and J. M. Quirk, *Journal of the American Chemical Society*, 1979, **101**, 7738–7740.

16 G. A. Russell and H. C. Brown, *Journal of the American Chemical Society*, 1955, **77**, 4578–4582.

17 W. Liu and J. T. Groves, *Journal of the American Chemical Society*, 2010, **132**, 12847–12849.

18 C. Bae, J. F. Hartwig, N. K. Boaen Harris, R. O. Long, K. S. Anderson and M. A. Hillmyer, *Journal of the American Chemical Society*, 2005, **127**, 767–776.

19 H. Chen, S. Schlecht, T. C. Semple and J. F. Hartwig, *Science*, 2000, **287**, 1995–1997.

20 P. R. Schreiner and A. A. Fokin, *The Chemical Record*, 2004, **3**, 247–257.

21 A. A. Fokin and P. R. Schreiner, *Advanced Synthesis & Catalysis*, 2003, **345**, 1035–1052.

22 H. Tu, S. Zhu, F.-L. Qing and L. Chu, *Tetrahedron Letters*, 2018, **59**, 173–179.

23 S. Roy, S. Panja, S. R. Sahoo, S. Chatterjee and D. Maiti, *Chemical Society Reviews*, 2023, **52**, 2391–2479.

24 P. Renaud and M. P. Sibi, Eds., *Radicals in Organic Synthesis*, Wiley, 1st edn., 2001.

25 F. Minisci, O. Porta, F. Recupero, C. Gambarotti, R. Paganelli, G. F. Pedulli and F. Fontana, *Tetrahedron Letters*, 2004, **45**, 1607–1609.

26 Y. Amaoka, S. Kamijo, T. Hoshikawa and M. Inoue, *The Journal of Organic Chemistry*, 2012, **77**, 9959–9969.

27 V. A. Schmidt, R. K. Quinn, A. T. Brusoe and E. J. Alexanian, *Journal of the American Chemical Society*, 2014, **136**, 14389–14392.

28 R. K. Quinn, Z. A. Könst, S. E. Michalak, Y. Schmidt, A. R. Szklarski, A. R. Flores, S. Nam, D. A. Horne, C. D. Vanderwal and E. J. Alexanian, *Journal of the American Chemical Society*, 2016, **138**, 696–702.

29 M. M. Tierney, S. Crespi, D. Ravelli and E. J. Alexanian, *The Journal of Organic Chemistry*, 2019, **84**, 12983–12991.

30 T. J. Fazekas, J. W. Alty, E. K. Neidhart, A. S. Miller, F. A. Leibfarth and E. J. Alexanian, *Science*, 2022, **375**, 545–550.

31 W. L. Czaplyski, C. G. Na and E. J. Alexanian, *Journal of the American Chemical Society*, 2016, **138**, 13854–13857.

32 A. Artaryan, A. Mardyukov, K. Kulbitski, I. Avigdori, G. A. Nisnevich, P. R. Schreiner and M. Gandelman, *The Journal of Organic Chemistry*, 2017, **82**, 7093–7100.

33 P. R. Schreiner, O. Lauenstein, E. D. Butova and A. A. Fokin, *Angewandte Chemie International Edition*, 1999, **38**, 2786–2788.

34 L. Liguori, H.-R. Bjorsvik, A. Bravo, F. Fontana, and F. Minisci, *Chemical Communications*, 1997, **16**, 1501-1502.

35 R. Montoro and T. Wirth, *Organic Letters*, 2003, **5**, 4729–4731.

36 D. D. Tanner and G. C. Gidley, *Journal of the American Chemical Society*, 1968, **90**, 808–809.

37 J. Barluenga, E. Campos-Gómez, D. Rodríguez, F. González-Bobes and J. M. González, *Angewandte Chemie International Edition*, 2005, **44**, 5851–5854.

38 S. H. Combe, A. Hosseini, L. Song, H. Hausmann and P. R. Schreiner, *Organic Letters*, 2017, **19**, 6156–6159.

39 J. B. Williamson, S. E. Lewis, R. R. Johnson, I. M. Manning and F. A. Leibfarth, *Angewandte Chemie International Edition*, 2019, **58**, 8654–8668.

40 Y. K. Kim, in *Polyolefin Fibres*, Elsevier, 2017, 135–155.

41 H. Zhou, S. Wang, H. Huang, Z. Li, C. M. Plummer, S. Wang, W.-H. Sun and Y. Chen, *Macromolecules*, 2017, **50**, 3510–3515.

42 C. M. Plummer, H. Zhou, W. Zhu, H. Huang, L. Liu and Y. Chen, *Polymer Chemistry*, 2018, **9**, 1309–1317.

43 G. D. Cooper and M. Prober, *Journal of Polymer Science*, 1960, **44**, 397–409.

44 S. E. Lehman, K. B. Wagener, L. S. Baugh, S. P. Rucker, D. N. Schulz, M. Varma-Nair and E. Berluche, *Macromolecules*, 2007, **40**, 2643–2656.

45 S. R. Holmes-Farley, R. H. Reamey, R. Nuzzo, T. J. McCarthy and G. M. Whitesides, *Langmuir*, 1987, **3**, 799–815.

46 A. Shoji, T. Adachi, M. Tsuchiya, M. Fujishima, D. S. Kumar and Y. Yoshida, *Journal of Photopolymer Science and Technology*, 2005, **18**, 251–254.

47 M. Fujishima, D. Kawabata, C. Funakoshi, Y. Yoshida, T. Yamashita, K. Kashiwagi and K. Higashikata, *Polymer Journal*, 1995, **27**, 575–578.

48 J. B. Williamson, W. L. Czaplyski, E. J. Alexanian and F. A. Leibfarth, *Angewandte Chemie*, 2018, **130**, 6369–6373.

49 L. Cluzeau, F. Robert, D. M. Bassani, Y. Landais and D. Taton, *Angewandte Chemie International Edition*, 2026, **65**, e20646.

50 J. Friedrich, S. Wettmarshausen and M. Hennecke, *Surface and Coatings Technology*, 2009, **203**, 3647–3655.

51 J. H. Dully, F. J. Wodarczyk and J. J. Ratto, *Journal of Polymer Science Part A: Polymer Chemistry*, 1987, **25**, 1187–1190.

52 H. S. Munro, R. J. Ward and E. Khor, *Journal of Polymer Science Part A: Polymer Chemistry*, 1990, **28**, 923–929.

53 J. F. Elman, L. J. Gerenser, K. E. Goppert-Berarducci and J. M. Pochan, *Macromolecules*, 1990, **23**, 3922–3928.

54 P. R. Schreiner, O. Lauenstein, I. V. Kolomitsyn, S. Nadi and A. A. Fokin, *Angewandte Chemie International Edition*, 1998, **37**, 1895–1897.

55 P. R. Schreiner, O. Lauenstein, E. D. Butova, P. A. Gunchenko, I. V. Kolomitsin, A. Wittkopp, G. Feder and A. A. Fokin, *Chemistry - A European Journal*, 2001, **7**, 4996–5003.

56 J. Chmelar, P. Matuska, T. Gregor, M. Bobak, F. Fantinel and J. Kosek, *Chemical Engineering Journal*, 2013, **228**, 907–916.

57 E. V. Dehmlow and M. Lissel, *Chemische Berichte*, 1978, **111**, 3873–3878.

58 G. H. Aylward and T. J. Findlay, *Datensammlung Chemie in SI-Einheiten*, John Wiley & Sons, 2014.

59 E. V. Dehmlow, M. Lissel and J. Heider, *Tetrahedron*, 1977, **33**, 363–366.

60 E. Boz, K. B. Wagener, A. Ghosal, R. Fu and R. G. Alamo, *Macromolecules*, 2006, **39**, 4437–4447.

61 M. D. Watson and K. B. Wagener, *Macromolecules*, 2000, **33**, 8963–8970.

62 J. V. Gulmine, P. R. Janissek, H. M. Heise and L. Akcelrud, *Polymer Testing*, 2002, **21**, 557–563.

63 B. Couturaud, A. Mas and J. J. Robin, *European Polymer Journal*, 2015, **70**, 276–285.

64 J. Coates, in *Encyclopedia of Analytical Chemistry*, ed. R. A. Meyers, Wiley, 1st edn., 2000.

65 S. S. Soomro, D. Cozzula, W. Leitner, H. Vogt and T. E. Müller, *Polymer Chemistry*, 2014, **5**, 3831–3837.

66 B. Lesiak, L. Kövér, J. Tóth, J. Zemek, P. Jiricek, A. Kromka and N. Rangam, *Applied Surface Science*, 2018, **452**, 223–231.

67 X. Wang, Y. Wang, X. Shi, J. Liu, C. Chen and Y. Li, *Macromolecules*, 2014, **47**, 552–559.

68 M. Zhang, R. H. Colby, S. T. Milner, T. C. M. Chung, T. Huang and W. deGroot, *Macromolecules*, 2013, **46**, 4313–4323.

69 G. Moad, *Progress in Polymer Science*, 1999, **24**, 81–142.

70 P. E. Gloor, Y. Tang, A. E. Kostanska and A. E. Hamielec, *Polymer*, 1994, **35**, 1012–1030.

71 D. Tripathi, *Practical guide to polypropylene*, iSmithers Rapra Publishing, 2002.

72 H. Ö. Gülsoy and M. Taşdemır, *International Journal of Polymeric Materials*, 2006, **55**, 619–626.

73 R. M. Khafagy and Y. A. Badr, *J. Polym. Sci. B Polym. Phys.*, 2005, **43**, 2829–2842.

CHAPTER 6

From Polyethylene to Conjugated Polyenes: A Mechanochemical One-Pot Upcycling Strategy for Selective Functionalisation



Ben Ayed E., Delcorps J., Coulembier O., *Advanced Sustainable Systems*, 2025, 9, 9, e00571. https://doi.org/10.1002/adsu.202500571

TABLE OF CONTENTS

I. INTRODUCTION 226

II. RESULTS AND DISCUSSION 228

III. CONCLUSION 237

IV. EXPERIMENTAL 238

A. Materials 238

B. Procedures 238

C. Methods 239

V. SUPPORTING INFORMATION 242

VI. REFERENCES 244

I. INTRODUCTION

Plastic materials have dominated nearly every aspect of daily life since the 1950s. Their versatility explains their widespread use: they are mouldable, dyeable to meet consumer preferences, chemically inert, lightweight, and offer tailored physical and mechanical properties.[1] These properties have led to their dominance, with global production reaching 413.8 million tons (Mt) in 2023 and projected to exceed 500 Mt by 2050.[2] Polyolefins account for at least 40% of the plastics consumed worldwide, primarily in short-lived applications like packaging, one of the most problematic plastic uses. A large portion of these plastics ends up in terrestrial and aquatic ecosystems, contributing significantly to greenhouse gas emissions[3] and exacerbating global warming, posing catastrophic threats to planetary health. Reports have shown that polyethylene is one of the largest emitters of methane and ethylene.[4] Various approaches to address post-consumer polyolefins, such as mechanical recycling, chemical recycling, and incineration, have been implemented. However, mechanical recycling compromises product quality, chemical recycling produces complex hydrocarbon blends that are difficult to separate, and incineration releases substantial quantities of greenhouse gases.[5,6] Recovering polymer subunits is also energetically inefficient.[5]

The concept of "upcycling" has emerged as a promising approach, involving the transformation of post-consumer polyolefins into value-added products by introducing active sites into their chemical structures. This process enables reactions that produce valuable products for further use. One of the most studied processes is dehydrogenation, which weakens the main polymer chains by forming double bonds. Dehydrogenation can be achieved using metallic catalysts, such as iridium complexes,[7] to introduce unsaturations or serve as an intermediate step for reactions like tandem ethenolysis and isomerisation (Iridium complex/$ZnSiO_2$, Na/γ-Al_2O_3-WO_3/SiO_2)[8,9] and cross-alkane metathesis (Ru-based complexes[10,11], Iridium complexes[12]). Additionally, dehydrogenation has been explored for Diels–Alder reactions to produce comonomers and break down high-density polyethylene into telechelic macromonomers for depolymerisation and repolymerisation.[13] Despite the potential of these reactions, several challenges hinder their large-scale application. Many catalysts are prohibitively expensive, air-sensitive, and occasionally toxic (especially Ru-based catalysts),[14] making them impractical for widespread use. Catalyst deactivation is another major limitation, often caused by the reaction duration or the presence of impurities and contaminants in post-consumer plastics.[10,15] Furthermore, some catalysts require a certain percentage of unsaturation to initiate the reaction, adding another layer of complexity.[16]

In this context, reactive extrusion has emerged as a powerful and scalable platform for polyolefin upcycling, combining mechanical, thermal, and chemical stimuli in a continuous process to selectively functionalise polymer chains while minimising undesired side reactions.[17–19] Recent advances demonstrate that radical-based C-H functionalisation can be

performed directly within twin-screw extruders, enabling the introduction of functional groups that improve polymer adhesion and mechanical properties without compromising polymer integrity.[19,20] Additionally, reactive extrusion has proven effective in treating mixed or incompatible polyolefin blends, where *in situ* cross-linking and grafting reactions generate phase-separated nanostructures that enhance ductility, dimensional stability, and recyclability.[18] Mechanochemical activation under extrusion conditions further allows for the initiation of radical chain reactions under mild, solvent-free conditions with energy efficiency and operational simplicity.[21,22] These attributes establish reactive extrusion as a key tool in developing innovative, sustainable approaches for polyolefin valorisation, motivating its application in the present study.

In the previous chapter, we developed a solvent-free, mild-temperature extrusion process that enables the direct iodination of polyolefins using iodoform (CHI_3) as the iodine source and sodium hydroxide (NaOH) as a free-radical initiator.[23] Operating at low temperature (106 °C), this method facilitates the efficient functionalisation of both polyethylene (PE) and polypropylene (PP), achieving up to 23 wt% iodine incorporation, without chain scission, in a kinetically controlled process. Notably, prolonged extrusion led to the formation of few in-chain C=C bonds, as demonstrated by various spectroscopic and thermal techniques. The extent of these unsaturations was found to correlate with both the initiator content and the applied shear forces, ultimately influencing the polymer solubility and reactivity. Investigations on a model *n*-hexadecane (*n*-C16) molecule, easy to characterise by NMR spectroscopy, revealed that although iodination proceeded efficiently at the onset of the reaction, the iodine conversion unexpectedly declined after extended reaction times. For instance, under reaction conditions with a $[n\text{-C16}]_0/[CHI_3]_0/[NaOH]_0$ ratio of 1/1/1 at 106 °C, ^{1}H NMR spectroscopy showed that after 2 hours, one iodine atom was incorporated per four *n*-C16 chains, while one chain out of 200 carried a carbon-carbon double bond. After 144 hours of reaction, however, the iodination decreased, with one iodine atom incorporated per six chains and one chain out of eight exhibiting a double bond (**Figures S6.1 – S6.2**, **p. 242**). This basic model indicated a dynamic interplay between iodination and elimination reactions, even under conditions not optimised for efficient elimination. Initially, CHI_3 and NaOH promoted iodination, but beyond a certain threshold, NaOH started acting as a base, inducing elimination and leading to the formation of unsaturated species. Unlike conventional dehydrogenation methods that require costly, air-sensitive metal catalysts, this transformation occurred under simple, metal-free conditions using NaOH - a widely available and inexpensive base - without the need for solvents or complex reaction setups. These advantages have motivated us to further explore this process to assess its potential as a scalable and cost-effective method for introducing double bonds into polyolefins under mild extrusion conditions (**Figure 6.1**).

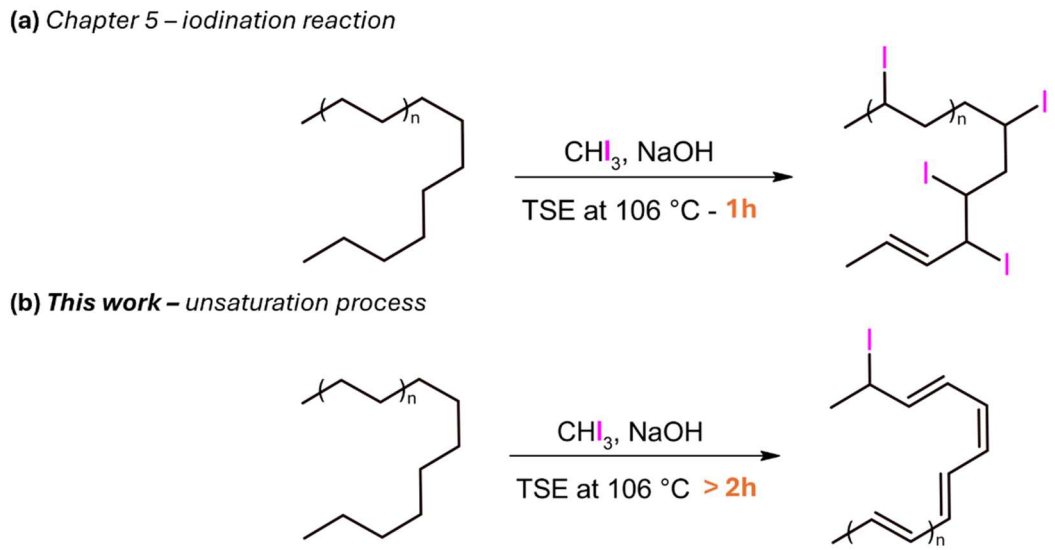


Figure 6.7. Iodination vs. elimination: tuning polyolefin reactivity under mild extrusion conditions. (a) Previously developed solvent-free iodination of polyethylene using CHI_3 and NaOH, leading to well-defined iodinated polymers. **(see Chapter 5) (b)** This work: controlled shear-induced elimination promotes the formation of polyolefins with multiple unsaturations while retaining residual iodine functionalities. TSE: Twin-screw extrusion.

Beyond its chemical innovation, this work contributes to the United Nations Sustainable Development Goals, particularly SDG 12 (Responsible Consumption and Production), by proposing a scalable and solvent-free upcycling strategy for polyolefins. It opens new avenues for converting plastic waste into higher-value functional materials, offering a more circular and sustainable approach to plastic use.

II. RESULTS AND DISCUSSION

To further investigate the influence of reaction parameters on the balance between iodination and elimination, the proportion of elimination reactions was enhanced by increasing shear force and reaction time while maintaining a minimal NaOH concentration. Although NaOH is a widely available and inexpensive base, its excessive use was avoided to limit unnecessary side effects. Instead, two samples were prepared under medium to high shear conditions (screw speed (SS) of 200 to 300 rpm), with reaction times of 2 hours (**PE_1**) and 5 hours (**PE_2**) for an initial $[C_2H_4]_0/[CHI_3]_0/[NaOH]_0$ of 1 (see Chapter 5). To facilitate processing and to enable precise structural modifications, the study was conducted on a low-molecular-weight linear low-density polyethylene (LLDPE; theoretical M_n ~1500 g/mol). This model system provides a controlled platform to probe chemical reactivity under mild conditions, with potential for extension to post-consumer polyolefin waste streams, including low-density polyethylene (LDPE). LDPE is widely used in packaging materials such as films and plastic bags, yet often regarded as challenging to recycle due to its low density and branched structure. Nevertheless, LDPE represents a significant portion of global plastic waste and is actively targeted in mechanical and chemical

recycling schemes. In Belgium alone, plastic packaging waste accounts for ~ 366,000 tons annually, with LDPE films constituting a major fraction.[24]

Encouragingly, Belgium ranks among the top EU performers in plastic recycling, with packaging plastics recycled at a rate of 54% in 2022 - up from 29% in 2002.[25] This improvement is largely attributed to the implementation of inclusive collection systems (e.g., the "New Blue Bag" scheme) that now encompass flexible LDPE-based materials.[26] Several industrial initiatives illustrate the strategic importance of LDPE recycling. For instance, Raff Plastics (Londerzeel) specialises in recycling industrial LDPE waste into high-quality compounds for construction and manufacturing.[27] Phoenix Plus SA handles post-consumer LDPE along with other polyolefins, transforming waste into reusable feedstocks for international markets.[28] In Beringen, Chiro has developed advanced AI-based sorting lines specifically tailored for LDPE films, producing recycled materials of commercial quality.[29]

These examples underscore the relevance of LDPE as a recyclable polyolefin. In line with this, we have previously demonstrated that our iodination procedure - applied to isotactic polypropylene at 106 °C, *ca.* 30 °C below its melting point - allowed successful functionalisation without chain scission. This supports the generalisability of our method to chemically modify polyolefin waste streams, including LDPE, under industrially relevant conditions. To evaluate the practical feasibility of such modifications, we revisited our iodination/elimination protocol under controlled conditions. Our previous studies had already demonstrated that 2 hours of reaction led to **PE** modified with 15 wt% iodine, while also exhibiting a significant degree of unsaturation, as attested by the appearance of a charring plateau around 19 wt% during thermogravimetric analysis (TGA, **Figure 6.2a,** see also **Figure 5.4a** in Chapter 5, page 189).[23] Extending the reaction time to 5 hours allowed a deeper assessment of the impact of prolonged extrusion on the competition between iodination and elimination. For **PE_2**, a 9 wt% iodine loss and a charring plateau of 32 wt% were observed (**Figure 6.2a**), providing additional insight into the dynamics of iodination and elimination under these conditions, thus reinforcing the understanding of the reaction balance under mild yet mechanically intense conditions. The moderated solubility of **PE_1** and the full insolubility of **PE_2** prevented direct comparison by ^{1}H NMR spectroscopy. A differential scanning calorimetry (DSC) study was used to observe the impact of the degree of unsaturation on the thermal behaviour of the samples, as it does not directly quantify carbon-carbon double bonds. Compared to pristine **PE** (T_m = 105 °C and X_c = 21%), **PE_1** exhibited a lower melting point and crystallinity (T_m = 83 °C, X_c = 7%), while **PE_2** displayed an even more pronounced decrease (T_m = 66.3 °C, X_c = 3%) (**Figure 6.2b**). This progressive loss of crystallinity with increasing reaction time under high shear conditions strongly suggests that elimination reactions disrupt the polymer ordered domains, leading to a higher incorporation of unsaturations within the polymer matrix.

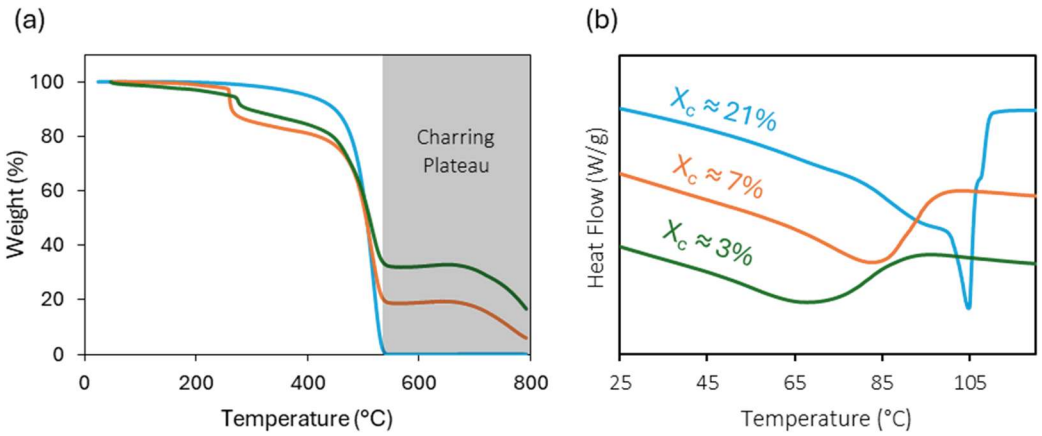


Figure 6.2. (a) TGA curves and **(b)** DSC third heating thermograms of pristine PE (blue) and functionalised samples **PE_1** (orange) and **PE_2** (green). Exo up.

To gain further insights into the nature of these unsaturations, attenuated total reflectance Fourier-transform infrared (ATR-FTIR) spectroscopy was employed to investigate the molecular structure of modified polyethylene samples (**PE_1** and **PE_2**) in comparison with pristine **PE**. The spectrum of pristine **PE** exhibited four distinct absorption bands at 2918, 2850, 1465, and 721 cm^{-1}, corresponding to CH_2 asymmetric stretching, CH_2 symmetric stretching, CH_2 bending vibrations, and CH_2 rocking motions, respectively.[30] In contrast, the spectra of **PE_1** and **PE_2** showed a broader CH_2 bending peak centred around 1463 cm^{-1}, suggesting alterations in the local molecular environment due to modification.[31] Moreover, new absorption bands emerged at ≈1330 and 779 cm^{-1}, attributable to CH_3 deformation modes. Particularly noteworthy were the broad absorption features observed in the 1645 - 1569 cm^{-1} region, characteristic of C=C stretching vibrations, along with a distinct band at 779 cm^{-1}, indicative of =C-H bending modes associated with the *cis* isomer of internal alkenes (**Figure 6.3a**).[32] Interestingly, this observation contrasts with the recent work by Zeng *et al.*,[33] where the elimination of bromine atoms led to the preferential formation of *trans*-internal alkenes, the thermodynamically more stable isomer.[34] Additionally, the stretching mode peak shifted to higher frequencies, suggesting the presence of conjugated double bonds and polyene sequences,[35,36] a hypothesis requiring further spectroscopic confirmation. Notably, no oxidation of the double bonds was detected, as evidenced by the absence of a peak at 1710 cm^{-1} associated with carbonyl groups.[32] To confirm the conjugation hypothesis inferred from FTIR analysis, Raman spectroscopy was performed using an excitation wavelength of 523 nm. For **PE_1**, a strong peak was observed at 1589 cm^{-1}, assigned to the C=C stretching mode within a conjugated system, specifically a *cis* isomer configuration.[37,38] As depicted in **Figure 6.3b**, a secondary peak merges with the primary peak, forming an intermediate frequency. Previous studies on short conjugated systems have attributed such behaviour to coupling between the C–C and C=C stretching modes, a phenomenon characteristic of relatively short polyene sequences.[39] In contrast, no significant Raman signal was detected for **PE_2**, even at a higher excitation wavelength of 783 nm, suggesting that extensive structural modifications hinder effective resonance enhancement.

Further insights into the nature of these polyenes were obtained via solid-state cross-polarisation magic-angle spinning (CP-MAS) ^{13}C NMR spectroscopy analyses performed by Dr. Chirstophe Detrembleur's team (**Figure 6.3c**). The **PE_1** and **PE_2**-based spectra displayed a broad peak around δ = 100 ppm, confirming the presence of the *cis* isomer previously identified by FTIR and Raman spectroscopy. Interestingly, the observed chemical shifts appeared at lower frequencies than those typically reported for conjugated polyenes,[40,41] likely due to the influence of iodine atoms. While iodine introduces polarity, it may also disrupt conjugation, affecting the electronic environment and spectral characteristics.[42] Additionally, factors such as polyene chain length, bond alternation, and angular strain further modulate the chemical shifts.[43]

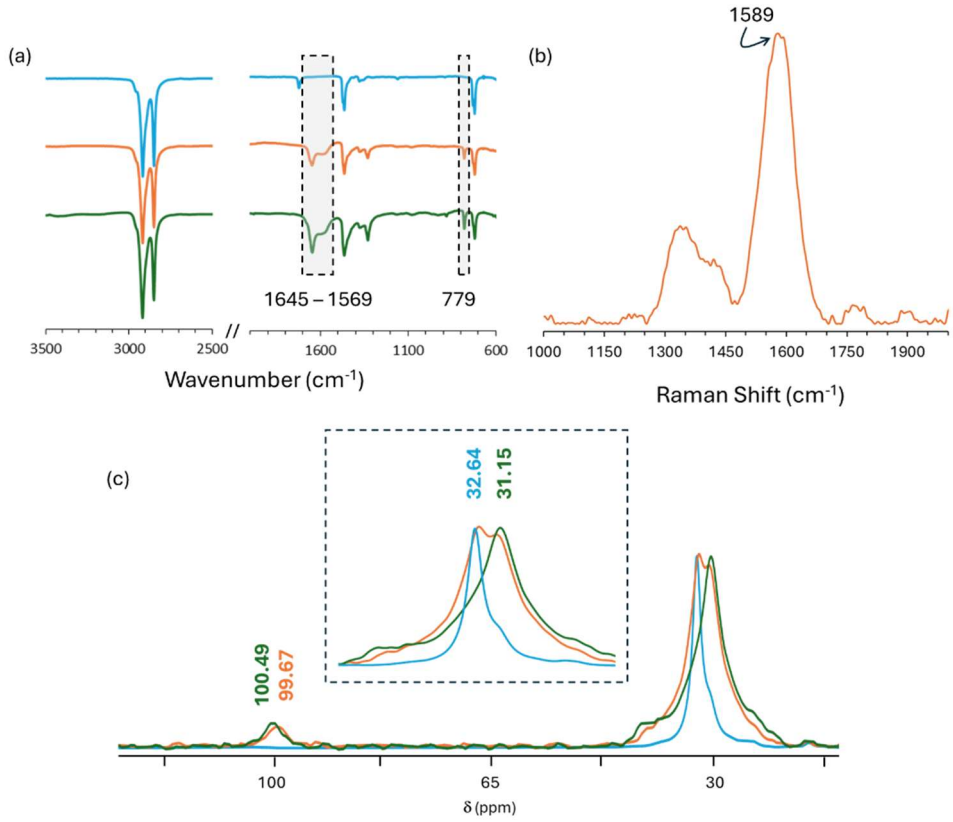
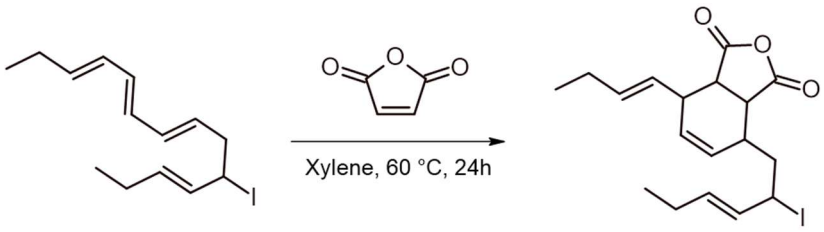


Figure 6.3. (a) ATR-FTIR spectra of pristine **PE** (blue), **PE_1** (orange), and **PE_2** (green), highlighting the appearance of C=C stretching vibrations and =C–H bending modes, indicative of unsaturation. **(b)** Raman spectrum of **PE_1** at an excitation wavelength of 523 nm, revealing a prominent peak at 1589 cm^{-1} associated with conjugated double bonds. **(c)** CP-MAS ^{13}C NMR spectra of pristine **PE** (blue), **PE_1** (orange), and **PE_2** (green), showing a broad resonance around δ = 100 ppm, further supporting the presence of unsaturated structures.

The CP-MAS ^{13}C NMR spectrum also provided insights into the polymer crystallinity: increasing structural disorder following functionalisation resulted in a shift in the methylene peak. For **PE_1**, two signals were observed at δ = 32.64 ppm and δ = 31.15 ppm, while for **PE_2**, the signal at δ = 31.15 ppm became predominant. These shifts support a reduction in crystallinity, with the signal at δ = 32.64 ppm typically assigned to the crystalline phase and the one at δ = 31.15 ppm associated with the amorphous region.[44,45] This shift is consistent with the increasing

disruption of the polymer ordered structure with prolonged reaction time, in accord to the DSC data.

To the best of our knowledge, only a very limited number of studies have reported [4+2] Diels-Alder reaction involving polyacetylene or even its oligomeric forms.[46,47] This scarce reactivity is likely due to the intrinsic properties of such systems, including their predominant *trans* configuration, extended conjugation length, and limited solubility. However, gathered spectroscopic data suggest the presence of short conjugated sequences in a *cis* conformation, along with iodine atoms covalently bound to the polymer backbone. These structural features may facilitate the [4+2] cycloaddition reaction by modulating the electronic environment of the diene units. To explore this reactivity, a model Diels-Alder reaction was performed between our polymer and maleic anhydride (MA). Given its superior solubility, **PE_1** was selected as the substrate, and the reaction was carried out in xylene at 60 °C for 24 hours (**Scheme 6.1**).



Scheme 6.1. Diels-Alder reaction between a modified polyethylene fragment bearing supposed conjugated double bonds in a *cis* configuration and iodine atoms, and maleic anhydride, conducted in xylene at 60 °C for 24 hours.

After purification, ^{1}H NMR analysis revealed the formation of a new functional group, with a signal at δ = 3.74 ppm, attributed to the methine protons in α position to the carbonyl groups of the generated tetrahydrophthalic anhydride unit (**Figure 6.4**). Notably, no vinyl signals corresponding to newly formed C=C bonds were detected, consistent with their absence in the NMR spectrum of unreacted **PE_1**. This absence is likely due to their restricted mobility in solution.[23] Interestingly, the signal assigned to the iodine-linked methine proton before reaction remained unchanged at δ = 4.11 ppm, confirming both the retention of iodine within the polymer structure and the non-radical nature of the Diels-Alder reaction. These results provide evidence of conjugated diene segments within the modified PE structure, suggesting that polyethylene derivatives adopt a conformation favourable to the Diels-Alder reaction. Furthermore, the carbonyl stretching vibration at ~1710 cm^{-1} in the FTIR spectrum (**Figure S6.3**, **p. 243**) further corroborates the successful functionalisation.

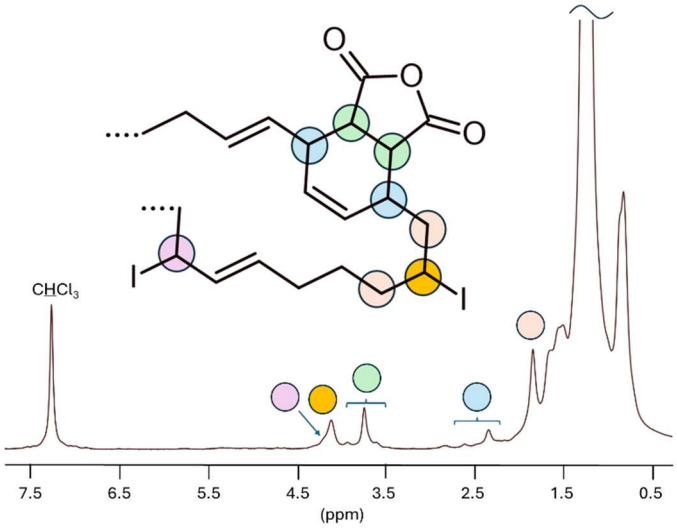
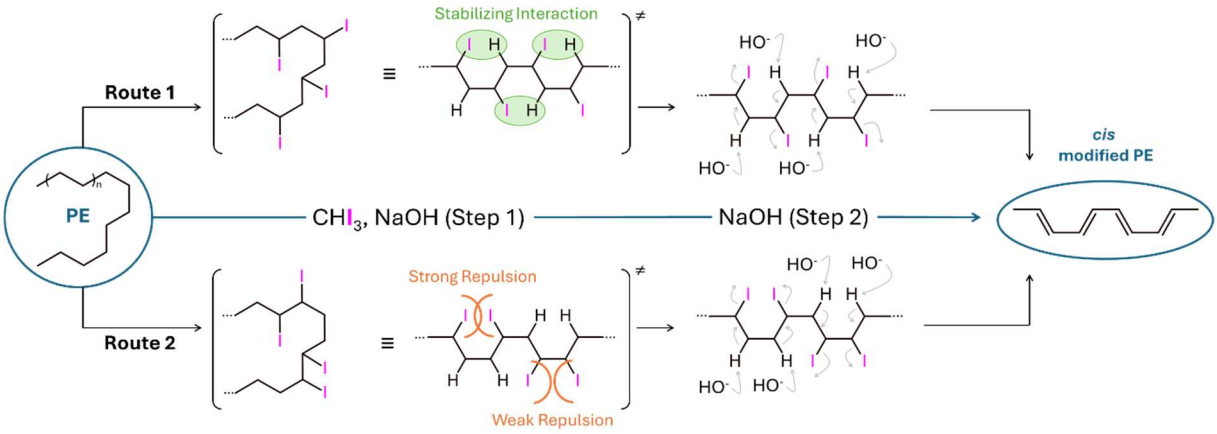


Figure 6.4. ^{1}H NMR spectrum (500 MHz, 21°C, $CDCl_3$) of modified **PE_1** after Diels-Alder reaction with MA. Coloured dots indicate the most relevant proton signals.

The formation of conjugated polyene sequences under these reaction conditions suggests an elimination pathway distinct from classical dehydrohalogenation observed in polyhalogenated polymers such as poly(vinyl chloride) (PVC), where base-induced elimination predominantly yields *trans* polyenes.[41]



Scheme 6.2. Proposed pathways for *cis* polyene formation. Route 1 stabilises iodine positioning on alternating methylene units, while Route 2 involves adjacent iodine atoms, leading to a less stable intermediate.

In contrast, the system presented here, involving PE, operates under conditions that induce a localised iodination followed by dehydroiodination, leading to the formation of conjugated polyene sequences in a *cis* conformation. To our opinion, the key to this process lies in the precise positioning of iodine atoms within the polymer backbone, which plays a critical role in stabilising the intermediate structure (Step 1) before elimination occurs (Step 2). Once iodine atoms are positioned, base-induced elimination, following a favourable E2 mechanism, takes place. In this process, a proton is eliminated in an anti-periplanar configuration relative to the iodine atom, promoting the formation of conjugated polyene sequences. The shear force and

temperature during the extrusion process increase the degrees of freedom in the polymer chains, favouring the alignment of hydrogen atoms in the anti-position with respect to iodine atoms, thereby facilitating the elimination process.

This dynamic system maintains a balance between iodination and elimination, with the final product governed by reaction time and shear force. For the formation of *cis* isomers, two potential iodine positioning modes can be considered. In the first scenario, iodine atoms are positioned on a carbon flanked by two methylene units (Route 1, **Scheme 6.2**), thereby interacting with neighbouring protons through halogen bonding, which stabilises the structure and promotes elimination. In the second scenario, iodine atoms are placed on α and β adjacent carbon atoms, twisted between ethylene and methylene units (Route 2, **Scheme 6.2**), leading to a less stable intermediate, where steric hindrance and electronic effects from the neighbouring iodine atoms reduce stability. The favourable iodine - hydrogen interaction in the first scenario enhances the stability of the intermediate structure, favouring the E2 elimination mechanism and driving the formation of conjugated polyenes.

Remarkably, our conditions enable the selective formation of short-length conjugated polyenes predominantly in the less thermodynamically stable *cis* isomer, a configuration typically accessible only through cryogenic routes (e.g., –78 °C) followed by thermal isomerisation to the more stable *trans* form.[48,49] In stark contrast, our mechanochemical approach achieves this uncommon isomer directly at 106 °C in a melt-processing environment - conditions compatible with industrial extrusion. This unprecedented access to *cis* polyenes under scalable conditions constitutes a significant departure from traditional synthetic routes. Although rarely explored, the *cis* configuration holds substantial promise: upon doping, it has exhibited electrical conductivities comparable to or even surpassing those of the *trans* isomer.[50] Moreover, its integration into optoelectronic[51] and photovoltaic devices, including LED systems,[52] has recently garnered attention. In our study performed in collaboration with Pr. Philippe Leclère, no measurable electrical conductivity could be detected by conductive atomic force microscopy (c-AFM), and thermal isomerisation to the *trans* form - as described in previous reports - proved unsuccessful. These results indicate that the *cis* architecture remains kinetically stabilised under our conditions, offering a unique opportunity to explore structure–property relationships beyond the thermodynamic landscape typically accessed in conjugated polymer chemistry.

Given these observations, the focus shifted toward leveraging the intrinsic reactivity of the conjugated sequences for further functionalisation. Since extended conjugation, as in an all-*trans* arrangement, disfavours post-functionalisation due to the disruption of electronic delocalisation, the *cis* configuration of modified PE may offer greater susceptibility to chemical modification. To probe this potential reactivity, an *in situ* mechanochemical epoxidation was carried out using *m*-chloroperoxybenzoic acid (*m*CPBA) (**Figure 6.5**). The incorporation of epoxide groups is particularly advantageous, as it addresses common limitations of polyolefins,

such as poor adhesion, low surface energy, and limited chemical reactivity, thereby broadening their potential applications.

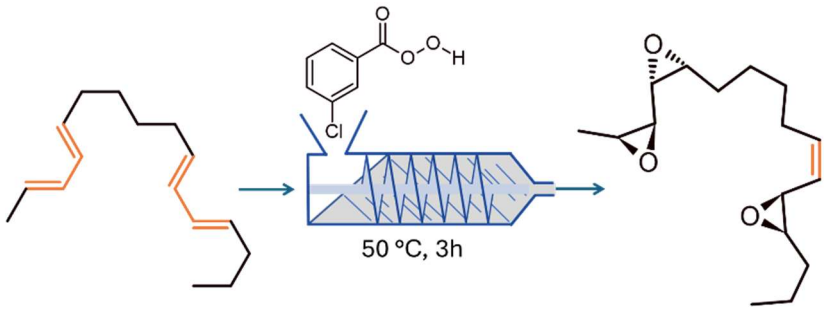


Figure 6.5. Mechanochemical epoxidation of a *cis* segment of a modified PE using *m*CPBA under reactive extrusion at 50 °C.

To complement the results obtained with **PE_1**, **PE_2** was selected for the epoxidation reaction due to its suspected higher content of olefinic moieties. As previously noted, **PE_2** exhibited significant resistance to solubilisation in various organic solvents. This insolubility is attributed to the polyene nature of the material, which likely complicates processing. To overcome this limitation, the epoxidation reaction was conducted in bulk through reactive extrusion (SS = 50 rpm) at 50 °C, slightly below the polymer's T_m. Interestingly, after a few minutes of reaction with an excess of *m*CPBA, the shear forces between the extruder screws gradually decreased, ultimately yielding an off-white solid after 3 hours under nitrogen. Following purification, the epoxidised **PE_2** (**e-PE_2**) exhibited enhanced solubility in organic solvents, such as DMSO, compared to pristine **PE_2** (**Figure 6.6a**). Notably, even after 15 hours at 80 °C, **PE_2** remained largely insoluble in DMSO, whereas **e-PE_2** showed significantly improved solubility. This suggests that epoxidation effectively disrupts intermolecular interactions and facilitates dissolution.[53,54] Importantly, the solubilisation of **e-PE_2** was not due to chain fragmentation, as Size Exclusion Chromatography (SEC) analysis (**Figure 6.6c**) revealed a shift to lower elution volume compared to pristine **PE**, further supporting the notion that the epoxidation of **PE_2** did not lead to chain degradation.

In the epoxidised sample, the presence of an undissolved fraction (**Figure 6.6a**, left) was attributed to incomplete conversion of double bonds or a possible formation of higher-molecular-weight species, as evidenced by the SEC data (**Figure 6.6c**), which shows a shoulder at lower elution volumes. This hypothesis is partially supported by the FTIR spectra (**Figure 6.6b**), where, despite the disappearance of the major peaks associated with carbon-carbon double bond stretching (~ 1647 cm^{-1}), a low-intensity tailing is still observed between 1672 and 1564 cm^{-1}. Interestingly, the epoxidation process resulted in the formation of oxirane groups, as indicated by new peaks at 790 and 1260 cm^{-1}, corresponding to the C-O-C stretching modes of epoxy groups. The low-temperature solid-state mechanochemical epoxidation conditions favoured the integration of oxirane groups into the unsaturated polyethylene chains, although ring-opening reactions may have led to the formation of additional functional groups, such as ketones and carboxylic acids, as suggested by the carbonyl stretching peak at 1710 cm^{-1}.

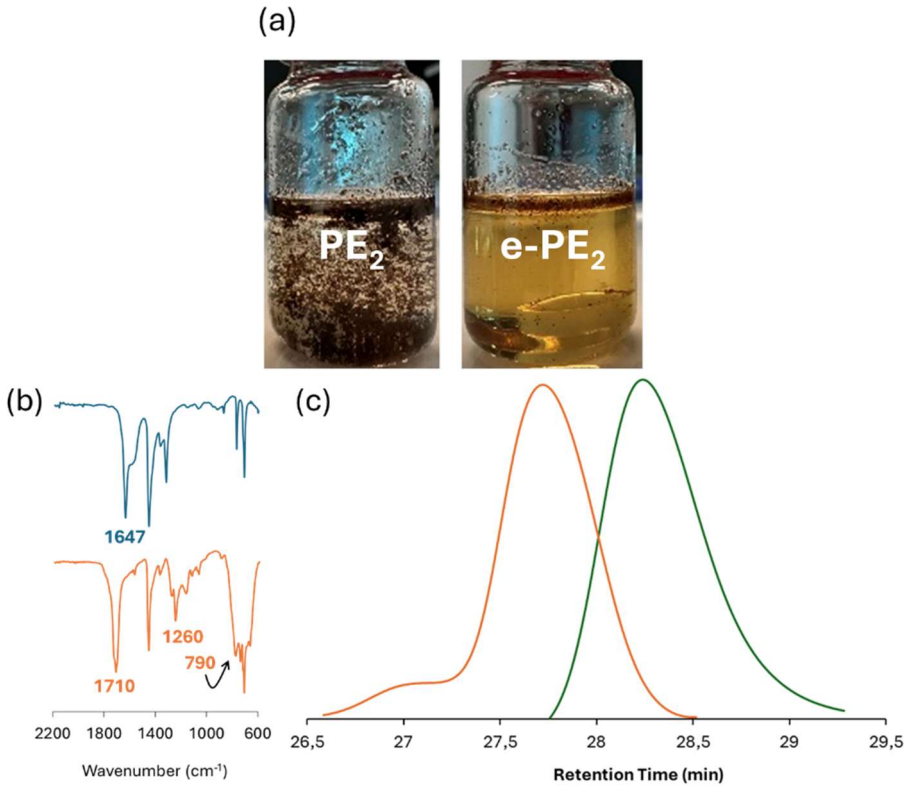
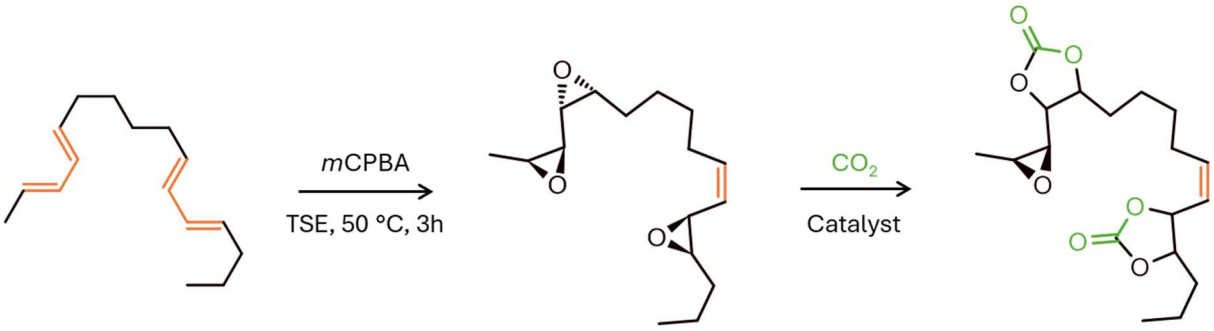


Figure 6.6. (a) Solubility comparison of **PE_2** (left) and **e-PE_2** (right) in DMSO at 80 °C for 15 h. **(b)** ATR-FTIR spectra of **PE_2** (blue) and **e-PE_2** (orange). **(c)** SEC traces of pristine **PE** (green) and **e-PE_2** (orange) recorded in DMSO at 50 °C.

III. CONCLUSION

A solvent-free and scalable approach for the selective functionalisation of polyethylene has been established through a twin-screw extrusion process, enabling the formation of conjugated polyene sequences in a stereoselective *cis* configuration. This structure, typically accessible only under cryogenic conditions, was obtained here at 106 °C under mild yet mechanically intense processing, underscoring the potential of extrusion as a tool for polyolefin transformation. The resulting polyene sequences were shown to be chemically addressable, as demonstrated by successful Diels–Alder and epoxidation reactions, thereby expanding the range of post-functionalisation strategies applicable to polyolefins. Indeed, the oxirane groups installed along the PE backbone open a direct avenue toward a further CO_2-based functionalisation of the polymer. The cycloaddition of CO_2 onto epoxides is indeed one of the most economically viable routes to CO_2-derived materials, and metal-free organocatalysts such as the DBU/I_2 dual system developed by our group[55] or the [HDBU]X salts rationalised by Fanjul-Mosteirín *et al*.[56] achieve it under mild, solvent-free conditions (1 atm CO_2, 65-70 °C) on a broad epoxide scope. Transposing this chemistry to the epoxidised PE developed here would form carbonate rings directly on-chain, thereby closing the loop between the CO_2 and polyolefin chemistries explored throughout this manuscript (**Scheme 6.2**). Moreover, while the methodology was developed using a low-molecular-weight linear PE as a model system, it is designed with scalability and transposability in mind, particularly toward challenging waste streams such as low-density polyethylene (LDPE). Given the relevance of LDPE in packaging and its growing importance in recycling infrastructures, the present strategy contributes to the development of viable chemical upcycling routes for polyolefin-rich waste.



Scheme 6.2. Envisioned CO_2-based extension of the present work: organocatalytic cycloaddition of CO_2 onto the epoxidised polyethylene derived from *cis* conjugated polyene sequences, affording a cyclic carbonate-functionalised polyolefin.

Like Chapter 5, this chapter is owed to Emna, who carried out the experimental work and authored the original article on which this chapter is based.

IV. EXPERIMENTAL

A. Materials

Sodium hydroxide powder (NaOH, >98.5%), iodoform (CHI_3, 99+%), 3-chloroperoxybenzoic acid (*m*CPBA, ≤77%), maleic anhydride (MA, 99%), deuterated chloroform (0.03 vol% TMS, deuteration degree ≥99.8%, stabilised with silver), and polyethylene (LLDPE) (SKU: 427772-250 g, M_n ~1.5 kg/mol, Đ = 2.2) were purchased from Sigma-Aldrich. Chloroform ($CHCl_3$, 99+%, stabilised with amylene), methanol (GPR Reactpur), and xylene (99+%, mixture of isomers) were sourced from AnalytiChem, Belgium, NV.

B. Procedures

The iodination and epoxidation of polyethylene were conducted in an Xplore DSM vertical microcompounder with a 5 cm^3 capacity. This system featured intermeshing conical twin screws, allowing precise speed control and continuous nitrogen purging. A manual floodgate facilitated seamless switching between extrusion and recirculation during reactive extrusion. The method is explained in detail according to our previously reported procedure (Chapter 5).

Representative Procedure for Functionalisation of LLDPE to Give PE_1 and PE_2

In a preheated extruder chamber, LLDPE (1.0 g, 35.7 mmol C_2H_4, 1.0 eq.) was fed into the extruder. Subsequently, at 30-minute intervals, four fractions of iodoform (35.7 mmol total, 1.0 eq.) and sodium hydroxide (35.7 mmol total, 1.0 eq.) were introduced at screw speed between 200-300 rpm for 2 hours (**PE_1**) and 5 hours (**PE_2**). Upon completion, the polymer was collected and stored in a sample holder for 24 hours to equilibrate to ambient relative humidity. Purification was performed by dissolving the polymer in a 50:50 mixture of xylene and water followed by precipitation in methanol. The resulting solid was isolated via vacuum filtration, rinsed with methanol, and dried overnight under vacuum before characterisation.

Representative Procedure for the Diels-Alder Cycloaddition of Polyethylene with Cis Polyene Sequences (PE_1)

In a 50 mL oven-dried round-bottom flask equipped with a Teflon-coated stir bar, dehydrogenated polyethylene (**PE_1**) (100 mg, 3.8 mmol, 1.0 eq.) was dissolved in xylene (50 mL) at 60 °C. Maleic anhydride (MA) (2.22 g, 7.6 mmol, 2.0 eq.) was added and the mixture was stirred for 24 hours under reflux. The dispersion was collected and cooled down before adding methanol to precipitate the polymer. The reaction mixture was then filtered, washed with acetone, and dried in the vacuum oven for 24 hours before characterisation.

Representative Procedure for the Epoxidation of Polyethylene with Cis Polyene Sequences (PE_2) to Give e-PE_2

PE_2 (400 mg, 15.3 mmol, 1.0 eq.) and 3-chloroperbenzoic acid (*m*CPBA) (2.64 g, 15.3 mmol, 1.0 eq.) were simultaneously introduced into the extruder chamber, with the screw speed set to 50 rpm. The reaction was carried out at 50 °C for 3 hours under an inert atmosphere. Upon completion, the mixture was precipitated in methanol, collected by filtration, and dried in a vacuum oven for 24 hours, yielding a yellowish solid product (**e-PE_2**).

Representative Procedure for the Iodination Reaction of the Small Model Molecule *n*-Hexadecane (*n*-C16)

In a brown glass round-bottom flask placed in a silicone oil bath, fitted with a reflux condenser and a magnetic stirrer bar, *n*-hexadecane (33.96 g, 0.15 mol, 1.0 eq.), an initial portion of CHI_3 (0.15 mol, 1.0 eq.), and finely powdered NaOH (0.15 mol, 1.0 eq.) were combined. The molar ratio of $[n\text{-C16}]_0/[CHI_3]_0/[NaOH]_0$ was 1/1/1. However, to optimise the conversion, iodoform and NaOH were added at 30-minute intervals during the 2-hour reaction and at daily intervals over the course of 4 days for the 5-day reaction at 106 °C. After the reaction was complete, the mixture was filtered under vacuum to remove solid by-products. The crude liquid product was then collected and analysed by ^{1}H NMR spectroscopy for structural characterisation.

Solubility Procedure of PE_2 and e-PE_2 in DMSO

10 mg of **PE_2** and **e-PE_2** were weighed into glass vials, followed by the addition of 5 mL of DMSO. The vials were then heated at 80 °C for 15 hours under constant magnetic stirring. Prolonged heating did not enhance the solubility of **PE_2**, while the epoxidised polymer began to disintegrate and dissolve within the first hour.

C. Methods

NMR Spectroscopy

^{1}H NMR spectra were recorded using an AVANCE II 500 MHz spectrometer equipped with a broadband Prodigy cryoprobe or a Bruker UltraShield 500 MHz spectrometer. All NMR experiments were conducted at room temperature, and the spectra were processed using MestReNova software. Chemical shifts (δ) for ^{1}H NMR spectra were referenced to the residual solvent peaks (7.26 ppm for $CDCl_3$).

Fourier Transform Infrared Spectroscopy

Fourier transform infrared spectroscopy (FTIR) spectra of the samples were collected using the attenuated total reflectance (ATR) technique on a Bruker Tensor 27 instrument, processed with OPUS 6.5 software. Measurements were performed over a wavelength range of 4000–600 cm^{-1} with 32 scans per spectrum.

Raman Spectroscopy

Raman spectra were recorded using a BRUKER SENTERRA micro-Raman spectrometer with a 523 nm excitation laser. The laser power was set to 20 mW, and the integration time for each acquisition was 15 seconds. To improve the signal-to-noise ratio, five accumulations were performed for each spectrum.

Thermogravimetric analysis

Thermogravimetric analysis (TGA) was used to evaluate the thermal decomposition of the samples. The analysis was conducted using a TGA Q500 (TA Instruments®, New Castle, USA). Sample masses ranging from 5 to 10 mg were placed in a platinum pan and heated from 30 to 800 °C at a rate of 10 °C.min^{-1} under a nitrogen atmosphere.

Differential scanning calorimetry

Differential scanning calorimetry (DSC) measurements of the polymer samples were performed using a DSC Q2000 (TA Instruments) equipped with a chiller and an autosampler. Approximately 5-10 mg of each polymer sample was sealed in a crimped aluminium pan for each run. The DSC analysis involved heating the samples from -60 to 150 °C at a rate of 10 °C.min^{-1} under a nitrogen atmosphere. The melting temperatures (T_m) were determined from the third heating cycle using TA software. The crystallinity degree (X_c) was calculated according to the following equation (1).

$$\chi_c\ (\%) = \frac{\Delta H_f}{\Delta H_f^0}\ x\ 100 \qquad (1)$$

Where ΔH_f is the melting enthalpy of the PE sample while ΔH_f^0 is the standard melting enthalpy of PE (293 J/g).

Size exclusion chromatography

Size exclusion chromatography (SEC) was performed in DMSO at 50 °C using an Agilent liquid chromatograph equipped with an Agilent degasser, an isocratic HPLC pump (flow rate = 0.7 mL.min^{-1}), an Agilent autosampler (loop volume = 100 µL, solution conc. = 1 mg/mL/ LiCl 0.1% (w/v)), an Agilent-DRI refractive index detector and three columns: a PL gel 10 µm guard column and two PL gel Mixed-D 10 µm columns (linear columns for separation of MwPS ranging from 500 to 10^6 g/mol). Polystyrene standards were used for calibration.

Atomic Force Microscopy

The current measurements at the nanoscale were carried out in air using a Bruker Dimension Icon microscope equipped with a Nanoscope VI controller and an Extended TUNA external module for current detection. Peak Force TUNA provides direct, precise force control and eliminates lateral forces. For the acquisition, a PtIr conductive coating on etched Si probes (Bruker SCM PITV2) tip ensured good electrical contact at the tip–sample contact, while low spring constant (3 N/m) and detection set-point guaranteed low contact forces, preventing mechanical or electrical damage upon scanning. This enables routine high sensitivity and high-resolution current imaging. The tip radius is about 25 nm and the resonance frequency is about 75 kHz.

V. SUPPORTING INFORMATION

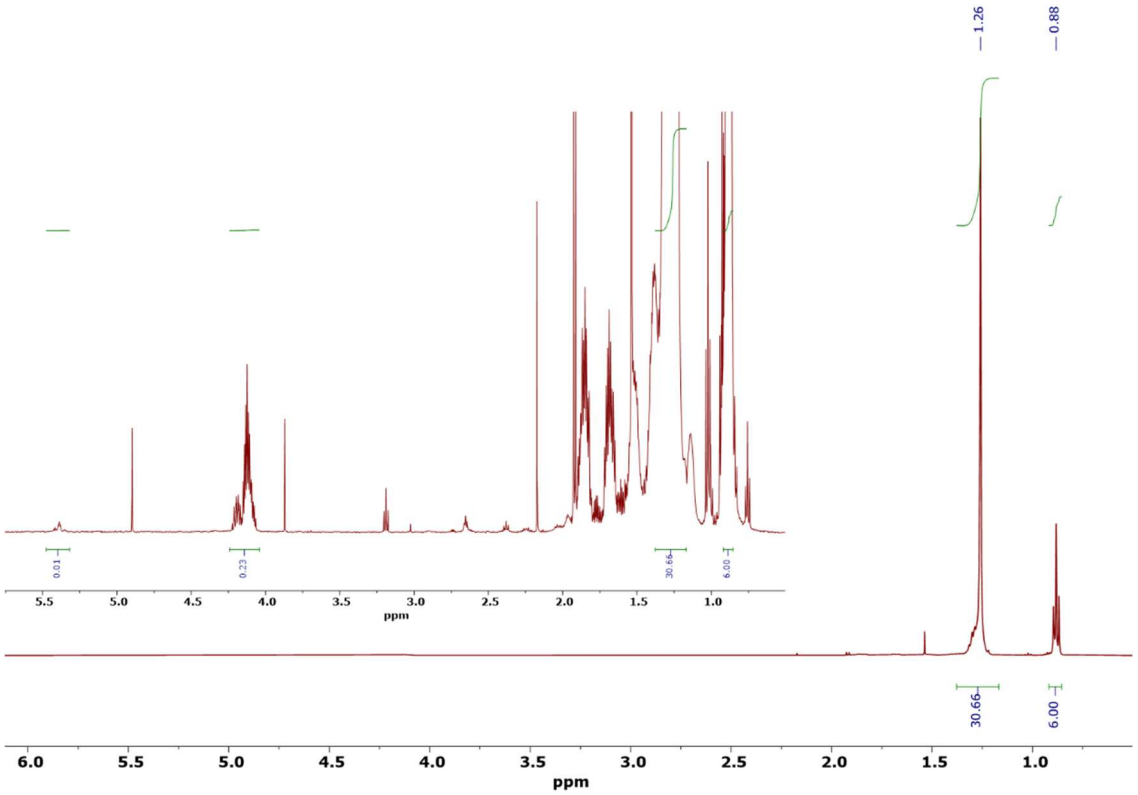


Figure S6.1. ^{1}H NMR spectrum of *n*-C16 after the iodination reaction for 2 hours at 106 °C (500 MHz, $CDCl_3$, room temperature).

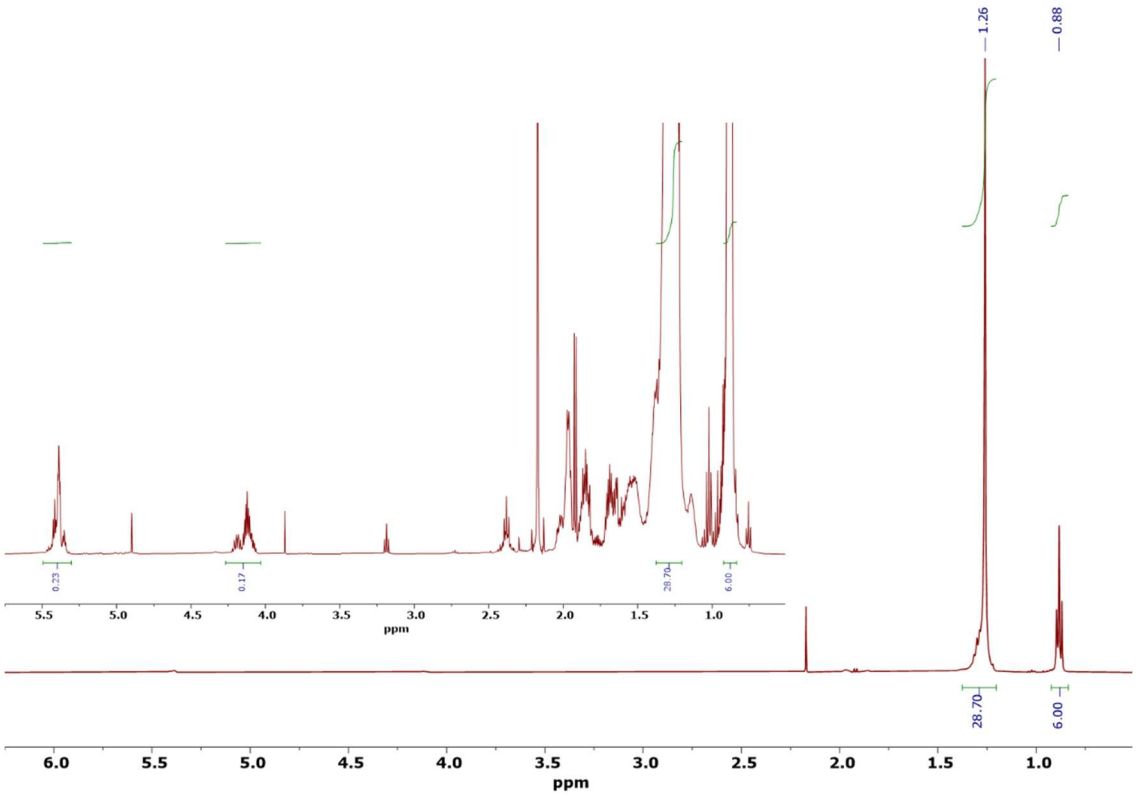


Figure S6.2. ^{1}H NMR spectrum of *n*-C16 after the iodination reaction for 144 hours at 106 °C (500 MHz, $CDCl_3$, room temperature).

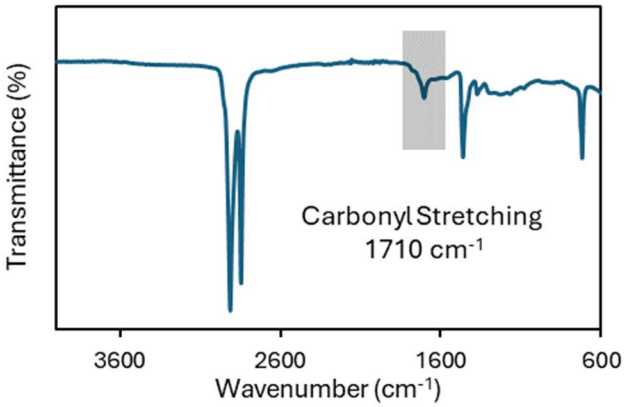


Figure S6.3. ATR-FTIR spectrum of modified polyethylene (**PE_1**) subjected to the Diels-Alder reaction.

VI. REFERENCES

1 J. R. Jambeck and I. Walker-Franklin, *One Earth*, 2023, **6**, 600–606.

2 *PlasticsEurope2024*, https://plasticseurope.org/knowledge-hub/plastics-the-fast-facts-2024/.

3 S. R. Nicholson, N. A. Rorrer, A. C. Carpenter and G. T. Beckham, *Joule*, 2021, **5**, 673–686.

4 R. Geyer, J. R. Jambeck and K. L. Law, *Sci. Adv.*, 2017, **3**, e1700782.

5 A. Rahimi and J. M. García, *Nat. Rev. Chem.*, 2017, **1**, 0046.

6 M. Shen, W. Huang, M. Chen, B. Song, G. Zeng and Y. Zhang, *Journal of Cleaner Production*, 2020, **254**, 120138.

7 A. Ray, K. Zhu, Y. V. Kissin, A. E. Cherian, G. W. Coates and A. S. Goldman, *Chem. Commun.*, 2005, 3388–3390.

8 R. J. Conk, S. Hanna, J. X. Shi, J. Yang, N. R. Ciccia, L. Qi, B. J. Bloomer, S. Heuvel, T. Wills, J. Su, A. T. Bell and J. F. Hartwig, *Science*, 2022, **377**, 1561–1566.

9 R. J. Conk, J. F. Stahler, J. X. Shi, J. Yang, N. G. Lefton, J. N. Brunn, A. T. Bell and J. F. Hartwig, *Science*, 2024, **385**, 1322–1327.

10 N. M. Wang, G. Strong, V. DaSilva, L. Gao, R. Huacuja, I. A. Konstantinov, M. S. Rosen, A. J. Nett, S. Ewart, R. Geyer, S. L. Scott and D. Guironnet, *J. Am. Chem. Soc.*, 2022, **144**, 18526–18531.

11 M. Nagyházi, Á. Lukács, G. Turczel, J. Hancsók, J. Valyon, A. Bényei, S. Kéki and R. Tuba, *Angew. Chem. Int. Ed.*, 2022, **61**, e202204413.

12 A. Arroyave, S. Cui, J. C. Lopez, A. L. Kocen, A. M. LaPointe, M. Delferro and G. W. Coates, *J. Am. Chem. Soc.*, 2022, **144**, 23280–23285.

13 S. M. Parke, J. C. Lopez, S. Cui, A. M. LaPointe and G. W. Coates, *Angew. Chem. Int. Ed.*, 2023, **62**, e202301927.

14 Y. Kratish, J. Li, S. Liu, Y. Gao and T. J. Marks, *Angewandte Chemie*, 2020, **132**, 20029–20033.

15 P. F. Britt, G. W. Coates, K. I. Winey, J. Byers, E. Chen, B. Coughlin, C. Ellison, J. Garcia, A. Goldman, J. Guzman, J. Hartwig, B. Helms, G. Huber, C. Jenks, J. Martin, M. McCann, S. Miller, H. O'Neill, A. Sadow, S. Scott, L. Sita, D. Vlachos and R. Waymouth, *Report of the Basic Energy Sciences Roundtable on Chemical Upcycling of Polymers*, 2019.

16 P. A. Kots, *Chem Catalysis*, 2024, **4**, 101194.

17 J. B. Williamson, C. G. Na, R. R. Johnson, W. F. M. Daniel, E. J. Alexanian and F. A. Leibfarth, *J. Am. Chem. Soc.*, 2019, **141**, 12815–12823.

18 T. Vialon, H. Sun, G. J. M. Formon, P. Galanopoulo, C. Guibert, F. Averseng, M.-N. Rager, A. Percot, Y. Guillaneuf, N. J. Van Zee and R. Nicolaÿ, *J. Am. Chem. Soc.*, 2024, **146**, 2673–2684.

19 M. Hua, Z. Peng, R. D. Guha, X. Ruan, K. C. Ng, J. Demarteau, S. Haber, S. N. Fricke, J. A. Reimer, M. B. Salmeron, K. A. Persson, C. Wang and B. A. Helms, *Sci. Adv.*, 2024, **10**, eadq3801.

20 T. J. Fazekas, J. W. Alty, E. K. Neidhart, A. S. Miller, F. A. Leibfarth and E. J. Alexanian, *Science*, 2022, **375**, 545–550.

21 J. Zhou, T. Hsu and J. Wang, *Angew. Chem. Int. Ed.*, 2023, **62**, e202300768.

22 K. Kubota, J. Jiang, Y. Kamakura, R. Hisazumi, T. Endo, D. Miura, S. Kubo, S. Maeda and H. Ito, *J. Am. Chem. Soc.*, 2024, **146**, 1062–1070.

23 E. Ben Ayed, J. Delcorps and O. Coulembier, *Ind. Eng. Chem. Res.*, 2024, **63**, 21455–21465.

24 Packaging Waste, https://statbel.fgov.be/en/themes/environment/waste-and-pollution/packaging-waste, (accessed 1 April 2025).

25 Belgium among the top EU nations for recycling plastic packaging, https://www.brusselstimes.com/eu-affairs/1284000/belgium-one-of-the-eus-best-performers-for-recycling-plastic-packaging, (accessed 6 April 2025).

26 Belgium exceeds European plastic recycling requirements, https://www.fostplus.be/en/blog/belgium-exceeds-european-plastic-recycling-requirements, (accessed 9 April 2025).

27 Our Services, https://www.raffplastics.be/en/our-services, (accessed 9 April 2025).

28 Recycling Solutions, https://www.phoenixplus.be/en/recycling-solutions, (accessed 15 April 2025).

29 Ecoo expands! A new recycling plant in Beringen., https://www.ecoo.eu/en/inspiration/ecoo-expands-a-new-recycling-plant-in-beringen, (accessed 13 April 2025).

30 M. A. Smook, E. T. Pieski and C. F. Hammer, *Ind. Eng. Chem.*, 1953, **45**, 2731–2737.

31 K. Nambu, *J. of Applied Polymer Sci.*, 1960, **4**, 69–73.

32 J. Coates, in *Encyclopedia of Analytical Chemistry*, ed. R. A. Meyers, Wiley, 1st edn., 2000.

33 M. Zeng, Y.-H. Lee, G. Strong, A. M. LaPointe, A. L. Kocen, Z. Qu, G. W. Coates, S. L. Scott and M. M. Abu-Omar, *ACS Sustainable Chemistry & Engineering*, 2021, **9**, 13926–13936.

34 De James C.W. Chien, *Polyacetylene: chemistry, physics, and material science*, Elsevier, 2012.

35 H. Shirakawa and S. Ikeda, *Polymer Journal*, 1971, **2**, 231–244.

36 A. J. Dias and T. J. McCarthy, *Macromolecules*, 1985, **18**, 869–871.

37 L. Dai, *Macro Chemistry & Physics*, 1997, **198**, 1723–1738.

38 H. Shirakawa, T. Ito and S. Ikeda, *Polym. J.*, 1973, **4**, 460–462.

39 R. L. Christensen, E. A. Barney, R. D. Broene, M. G. I. Galinato and H. A. Frank, *Archives of Biochemistry and Biophysics*, 2004, **430**, 30–36.

40 T. C. Clarke and J. C. Scott, *Solid State Communications*, 1982, **41**, 389–391.

41 H. J. Bowley, D. L. Gerard, W. F. Maddams, M. R. Paton, *Macromolecular Chemistry and Physics*, 1985, **186**, 695–705.

42 T. Yamanobe and I. Ando, *The Journal of Chemical Physics*, 1985, **83**, 3154–3160.

43 H. W. Gibson, J. M. Pochan and S. Kaplan, *J. Am. Chem. Soc.*, 1981, **103**, 4619–4620.

44 N. Chaiyut, T. Amornsakchai, H. Kaji and F. Horii, *Polymer*, 2006, **47**, 2470–2481.

45 R. A. Assink, M. Celina, K. T. Gillen, R. L. Clough and T. M. Alam, *Polymer Degradation and Stability*, 2001, **73**, 355–362.

46 R. Cosmo and H. Naarmann, *Molecular Crystals and Liquid Crystals Incorporating Nonlinear Optics*, 1990, **185**, 89–98.

47 I. C. McNeill, M. H. Mohammed, E. Ya. Davydov and G. E. Zaikov, *Polymer Degradation and Stability*, 1997, **58**, 61–67.

48 H. Shirakawa, E. J. Louis, A. G. MacDiarmid, C. K. Chiang and A. J. Heeger, *J. Chem. Soc., Chem. Commun.*, 1977, 578–580.

49 M. Goh, G. Piao, M. Kyotani and K. Akagi, *Macromolecules*, 2009, **42**, 8590–8593.

50 T. Yamabe, K. Tanaka, H. Terama-e, K. Fukui, A. Imamura, H. Shirakawa and S. Ikeda, *Solid State Communications*, 1979, **29**, 329–333.

51 S. Wang, X. Sun, H. Zeng, S. Xie, J. Zhang and X. Wan, *Macromolecules*, 2025, **58**, 1235–1244.

52 K. N. Keya, M. A. Jabed, W. Xia and D. Kilin, *Applied Sciences*, 2022, **12**, 2830.

53 X. Jian and A. S. Hay, *J. Polym. Sci. C Polym. Lett.*, 1990, **28**, 285–288.

54 Q. Xiong, S. Yang, C. Peng, F. Xie, Z. Gu, Y. Fu, H. Tan, Q. Dai, W. Yi, L. Li and K. Liu, *J. Polym. Res.*, 2023, **30**, 326.

55 O. Coulembier, S. Moins, V. Lemaur, R. Lazzaroni and P. Dubois, *Journal of CO_2 Utilization*, 2015, **10**, 7–11.

56 N. Fanjul-Mosteirín, C. Jehanno, F. Ruipérez, H. Sardon and A. P. Dove, *ACS Sustainable Chem. Eng.*, 2019, **7**, 10633–10640.

CHAPTER 7

Conclusion And Perspectives



The work presented in this manuscript was motivated by two of the most pressing environmental challenges of the 21st century, i.e. the continuous accumulation of anthropogenic carbon dioxide in the atmosphere and the persistent generation of plastic waste, two problematics that are traditionally addressed as independent issues. Guided by the conviction that these seemingly disconnected streams could actually benefit from being tackled jointly, this thesis explored an integrated strategy in which CO_2 is activated through organic carriers and covalently incorporated into pre- or post-modified polyolefin backbones. The three research axes defined in the general introduction, namely the preparation of CO_2-derived reactive synthons, the halogenation of commodity polyolefins, and the coupling of both chemistries into a unified upcycling process, were addressed successively across five experimental chapters, each building upon the observations and limitations of the previous ones.

Chapter 2 established the conceptual and mechanistic foundation of the work by demonstrating that 1,5,7-triazabicyclo[4.4.0]dec-5-ene (TBD) is a particularly well-suited organic base for the formation of CO_2-binding organic liquids (CO_2BOLs) from primary and secondary alcohols. Combining experimental observations and density functional theory calculations, we showed that TBD-based CO_2BOLs outperform their 1,8-diazabicyclo[5.4.0]undec-7-ene (DBU) homologues in terms of selectivity, allowing the clean preparation of linear dialkyl carbonates from highly reactive alkyl iodides through bimolecular nucleophilic substitution. The high S_N2 selectivity observed at room temperature was rationalised in terms of a unique, metal-free cation-assisted ion-pair mechanism in which the in situ generated TBD.H^+ guanidinium stabilises the transition state while suppressing competing N-alkylation pathways. Importantly, the sole by-product of the reaction, the TBD.H^+,I^- salt, exhibits no detectable cytotoxicity on human intestinal epithelial FHs74Int cells, further supporting the potential compatibility of this chemistry with pharmaceutical-grade applications. This chapter therefore not only introduced TBD-based CO_2BOLs as versatile reagents but also delineated the mechanistic framework onto which the remaining experimental chapters were constructed.

Translating this reactivity to macromolecular substrates, Chapter 3 investigated the direct functionalisation of pristine poly(vinyl chloride) (PVC) using TBD-based CO_2-binding alcohols (CO_2BALs) as nucleophilic partners. By systematically varying the nature of the solvent, the conversion of the CO_2BAL and the reaction time, a carbonate grafting of approximately 2.5 mol% of the methine sites was achieved at 21 °C in N,N-dimethylformamide, with a remarkable S_N2/E2 selectivity of 94/6 and the exclusive release of a benign, recoverable TBD.HCl by-product. Although the degree of substitution remained modest, this chapter confirmed that CO_2 can be covalently introduced onto PVC under genuinely mild conditions, while also identifying the main factors limiting the overall efficiency, namely the strong stabilisation of CO_2BALs in polar aprotic media and the steric constraints imposed by the statistical coil conformation of PVC.

Building on these insights, Chapter 4 proposed a dual strategy to circumvent these limitations. On the one hand, a partial iodination of PVC was performed through an aqueous phase-transfer catalysis protocol, which avoids the conventional THF/acetone solvent mixture and delivers a more reactive iodinated PVC. On the other hand, carbamate-based analogues of CO_2BALs, denoted CO_2BAMs, were prepared from 1-hexylamine in the presence of DBU, thereby replacing the moisture-sensitive and costly TBD guanidine by a cheaper, more robust superbase. Reacting the iodinated PVC with the DBU-based CO_2BAM under conditions directly comparable to those of Chapter 3 resulted in a roughly fourfold increase in the degree of substitution (~ 10 mol%) while preserving the full solubility of the modified material in organic media. Moreover, the intrinsic thermodynamic stability of the newly formed carbamate linkages is expected to confer enhanced durability and compatibility with subsequent transformations. Taken together, Chapters 3 and 4 therefore describe a coherent and increasingly efficient CO_2-based route for the chemical modification of PVC, from proof-of-concept to a markedly more productive and greener protocol.

A complementary line of investigation, developed in Chapter 5, addressed one of the most long-standing challenges of polyolefin chemistry, namely the selective functionalisation of the chemically inert C-H bonds of polyethylene (PE). Adapting the phase-transfer single-electron approach originally proposed by Schreiner and co-workers for small alkanes, a solvent-free iodination protocol was designed and implemented in a twin-screw extruder operating under mild conditions (106 °C), using iodoform as iodine source and powdered sodium hydroxide as initiator. This mechanochemical strategy allowed the incorporation of up to 23 wt% of iodine into low-molecular-weight linear PE, with a controlled balance between iodination and elimination, and without detectable chain cleavage. The concept was subsequently extended to isotactic polypropylene (22 wt% iodine), providing, to the best of our knowledge, the first example of a scalable, solvent-free and metal-free iodination of commodity polyolefins through reactive extrusion. Beyond its chemical novelty, this approach is directly compatible with industrial melt-processing infrastructures and therefore offers a tangible bridge between laboratory-scale polymer functionalisation and real process engineering.

The final experimental chapter exploited the unique reactivity of the iodinated PE obtained by reactive extrusion to generate, in a controlled manner, conjugated polyene sequences of well-defined stereochemistry. By fine-tuning the residence time and shear conditions, the competition between iodination and dehydroiodination was deliberately shifted toward elimination, yielding a modified PE that unambiguously exhibits short conjugated sequences adopting a *cis* configuration. This stereoselective outcome, obtained at 106 °C in a melt-processing environment, is particularly noteworthy given that such isomers are typically accessible only through cryogenic routes followed by thermal isomerisation. The successful Diels-Alder cycloaddition with maleic anhydride, and the mechanochemical *in situ* epoxidation with *m*-chloroperoxybenzoic acid collectively evidence the chemical versatility of these *cis*

sequences and confirm their suitability as reactive handles for further post-functionalisation of polyolefin waste streams.

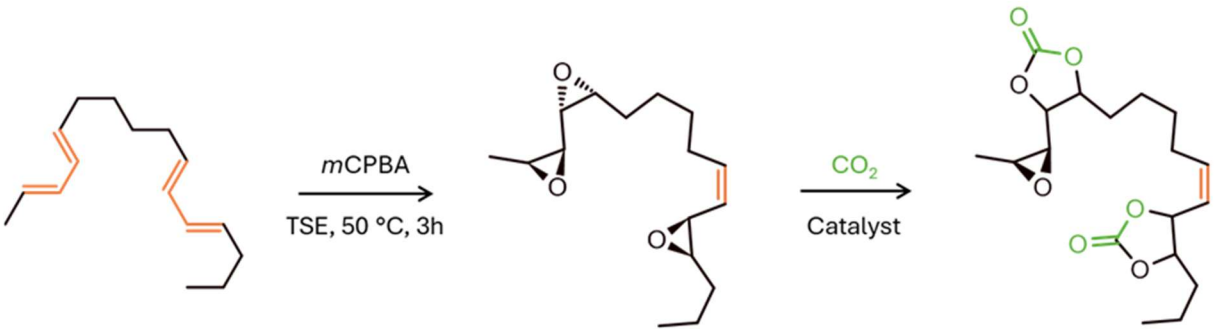
Although each chapter delineates a self-contained contribution, several research avenues remain to be explored in order to move these different strategies beyond the proof-of-concept stage and, more importantly, to fully realise the integrated vision outlined in the general introduction.

A first set of perspectives directly concerns the CO_2BAM-based upcycling process introduced in Chapter 4. Although this strategy already increased the efficiency of S_N2 substitution by roughly fourfold compared to the CO_2BAL chemistry of Chapter 3, the proof-of-concept was established with a single CO_2BAM, namely the DBU-based formulation derived from 1-hexylamine. Systematic investigations of CO_2BAMs bearing different alkyl substituents are thus still required, not only to probe the robustness of the S_N2 pathway across a broader chemical space, but also to tune the nature of the grafted side chain, and thereby the macroscopic properties of the modified PVC. In the same line, dedicated studies on reaction time, $[CO_2BAM]_0/[halogen]_0$ ratios, and on the resulting polymer properties are needed to determine the intrinsic limits of the approach and to establish clear correlations between the degree of grafting and the thermal, mechanical and processing behaviour of the functionalised material. From a sustainability standpoint, the replacement of DMF by a fully benign polar aprotic solvent, represents a concrete priority before any scale-up can be envisioned. Taken together, these investigations will be decisive to firmly translate the strategy developed in Chapter 4 beyond its current proof-of-concept status.

A second perspective directly emerges from the comparison of the different chapters of this manuscript. The CO_2BOL chemistry established in Chapters 2, 3 and 4 was applied to small alkyl iodides and, at the macromolecular level, to PVC and iodinated PVC, whereas the solvent-free TSE-based iodination developed in Chapter 5 provides ready access to iodinated polyethylene and polypropylene bearing iodine contents of up to 23 and 22 wt %, respectively. The reaction between these iodinated polyolefins and CO_2BOLs could not be carried out within the timeframe of the present work but constitutes the most natural extension of the strategies developed throughout this thesis. Its implementation would allow the two research axes pursued here to converge on the upcycling of commodity polyolefins through the covalent incorporation of CO_2 along the polymer backbone. The success of this approach will however depend on the thermal robustness of CO_2BOLs under the processing conditions required for polyethylene and polypropylene, and in particular for any reactive-extrusion implementation operating well above the softening points of these polyolefins. As shown by the TGA data collected in Chapter 3 and the Appendix (page 241), the degradation onset temperatures (T5%) of the CO_2BOLs investigated in this work consistently remain below 100 °C, regardless of the alkyl chain length, which is too low to ensure their integrity in the melt state of typical commodity polyolefins. Pushing this T5% to approximately 150 °C would already represent a

meaningful step forward, as it would provide sufficient operating margin above the melting and processing temperatures of low-density polyethylene while preserving the carbonate or carbamate functionality long enough for the substitution reaction to take place. Achieving such an improvement, for example through judicious tuning of the alcohol or amine partner, or of the organic base, therefore constitutes a key prerequisite for bringing the two research axes developed in this thesis together.

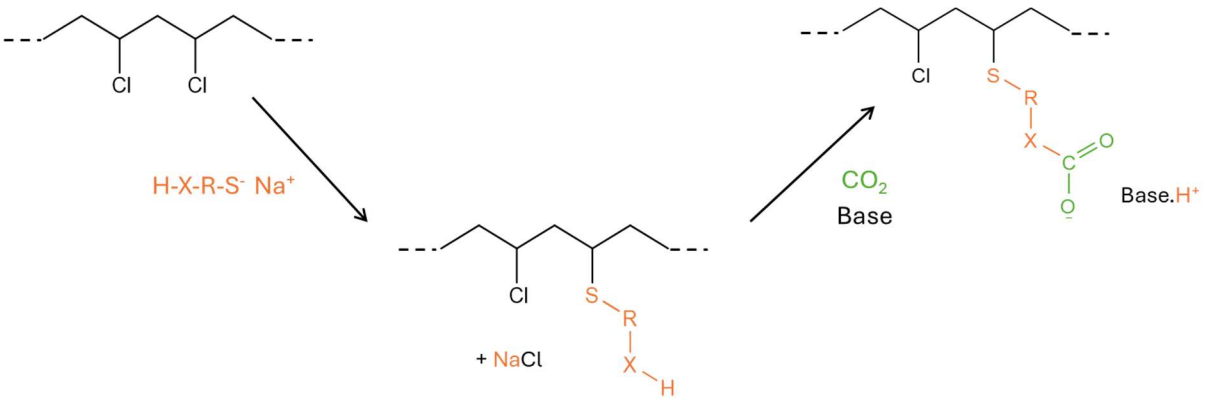
A third, more exploratory perspective concerns the direct use of CO_2 as a reactive partner for the epoxidised polyethylene obtained in Chapter 6. The *in situ* mechanochemical epoxidation of the *cis* polyene sequences with *m*-chloroperoxybenzoic acid was indeed shown to install oxirane groups along the PE backbone without detectable chain degradation, while simultaneously improving the solubility and processability of the material. These oxirane moieties open a direct avenue toward a further CO_2-based functionalisation of the polymer. Indeed, the incorporation of CO_2 into epoxides constitutes one of the most economically viable routes to value-added CO_2-derived materials. Reacting the epoxidised polyethylene with CO_2 could therefore provide an original strategy in which CO_2 is incorporated along a polyolefin backbone through carbonate rings formed directly on-chain, potentially yielding cyclic carbonate-functionalised polyethylene derivatives. Such an approach would offer an additional route to close the loop between the CO_2 and the polyolefin chemistries explored throughout this manuscript, thereby extending the CO_2-plastics valorisation concept developed in this thesis (**Scheme 7.1**).



Scheme 7.1. Envisioned CO_2-based extension of the present work: organocatalytic cycloaddition of CO_2 onto the epoxidised polyethylene derived from *cis* conjugated polyene sequences, affording a cyclic carbonate-functionalised polyolefin.

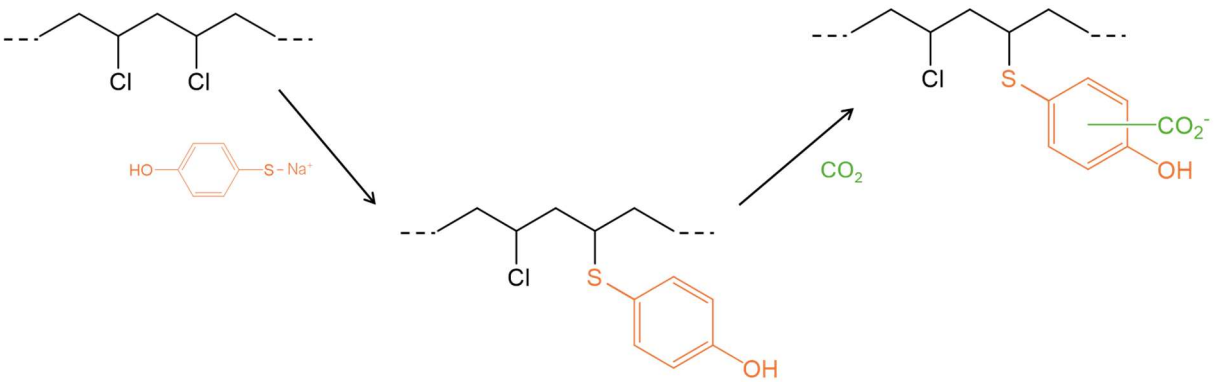
Beyond these direct extensions, additional perspectives emerge from the possibility of diversifying the chemistry employed to tether CO_2-derived functionalities onto polymer chains, either by complementing the CO_2BOL platform developed in this thesis or by replacing it altogether with fundamentally different reactions. A first direction concerns the well-established use of thiols for the nucleophilic substitution of chlorine atoms along the PVC backbone.[1–3] Aromatic thiols in particular have long been known to behave as highly efficient nucleophiles toward PVC, combining strong nucleophilic character with a relatively low basicity that suppresses the competing dehydrochlorination pathway observed with more basic nucleophiles.[3,4] Under appropriate conditions, this reaction proceeds selectively without

detectable elimination and enables degrees of modification that can reach values considerably higher than those achieved with the CO_2BAL and CO_2BAM strategies developed in Chapters 3 and 4.[2–4] The versatility of this chemistry is further illustrated by the large variety of aromatic and hetero-aromatic thiol platforms that can be designed to carry additional functional groups, and thereby to introduce a broad range of chemical handles along the polymer.[5] In the context of this thesis, and by extension to the halogenated polyolefins obtained through the TSE-based iodination of Chapter 5, such a thiol-mediated route could be employed to anchor functional building blocks onto the polymer prior to CO_2 activation. In particular, the grafting of thiols bearing hydroxyl or amine functionalities could subsequently provide polymer-supported alcohols or amines amenable to CO_2 binding, thereby enabling the post-functionalisation synthesis of CO_2BOLs directly on the polymer backbone, rather than pre-functionalisation as explored throughout Chapters 2 to 4 (**Scheme 7.2**).



Scheme 7.2. Proposed two-step post-functionalisation route towards polymer-supported CO_2BOLs. Nucleophilic substitution of PVC chlorine atoms with bifunctional thiol compounds (where X = O or NH) and subsequent CO_2BOL formation.

A second, complementary direction can be envisaged as a natural extension of this thiol-based strategy, by selecting a mercaptophenol as the bifunctional nucleophile. The thiolate function would first ensure the S_N2 substitution of the halogen atoms along the polymer backbone, in line with the chemistry described above, while the phenol moiety would be left dangling on the polymer chain as a latent CO_2-reactive handle. The pendant phenol groups thereby introduced could then undergo a Kolbe-Schmitt carboxylation, yielding polymer-supported hydroxybenzoic acid motifs and providing an alternative route to covalently incorporate CO_2 along a polymer backbone. Although the classical Kolbe-Schmitt reaction typically requires elevated temperatures and pressures, recent developments such as the para-selective variant reported by Liu, Perry and Kong indicate that significantly milder conditions are now within reach,[6] which would render the post-functionalisation of polymer-bound phenols increasingly realistic. Should this two-step strategy prove feasible, its implementation under reactive-extrusion conditions, in line with the solvent-free TSE-based methodology established in Chapter 5, would constitute an even more attractive outcome, by combining the thiol-mediated grafting and the CO_2 fixation within a single solvent-free, melt-state polymer process (**Scheme 7.3**).



Scheme 7.3. Envisioned route for the CO_2-based functionalisation of a halogenated polymer backbone via the Kolbe-Schmitt reaction.

The extensions and alternative directions discussed above are not intended as an exhaustive roadmap, but rather as a glimpse of the many opportunities that remain to be explored at the interface between CO_2 valorisation and plastic upcycling. The chemistries developed throughout this manuscript are meant as stepping stones rather than endpoints, and much work is still required to translate these concepts into mature processes. Further studies, both along the lines suggested here and beyond, will be needed to progressively shape a more circular and sustainable use of carbon and polymeric resources.

References

1 H. Reinecke and C. Mijangos, *Polymer Bulletin*, 1996, **36**, 13–18.

2 H. Reinecke and C. Mijangos, *Macromol. Chem. Phys.*, 1998, **199**, 2199–2204.

3 R. Navarro, K. Bierbrauer, C. Mijangos, E. Goiti and H. Reinecke, *Polymer Degradation and Stability*, 2008, **93**, 585–591.

4 M. Herrero, P. Tiemblo, J. Reyes-Labarta, C. Mijangos and H. Reinecke, *Polymer*, 2002, **43**, 2631–2636.

5 R. Navarro, M. Perrino, C. García, C. Elvira, A. Gallardo and H. Reinecke, *Polymers*, 2016, **8**, 152.

6 X. Liu, G. J. P. Perry and D. Kong, *Angew. Chem. Int. Ed.*, 2026, **65**, e22503.

APPENDIX

Evaluation of CO_2-Binding Organic Liquids as Electrolytes



TABLE OF CONTENTS

I. INTRODUCTION 258

II. RESULTS AND DISCUSSION 260

A. CO_2BOL screening 260

B. Temperature dependence and activation energy 265

C. Conductivity recovery and impedance evolution 267

D. ACN–based solutions: concentration dependence and LiTFSI compatibility 273

III. CONCLUSION 276

IV. EXPERIMENTAL 277

A. Materials 277

B. Procedures 277

C. Methods 279

V. SUPPORTING INFORMATION 281

VI. REFERENCES 289

I. INTRODUCTION

In 2023, global greenhouse gas (GHG) emissions reached a record high of 57.1 Gt of CO_2 equivalent ($GtCO_2e$), with carbon dioxide (CO_2) accounting for roughly 75% of the total.[1] Strategies to address CO_2 emissions can be broadly categorised into two approaches. The first, upstream mitigation, focuses on reducing emissions at their source, primarily through decreasing reliance on fossil fuels. While this approach remains essential, increasing research efforts have also been directed toward downstream strategies, including atmospheric carbon removal, carbon capture and storage (CCS), and carbon capture and utilisation (CCU).[2,3] Among CCU technologies, significant research efforts have been devoted to the chemical conversion of CO_2 into value-added products, including fuels, chemicals, and polymers.[4–6] A key prerequisite for CCU is the efficient capture of CO_2. Currently, the industrial benchmark for post-combustion CO_2 capture relies on aqueous amine solutions, most notably monoethanolamine (MEA). However, this technology suffers from several well-documented drawbacks: high energy requirements for solvent regeneration, solvent degradation, corrosion, and the large amount of water that must be heated during the stripping step.[7] These limitations have motivated the development of water-lean capture systems with improved energy efficiency. Among these, CO_2-binding organic liquids (CO_2BOLs) - anhydrous mixtures of an alcohol and an amidine or guanidine base - have attracted considerable attention as CO_2 capture agents. Indeed, upon exposure to CO_2, the alcohol and the base react together to reversibly form amidinium or guanidinium alkyl carbonate salts, enabling CO_2 capture without the thermodynamic penalty associated with water.[8–11] This switchable polarity, combined with the tunability of their molecular structure, makes CO_2BOLs particularly promising not only for CO_2 capture but also for its direct utilisation. Indeed, CO_2BOLs have recently been employed in the synthesis of cyclic[12–15] and linear dialkyl carbonates,[16**] polycarbonates,[17,18] and for the functionalisation of poly(vinyl chloride) (PVC).[19,20††]

Several works utilising the same strategy also make use of amines instead of alcohols.[21–24] In recent work, our group broadened the original definition of CO_2BOLs to include the amine-based compounds (CO_2-binding amines, CO_2BAMs) in addition to the alcohol-based ones (CO_2-binding alcohols, CO_2BALs). While the latter fits the original definition of CO_2BOLs introduced by Heldebrant, the former produce alkylcarbamate salts rather than alkycarbonate ones, circling back to the well-known CO_2 capture by amines.[22,25–28] In solvent-free conditions, the synthesis of CO_2BAMs generally yields higher conversion rates than the one of CO_2BALs. Moreover, it was shown that the choice of the base strongly impacted CO_2 capture ability as well.[10,16,29] Beyond their use as CO_2 capture agents and as reactive intermediates in organic synthesis, the CO_2-derived ionic salts formed by both CO_2BALs and CO_2BAMs constitute an emerging class of

** See **Chapter 2** – Turning Carbon Dioxide into Dialkyl Carbonates through Guanidinium-Assisted S_N2 Ion-Pair Process

†† See **Chapter 3** – CO_2-Binding Alcohols as Potential Candidates for Poly(Vinyl Chloride Upcycling) and **Chapter 4** – Boosting PVC Reactivity through Iodination for CO_2-Derived Functionalisation

structurally tuneable ionic compounds in their own right. Their intrinsic ionic nature - arising directly from the CO_2 fixation reaction - raises a broader question: could such compounds find utility in applications that are typically the domain of ionic liquids ? In particular, although CO_2BALs and CO_2BAMs have not yet been explored as battery electrolytes, their tunability in terms of both cation and CO_2-derived anion structure suggests that they could offer modulable electrolytic properties, analogous to the effects observed in conventional ionic liquids where modification of the ion pair influences conductivity, viscosity, and electrochemical stability.[30–32] Their chemical modularity and their ability to generate ionically conductive phases thus pave the way for a new exploratory approach to the design of safe and high-performance electrolytes, whilst taking advantage of the inherent reversibility of CO_2 capture.

Ionic liquids have been investigated as electrolytes for lithium-ion batteries for over two decades,[33] initially motivated by safety concerns associated with conventional organic carbonate-based electrolytes. Lithium-ion batteries are susceptible to thermal runaway upon overcharging or elevated temperatures. This process involves exothermic reactions between electrolyte and electrode materials, leading to gas evolution (release of gases including CO_2 and flammable species), pressure buildup within the cell, and, in severe cases, fire or explosion.[34,35] Ionic liquids were therefore considered attractive alternatives due to their non-flammability, high thermal stability, and good ionic conductivity. Additionally, their ability to dissolve gases such as CO_2 may help mitigate pressure buildup during thermal runaway events.[34] However, while this property can contribute to reducing overpressure during failure events, the use of ionic liquids in batteries does not constitute a CO_2 mitigation strategy, as the dissolved carbon is produced within the system rather than captured for valorisation in battery technology.

Batteries actually making use of CO_2 in the electrolytic system as a CCU strategy – known as metal-CO_2 batteries – have been developed in recent years.[36] These devices employ a metallic anode and a cathode typically composed of nanostructured carbon-based materials (e.g., carbon nanotubes, carbon fibres), through which CO_2 diffuses toward a catalyst layer located at the electrolyte interface. There, CO_2 can be converted into various compounds, including alkali carbonates, depending on the battery configuration during discharge. At the same time, metallic ions are released into the electrolyte as the anode is oxidised. On the other hand, during charge, CO_2 is regenerated at the cathode while the metallic ions are deposited back onto the anode.[36–38] In 2018, Khurram *et al*. even combined metal-CO_2 battery technology with CO_2 capture by alkylamines.[39] However, while promising, such technology faces challenges. Notably, safety concerns involving gas management at the CO_2-feed level as well as the hazardous gaseous by-products potentially generated.[36]

In this work, we explore the possibility of CO_2 capture chemistry incorporation into conventional Li-ion batteries by employing CO_2BOLs as electrolyte components. Unlike metal-CO_2 batteries, which require external CO_2 supply and associated gas management systems, this approach relies on chemically bound CO_2 within the electrolyte, thereby potentially reducing

safety concerns related to gas handling. In addition, the use of CO_2BOLs is motivated by their organic nature and their reversible decomposition at elevated temperatures, which leads to the release of CO_2. Herein, we present preliminary studies evaluating the electrochemical behaviour and potential applicability of CO_2BOL-derived electrolytes in Li-ion battery systems. Moreover, we show that CO_2BOLs' decomposition at elevated temperatures leads to a decrease in ionic conductivity. Upon cooling, the CO_2BOL is restored, in turn restoring ionic conductivity. This could allow for the system to regulate itself in the event of a thermal runaway, thereby reducing risks.

II. RESULTS AND DISCUSSION

A. CO_2BOL screening

Given that the mixing and matching of nucleophiles and bases impacts CO_2BOLs' chemical and physical properties, a selected variety of compounds were prepared to screen parameters such as the nature of the base, the nature of the nucleophile, and the alkyl chain length of the nucleophile. As the goal is to evaluate the potential of CO_2BOLs as liquid electrolytes, our focus was set on short-chain nucleophiles such as 1-butanol, 1-hexanol, 1-butylamine, and 1-hexylamine. This choice was supported by the melting points reported both by Phan *et al.*[40] and our own group.[19] CO_2BOLs were systematically prepared from an equimolar mixture of nucleophile and base, using a CO_2 pressure of 0.2 bar for a duration of three hours. Other preparation conditions and CO_2BOL conversion rates are shown in **Table A.1**. The exact synthetic procedures are found in the experimental section.

To facilitate consistent comparisons throughout this chapter, samples are designated using a short code of the form "nucleophile-base". The studied nucleophiles include 1-butanol (ButOH), 1-hexanol (HexOH), 1-butylamine ($ButNH_2$), and 1-hexylamine ($HexNH_2$). The organic bases used are 1,5,7-triazabicyclo[4.4.0]dec-5-ene (TBD) and 1,8-diazabicyclo[5.4.0]undec-7-ene (DBU). For example, the combination of ButOH and DBU is denoted as ButOH-DBU, whereas $HexNH_2$ combined with TBD is labelled $HexNH_2$-TBD. Amines used without DBU or TBD are referred to simply by the nucleophile ($ButNH_2$ or $HexNH_2$). Samples prepared in the absence of CO_2 are indicated by appending the suffix "-free" to the corresponding code, denoting the CO_2-free mixture derived from the same precursor pair (e.g. ButOH-DBU-free or $HexNH_2$-TBD-free).

At 25 °C, most DBU-based systems (and their CO_2-free counterparts) were liquids or viscous liquids, whereas the TBD-based and amine-only CO_2BAMs were obtained as solid powders (**Table SA.1**, **p. 281**). Because neat conductivity measurements require dispensing a defined volume (60 µL) onto a glass-fibre separator, only flowable samples could be evaluated as neat electrolytes at 25 °C. Samples that were solid at 25 °C are therefore discussed using measurements at elevated temperature and/or as solutions in acetonitrile (ACN).

Table A.1. CO_2BOL preparation conditions [a]

Entry	Nucleophile	Base	Reaction Temperature (°C)	Conversion in CO_2BOL[b] (%)
1	ButOH	DBU	21	63
2	HexOH		21	49
3	$ButNH_2$		60	90
4	$HexNH_2$		90	88
5	ButOH	TBD	90	70.5
6	HexOH		90	68
7	$ButNH_2$		60	94.5
8	$HexNH_2$		90	88.5
9	$ButNH_2$	$ButNH_2$	60	80
10	$HexNH_2$	$HexNH_2$	90	44

[a] The reaction was systematically performed from an equimolar mixture of the nucleophile and the base for 3 hours, under 0.2 bar of CO_2.

[b] Conversion rates are calculated based on ^{1}H NMR spectra (500 MHz, $CDCl_3$) of the final CO_2BOL products.

The temperature-dependent ionic conductivity of the neat systems were measured in symmetric SS | electrolyte | SS cells (SS = stainless steel) in the 20-60 °C temperature range. Temperatures higher than 60 °C were not investigated due to the risk of thermal decomposition of CO_2BOL systems with the concomitant release of CO_2. Indeed, thermogravimetric analysis systematically shows degradation onset temperatures (T5%) below 100 °C regardless of the nucleophile/base pair, going as low as ~58 °C in the case of $HexNH_2$ (**Figures SA.1 – SA.4, p. 281 – 282**).

For all compositions that could be evaluated in the neat state (**Table SA.1**, **p.281**), conductivity increases with temperature, consistent with thermally activated ion transport.[41,42] CO_2BOL samples (**Figure A.1a**) show the highest conductivities, reaching ~10^{-6}–10^{-4} S.cm^{-1} across the investigated temperature range. In contrast, CO_2-free counterparts prepared from the same nucleophile/base pairs (**Figure A.1b**) are typically one to two orders of magnitude less conductive, highlighting the strong impact of CO_2BOL formation on ion transport in the neat mixtures.

As a reference, the individual components (ButOH, HexOH, $ButNH_2$, $HexNH_2$, and pristine DBU) are far less conductive on their own (**Figure A.1c**), remaining within ~10^{-8}–10^{-5} S.cm^{-1} under the same measurement conditions. This baseline indicates that the conductivity of the formulated neat CO_2BOL systems is dominated by the ionic species and their local solvation/association environment rather than by intrinsic conduction of the neutral reactants.[43]

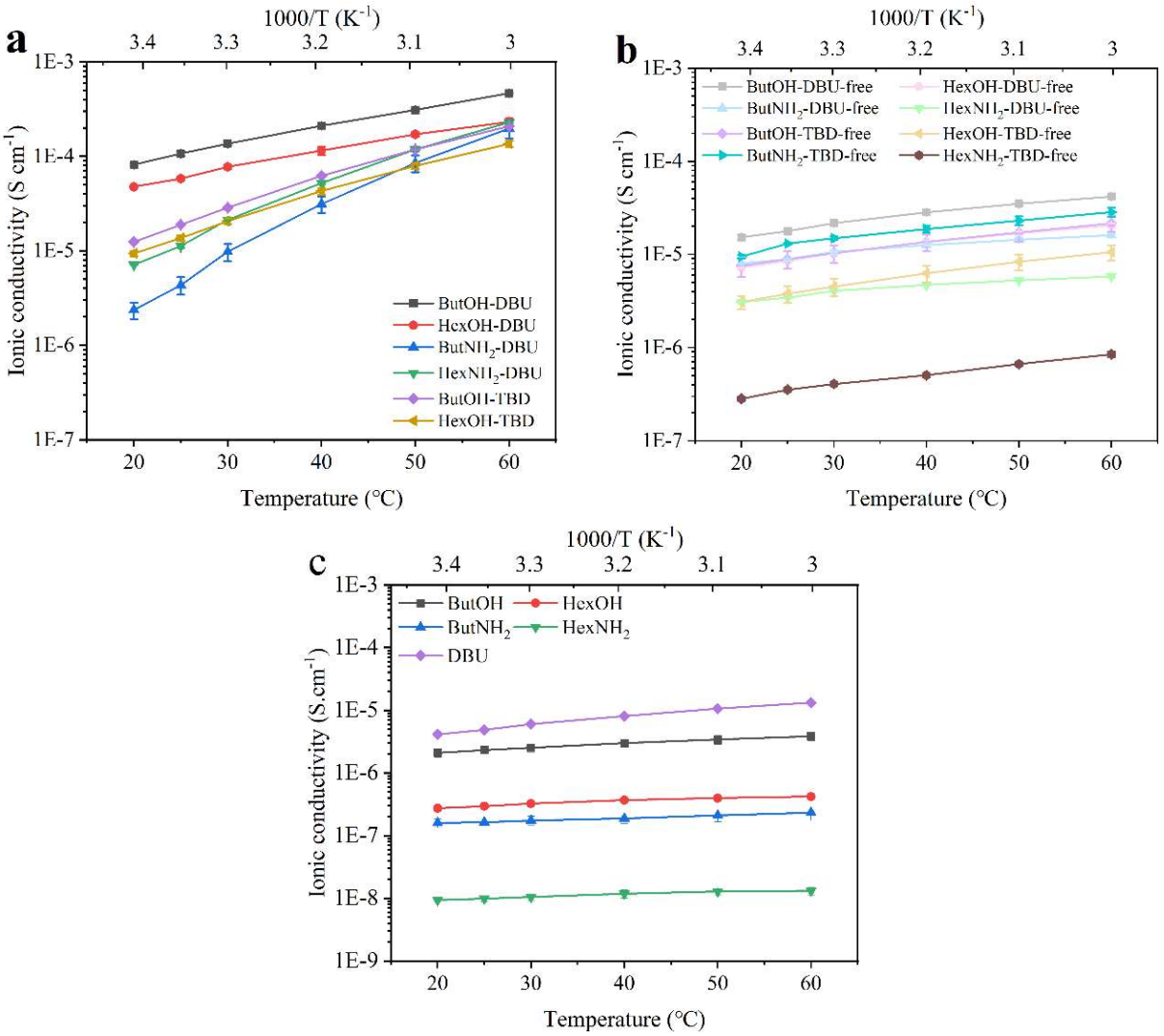


Figure A.1. Temperature-dependent ionic conductivity of neat samples (20-60 °C): **(a)** CO_2BOLs, **(b)** CO_2-free counterparts, and **(c)** neat individual reactants.

The conductivity/temperature (σ–T) profiles from **Figure A.1**, show that the ionic transport in these neat protic molecular systems is strongly dependent on molecular structure and composition. In other words, each of the three selected variables, i.e. chain length (butyl vs hexyl), base identity (DBU vs TBD), and nucleophile type (alcohol vs amine), has a clear impact on ionic conductivity. The investigation of each parameter is detailed below.

Chain-length effects were assessed by comparing butyl- and hexyl-derived samples within the same nucleophile/base pair (**Figure A.2**). In the CO_2BAL systems at 25 °C (**Figure A.2a**), butyl analogues are consistently more conductive than the corresponding hexyl analogues for both DBU and TBD. This trend is consistent with reduced viscosity and improved ionic mobility in the shorter-chain formulations.[44] Conversely, an opposite behaviour is observed for DBU-based CO_2BAMs where the hexyl analogue exhibits higher conductivity than the butyl analogue (**Figure A.2a**). The TBD-based CO_2BAMs, however, could not be evaluated as neat electrolytes due to its solid nature at 25 °C, which prevents their dispensing onto the glass-fibre separator in the present SS | electrolyte | SS configuration (**Table SA.1**, **p. 281**).

For the CO_2-free counterparts at 25 °C (**Figure A.2b**), the chain-length effect is generally modest: butyl-based systems tend to be slightly more conductive than the corresponding hexyl analogues.

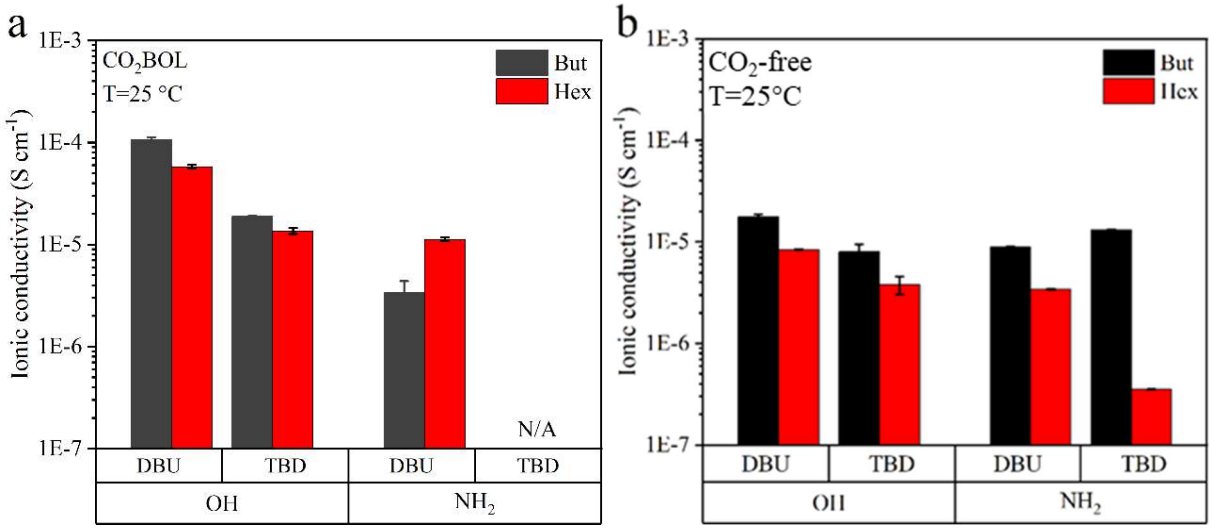


Figure A.2. Effect of chain length on ionic conductivity at 25 °C: **(a)** CO_2BOL systems and **(b)** CO_2-free counterparts.

The nature of the base also has a clear impact on ionic conductivity at 25 °C (**Figure A.3**). In the CO_2BAL systems (**Figure A.3a**), DBU formulations are consistently more conductive than the corresponding TBD formulations for both butyl- and hexyl-derived samples. For CO_2BAM systems, a direct DBU-TBD comparison at 25 °C is not possible again due to the inability to test the TBD-based CO_2BAMs as neat electrolytes with the present SS | electrolyte | SS configuration.

The same overall tendency is retained in the CO_2-free series (**Figure A.3b**), where DBU generally yields higher conductivity than TBD for both alcohol- and amine-based systems. Taken together, these results identify DBU as the more favourable base for achieving higher room-temperature conductivity in the neat state within the compositions accessible to measurement.

Differences between DBU and TBD likely arise from how the base shapes both charge-carrier speciation and mobility. In addition, the base can indirectly control measured performance by determining whether the material remains flowable at room temperature, as illustrated by the solid TBD-based CO_2BAM samples at 25 °C.

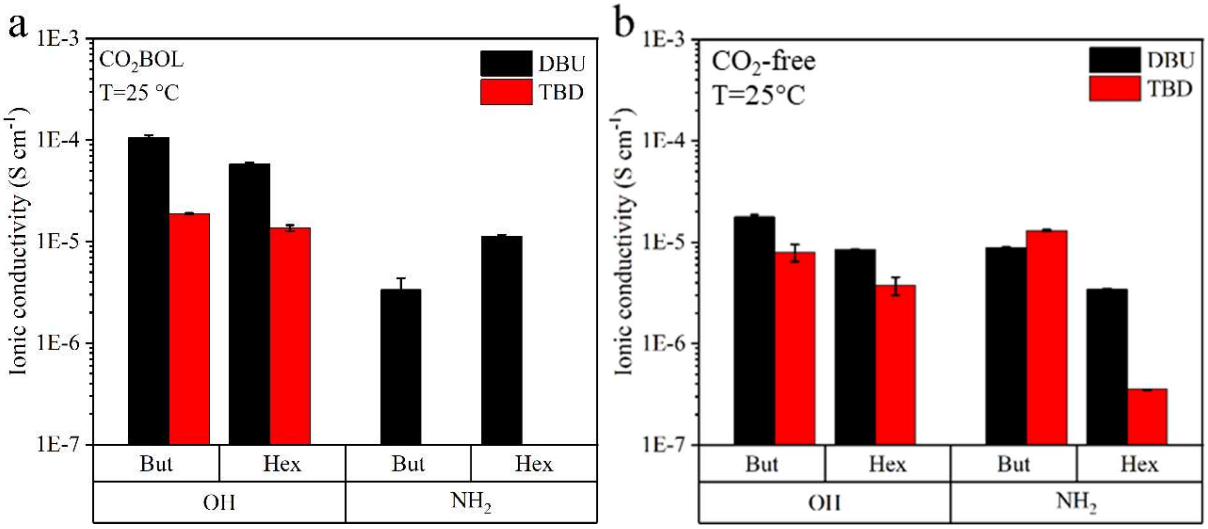


Figure A.3. Effect of base (DBU vs TBD) on ionic conductivity at 25 °C: **(a)** CO_2BOL systems and **(b)** CO_2-free counterparts.

Finally, the nature of the nucleophile strongly affects room-temperature conductivity as well (**Figure A.4**). CO_2BAL systems are markedly more conductive than the corresponding CO_2BAM systems under DBU conditions for both chain lengths (**Figure A.4a**). The same qualitative contrast is expected for TBD-based formulations. However, as the TBD-based CO_2BAM samples cannot be assessed, this cannot be confirmed.

In the CO_2-free series (**Figure A.4b**), the OH/NH_2 difference is not uniform and varies with both base identity and chain length. However, those systems cannot be qualified as electrolytes owing to their low intrinsic ionic conductivity.

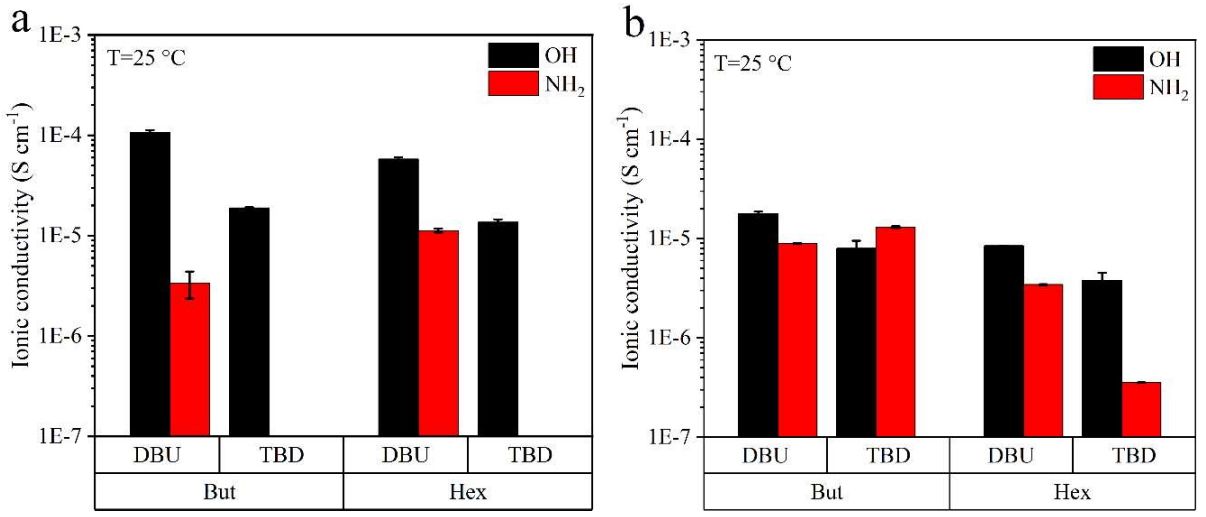


Figure A.4. Effect of nucleophile identity (OH vs NH_2) on ionic conductivity at 25 °C: **(a)** CO_2BOL systems and **(b)** CO_2-free counterparts.

B. Temperature dependence and activation energy

The temperature dependence was analysed using an Arrhenius relationship (**Eq. A.1**) to estimate the activation energy (E_a).

$$\ln(\sigma T) = \ln(A_0) - \frac{E_a}{RT} \qquad \textit{Eq. A.1}$$

where σ is the measured ionic conductivity, T is the temperature, A_0 is the pre-exponential factor, and R is the universal gas constant (8.3144 $J.mol^{-1}.K^{-1}$).

Plotting ln(σT) as a function of 1000/T yields a straight line whose slope b is related to E_a according to:

$$b = -\frac{E_a}{1000R} \qquad \textit{Eq. A.2}$$

The resulting plots for the CO_2BOL and CO_2-free systems (**Figure A.5**) exhibit excellent linearity without curvature, indicating Arrhenius behaviour typical of low-viscosity liquid electrolytes, rather than a Vogel–Tamman–Fulcher (VTF) behaviour.[45]

The resulting E_a values are summarised in **Table A.2** and fall within the range typical of liquid electrolytes for both CO_2BOL systems and their CO_2-free counterparts. Notably, the higher activation energies observed for CO_2BOL systems over 20-60 °C range indicate a stronger temperature dependence of ionic conductivity, consistent with their steeper increase in conductivity upon heating.

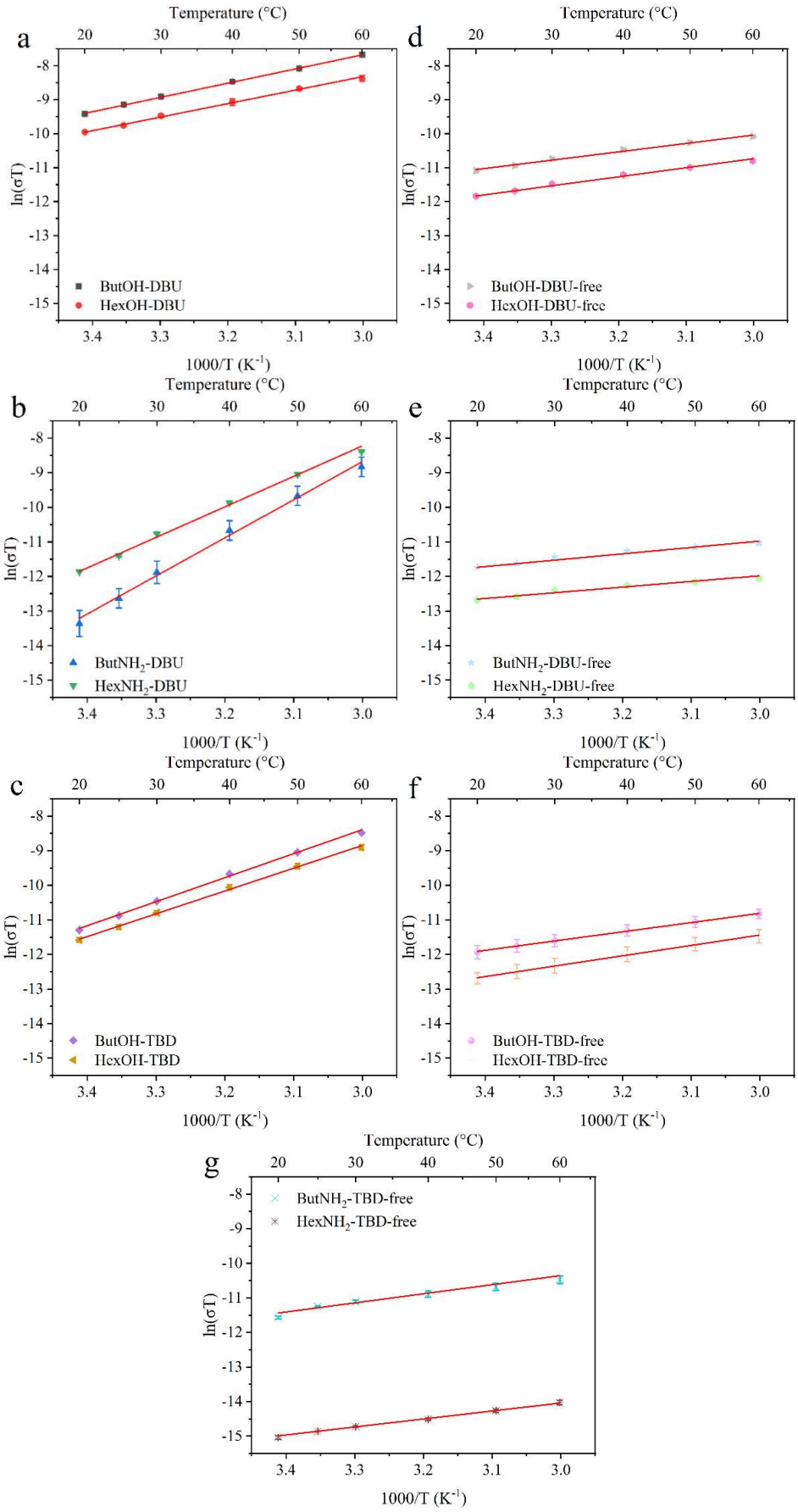


Figure A.5. Arrhenius analysis of ionic conductivity in neat systems: ln(σT) versus 1000/T (20-60 °C) with linear fits of **(a-c)** CO_2BOL systems and **(d-g)** CO_2-free counterparts (see panel labels for compositions).

Table A.2. Apparent activation energies for ionic conduction derived from Arrhenius fits.

CO_2BOL		CO_2-free	
Sample	**Ea (kJ/mol)**	**Sample**	**Ea (kJ/mol)**
ButOH–DBU	34.91	ButOH–DBU–free	19.64
HexOH–DBU	33.15	HexOH–DBU–free	21.60
$ButNH_2$–DBU	90.92	$ButNH_2$–DBU–free	14.68
$HexNH_2$–DBU	73.39	$HexNH_2$–DBU–free	13.28
ButOH–TBD	57.44	ButOH–TBD–free	21.30
HexOH–TBD	54.86	HexOH–TBD–free	24.72
$ButNH_2$–TBD	N/A[a]	$ButNH_2$–TBD–free	20.34
$HexNH_2$–TBD	N/A[a]	$HexNH_2$–TBD–free	23.37

[a] N/A indicates samples that are solid at 25 °C and not measurable in the neat state.

C. Conductivity recovery and impedance evolution

Thermal stability and temperature history can strongly influence ion transport in electrolytes. In addition, CO_2BOL systems are prone to thermal decomposition, which is accompanied by the release of CO_2. To assess those effects, selected samples were thermally treated at 70 °C under sealed or open conditions and their conductivity/impedance were compared before and after heating.

Under sealed conditions, neat samples were heated at 70 °C (typically 15 h) and then cooled to 20 °C prior to electrochemical impedance spectroscopy (EIS) measurements. This protocol allows the decoupling of the changes induced by the instantaneous temperature dependence of σ from those originating from the sample's thermal history. The increase in σ after sealed heating is mirrored by the impedance response. For CO_2BOL samples, the high-frequency intercept shifts to lower resistance after heating and cooling, indicating improved ionic transport under sealed conditions (**Figure A.6** and **Figures SA.5 – SA.18**, **p. 283 – 287**).

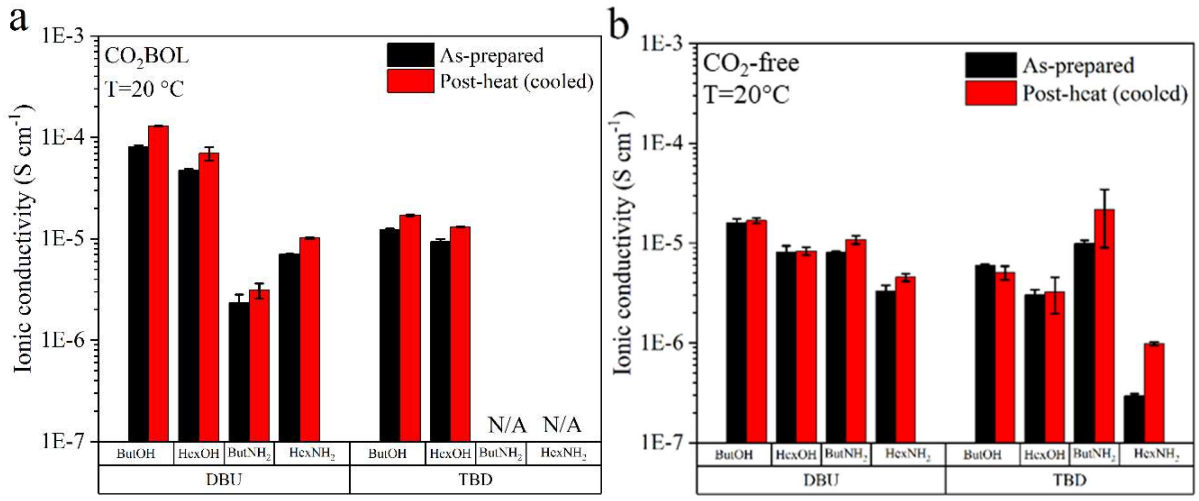


Figure A.6. Effect of sealed thermal treatment on ionic conductivity measured after cooling to 20 °C: **(a)** CO_2BOL systems and **(b)** CO_2-free counterparts (as-prepared vs post-heat (cooled)).

CO_2BOL samples were heated at 70 °C under either sealed or open conditions to assess how exposure to the atmosphere affects composition and transport behaviour. Open-vial heating produced clear mass loss across the CO_2BOL sample set (**Table A.3**), motivating a closer electrochemical examination using ButOH–DBU (**Table A.3, entry 1**) as a representative formulation.

Table A.3. Mass loss of CO_2BOL-containing samples during open-vial heating at 70 °C.

Entry	Sample (CO_2BOL)	m_0 (AP, mg)	m_{30} (Open 30 h, mg)	m_{60} (Open 60 h, mg)	Mass loss[a] (0→60 h, %)
1	ButOH–DBU	318.0	231.3	187.5	41
2	HexOH–DBU	325.2	290.1	245.1	25
3	$ButNH_2$–DBU	165.4	113.1	85.2	48
4	$HexNH_2$–DBU	184.9	119.0	76.7	55
5	ButOH–TBD	282.6	237.3	199.3	29
6	HexOH–TBD	347.2	340.1	320.8	11

[a] Mass loss (%) was calculated as $(m_0 - m_{60})/m_0 \times 100\%$

Impedance measurements were therefore carried out in symmetric SS | electrolyte | SS cells at 20 °C after different thermal histories. As shown in **Figure A.7a**, the bulk resistance (R_b, high-frequency intercept) is essentially unchanged after sealed heating for 15 h relative to the as-prepared state (126 Ω vs 127 Ω), indicating that the low-resistance state is maintained under sealed conditions. In contrast, under open heating, the resistance increases steadily with time, from 210 Ω (15 h) to 309 Ω (30 h) and 533 Ω (45 h), reaching 955 Ω (60 h) close to the CO_2-free baseline (979 Ω). The corresponding Nyquist plots (**Figure A.7b**) show the same evolution as a progressive right shift of the high-frequency intercept occurs with increasing open-vial heating time.

Overall, **Table A.3** and **Figure A.7** demonstrate that open-vial heating at 70 °C leads to substantial mass loss and a strong increase in bulk resistance, effectively driving the impedance response toward CO_2-free behaviour, whereas sealed heating suppresses this drift. This strongly suggests that open-vial heating at 70 °C results in the thermal decomposition of CO_2BOL samples releasing CO_2, and that those samples start to resemble to CO_2-free ones.

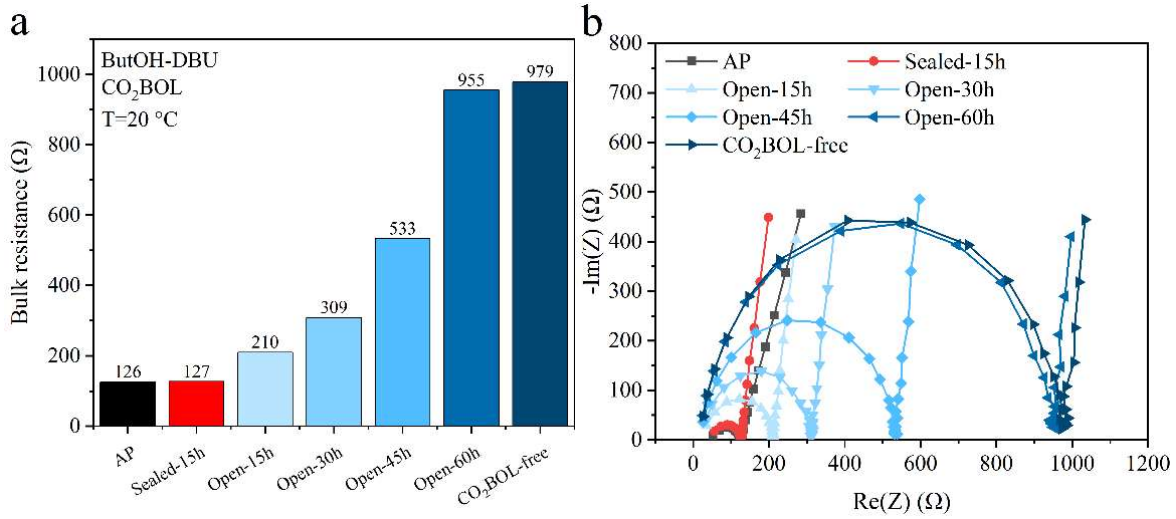


Figure A.7. Open-vial heating induces impedance reversion toward CO_2-free behaviour (ButOH–DBU, CO_2BOL): **(a)** bulk resistance after different thermal histories and **(b)** corresponding Nyquist plots (20 °C, AP = as prepared).

To assess the thermal behaviour of CO_2BOL electrolytes under prolonged heating in a sealed environment, symmetric SS | electrolyte | SS coin cells were aged at 70 °C and monitored by in situ EIS. ButOH–DBU and HexOH–DBU were selected as representative CO_2BOL systems, and three independently assembled cells were tested for each composition.

Both systems show a clear decrease in bulk resistance with aging time (**Figure A.8** and **Table A.4**). For ButOH–DBU, R_b drops from 18.60 ± 1.33 Ω to 11.57 ± 0.57 Ω after 108 h. HexOH–DBU follows the same trend, decreasing from 30.78 ± 8.76 Ω to 17.82 ± 0.59 Ω over the same timeframe. Most of the resistance reduction occurs within the first 18 h, after which R_b declines more slowly and approaches a near-steady value by 96–108 h.

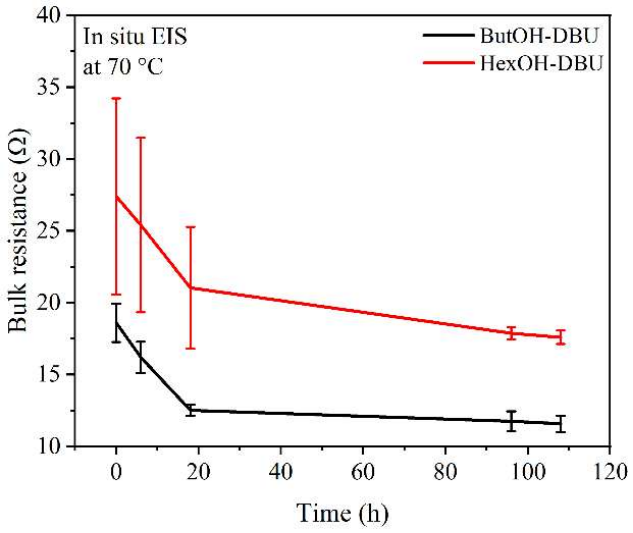


Figure A.8. Evolution of bulk resistance during coin-cell aging at 70 °C (in situ EIS).

High-frequency Nyquist plots (**Figures SA.19 and SA.20**, **p. 288**) show the same evolution across all independently assembled cells: the high-frequency intercept shifts to lower values with aging time and changes only marginally after ~96–108 h.

Compared with open-vial heating, coin-cell aging provides a clear example of how a closed environment alters the thermal response. Under open conditions, mass loss is accompanied by a strong increase in resistance and a drift toward CO_2-free behaviour, whereas the sealed coin-cell configuration prevents volatilisation and allows the electrolyte to relax toward a lower-resistance state. These results suggest that CO_2BOL-based protic molecular systems can remain impedance-stable under sealed, device-relevant thermal exposure, at least within the time window examined here.

Table A.4. Bulk resistance (R_b) during coin-cell aging at 70 °C (in situ EIS).

	ButOH–DBU		HexOH–DBU	
Time (h)	R_b (Ω)	SD (Ω)	R_b (Ω)	SD (Ω)
0	18.60	1.33	30.78	8.76
2	17.55	1.23	29.05	7.02
4	16.67	1.12	28.18	6.84
6	16.20	1.09	27.77	6.85
15	13.73	1.64	25.04	6.87
18	12.51	0.38	21.65	3.68
96	11.75	0.70	18.07	0.53
108	11.57	0.57	17.82	0.59

To further evaluate the effect of repeated temperature changes, impedance cycling tests were performed between 25 and 70 °C. This experiment complements the sealed-heating and coin-cell aging results discussed above. ButOH–DBU-based samples with and without CO_2 were compared in terms of impedance evolution and recovery behaviour.

Overall, the CO_2BOL sample exhibits consistently lower impedance than its CO_2-free counterparts, and both systems show reduced impedance at 70 °C compared to 25 °C. The relative decrease is more pronounced for the CO_2BOL system.

Figure A.9a and **b** show the impedance values measured during repeated cycling. The CO_2BOL sample remains less resistive than the CO_2-free one over the full sequence, with values of ~67–75 Ω at 25 °C and 13 - 23 Ω at 70 °C, compared to ~525–550 Ω and 195 - 250 Ω, respectively, for the CO_2-free system. The normalised data (**Figure A.9c,d**) confirm the larger relative decrease at elevated temperature for the CO_2BOL sample. A gradual cycle-dependent decrease is also observed, particularly at 70 °C.

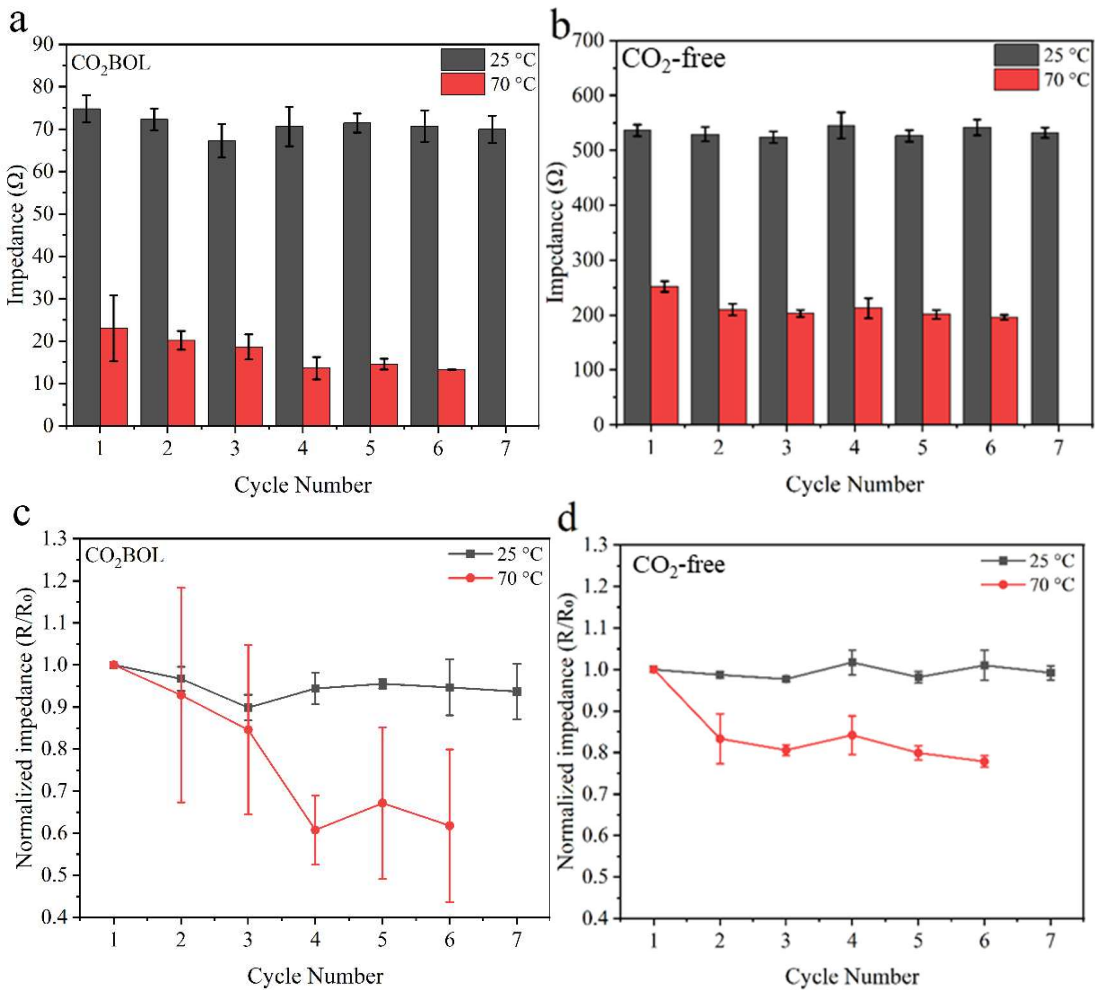


Figure A.9. Absolute **(a,b)** and normalised **(c,d)** impedance evolution during repeated temperature cycling between 25 and 70 °C. **(a,c)** CO_2BOL system. **(b,d)** CO_2-free system.

To examine reversibility, the CO_2BOL system was monitored during aging at 70 °C followed by recovery at 25 °C (**Figure A.10**). During aging, the impedance decreases from about ~15.2 Ω to 13.0 Ω over 10 h. Upon returning to 25 °C, the impedance increases with time, with most recovery occurring within the first 2 h before reaching a plateau (~68.1 Ω after 10h). This behaviour indicates partial reversibility, with a remaining thermal-history effect.

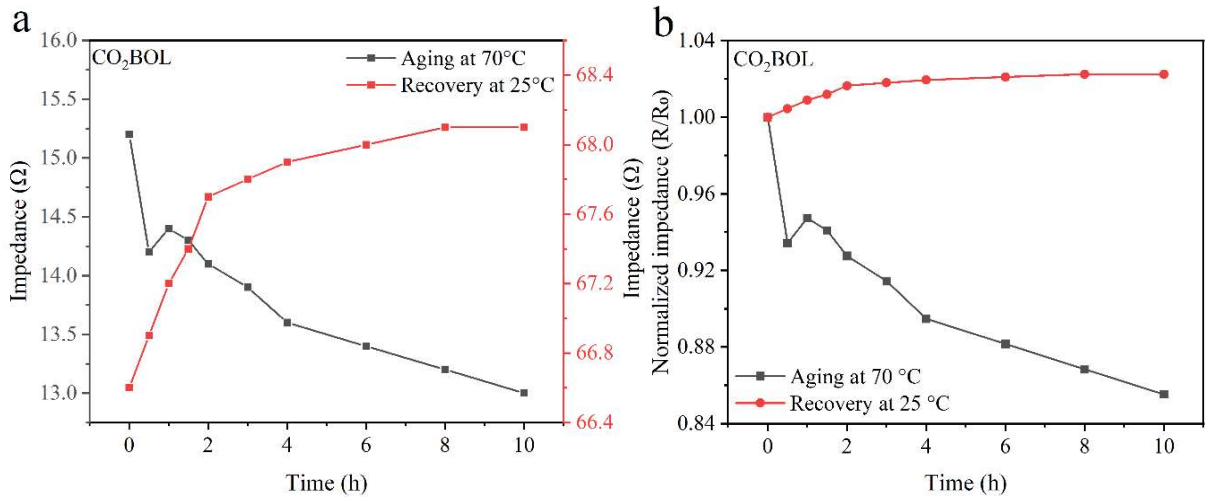


Figure A.10. Impedance evolution of the CO_2BOL system during aging at 70 °C and subsequent recovery at 25 °C. (a) Absolute impedance as a function of time. **(b)** Normalised impedance as a function of time.

The recovery of impedance after thermal cycling was quantified for both systems (**Figure A.11**). At 25 °C, recovery is high for both samples (94% for CO_2BOL and 99% for CO_2-free), whereas lower values are observed at 70 °C (62% and 78%, respectively).

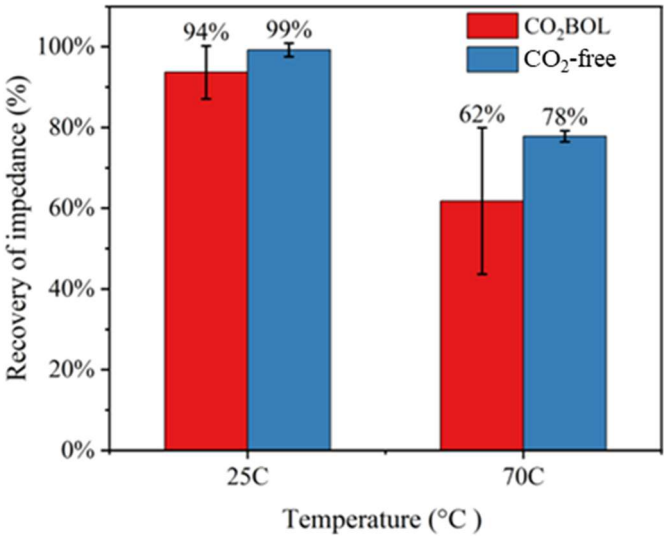


Figure A.11. Recovery of impedance after thermal cycling for CO_2BOL and CO_2-free systems at 25 and 70 °C.

Taken together, these results show that the CO_2BOL system combines lower impedance with a stronger and more dynamic thermal response, characterised by a larger conductivity gain at elevated temperature and a partially reversible behaviour upon cooling, indicative of a marked sensitivity to thermal history.

D. ACN–based solutions: concentration dependence and LiTFSI compatibility

Several CO_2BOL formulations are difficult to evaluate in the neat state at room temperature because they are highly viscous or solid. To improve processability, the electrolytes were therefore dissolved in acetonitrile (ACN). **Figure A.12a** compares conductivities measured at 20 °C for selected systems as neat samples and as ACN solutions at a concentration of 200 mg.mL^{-1}. For compositions that can be tested in the neat state, dissolution in ACN increases σ by roughly one to two orders of magnitude, from the 10^{-6} - 10^{-4} S.cm^{-1} range to around 10^{-3} S.cm^{-1}. ACN also allows measurements for formulations that cannot be tested as neat electrolytes at 20 °C (N/A in **Figure A.12a**), extending the accessible composition space. However, while most formulations produced clear, single-phase solutions at a concentration of 200 mg.mL^{-1} at room temperature, the HexNH$_2$–TBD, ButNH$_2$, and HexNH$_2$ CO_2BAMs displayed visible phase separation/precipitation. These systems' ionic conductivity could therefore not be assessed in solution either.

The ACN solutions also show the expected increase in σ with temperature from 20 to 60 °C (**Figure A.12b**). Most DBU- and TBD-based formulations cluster within a similar conductivity range in ACN, whereas ButNH$_2$-TBD remains consistently lower across the full window, (indicating that the chemical nature of the CO_2BOL still influences ion transport in solution.). For reference, neat ACN is far less conductive, confirming that the measured response arises from the dissolved CO_2BOL species rather than the solvent itself.

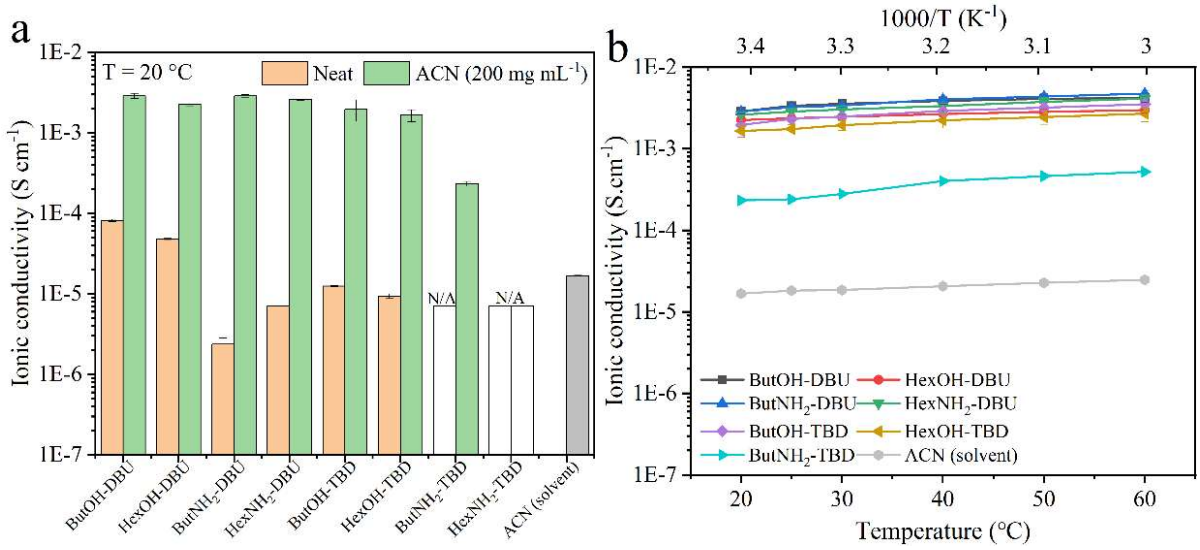


Figure A.12. Ionic conductivity of CO_2BOL-containing systems as neat samples and as acetonitrile solutions: **(a)** σ at 20 °C (neat vs 200 mg.mL^{-1}), and **(b)** temperature dependence for 200 mg.mL^{-1} solutions (20–60 °C).

Concentration effects were examined by preparing ACN solutions at 100 and 200 mg.mL^{-1} at fixed solvent volume. **Figure A.13** shows a representative case (HexOH–DBU): the 200 mg.mL^{-1}

solution is more conductive than the 100 mg.mL^{-1} solution over the full 20–60 °C range, and the gap between the two remains visible at every temperature point. This behaviour indicates that increasing the CO_2BOL loading raises the conductivity of the solution, although the absolute values and the magnitude of the gain remain formulation dependent. Both concentrations also show the expected increase in σ with temperature. In practice, increasing CO_2BOL concentration thus offers a straightforward way to boost conductivity while retaining manageable handling, provided the solution remains single-phase with the chosen formulation.

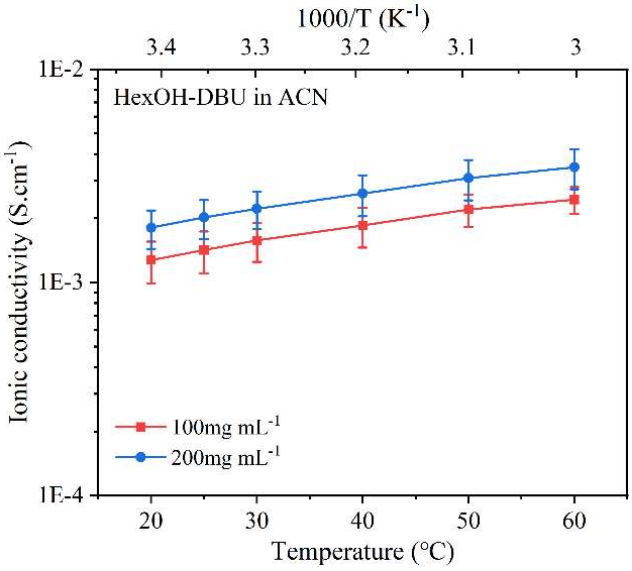


Figure A.13. Concentration dependence of ionic conductivity for HexOH–DBU in acetonitrile.

In order to check the possibility to use CO_2BOL-based electrolytes for Li-ion batteries, LiTFSI was added to the CO_2BOL (some CO_2-free samples were also investigated, see below) solutions in ACN (note that LiTFSI was insoluble in all the investigated pure CO_2BOL and CO_2-free samples). Practically, LiTFSI compatibility was screened by checking solution appearance before and after salt addition in CO_2BOL/ACN solutions. While precipitation was observed for $HexNH_2$–TBD at 200 mg.mL^{-1}, a visually homogeneous solution was obtained in ACN at 100 mg.mL^{-1}. However, when LiTFSI (0.5 M) is added, it becomes visibly inhomogeneous, consistent with a reduced solubility in the salted solution. The CO_2-free $HexNH_2$–TBD reference is clear at both 100 and 200 mg.mL^{-1} without salt. Yet, it turns strongly turbid upon LiTFSI addition, indicating an even stronger sensitivity to salt-induced phase destabilisation.[46] These observations show that phase stability upon salt addition must be evaluated alongside conductivity when selecting ACN-based CO_2BOL electrolytes, and that TBD/amine-containing formulations can be particularly prone to salt-triggered inhomogeneity.

Acetonitrile is not suitable for Li-metal-based measurements, as reported for LiTFSI/ACN electrolytes.[47] Therefore, dimethoxyethane (DME) was used as an alternative solvent for Li-referenced electrochemical tests.[48] For $HexNH_2$–DBU solutions at the same concentration (200 mg.mL^{-1}), the ionic conductivity in DME is consistently lower than that in ACN over the same

temperature range (20–60 °C) (**Figure A.14a**), indicating a strong solvent dependence of ion transport. Linear sweep voltammetry (LSV) of the DME-based solution shows a reproducible rise in anodic current at high potentials (**Figure A.14b**), indicating electrolyte stability up to 4 – 5 V in the applied conditions. It should be noted that conventional LSV can overestimate oxidative stability and is used here only as a comparative screening metric.

Moreover, addition of LiTFSI (0.5 M) in the $HexNH_2$–DBU CO_2BOL system resulted in a milky dispersion and phase separation upon standing, indicating limited salt compatibility in this solvent system at high salt concentration.

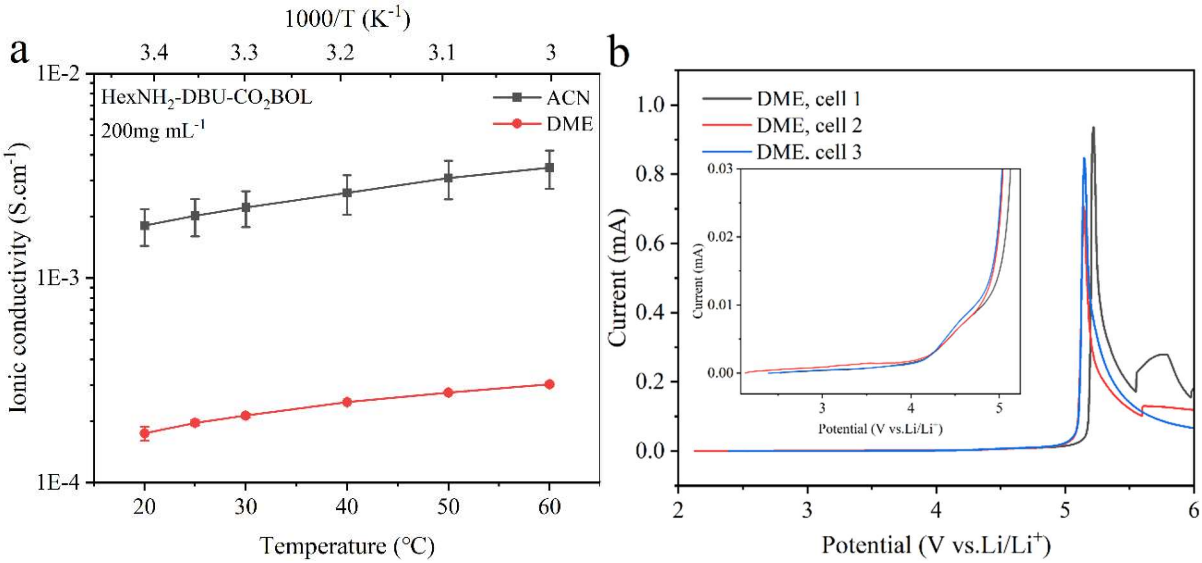


Figure A.14. Solvent effect of $HexNH_2$–DBU CO_2BOL solution (200 mg.mL^{-1}) in ACN and DME. **(a)** Ionic conductivity. **(b)** LSV in DME.

III. CONCLUSION

This work shows that CO_2BOL-containing formulations exhibit significantly enhanced ionic conductivity compared with their CO_2-free counterparts over the 20 – 60 °C temperature range, with improvements of up to one to two orders of magnitude depending on composition. In neat systems, ionic transport is strongly governed by molecular structure: increasing alkyl chain length reduces conductivity, while both the choice of base (DBU vs. TBD) and nucleophile nature (alcohol vs. amine) substantially influence charge transport. Arrhenius analysis confirms thermally activated conduction in all measurable formulations, allowing meaningful comparison of apparent activation energies across compositions. Thermal treatment experiments further reveal that sealed heating at 70 °C induces reproducible changes in impedance and conductivity that persist upon cooling, whereas open-vial heating promotes a reversion toward CO_2-free-like impedance behaviour, highlighting the role of CO_2 retention in determining transport properties. Finally, while acetonitrile solutions show formulation- and concentration-dependent conductivity, practical considerations related to Li-metal testing motivate solvent substitution. In this context, HexNH_2–DBU CO_2BOL solutions in DME display lower conductivity than in ACN, and the addition of 0.5 M LiTFSI results in phase separation, indicating limited compatibility with high salt concentrations. Together, these findings provide insight into the structure–property relationships governing ionic transport in CO_2BOL-based systems and highlight their dynamic thermal response as a key feature to consider for their implementation in electrochemical environments.

IV. EXPERIMENTAL

A. Materials

Carbon dioxide N50 (≥ 99.999 %) was supplied by Air Liquide. 1-Butanol (99 %), 1-hexanol (anhydrous, ≥ 99 %), as well as deuterated chloroform (0.03 vol% TMS, deuteration degree min. 99.8% for NMR spectroscopy, stabilised with silver) were purchased from Sigma-Aldrich. Butylamine (for pharma synthesis, non GMP) was supplied by Merck. Hexylamine (99%) and 1,8-diazabicyclo[5.4.0]undec-7-ene (DBU, 98+ %) were purchased from Thermoscientific. 1,5,7-Triazabicyclo[4.4.0]dec-5-ene (TBD) was supplied by Apollo Scientific. Lithium bis(trifluoromethanesulfonyl)imide (LiTFSI) was purchased from BLDPharm while acetonitrile (ACN) and 1,2-dimethoxyethane (DME, > 99.0 %) were supplied by VWR and TCI, respectively. All reagents were used as received. Glass fibre separators (diameter, ϕ = 1.58 cm; thickness, t = 0.020 cm), stainless–steel electrodes (ϕ = 1.58 cm; t = 0.010 cm), and CR2032 coin cells were purchased from Xiamen TOB New Energy Technology Co., Ltd.

B. Procedures

CO_2BOL synthesis

A Schlenk tube, equipped with a septum and a stir bar, is charged with an equimolar mixture of a primary alcohol (1-butanol or 1-hexanol) or amine (1-butylamine or 1-hexylamine) and a base (DBU, TBD, or the amine itself) in bulk. A butyl pipe is used to link the Schlenk tube to a Schlenk line. This Schlenk line is used to first put the reaction mixture under vacuum, then under a carbon dioxide atmosphere (pCO_2 = 0.2 bar). In the case of the DBU-based CO_2BALs the reaction is performed at room temperature (21 °C). For the other CO_2BOLs, the reaction is carried out at 60°C for butylamine-based CO_2BAMs (b.p. butylamine = 78 °C) or 90 °C for all other samples in an oil bath and under maximum stirring for 3 hours.

- $ButOCO_2^-$, $DBU.H^+$: ^1H NMR (500 MHz, $CDCl_3$) : δ (ppm) = 3.91 (t, 2H), 3.42 (m, 6H), 2.73 (br. s, 2H), 1.96 (quint, 2H), 1.72 (br. s, 4H), 1.66 (br. s, 2H), 1.56 (m, 2H), 1.38 (m, 2H), 0.91 (t, 3H).

- $HexOCO_2^-$, $DBU.H^+$: ^1H NMR (500 MHz, $CDCl_3$) : δ (ppm) = 3.90 (t, 2H), 3.37 (m, 6H), 2.63 (br. s, 2H), 1.91 (quint, 2H), 1.70 (br. s, 4H), 1.64 (br. s, 2H), 1.59 (m, 2H), 1.36 (m, 2H), 1.30 (m, 4H), 0.91 (t, 3H).

- $ButNHCO_2^-$, $DBU.H^+$: ^1H NMR (500 MHz, $CDCl_3$) : δ (ppm) = 3.45 (m, 6H), 3.11 (t, 2H), 2.84 (br. s, 2H), 1.98 (quint, 2H), 1.75 (br. s, 4H), 1.67 (br. s, 2H), 1.45 (quint, 2H), 1.35 (sx, 2H), 0.90 (t, 3H).

- $HexNHCO_2^-$, $DBU.H^+$: ^1H NMR (500 MHz, $CDCl_3$) : δ (ppm) = 3.41 (m, 6H), 3.11 (t, 2H), 2.82 (br. s, 2H), 1.97 (quint, 2H), 1.74 (br. s, 4H), 1.67 (br. s, 2H), 1.46 (quint, 2H), 1.28 (m, 6H), 0.90 (t, 3H).
- $ButOCO_2^-$, $TBD.H^+$: ^1H NMR (500 MHz, $CDCl_3$) : δ (ppm) = 3.91 (t, 2H), 3.29 (m, 8H), 1.99 (quint, 4H), 1.59 (quint, 2H), 1.40 (sx, 2H), 0.91 (t, 3H).
- $HexOCO_2^-$, $TBD.H^+$: ^1H NMR (500 MHz, $CDCl_3$) : δ (ppm) = 3.90 (t, 2H), 3.31 (m, 8H), 1.99 (quint, 4H), 1.60 (m, 2H), 1.38 (m, 2H), 1.29 (m, 4H), 0.87 (t, 3H).
- $ButNHCO_2^-$, $TBD.H^+$: ^1H NMR (500 MHz, $CDCl_3$) : δ (ppm) = 3.29 (m, 8H), 3.10 (t, 2H), 1.96 (quint, 2H), 1.45 (quint, 2H), 1.35 (sx, 2H), 0.90 (t, 3H).
- $HexNHCO_2^-$, $TBD.H^+$: ^1H NMR (500 MHz, $CDCl_3$) : δ (ppm) = 3.30 (m, 8H), 3.11 (t, 2H), 1.96 (quint, 2H), 1.46 (quint, 2H), 1.28 (m, 6H), 0.87 (t, 3H).
- $ButNHCO_2^-$, $ButNH_3^+$: ^1H NMR (500 MHz, $CDCl_3$) : δ (ppm) = 3.05 (t, 2H), 2.74 (t, 2H), 1.55 (quint, 2H), 1.42 (quint, 2H), 1.35 (sx, 4H), 0.92 (t, 6H).
- $HexNHCO_2^-$, $HexNH_3^+$: ^1H NMR (500 MHz, $CDCl_3$) : δ (ppm) = 3.03 (t, 2H), 2.73 (t, 2H), 1.57 (quint, 2H), 1.42 (quint, 2H) 1.28 (m, 12H), 0.88 (t, 6H).

Preparation of samples for ionic conductivity measurements

- **Neat samples**

All procedures were carried out in an argon-filled glovebox. An aliquot of the electrolyte (60 µL) was dispensed onto a glass-fibre separator (diameter, 1.58 cm) and allowed to fully wet the separator. The wetted separator was then sandwiched between two stainless-steel (SS) blocking electrodes to assemble a symmetric cell (SS | electrolyte | SS). The cell was crimped in CR2032 coin cells under a uniaxial pressure of 75 $kgf.cm^{-2}$ (≈ 7.35 MPa) and equilibrated for 12 h prior to impedance measurements.

- **ACN–based solutions**

ACN–based electrolyte solutions were prepared by dissolving the sample in acetonitrile (ACN, 1.0 mL) under vigorous stirring for 2 h to obtain a homogeneous solution. Two concentrations were investigated by varying the sample mass while keeping the ACN volume fixed at 1.0 mL, namely 100 $mg.mL^{-1}$ (100 mg in 1.0 mL) and 200 $mg.mL^{-1}$ (200 mg in 1.0 mL).

The ionic conductivity cells were assembled following the same procedure as described for the neat samples. Briefly, 60 µL of the solution were dispensed onto a glass–fibre separator (diameter = 1.58 cm), sandwiched between two SS blocking electrodes (SS | electrolyte | SS), and assembled into a CR2032 coin cell under 75 $kgf.cm^{-2}$. The sealed cells were rested for 12 h prior to ionic conductivity measurements.

Thermal treatment and aging protocols

- **Open vials**

For open-vial thermal treatment, neat samples were placed in vials with the caps removed and heated in an oven at 70 °C (typically 15–60 h, as indicated for each experiment). After heating, samples were cooled down to room temperature before cell assembly and electrochemical measurements. When relevant, mass loss (%) was calculated as $[(m_0-m_t)/m_0]\times100$, where m_0 is the initial mass and m_t is the mass after heating.

- **Sealed vials**

For sealed-vial thermal treatment, a defined mass of neat sample was loaded into a vial, tightly sealed, and heated at 70 °C for 15 h. After heating, the vial was cooled to room temperature and the sample mass and appearance were recorded. The electrolyte cell was then assembled and measured following the procedure previously described.

- **Coin cell aging**

For coin-cell aging, CR2032 symmetric cells (SS | electrolyte | SS) assembled as described previously were stored at 70 °C. Electrochemical impedance spectroscopy was collected *in situ* at 70 °C at defined aging times (0, 2, 4, 6, 15, 18, 96, and 108 h) to track impedance evolution.

C. Methods

Nuclear Magnetic Resonance (NMR) spectroscopy

CO_2BOLs were all characterised by ^{1}H NMR using a Bruker AVANCEII 500 MHz apparatus at room temperature in chloroform-d_1 ($CDCl_3$). All spectra were acquired according to the following parameters: aq = 2.75 sec, d1 = 1 sec, sw = 20, ns = 32.

Thermogravimetric analysis (TGA)

The CO_2BOLs were subjected to thermogravimetric analysis to determine their degradation onset temperatures. Measurements were performed under nitrogen flow at a rate of 5 °C per minute using a TA Q500 TGA.

Electrochemical measurement

- **Electrochemical impedance spectroscopy (EIS)**

Electrochemical impedance spectroscopy (EIS) was performed using a Bio–Logic VMP–300 potentiostat/impedance analyser. Impedance spectra were recorded over a frequency range of 7 MHz to 10 mHz with an AC amplitude of 30 mV. Temperature–dependent measurements were

conducted at 20, 25, 30, 40, 50, and 60 °C, and the cell was equilibrated for 1 h at each temperature prior to data acquisition.[49,50]

The bulk resistance (R_b) was determined from the high-frequency intercept of the Nyquist plot on the real axis (Z'). Ionic conductivity (σ, S cm^{-1}) was calculated from the separator thickness and the effective electrode area as described below (**Eq. A.3**).[49]

$$\sigma = \frac{L}{R_b \cdot A} \qquad \textit{Eq. A.3}$$

where L is the electrolyte thickness (taken as the nominal thickness of the glass–fibre separator, $t = 0.020$ cm) and A is the effective electrode area defined by the stainless–steel electrode diameter ($\varphi = 1.58$ cm). For each sample, three independent cells were assembled and measured; the reported conductivity values are the average of three measurements (n = 3) unless otherwise stated.

- **Activation energy**

The apparent activation energy for ionic conduction was estimated from the temperature-dependent conductivity using an Arrhenius-type analysis. Specifically, ln(σT) was fitted as a linear function of reciprocal temperature over the 20 to 60 °C range to extract the slope, from which the apparent activation energy was calculated.[43]

$$\sigma T = \sigma_0 \exp\left(-\frac{E_a}{RT}\right) \qquad \textit{Eq. A.4}$$

Here, T is the absolute temperature (K) and R is the gas constant. When 1000/T is used as the x-axis, the corresponding conversion factor is included in the activation-energy calculation to ensure consistency of units.

$$\ln(\sigma T) = \ln(\sigma_0) - \frac{E_a}{R} \cdot \frac{1}{T} \qquad \textit{Eq. A.5}$$

The resulting apparent activation energies are reported in **Table A.2**. Samples that are solid at 25 °C could not be evaluated in the neat state; these entries are reported as N/A.

- **Linear sweep voltammetry**

Linear sweep voltammetry (LSV) was conducted in a Li | electrolyte | stainless-steel (SS) cell at 25 °C. The potential was swept from the open-circuit voltage (OCV) to 6.0 V at a scan rate of 0.1 $mV.s^{-1}$.

V. SUPPORTING INFORMATION

Table SA.1. Sample nomenclature and physical state at 25 °C.

Short code	Physical state at 25 °C	Short code	Physical state at 25 °C
ButOH–DBU	viscous liquid	ButOH–DBU–free	liquid
HexOH–DBU	viscous liquid	HexOH–DBU–free	liquid
$ButNH_2$–DBU	viscous liquid	$ButNH_2$–DBU–free	liquid
$HexNH_2$–DBU	viscous liquid	$HexNH_2$–DBU–free	liquid
ButOH–TBD	viscous liquid	ButOH–TBD–free	liquid
HexOH–TBD	viscous liquid	HexOH–TBD–free	liquid
$ButNH_2$–TBD	solid powder	$ButNH_2$–TBD–free	liquid
$HexNH_2$–TBD	solid powder	$HexNH_2$–TBD–free	liquid
$ButNH_2$	solid powder	$ButNH_2$–free	liquid
$HexNH_2$	solid powder	$HexNH_2$–free	liquid

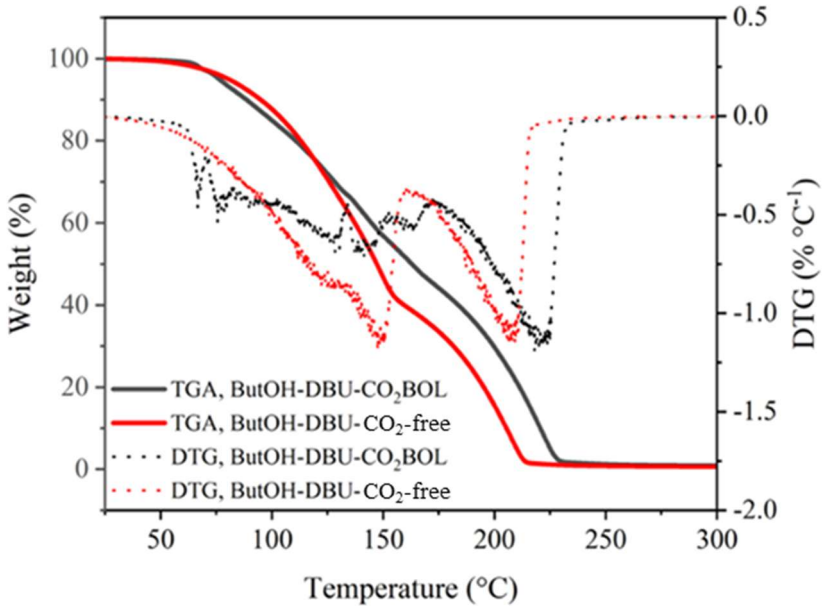


Figure SA.1. TGA of the ButOH-DBU CO_2BOL and the CO_2-free mixture.

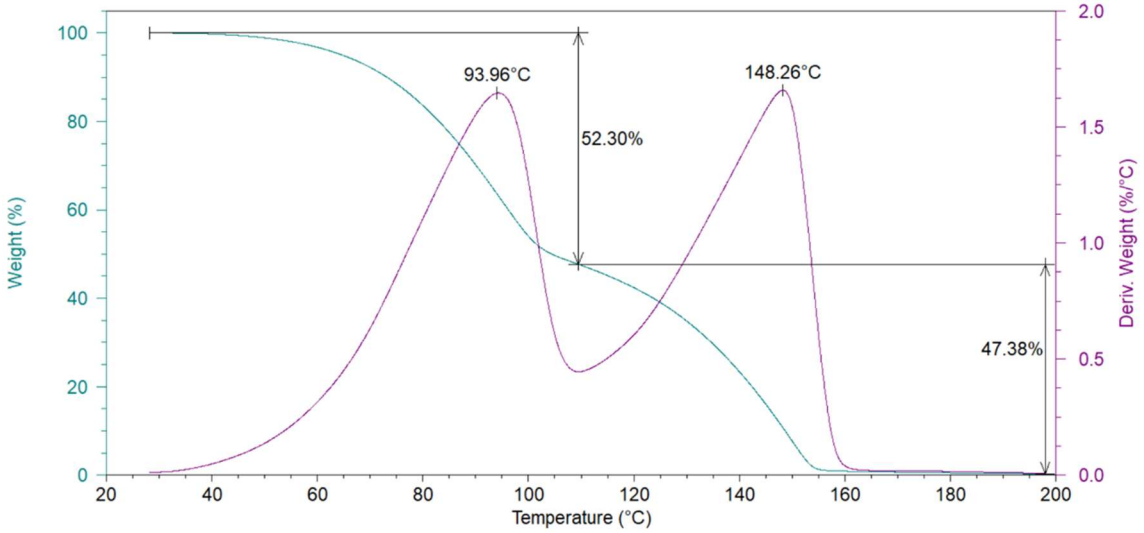


Figure SA.2. TGA of the HexNH$_2$-DBU CO$_2$BAM.

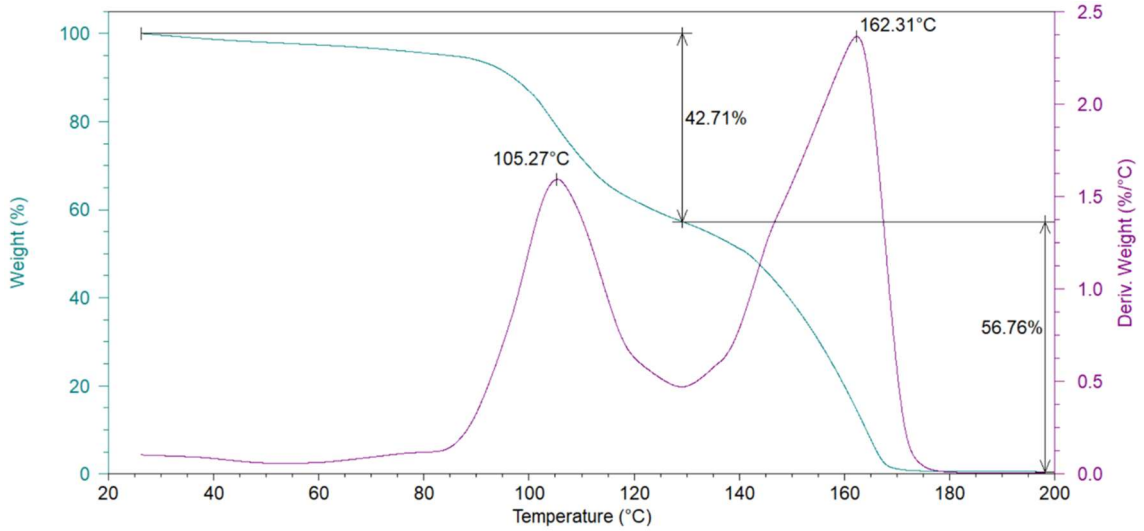


Figure SA.3. TGA of the ButOH-TBD CO$_2$BAL.

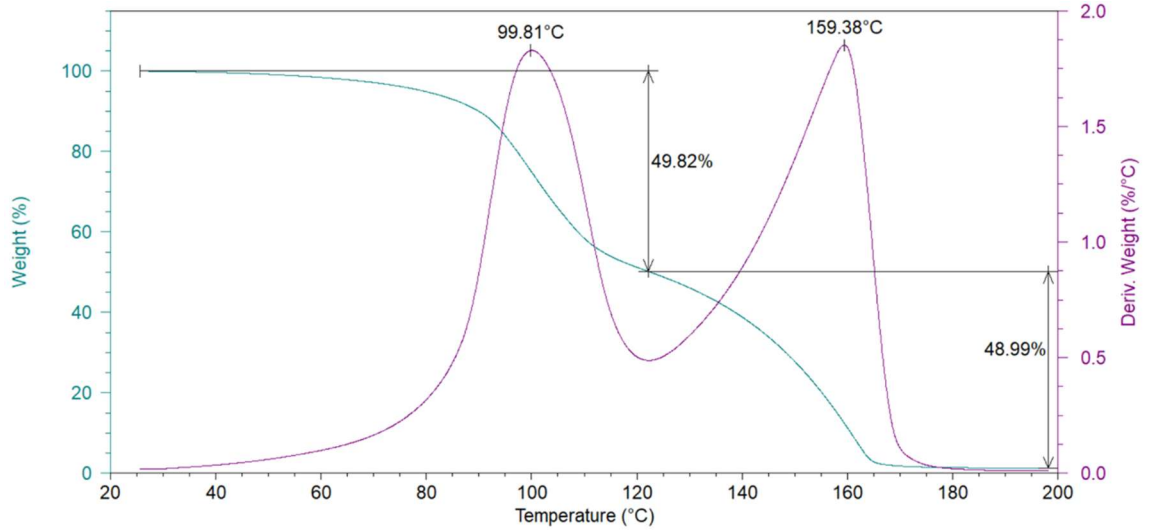


Figure SA.4. TGA of the HexOH-TBD CO$_2$BAL.

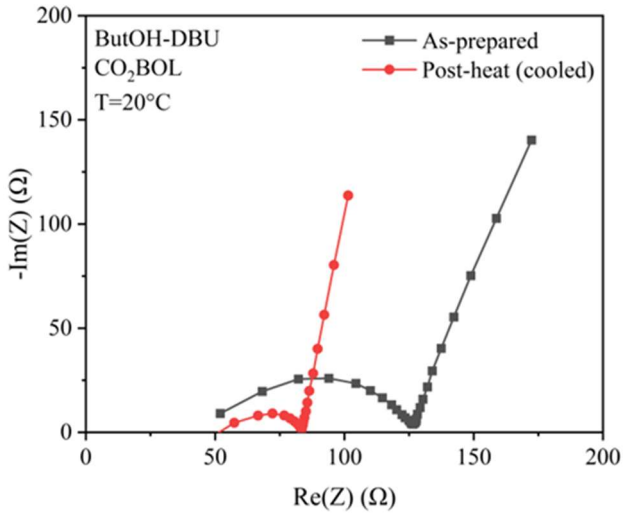


Figure SA.5. Nyquist plots of ButOH-DBU CO_2BOL neat system measured at 20 °C before heating (as-prepared) and after sealed thermal treatment at 70 °C followed by cooling (post-heat (cooled)).

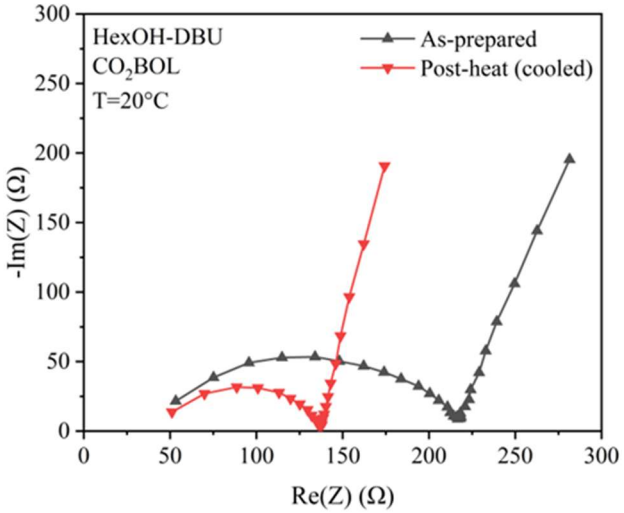


Figure SA.6. Nyquist plots of HexOH-DBU CO_2BOL neat system measured at 20 °C before heating (as-prepared) and after sealed thermal treatment at 70 °C followed by cooling (post-heat (cooled)).

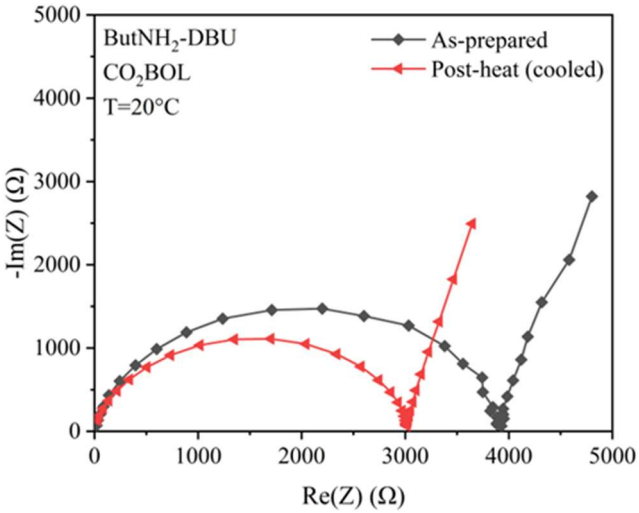


Figure SA.7. Nyquist plots of ButnH_2-DBU CO_2BOL neat system measured at 20 °C before heating (as-prepared) and after sealed thermal treatment at 70 °C followed by cooling (post-heat (cooled)).

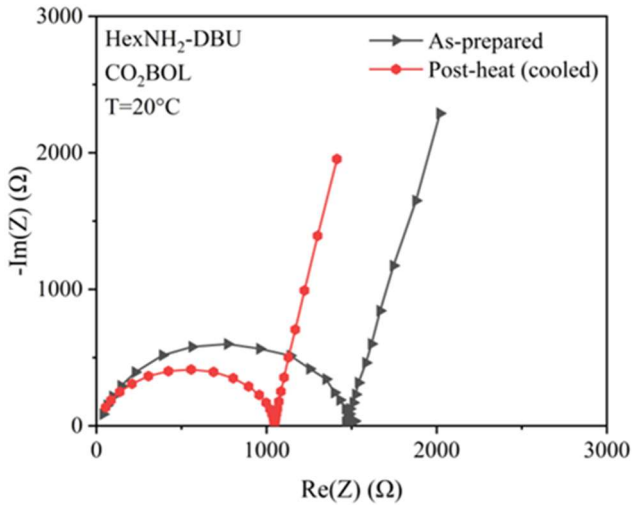


Figure SA.8. Nyquist plots of HexNH$_2$-DBU CO_2BOL neat system measured at 20 °C before heating (as-prepared) and after sealed thermal treatment at 70 °C followed by cooling (post-heat (cooled)).

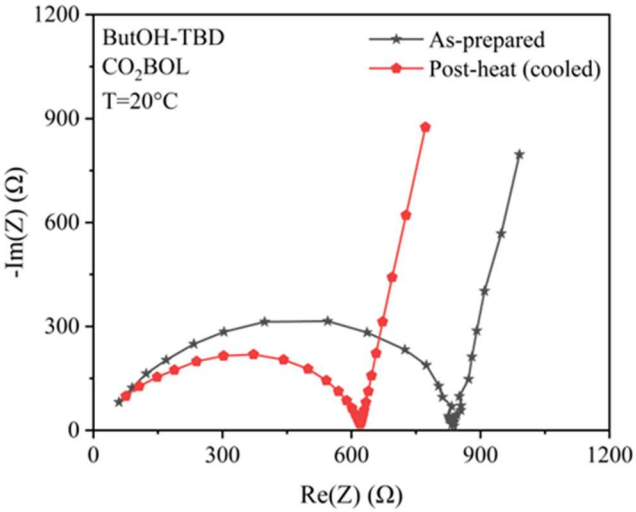


Figure SA.9. Nyquist plots of ButOH-TBD CO_2BOL neat system measured at 20 °C before heating (as-prepared) and after sealed thermal treatment at 70 °C followed by cooling (post-heat (cooled)).

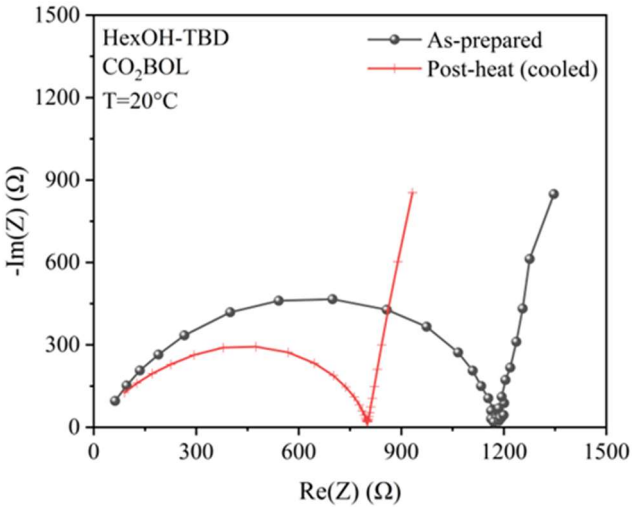


Figure SA.10. Nyquist plots of HexOH-TBD CO_2BOL neat system measured at 20 °C before heating (as-prepared) and after sealed thermal treatment at 70 °C followed by cooling (post-heat (cooled)).

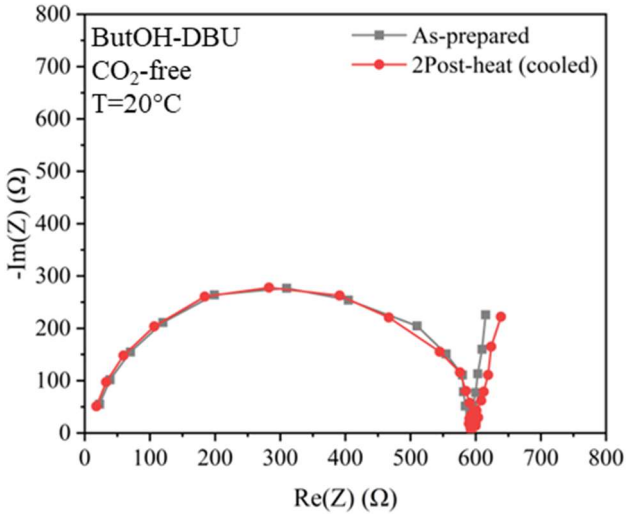


Figure SA.11. Nyquist plots of ButOH-DBU CO_2-free neat systems measured at 20 °C before heating (as-prepared) and after sealed thermal treatment at 70 °C followed by cooling (post-heat (cooled)).

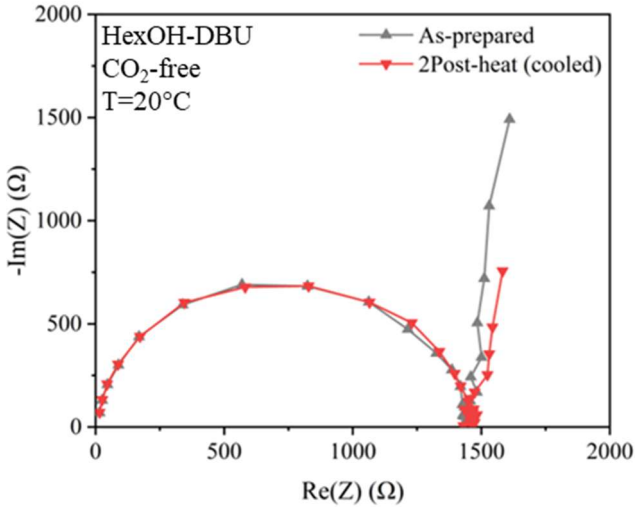


Figure SA.12. Nyquist plots of HexOH-DBU CO_2-free neat systems measured at 20 °C before heating (as-prepared) and after sealed thermal treatment at 70 °C followed by cooling (post-heat (cooled)).

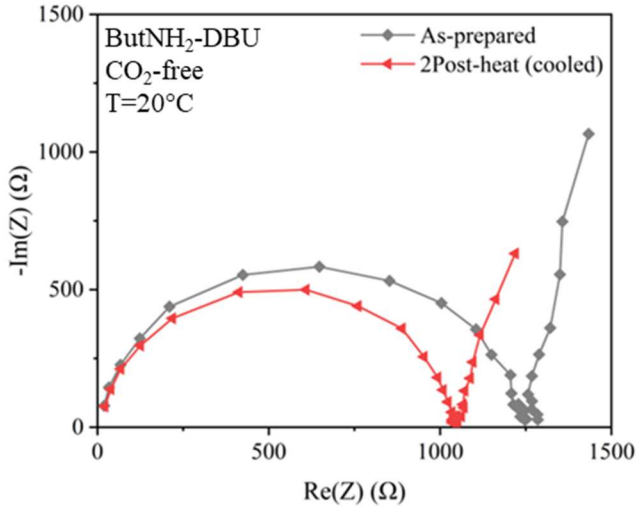


Figure SA.13. Nyquist plots of ButNH$_2$-DBU CO_2-free neat systems measured at 20 °C before heating (as-prepared) and after sealed thermal treatment at 70 °C followed by cooling (post-heat (cooled)).

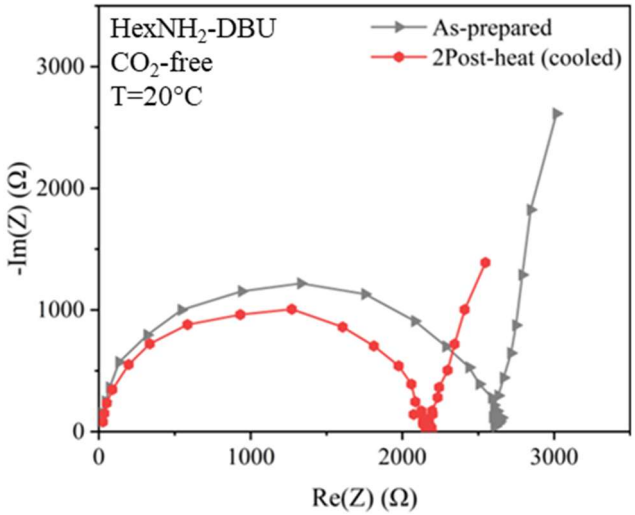


Figure SA.14. Nyquist plots of $HexNH_2$-DBU CO_2-free neat systems measured at 20 °C before heating (as-prepared) and after sealed thermal treatment at 70 °C followed by cooling (post-heat (cooled)).

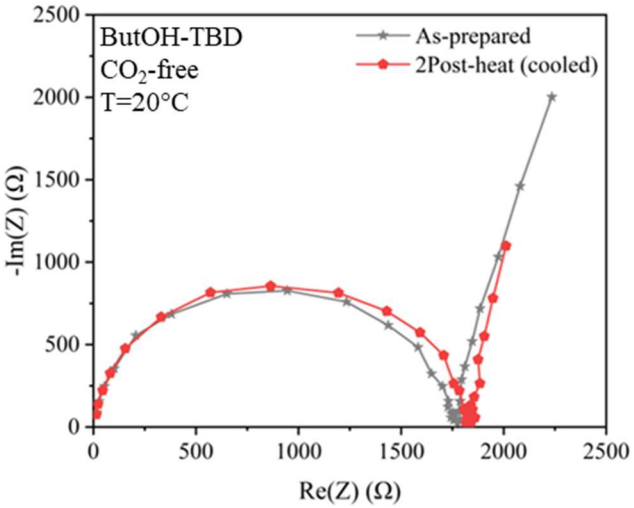


Figure SA.15. Nyquist plots of ButOH-TBD CO_2-free neat systems measured at 20 °C before heating (as-prepared) and after sealed thermal treatment at 70 °C followed by cooling (post-heat (cooled)).

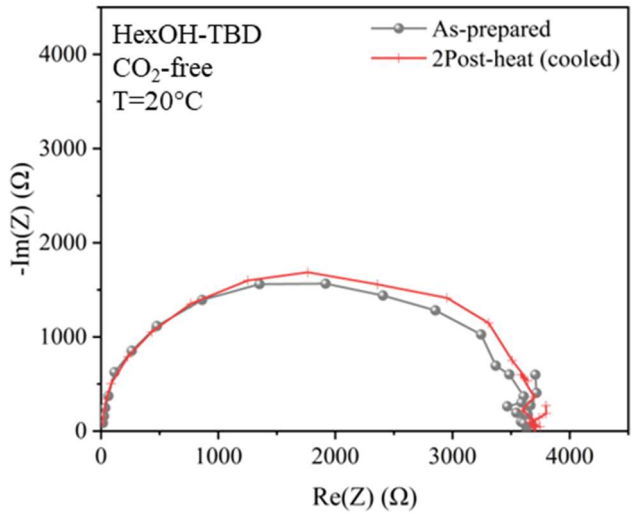


Figure SA.16. Nyquist plots of HexOH-TBD CO_2-free neat systems measured at 20 °C before heating (as-prepared) and after sealed thermal treatment at 70 °C followed by cooling (post-heat (cooled)).

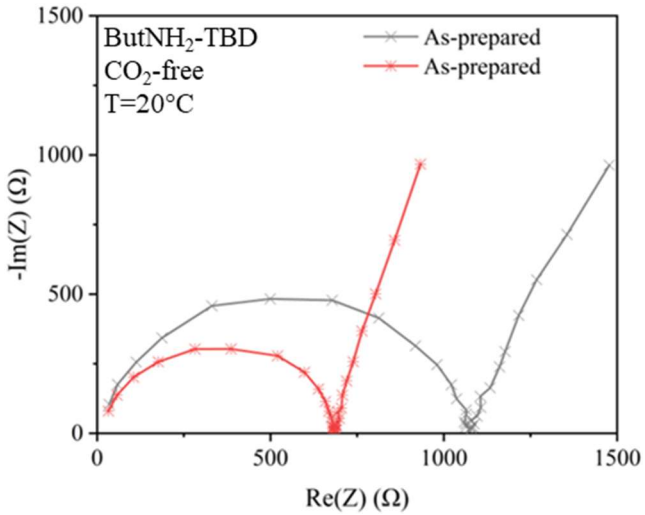


Figure SA.17. Nyquist plots of $ButNH_2$-TBD CO_2-free neat systems measured at 20 °C before heating (as-prepared) and after sealed thermal treatment at 70 °C followed by cooling (post-heat (cooled)).

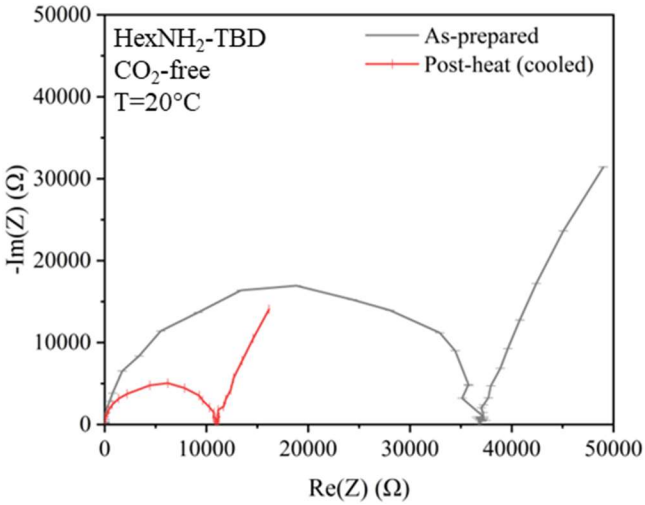


Figure SA.18. Nyquist plots of $HexNH_2$-TBD CO_2-free neat systems measured at 20 °C before heating (as-prepared) and after sealed thermal treatment at 70 °C followed by cooling (post-heat (cooled)).

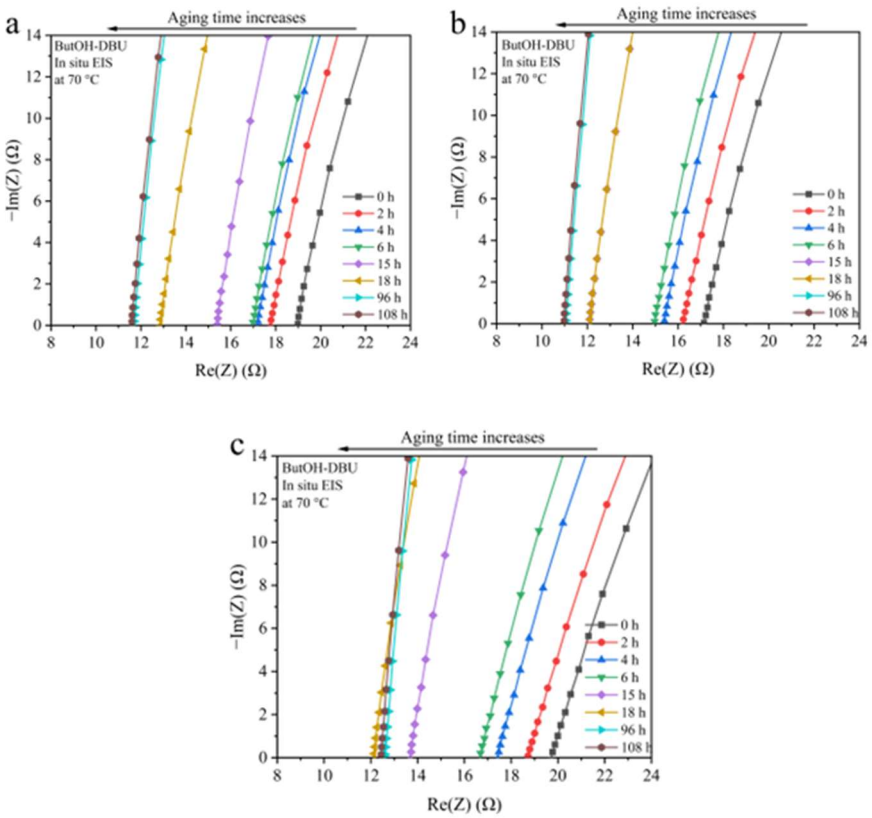


Figure SA.19. *In situ* impedance evolution during coin-cell aging at 70 °C for ButOH–DBU in three independently assembled cells. Arrow indicates increasing aging time.

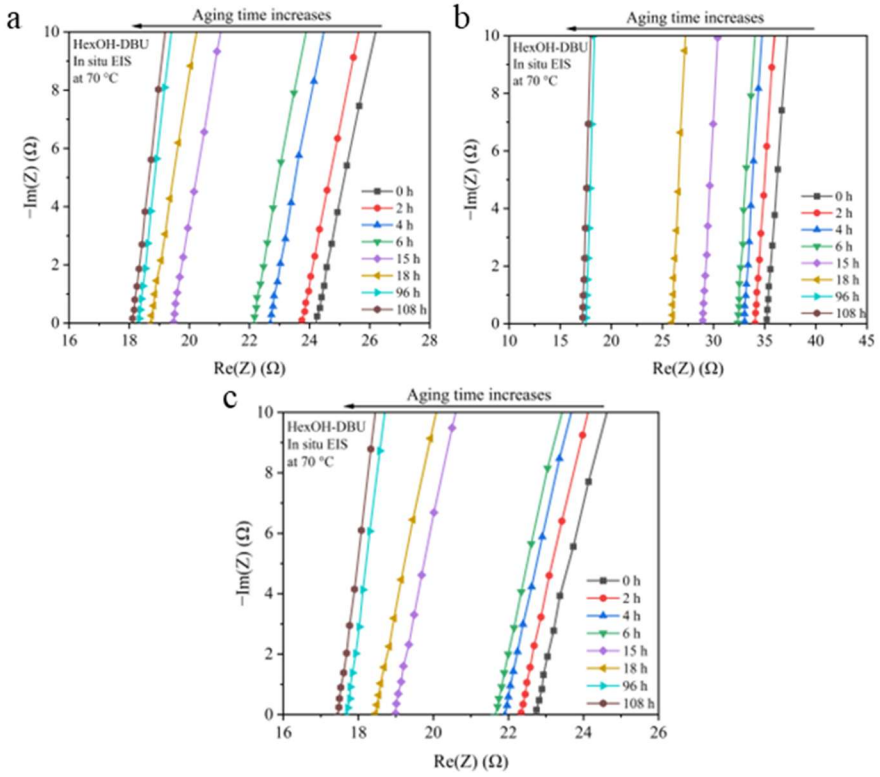


Figure SA.20. *In situ* impedance evolution during coin-cell aging at 70 °C cells for HexOH–DBU in three independently assembled. Arrow indicates increasing aging time.

VI. REFERENCES

1 *Emissions Gap Report 2024: No more hot air ... please!*, United Nations Environment Programme, 2024.

2 S. Chowdhury, Y. Kumar, S. Shrivastava, S. K. Patel and J. S. Sangwai, *Energy Fuels*, 2023, **37**, 10733–10757.

3 M. H. Islam and S. R. Patlolla, *Energies*, 2025, **18**, 3937.

4 W. Gao, S. Liang, R. Wang, Q. Jiang, Y. Zhang, Q. Zheng, B. Xie, C. Y. Toe, X. Zhu, J. Wang, L. Huang, Y. Gao, Z. Wang, C. Jo, Q. Wang, L. Wang, Y. Liu, B. Louis, J. Scott, A.-C. Roger, R. Amal, H. He and S.-E. Park, *Chem. Soc. Rev.*, 2020, **49**, 8584–8686.

5 I. Ghiat and T. Al-Ansari, *Journal of CO_2 Utilization*, 2021, **45**, 101432.

6 C. B. Peres, P. M. R. Resende, L. J. R. Nunes and L. C. D. Morais, *Clean Technol.*, 2022, **4**, 1193–1207.

7 M. Ç. Öztürk, C. S. Ume and E. Alper, *Chem. Eng. & Technol.*, 2012, **35**, 2093–2098.

8 D. J. Heldebrant, P. G. Jessop, C. A. Thomas, C. A. Eckert and C. L. Liotta, *J. Org. Chem.*, 2005, **70**, 5335–5338.

9 D. J. Heldebrant, C. R. Yonker, P. G. Jessop and L. Phan, *Energy Environ. Sci.*, 2008, **1**, 487–493.

10 D. J. Heldebrant, C. R. Yonker, P. G. Jessop and L. Phan, *Energy Procedia*, 2009, **1**, 1187–1195.

11 D. J. Heldebrant, P. K. Koech, M. T. C. Ang, C. Liang, J. E. Rainbolt, C. R. Yonker and P. G. Jessop, *Green Chem.*, 2010, **12**, 713–721.

12 S. G. Khokarale and J.-P. Mikkola, *RSC Adv.*, 2019, **9**, 34023–34031.

13 J. L. Hedrick, V. Piunova, N. H. Park, T. Erdmann and P. L. Arrechea, *ACS Macro Lett.*, 2022, **11**, 368–375.

14 T. M. McGuire, E. M. López-Vidal, G. L. Gregory and A. Buchard, *Journal of CO_2 Utilization*, 2018, **27**, 283–288.

15 G. L. Gregory, M. Ulmann and A. Buchard, *RSC Adv.*, 2015, **5**, 39404–39408.

16 J. Delcorps, K. S. Rawat, M. Wells, E. Ben Ayed, B. Grignard, C. Detrembleur, B. Blankert, P. Gerbaux, V. Van Speybroeck and O. Coulembier, *Cell Reports Physical Science*, 2024, **5**, 102057.

17 G. L. Gregory, L. M. Jenisch, B. Charles, G. Kociok-Köhn and A. Buchard, *Macromolecules*, 2016, **49**, 7165–7169.

18 G. L. Gregory, E. M. Hierons, G. Kociok-Köhn, R. I. Sharma and A. Buchard, *Polym. Chem.*, 2017, **8**, 1714–1721.

19 J. Delcorps, E. Ben Ayed and O. Coulembier, *Polym. Chem.*, 2025, **16**, 2923–2932.

20 J. Delcorps, E. Ben Ayed and O. Coulembier, *RSC Adv.*, 2026, **16**, 12798–12805.

21 W. D. McGhee, D. P. Riley, M. E. Christ and K. M. Christ, *Organometallics*, 1993, **12**, 1429–1433.

22 W. McGhee, D. Riley, K. Christ, Y. Pan and B. Parnas, *J. Org. Chem.*, 1995, **60**, 2820–2830.

23 J. K. Mannisto, L. Pavlovic, T. Tiainen, M. Nieger, A. Sahari, K. H. Hopmann and T. Repo, *Catal. Sci. Technol.*, 2021, **11**, 6877–6886.

24 K. Stagel, L. Ielo and K. Bica-Schröder, *ACS Omega*, 2023, **8**, 48444–48450.

25 G. F. Versteeg, L. A. J. Van Dijck and W. P. M. Van Swaaij, *Chemical Engineering Communications*, 1996, **144**, 113–158.

26 P. V. Kortunov, M. Siskin, L. S. Baugh and D. C. Calabro, *Energy Fuels*, 2015, **29**, 5919–5939.

27 N. McCann, D. Phan, X. Wang, W. Conway, R. Burns, M. Attalla, G. Puxty and M. Maeder, *J. Phys. Chem. A*, 2009, **113**, 5022–5029.

28 M. Costa, G. P. Chiusoli and M. Rizzardi, *Chem. Commun.*, 1996, 1699.

29 G. Lu, S. Farrukh and X. Fan, *Fuel*, 2025, **391**, 134740.

30 M. Armand, F. Endres, D. R. MacFarlane, H. Ohno and B. Scrosati, *Nature Mater.*, 2009, **8**, 621–629.

31 M. Watanabe, M. L. Thomas, S. Zhang, K. Ueno, T. Yasuda and K. Dokko, *Chem. Rev.*, 2017, **117**, 7190–7239.

32 D. R. MacFarlane, M. Forsyth, P. C. Howlett, M. Kar, S. Passerini, J. M. Pringle, H. Ohno, M. Watanabe, F. Yan, W. Zheng, S. Zhang and J. Zhang, *Nat. Rev. Mater.*, 2016, **1**, 15005.

33 A. Lewandowski and A. Świderska-Mocek, *Journal of Power Sources*, 2009, **194**, 601–609.

34 C. Locati, U. Lafont, C. J. Peters and E. M. Kelder, *Journal of Power Sources*, 2009, **189**, 454–457.

35 P. Liu, L. Yang, B. Xiao, H. Wang, L. Li, S. Ye, Y. Li, X. Ren, X. Ouyang, J. Hu, F. Pan, Q. Zhang and J. Liu, *Adv. Funct. Materials*, 2022, **32**, 2208586.

36 J. Zou, D. Gupta, J. A. Yuwono, S. Zhang and Z. Guo, *Nat. Rev. Clean Technol.*, 2025, **1**, 699–718.

37 C. J. Fetrow, C. Carugati, X.-D. Zhou and S. Wei, *Energy Storage Materials*, 2022, **45**, 911–933.

38 B. He, Y. Ge, F. Zhang, H. Tian, Y. Xin, Y. Lei and Y. Yang, *Nano-Micro Lett.*, 2025, **17**, 299.

39 A. Khurram, M. He and B. M. Gallant, *Joule*, 2018, **2**, 2649–2666.

40 L. Phan, D. Chiu, D. J. Heldebrant, H. Huttenhower, E. John, X. Li, P. Pollet, R. Wang, C. A. Eckert, C. L. Liotta and P. G. Jessop, *Ind. Eng. Chem. Res.*, 2008, **47**, 539–545.

41 T. L. Greaves and C. J. Drummond, *Chem. Rev.*, 2015, **115**, 11379–11448.

42 T. L. Greaves and C. J. Drummond, *Chem. Rev.*, 2008, **108**, 206–237.

43 G. G. Cameron, M. D. Ingram and J. L. Harvie, *Faraday Discuss. Chem. Soc.*, 1989, **88**, 55.

44 A. Pinkert, K. L. Ang, K. N. Marsh and S. Pang, *Phys. Chem. Chem. Phys.*, 2011, **13**, 5136.

45 K. Yasui and K. Hamamoto, *Materials*, 2024, **17**, 5134.

46 N. Xin, Y. Sun, M. He, C. J. Radke and J. M. Prausnitz, *Fluid Phase Equilibria*, 2018, **461**, 1–7.

47 V. Nilsson, R. Younesi, D. Brandell, K. Edström and P. Johansson, *Journal of Power Sources*, 2018, **384**, 334–341.

48 E. Park, J. Park, K. Lee, Y. Zhao, T. Zhou, G. Park, M.-G. Jeong, M. Choi, D.-J. Yoo, H.-G. Jung, A. Coskun and J. W. Choi, *ACS Energy Lett.*, 2023, **8**, 179–188.

49 P. Vadhva, J. Hu, M. J. Johnson, R. Stocker, M. Braglia, D. J. L. Brett and A. J. E. Rettie, *ChemElectroChem*, 2021, **8**, 1930–1947.

50 J. A. Isaac, L. R. Mangani, D. Devaux and R. Bouchet, *ACS Appl. Mater. Interfaces*, 2022, **14**, 13158–13168.